Convergent-Beam Electron Diffraction IV

by

Michiyoshi Tanaka
Masami Terauchi
Kenji Tsuda
Koh Saitoh

JEOL

Convergent-Beam Electron Diffraction IV

by

Michiyoshi Tanaka
Masami Terauchi
Kenji Tsuda
Koh Saitoh

Research Institute for
Scientific Measurements

Institute of Multidisciplinary
Research for Advanced Materials

Tohoku University

JEOL LTD.

Published by JEOL Ltd.
1-2, Musashino 3-chome, Akishima, Tokyo 196-8558, Japan

Printed in Japan

Contents

Preface

The convergent-beam electron diffraction (CBED) method has entirely obtained the citizenship in the electron microscope world and has grown to be a very important technique among the analytical methods for materials. In its period of growth, Professor A. Eades used to count every year the number of papers concerning the CBED method. Nowadays the method has appeared in many papers of various fields and become very popular so that counting the number of related papers has lost its meaning. When the large-angle technique which we developed was applied to a microscope study in the early days, the original reference was quoted in every paper, but it is now so popular as to be referred to only as LACBED without quoting the reference. The CBED method is widely used, for example, as a tool for symmetry determination in fundamental materials science and as an effective tool for strain measurements of multi-layers in the applied materials science.

Since 1990, our major target has been to develop a high-precision crystal structure refinement method based on the full dynamical theory of electron diffraction. Thereby, we strongly recognized the necessity of developing an electron microscope which enables the energy filtering of an entire CBED pattern containing both ZOLZ and HOLZ reflections. We manufactured, with JEOL, an electron microscope JEM-2010FEF, which is equipped with a field emission gun, an objective lens with a small Cs and an omega filter. The microscope was developed under the Grant-in-Aid for Specially Promoted Research (No. 06102003) from the Ministry of Education, Science, Sports and Culture of Japan. We this time reached the final volume of our CBED book series. In this volume we exhibit many examples of energy-filtered CBED patterns, which were taken by the JEM-2010FEF microscope. We also include a new space-group determination method which uses the coherent CBED technique, the case studies of crystal structure refinements of CdS, $LaCrO_3$ and h-$BaTiO_3$ including charge density determination, simulations of Kikuchi patterns due to thermal diffuse scattering, recent studies of quasicrystals, interface analysis, which is an important application to device technology, and a future trend of the electron microscope. We add an atlas of CBED symmetries for handy reference and CBED pictures for the reader's enjoyment.

The data shown herein was obtained with the cooperation of successive graduate students of Physics Course, Tohoku University. They include Dr. S. Yamada (Central Research Institute of Electric Power Industry), Mr. S. Fukushima (Foundation for Promotion of Material Science and Technology of Japan), Mr. K. Tanaka (Fujitsu Ltd.), Ms. N. Kanda, Dr. K. Omoto and Dr. T. Yokosawa (Doctor Course of Physics, Tohoku Univ.), Mr. A. Sakamoto (BJ Products Design Center, Canon Inc.), Mr. K. Takagi (VLSI Division, NEC Corporation), Mr. H. Yamamoto (Murata Manufacturing Co., Ltd.), Mr. Y. Ogata (Master Course of Physics, Tohoku Univ.), and Mr. T. Akaogi (Analytical Res. Lab., Asahi Kasei Corporation). Other important data was obtained by the collaboration with Dr. Y. Yan (National Renewable Energy Lab., US) and Dr. U. Kaiser (Inst. for Solid State Physics, Friedrich-Schiller Univ., Germany). The photographs included in this publication were taken mainly with JEOL electron microscopes JEM-2010 and JEM-2010FEF using an imaging plate system.

I express my gratitude to the JEOL Ltd. staff, especially Mr. T. Eto (President), Dr. Y. Harada and Mr. H. Akimoto for promoting and supporting this publication and to Mr. Y. Ishida, Mr. T. Honda and Mr. M. Naruse for their devoted collaboration in instrument development. I wish to thank Mr. F. Sato of our lab for his dedicated maintenance of the JEM-100CX-FEG, JEM-2000FX, JEM-2010 and JEM-2010FEF, and for his highly skilled photography.

Also, without the unstinting help of Mr. T. Handa and Mr. H. Tasaka of JEOL Ltd. in the compilation of the book, and of Mr. K. Takayanagi and Mr. T. Izui of JEOL Technoservice Co., Ltd. in the critical reading of the manuscript, this edition would never have been possible. It is my pleasure to pay tribute also to Mr. T. Kondo of Kyoritsu Printing Co., Ltd. for the excellent printing of this book. Some of the photographs contained herein were reprinted from our papers with the publishers' kind permission.

This work was supported financially by the Grant-in-Aid for Specially Promoted Research (No. 06102003), the Grant-in-Aid for International Scientific Research Program: Joint Research (No. 10044056), the Grant-in-Aid for Co-operative Research (No. 06302022), the Grant-in-Aid for Scientific

Research A (No. 11304020), the Grant-in-Aid for Scientific Research C (Terauchi: No. 10640295) and B (Terauchi: No. 12440079), Grant-in-Aid for Scientific Research on Priority Areas A (Terauchi: No. 11165204) and Grant-in-Aid for the Encouragement of Young Scientists A (Tsuda: No. 10740138 and No. 12740199), from the Ministry of Education, Science, Sports and Culture of Japan.

We, with JEOL, have now started to construct a new electron microscope equipped with a Wien filter monochromator and an omega filter analyzer, which allows us to take not only energy-filtered HREM images and CBED patterns but also electron energy-loss spectra with an energy resolution of better than 0.2eV from a specimen area less than 2nm in diameter, under a project "Development of updated fundamental technology" of Japan Science and Technology Corporation (JST). The performance of the microscope will be reported elsewhere in the future.

Finally, I must thank my wife Kyoko for her strong and long years of support to my dedication to the research life. My tiny contribution to electron microscopy and electron crystallography is attributed to her.

Sendai, Spring 2002

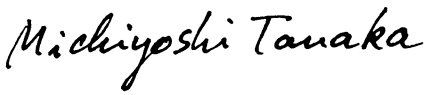

Michiyoshi Tanaka

Introduction

The space-group determination method using dynamical extinction lines cannot distinguish 23 sets of space groups. Most of the indistinguishable sets have 4_2, $3_1(3_2)$ and $6_2(6_4)$ screw axes, which do not produce the extinction lines. There is, however, a practical method of distinguishing a rotation axis and a screw axis. This method is to observe the changes of the intensities of the reflections which can be kinematically forbidden, by tilting the incident beam so that *Umweganregung* paths to the reflections disappear. By this test, each space group of the indistinguishable pairs, for instance $P3$ and $P3_1$, can be distinguished except for the pairs of opposite handedness and the special pairs of ($I23$ and $I2_13$) and ($I222$ and $I2_12_12_1$).

Identifications of the handedness of space groups were reported for quartz by Goodman and Secomb [1] and Goodman and Johnson [2], and for MnSi by Tanaka *et al.* [3]. The senses of the first and second crystal axes of these space groups were determined with the aid of kinematical structure-factor calculations, and the sense of the third crystal axis was determined by dynamical intensity calculations. The special pairs of ($I23$ and $I2_13$) and ($I222$ and $I2_12_12_1$), however, cannot be distinguished by the above methods because these pairs show the same kinematical extinction and no dynamical extinction lines. A method of detecting the phases of the structure factors is needed to distinguish the special pairs.

Coherent CBED, which uses a highly coherent electron source (*i.e.* a field-emission gun), is a method of directly providing phase information on crystal structure factors. The coherent CBED technique produces interference fringes in the overlapping regions of CBED disks. From the relative positions of the fringes, the phase differences between two diffraction waves can be determined. We theoretically clarified that the coherent CBED method can distinguish 12 space-group pairs among the 23 indistinguishable sets by observing the relative arrangements of the 2-fold-rotation or 2_1-screw axis with respect to the principal rotation or screw axes [4], [5], the 12 pairs being composed of a principal rotation or screw axis and of other 2-fold-rotation axes and/or 2_1-screw axes such as ($I222$ and $I2_12_12_1$) and ($P321$ and $P3_121$). The present method provides an effective use of coherent CBED for determination of the crystal symmetry. The experimental proof should be done in the future.

We proposed a full-dynamical method to refine crystal structure parameters (atom positions and Debye-Waller factors) in a nanometer-size area using higher-order Laue zone (HOLZ) reflections of CBED patterns for the first time (Tsuda and Tanaka [6], Tanaka *et al.* [7]). The use of HOLZ reflections is essential for the refinement method because small displacements of atoms are sensitively detected using reflections with large reciprocal vectors. Energy filtering to remove inelastically scattered background is now becoming indispensable for quantitative analysis of CBED patterns. Measurements of low-order structure factors were successfully conducted using energy-filtered CBED patterns by several researchers. The energy-filtered data was obtained using a serial electron energy-loss spectrometer and a scanning unit (Zuo *et al.*, [8]; Tanaka *et al.*, [7]; Saunders *et al.*, [9]), an omega (Ω)-filter (Deininger *et al.*, [10]; Zuo *et al.*, [11]) or using a post-column filter (Saunders *et al.*, [12]). All these instruments are limited to detect diffraction intensities at small scattering angles. Thus, these cannot be applied to our method which uses the intensities of HOLZ reflections at high scattering angles. An energy filter with a high acceptance angle is needed for our method. The distortion of the CBED patterns due to aberrations of the lenses and the energy filter is appreciable for HOLZ reflections in the existing microscopes, though they are disregarded for zeroth-order Laue zone (ZOLZ) reflections at small scattering angles. Small distortion is important for the accurate fitting of HOLZ reflection intensities. For these purposes, we developed a new Ω-filter electron microscope, which can take energy-filtered CBED patterns covering high angles of about up to 10 degrees with small distortions (Tsuno *et al.*, [13]; Tanaka *et al.*, [14]).

The microscope is designed not only to take such energy-filtered CBED patterns but also to achieve the highest performance in high-resolution imaging, element mapping, energy-dispersive X-ray analysis, etc. The microscope was constructed by introducing advanced technologies such as systems for remote control, image observation using high-definition TV, active vibration cancellation and digital image recording. The microscope was manufactured by JEOL as the JEM-2010FEF, based on the JEM-2010F already on the market. We shortly describe the design and performance of the JEM-2010FEF and display various examples of CBED patterns to show the effectiveness of energy filtering.

We have extended our method for refining crystal structural parameters using convergent-beam electron diffraction so as to fit the theoretical calculations with the experimental intensities of energy-filtered two-dimensional ZOLZ and HOLZ CBED patterns [15]. For this purpose, a JEM-2010FEF has been fully used. We have developed an analysis program (MBFIT) to refine positional parameters, Debye-Waller factors and low-order structure factors. It is based on many-beam Bloch-wave calculations and nonlinear least-squares fitting. First, we refined the positional parameter of sulfur and the isotropic and anisotropic Debye-Waller factors of a noncentrosynmetric crystal of CdS. Then, we refined the positional parameter of oxygen atoms and anisotropic Debye-Waller factors of all atoms of the high-temperature phase of $LaCrO_3$. Clear anisotropy of thermal vibration of the oxygen atoms was obtained for the first time. We have further made a similar refinement for the intermediate phase of hexagonal $BaTiO_3$.

Charge ordering and orbital ordering in perovskite and related materials are topics concerning the research of the colossal magneto-resistance materials and the high T_c superconductors. For such studies, the accurate measurement of the charge density is essential. It has long been performed by X-ray diffraction using single and powder crystals. The CBED method can be applied to the determination of charge density distribution, because together with the atom positions and Debye-Waller factors, the low-order Fourier coefficients of the electrostatic potential (low-order crystal structure factors for electron diffraction), which are sensitive to valence electrons, can be refined. Through Poisson's equation, the structure factors for electron diffraction are converted to those for X-ray diffraction, or the Fourier coefficients of the charge density. According to the nature of Poisson's equation, a small change in the low-order structure factors for X-ray diffraction causes a large change in those for electron diffraction. That is, the determination of the low-order structure factors for electron diffraction by the electron diffraction method takes an advantage in determining more accurate low-order structure factors for X-ray diffraction compared with the X-ray diffraction method. Saunders *et al.* determined six low-order crystal structure factors of Si by fitting a [110] CBED pattern with the theoretical calculations. They displayed the bonding charge density using four low-order structure factors and compared it with that obtained by using the structure factors determined by the X-ray diffraction method [9], [16]. Nuechter *et al.* determined the charge density of NiAl using the six low-order structure factors and temperature factors determined by them [17]. They honestly stated there is a certain discrepancy between the experimental and theoretical structure factors. To obtain high precision structure factors is a common target of electron crystallographers. Zuo *et al.* [18] showed the charge density distribution of Cu_2O using the low-order structure factors obtained from a ZOLZ-CBED pattern and the high-order structure factors determined by X-ray diffraction. It should be noted that the accurate determination of Debye-Waller factors, which can be performed successfully by our refinement method with the use of HOLZ reflections, is crucial to obtaining high-precision low-order structure factors for X-ray diffraction. Thus, our method would have the potential to provide the behavior of valence electrons more accurately than the X-ray diffraction method and the electron diffraction method which uses only ZOLZ reflections. We will show the charge density distributions of $LaCrO_3$ obtained by the present method.

We have been involved in the study of the symmetry determination of quasicrystals. It was believed and assumed that the decagonal quasicrystal has a space group of $P10_5/mmc$ on the basis of electron diffraction patterns and HREM images. Using CBED, we discovered decagonal quasicrystals with noncentrosymmetric space group $P\overline{1}0m2$. We confirmed from an HREM study that the 2nm diameter cluster of the quasicrystals, which are seen at the projection along the decagonal axis, have a fivefold symmetry. We discovered from HREM studies that many decagonal quasicrystals with space group $P10_5/mmc$ consist of 2nm diameter clusters of fivefold symmetry. That is, the basic unit is noncentrosymmetric though the resultant symmetry is centrosymmetric. The rest of the decagonal quasicrystals with $P10_5/mmc$ has been believed to have 2nm diameter clusters of tenfold symmetry. We introduced the high-angle annular dark-field (HAADF) method [19] for revealing the true symmetry and constructing better models of the decagonal quasicrystals. That is, we revealed using HAADF that the 2nm diameter cluster in one of the highest-quality quasicrystals, $Al_{72}Ni_{20}Co_8$ with space group $P10_5/mmc$, does not have tenfold symmetry but only one mirror symmetry [20]. The result overthrew what had been believed by the qua-

sicrystal researchers, "the basis or the 2nm diameter cluster of high-quality decagonal quasicrystals with space group $P10_5/mmc$ is of tenfold symmetry". To date, the mirror symmetry cluster has been widely accepted and consistent with the Gummelt tiling, which covers a two dimensional plane in a quasiperiodic way by a decagonal tile with mirror symmetry [21], [22].

Decagonal quasicrystals are usually composed of three elements, for example, aluminum and two transition metals. It has long been a question whether two transition metals take an ordered or a disordered arrangement. We applied the atom location by channeling enhanced microanalysis (ALCHEMI) method [23] to decagonal quasicrystals to reveal the role of the second transition metal. We have found that the two kinds of transition metals are arranged in disorder [24]. This means that the second element varies the electron-atom ratio and thus the quasicrystal is a Hume-Rothery compound [25]. We have revealed to a certain extent the development from an approximant crystal to a decagonal quasicrystal, by considering an appropriate tile or an elongated hexagonal tile [26]. Through these investigations, we are approaching constructing a correct model of the basic unit or the basis of the quasicrystal. We are continuing the structure determination of quasicrystals by CBED.

We already know that the elastic scattering part of CBED patterns is well reproduced by theoretical simulations when proper structural and absorption parameters and a sufficient number of beams are taken into account. The CBED patterns, however, contain Kikuchi patterns formed by thermal diffuse scattering (TDS) even when the energy-filtering technique is used. Takagi [27] re-formulated Kainuma's theory [28] based on the Bloch-wave method and gave the intensity distribution of the Kikuchi-band profile due to TDS using the two-beam dynamical theory. Hall and Hirsch [29] considered TDS from two-beam Bloch waves in the kinematical fashion under the Einstein model for thermal vibrations and provided a very important formula or a scattering factor to calculate the TDS diffuse intensity. They calculated the normal and anomalous absorption coefficients of the imaginary potential due to TDS and showed TDS to be a major source of the anomalous absorption. Later, Rossouw and Bursill [30] provided a many-beam dynamical theory of the Kikuchi pattern using the scattering factor of TDS given by Hall and Hirsch [29], which permits the angular intensity distribution of TDS or the Kikuchi pattern to be calculated. They preliminarily carried out computer simulations of the TDS distribution of TiO_2 under a nine-beam approximation. Accurate theoretical calculations of the intensity distribution of Kikuchi patterns are an important hurdle to be cleared. If the Kikuchi pattern is well reproduced by simulations, the theoretical pattern is useful for subtracting the background intensity of a CBED pattern. Calculation of an accurate Kikuchi pattern is a very big task. A rapid progress in the performance of computers will overcome the difficulty and accelerate the execution of better theoretical calculations.

Omoto, our student, derived a comprehensive theoretical expression for the intensity of inelastically scattered electrons, which corresponds to Fujimoto's formulation for elastic scattering. He showed that the simulations of the Kikuchi patterns formed by TDS using a sufficient number of beams well reproduce the experimental patterns [31]. Simulated Kikuchi patterns of MgO, Al and TiO_2 at zone-axis incidences are shown and compared with experimental results. The Kikuchi patterns of MgO were calculated at the exact 020 excitation under the two-beam approximation using Takagi's independent Bloch-wave treatment. Excess and defect Kikuchi bands are analyzed in terms of the transitions between the branches of the dispersion surface. The thickness dependence and other features of the Kikuchi patterns are shown, which cannot be expected from Takagi's treatment. The Kikuchi patterns of MgO for systematic reflection cases are simulated and compared with experimental results.

Interface analysis or the determination of lattice-parameter changes at interfaces of multilayer materials is an important need for the device technology. Such determination using large-angle CBED [32], [33] originated from Cherns [34] of Bristol group. Recently, lattice-parameter determinations with an accuracy of about 10^{-4} have been performed by Zuo *et al.* [35], Kraemer *et al.* [36] and Wittmann *et al.* [37] using more automatic analysis programs, which take account of dynamical diffraction effects. Interface analysis is often carried out together with spectroscopic investigations, but we omit the spectroscopic investigations and confine ourselves in this volume to microscopy and diffraction analysis of interfaces. We will show the studies of structures of a stacking fault of TiO_2 [38], [39] and inversion domain boundaries of AlN [40]

under the combined use of CBED [7], [41] and HREM techniques. The lattice-parameter determinations of a thin cubic SiC film on a 6H-SiC substrate [42] and of a strained area at the substrate of InAs/GaAs are given. We investigate the effect of surfaces causing the asymmetric feature of reflection line profiles at a stacking fault and strong bending of reflection lines at a dislocation, which are often seen in LACBED patterns.

Microscopy, diffractometry and spectroscopy using electron microscopes have made a great contribution to materials research. The combined use of spectroscopy and diffractometry as well as spectroscopy and microscopy will be a weighty subject in the future, which includes studies of the momentum dependence of electron energy-loss spectra and the spatial variation of electronic structures. For this purpose, better energy resolutions of electron energy-loss spectroscopy (EELS) and X-ray emission spectroscopy (XES) are required at a nanometer area illumination.

We have developed a high energy-resolution EELS microscope (JEM-HREA80) to investigate detailed electronic structures of materials [43]. The microscope is equipped with a Wien-filter monochromator and analyzer. The energy resolutions for routine measurements are 50meV to 0.2eV depending on the setting of the filters. The microscope has been applied to reveal the detailed analysis of electronic structures of many materials [44]. The momentum and spatial resolutions are $3nm^{-1}$ in diameter and 30 to 100nm in diameter, respectively, the latter value being unfortunately not high enough for the recent sub-nanometer characterization of materials. On the other hand, we have manufactured an Ω-filter electron microscope (JEM-2010FEF) [14], which enables us to perform precise crystal structure analysis at a sub-nanometer scale using the CBED method. However, since it does not have a monochromator, its energy resolution of EELS spectra remains at about 1eV, which is not sufficient for the detailed study of electronic structures of materials.

Thus, analytical electron microscopes, which permit us to study both the crystal structures and electronic structures at a sub-nanometer scale, are strongly expected to appear on the market. For STEM, Krivanek developed a quadrupole-octupole spherical-aberration corrector to obtain a sub-Å electron beam without monochromating it [45]. Mook and Kruit constructed a short Wien-filter monochromator [46]. The German group headed by Ruehle is developing a new microscope which is equipped with an electrostatic Ω-filter as a monochromator and a mandolin filter as an analyzer designed by Rose [47]. FEI Company is developing a Wien-filter monochromator for a transmission electron microscope (TEM) [48].

Since 1999, we have continued to manufacture a new electron microscope under a project named "MIRAI 21" of Japan Science and Technology Corporation (JST), which enables us to investigate both the crystal and electronic structures of advanced materials at a sub-nanometer scale [49]. We describe the basic design of the microscope. MIRAI means "Future" in Japanese and is the abbreviation of "Microscope for Innovative Research and Advanced Investigation". The microscope is of an accelerating voltage of 200kV and has a point resolution of 0.19nm and an energy resolution of 0.2eV at a probe less than 2nm in diameter. It should be noted that a higher energy resolution is attainable at a larger probe size. The microscope is constructed on the basis of the JEM-2010FEF, but equipped with a double Wien-filter monochromator and an improved Ω-filter analyzer. A new and the most important element of the microscope is the Wien-filter monochromator.

The electron energy-loss near-edge fine structure (ELNES) gives the partial density of states (DOS) of the conduction band. If we measure a valence-electron excitation spectrum, it can be transformed to the dielectric function by the Kramers-Kronig analysis. The imaginary part of the dielectric function is proportional to the joint DOS of the valence and conduction bands multiplied by transition probabilities. Unfortunately, it is not easy to deduce the DOS of the valence band from the experimentally obtained joint DOS. Thus, the DOS of the valence band cannot be reached directly by EELS. Together with the DOS of the conduction band (unoccupied states), the DOS of the valence band (occupied states) is required for an understanding of the whole electronic structure.

A partial DOS of the valence band can be obtained by X-ray emission spectroscopy (XES). An energy-dispersive X-ray spectroscopy (EDS) device attached to an analytical TEM is a tool for taking X-ray emission spectra from a small specimen area. However, since the energy resolution of the conventional EDS device using a semiconductor detector is about 130eV, it is insufficient for the study of the electronic structures. A new microcalorimeter EDS device [50], [51] and a con-

ventional wavelength-dispersive X-ray spectroscopy device for scanning electron microscopes have energy resolutions of about 10eV, which are higher than that of the conventional EDS, but do not yet have enough energy resolution to obtain the DOS of the valence band. A conventional EELS instrument attached to a TEM usually takes spectra with an energy resolution of about 1eV, by which the DOS of conduction bands has been studied through ELNES up to now [52]. Thus, an energy resolution of about 1eV is a target resolution for the study of the DOS of the valence band, though a high energy-resolution XES device for a TEM with an energy resolution of about 0.2eV should be desired in the future to study the fine structures of the DOS of the valence band.

We constructed a grazing-incidence soft-X-ray spectrometer for a TEM. The spectrometer, which is composed of a grating and a CCD detector, was attached to a JEM-2000FX transmission electron microscope. Boron *K*-emission spectra of hexagonal boron nitride, which give the DOS of the valence band of the material, were obtained with an energy resolution of about 0.6eV [53]. Since our spectrometer is making progress in its performance, the latest information on our development should be referred to our papers in the proceedings of the related conferences.

We showed and used the CBED symmetries for the point- and space-group determinations in the three previous volumes. We herewith summarize the most basic CBED pattern symmetries, which are not experimental patterns but simulated patterns for a little unfamiliar materials in some cases to display clear symmetries.

Finally, we give several pictures for attraction, most of which are created by the decoration of masterpieces of paintings using CBED patterns. The photos of our team and our JEM-2010FEF are appended for our memory.

References

[1] P. Goodman and T. W. Secomb: *Acta Cryst.*, **A33** (1977) 126.

[2] P. Goodman and A. W. S. Johnson: *Acta Cryst.*, **A33** (1977) 997.

[3] M. Tanaka, H. Takayoshi, M. Ishida and Y. Endoh: *J. Phys. Soc. Jpn.*, **54** (1985) 2970.

[4] K. Tsuda, K. Saitoh, M. Terauchi, M. Tanaka and P. Goodman: *Acta Cryst.*, **A56** (2000) 359.

[5] K. Saitoh, K. Tsuda, M. Terauchi and M. Tanaka: *Acta Cryst.*, **A57** (2001) 219.

[6] K. Tsuda and M. Tanaka: *Acta Cryst.*, **A51** (1995) 7.

[7] M. Tanaka, M. Terauchi and K. Tsuda: Convergent-Beam Electron Diffraction III, JEOL-Maruzen, Tokyo, 1994.

[8] J. M. Zuo, J. C. H. Spence, J. Downs and J. Mayer: *Acta Cryst.*, **A49** (1993) 422.

[9] M. Saunders, D. M. Bird, N. J. Zaluzec, W. G. Burgess, A. R. Preston and C. J. Humphreys: *Ultramicroscopy*, **60** (1995) 311.

[10] C. Deininger, G. Necker and J. Mayer: *Ultramicroscopy*, **54** (1994) 15.

[11] J. M. Zuo: *Microscopy Research and Technique*, **46** (1999) 220.

[12] M. Saunders, D. M. Bird, O. F. Holbrook, P. A. Midgley and R. Vincent: *Ultramicroscopy*, **65** (1995) 45.

[13] K. Tsuno, T. Kaneyama, T. Honda, K. Tsuda, M. Terauchi and M. Tanaka: *J. Electron Microsc.*, **46** (1997) 357.

[14] M. Tanaka, K. Tsuda, M. Terauchi, K. Tsuno, T. Kaneyama, T. Honda and M. Ishida: *J. Microscopy*, **194** (1999) 219.

[15] K. Tsuda and M. Tanaka: *Acta Cryst.*, **A55** (1999) 939.

[16] P. A. Midgley, M. Saunders, R. Vincent, J. W. Steeds: *Ultramicroscopy*, **59** (1995) 1.

[17] W. Nuechter, A. L. Weickenmeier and J. Mayer: *phys. stat. sol.* (*a*), **166** (1998) 367.

[18] J. M. Zuo, M. Kim, M. O'Keeffe and J. C. H. Spence: *Nature*, **401** (1999) 49.

[19] S. J. Pennycook and D. E. Jesson: *Phys. Rev. Lett.*, **64** (1990) 938.

[20] K. Saitoh, K. Tsuda, M. Tanaka, K. Kaneko and A. P. Tsai: *Jpn. J. Appl. Phys. Lett.*, **36** (1997) L1400.

[21] P. Gummelt: *Geometriae Dedicata*, **62** (1996) 1.

[22] P. J. Steinhardt, H. C. Jeong, K. Saitoh, M. Tanaka, E. Abe and A. P. Tsai: *Nature*, **396** (1998) 55.

[23] J. C. H. Spence and J. Taftø: *J. Microscopy*, **130** (1983) 147.

[24] K. Saitoh, M. Tanaka and A. P. Tsai: *J. Phys. Soc. Jpn.*, **69** (2000) 2379.

[25] A. P. Tsai, A. Inoue and T. Masumoto: *Mater. Trans. JIM*, **30** (1989) 463.

[26] K. Saitoh, T. Yokosawa, M. Tanaka and A. P. Tsai:

J. Phys. Soc. Jpn., **68** (1999) 2886.
[27] S. Takagi: *J. Phys. Soc. Jpn.*, **13** (1958) 287.
[28] Y. Kainuma: *Acta Cryst.*, **8** (1955) 247.
[29] C. R. Hall and P. B. Hirsch: *Proc. R. Soc. London Ser. A*, **286** (1965) 158.
[30] C. J. Rossouw and L. A. Bursill: *Acta Cryst.*, **A41** (1985) 320.
[31] K. Omoto, K. Tsuda and M. Tanaka: *J. Electron Microsc.*, **51** (2002) 67.
[32] M. Tanaka, R. Saito, K. Ueno and Y. Harada: *J. Electron Microsc.*, **29** (1980) 408.
[33] M. Tanaka and M. Terauchi: Convergent-Beam Electron Diffraction, JEOL-Maruzen, Tokyo, 1985.
[34] D. Cherns, C. J. Kiely and A. R. Preston: *Ultramicroscopy*, **24** (1988) 355.
[35] J. M. Zuo, M. Kim and R. Holmestad: *J. Electron Microsc.*, **47** (1998) 121.
[36] S. Kraemer, J. Mayer, C. Witt, A. Weikenmeier and M. Ruehle: *Ultramicroscopy*, **81** (2000) 245.
[37] R. Wittmann, C. Parzinger and D. Gerthsen: *Ultramicroscopy*, **70** (1998) 145.
[38] S. Yamada and M. Tanaka: *J. Electron Microsc.*, **44** (1995) 212.
[39] S. Yamada and M. Tanaka: *J. Electron Microsc.*, **46** (1997) 67.
[40] Y. Yan, M. Terauchi and M. Tanaka: *Phil. Mag.*, **A75** (1997) 1005.
[41] M. Tanaka, M. Terauchi and T. Kaneyama: Convergent-Beam Electron Diffraction II, JEOL-Maruzen, Tokyo, 1988.
[42] U. Kaiser, K. Saitoh, K. Tsuda and M. Tanaka: *J. Electron Microsc.*, **48** (1999) 221.
[43] M. Terauchi, M. Tanaka, K. Tsuno and M. Ishida: *J. Microscopy*, **194** (1999) 203.
[44] For example, M. Terauchi and M. Tanaka: *J. Surface Analysis*, **3** (1997) 240.
[45] O. L. Krivanek, N. Dellby and A. R. Lupin: *Ultramicroscopy*, **78** (1999) 1.
[46] H. W. Mook and P. Kruit: *Ultramicroscopy*, **78** (1999) 43.
[47] H. Rose: *Ultramicroscopy*, **78** (1999) 13.
[48] P. C. Tiemeijier: *Ultramicroscopy*, **78** (1999) 53.
[49] M. Tanaka, M. Terauchi, K. Tsuda, K. Saitoh, T. Honda, K. Tsuno, M. Naruse, T. Tomita and T. Kaneyama: *Inst. Phys. Conf. Ser.*, No.**165** (2000) 217.
[50] D. A. Wollman, K. D. Irwin, G. C. Hilton, L. L. Dulcie, D. E. Newbury and J. M. Martinis: *J. Microscopy*, **188** (1997) 196.
[51] D. Newbury, D. Wollman, K. Irwin, G. Hilton and J. Martinis: *Ultramicroscopy*, **78** (1999) 73.
[52] R. F. Egerton: Electron Energy-Loss Spectroscopy in the Electron Microscope (2nd edition), Plenum Press, 1996.
[53] M. Terauchi, H. Yamamoto and M. Tanaka: *J. Electron Microsc.*, **50** (2001) 101.

Abbreviations of Technical Terms

CBED	Convergent-Beam Electron Diffraction
ZAP	Zone-Axis Pattern
WP	Whole Pattern
BP	Bright-Field Pattern
DP	Dark-Field Pattern
±DP	±G Dark-Field Pattern
ZOLZ	Zeroth Order Laue-Zone
H(F,S)OLZ	Higher (First, Second) Order Laue-Zone
LACBED	Large-Angle CBED
CTEM	Conventional Transmission Electron Microscopy
STEM	Scanning Transmission Electron Microscopy
HREM	High-Resolution Electron Microscopy
EFTEM	Energy-Filtering Transmission Electron Microscopy
FEG	Field Emission Gun
CL	Condenser Lens
OL	Objective Lens
IL	Intermediate Lens
PL	Projector Lens
IP	Imaging Plate
CCD	Charge-Coupled Device
MBFIT	Many-Beam Dynamical Calculations and Least-Squares Fitting
GOF	Goodness-of-Fit
GBP	Generalized Bethe Potential
HAADF	High-Angle Annular Dark-Field
ALCHEMI	Atom Location by Channeling-Enhanced Microanalysis
SAD	Selected-Area Diffraction
TDS	Thermal Diffuse Scattering
IDB	Inversion Domain Boundary
EELS	Electron Energy-Loss Spectroscopy
ELNES	Electron Energy-Loss Near-Edge Fine Structure
XES	X-ray Emission Spectroscopy
EDS	Energy-Dispersive X-ray Spectroscopy
WDS	Wavelength-Dispersive X-ray Spectroscopy
DOS	Density of States
FWHM	Full Width at Half Maximum
XAS	X-ray Absorption Spectroscopy
PES	Photoelectron-Emission Spectroscopy
IPES	Inverse Photoelectron-Emission Spectroscopy

Space-Group Determination by Coherent CBED

Space Groups Indistinguishable by Dynamical Extinction Lines

Convergent-beam electron diffraction (CBED) is known as a very effective method for determining crystal point- and space-groups. However, the method cannot distinguish 23 space-group sets in the table on the right-side page for the following five reasons.

i) $3_1(3_2)$-, 4_2- and $6_2(6_4)$-screw axes cannot be distinguished from their corresponding non-screw axes because the screw axes do not form dynamical extinction lines. Thus, the space-group sets Nos.1 to 5, 8, 10 to 13 and 18 in the table cannot be distinguished.

ii) A 6_3-screw axis cannot be distinguished from a 6_1 (6_5)-screw axis because the three screw axes show dynamical extinction lines in the same manner. Thus, the space-group sets Nos.6 and 7 cannot be distinguished.

iii) Enantiomorphous space-group pairs cannot be distinguished because they show the same CBED symmetry. Thus, the space-group pairs indicated by the parentheses in the table (Nos.1 to 7, 9, 19, 22 and 23) cannot be distinguished.

iv) The space-group pairs of Nos.16 and 17 show the same CBED symmetries because they have completely the same symmetry elements in each pair despite the different space-group symbols.

v) The space-group pairs of Nos.14, 15, 20 and 21 can not be distinguished because reflections which should show dynamical extinction lines due to a 4_1-screw axis are forbidden by the extinction rule of the lattice types *I* and *F*.

In this chapter, it is shown theoretically that the coherent CBED method can distinguish space groups, which are composed of principal rotation and screw axes accompanying other 2-fold-rotation axes, or the twelve space-group sets of Nos.2, 3, 5, 7, 12, 13, 15, 16, 17, 18, 20 and 21 in the table on the right-side page. It is demonstrated by computer simulations that the relative arrangement of 2-fold-rotation and 2_1-screw axes can be distinguished by examining the relative phases of specific reflections through the interference fringes of coherent CBED patterns.

No.1	$P3$, ($P3_1$, $P3_2$)
No.2	$P312$, ($P3_112$, $P3_212$)
No.3	$P321$, ($P3_121$, $P3_221$)
No.4	$P6$, ($P6_2$, $P6_4$)
No.5	$P622$, ($P6_222$, $P6_422$)
No.6	$P6_3$, ($P6_1$, $P6_5$)
No.7	$P6_322$, ($P6_122$, $P6_522$)
No.8	$P4$, $P4_2$
No.9	($P4_1$, $P4_3$)
No.10	$P4/m$, $P4_2/m$
No.11	$P4/n$, $P4_2/n$
No.12	$P422$, $P4_222$
No.13	$P42_12$, $P4_22_12$
No.14	$I4$, $I4_1$
No.15	$I422$, $I4_122$
No.16	$I23$, $I2_13$
No.17	$I222$, $I2_12_12_1$
No.18	$P432$, $P4_232$
No.19	($P4_132$, $P4_332$)
No.20	$I432$, $I4_132$
No.21	$F432$, $F4_132$
No.22	($P4_122$, $P4_322$)
No.23	($P4_12_12$, $P4_32_12$)

23 space-group sets indistinguishable by dynamical extinction lines.

Coherent CBED

Figure (a) on the right-side page shows a schematic diagram of the coherent CBED method. A convergence angle of the incident beam is set to overlap the neighboring reflection disks. Two plane waves with wave vectors of $\boldsymbol{k}_1$ and $\boldsymbol{k}_2 = \boldsymbol{k}_1 - \boldsymbol{g}$ form interference fringes at **P** in the overlapping region. If the focused point of the incident beam is on the specimen, each overlapping region of the CBED disks shows a uniform intensity. If the beam is defocused from the specimen by a certain amount, interference fringes appear in the overlapping regions. Formation of the interference fringes was explained in detail by Cowley [a], Vine *et al.* [b] and Terauchi *et al.* [c]. The entire-fringe set is displaced with a shift of the probe position. The relative position of the fringes is determined by the probe position and the phase difference between crystal structure factors of the reflections. The former effect is given by a phase factor of $\exp(2\pi i\, \boldsymbol{g}\cdot\Delta\boldsymbol{r})$, where $\boldsymbol{g}$ and $\Delta\boldsymbol{r}$ respectively indicate a reflection vector and a vector pointing the probe position from the origin of a unit cell.

First, we consider the interference fringes between the transmitted wave (000) and its two neighboring reflection waves ($\pm\boldsymbol{g}$), whose reflection vectors are perpendicular to the direction of a 2-fold-rotation axis. It is noted that the 2-fold axis is not necessarily perpendicular to the incident beam direction [4], [5]. When the probe is located on the 2-fold axis, the phases of the crystal structure factors and that for the probe position are the same for the two reflections. This is caused by the fact that the reflections $\boldsymbol{g}$ and $-\boldsymbol{g}$ are equivalent with respect to the 2-fold axis. As a result, the interference-fringe sets appearing in the two overlapping regions show mirror symmetry m with respect to the center of the transmitted wave as shown in Fig. (b). If the probe is not on the axis, the fringe sets do not show mirror symmetry as shown in Fig. (c). Thus, we can identify the position of the 2-fold axis from the coherent CBED pattern. The positions of the 2-fold axes in the other orientations are examined using the reflection pairs whose reflection vectors are perpendicular to the 2-fold axes. If the probe is put on an intersection point of two 2-fold axes, the coherent CBED pattern shows two sets of mirror symmetry. Similarly, the coherent CBED pattern shows three sets of mirror symmetry at an intersection point of three 2-fold axes. Therefore, the intersection points of the 2-fold axes can be revealed by observing the interference fringes in the coherent CBED patterns. It should be noted that a 2_1-screw axis also forms mirror symmetry as a 2-fold axis does when the probe is positioned on the 2_1-screw axis, and thus the arrangement of 2_1-screw axes can also be identified by the same procedure.

References

[a] J. M. Cowley: *Ultramicroscopy*, **4** (1979) 435.

[b] W. J. Vine, R. Vincent, P. Spellward and J. W. Steeds: *Ultramicroscopy*, **41** (1992) 423.

[c] M. Terauchi, K. Tsuda, O. Kamimura, M. Tanaka, T. Kaneyama and T. Honda: *Ultramicroscopy*, **54** (1994) 268.

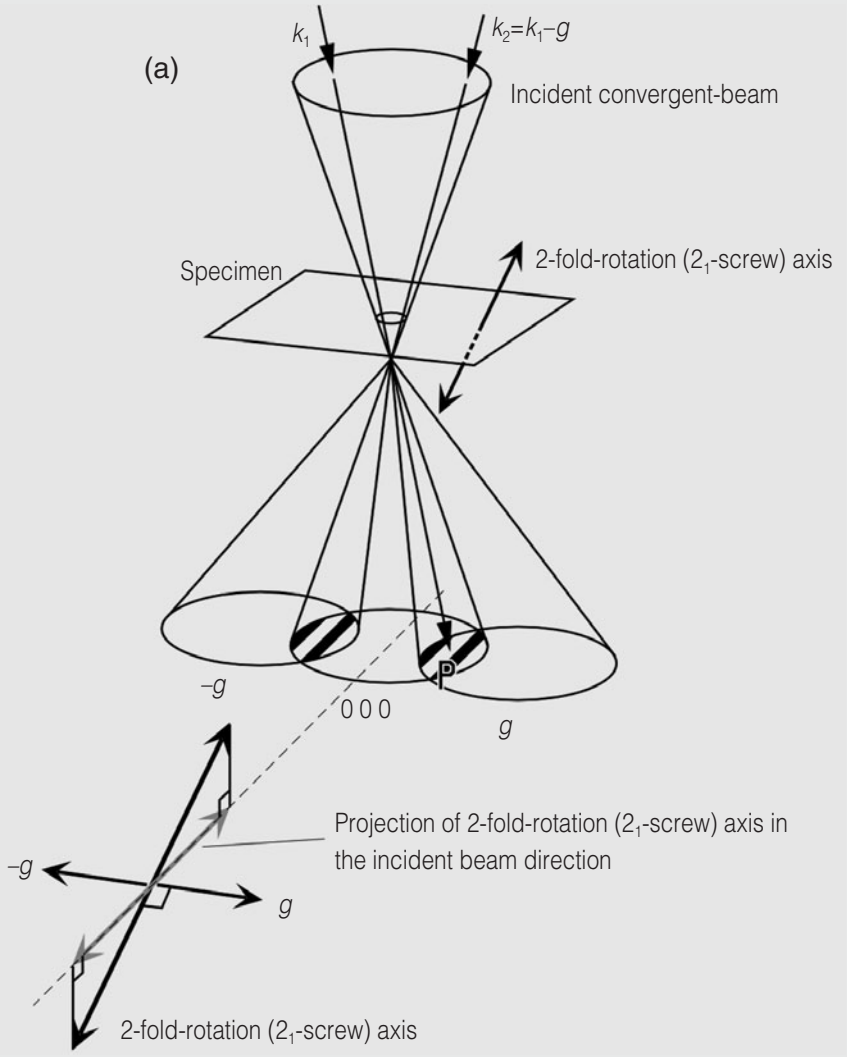

(b) The probe is on a 2-fold-rotation (2_1-screw) axis

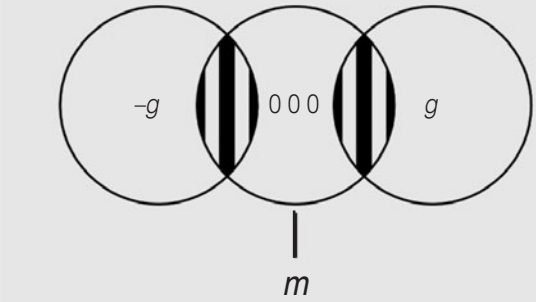

(c) The probe is not on a 2-fold-rotation (2_1-screw) axis

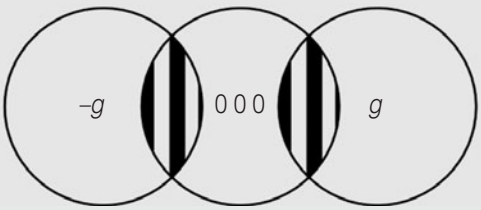

Effect of probe size on CBED patterns

In conventional calculations of CBED patterns, the effect of the electron-probe size is not taken into account, but an incident plane wave is used for obtaining the diffraction intensity at each point of a diffraction disk because the diffraction waves are independent of each other. The relative phases between the incident waves are not considered in the calculations of CBED patterns. A plane wave does not illuminate a small specimen area but does an infinite specimen area. Here, we consider the effect of the finite size of the probe on the CBED patterns of perfect crystals. The effect of the probe size can be explained appropriately by the artificial superlattice method [a].

Figures on the opposite page schematically show a parallel-beam illumination in the conventional calculation method (Fig. (a)) and a convergent-beam illumination in the artificial superlattice method (Fig. (b)). The black dots in the figures indicate the reciprocal lattice points corresponding to a fundamental lattice. The white dots correspond to the reciprocal lattice points of an artificial superlattice. For a convergent-beam illumination, a number of incident plane waves traveling in different directions pass through the condenser-lens aperture and form a finite-size probe on the top surface of the specimen. A certain phase relation exists between the different incident plane waves on the top surface, which is determined by the spherical aberration and the amount of defocus of the probe-forming lens. The convergent-beam illumination to the artificial superlattice produces enough diffraction points to cover the diffraction disks (see Fig. (b)), the density of the diffraction points being dependent on the size of the superlattice.

When the probe size at the specimen is smaller than the fundamental lattice spacing concerned, two adjacent reflections give rise to coherent interference, producing interference fringes at their overlapping area. The interference fringes due to the finite-size probe are correctly reproduced by the artificial superlattice calculation, while they are not reproduced by the conventional incoherent calculation. This is because the artificial superlattice method can deal with the whole convergent illumination beams in one Bethe's basic equation and assign the phases to all the illumination beams correctly through the boundary condition on the top surface. When the probe size exceeds the lattice spacing, the fringes rapidly disappear. This is because other fringes displaced from those fringes begin to overlap, which is called incoherent interference. For such a large probe size beyond the lattice spacing, the conventional incoherent calculation, where the illuminated area is infinite, is enough to explain the experimental result, though the superlattice method can reproduce thoroughly the dependence of the probe size on the interference fringes.

On the other hand, the intensities of the non-overlapping areas of diffraction disks do not depend on the probe size. The conventional calculation can reproduce the experimental results because the intensities of the neighboring points are independent of each other for perfect crystals. It should be noted that the artificial superlattice calculation can also provide the same intensities. This can be deduced from the premise that even in the artificial superlattice calculation, only the fundamental reflections have finite values of their structure factors, but the superlattice reflections have zero values of their structure factors. In other words, the superlattice method assumes that the dynamical interaction takes place only between the fundamental reflections for each incident plane wave, or that the diffraction intensities produced by the constituent beams of the convergent incident beam are independent of each other.

The conventional calculation method, which uses an incident plane wave that illuminates an infinite area, provides correct results for the simulation of CBED patterns of perfect crystals, except for the calculations of interference fringes at the overlapping areas of CBED patterns.

Reference

[a] J. C. H. Spence: *Acta Cryst.*, **A34** (1978) 112.

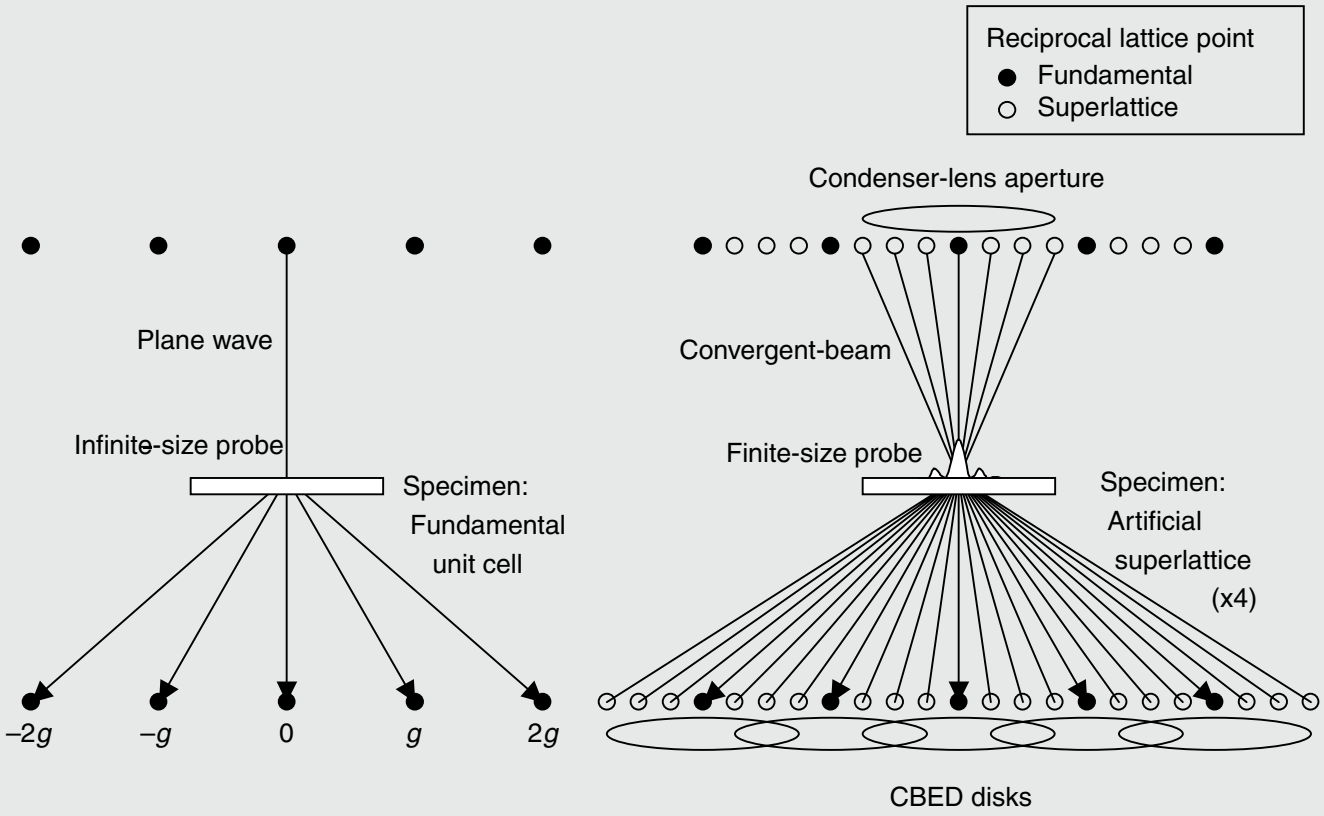

(a) Conventional method

(b) Artificial superlattice method

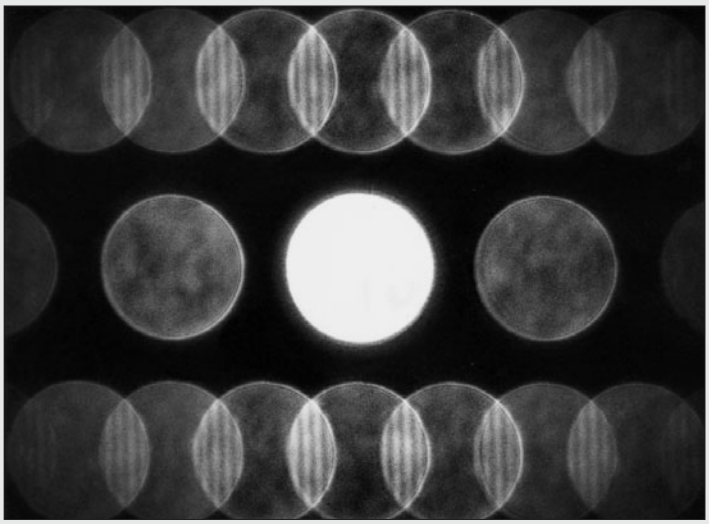

FeS_2 [100] 200kV

Coherent CBED pattern

$Sr_2Nb_2O_7$ **80kV**

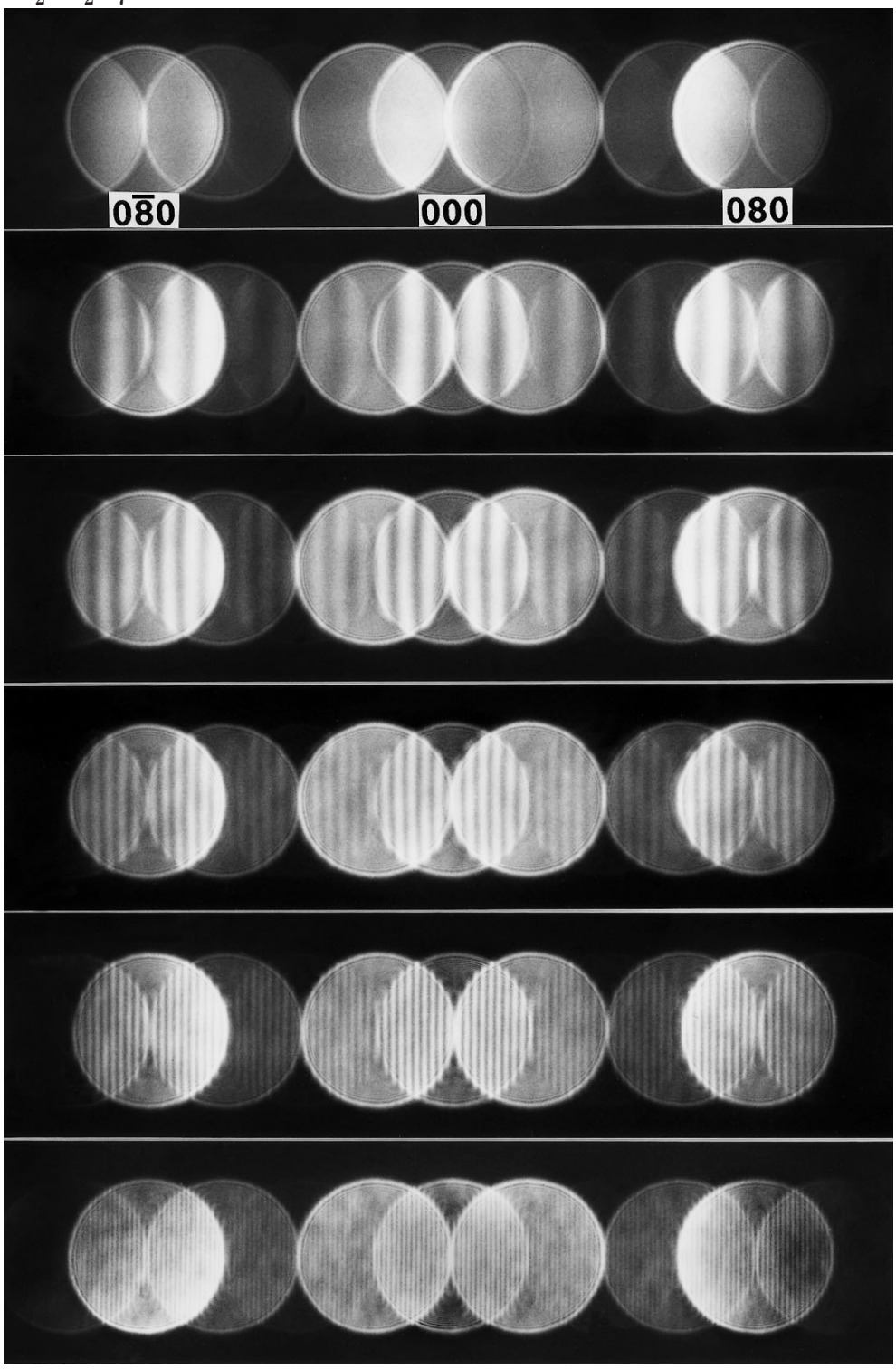

d_{020} = 1.34nm

Coherent CBED patterns taken with six different amounts of illumination defocus from $Sr_2Nb_2O_7$ by exciting the 0k0 systematic reflections.

Cubic BN [111] **100kV**

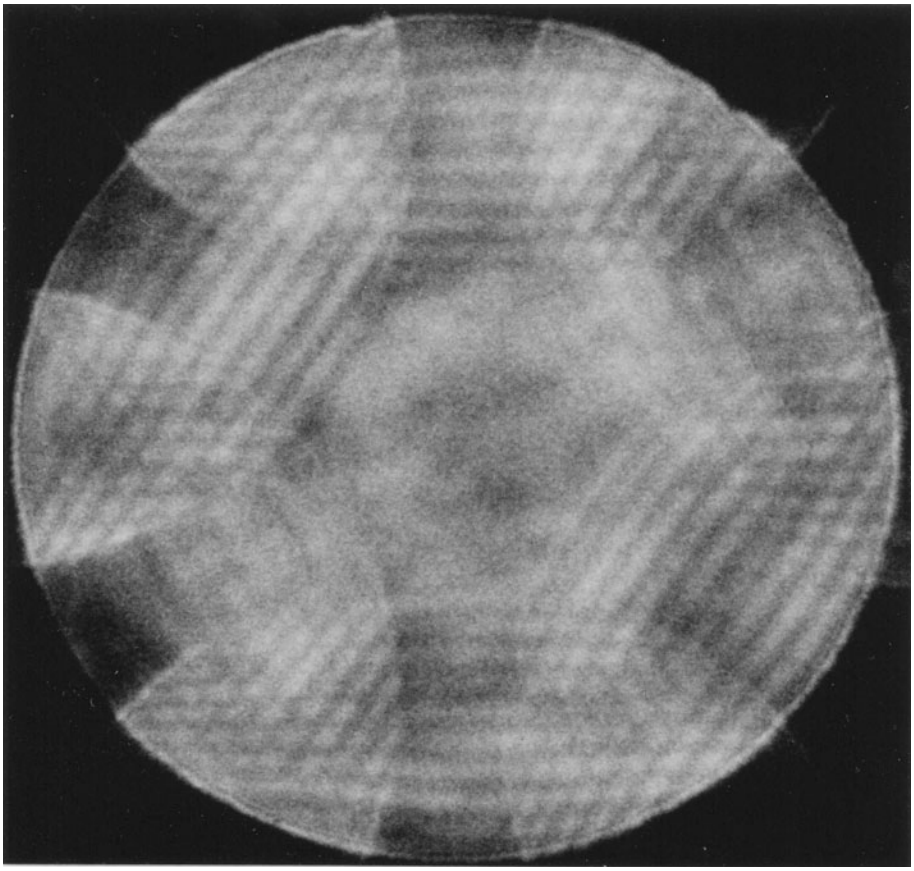

d_{220} = 0.128nm

Coherent CBED pattern of cubic boron nitride. Interference fringes of the 220 spacing (0.128nm) are seen in the three directions, which are of the world's highest resolution. The result indicates that a probe size of less than 0.128nm is achieved [a].

Reference

[a] K. Tsuda and M. Tanaka: *J. Electron Microsc.*, **45** (1996) 59.

Distinction Between I23 and I2$_1$3

Arrangements of 2-fold-rotation axes

The figures illustrate the arrangements of symmetry elements of space groups *I*23 and *I*2$_1$3 in projection in the [100] direction [a], where 2-fold and 2$_1$-screw axes are indicated by usual symbols. It should be noted that the two space-groups have both 2-fold and 2$_1$-screw axes irrespective of their symbols *I*23 and *I*2$_1$3. We do not distinguish between 2-fold and 2$_1$-screw axes because both the 2-fold and 2$_1$-screw axes cause no difference in the formation of mirror symmetry of the interference-fringe patterns appearing at the overlapping areas between 000 and $\pm\boldsymbol{g}$ reflections.

Space groups *I*23 and *I*2$_1$3 have the same relative arrangements of the 2-fold and 2$_1$-screw axes, when they are projected along the [100] zone axis, as seen in the figures. The figures on the right-side page show the arrangements of the 2-fold and 2$_1$-screw axes in projections in the [110] and [111] directions. The [110] projection makes no difference for the two space-groups as well, except a relative shift. However, in the [111] projection, it is clearly seen that the three perpendicular 2-fold and 2$_1$-screw axes intersect at the same positions of "a", "c", "g" and "i" for *I*23, but only two of them intersect at the positions of "b", "d", "e", "f" and "h" for *I*2$_1$3. It should be noted that the 2-fold and 2$_1$-screw axes do not produce any symmetry in the conventional CBED patterns taken with the [111] incidence because the 2-fold and 2$_1$-screw axes are neither parallel nor perpendicular to the [111] direction. It is, however, shown in the following pages that the coherent CBED technique can directly reveal the difference of the relative arrangement of 2-fold and 2$_1$-screw axes.

[100] projection

***I*23**

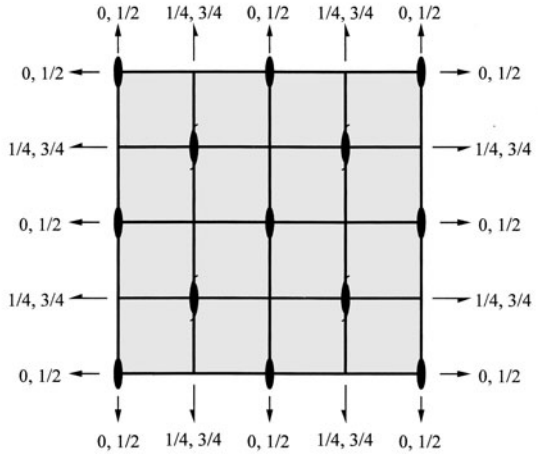

***I*2$_1$3**

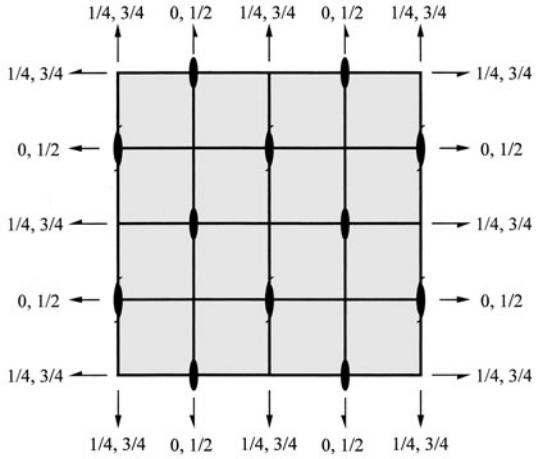

Reference

[a] International Tables for Crystallography, Vol. A, ed. Th. Hahn, Kluwer Academic Publishers, 1989.

[110] projection

***I*23**

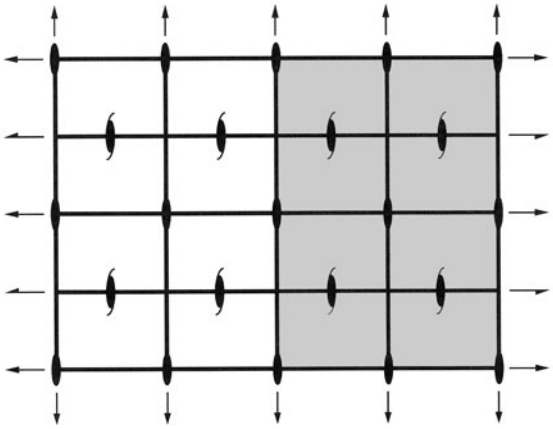

***I*2$_1$3**

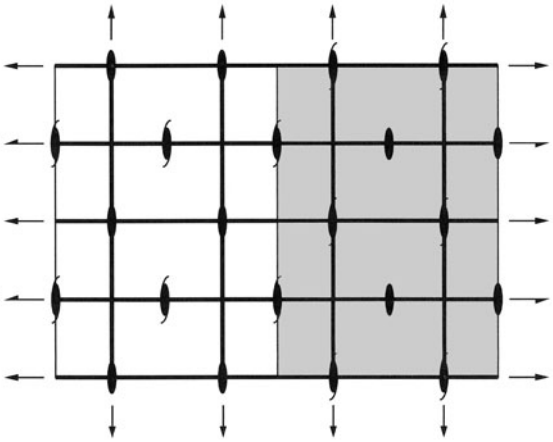

[111] projection

***I*23**

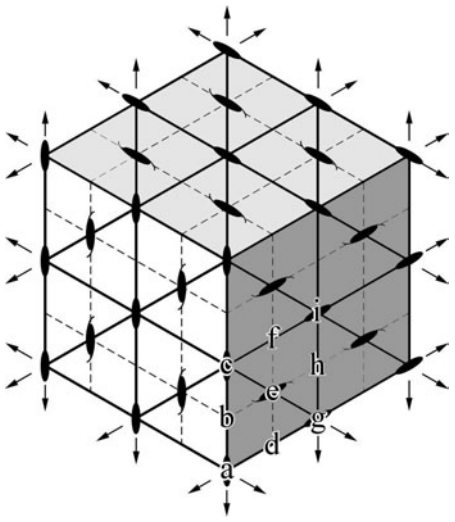

***I*2$_1$3**

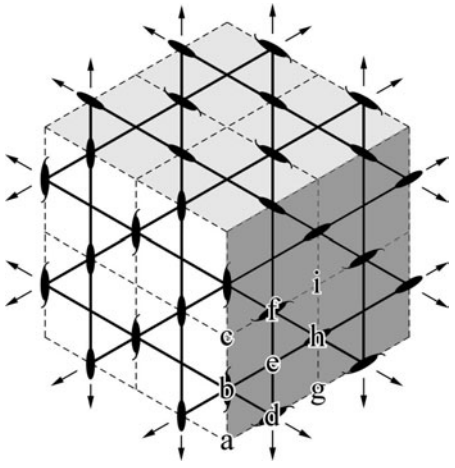

Coherent CBED patterns of *I*23

Phases of structure factors

Figures (a) to (i) show the phases of kinematical crystal structure factors of 110-type reflections for a structure model of *I*23 at the probe positions of "a" to "i" illustrated in the right figure, respectively, where the relative phase depending on the probe positions, $2\neq i\boldsymbol{g}\cdot\Delta\boldsymbol{r}$, are included to the phases of the structure factors. The model structure has a lattice parameter of a = 0.4nm and is composed of atoms whose positions are generated from a general position of (0.05, 0.10, 0.15) by the symmetry operations of space group *I*23. It should be noted that, when the probe is placed on the 2-fold and 2_1-screw axes, the structure factors of the reflections $\boldsymbol{g}$ and $-\boldsymbol{g}$ perpendicular to the axes have the same phase as shown by a pair of arrows in the figures.

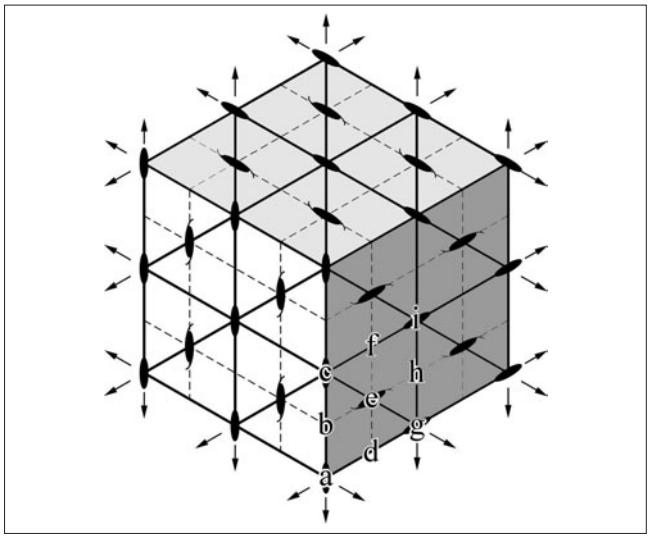

Lattice parameter a = 0.4nm		
Site	Position (x, y, z)	Element
24*f*	(0.05, 0.10, 0.15)	Si

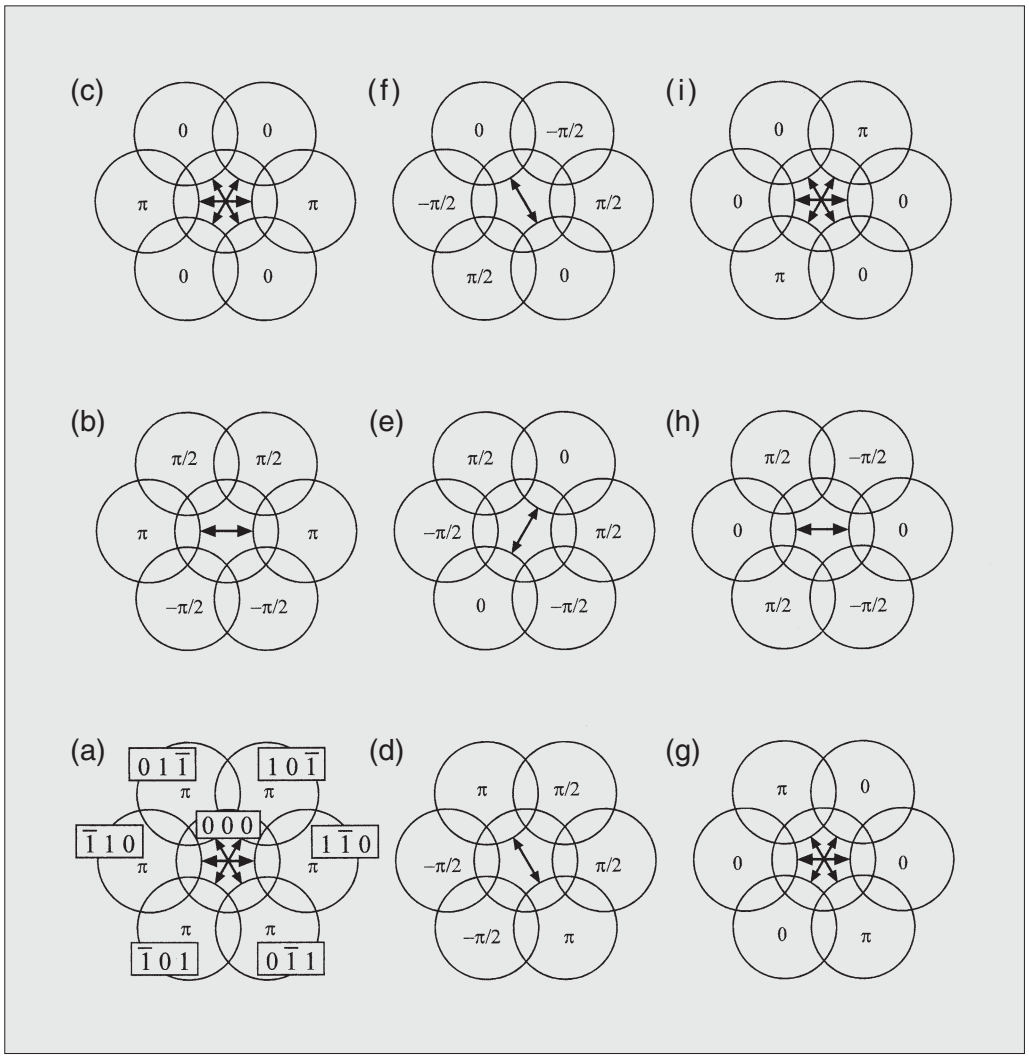

Simulations

Figures (a) to (i) show coherent CBED simulation patterns for the model of *I*23, which were calculated under the kinematical approximation with a certain defocus of the illumination, respectively, at the probe positions of "a" to "i" illustrated on the previous page. It is noted that the interference fringes agree well with those calculated by the dynamical theory if the specimen thickness is less than about 10nm at an accelerating voltage of 100kV.

When the two overlapping areas which face each other show the symmetric interference fringes with respect to the center of the incident beam (indicated by a pair of arrows), the structure factors of the $\pm\boldsymbol{g}$ reflections have the same phase, indicating the existence of 2-fold and 2_1-screw axes at the probe position. Figures (a), (c), (g) and (i) exhibit three sets of such pairs, confirming the intersection of three perpendicular 2-fold and 2_1-screw axes at positions "a", "c", "g" and "i" in the figure on the previous page.

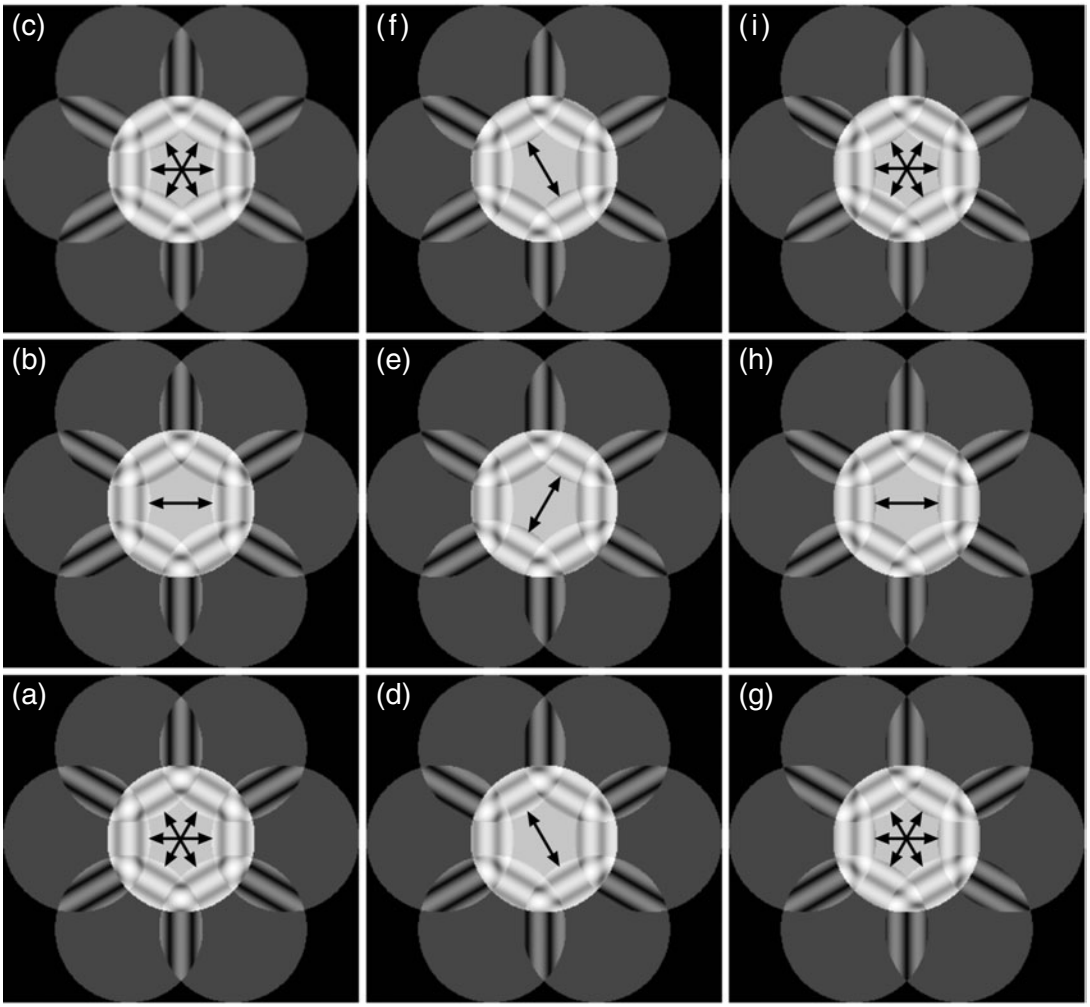

Coherent CBED patterns of $I2_13$

Phases of structure factors

Figures (a) to (i) show the phases of kinematical crystal structure factors of 110-type reflections for a structure model of $I2_13$ at the probe positions of "a" to "i" illustrated in the right figure, respectively. The model structure has a lattice parameter of a = 0.4nm and is composed of atoms whose positions are generated from a general position of (0.05, 0.10, 0.15) by the symmetry operations of space group $I2_13$. It is seen that, when the probe is placed on the 2-fold and 2_1-screw axes, the structure factors of the reflections $\boldsymbol{g}$ and $-\boldsymbol{g}$ perpendicular to the axes have the same phase as shown by a pair of arrows in the figures.

Lattice parameter a = 0.4nm		
Site	Position (x, y, z)	Element
24c	(0.05, 0.10, 0.15)	Si

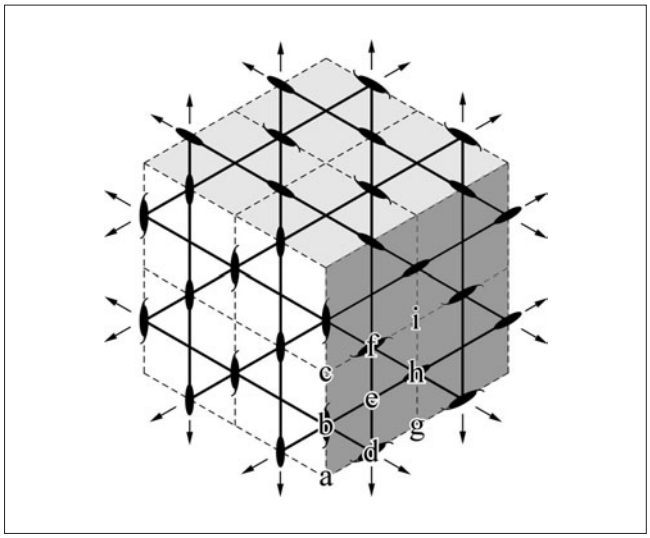

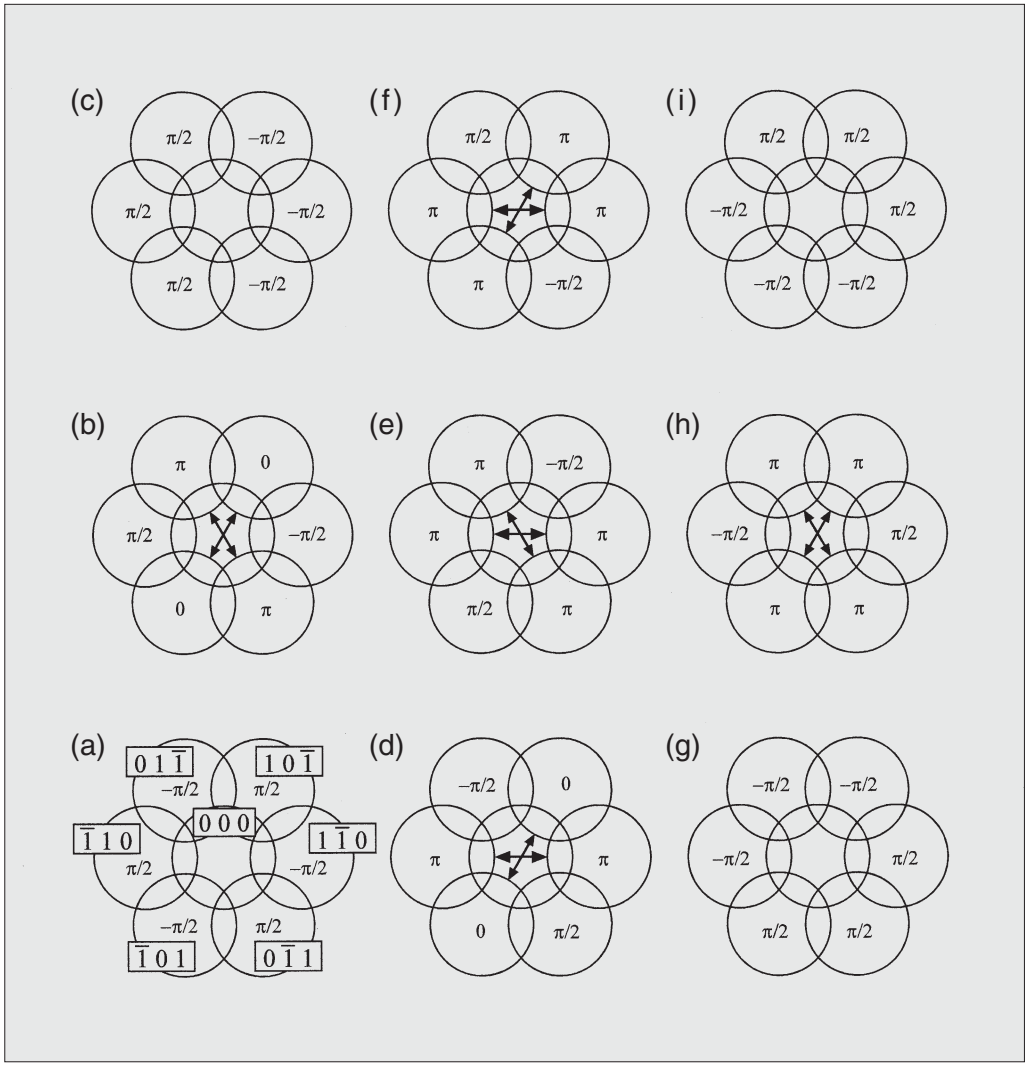

Simulations

Figures (a) to (i) show coherent CBED simulation patterns for the model of $I2_13$, calculated under the kinematical approximation with the same defocus condition as that of the $I23$ case at the probe positions of "a" to "i" illustrated on the previous page. The pairs of the overlapping areas with symmetric fringes with respect to the center of the incident beam are indicated by pairs of arrows. In contrast to the case of $I23$, there are no patterns that have three such pairs, but only two such pairs are seen in the case of $I2_13$, indicating the absence of intersection of three perpendicular 2-fold and 2_1-screw axes.

Therefore, the space groups $I23$ and $I2_13$ can be distinguished by using the [111] coherent CBED patterns. That is, if the [111] coherent CBED pattern shows the three pairs of interference fringes in the overlapping regions, and if each of which is symmetric with respect to the center of the incident beam, the space group is $I23$. On the other hand, if the pattern shows only two such pairs, the space group is $I2_13$.

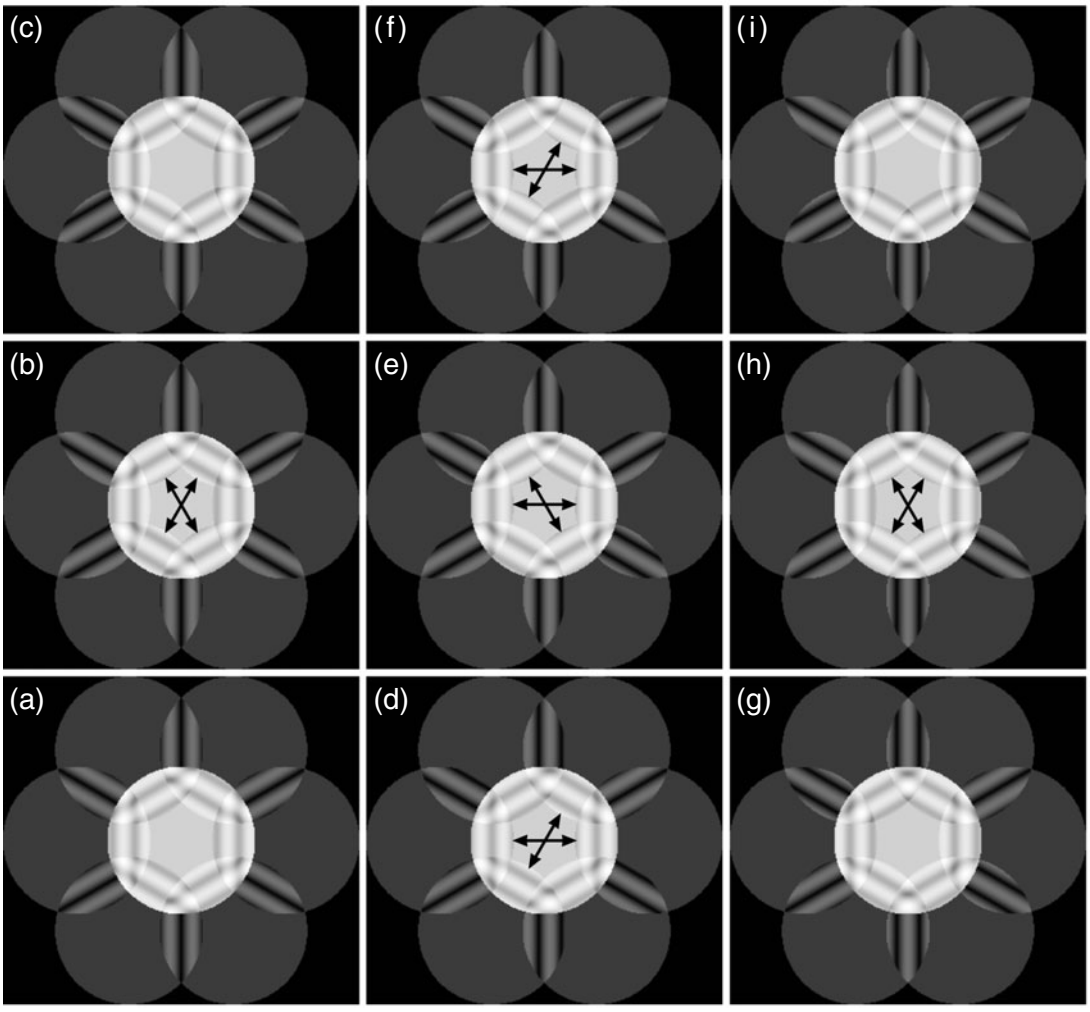

Distinction Between P321 and $P3_121$ ($P3_221$)

Arrangement of 2-fold-rotation axes

Figures (a), (b) and (c) schematically show the arrangements of 2-fold axes of space groups $P321$, $P3_121$ and $P3_221$ projected in the [0001] direction, where the lines indicate 2-fold axes. The fractional numbers beside the small arrows indicate fractional coordinates of the 2-fold axes in the [0001] direction. There are three 2-fold axes perpendicular to the [0001] direction, two of which form an angle of 120 degrees. The three 2-fold axes are at the same height in the [0001] direction for $P321$. The corresponding three 2-fold axes are separated by c = 1/6 in the [0001] direction with a 120° clockwise rotation for $P3_121$ and with a 120° counter-clockwise rotation for $P3_221$. Since the three space-groups have the same arrangement of the three 2-fold axes when they are projected in the [0001] direction, the space groups cannot be distinguished in this projection.

Figures (d), (e) and (f) respectively show the arrangements of the 2-fold axes of space groups $P321$, $P3_121$ and $P3_221$ projected in the $[11\bar{2}3]$ direction. In this projection, the arrangements of the three 2-fold axes are different in the three space groups. $P321$ has points where the three 2-fold axes intersect (“a”, “c”, “g” and “i”). $P3_121$ and $P3_221$ do not have such points but have points where only two of the three 2-fold axes intersect (“a” to “l”). Conventional CBED patterns taken at $[11\bar{2}3]$ incidence do not show any symmetry because these 2-fold axes are neither parallel nor perpendicular to the incident beam. Coherent CBED, however, shows different symmetries for $P321$, $P3_121$ and $P3_221$, allowing us to distinguish them at the incidence. It is noted that $P3_121$ cannot be distinguished from $P3_221$ because the coherent CBED patterns of both the space groups show the same symmetry. The distinction between such enantiomorphous space-group pairs can be made by a different method [1], [2], [3].

[0001] projection

(a)

***P*321**

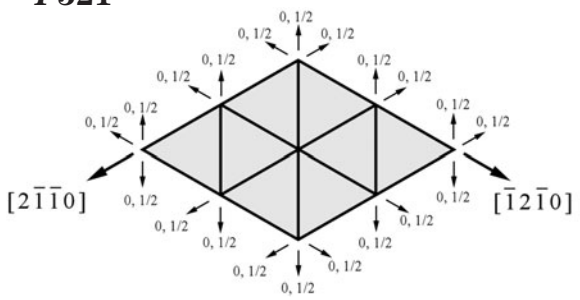

(b)

***P*3$_1$21**

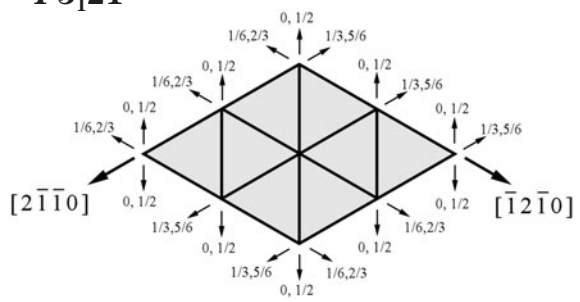

(c)

***P*3$_2$21**

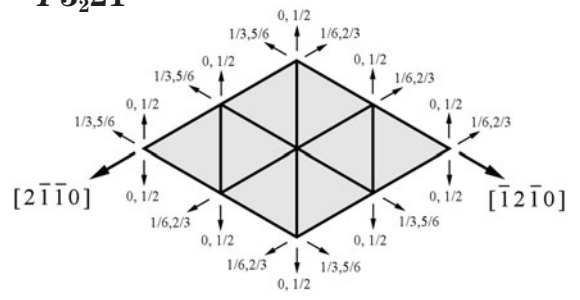

[11$\bar{2}$3] projection

(d)

***P*321**

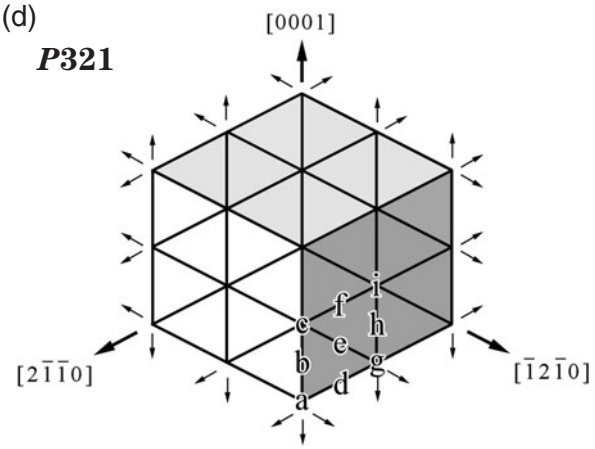

(e)

***P*3$_1$21**

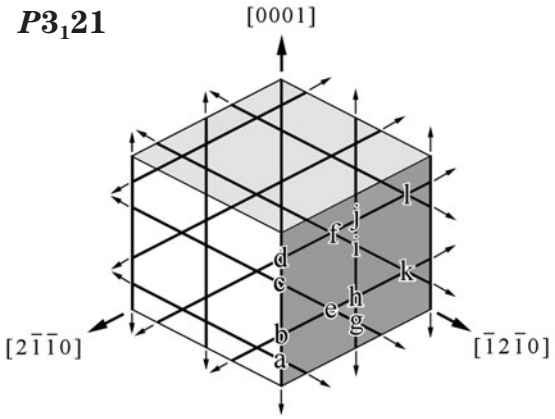

(f)

***P*3$_2$21**

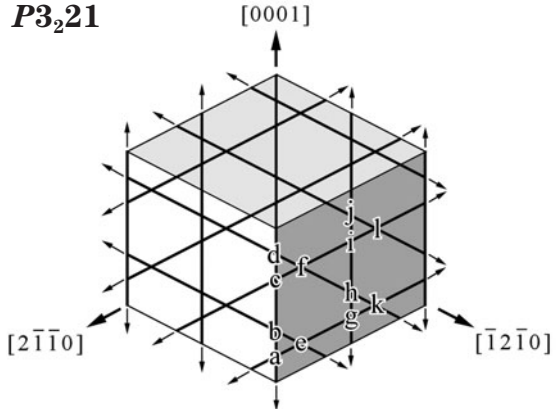

Coherent CBED patterns of *P*321

Phases of structure factors

Figures (a) to (i) show the phases of the kinematical crystal structure factors of reflections for a structure model of *P*321 at the probe positions of "a" to "i" illustrated in the right figure, respectively. The model structure has lattice parameters of a = 0.4nm and c = 0.8nm, and is composed of the atoms whose positions are generated from general positions given in the table by the symmetry operations of space group *P*321. It should be noted that, when the probe is placed on the 2-fold axis, the structure factors of the reflections $\boldsymbol{g}$ and $-\boldsymbol{g}$ perpendicular to the axis have the same phase as already seen in the cases of *I*23 and $I2_13$.

Lattice parameters a = 0.4nm and c = 0.8nm		
Site	Position (x, y, z)	Element
6g	(0.18, 0.20, 0.15)	Si
6g	(0.25, 0.10, 0.05)	C

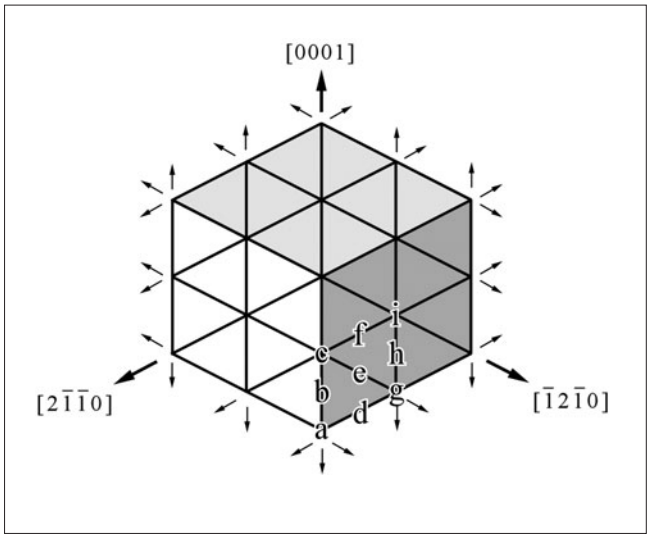

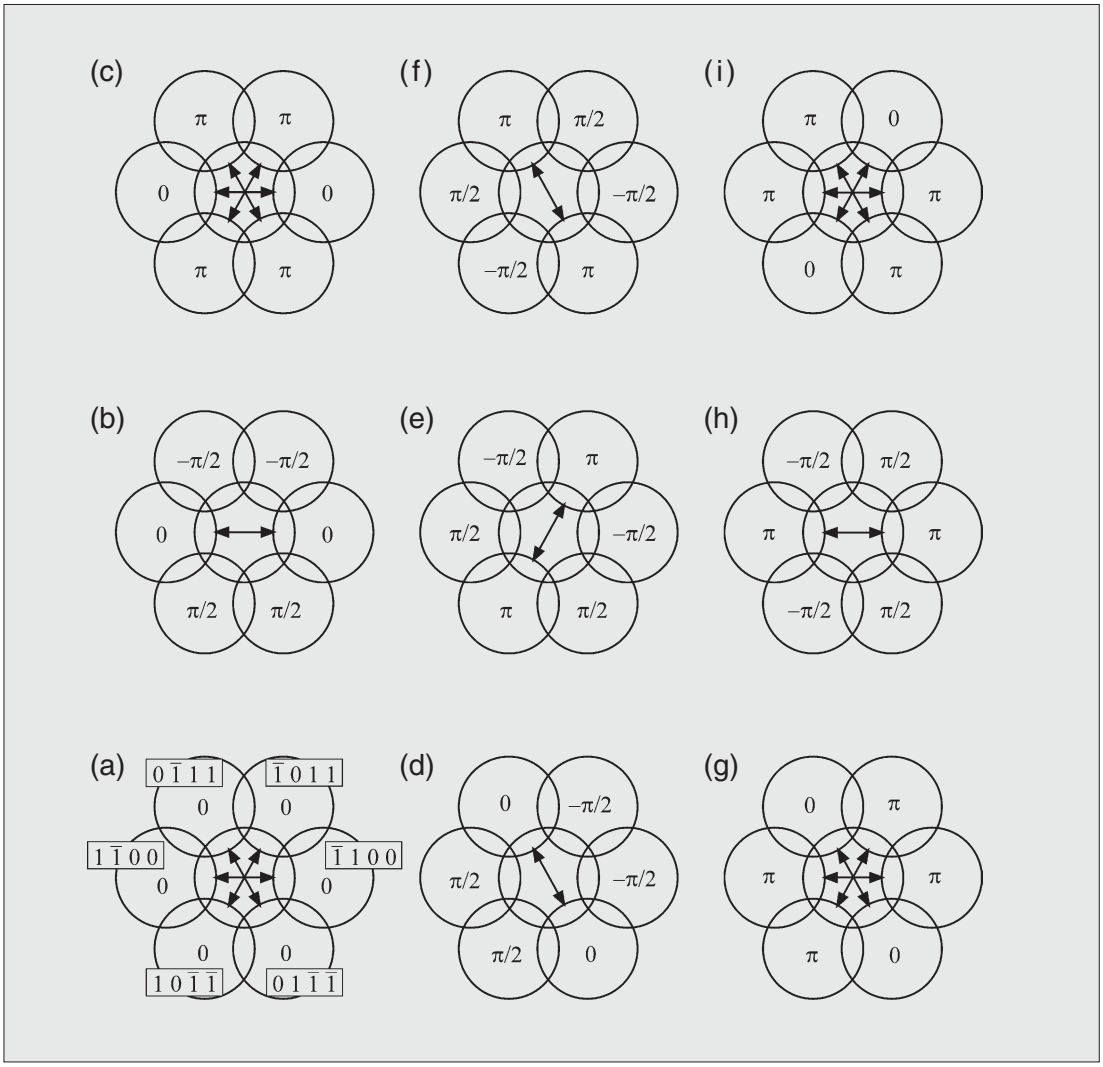

Simulations

Figures (a) to (i) show coherent CBED simulation patterns for the model of *P*321 under the kinematical approximation with a certain defocus of the illumination at the probe positions of “a” to “i” in the figure on the previous page, respectively. At positions “a”, “c”, “g” and “i”, three sets of mirror symmetry appear, clarifying that these positions are the intersection points of the three 2-fold axes.

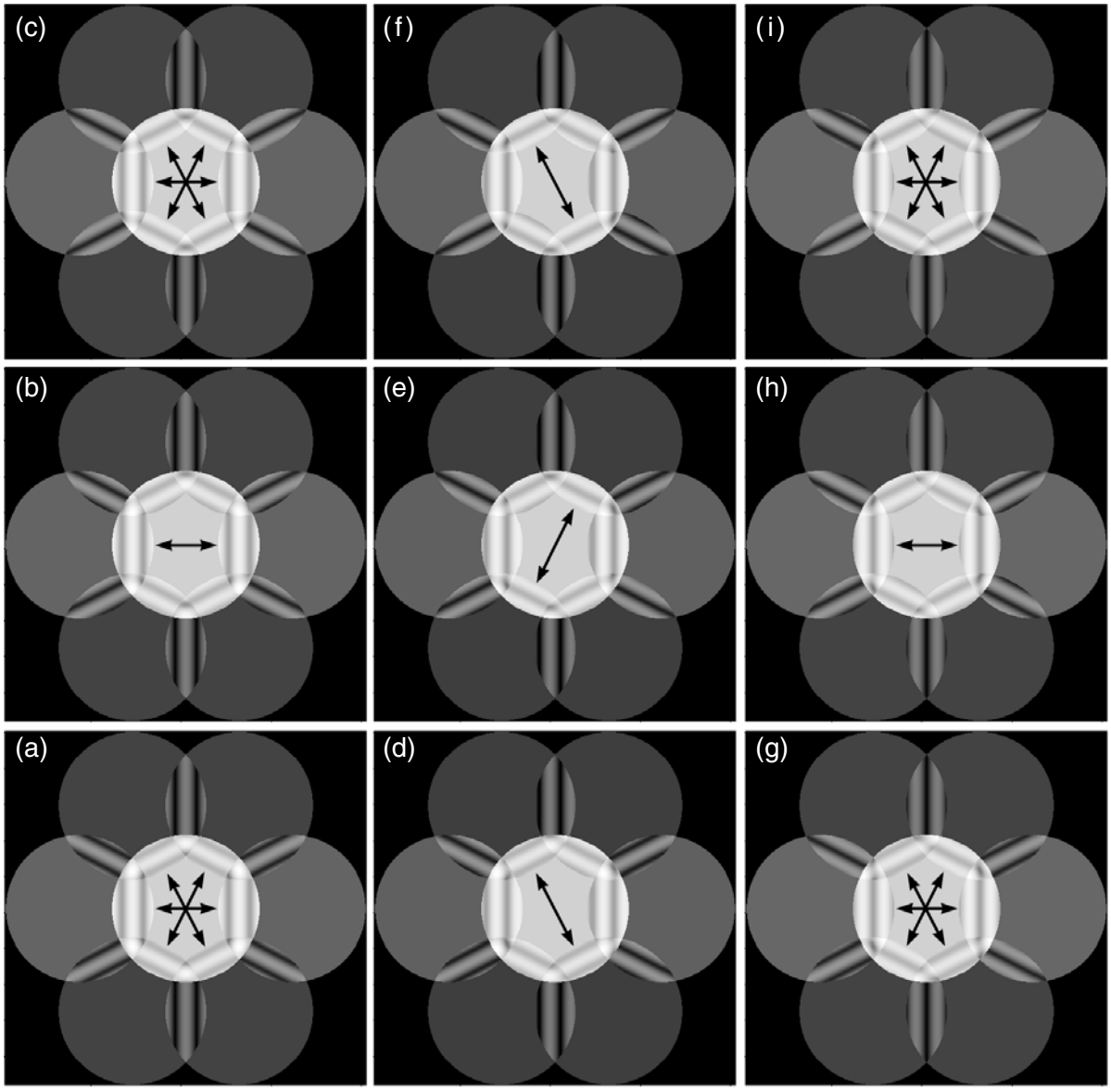

Coherent CBED patterns of $P3_121$

Phases of structure factors

Figures (a) to (l) show the phases of the kinematical crystal structure factors of reflections for a structure model of $P3_121$ at the probe positions of "a" to "l" illustrated in the right figure, respectively. The atomic positions of the model structure are given in the table. By referring to the right figure, the phases of the reflections $\pm\boldsymbol{g}$ perpendicular to a 2-fold axis are the same when the probe is located on the positions of "a" to "l".

Lattice parameters a = 0.4nm and c = 0.8nm		
Site	Position (x, y, z)	Element
6c	(0.18, 0.20, 0.15)	Si
6c	(0.25, 0.10, 0.05)	C

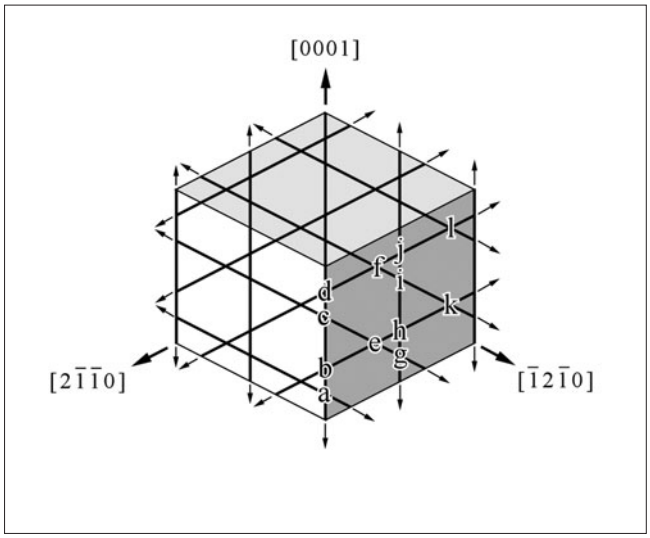

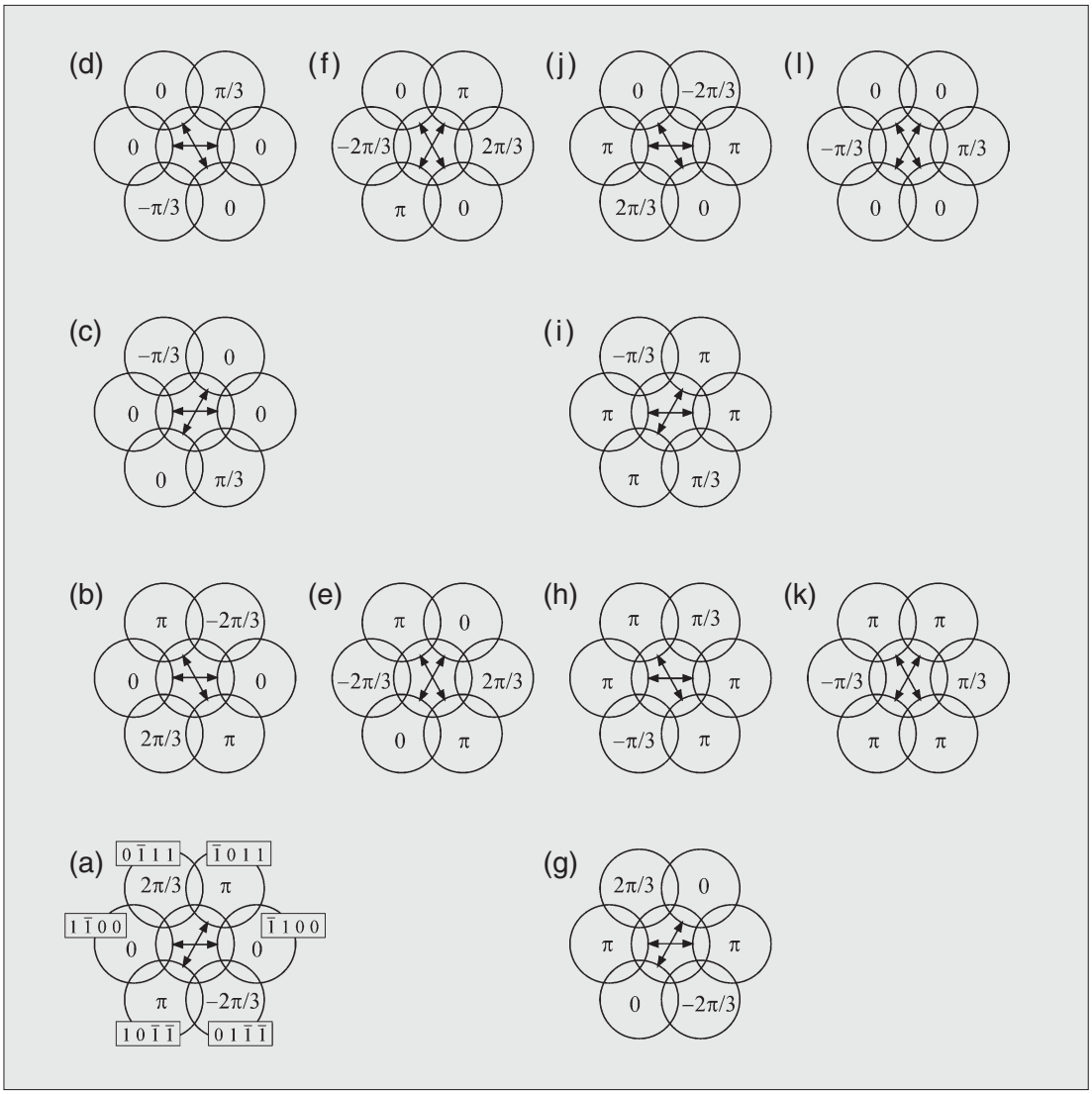

Simulations

Figures (a) to (l) show coherent CBED simulation patterns for the model structure of $P3_121$ calculated under the same condition as that for $P321$ respectively at the probe positions of "a" to "l" in the figure on the previous page. Two of the three fringe pairs show mirror symmetry, but the rest of them does not show mirror symmetry.

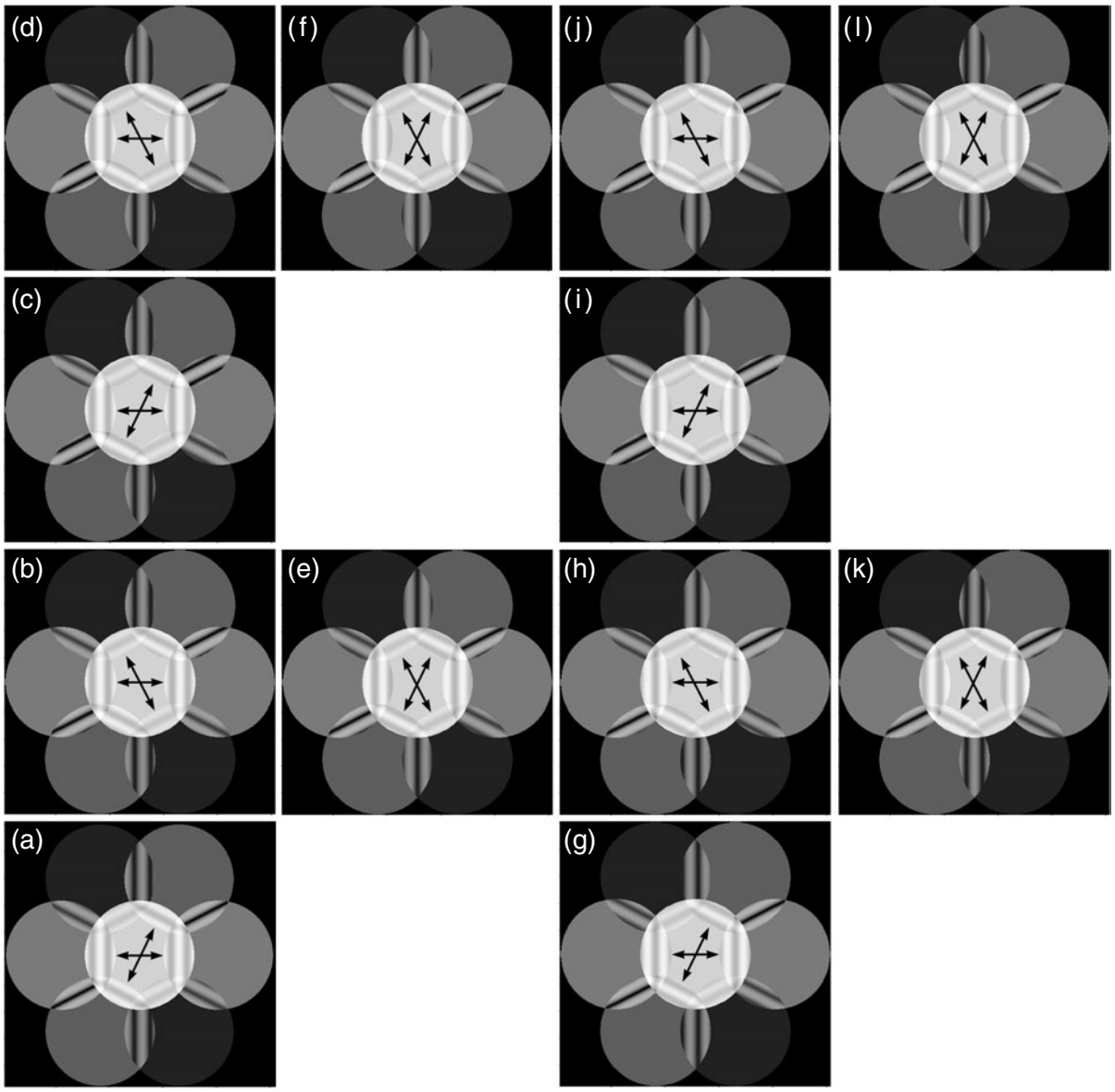

Coherent CBED patterns of $P3_221$

Phases of structure factors

Figures (a) to (l) show the phases of the kinematical crystal structure factors of reflections for a structure model of $P3_221$ at the probe positions of "a" to "l" illustrated in the right figure, respectively. The model structure is given in the table. By referring to the right figure, the phases of the reflections $\pm\boldsymbol{g}$ perpendicular to a 2-fold axis are the same when the probe is located on the positions of "a" to "l".

Lattice parameters a = 0.4nm and c = 0.8nm		
Site	Position (x, y, z)	Element
6c	(0.18, 0.20, 0.15)	Si
6c	(0.25, 0.10, 0.05)	C

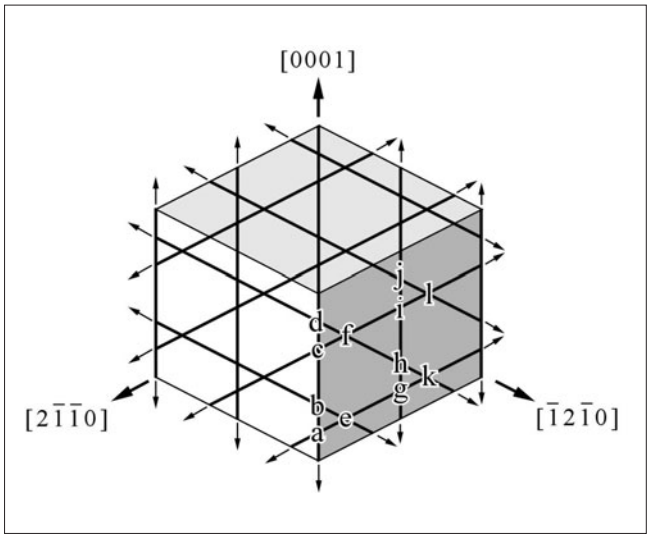

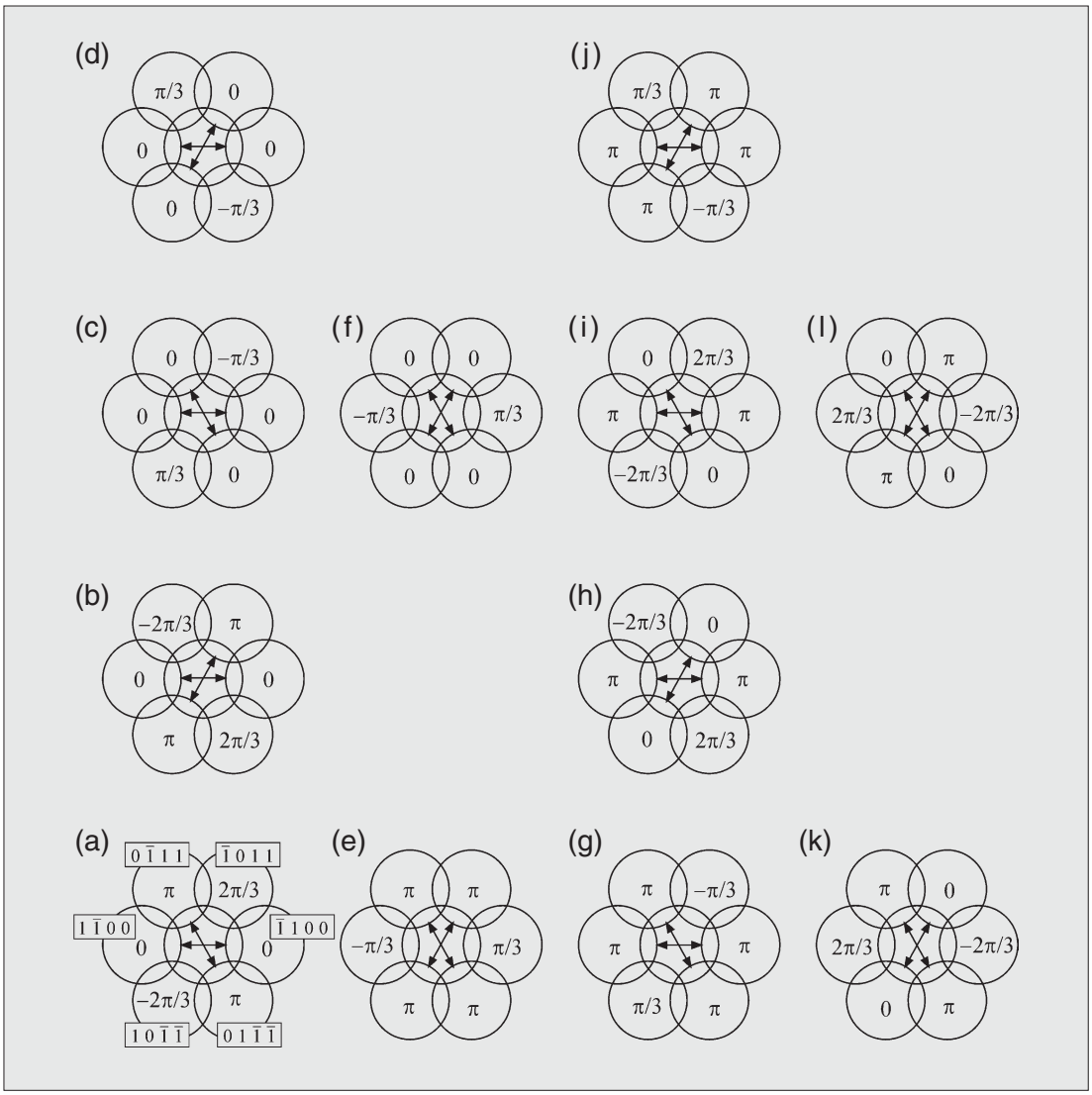

Simulations

Figures (a) to (l) show coherent CBED simulation patterns for the model structure of $P3_221$ at the probe positions of "a" to "l" in the figure on the previous page. Only two of the three fringe pairs show mirror symmetry as well as those of $P3_121$, clarifying that the two 2-fold axes intersect at those positions.

Therefore, space group $P321$ can be distinguished from $P3_121$ and $P3_221$ by using the $[11\bar{2}3]$ coherent CBED patterns. That is, if the pattern shows three sets of mirror symmetry, the space group is $P321$. On the other hand, if the pattern shows only two sets of mirror symmetry, the space group is $P3_121$ or $P3_221$.

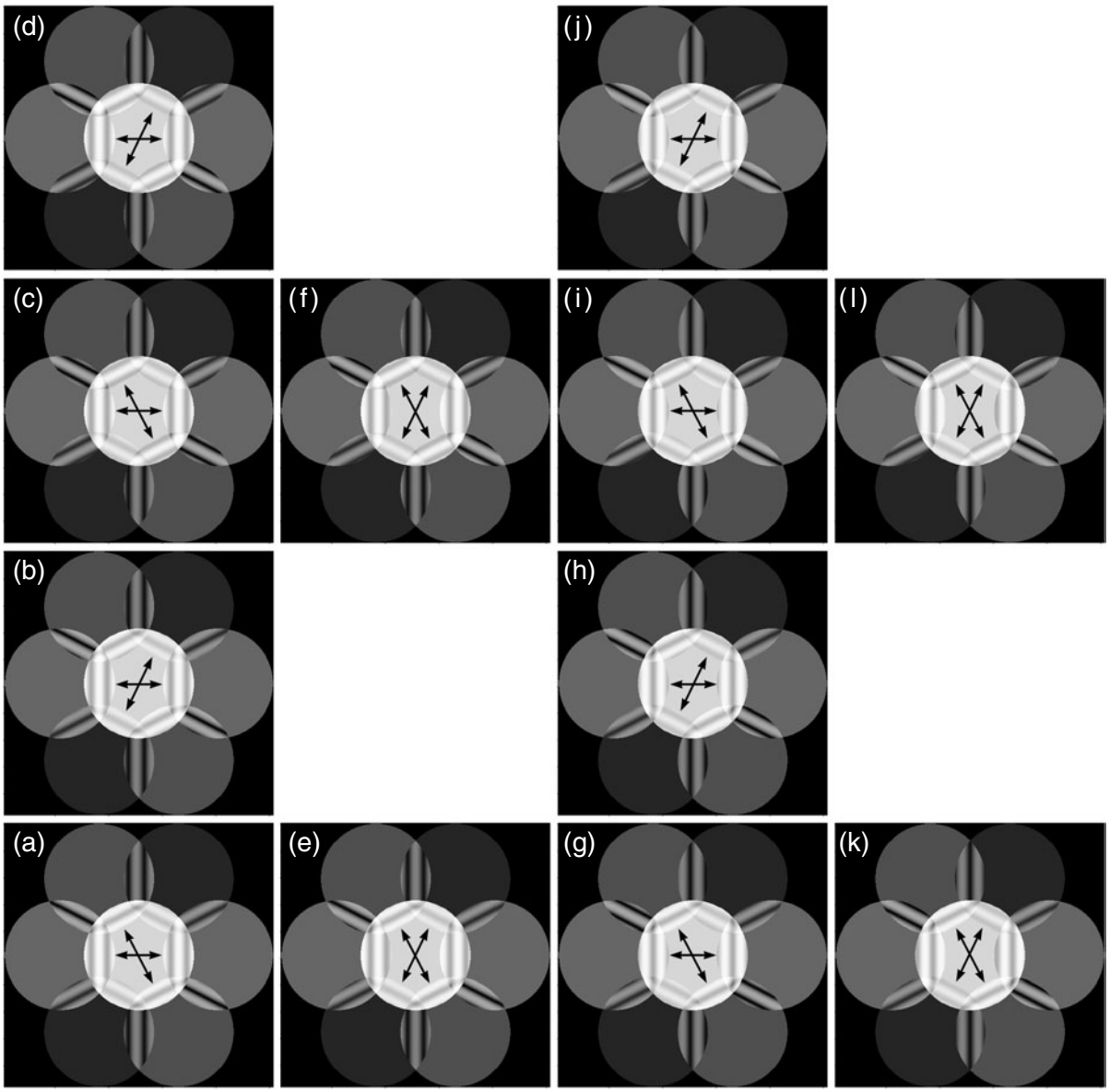

Retrieval of the Intersection Characteristics of the 2-Fold-Rotation Axes

In the distinction procedures already described, the probe has to be located at the points where multiple numbers of 2-fold and/or 2_1-screw axes intersect. We describe a retrieval procedure of the intersection characteristics of the 2-fold and 2_1-screw axes from one coherent CBED pattern taken at a probe position where the 2-fold or 2_1-screw axes do not intersect. The space-group pair of No.15 ($I422$, $I4_122$) is taken as an example. The model structures are given in the tables presented at the bottom of this page. Figures (a) and (b) respectively show the arrangements of the 2-fold and 2_1-screw axes of $I422$ and $I4_122$ in the [111] projection, which are observable when three reflection pairs $(01\bar{1}, 0\bar{1}1)$, $(10\bar{1}, \bar{1}01)$ and $(1\bar{1}0, \bar{1}10)$ are used to form interference fringes.

Figures (c) and (d) on the right-side page show simulation patterns respectively for the model structures of $I422$ and $I4_122$ under conditions where the probe is positioned neither on 2-fold nor on 2_1-screw axes. Line pairs 1, 2, 3 and 4 are drawn at the peak positions of the fringe pairs with a distance of $|\boldsymbol{g}|$. Lines 1c, 2c, 3c and 4c are respectively drawn parallel to the line pairs 1, 2, 3 and 4 so that each of the lines 1c to 4c passes midway between the corresponding line pairs. Lines 5c to 7c and 8c to 11c are drawn by the same procedure for fringe pairs 5 to 7 and 8 to 11 in the different orientations, respectively. It is seen that there exist the points where the midway lines in the three different orientations intersect. Since the midway lines move as an entire set with the shift of the probe position, the relative positions between the lines in different orientations do not change. The intersection characteristics of the 2-fold and 2_1-screw axes are always seen somewhere in the pattern irrespective of the probe position. In other words, the lines of Fig. (c) express the relative arrangement of the 2-fold and 2_1-screw axes of $I422$ in the [111] projection. Figure (d) shows the arrangements of the midway lines of a simulated coherent CBED patterns for the model of $I4_122$ at a point where the 2-fold or 2_1-screw axes do not intersect. It is seen that three midway lines do not intersect at a point, indicating the space group not being $I422$ but $I4_122$. Thus, space group $I422$ can be distinguished from $I4_122$ by using any single coherent CBED pattern. The other space-group sets can also be distinguished from a single coherent CBED pattern by the same procedure.

[111] projection

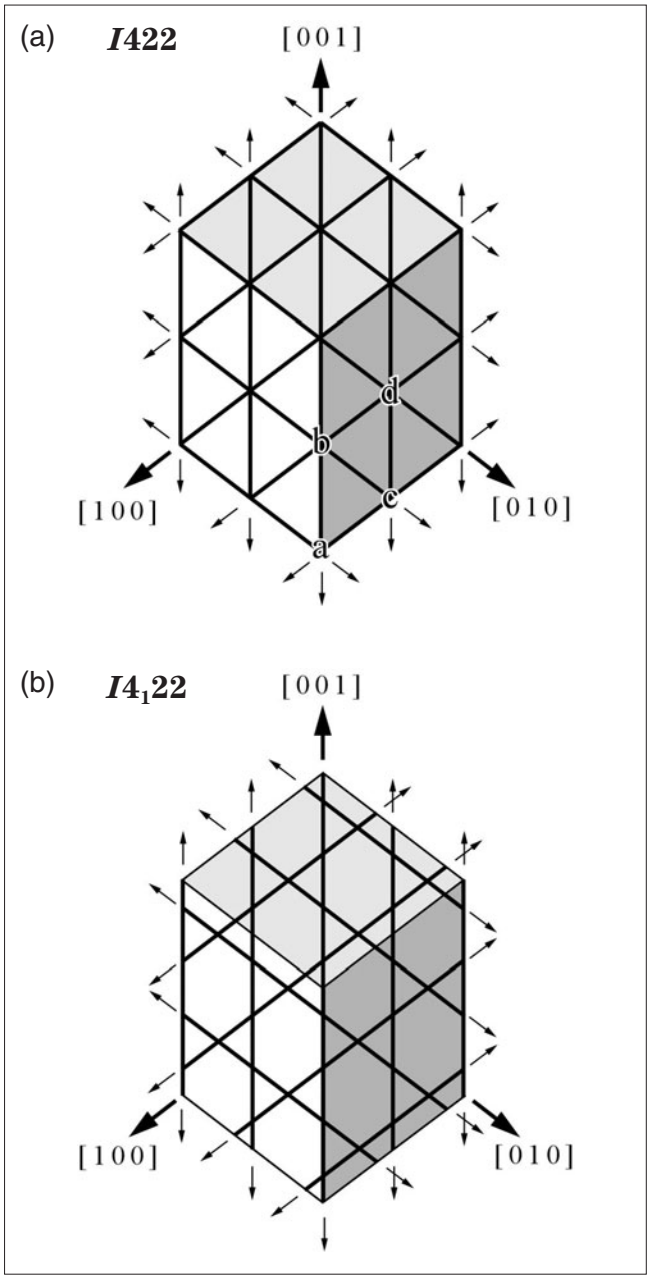

***I*422**

Lattice parameters a = 0.4nm and c = 0.4nm		
Site	Position (x, y, z)	Element
16k	(0.10, 0.15, 0.20)	Si

***I*4$_1$22**

Lattice parameters a = 0.4nm and c = 0.4nm		
Site	Position (x, y, z)	Element
16g	(0.10, 0.15, 0.20)	Si

(c)

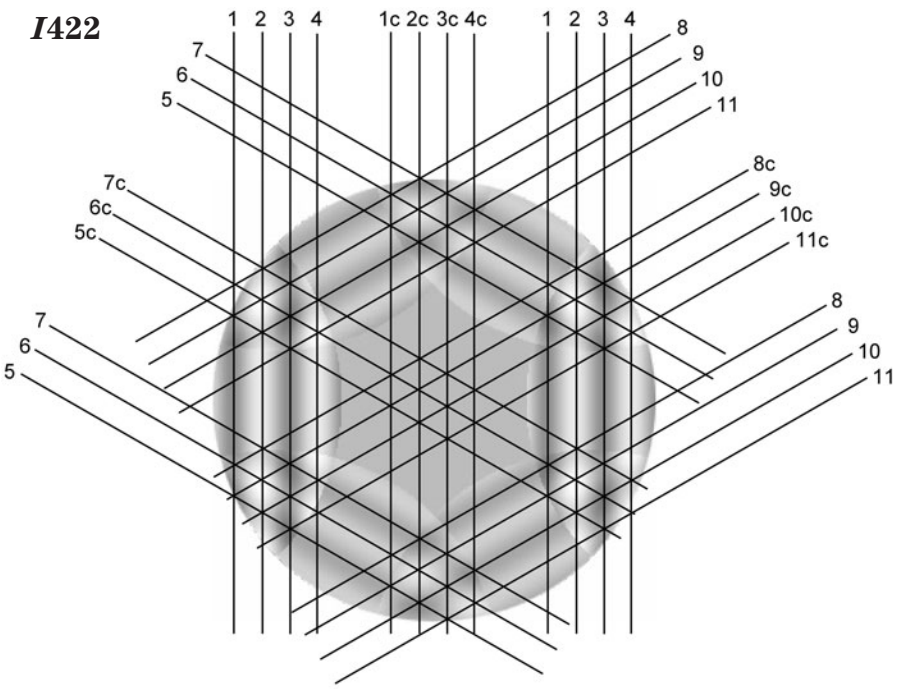
I422
1 2 3 4
1c 2c 3c 4c
1 2 3 4
8
9
10
11
7
6
5
8c
9c
10c
11c
7c
6c
5c
8
9
10
11
7
6
5

(d)

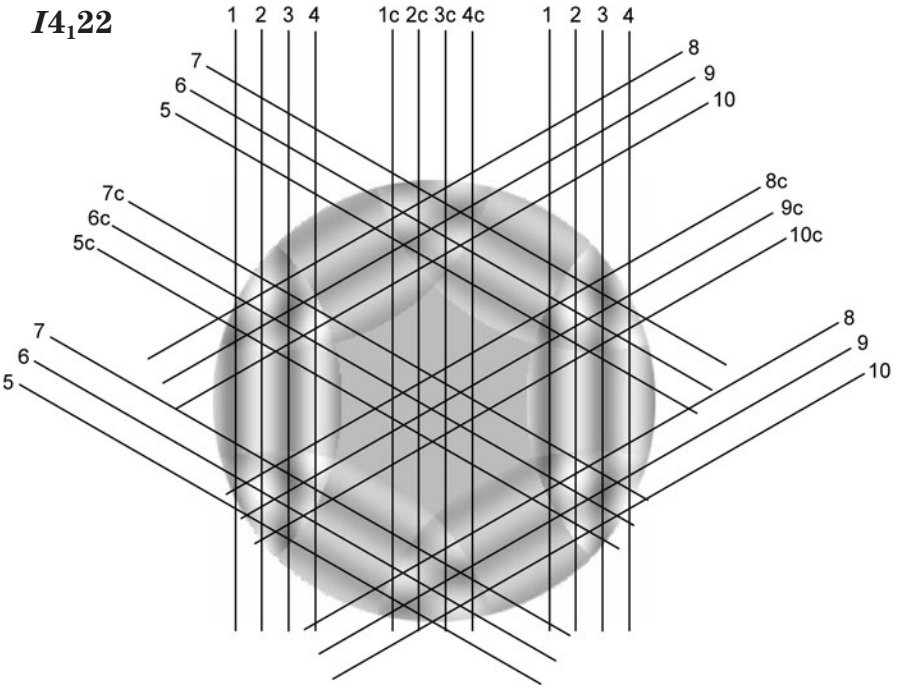
I4₁22
1 2 3 4
1c 2c 3c 4c
1 2 3 4
8
9
10
7
6
5
8c
9c
10c
7c
6c
5c
8
9
10
7
6
5

Many-Wave Interference

The coherent CBED method thus far allows us to distinguish the space groups using interference fringes formed by the transmitted wave and its neighboring reflection waves $\pm\boldsymbol{g}$. Unfortunately, some of the possible incidences have relatively high-order indices, which may not be preferable from the experimental viewpoint. Low-order incidences are available for the distinction if we observe interference fringes formed by the transmitted wave and reflected waves which are not neighboring to the transmitted waves.

For example, the [112] incidence is useful for the distinction between $P422$ and $P4_222$. The [112] coherent CBED simulation patterns (a) and (b) for the model structures of $P422$ and $P4_222$ (see the tables) at probe position "a" of the figures are composed of four reflection pairs ($1\bar{1}0$, $\bar{1}10$), ($11\bar{1}$, $\bar{1}\bar{1}1$), ($\bar{2}01$, $20\bar{1}$) and ($0\bar{2}1$, $02\bar{1}$). Figure (a) exhibits four sets of mirror symmetry, confirming the intersection of four perpendicular 2-fold and 2_1-screw axes at probe position "a". Figure (b) shows only three sets of mirror symmetry, indicating the absence of intersection of the fourth 2-fold and 2_1-screw axes.

***P*422**

Lattice parameters a = 0.4nm and c = 0.8nm		
Site	Position (x, y, z)	Element
8p	(0.23, 0.30, 0.15)	Si
8p	(0.08, 0.12, 0.05)	C

***P*4$_2$22**

Lattice parameters a = 0.4nm and c = 0.8nm		
Site	Position (x, y, z)	Element
8d	(0.18, 0.25, 0.15)	Si
8d	(0.07, 0.15, 0.05)	C

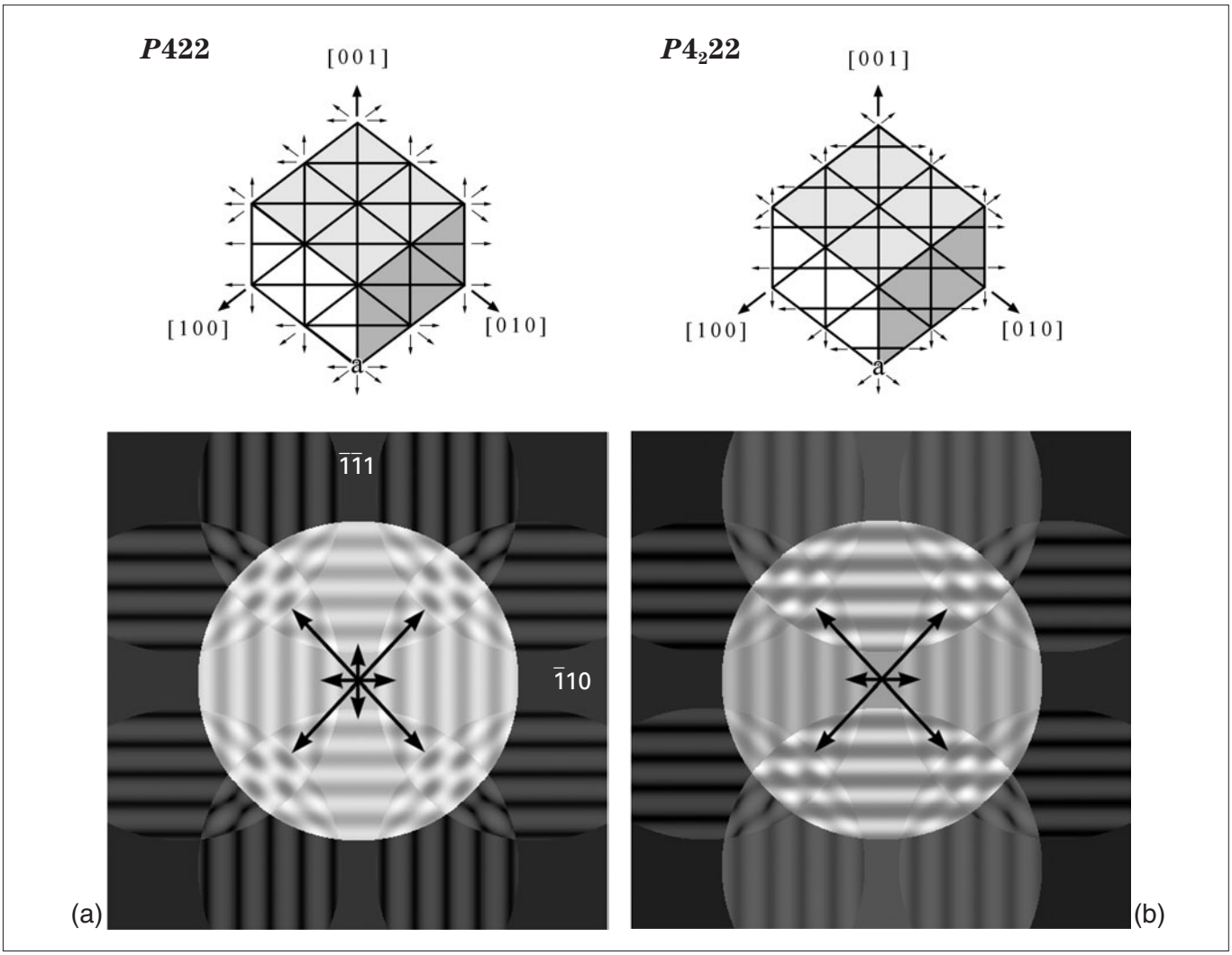

Space Groups Distinguishable by Coherent CBED

The electron incidences available for distinguishing the space-group sets already described are summarized in the following table. The indices with an asterisk indicate the incidences at which differentiation is performed by many-wave interference. Experimental proof should be carried out in the future.

Space-group set	Incidence
No.2 $P312$, ($P3_112$, $P3_212$)	$[1\bar{1}01]$
No.3 $P321$, ($P3_121$, $P3_221$)	$[11\bar{2}3]$
No.5 $P622$, ($P6_222$, $P6_422$)	$[11\bar{2}3]$
No.7 $P6_322$, ($P6_122$, $P6_522$)	$[11\bar{2}3]$
No.12 $P422$, $P4_222$	[321], [211], [112]*
No.13 $P42_12$, $P4_22_12$	[211]
No.15 $I422$, $I4_122$	[111]
No.16 $I23$, $I2_13$	[111]
No.17 $I222$, $I2_12_12_1$	[111]
No.18 $P432$, $P4_232$	[321], [211]*
No.20 $I432$, $I4_132$	[111]
No.21 $F432$, $F4_132$	[432]

12 spece-group sets distinguishable by coherent CBED.

Energy Filtering

Instrumentation

Energy filtering to remove the intensities of inelastically scattered electrons is now becoming indispensable for quantitative analysis of CBED patterns. Tanaka and Tsuda [a] demonstrated using a magnetic prism-type energy-filter that removal of plasmon-loss electrons is very important to compare the experimental intensity with the theoretical intensity. Furthermore, simultaneous energy filtering of both ZOLZ and HOLZ reflections is necessary for the high precision refinement of structural parameters.

We developed a 200kV Ω-filter electron microscope under a project (1994–1997) supported by a Grant-in-Aid for Specially Promoted Research of the Ministry of Education, Science, Sports and Culture of Japan. The microscope was manufactured with JEOL under the name of JEM-2010FEF based on the JEM-2010F already on the market. The microscope is aimed at not only taking energy-filtered ZOLZ and HOLZ CBED patterns but also achieving the highest performance in high resolution imaging, element mapping, energy dispersive X-ray analysis, etc.

Photographs on the right-side page show the column (a) and the console (b) of the JEM-2010FEF installed in our laboratory. The microscope has a field-emission gun (FEG), an Ω-filter, a high-definition TV instead of a fluorescent screen, a Peltier-cooled slow-scan CCD camera, a TV-rate camera and imaging plates together with standard films as the recording system. To avoid the mechanical vibration from outside, an active vibration cancellation system is integrated into the mount of the microscope.

The FEG is of a Schottky type with a ZrO/W(100) emitter. Its brightness is 4×10^8A/cm^{2}sr at an accelerating voltage of 200kV. The gun enables us to take electron diffraction patterns, energy-loss spectra and energy-dispersive X-ray spectra from a 0.5nm diameter area on a specimen with the use of an objective lens polepiece with C_s = 0.5mm and C_c = 1.1mm. The spatial resolutions of the microscope for the point image and the lattice image are 0.19nm and 0.1nm, respectively. The performance of the Ω-filter is described on the following pages.

For observing diffraction patterns and microscope images, the high-definition TV is used instead of a traditional fluorescent screen. To correct the astigmatism of the objective lens for high resolution microscopy, the TV-rate camera is used. Diffraction patterns and microscope images are taken digitally by the slow-scan CCD camera. We use the CCD camera for qualitative studies. We use imaging plates for quantitative analysis of CBED patterns because the imaging plate is advantageous to take a large-size picture like a CBED pattern containing HOLZ reflections, and has a wide dynamic range, nearly free from the point-spread function and the positional fluctuations of detection efficiency. These advantages are often very useful for compensating for its off-line use. Observation and recording can be carried out in a bright room, which has brought a great innovation into electron microscopy.

The microscope is entirely controlled from the console part which is separated from the column part, except manual setting of the specimen holder. All lens currents are controlled digitally from the computer. Specimen positioning is operated by a tracker ball on the console. All apertures are positioned by analog motors which are controlled from the console. Thus, the microscope column and the console are not necessary to be placed in the same room, enabling the microscope to be controlled from a separate room. Therefore, the present microscope has opened a way of remote control and simultaneous observation of microscope images at many distant places (Fig. (c)). Such a remote control system has recently been commercially supplied as FasTEM by JEOL.

Reference

[a] M. Tanaka and K. Tsuda: 25th Meeting of Microbeam Analysis Soc., San Jose, 1991, p.145.

Energy-filter TEM

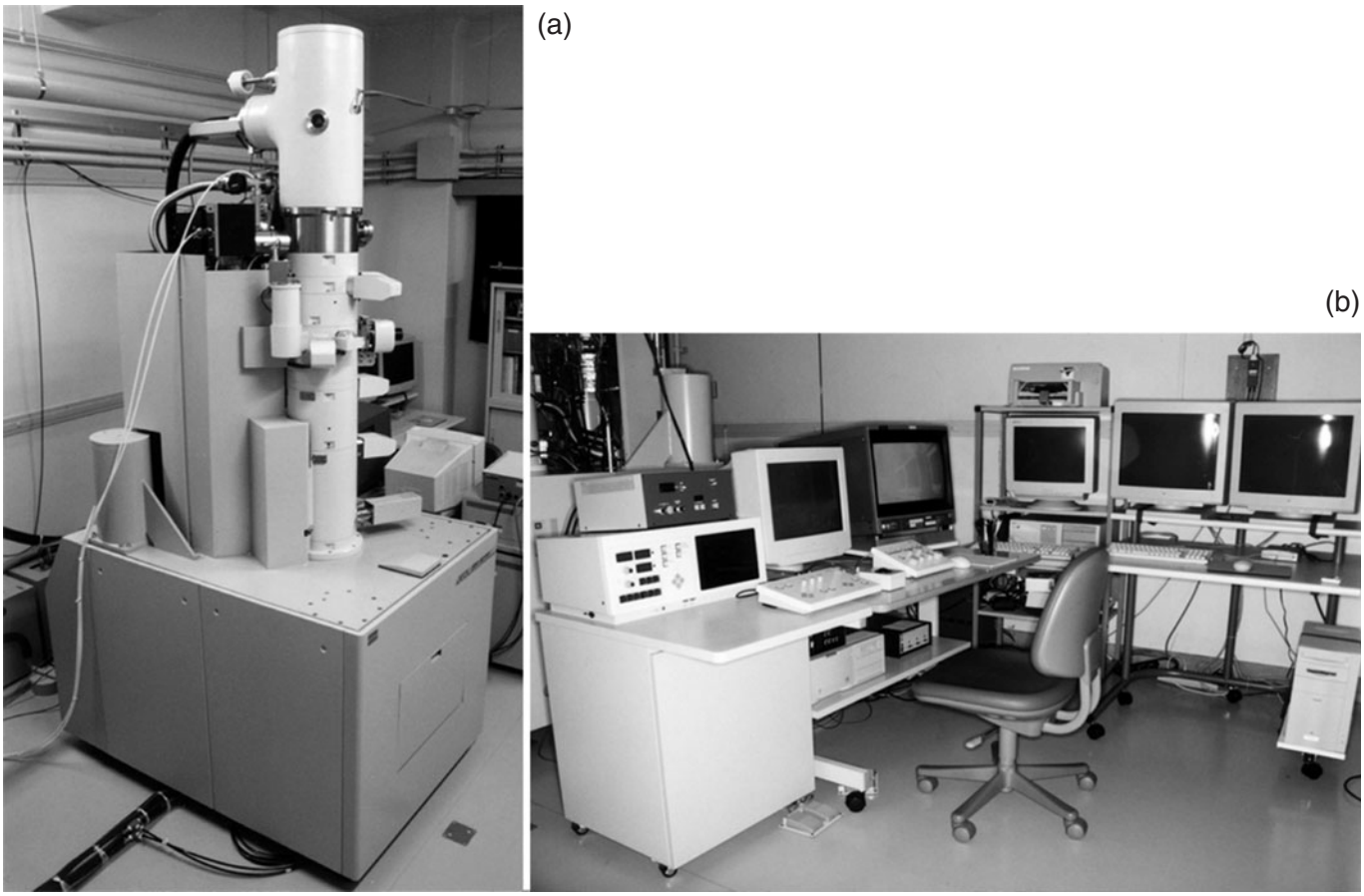

200kV Ω-filter electron microscope JEM-2010FEF. (a) Column part and (b) console part.

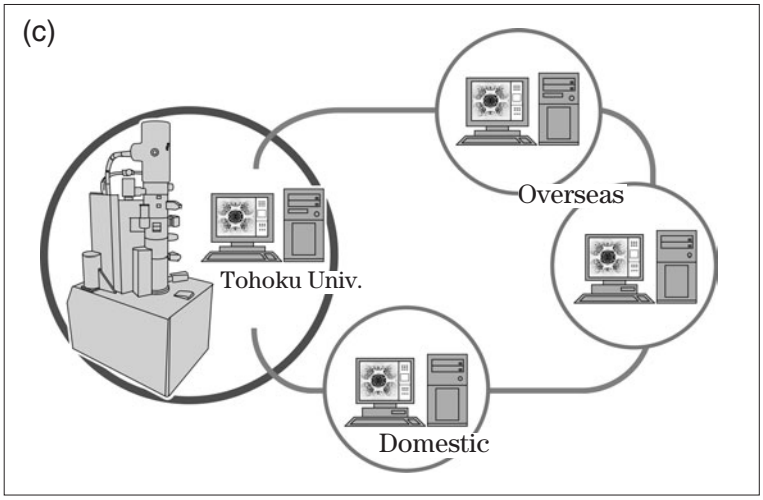

Remote control of the electron microscope and simultaneous observation of microscope images at many distant places.

Energy-filtering system

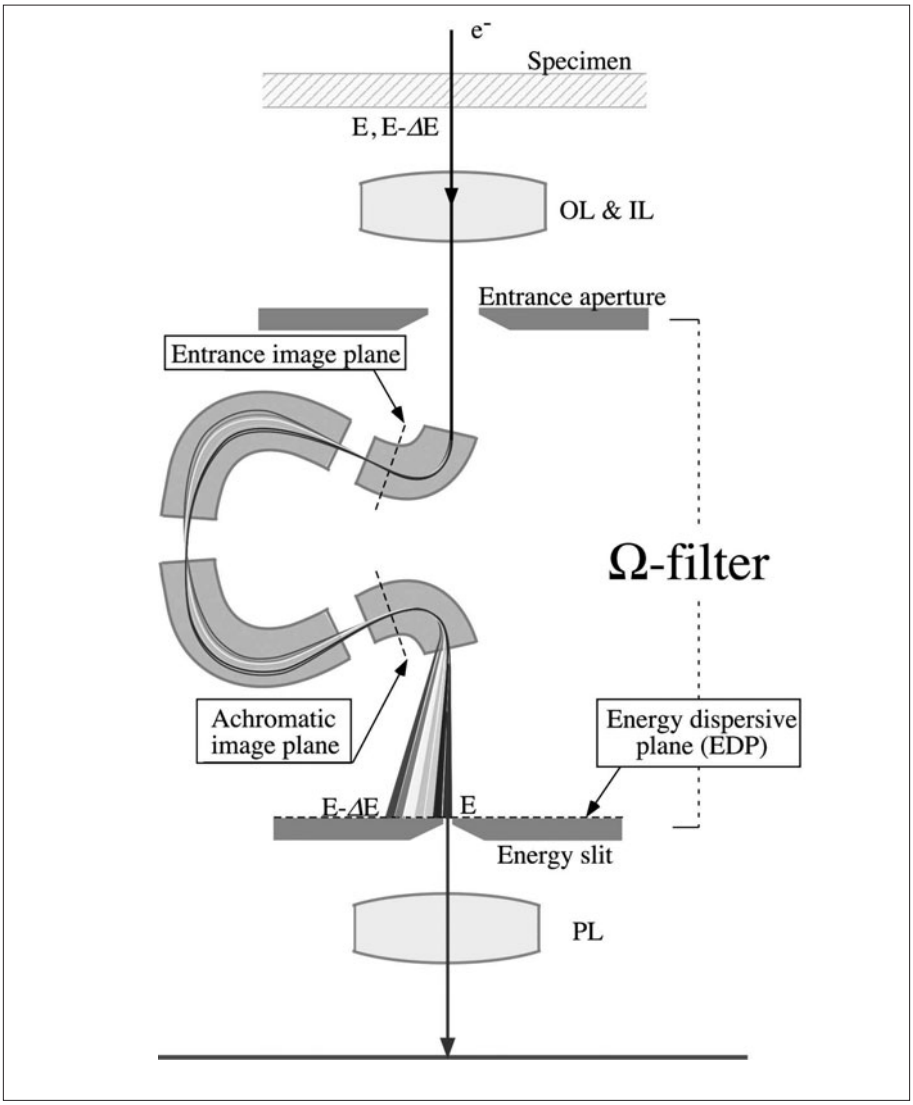

Schematic diagram of the energy-filtering system of the microscope.

Figure shows a schematic diagram of the energy-filtering system of the microscope. The Ω-filter acts as a lens of magnification ×1 with energy dispersion. In the CBED mode, the CBED pattern is formed on the entrance-image plane of the filter, which is the final image plane of the intermediate-lenses, and then the achromatic image (image without energy dispersion) is obtained on a plane conjugate with the entrance-image plane. In this mode, the image of the focused electron probe at the specimen is formed on the entrance-aperture plane and the energy-dispersive plane (EDP). The energy-selection slit is inserted into the EDP to select the electron beam with a definite energy-loss. In order to take zero-loss filtered ZOLZ and HOLZ CBED patterns, the electron-probe image of the zero-loss electrons has to be separated from those of the harmful plasmon-loss electrons at the EDP. This has been achieved by the large energy-dispersion of the Ω-filter and the small C_s of the objective lens. In particular, the latter is very important to reduce the electron-probe size at the EDP because HOLZ reflections have large scattering angles. We have succeeded for the first time in taking zero-loss filtered CBED patterns containing both the ZOLZ and HOLZ reflections at the same time, which are indispensable to the high precision refinement of the structural parameters.

Ω-filter

We designed and manufactured a new Wollnik type Ω-filter. Photograph shows the appearance of the filter. The optical characteristics were described in detail in a paper of Tsuno *et al.* [13]. The filter has energy dispersions of 2.1μm/eV and 1.2μm/eV at accelerating voltages of 100kV and 200kV, respectively. The distortion of the diffraction pattern is corrected to less than 1% by adjusting the balance of electric currents for the upper and lower halves of the filter.

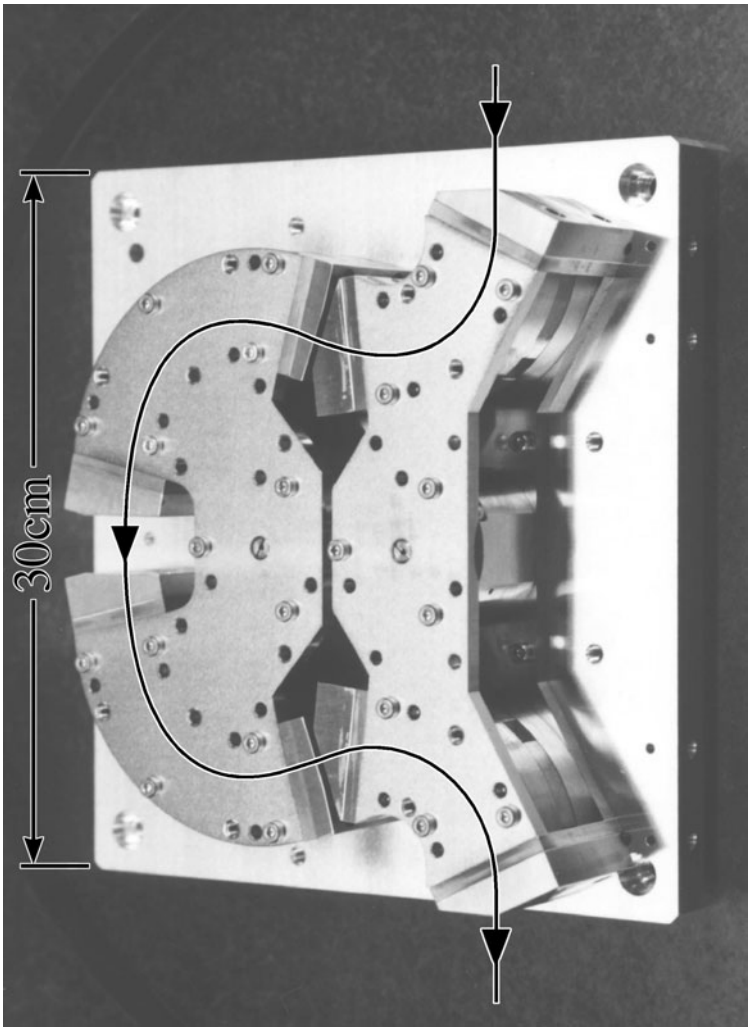

Ω-filter of JEM-2010FEF.

Effectiveness of energy filtering

Cubic BN [110]

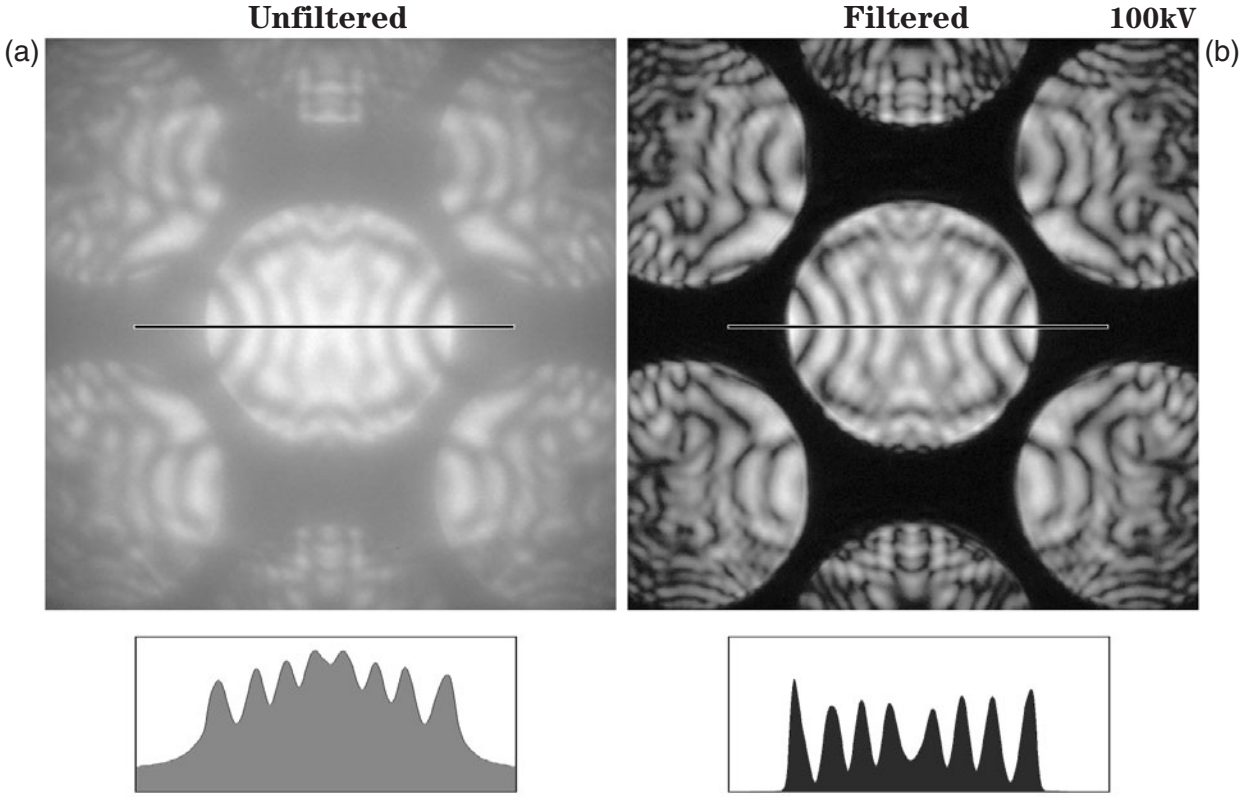

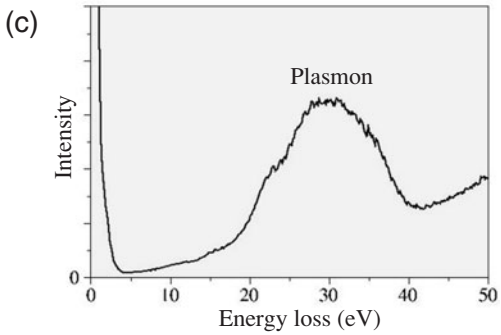

Photographs (a) and (b) respectively show unfiltered and zero-loss filtered CBED patterns of cubic BN taken with the [110] incidence at 100kV and an acceptance energy-width of $\Delta E = \pm 8$eV. Intensity line-profiles along the black lines in Photos (a) and (b) are shown below the patterns. The effect of removing the plasmon-loss intensity is clearly seen. This shows that energy filtering is necessary for quantitative comparison between experimental and theoretical intensities. Figure (c) shows the energy-loss spectrum of the specimen. It is seen that the plasmon-loss intensities can be fully removed by setting the width of the energy-selection slit to $\Delta E = \pm 8$eV.

High-acceptance angle

$LaMnO_3$ [010]

100kV

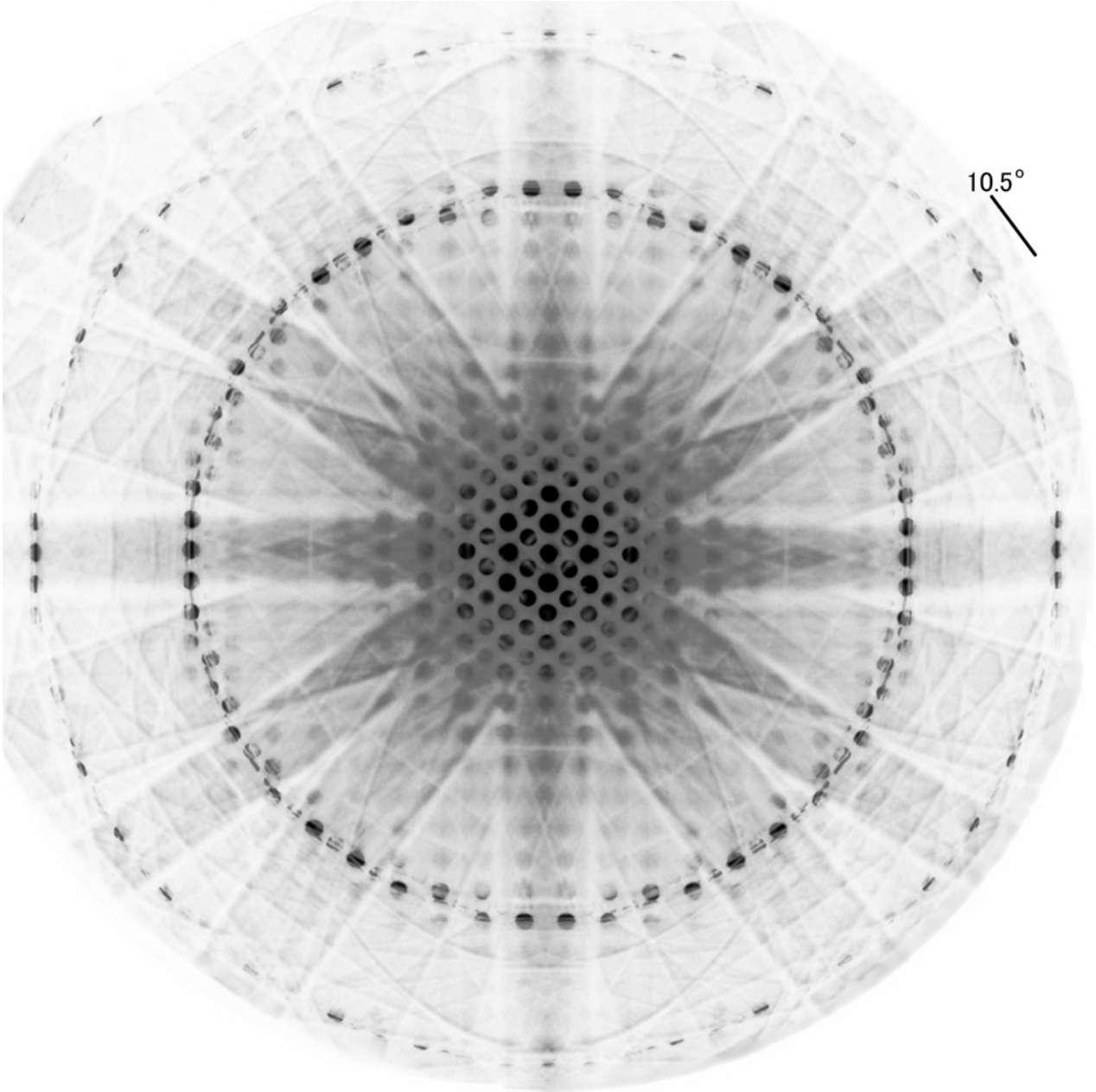

Photograph shows a zero-loss filtered CBED pattern of $LaMnO_3$ [010] taken at 100kV with $\Delta E = \pm 10$eV. The HOLZ reflections are seen together with the ZOLZ reflections. The acceptance angle is about 10° at filtering.

Cubic $BaTiO_3$ [100]

100kV

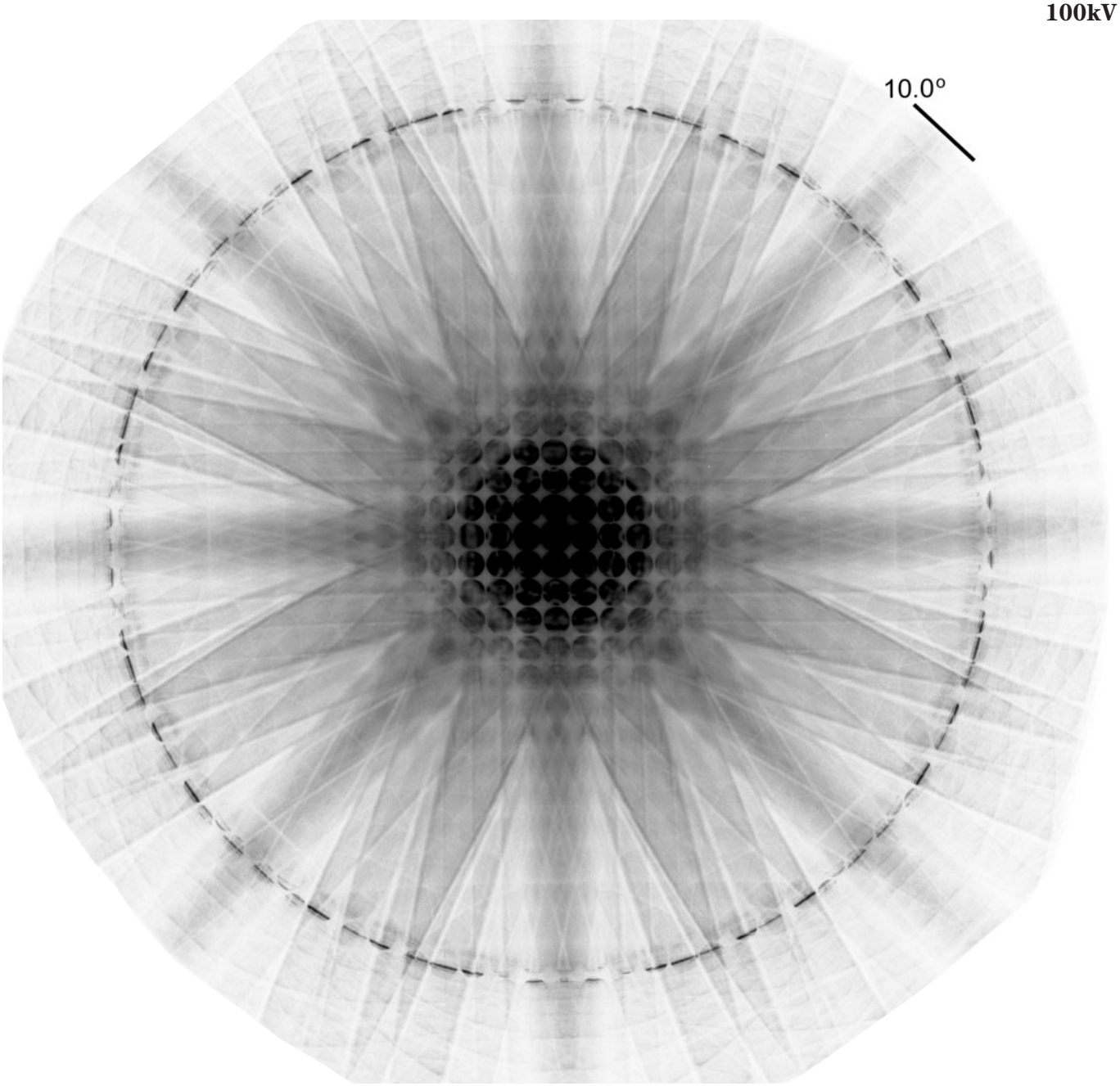

Photograph shows a zero-loss filtered CBED pattern of cubic $BaTiO_3$ [100] taken at 100kV with $\Delta E = \pm 10$eV. The HOLZ reflections are seen together with the ZOLZ reflections. The acceptance angle is about 10° at filtering.

HREM image

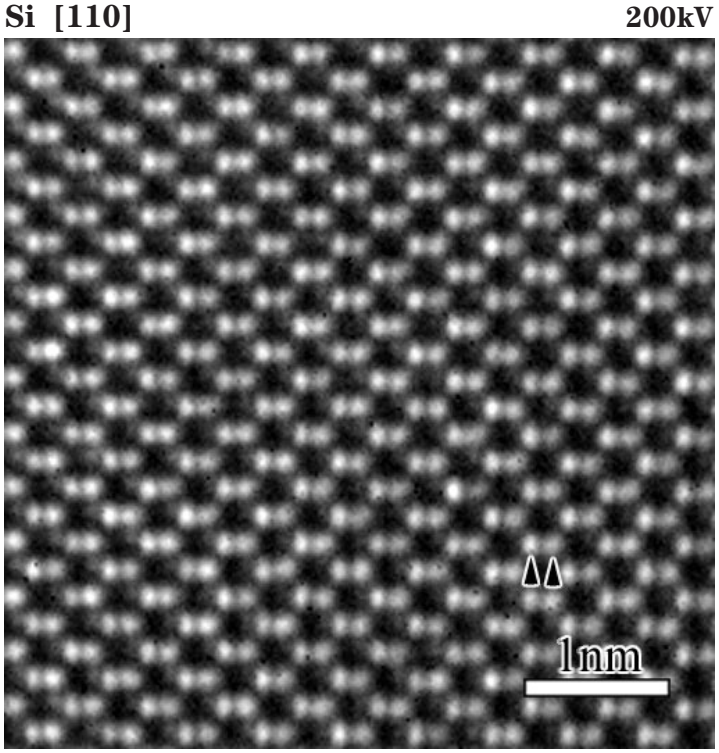

Zero-loss filtered high-resolution image of Si [110] taken at 200kV and $\Delta E = \pm 10$eV.

Photograph shows a zero-loss filtered high-resolution image of Si taken with the [110] incidence at 200kV and acceptance energy $\Delta E = \pm 10$eV. The two light dots of dumbbell-shaped contrasts are clearly resolved as indicated by arrowheads. This shows that the zero-loss filtered image suffers no deterioration of spatial resolution in the Ω-filter.

Element mapping images

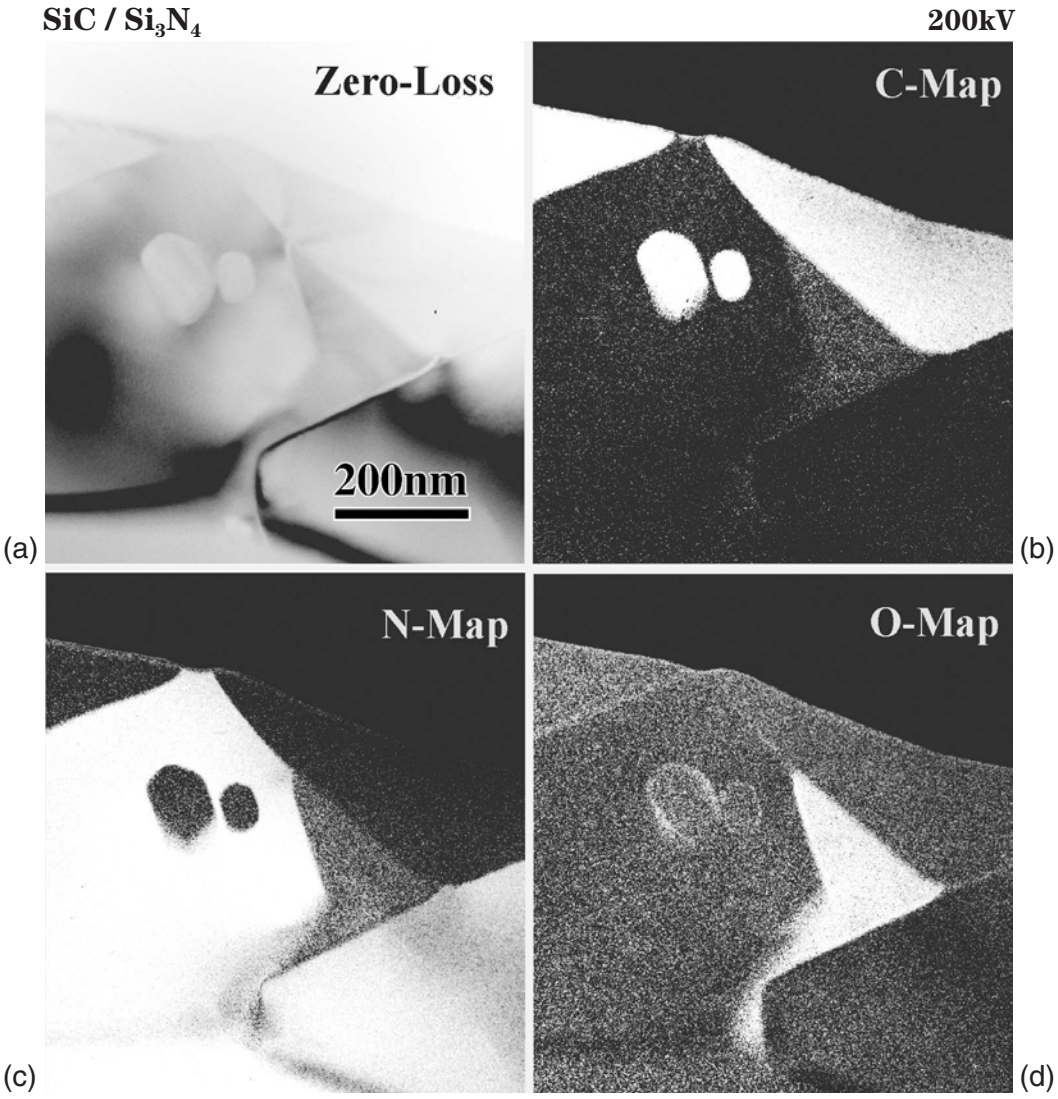

Element mapping images of SiC/Si_3N_4. (a) Zero-loss bright-field image, (b) carbon, (c) nitrogen and (d) oxygen images taken at 200kV and $\Delta E = \pm 15$eV.

Photograph (a) shows a zero-loss bright-field image of a SiC/Si_3N_4 ceramic taken at 200kV with $\Delta E = \pm 15$eV. Photographs (b), (c) and (d) are the element-distribution images of carbon, nitrogen and oxygen taken with $\Delta E = \pm 15$eV. For each element, background subtraction was carried out by the three-window method (e.g. [a]). Oxygen concentrations are clearly seen between the blocks.

Reference

[a] L. Reimer (ed.): Energy-Filtering Transmission Electron Microscopy, Springer-Verlag, 1995.

Energy-Filtered CBED Patterns

The effectiveness of energy filtering is demonstrated on many materials by displaying various energy-filtered pattems together with the energy-loss spectra. Unfiltered and zero-loss filtered patterns are presented. Also, we show plasmon-loss, core-loss and other loss pattems, which were taken by selecting the energy-loss ranges as indicated by the arrows in each spectrum. It is seen that the effect of energy filtering is more conspicuous for the materials composed of light elements. All of the data were taken by the JEM-2010FEF.

Si [111] **100kV**

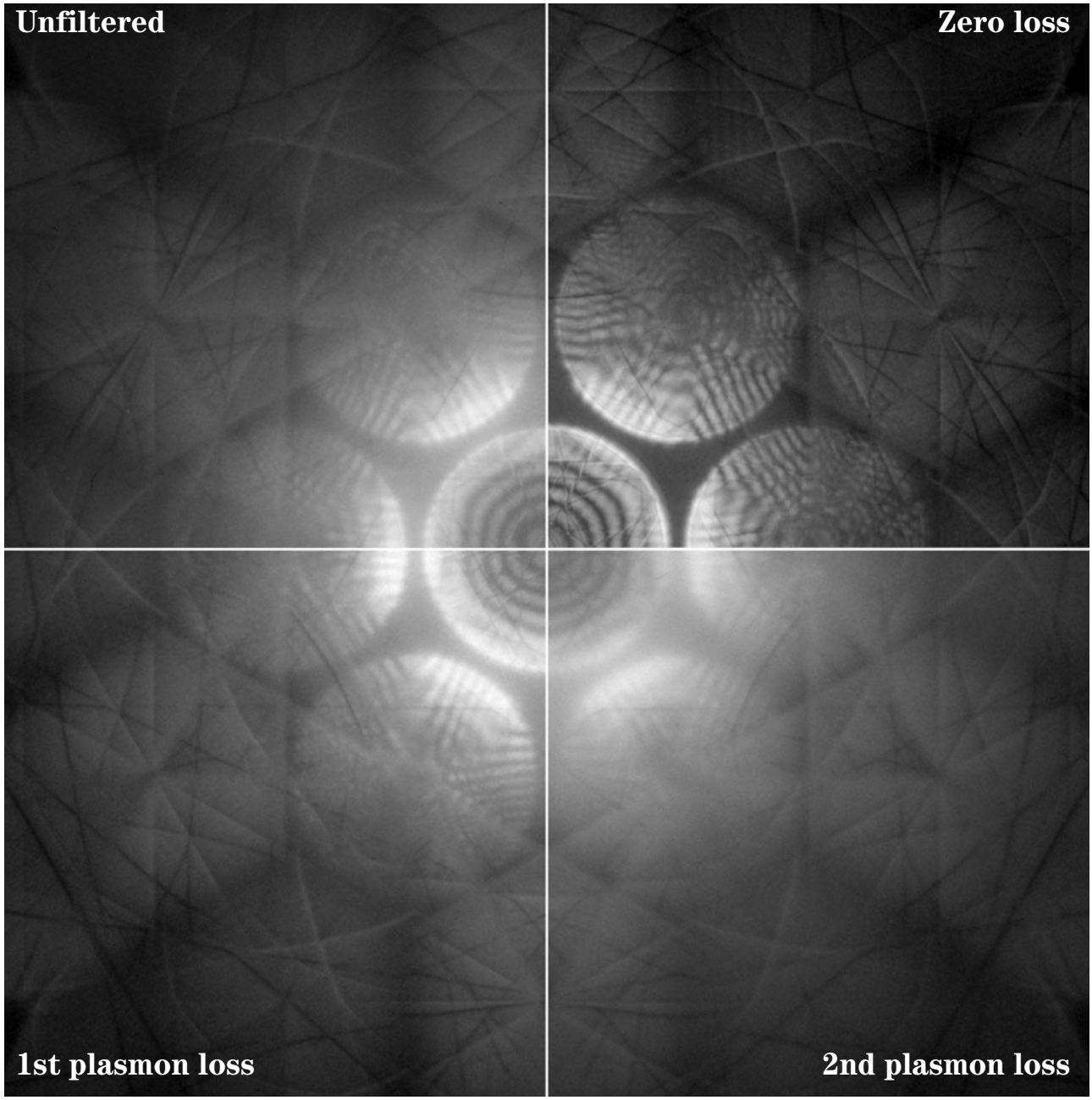

CBED patterns on this page are displayed with raw intensities. When the intensity scale is adjusted appropriate for the zero-loss pattern, the unfiltered pattern shows an oversaturation around the central area because it has high intensity. CBED patterns on the right-side page are displayed after adjusting the maximum intensity in each pattern to take the same full scale. All the patterns on the following pages are displayed with such intensity adjustments to avoid saturation and insufficiency of the pattern intensities.

Si [111] **100kV**

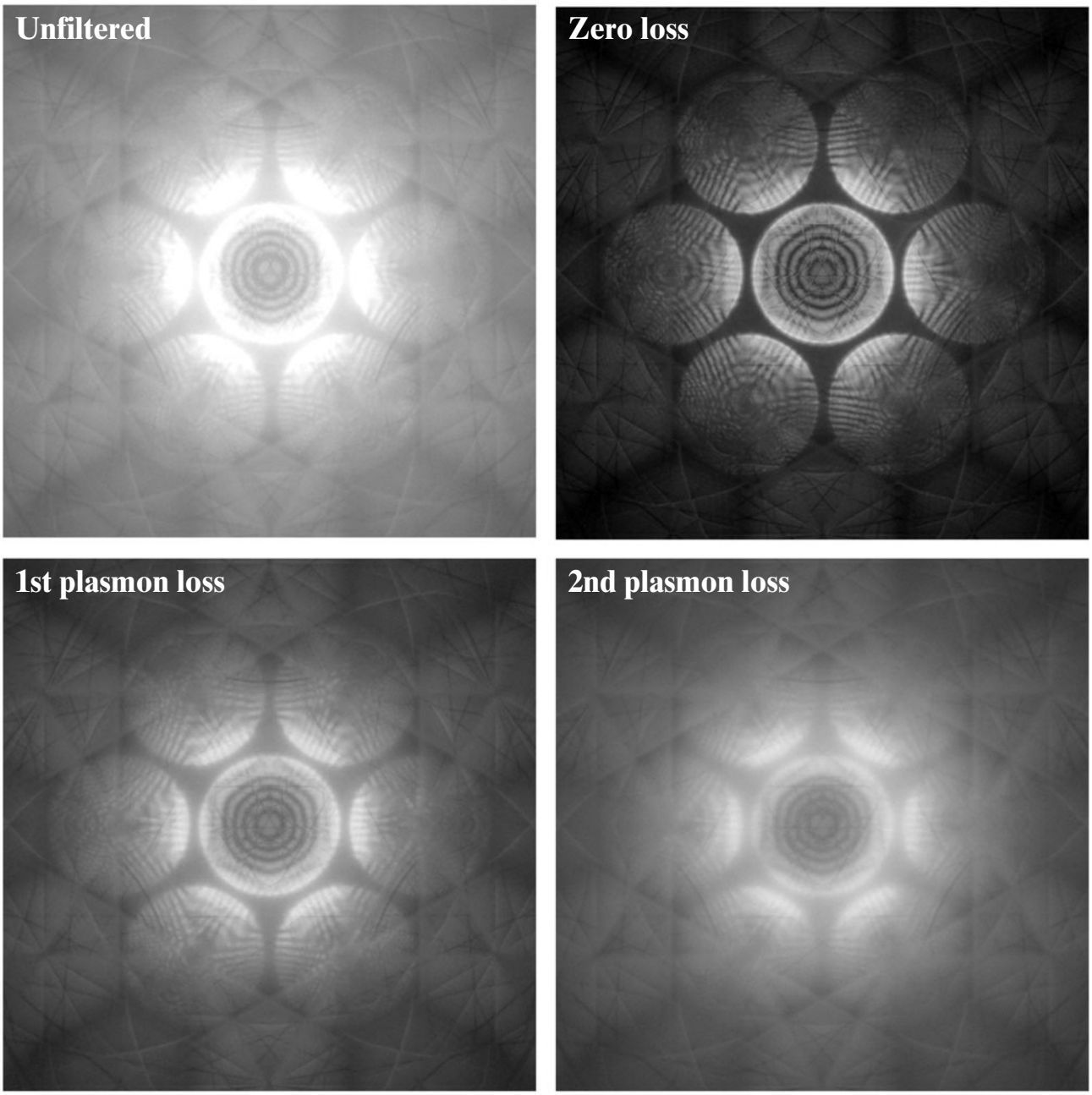

Si [111] 100kV

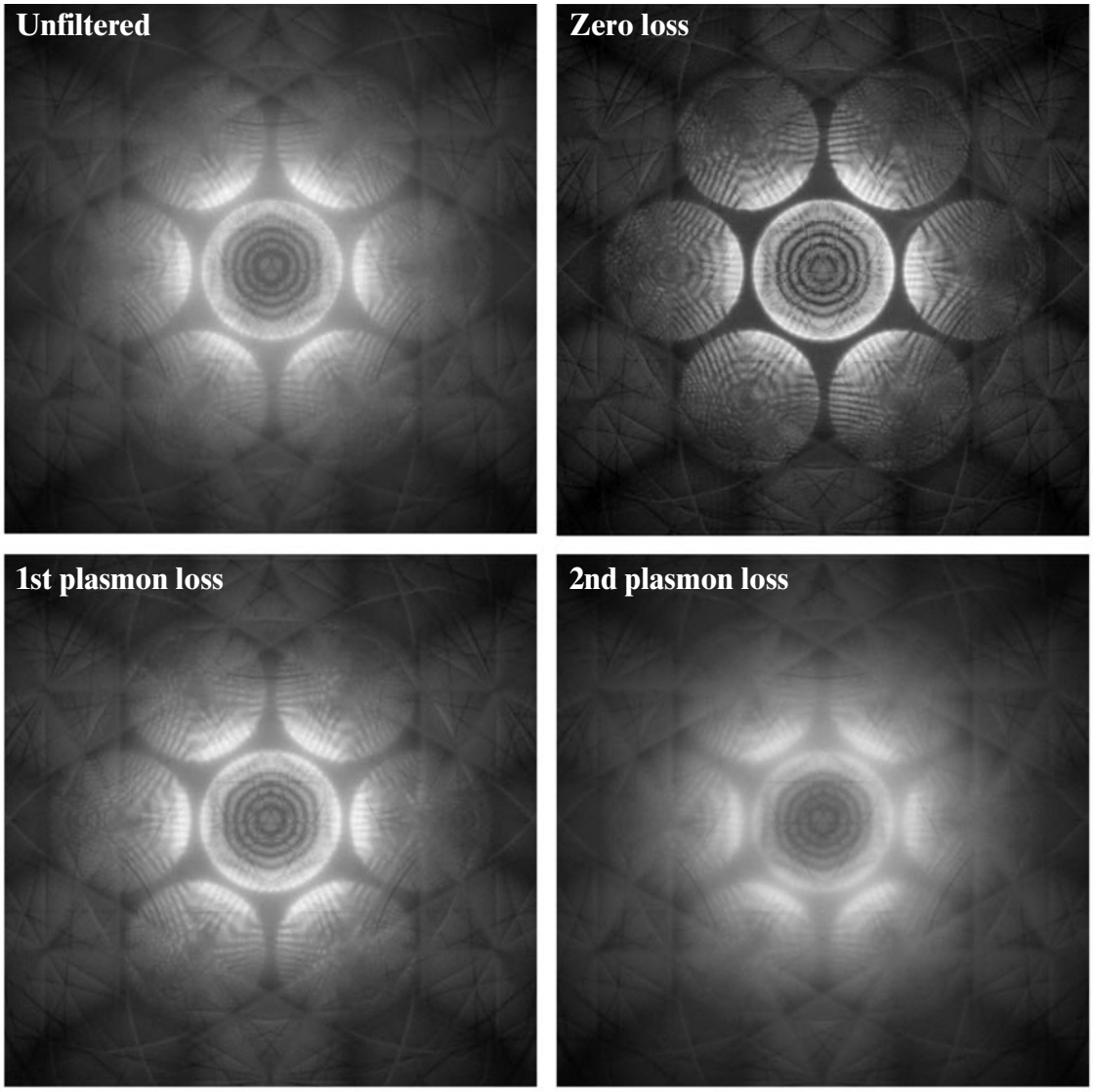
Unfiltered
Zero loss
1st plasmon loss
2nd plasmon loss

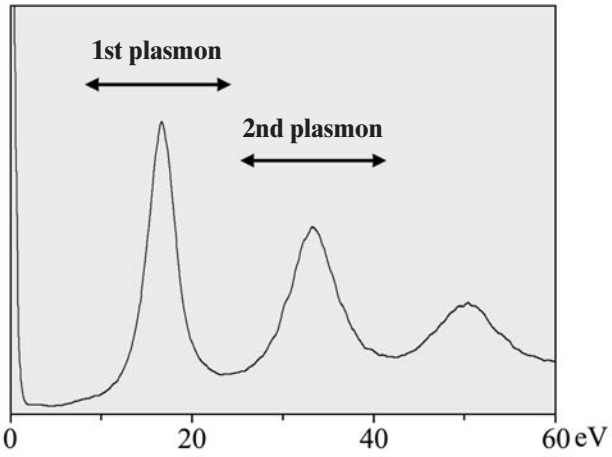
1st plasmon
2nd plasmon
0
20
40
60 eV

α-Boron [11$\bar{3}$] 100kV

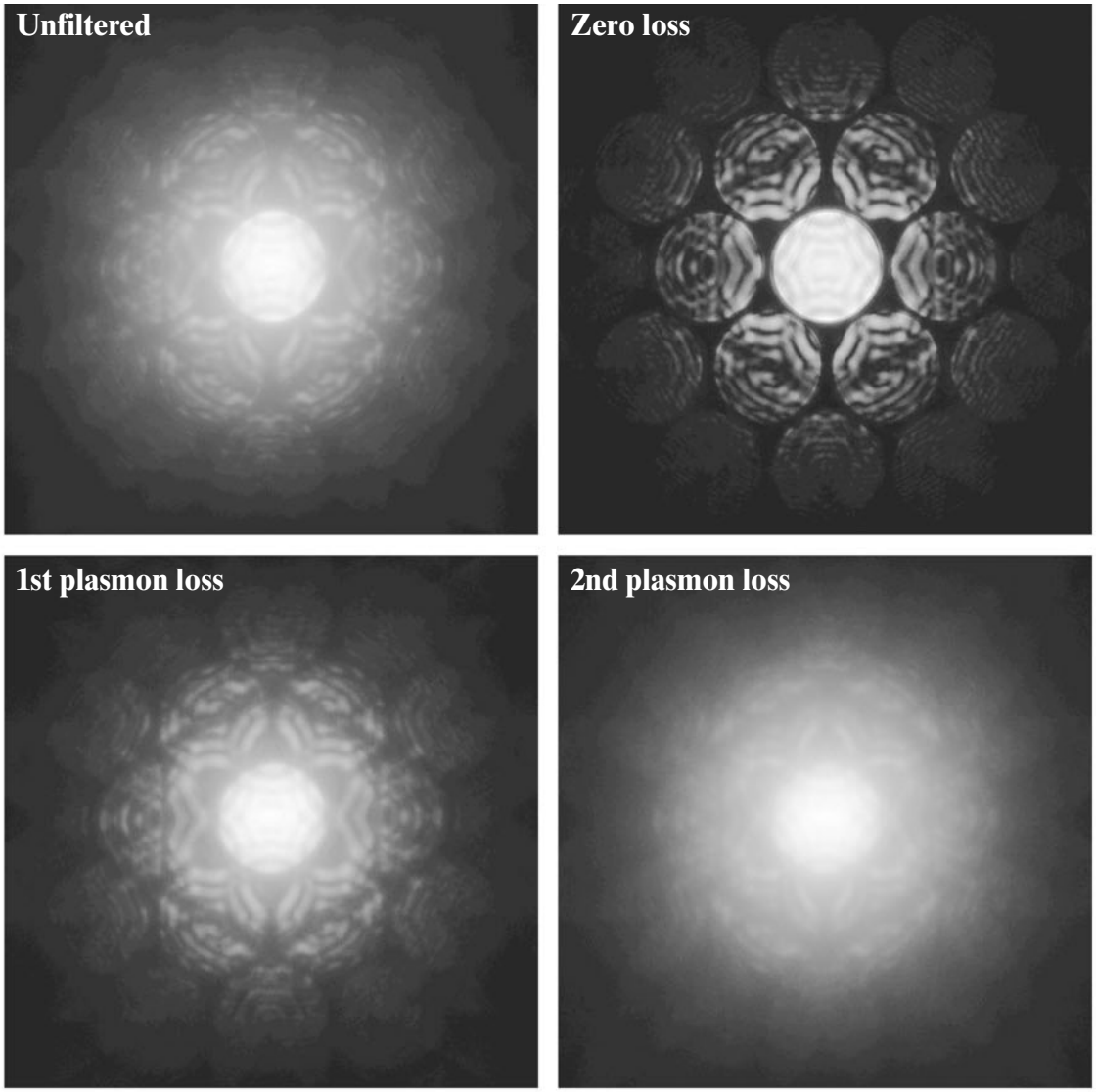

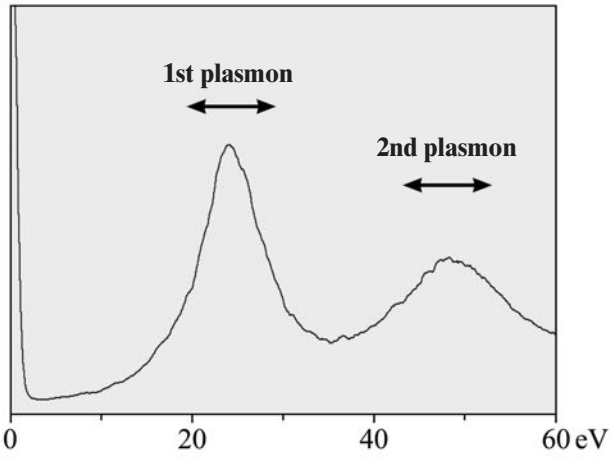

Graphite [0001] **100kV**

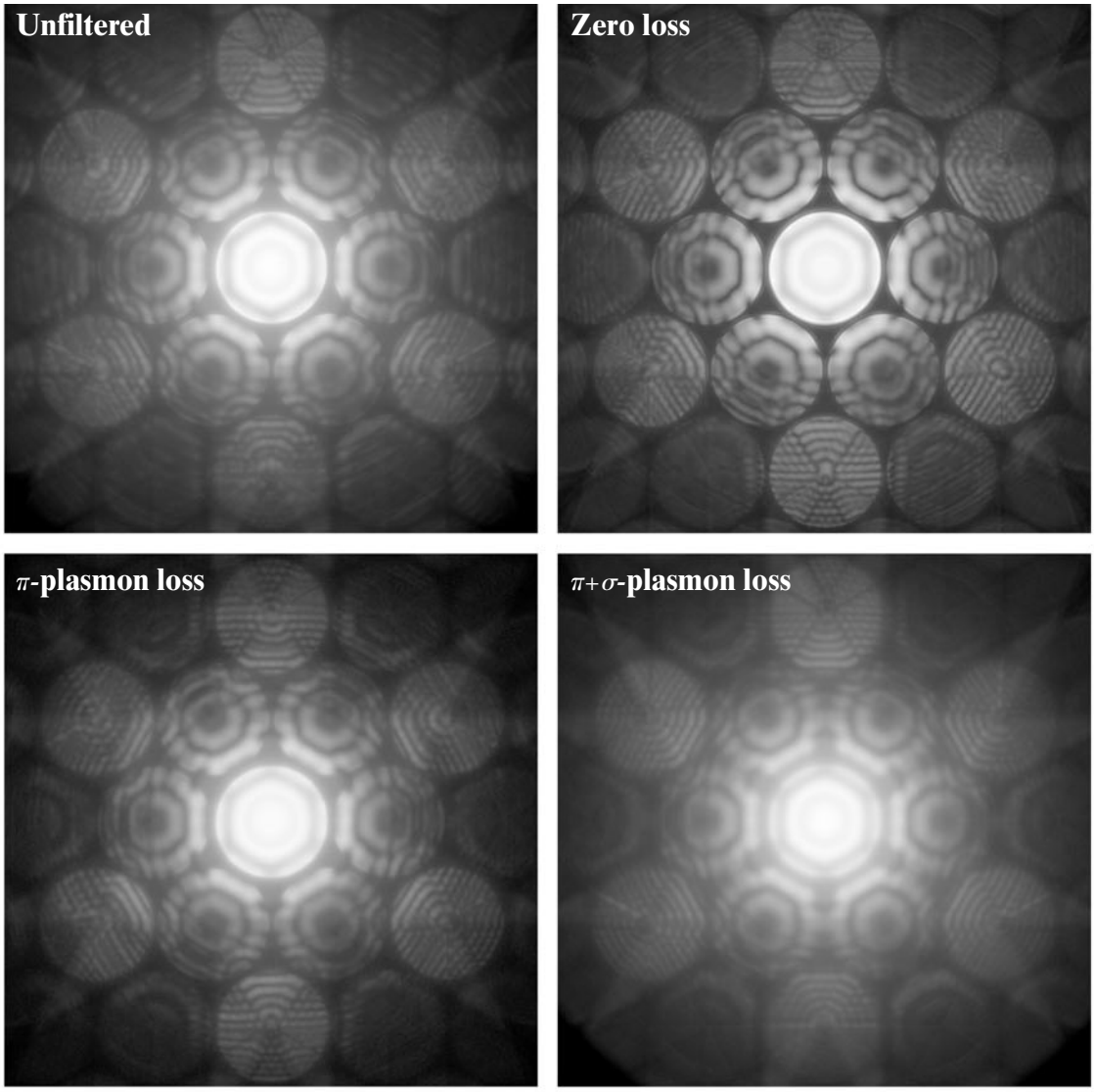

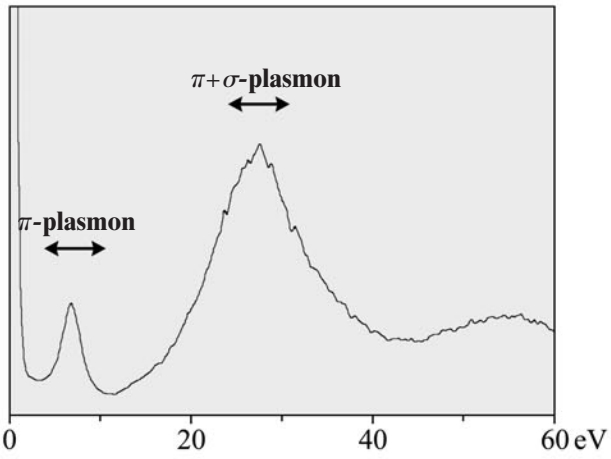

Diamond [111] **100kV**

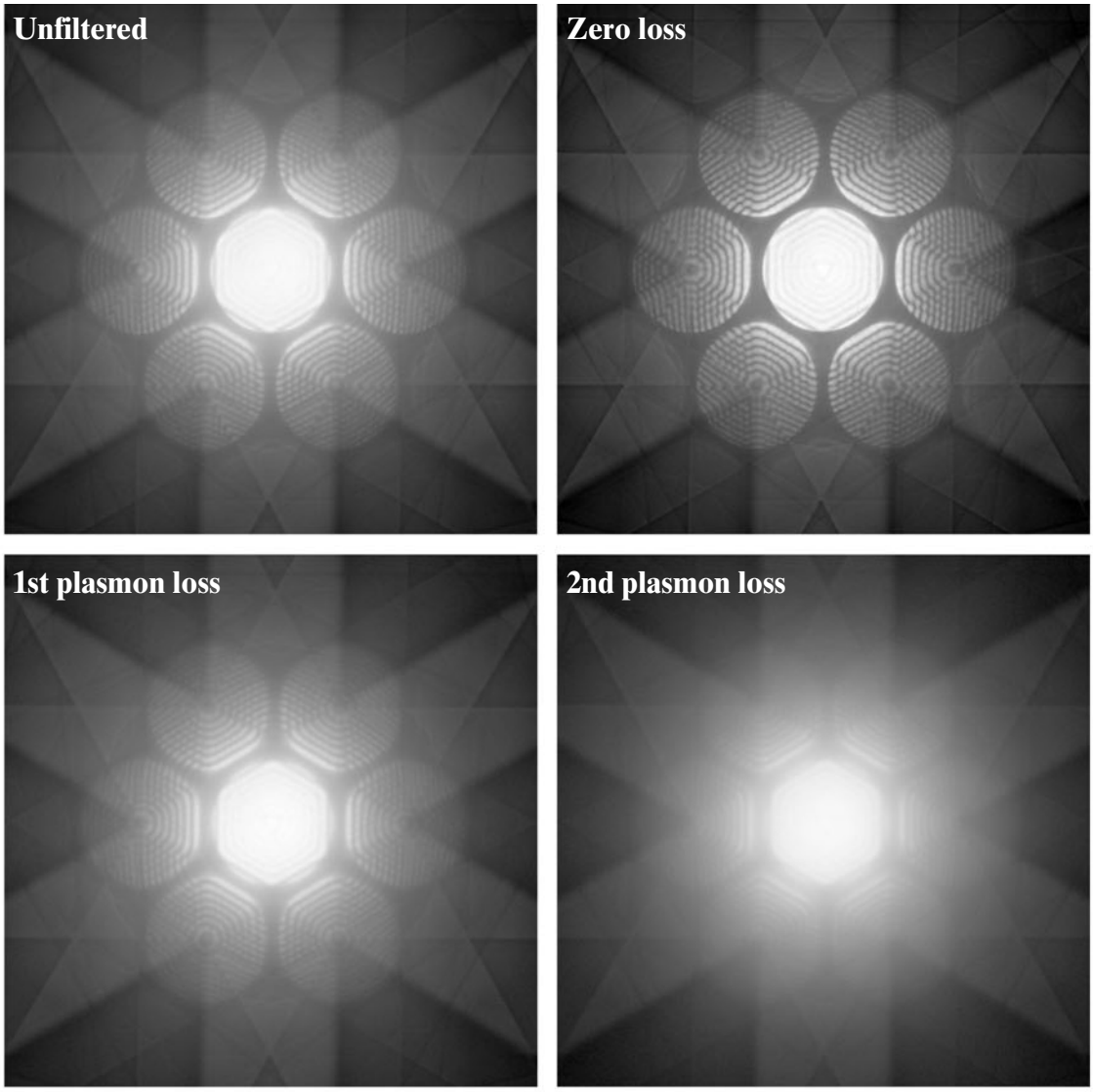

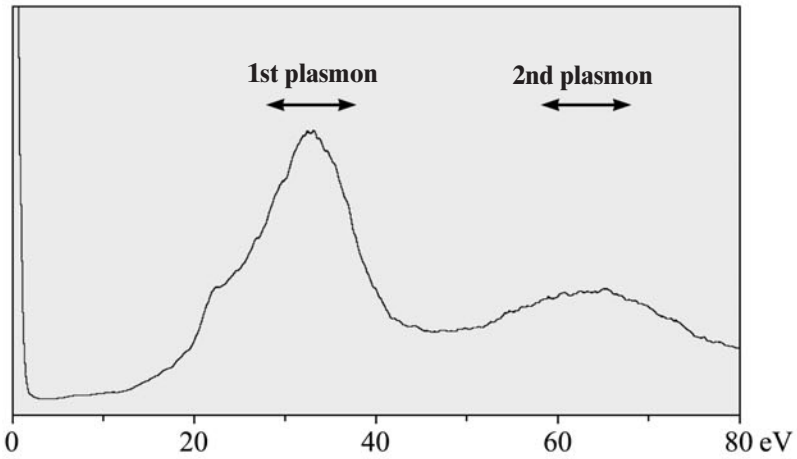

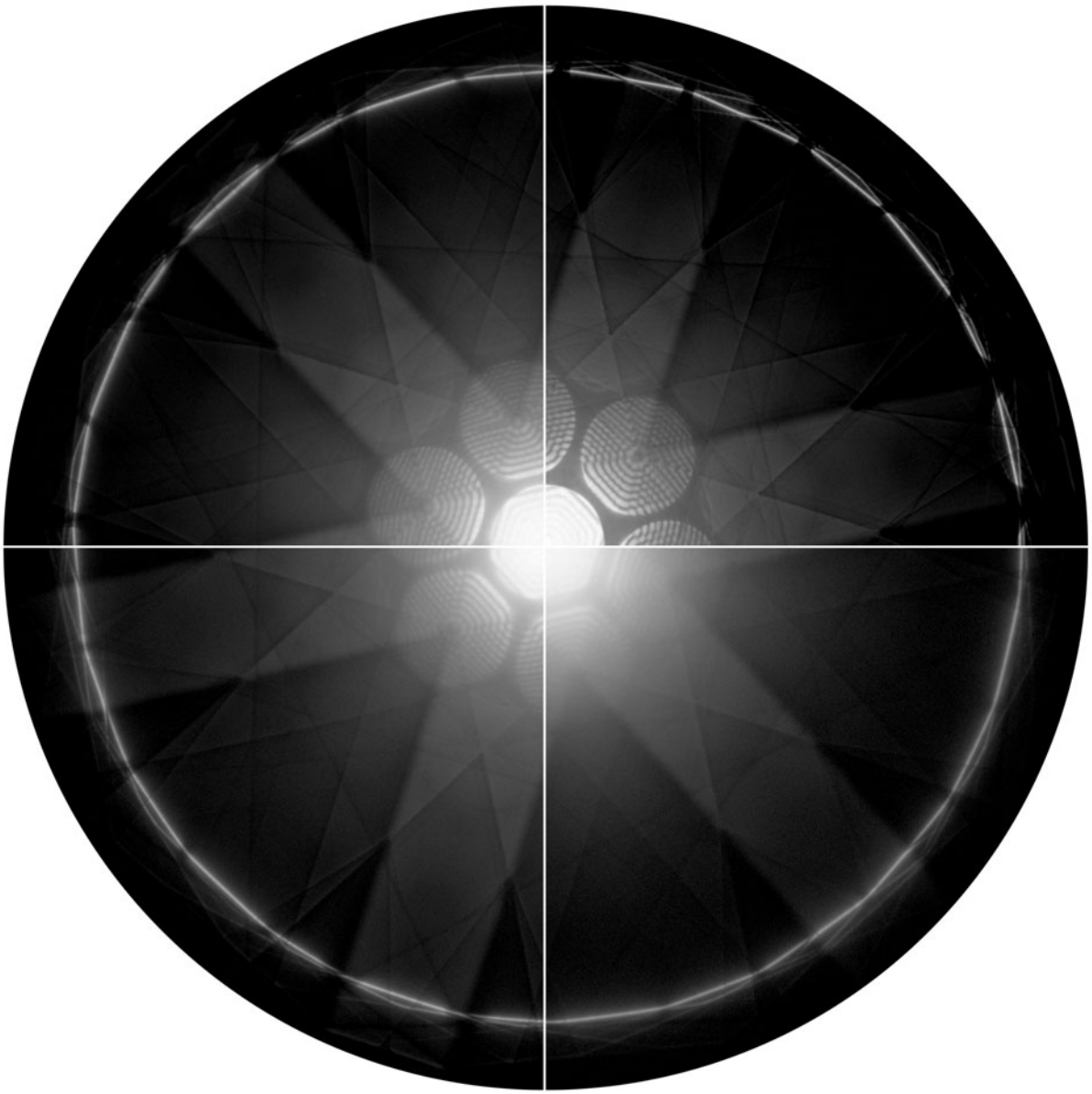

Ge [111] 100kV

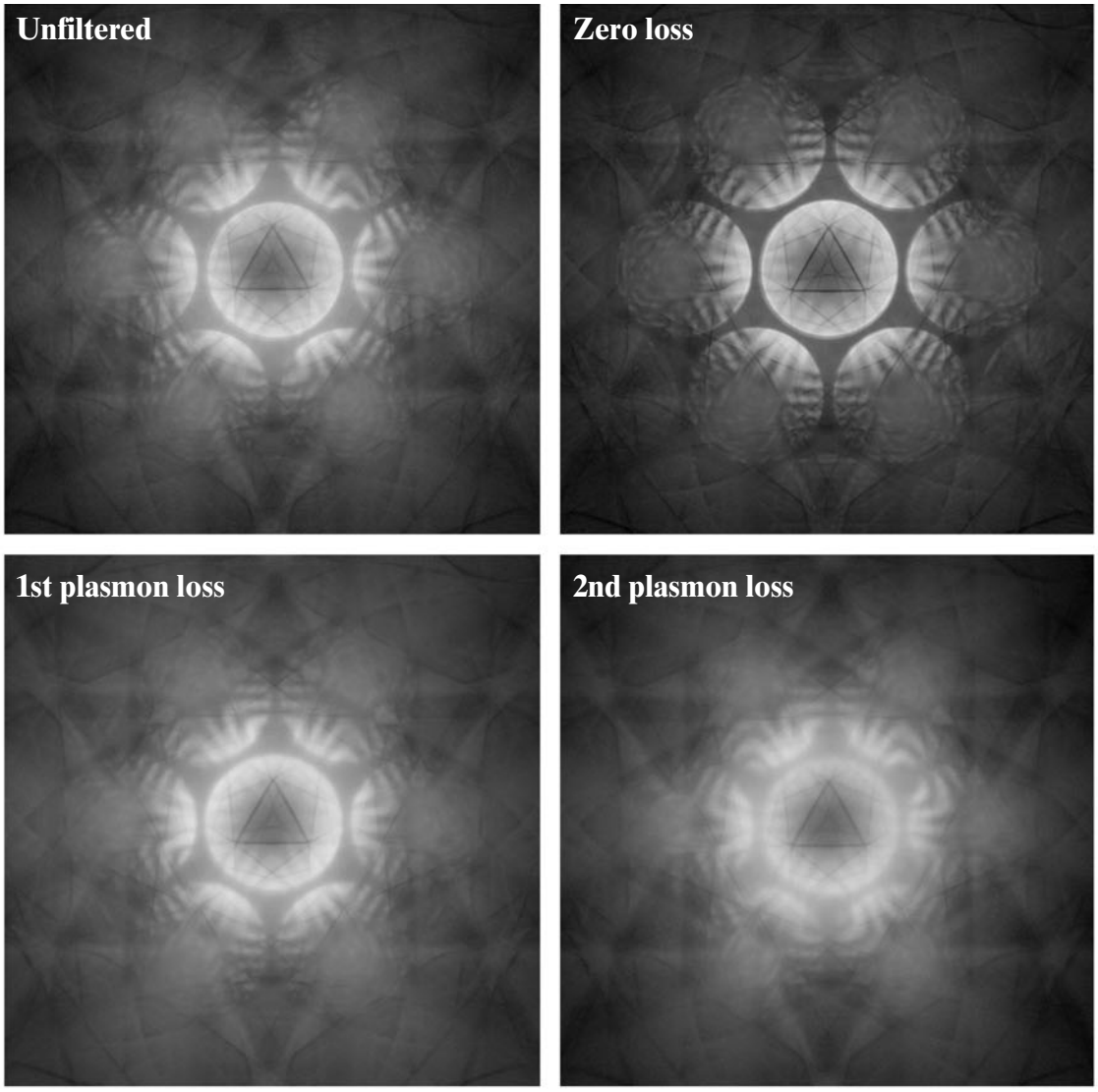
Unfiltered
Zero loss
1st plasmon loss
2nd plasmon loss

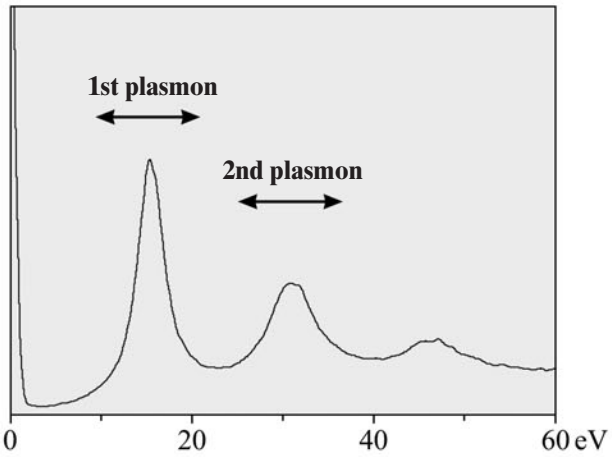
1st plasmon
2nd plasmon
0
20
40
60 eV

Al [100] 100kV

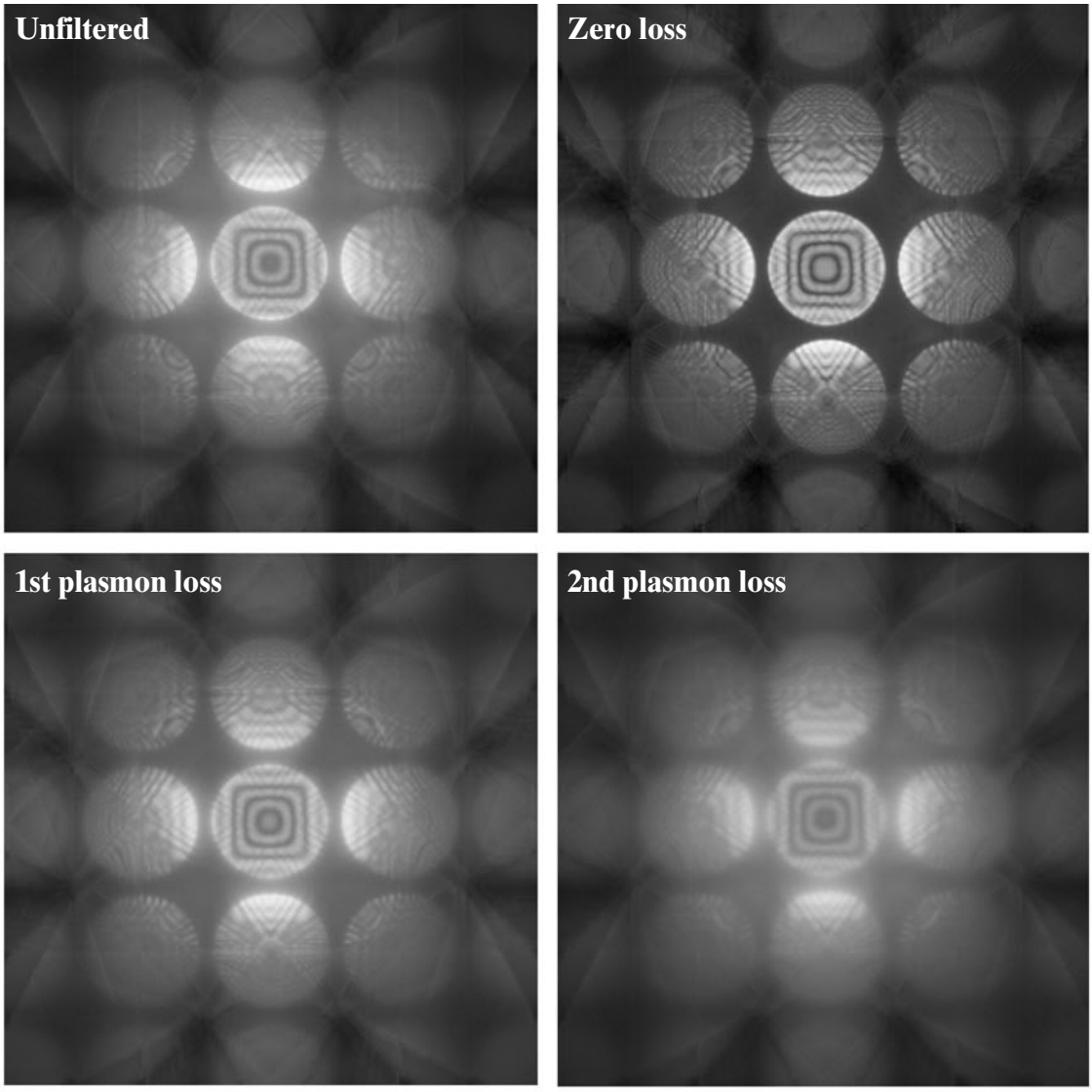
Unfiltered
Zero loss
1st plasmon loss
2nd plasmon loss

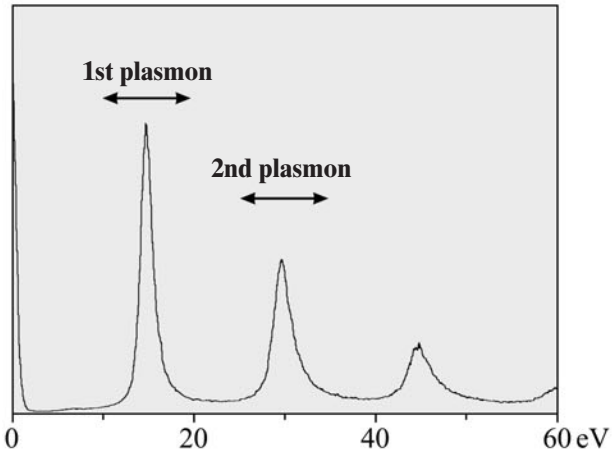
1st plasmon
2nd plasmon
0
20
40
60 eV

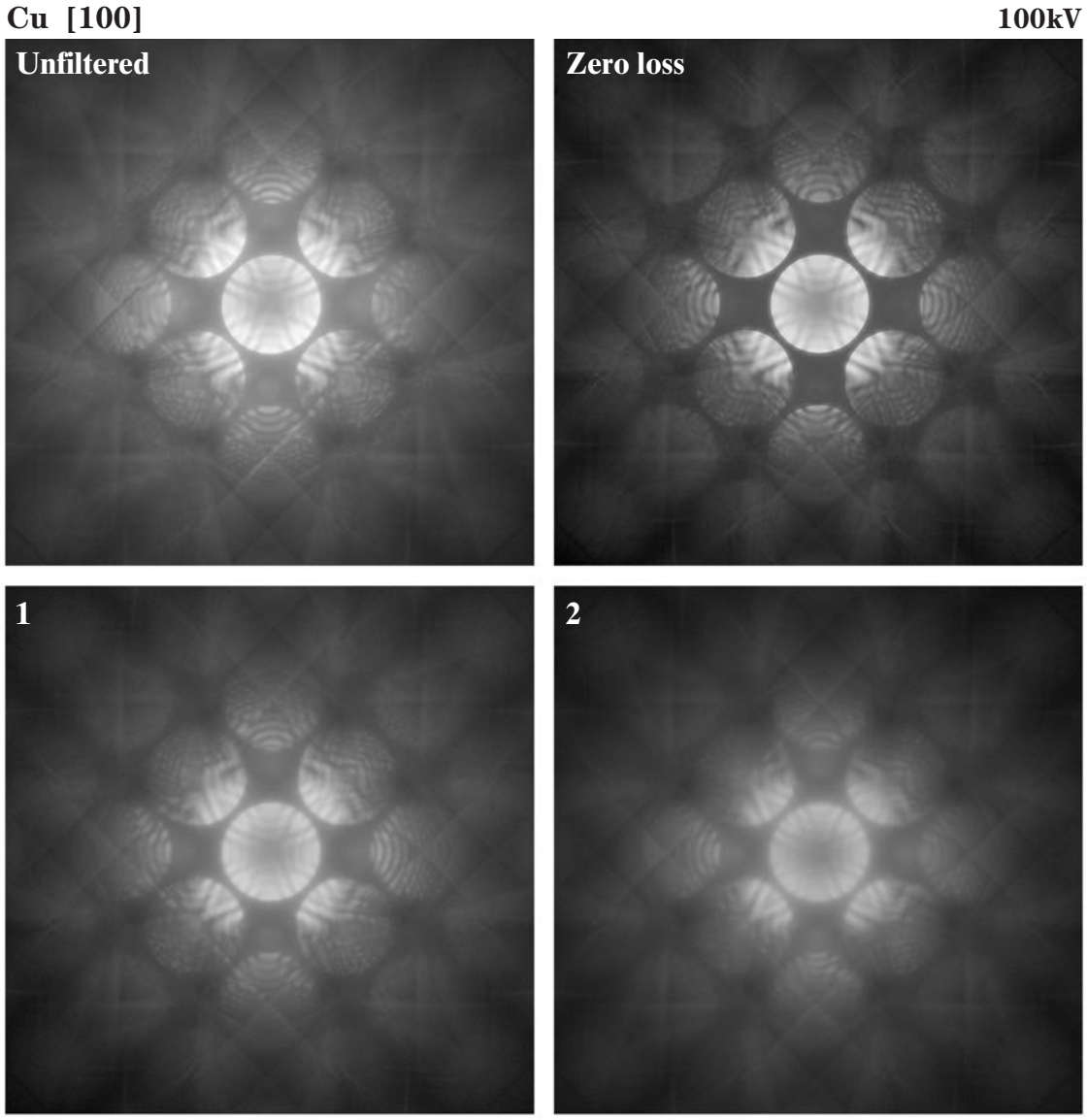
Cu [100]
100kV
Unfiltered
Zero loss
1
2

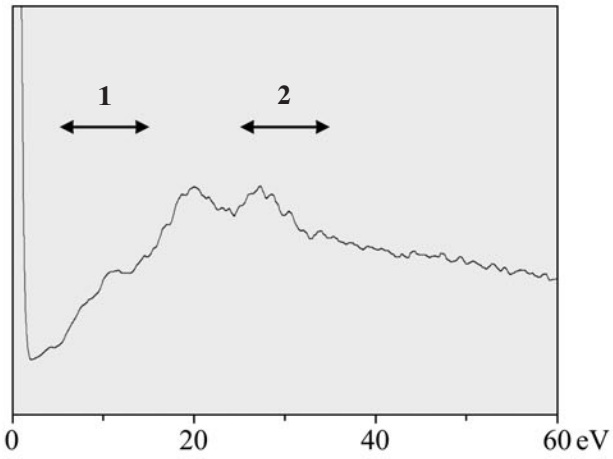
1
2
0
20
40
60 eV

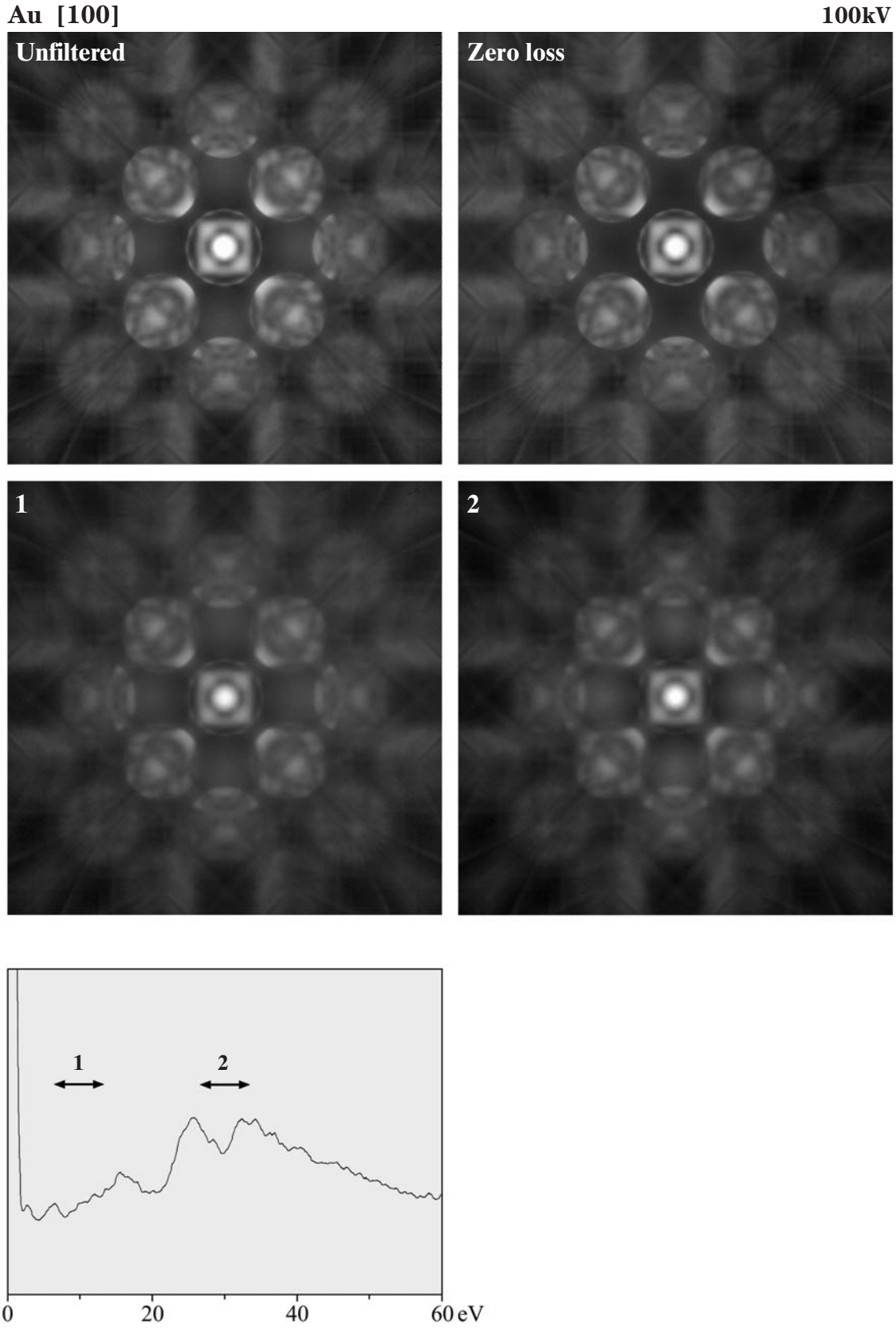
Au [100]
100kV
Unfiltered
Zero loss
1
2
1
2
0
20
40
60 eV

Cubic BN [111] **100kV**

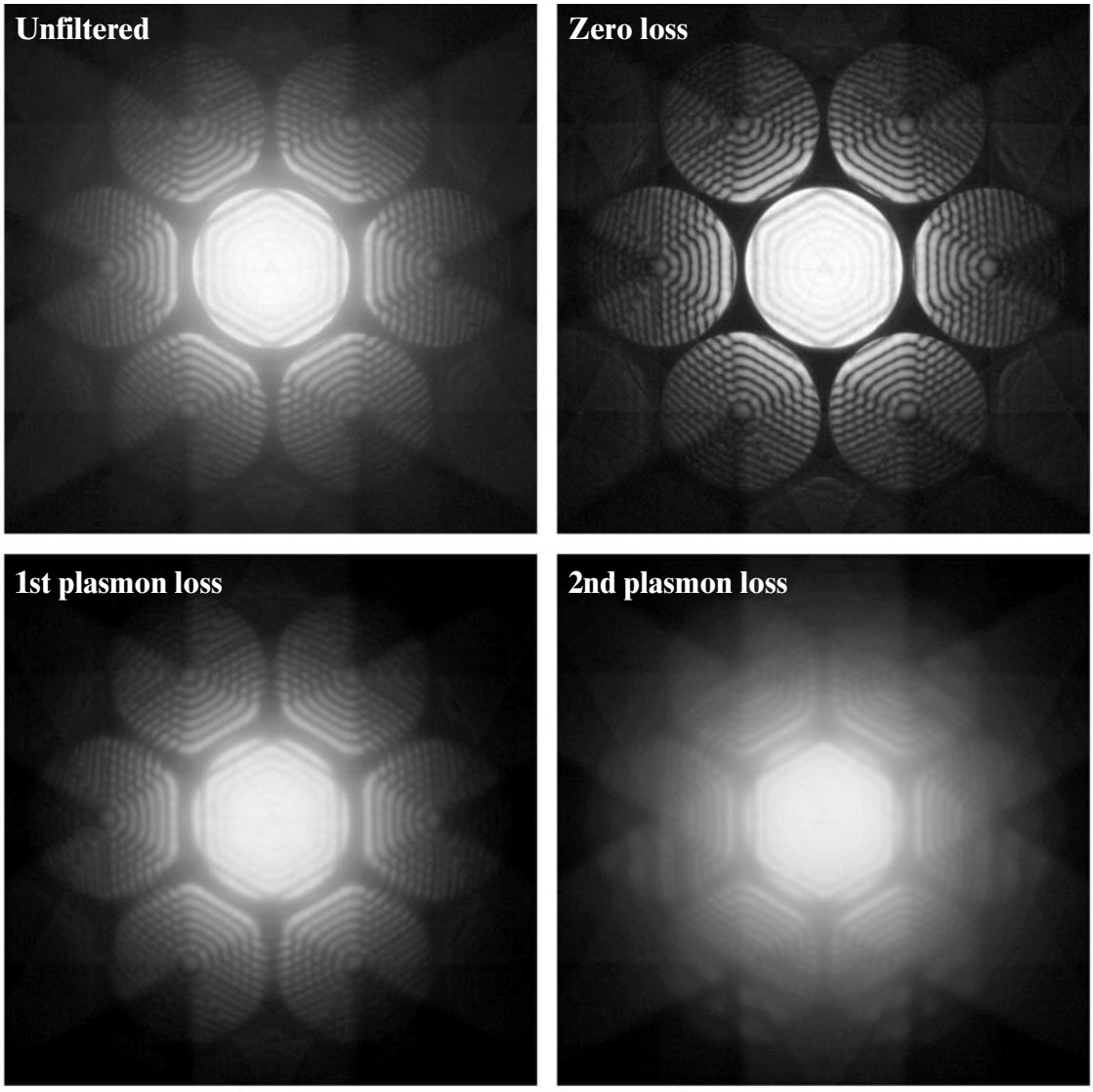

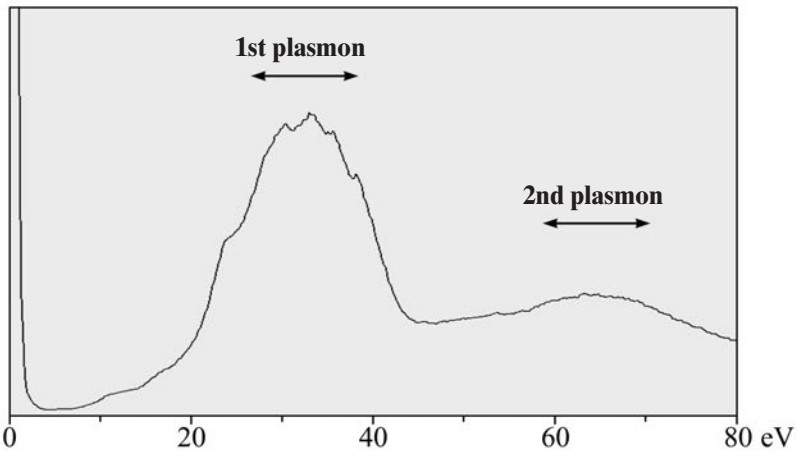

Cubic BN [110] **100kV**

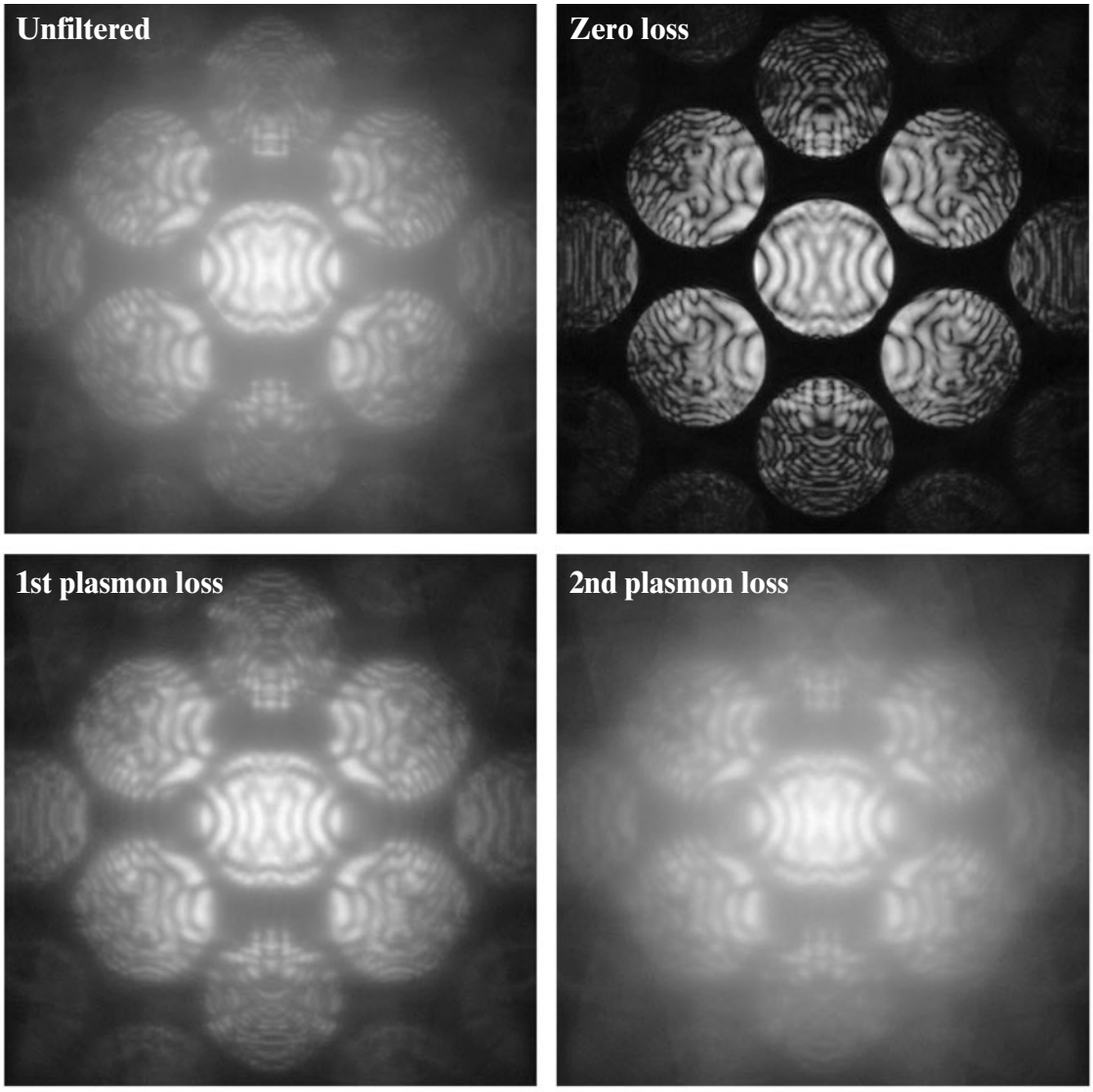

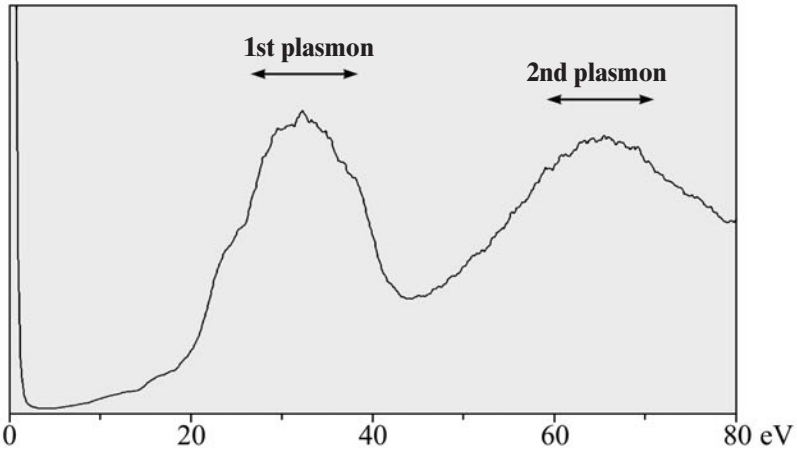

Hexagonal BN [0001] **100kV**

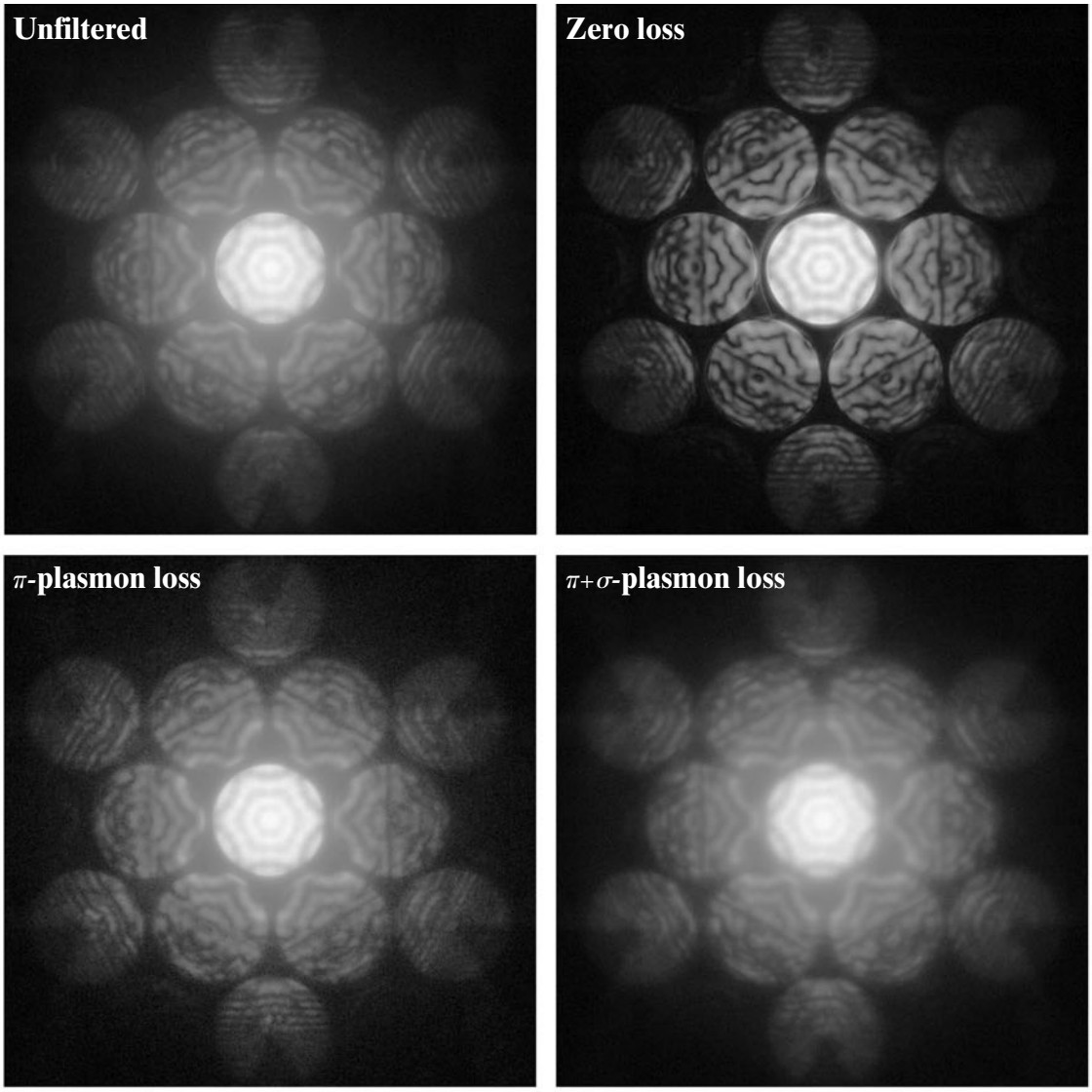

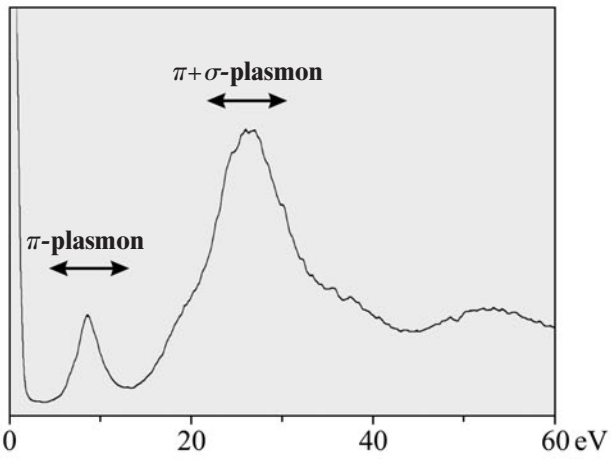

6H-SiC [0001] 100kV

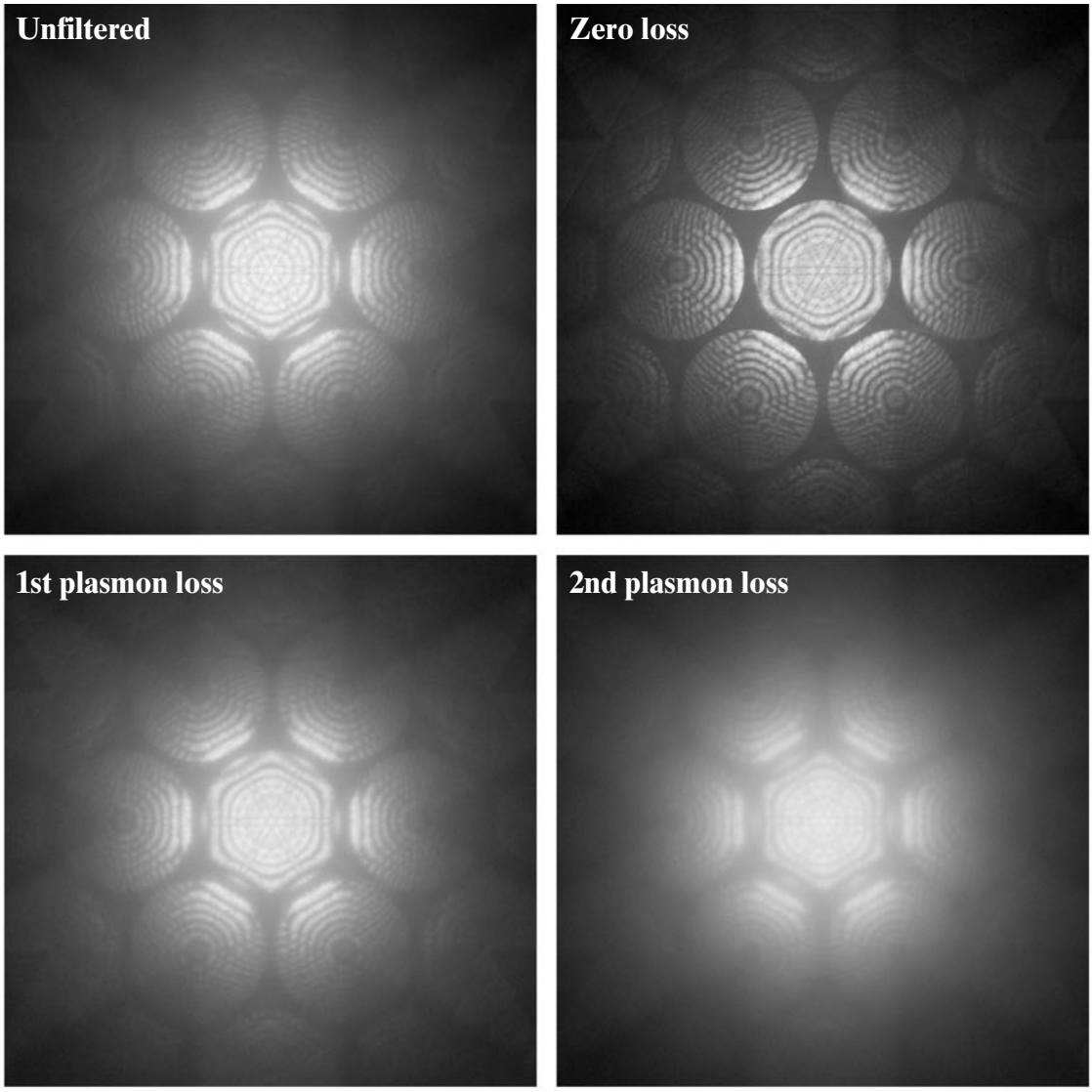

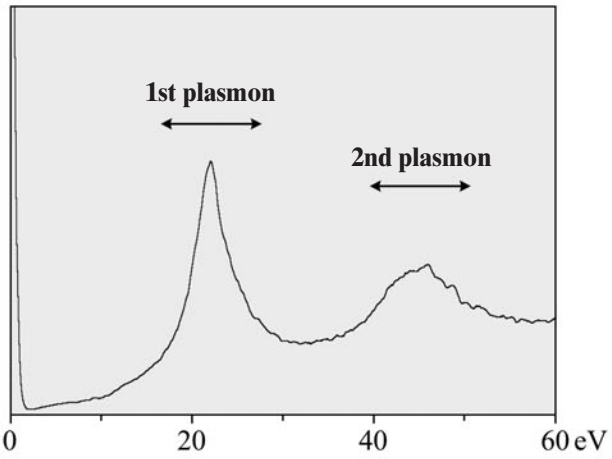

AlN [0001] 100kV

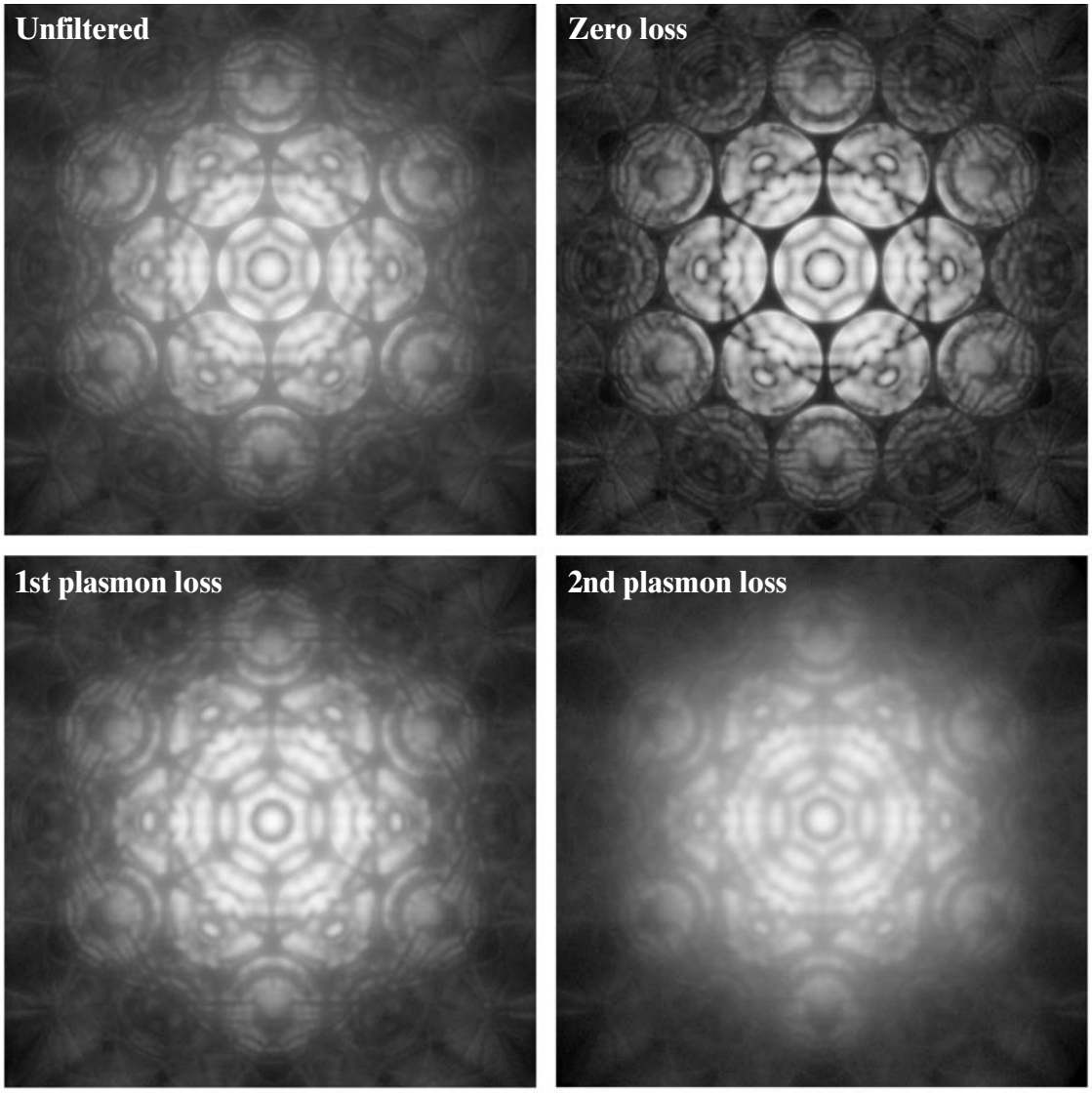

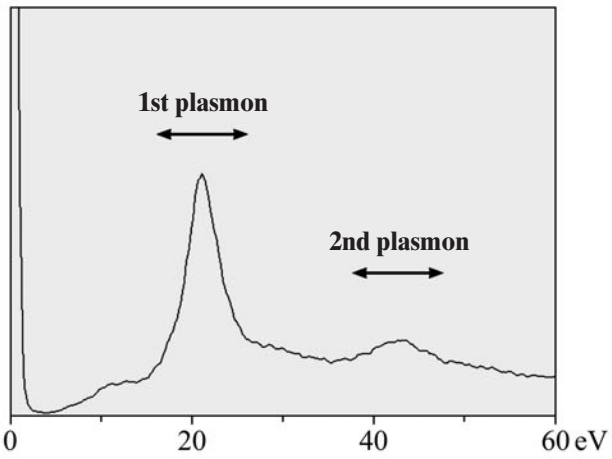

GaN [0001] **100kV**

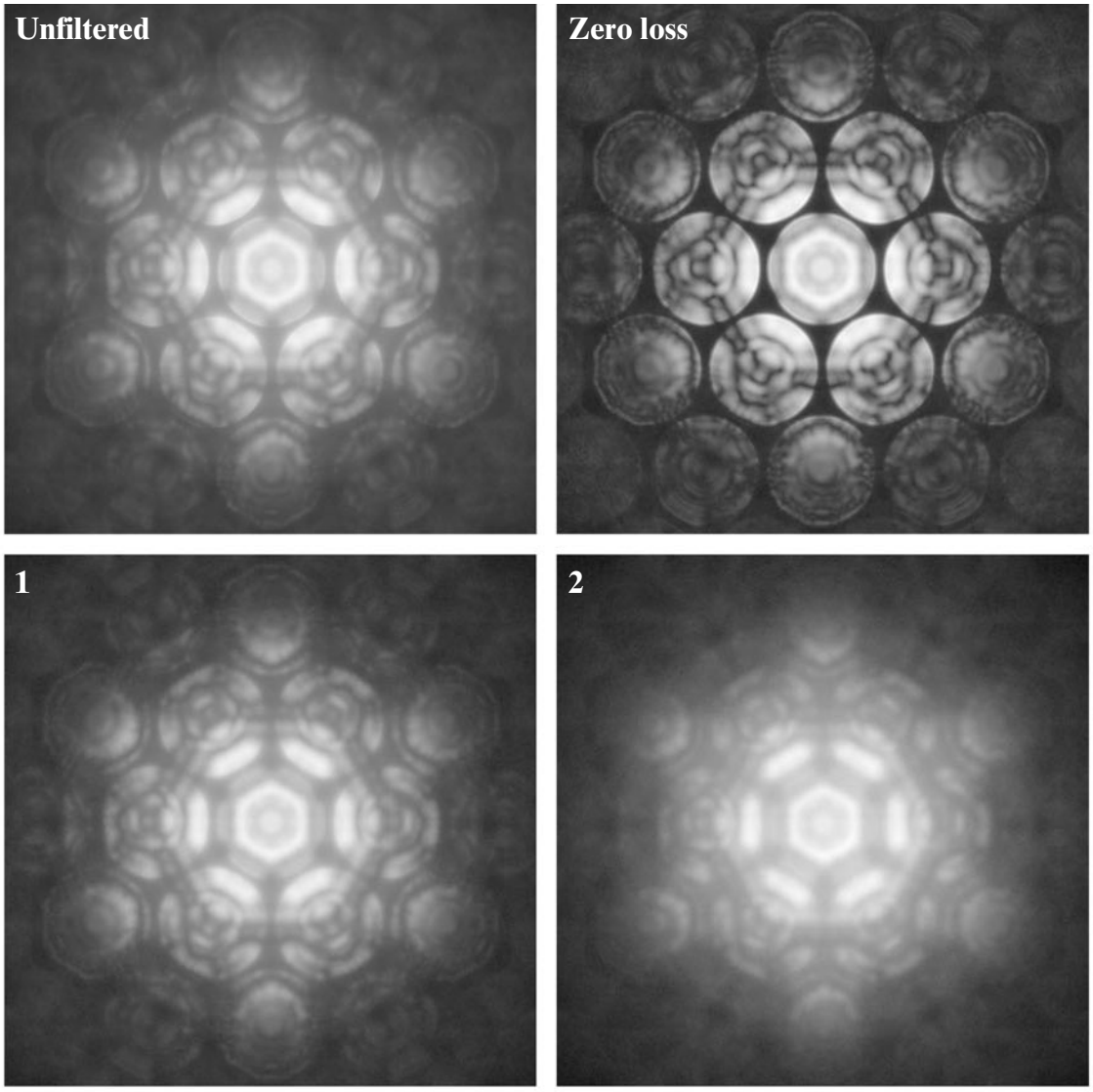

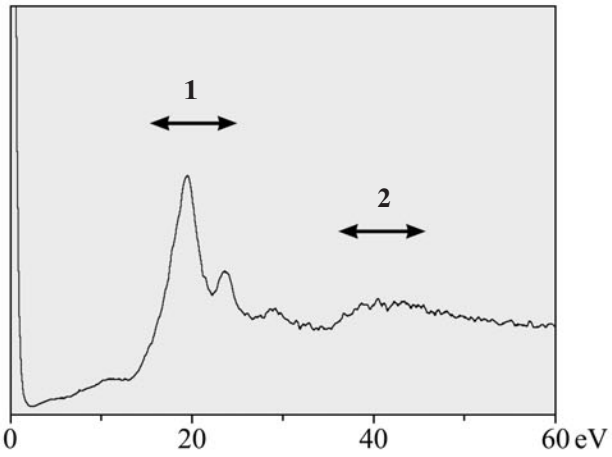

CdS [0001] 100kV

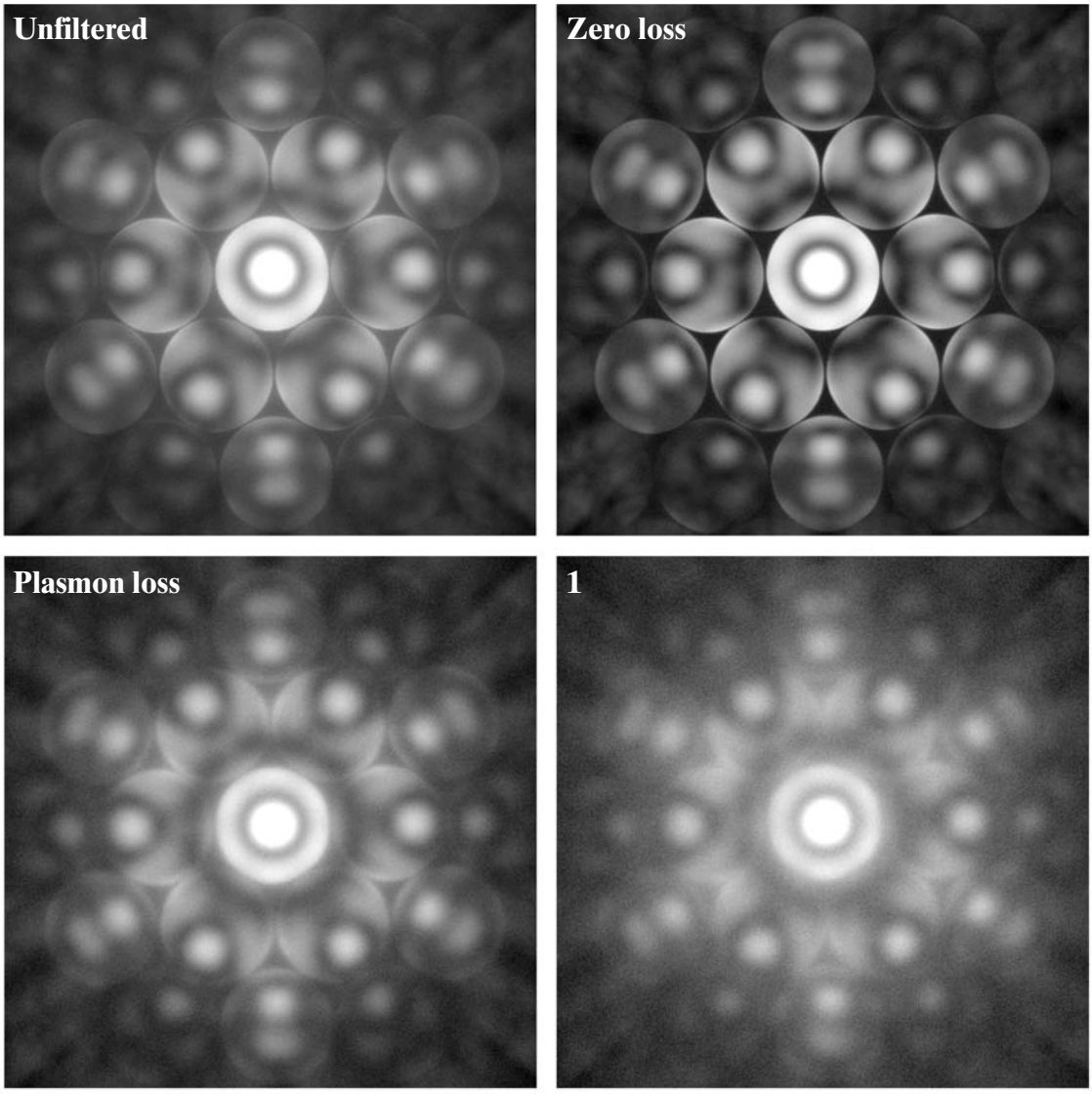

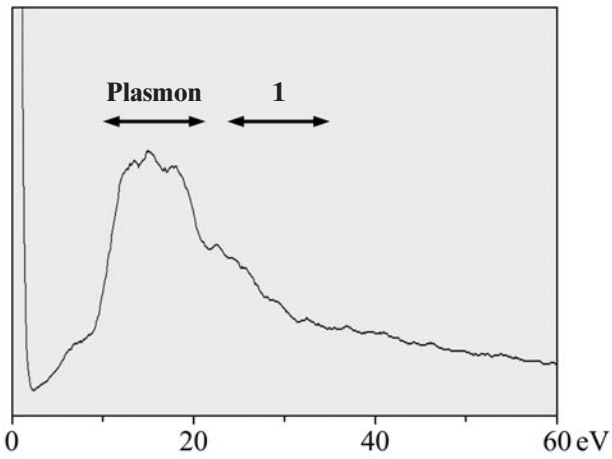

GaAs [100] **100kV**

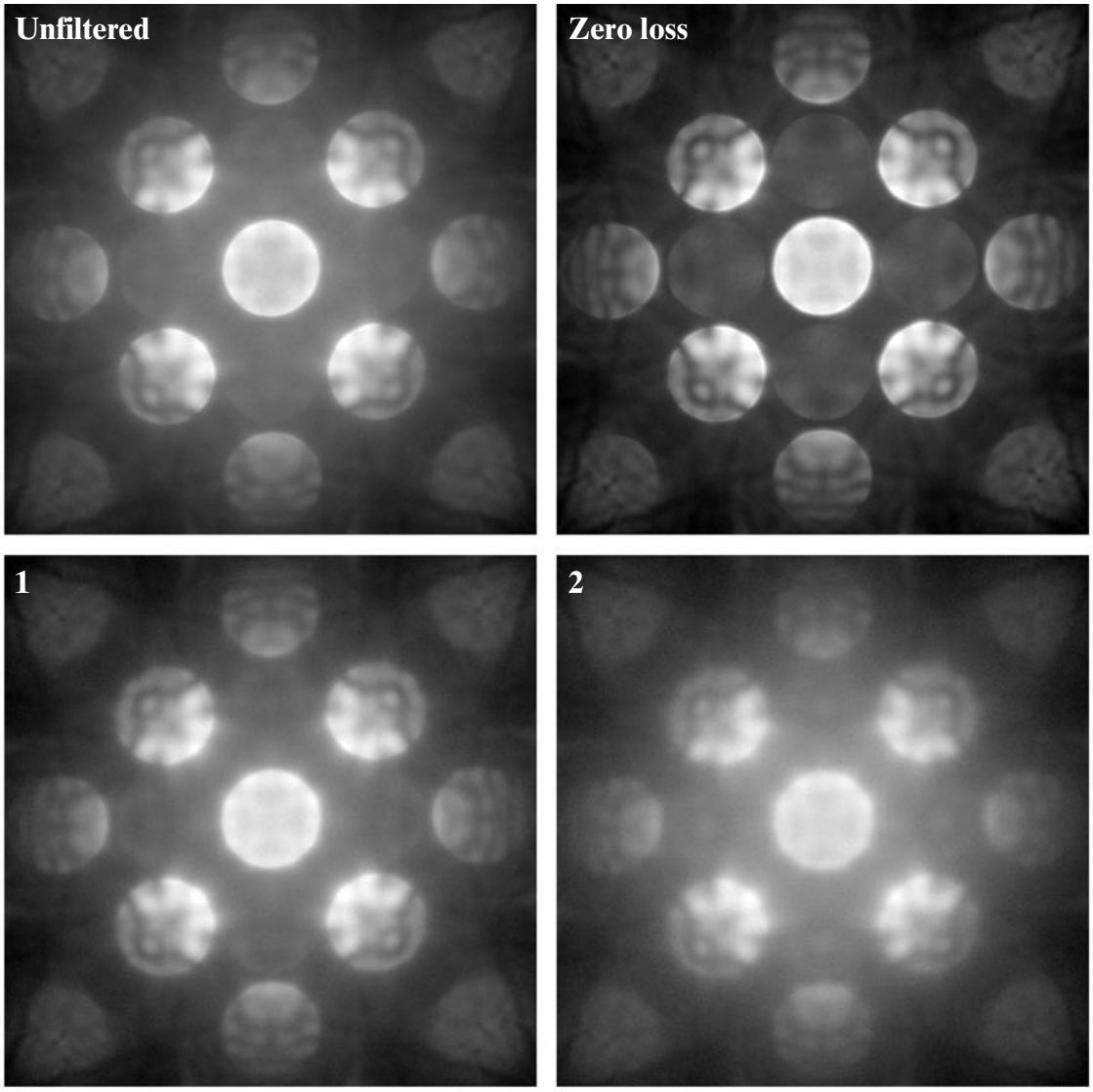

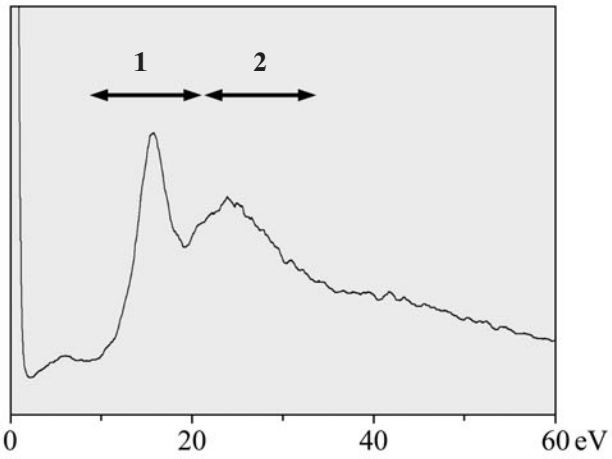

ZnS [100] **100kV**

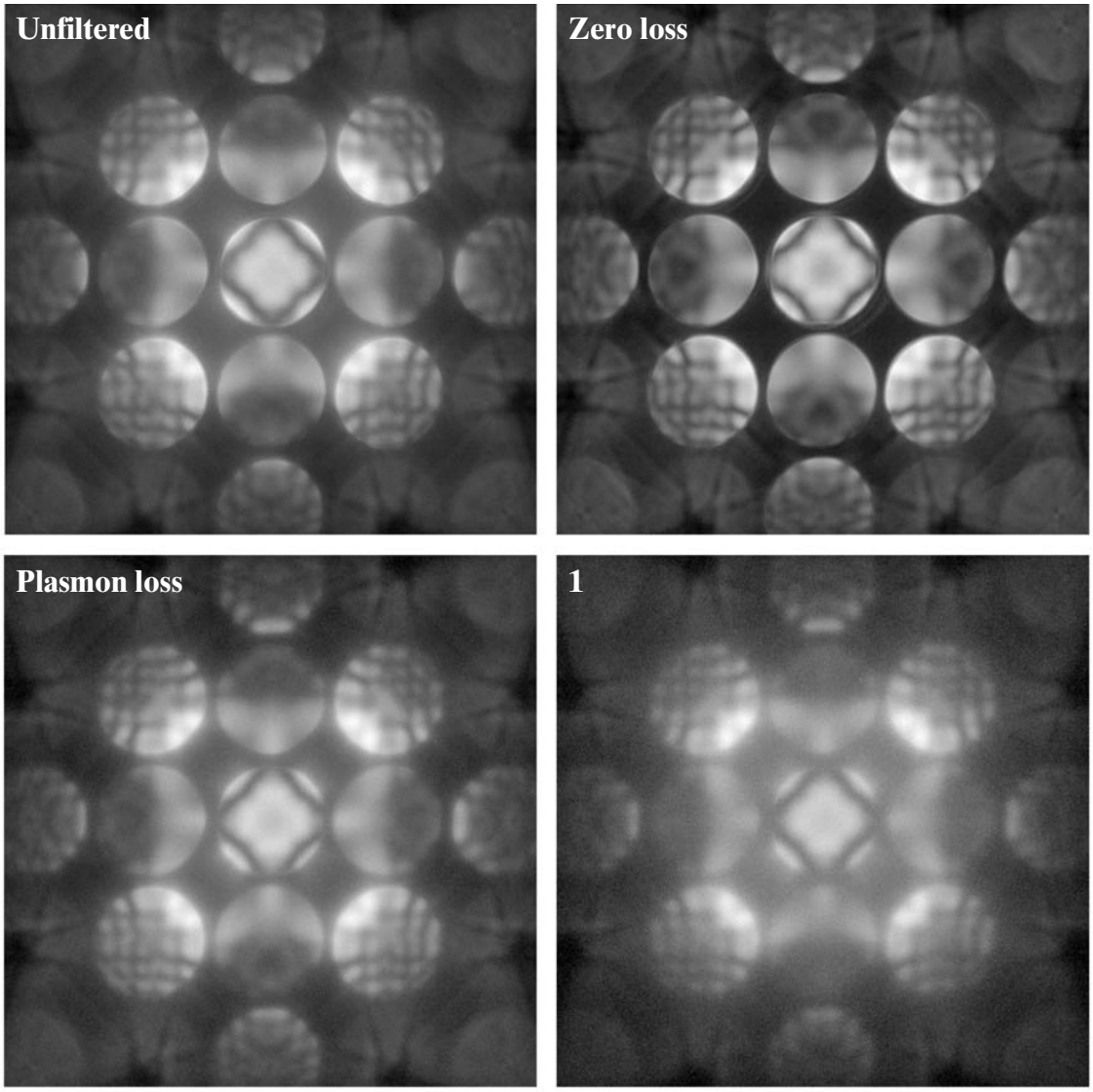

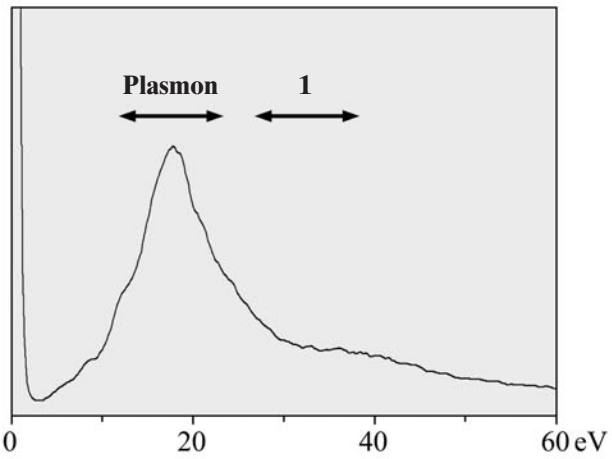

CdTe [100] **100kV**

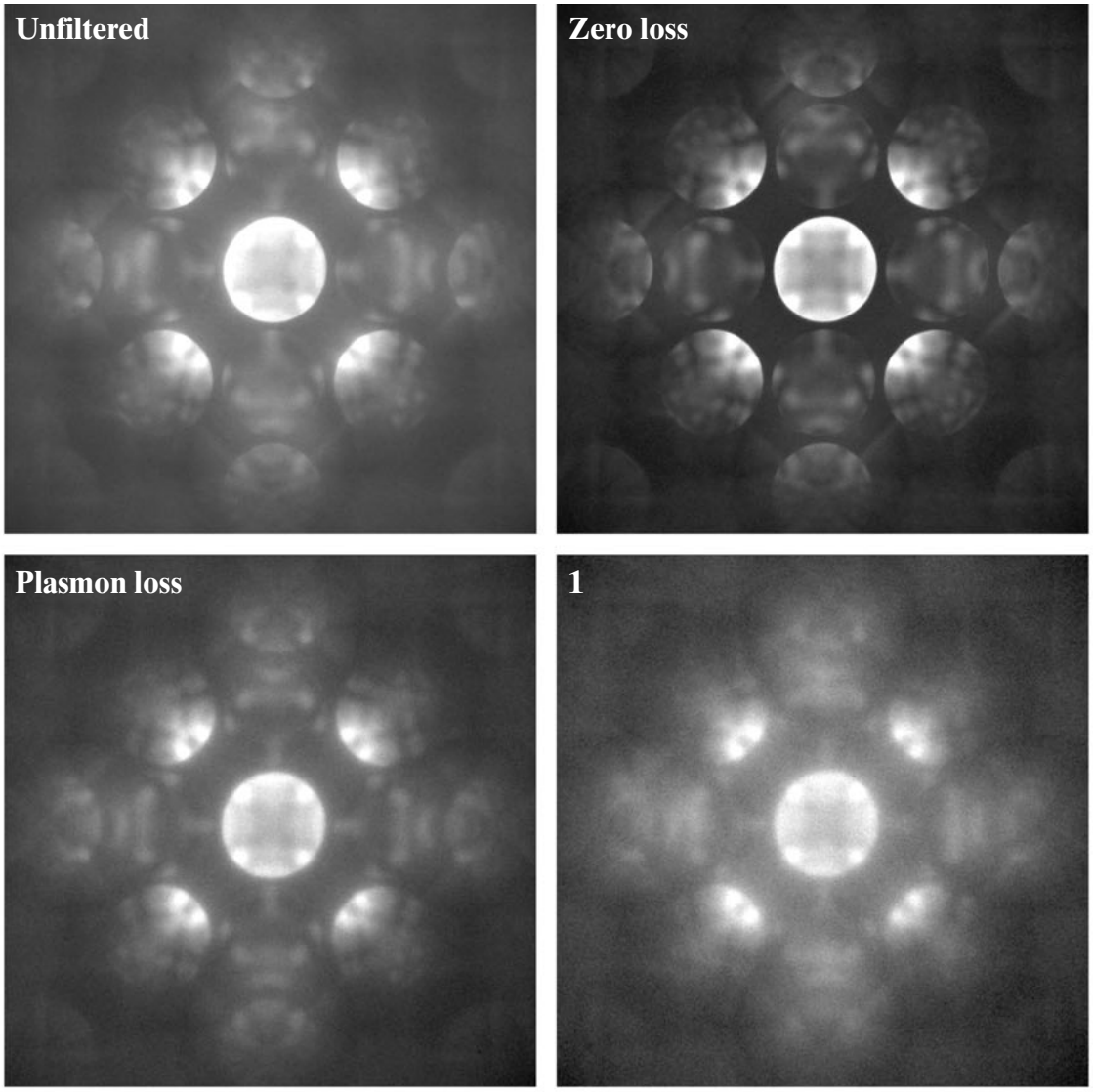

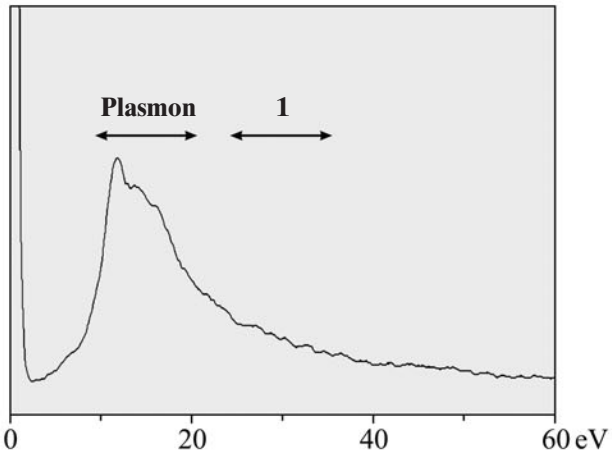

CaB_6 [100] **100kV**

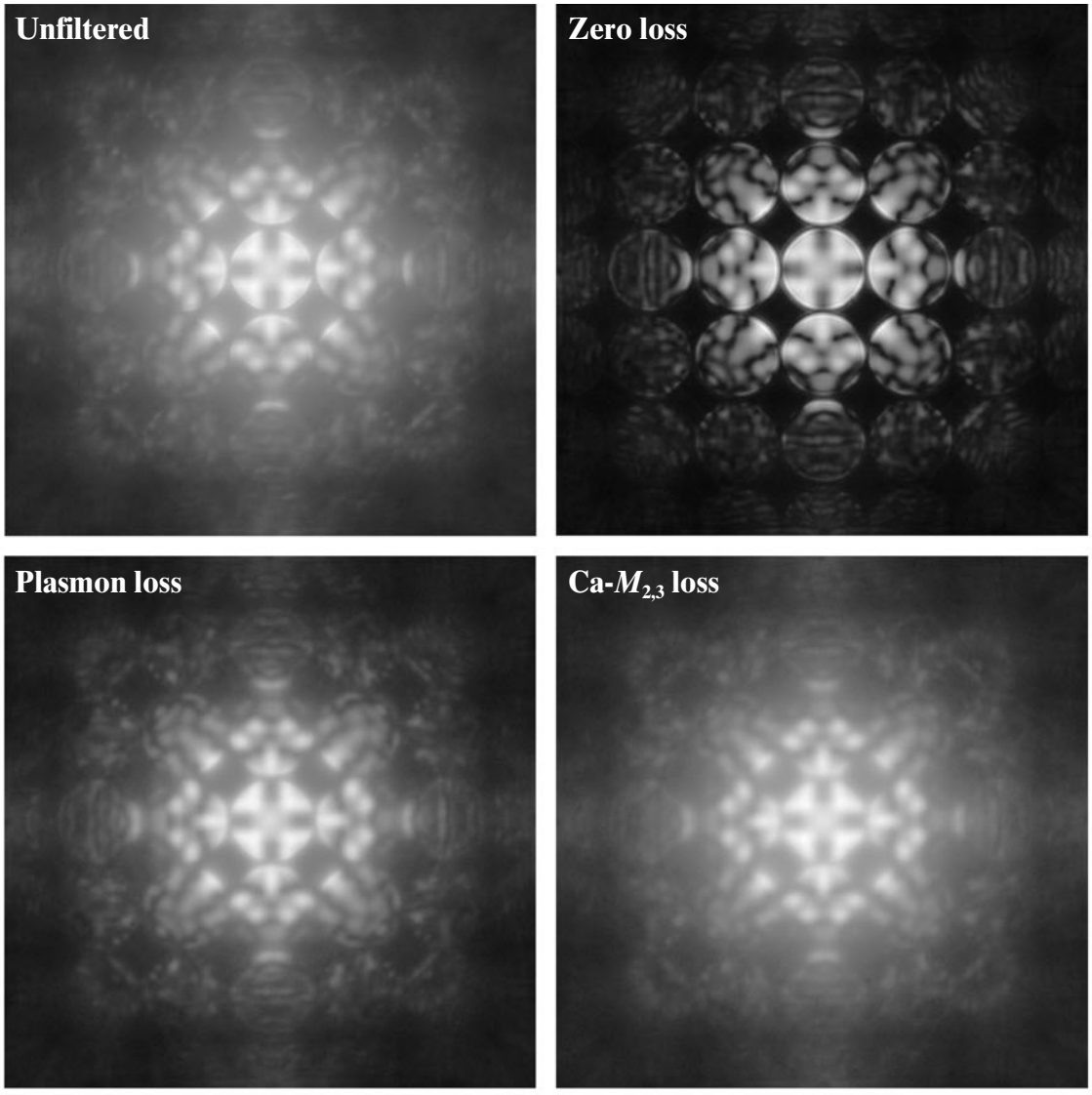

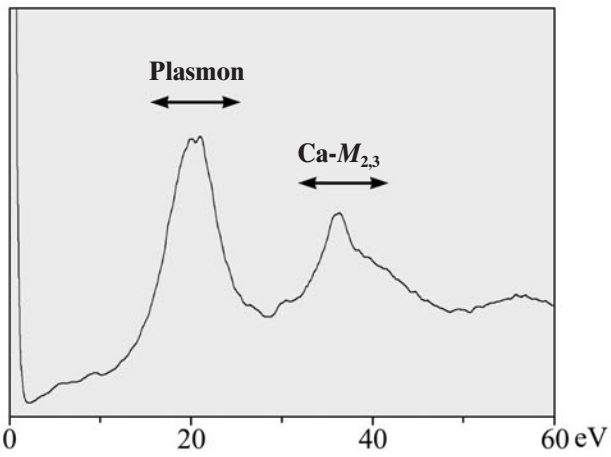

LaB_6 [100] **100kV**

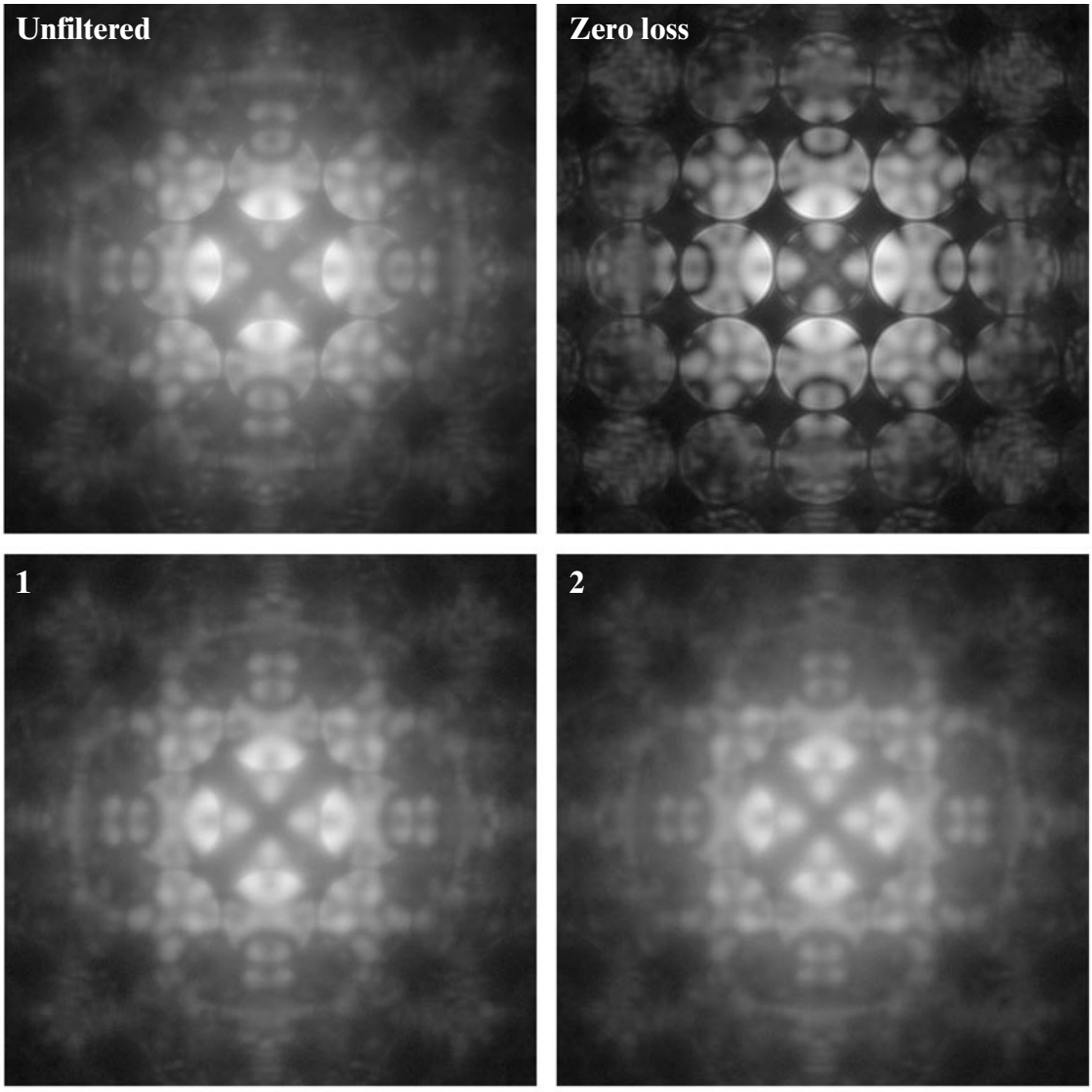

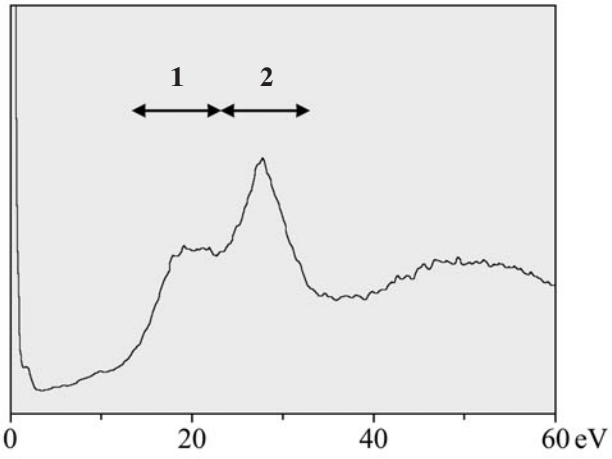

Fe_3O_4 [100] 100kV

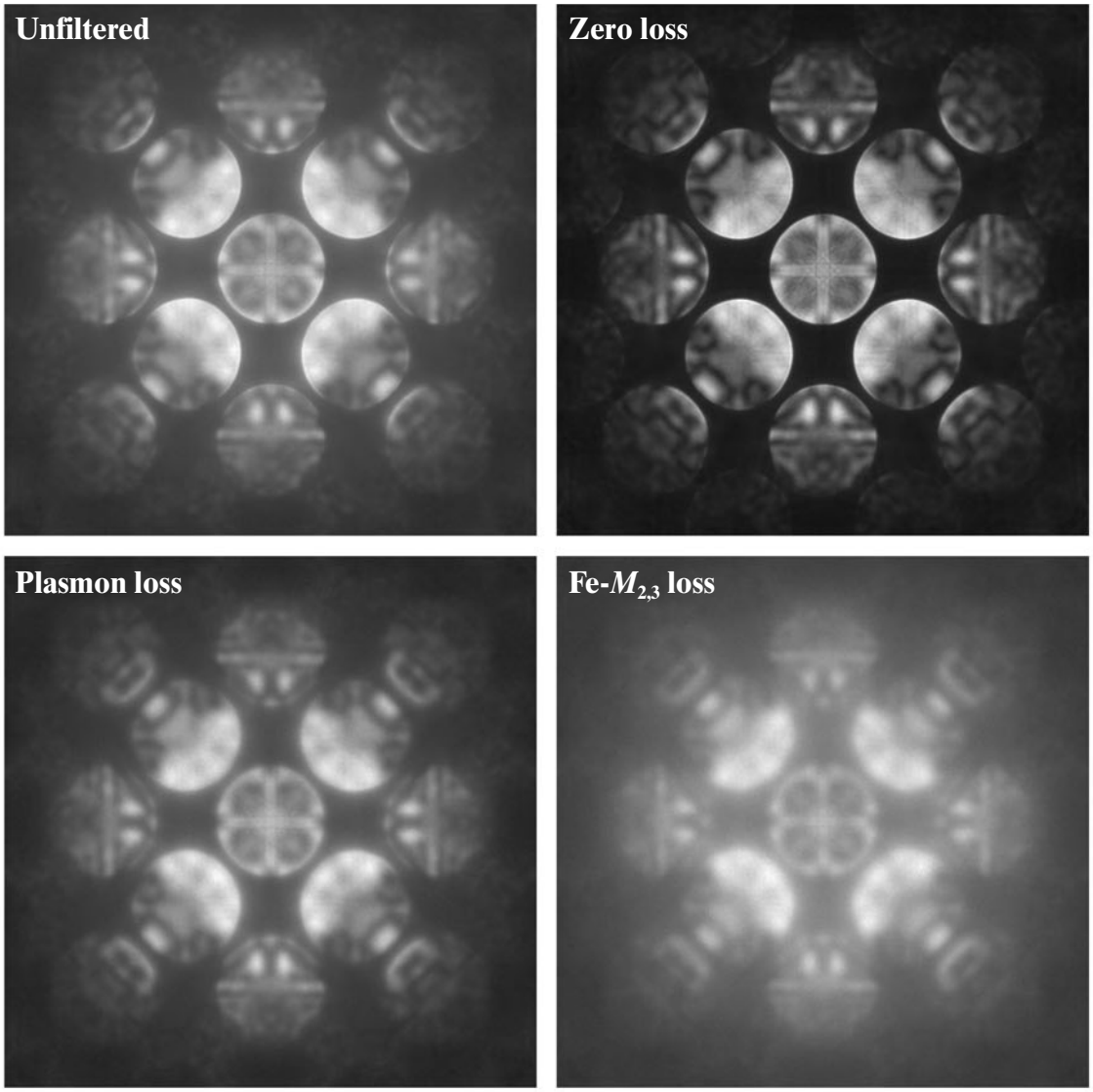

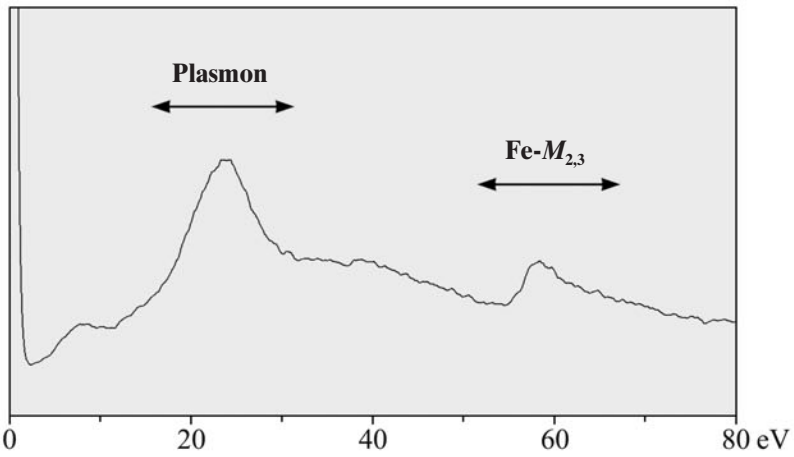

NiO [100] 100kV

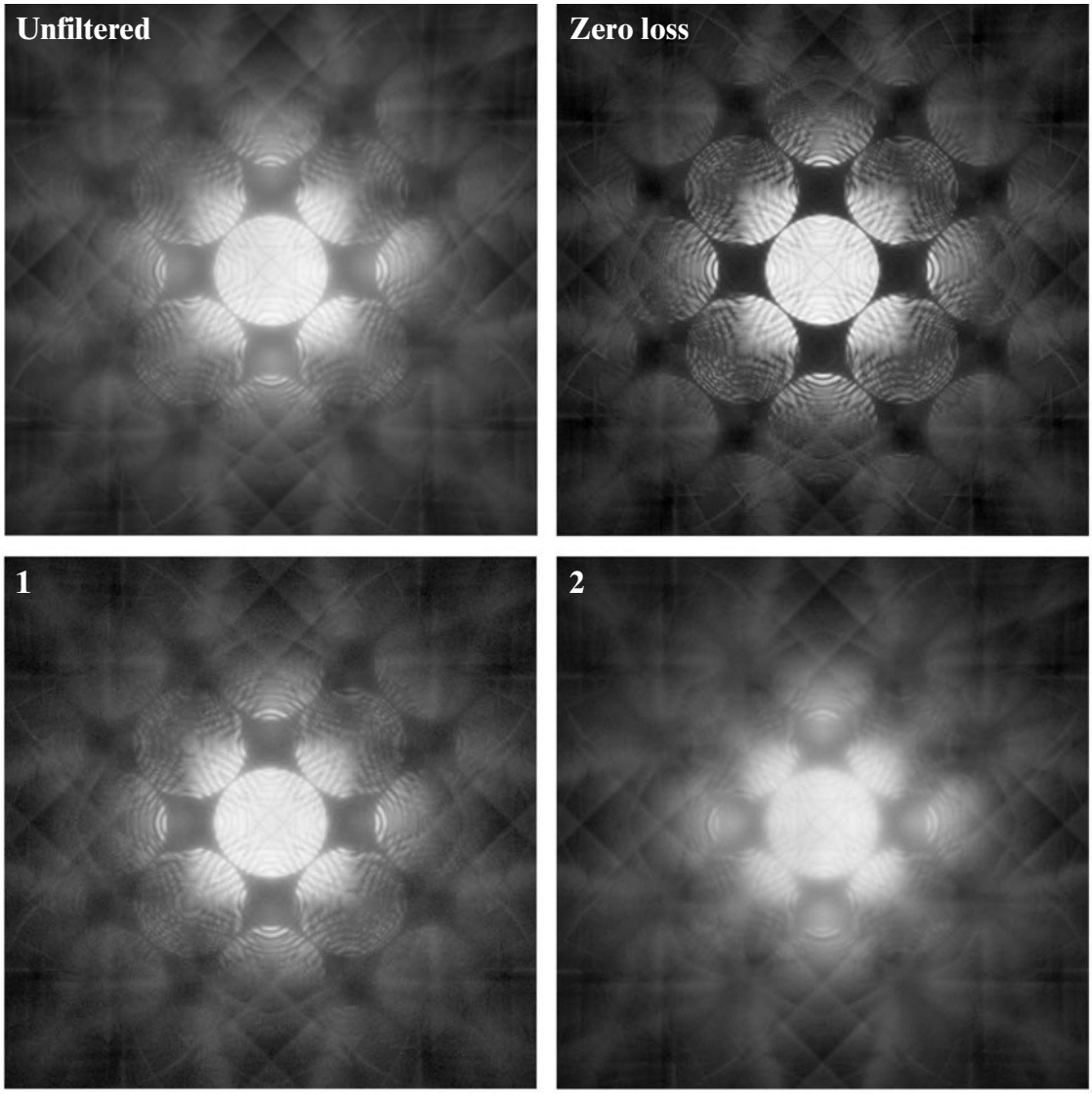

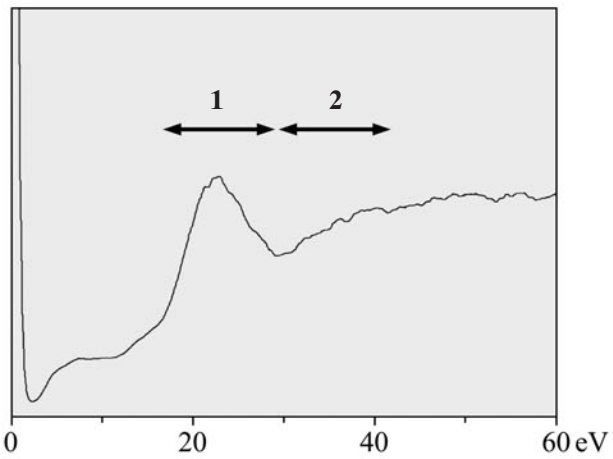

$SrTiO_3$ [100] 100kV

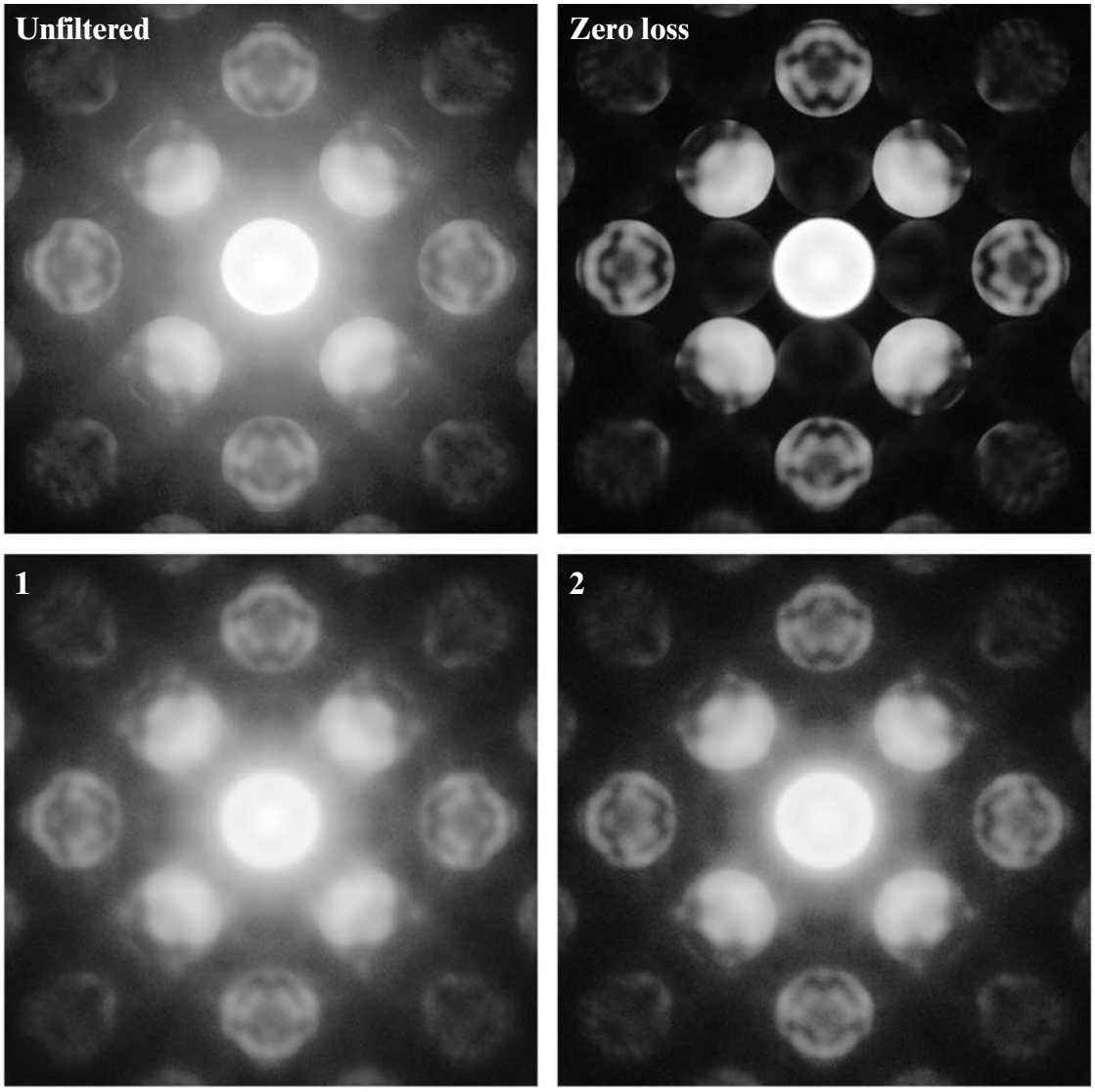

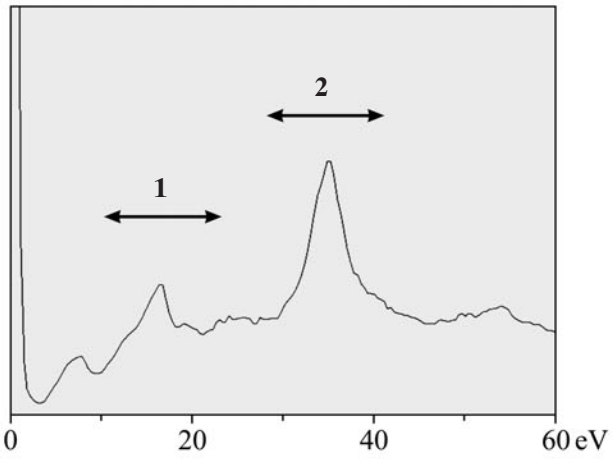

Cubic $BaTiO_3$ [001] **100kV**

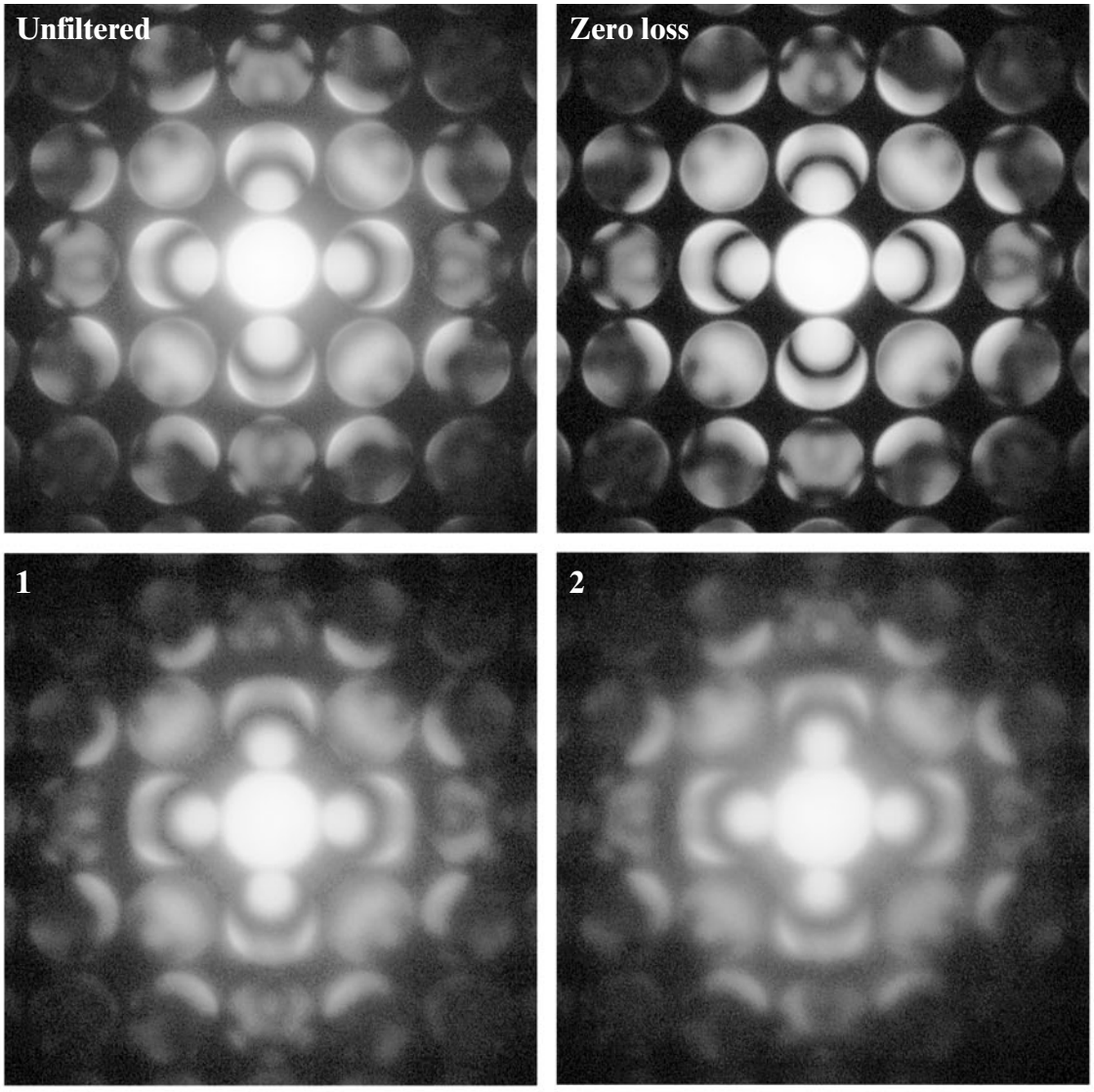

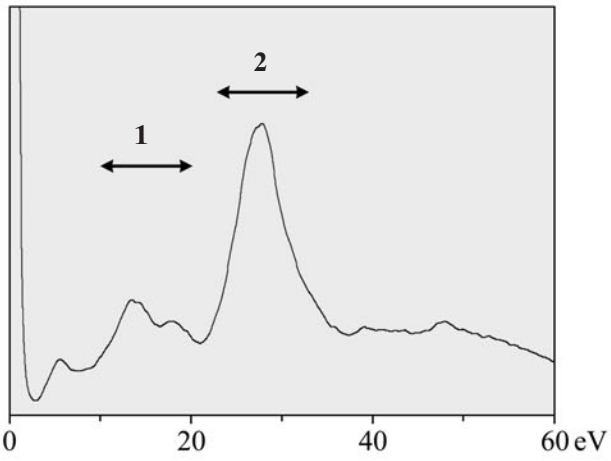

La_2CuO_4 [001] **100kV**

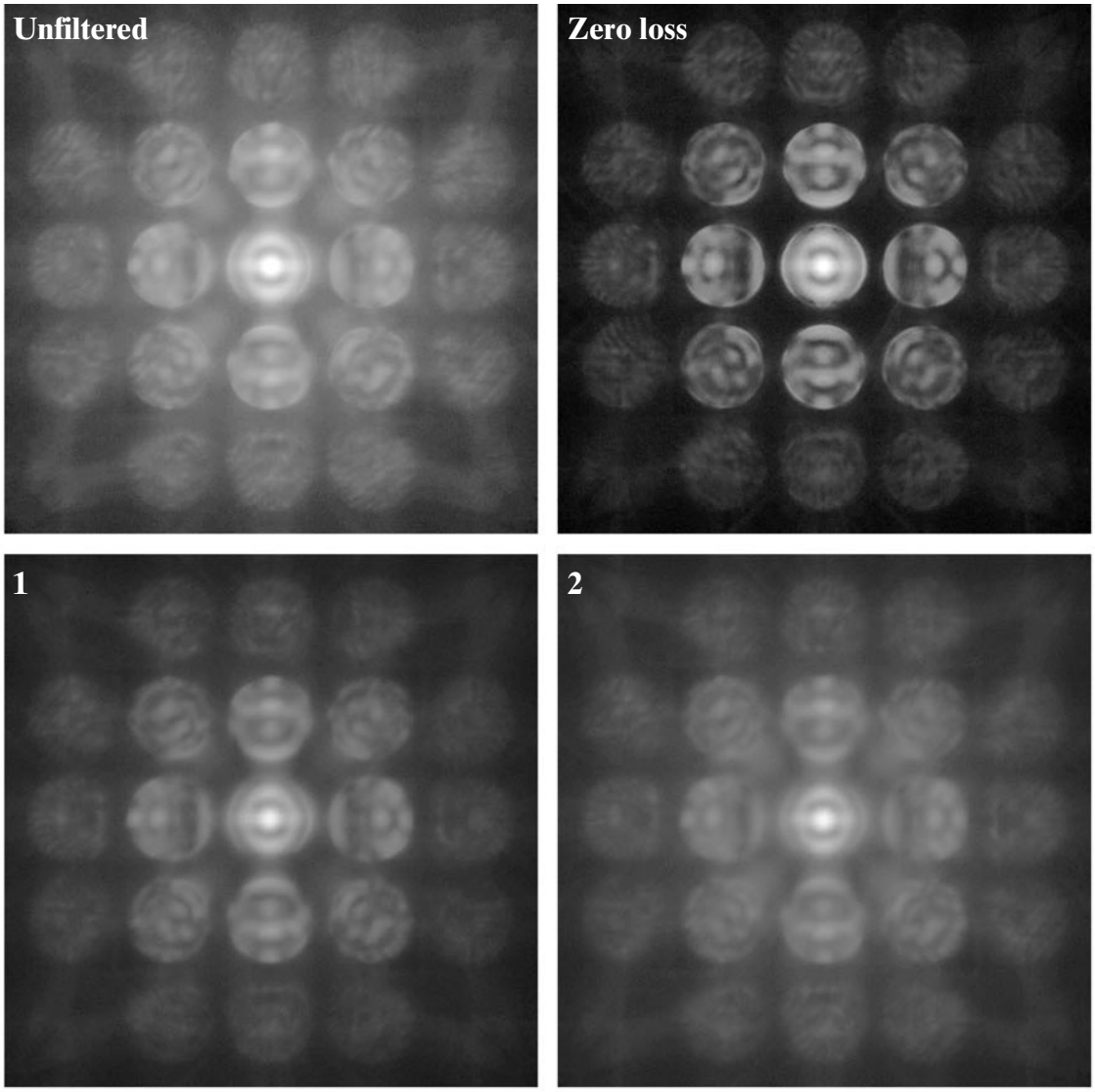

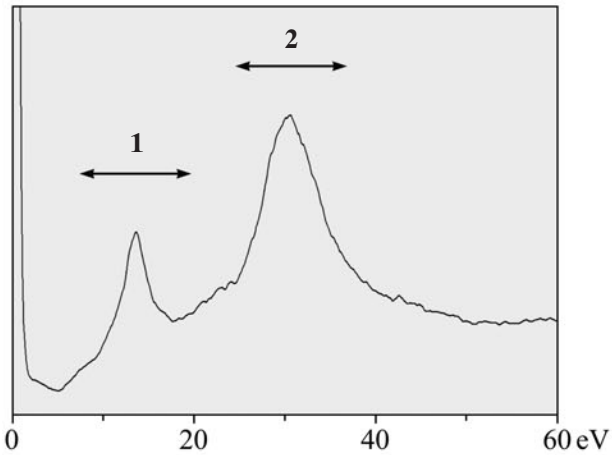

$La_{0.8}Sr_{0.2}CrO_3$ [110] **100kV**

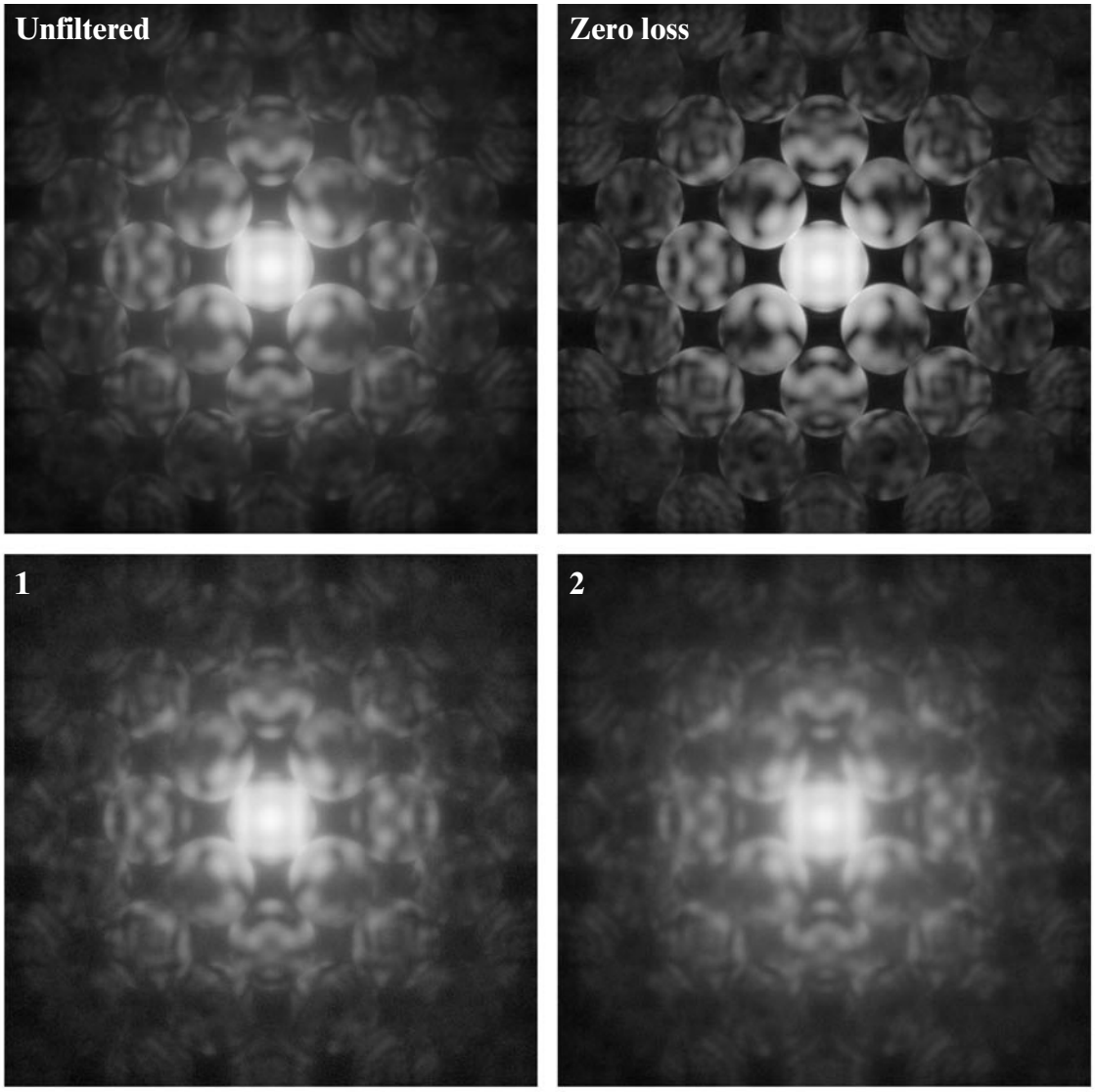

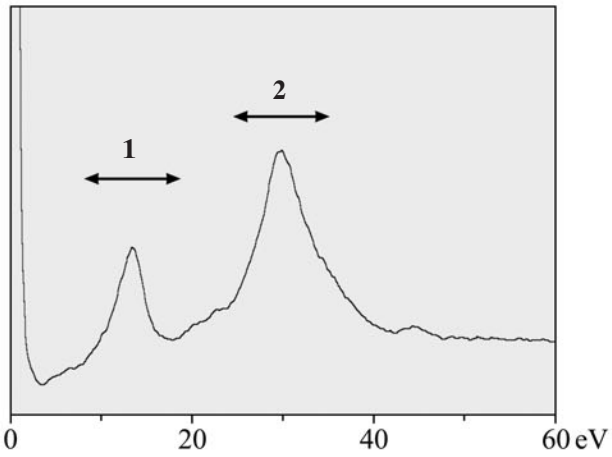

$Cd_2Re_2O_7$ [111] 100kV

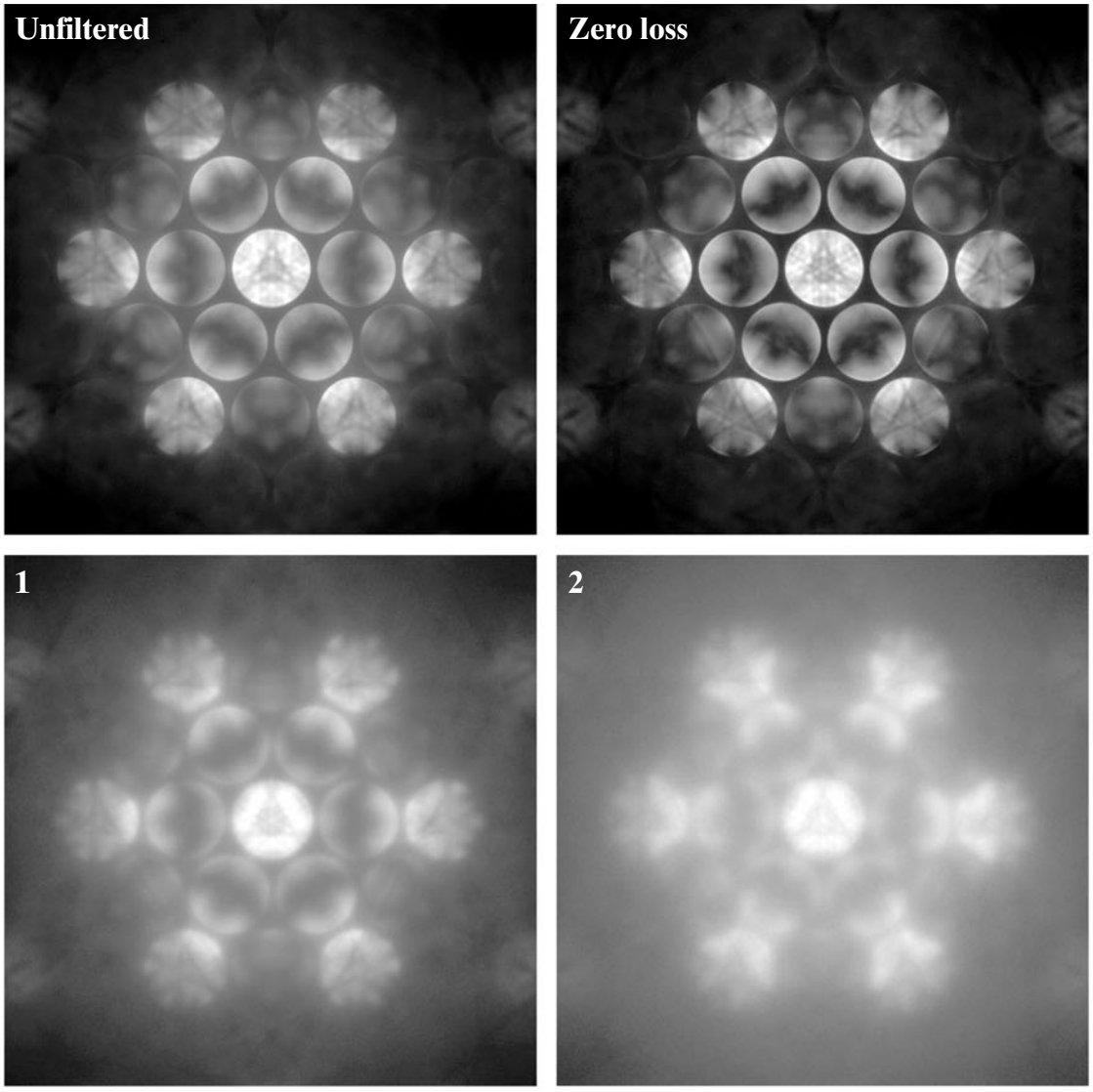

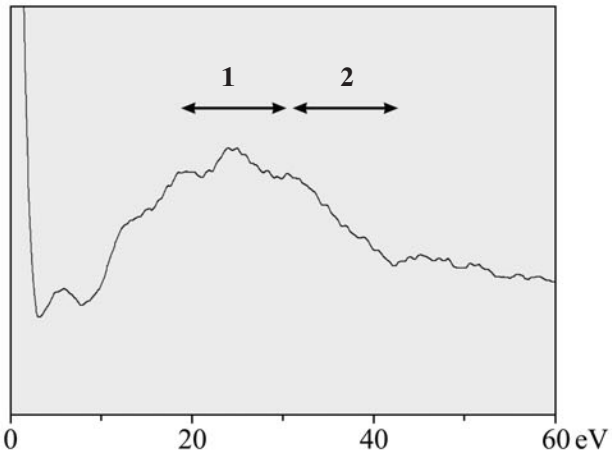

$MgAl_2O_4$ [100] 100kV

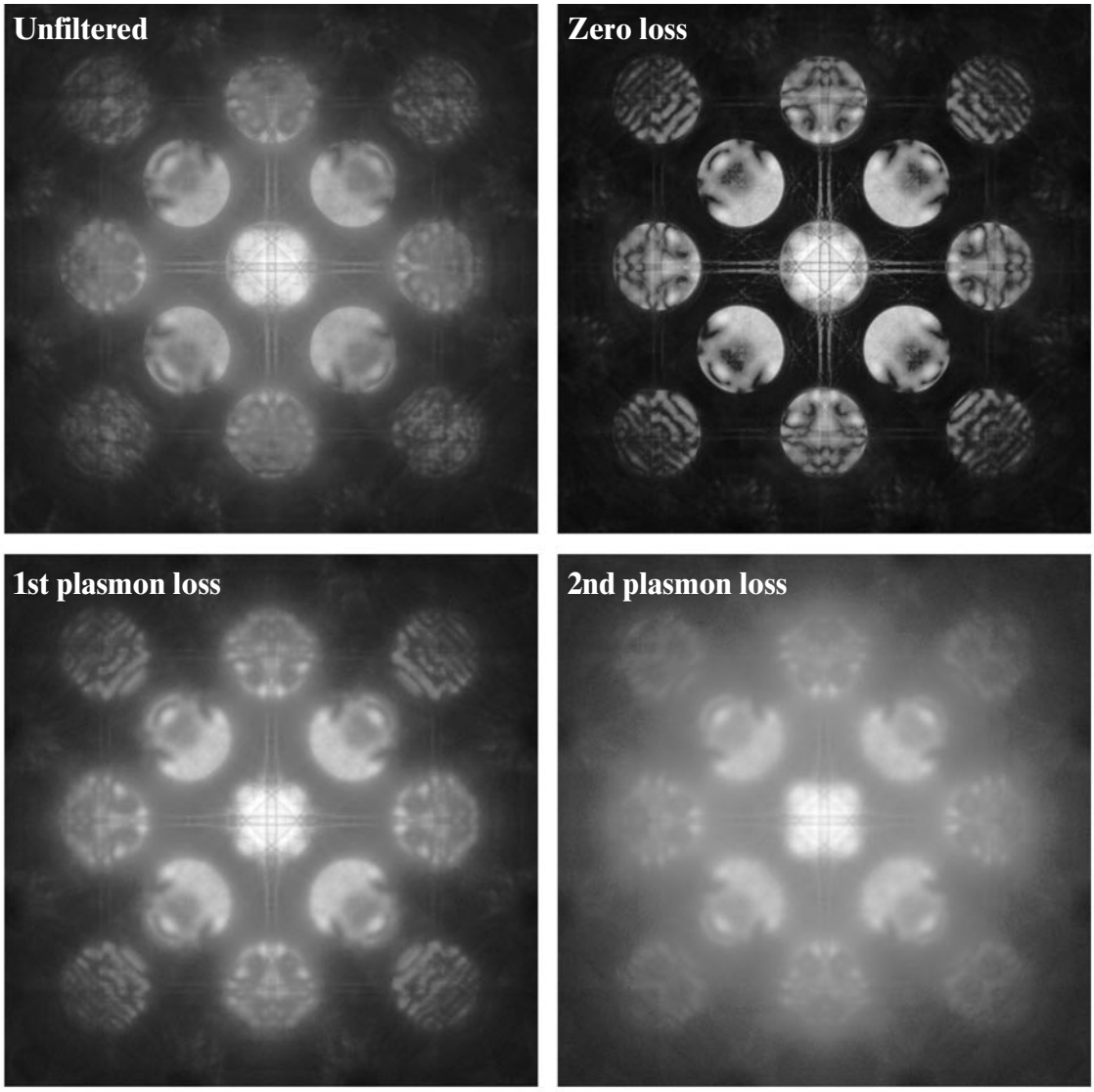

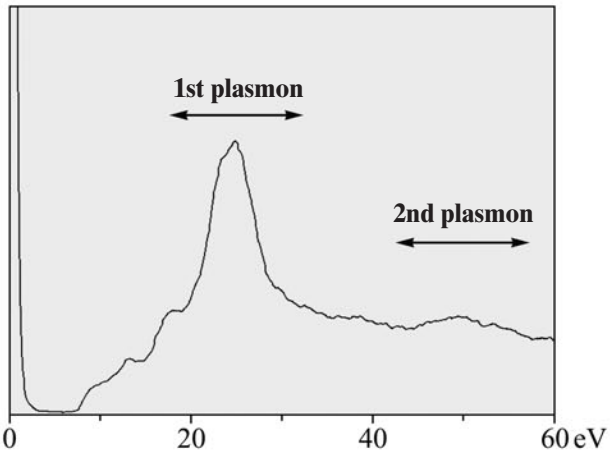

$NbSi_2$ [0001] **100kV**

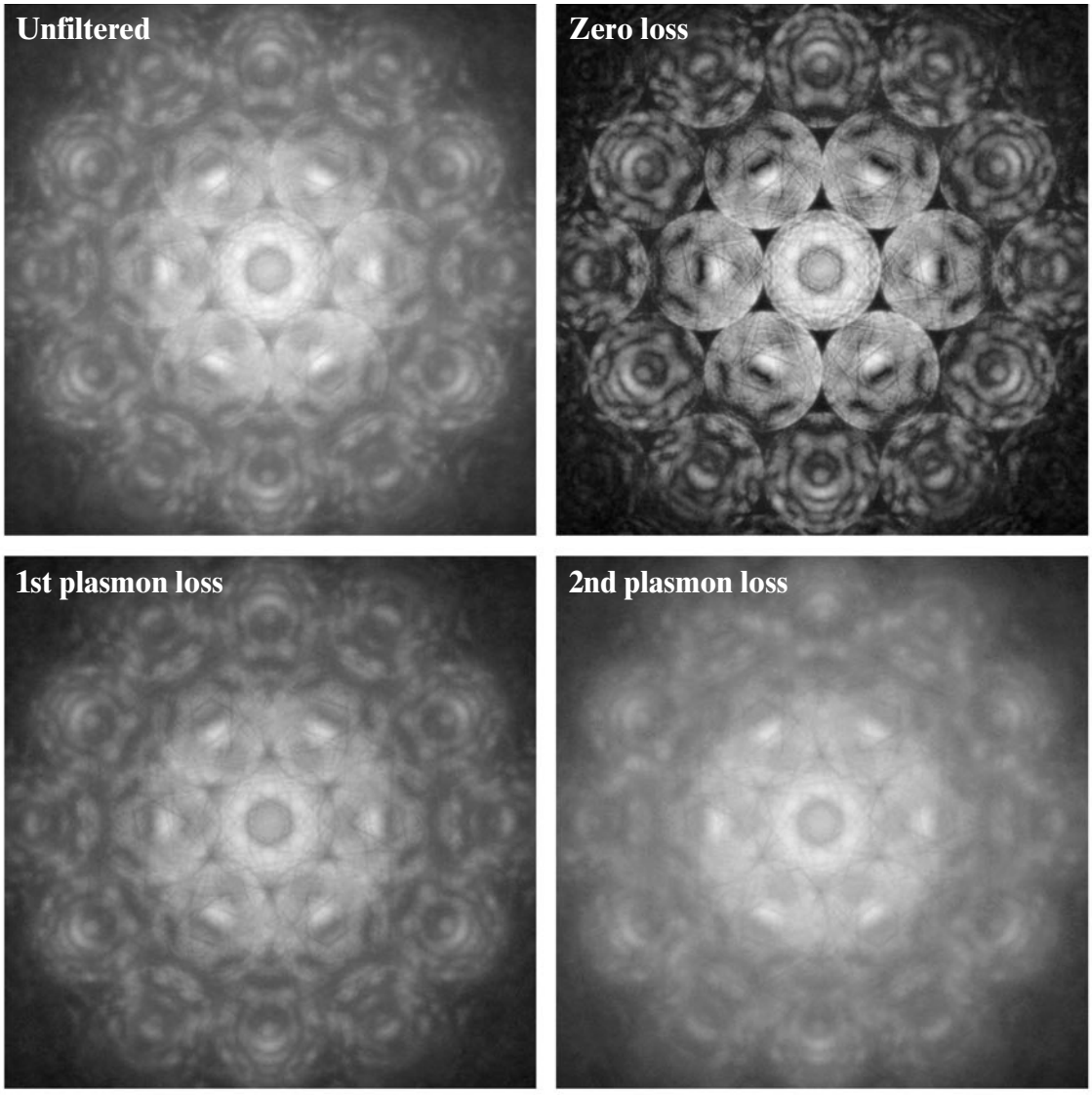

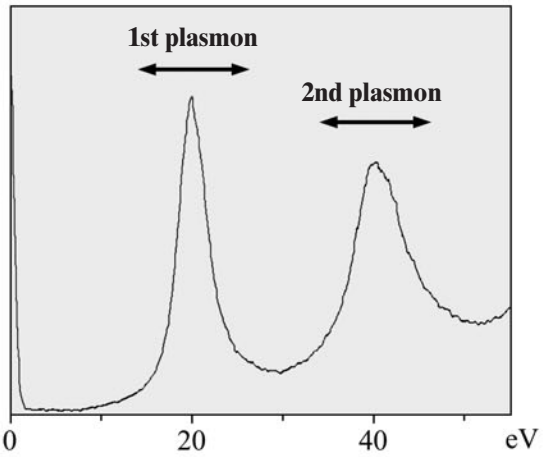

$Al_{72}Ni_{20}Co_8$ [00001] 100kV

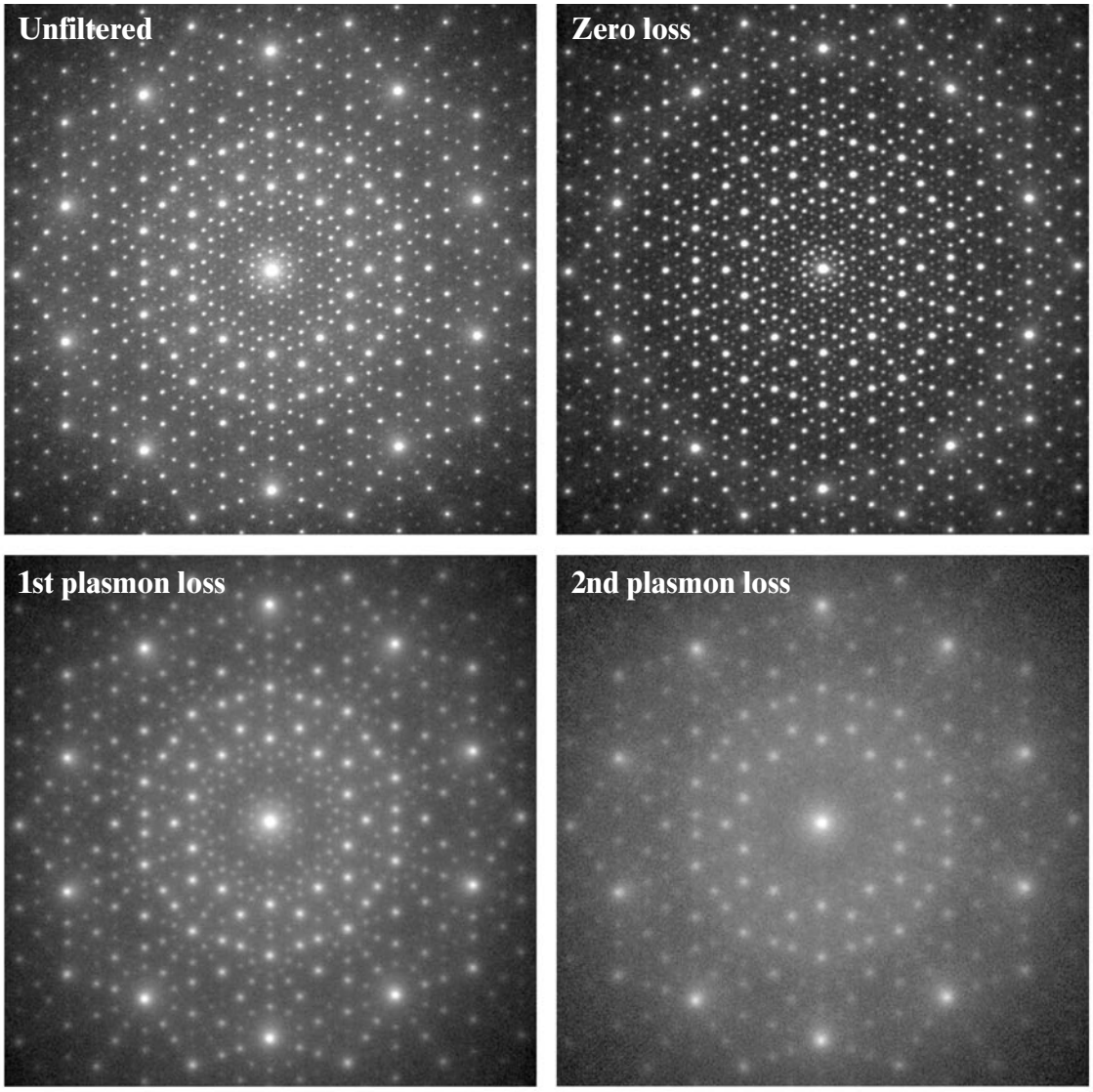

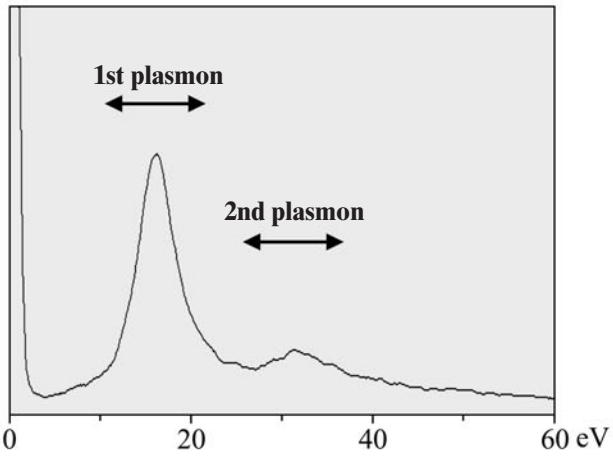

Structure Analysis

Structure Analysis by CBED

Crystal structure analysis by the CBED method has the following advantages in contrast to the X-ray and neutron diffraction methods: (1) *nm-size crystal structure analysis:* CBED patterns can be obtained from specimen areas of a few nm in diameter. Thus, the CBED method enables us to conduct the structure determination of not only perfect crystals but also local areas of crystals. (2) *Dynamical diffraction effect:* The CBED intensities contain phase information on crystal structure factors through the strong dynamical effect. (3) *Site-selective analysis:* Incident electrons form Bloch states in a specimen also due to the strong dynamical diffraction effect, each Bloch state being concentrated on specific atom positions. The use of the Bloch states allows site-selective structure analysis, or structure determination weighted for specific atom sites. (4) *High sensitivity to charge distribution:* Structure factors of low-order reflections for electron diffraction are more sensitive to the distributions of valence electrons than those for X-ray diffraction. These are the characteristic features only for the CBED method.

In the field of materials science, the structure refinement is more important than an *ab-initio* structure analysis. Since rough structures of most materials are already identified, what is expected to be investigated is secondary structures, namely small changes from the average structure, the displacements from the high symmetry phase, etc. Our method is not aimed at an *ab-initio* structure analysis but at a structure refinement. Thus, we need an initial structure model. We proposed a fully dynamical method to refine crystal structural parameters (atom positions and Debye-Waller factors) using CBED patterns with HOLZ reflections for the first time (Tsuda and Tanaka [6]; Tanaka *et al.* [7]). The use of HOLZ reflections is essential for the method because small displacements of atoms can be sensitively detected using HOLZ reflections with large reciprocal vectors. The method is based on the least-squares fitting between dynamical calculations and experimental intensities measured by imaging plates. The method was successfully applied to refine the structural parameters of the low-temperature phase of $SrTiO_3$. The experimental intensities in this case were acquired from a thin specimen area without the use of any energy filter. The fitting of the intensities was carried out using both integrated intensities (zero-dimensional data) and one-dimensional line profiles of HOLZ reflections. When the method is applied to the comparison with the experiments without the use of any energy filter, very thin specimens are required for reducing inelastic background intensities and suppressing the intensity variation of HOLZ reflections in the azimuthal direction due to dynamical diffraction. The accuracy and reliability of the method can be improved remarkably by the use of an energy filter and two-dimensional data of CBED patterns.

Energy filtering to remove inelastically scattered background is now becoming indispensable for quantitative analysis of CBED patterns. Measurements of low-order structure factors were successfully conducted using energy-filtered CBED patterns by several researchers. The energy-filtered data were obtained using a serial electron energy-loss spectrometer and a scanning unit (Zuo *et al.* [8]; Tanaka *et al.* [7]; Saunders *et al.* [9]), an Ω-filter (Deininger *et al.* [10]; Zuo *et al.* [11]) and using a post-column filter (Saunders *et al.* [12]). All these instruments are limited to detect diffraction intensities at small scattering angles. Thus, these cannot be applied to our method which uses the intensities of HOLZ reflections at high scattering angles. An energy filter with a high acceptance angle is needed for our method.

The distortion of the CBED patterns due to aberrations of the lenses and the energy filter is appreciable for HOLZ reflections in the existing filters, though they are disregarded for ZOLZ reflections at small scattering angles. Small distortion is important for the accurate fitting of HOLZ reflection intensities. For these purposes, we developed a new Ω-filter microscope which can take CBED patterns covering high angles of about up to 10 degrees with small distortion (Tsuno *et al.* [13]; Tanaka *et al.* [14]). The performance of the microscope is described in detail in the chapter of energy filtering.

The use of two-dimensional CBED intensities provides much more information on structural parameters. It enables us to perform accurate fitting between experimental and theoretical intensities, thus improving the accuracy and reliability of the analysis. We have extended our method for refining crystal structural parameters using CBED so as to fit the theoretical calculations with the experimental intensities of energy-filtered two-dimensional ZOLZ and HOLZ CBED patterns [15]. For this purpose, the JEM-2010FEF has been fully used. We have developed an analysis program (MBFIT) to refine structural parameters, which is based on many-beam Bloch-wave calculations and nonlinear least-squares fitting.

The present method can be applied to the determination of charge density distribution because the low-order Fourier coefficients of the electrostatic potential (low-order structure factors for electron diffraction), which are sensitive to valence electrons, can be refined together with the atom positions and Debye-Waller factors. Through Poisson's equation, the structure factors

for electron diffraction are converted to those for X-ray diffraction, or the Fourier coefficients of the charge density. According to the nature of Poisson's equation, a small change in the low-order structure factors for X-ray diffraction causes a large change in those for electron diffraction. That is, the determination of the low-order structure factors for electron diffraction by the electron diffraction method has an advantage in determining more accurate low-order structure factors for X-ray diffraction, compared with the X-ray diffraction method. Refinements of the low-order structure factors using ZOLZ CBED patterns were performed by Saunders *et al.* [9], [16], Nuechter *et al.* [17] and Zuo *et al.* [18]. It should be noted that the accurate determination of Debye-Waller factors, which can be performed successfully by our refinement method with the use of HOLZ reflections, is crucial to obtaining high-precision low-order structure factors for X-ray diffraction. Thus, the present method would have a potential to determine the behavior of valence electrons more accurately than the X-ray diffraction method and the electron diffraction method which uses only ZOLZ reflections.

In this chapter, structural parameters of CdS, $LaCrO_3$ and hexagonal $BaTiO_3$ are refined by the present method using the energy-filtered two-dimensional CBED patterns. In particular, the charge density distribution of $LaCrO_3$ is given together with the atom positions and anisotropic Debye-Waller factors. Lastly, Bloch states formed by incident electrons are simulated for some perovskite-type materials in order to demonstrate how the Bloch states change depending on the depth of the potential.

Analysis procedure

First of all, we need the tentative positional parameters of atoms of a specimen. The space group, the lattice parameters of the specimen and the accelerating voltage of the incident electrons are assumed to be determined by the CBED method in advance of analysis. The analysis procedure is as follows:

(i) Zero-loss energy-filtered CBED patterns containing HOLZ and ZOLZ reflections are obtained from the crystal using the Ω-filter transmission electron microscope JEM-2010FEF [13], [14]. The intensities are recorded on imaging plates. The use of energy-filtered CBED patterns of HOLZ and ZOLZ reflections is essential for the analysis. Appropriate electron incidences are selected so as to make CBED patterns sensitive to the displacements of the atoms to be refined.

(ii) The distortions of the CBED patterns due to the aberrations of the lenses and the | -filter are corrected numerically. Remaining background intensities due to thermal diffuse scattering (TDS) are subtracted by referring to the intensities just outside the reflection disks. Two-dimensional intensity distributions in reflection disks are extracted from the patterns.

(iii) The structural parameters are refined by a nonlinear least-squares fitting so as to minimize the residual sum of squares between the experimental two-dimensional data of HOLZ and ZOLZ reflections and calculated intensities. Intensity calculations are carried out based on the Bloch wave dynamical theory of electron diffraction. The structural parameters refined by the present method are atom positions, isotropic and anisotropic Debye-Waller factors, site occupancies and structure factors of low-order reflections. The intensity calculations and the nonlinear least-squares fitting are performed using an analysis software MBFIT which we have developed.

The analysis procedure is schematically shown on the right-side page. The procedures for correcting the distortion of CBED patterns, background subtraction due to TDS, dynamical calculation and nonlinear least-squares fitting are described on the following pages.

Schematic diagram of structure refinement by CBED

Experiments

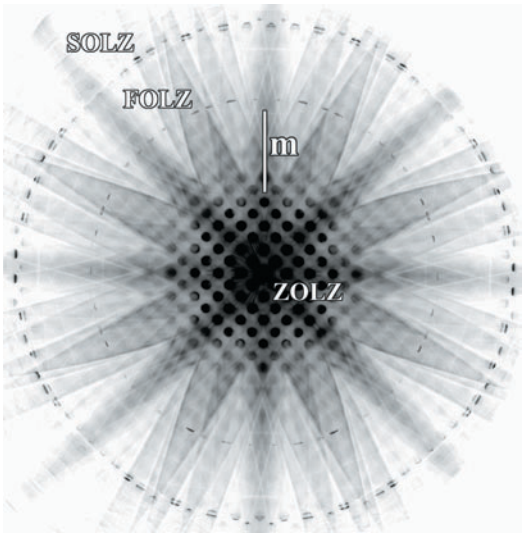

Two-dimensional energy-filtered HOLZ- and ZOLZ-CBED patterns

Data preprocessing:
- Distortion correction
- Background subtraction

Calculations

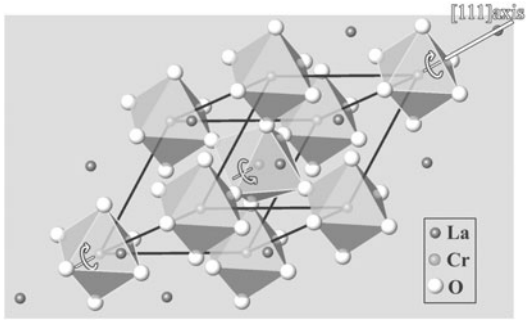

Structural model

Many-beam dynamical calculations

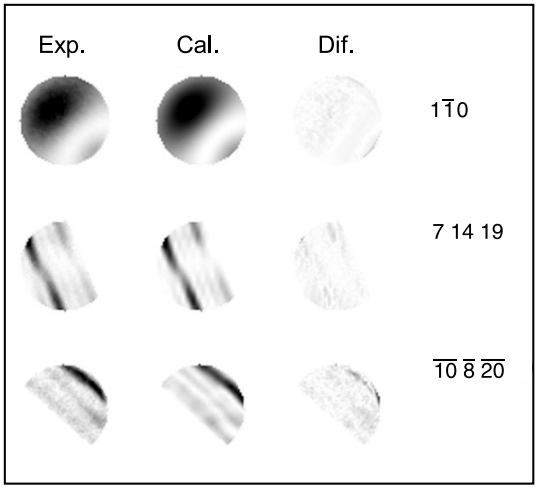

Fitting between experimental data and theoretical calculations by a nonlinear least-squares method

Weighted *R*-factor:

$$R_{\mathrm{w}} = \left[\frac{\sum_i w_i (I_i^{\mathrm{exp}} - s I_i^{\mathrm{cal}})^2}{\sum_i w_i (I_i^{\mathrm{exp}})^2}\right]^{1/2}$$

Goodness-of-fit:

$$GOF = \left[\frac{\sum_i w_i (I_i^{\mathrm{exp}} - s I_i^{\mathrm{cal}})^2}{(N - M)}\right]^{1/2}$$

(N: number of data points, M: number of parameters to be refined)

Structural parameters (Atom positions, *B*-factors, site occupancies, low-order F_g, etc.)

Preprocessing of experimental data

Correction of distortion of CBED patterns

To use two-dimensional HOLZ intensities, it is necessary to correct the distortion of an energy-filtered CBED pattern due to aberrations of the lenses and the Ω-filter of the electron microscope. The distortion due to the lenses can be described by radial and spiral distortions [6]. The displacements Δr of the radial distortion in the radial direction and Δs of the spiral distortion in the azimuthal direction are expressed by $\Delta r = C_r r^3$ and $\Delta s = C_{sp} r^3$, where r is the distance from the optical axis, and C_r and C_{sp} are the coefficients of the radial and spiral distortions, respectively. The distortion due to the Ω-filter is well approximated to be elliptical. That is, the displacements Δe_x and Δe_y of the elliptical distortion along the x- and y-axes are given by

$$\Delta e_x = C_{el}\,(r\cos(t+\theta)\cos\theta + r\sin(t+\theta)\sin\theta\,) \quad \text{and}$$
$$\Delta e_y = -C_{el}(-r\cos(t+\theta)\sin\theta + r\sin(t+\theta)\cos\theta\,) / (C_{el}+1),$$

where θ is the angle between the major axis of the ellipse of the distortion and the x-axis, t is the angle from the major axis, r is the distance from the optical axis and C_{el} is the coefficient of the elliptical distortion.

The distortion of the entire CBED pattern is corrected by the following procedure.

(a) The perimeters (central positions) of nearly a half of all the reflection disks are determined manually.
(b) Distortion coefficients of the radial, spiral and elliptical distortions are determined from the central positions obtained by the nonlinear least-squares fitting.
(c) The distortions of the entire CBED pattern are corrected by the equations using the distortion coefficients determined at the previous step. Two-dimensional intensity distributions of the reflections are extracted from the distortion-corrected pattern.

Subtraction of the background due to TDS

The distortion-corrected CBED patterns still contain weak diffuse background intensity and Kikuchi lines and bands, which are formed by TDS. We assumed that background intensities in each reflection disk change linearly along the lines parallel to the Kikuchi line or band which crosses the reflection disk or is nearest to the disk. Background intensities in each reflection disk were subtracted by linear interpolation between the background intensities of both sides of the disk along the lines.

References

[a] *e.g.* H. A. Bethe: *Ann. Phys. (Leipzig)*, **87** (1928) 55.; P. B. Hirsch, A. Howie, R. B. Nicholson, D. W. Pashley and M. J. Whelan: Electron Microscopy of Thin Crystals, 2nd ed., Krieger, 1977.; J. C. H. Spence and J. M. Zuo: Electron Microdiffraction, Plenum Press, 1992.
[b] P. A. Doyle and P. S. Turner: *Acta Cryst.*, **A24** (1968) 390.
[c] D. M. Bird and Q. A. King: *Acta Cryst.*, **A46** (1990) 202.
[d] M. Ichikawa and K. Hayakawa: *J. Phys. Soc. Jpn.*, **42** (1977) 1957.
[e] *e.g.* W. H. Press, B. P. Flannery, J. A. Teukolsky and W. T. Vetterling: Numerical Recipes, Cambridge University Press, 1992.
[f] J. M. Zuo: *Acta Cryst.*, **A47** (1991) 87.

Calculations

Dynamical calculations

The intensity calculations of CBED patterns are based on the Bloch-wave formulation of the dynamical theory, namely matrix diagonalizations of many beam equations [a]. The atomic scattering factors for electrons are calculated not by a Gaussian parameterization [b] but by a quadratic interpolation [c] to obtain the accurate values of the factors at scattering angles higher than $g = 4.0$Å^{-1}, where g is the scattering vector. Crystal structure factors are calculated with the atomic scattering factors obtained by the above method and with the full use of space-group symmetries. The tables of the atomic scattering factors for electrons and the space-group symmetries are contained in the program MBFIT.

The absorption (imaginary) potential is used in the dynamical calculations. The most significant contribution to the absorption potential is the contribution due to TDS, which is calculated by the scattering factors given by Hall and Hirsch [29] using the Einstein model of lattice vibrations, the table of the Fourier coefficients of the absorption potentials due to TDS being included in MBFIT [c]. To obtain accurate intensities of HOLZ reflections, the imaginary potential is treated not by perturbation but by exactly solving the matrix of the dynamical theory.

The reflections used in the scattering matrix are selected so that the values of their excitation errors s_g and reciprocal vectors g respectively satisfy $s_g < s_{max}$ and $g < g_{max}$. It is noted that magnitudes of their structure potentials U_g are not used as a criterion of selection because even forbidden reflections with $U_g = 0$ are often important through dynamical interaction.

The generalized-Bethe-potential (GBP) method [d] is adopted to reduce the dynamical calculation time. In the GBP method, the effects of weakly excited beams are incorporated into the crystal-potential coefficients of strongly excited beams, thereby the order of the initial matrix to be diagonalized being reduced. The GBP method gives more accurate intensities than the original Bethe-potential method because the former includes all the higher-order Bethe-potential terms, which are neglected in the latter. The reflections with excitation errors $s_g \leq s_{smax}$ are regarded as the strongly excited reflections and the reflections with $s_{smax} < s_g \leq s_{max}$ the weakly excited ones.

Nonlinear least-squares fitting

The structural parameters are refined so as to minimize the residual sum of squares S between the experimental CBED intensities and the theoretical CBED intensities by a nonlinear least-squares fitting. The quantity S is defined as $S = \Sigma_i w_i [I_i^{exp} - sI_i^{cal}(\boldsymbol{x})]^2$, where I_i^{exp} is the i-th experimental intensity, I_i^{cal} is the calculated intensity corresponding to I_i^{exp} for all the structural parameters $\boldsymbol{x}$, w_i is a weight factor and s is a scale factor common to all the calculated intensities.

We set the weight factor $w_i = w_{LZ}/(\sigma_i^{exp})^2$, where σ_i^{exp} is the experimental error of I_i^{exp}. w_{LZ} is an additional weight factor to decrease the weight of ZOLZ reflections in the residual sum of squares S. Both the HOLZ reflections and ZOLZ reflections are necessary to determine the Debye-Waller factors. Since intensities of ZOLZ reflections are more than 10^2 times those of HOLZ reflections and rather insensitive to positional parameters, the weights of ZOLZ reflections should be decreased using w_{LZ} for precise determination of the positional parameters.

Minimization of S is performed by the Levenberg-Marquardt method [e], which is known as a standard algorithm of the nonlinear least-squares fitting. The fitting starts with a set of initial values of the structural parameters and continues until S reaches a minimum. The structural parameters (atom positions, Debye-Waller factors and site occupancies), the scale factor common to all the calculated intensities, the specimen thickness, the low-order structure factors and the geometrical parameters are refined at the same time in the fitting. The geometrical parameters are introduced for correcting the small residual displacements of reflection disks, which exist even after the distortion correction. The standard deviations of the refined parameters are evaluated according to the error propagation rule.

The Levenberg-Marquardt method requires gradients of the theoretical intensities as a function of the fitting parameters. We have applied a perturbation method proposed by Zuo [f] to the evaluation of the gradients, where we have extended his method including HOLZ reflections. That is, intensity changes caused by small changes of structural parameters are calculated by the perturbation method without a new diagonalization of the scattering matrix, where the gradients are calculated from the intensity changes under a finite difference approximation. This method allows a large increase in the number of structural parameters without a great increase of computing time.

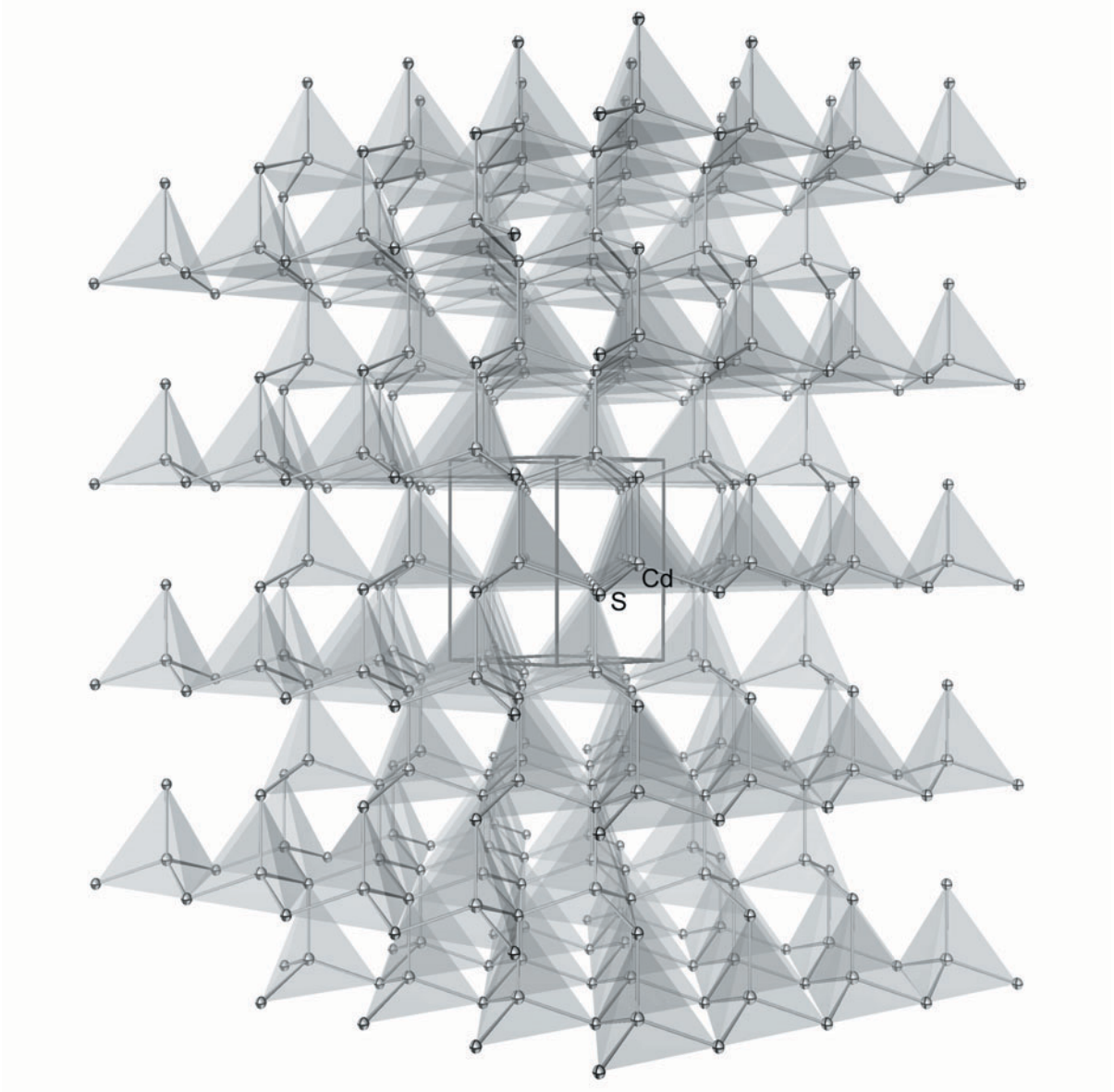

ORTEP diagram of the fitting result of CdS viewed from the [100] direction.

Thickness variation in the illuminated area

The experimental intensities should be the intensities averaged over an illuminated area with a thickness variation. However, we did not take into account the thickness variation. The thickness variation over the illuminated areas in the present experiments may be less than a few nm because the electron probe size used was approximately 1nm in full width at half maximum. Figures (a) to (d) show simulated line profiles of ZOLZ reflections 004, 002, 000 and $00\overline{2}$ in the c^*-direction with specimen thicknesses 88, 89, 90, 91 and 92nm. It is seen that the line profile averaged over these five thicknesses with the same weight for each thickness is almost the same as the line profile of the mean thickness of 90nm. Furthermore, HOLZ reflections which play an important role in the determination of parameter u are much more insensitive to the thickness change than ZOLZ reflections because of their large extinction distances. For these reasons, a small thickness variation in the illuminated area does not affect the fitting result. Therefore, we can use the mean value of the thicknesses.

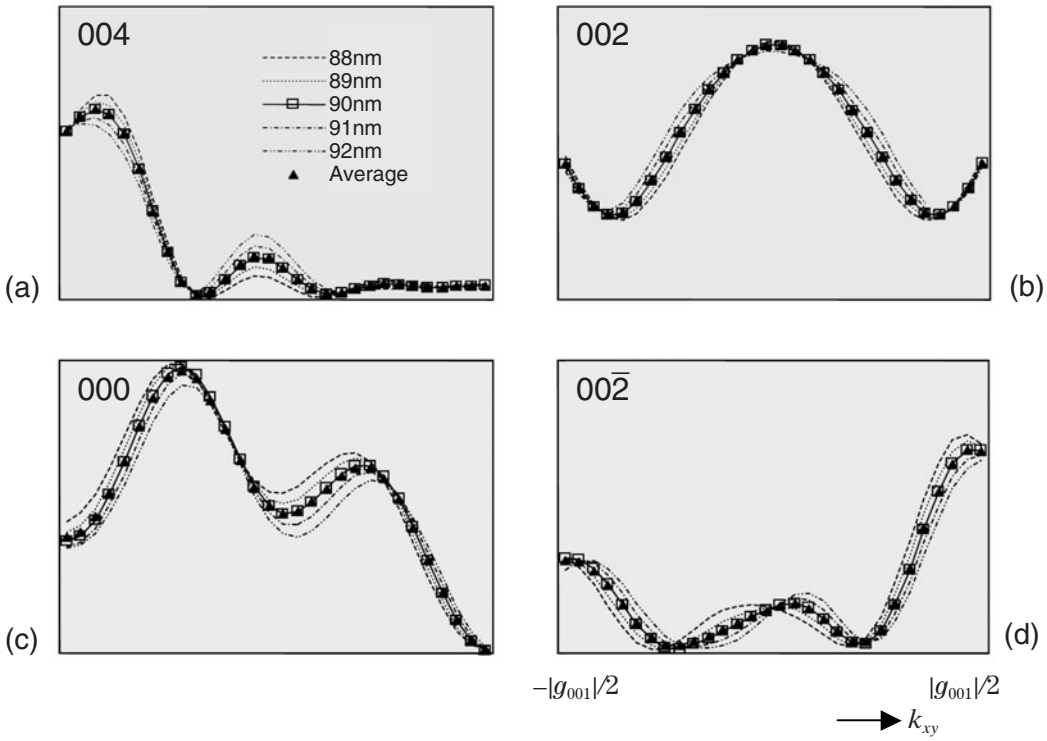

Refined parameters

Table shows the averaged values of the structural parameters of the two results described on page 96. The present result well agrees with the result of a single crystal X-ray diffraction experiment [a] except for small discrepancies of anisotropic B factors.

Parameter	Present result	X-ray [a]
u	0.3774(3)	0.37715(8)
B(Cd) (Å^2)	1.46(3)	1.394(4)
B(S) (Å^2)	1.10(2)	1.13(1)
B_{11}(Cd) (Å^2)	1.40(3)	1.376(3)
B_{33}(Cd) (Å^2)	1.50(2)	1.430(3)
B_{11}(S) (Å^2)	1.05(8)	1.136(7)
B_{33}(S) (Å^2)	1.21(6)	1.126(20)

The averaged values of the structural parameters obtained from the two data sets taken at the 002 and 00$\bar{2}$ excitations.

Plots of R_w as a function of parameter u

To confirm the nonexistence of local minima in the fitting, we plot the values of R_w against parameter u. Figure shows the plots of R_w, R_w^{ZOLZ} and R_w^{HOLZ} for the data taken at the 002 Bragg condition, where R_w^{ZOLZ} and R_w^{HOLZ} were calculated from the data of ZOLZ reflections and HOLZ reflections, respectively. Since all R_w's show no local minima, the values of the parameters obtained are the unique solution corresponding to the global minimum. It should be noted that R_w^{HOLZ} curve shows a deep minimum, but R_w^{ZOLZ} curve shows a shallow minimum at a u value, which is little different from that of R_w^{HOLZ}. This evidently shows that the HOLZ reflections are more sensitive to parameter u than the ZOLZ reflections. Thus, the use of HOLZ reflections is indispensable for determination of structural parameters.

The both curves of R_w and R_w^{HOLZ} are very close and have the minima at the same position because the weight factors w_{LZ} was set to a small value. With the increase of the w_{LZ} value for ZOLZ reflections, the curve R_w approaches the curve of R_w^{ZOLZ}, which makes it difficult to accurately determine the positional parameters. On the other hand, when w_{LZ} is decreased to a very small value, the correlation between scale factor s and Debye-Waller factors B increases, and thus unique determination of the parameters becomes unfeasible. The value ~0.001 of the weight factor w_{LZ} was selected by satisfying the two requirements in the present analysis.

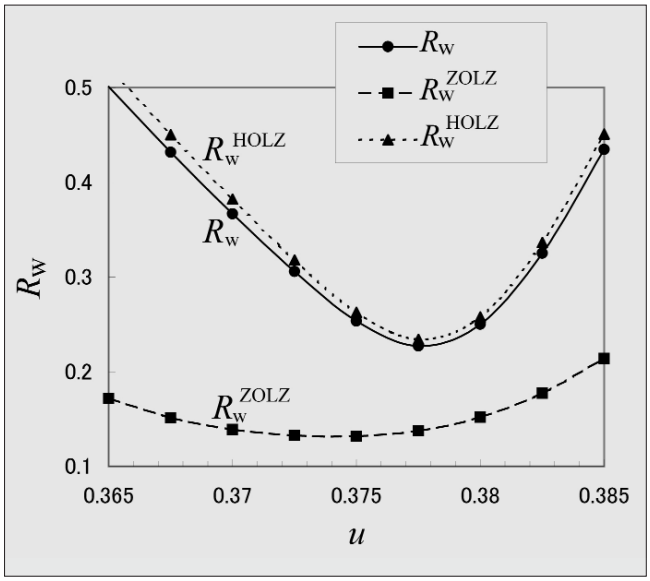

Plots of R_w as a function of parameter u.

Reference

[a] A. W. Stevenson, M. Milanko and Z. Barnea: *Acta Cryst.*, **B40** (1984) 521.

Fitting results (CdS $00\bar{2}$ excitation)

(b)

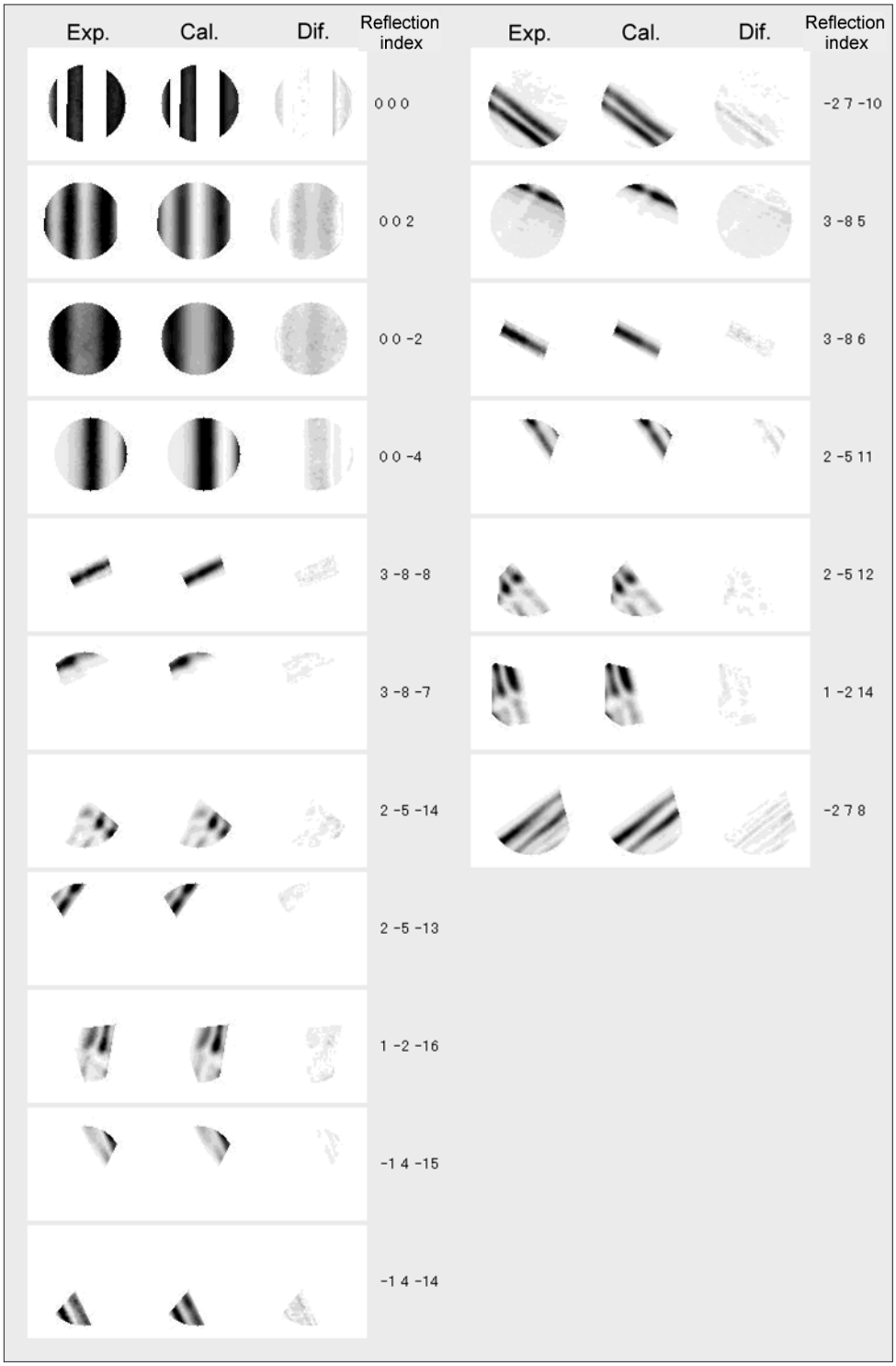

Fitting results for the data taken at the $00\bar{2}$ excitation.

Fitting results (CdS 002 excitation)

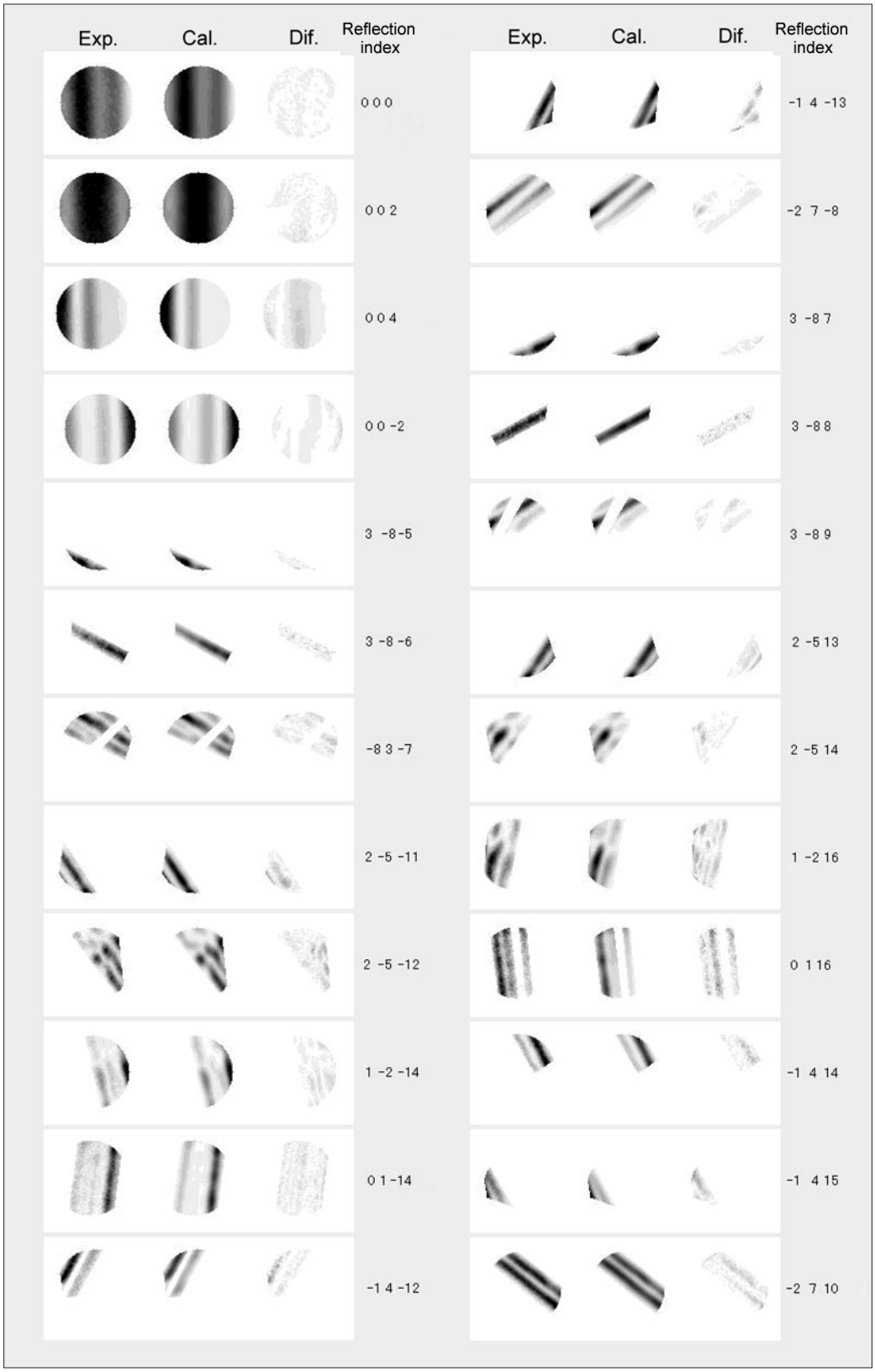

(a)

Fitting results for the data taken at the 002 excitation.

Fitting

After the distortion correction and background subtraction, two-dimensional intensities of four ZOLZ reflections and twenty FOLZ reflections were taken out of the CBED pattern. The specimen thickness was determined to be 93.0nm by comparing the experimental ZOLZ CBED patterns with calculated ones, where parameter u of 0.375 and Debye-Waller factors B(Cd) and B(S) of 1.0Å^2 were assumed. This value of the specimen thickness was used as the starting value to refine all parameters. The number of total data points in the present pattern was 36252, which is extremely greater than the data points used in the case of line profiles. Since intensities of ZOLZ reflections are more than 10^2 times those of HOLZ reflections and less sensitive to positional parameters, the weights of ZOLZ reflections are decreased using an additional weight factor w_{LZ} for precise determination of the positional parameters. The weight factor w_{LZ} for ZOLZ reflection intensities was set to be 0.0015. From the results of the convergence tests of intensities about the number of reflections, 279 reflections were chosen for the dynamical calculations by using the selection parameters g_{max} = 4.0Å^{-1}, s_{smax} = 0.015Å^{-1} and s_{max} = 0.03Å^{-1}. 119 weak reflections among the 279 reflections were treated by the GBP method [a].

The parameters to be refined in the fitting are structural parameters u, B(Cd) and B(S), scale factor s, specimen thickness t and 28 geometrical parameters to adjust the positions of reflection disks. The nonlinear least-squares fitting was converged in three iterations. It took about 15 hours to perform the fitting on a Alpha workstation. Figure (a) on the right-side page shows the final result of the fitting for the isotropic Debye-Waller factors between experimental and calculated reflection patterns. The patterns in the left, center and right columns respectively show experimental, calculated and difference patterns. The calculated patterns are seen to agree very well with experimental patterns. It should be noted that large intensity variations in the azimuthal directions seen in reflections 2 $\bar{5}$ $\bar{1}\bar{2}$, 2 $\bar{5}$ 14 and 1 $\bar{2}$ 16 were well reproduced in the calculated patterns. If such reflections are used for line profile fitting, the intensity distribution of the line profile is very sensitive to the azimuthal position. The intensity fitting to use such line profiles is not reliable. Thus, the two-dimensional fitting is required for the accurate refinement. The refined values of the structural parameters were u = 0.37775(2), B(Cd) = 1.492(1)Å^2 and B(S) = 1.079(2)Å^2 with thickness t = 91.50(3)nm and reliability factors of R = 0.081, R_w = 0.227 and GOF = 1.61. This value of GOF implies that the fitting is very good.

Subsequently, we refined anisotropic Debye-Waller factors $B(\mathrm{Cd})_{11}$, $B(\mathrm{Cd})_{33}$, $B(\mathrm{S})_{11}$ and $B(\mathrm{S})_{33}$ instead of the isotropic ones. The values of the parameters obtained above were used as the starting values in this fitting. The refined values were u = 0.37797(2), $B(\mathrm{Cd})_{11}$ = 1.437(2)Å^2, $B(\mathrm{Cd})_{33}$ = 1.517(2)Å^2, $B(\mathrm{S})_{11}$ = 0.965(4)Å^2 and $B(\mathrm{S})_{33}$ = 1.264(3)Å^2 with thickness t = 91.33(3)nm and reliability factors of R = 0.083, R_w = 0.220 and GOF = 1.56. A small improvement of R_w and GOF is seen with a small change of parameter u.

In a similar manner, the structural parameters were refined using the pattern taken at the 00$\bar{2}$ Bragg condition. The final result of the fitting is shown in Fig. (b) on page 98 with the use of the isotropic Debye-Waller factors. The number of total data points in the present pattern was 32099. The refined values were u = 0.37707(2), B(Cd) = 1.430(1)Å^2 and B(S) = 1.119(2)Å^2 with thickness t = 93.50(3)nm and reliability factors of R = 0.172, R_w = 0.208 and GOF = 1.836. When the anisotropic Debye-Waller factors were used instead of the isotropic Debye-Waller factors, the refined values were u = 0.37751(2), $B(\mathrm{Cd})_{11}$ = 1.371(2)Å^2, $B(\mathrm{Cd})_{33}$ = 1.486(2)Å^2, $B(\mathrm{S})_{11}$ = 1.135(5)Å^2 and $B(\mathrm{S})_{33}$ = 1.155(4)Å^2 with thickness t = 93.57(3)nm and reliability factors of R = 0.168, R_w = 0.208 and GOF = 1.765.

Reference

[a] M. Ichikawa and K. Hayakawa: *J. Phys. Soc. Jpn.*, **42** (1977) 1957.

Data preprocessing: distortion correction and background subtraction

An example of the correction of the displacement of HOLZ reflections is shown in Photos (a) and (b). Photograph (a) is an experimental CBED pattern of CdS including HOLZ reflection disks. The calculated (or expected) positions of the HOLZ reflections are indicated by black circles. It is seen that a considerable discrepancy exists between the experimental and expected patterns. Photograph (b) shows the calculated positions after the correction of the distortion due to the lens system. It is seen that the positions of the black circles agree quite well with the perimeters of the HOLZ reflections.

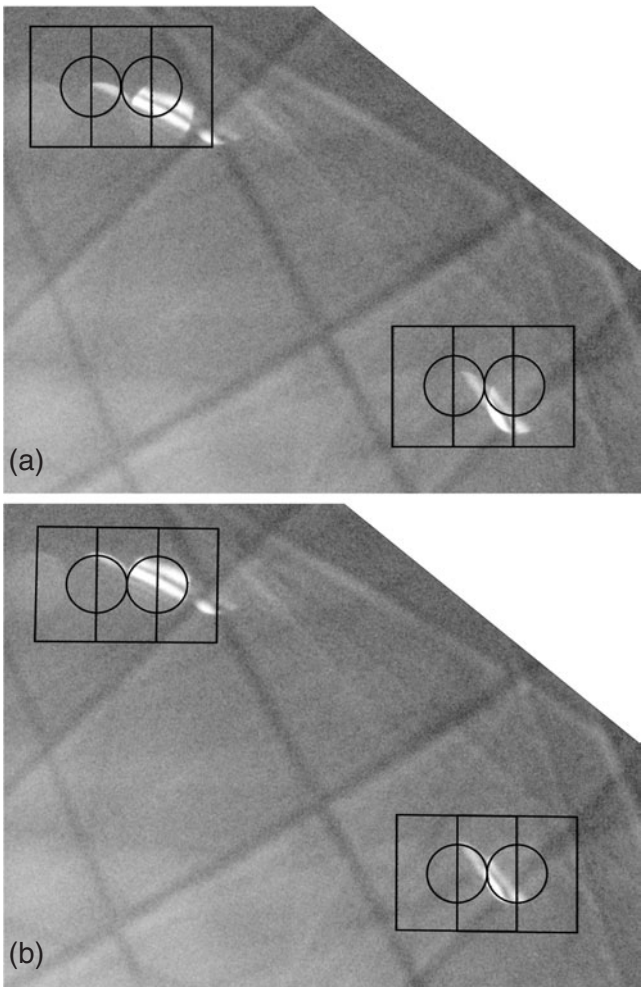

The black circles indicate the calculated (or expected) positions of HOLZ reflections (a) without and (b) with correction of distortion due to the lens system.

Figure (c) shows an example of the subtraction of background due to TDS, which are depicted as both conventional and bird's-eye view images. The patterns in the left, center and right columns respectively show raw data containing a HOLZ reflection disk, the background intensities evaluated from the intensities just outside the disk and the background-subtracted intensities of the HOLZ reflection. A weak Kikuchi line intersecting the HOLZ reflection disk is seen in the background intensities.

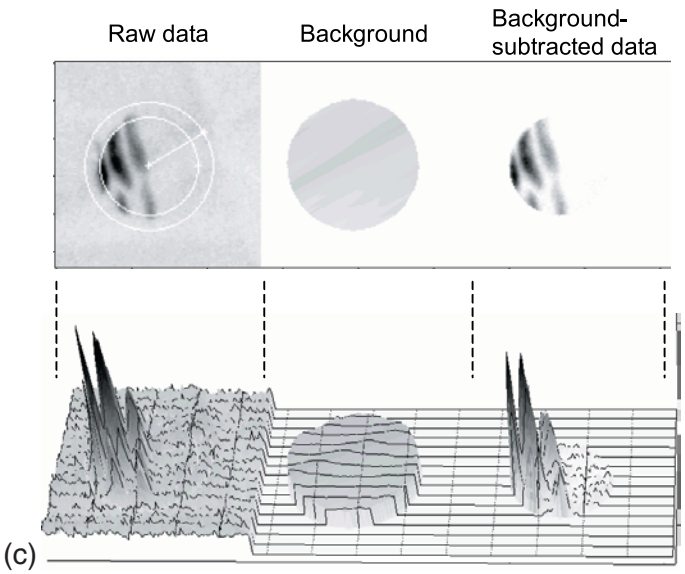

Subtraction of the background due to TDS.

Experiments

CdS [310] 002 excitation 100.7kV

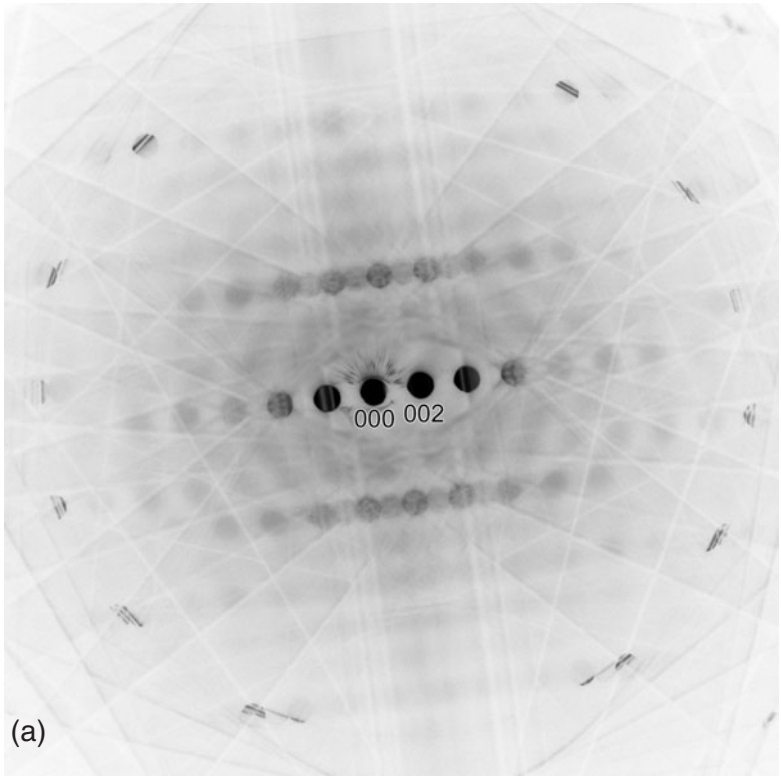

We took CBED patterns with the incidences slightly tilted from the [310] zone axis so that the 002 and $00\bar{2}$ reflections satisfied their Bragg conditions.

Photograph (a) shows a CBED pattern of CdS taken with the 002 Bragg excitation at room temperature using the JEM-2010FEF energy-filter microscope. The patterns were taken from about a 1nm-diameter area with an acceptance energy of 0±8eV. ZOLZ reflections are seen at the center of the pattern and HOLZ reflections in the outer part as a ring. The intensities of remaining background outside the reflection disks were approximately 2% of the intensity maxima inside the disks for the ZOLZ reflections and approximately 10% for the first-order Laue zone (FOLZ) reflections.

Photograph (b) shows another CBED pattern of CdS taken with the $00\bar{2}$ Bragg excitation at room temperature under similar conditions to Fig. (a).

CdS [310] $00\bar{2}$ excitation 100.7kV

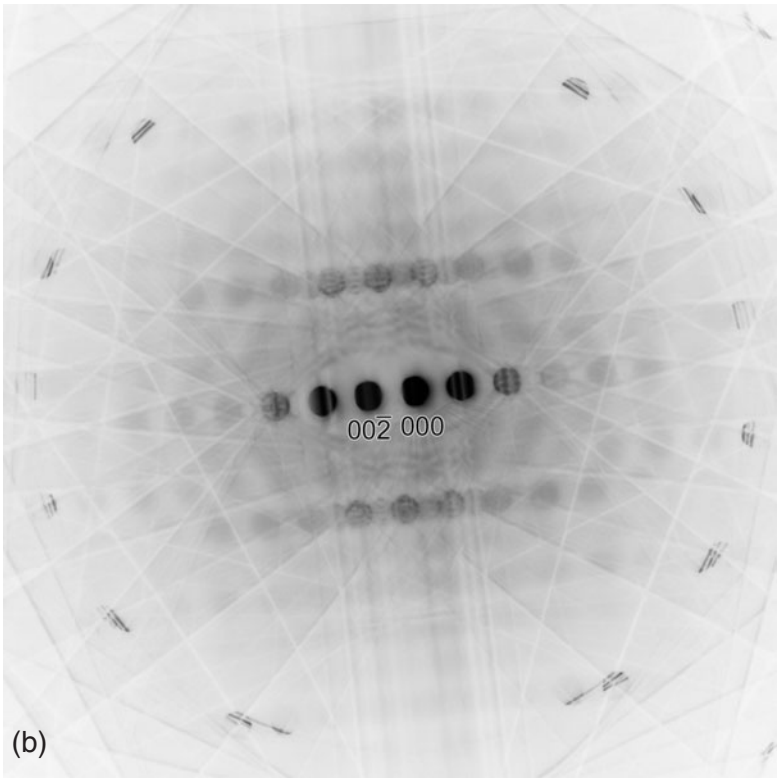

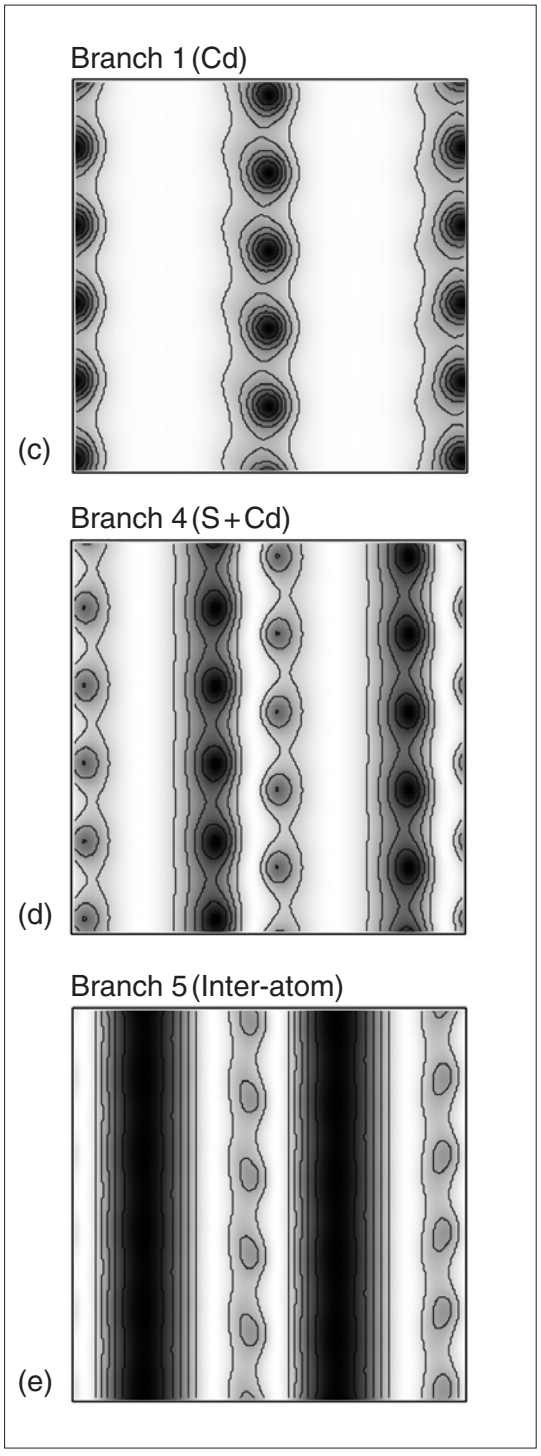

Electron density distributions of the Bloch states at the [310] incidence.

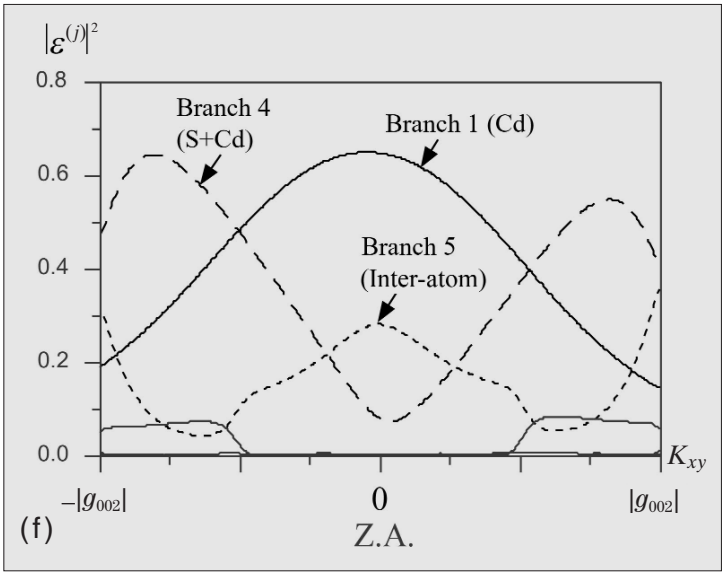

Excitations of branches 1, 4 and 5 at the [310] incidence.

Bloch states and excitations of branches

Figures (a) and (b) show the projected structure and projected potential of CdS in the [310] direction, respectively. It is seen that the projected structure consists of the rows of Cd atoms and the rows of S atoms. Figures (c) to (e) on the next page show electron-density distributions of the Bloch states of branches 1, 4 and 5, respectively, which were calculated using 101 ZOLZ reflections at the [310] incidence for an accelerating voltage of 100kV. The electron density of branch 1 is concentrated on the rows of Cd atoms (Fig. (c)), that of branch 4 strongly on the rows of S atoms and weakly on the rows of Cd atoms (Fig. (d)) and the electron density of branch 5 is between the rows of Cd and S atoms (Fig. (e)). The branch which has electron density maxima on the both rows of Cd and S atoms should be sensitive to the relative distance u between Cd and S atoms. That is, the intensity peak of the HOLZ reflection due to branch 4 is most sensitive to parameter u.

Figure (f) shows the absolute squares of the excitation amplitudes of the branches around the [310] incidence as a function of k_{xy}, where k_{xy} is the component of the incident wave vector along the c^*-axis. It is seen that the excitation of branch 4 has maxima around $k_{xy} = +3g_{002}/4$ and $-3g_{002}/4$, where reflections 003 and $00\overline{3}$ are respectively at the Bragg condition. Therefore, CBED patterns taken at the incidences to excite these reflections are expected to show a high sensitivity to parameter u.

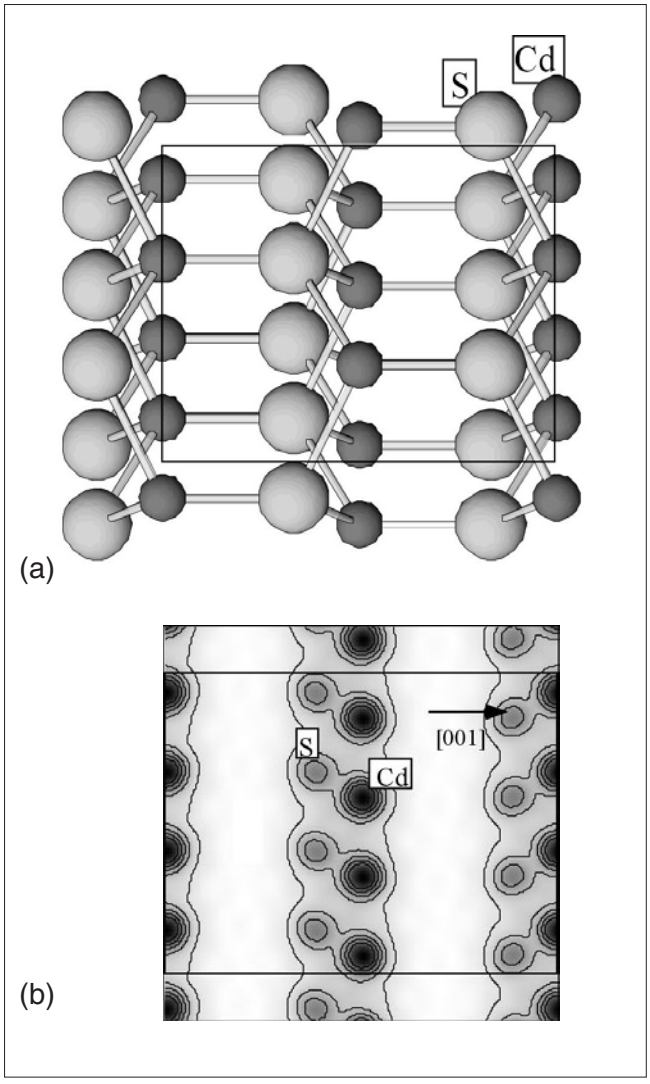

(a) Projected structure and (b) projected potential of CdS in the [310] direction.

Site-selective analysis

Selection of the [310] zone and the profile of a HOLZ reflection

CBED patterns taken at incidences [*UV*0] (*U*,*V*: integer) are sensitive to parameter u of the sulfur atoms because parameter u is parallel to the c-axis. The HOLZ reflection intensities of the patterns taken at incidences of [100] (equivalent to [010] and [110]) and [210] (equivalent to [120] and [1$\bar{1}$0]) are too weak to analyze. Those at incidences [310] and [410] are relatively strong, but less numbers of HOLZ reflections are excited at incidence [410]. For these reasons, we used [310] CBED patterns for the determination of the structural parameters.

Prior to the fitting between experimental and theoretical data, we interpret intensity profiles of HOLZ reflections in terms of Bloch waves. Figure (a) shows a section of the dispersion surface along the c^*-axis around the [310] incidence. For simplicity, only one HOLZ reflection 0 1 15 was considered. The dispersion surface was calculated with 101 ZOLZ reflections and the HOLZ reflection at an accelerating voltage of 100kV. The branch of the dispersion surface originating from the HOLZ reflection is clearly distinguished from those of ZOLZ reflections because the HOLZ branch makes a large angle with the ZOLZ branches, which lie almost perpendicular to the [310] direction. The line profile of the 0 1 15 reflection is shown in Fig. (b). Intensity peaks of the HOLZ reflection appear at the intersections between HOLZ and ZOLZ branches. It should be noted that only ZOLZ branches with large excitation amplitudes $\epsilon^{(j)}$ cause intensity peaks in the HOLZ reflection. In the present case, the three peaks of the line profile seen in Fig. (b) are assigned to the intersection between the HOLZ branch and the ZOLZ branches 1, 4 and 5. The other small peaks can be regarded as subsidiary peaks of the three principal peaks. It is noted that the branches 2, 4 and 6 are scarcely excited because they are antisymmetric with respect to the [310] zone axis.

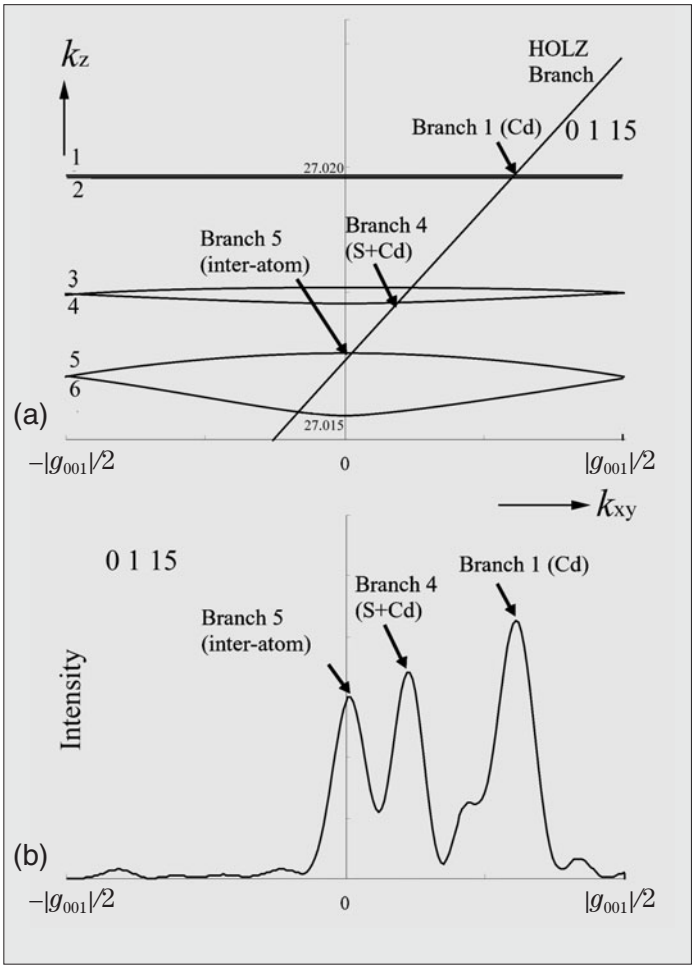

(a) Branches of the dispersion surface of CdS around the [310] incidence. (b) The line profile of the 0 1 15 HOLZ reflection. Peaks of the line profile appear at the intersections between the HOLZ branch and the ZOLZ branches 1, 4 and 5.

CdS

We selected cadmium sulphide (CdS) as the first test material for developing the CBED structure refinement using two-dimensional HOLZ and ZOLZ CBED patterns [15]. CdS is a semiconducting material with pyroelectricity and possesses the noncentrosymmetric hexagonal wurtzite structure belonging to space group $P6_3mc$. The atomic coordinates are expressed as Cd: (1/3, 2/3, 0), (2/3, 1/3, 1/2) and S: (1/3, 2/3, u), (2/3, 1/3, 1/2+u), where u is the ratio of the distance between the adjacent Cd and S atoms along the c-axis to the lattice parameter c. The structural parameters to be refined in this analysis are u and isotropic Debye-Waller factors B(Cd) and B(S) as the first step. Anisotropic Debye-Waller factors B_{11} and B_{33} for both atoms are determined at the second stage. The lattice parameters used for the fitting are a = 0.4136nm and c = 0.6713nm [a].

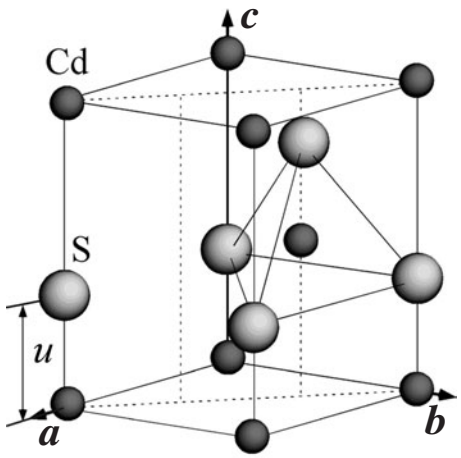

Crystal structure of CdS. The coordinates of the atoms shown here are displaced from those described in the text by (–1/3, 1/3, 0) to clarify the three-dimensional arrangement of the atoms.

Reference

[a] National Bureau of Standards (1957). Natl. Bur. Stand. (US) Circ. No. 539, Vol. 7, p.12.

$LaCrO_3$

Atom positions and anisotropic Debye-Waller factors of the rhombohedral phase of $LaCrO_3$ were refined by our method using energy-filtered two-dimensional HOLZ and ZOLZ CBED patterns.

$LaCrO_3$ is a material for the interconnector of solid oxide fuel cells. It is known that $LaCrO_3$ has two structural phase transformations approximately at 2000K and 537K. The phase above 2000K is expected to have the cubic perovskite structure [a]. The two phases below 2000K have distorted perovskite structures. It was reported that the space group of the phases above and below the transition temperature of 537K are rhombohedral $R\bar{3}m$ [b] and orthorhombic $Pbnm$ [c], [d], respectively. These space groups are, however, not decisive because they were determined by powder X-ray diffraction experiments. Prior to the structure refinement, we determined by the CBED method that the space groups above and below the transition temperature are respectively $R\bar{3}c$ and $Pbnm$ [e].

The relation between the rhombohedral axes and the pseudo-cubic axes is given by $\boldsymbol{a}_r = \boldsymbol{a}_c + \boldsymbol{c}_c$, $\boldsymbol{b}_r = \boldsymbol{a}_c + \boldsymbol{b}_c$ and $\boldsymbol{c}_r = \boldsymbol{b}_c + \boldsymbol{c}_c$, where $\boldsymbol{a}_r$, $\boldsymbol{b}_r$ and $\boldsymbol{c}_r$ are lattice parameters of the rhombohedral lattice and $\boldsymbol{a}_c$, $\boldsymbol{b}_c$ and $\boldsymbol{c}_c$ are those of the pseudo-cubic lattice. On the following pages, the incident beam directions and reflection indices are expressed by the rhombohedral system.

Since the rhombohedral phase belonging to space group $R\bar{3}c$ has two molecular units in the unit cell, La and Cr atoms occupy special positions of 2*a* and 2*b*, respectively, and O atoms occupy positions of 6*e*. Referring to the positions of 6*e*, it is seen that the neighboring oxygen octahedra along the [111] axis can rotate in directions opposite to each other with respect to the axis.

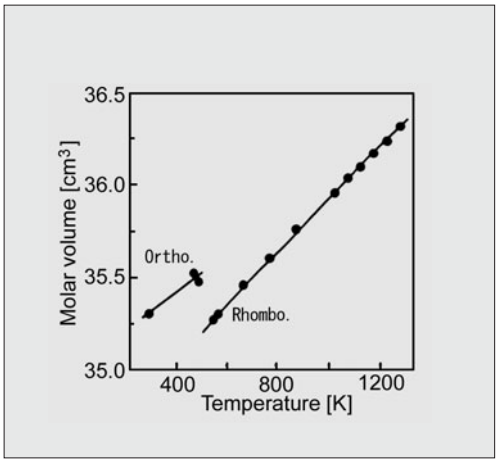

Temperature dependence of the molar volume of $LaCrO_3$ [f].

References

[a] S. Geller and P. M. Raccah: *Phys. Rev. B*, **2** (1970) 1167.

[b] H. E. Hoefer and W. F. Kock: *J. Electrochem. Soc.*, **140** (1993) 2889.

[c] C. P. Khattak and D. E. Cox: *Mater. Res. Bull.*, **12** (1977) 463.

[d] R. Berjoan, C. Romand and J. P. Coutures: *High Temp. Sci.*, **13** (1980) 173.

[e] T. Hashimoto, K. Takagi, K. Tsuda, M. Tanaka, K. Yoshida, H. Tagawa and M. Dokiya: *J. Electrochem. Soc.*, **147** (2000) 4408.

[f] T. Hashimoto, N. Matsushita, Y. Murakami, N. Kojima, K. Yoshida, H. Tagawa, M. Dokiya and T. Kikegawa: *Sol. Stat. Com.*, **108** (1998) 691.

Structural phase transformations of $LaCrO_3$

(a)

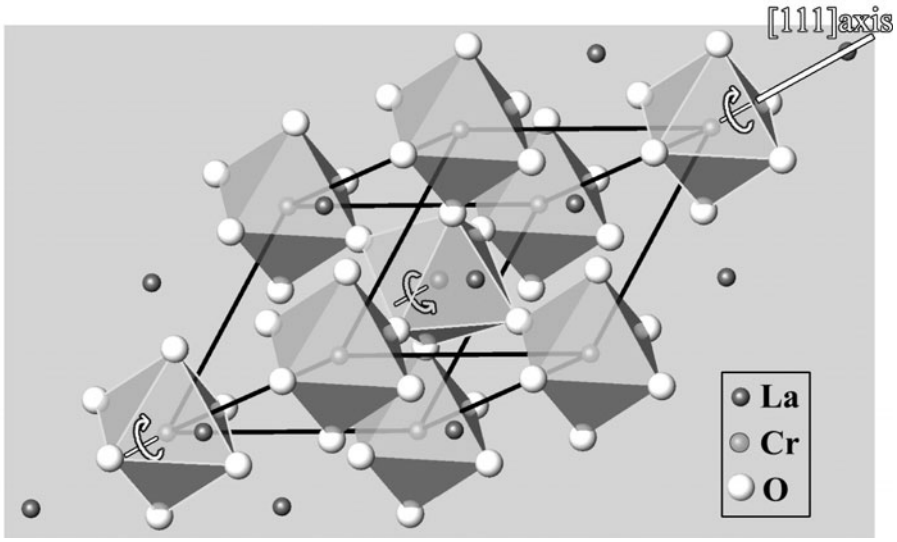

Crystal structure of the rhombohedral phase of $LaCrO_3$, which belongs to space group $R\bar{3}c$. The neighboring oxygen octahedra along the [111] axis rotate in directions opposite to each other with respect to the axis.

(b)

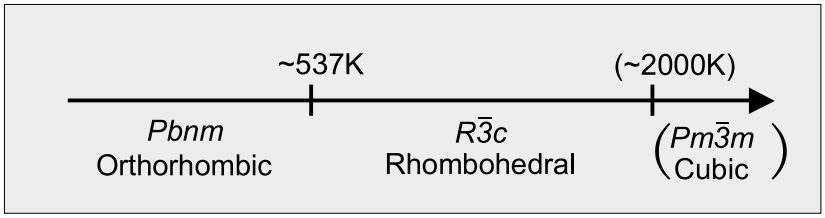

Sequence of the structural phase transformations of $LaCrO_3$.

Space-group determination

Figure (a) shows a CBED pattern of $LaCrO_3$ taken with the [111] incidence at 573K [a]. Magnified patterns of the HOLZ reflections are shown in the insets. Since the HOLZ reflections exhibit $3m$ symmetry, possible diffraction groups are $3m$, $3m1_R$ and 6_Rmm_R. ZOLZ reflections of the central part of Fig. (a) are enlarged in Fig. (b). The ZOLZ reflections exhibit $6mm$ symmetry, the projection diffraction group being $6mm1_R$. Thus, the diffraction group satisfying the symmetries of the CBED patterns of Figs. (a) and (b) is only 6_Rmm_R. Possible point groups for diffraction group 6_Rmm_R are $\bar{3}m$ and $m\bar{3}m$ according to the table of Buxton *et al.* [b]. In the case of the present material, it is known from X-ray diffraction experiments that the reflections can be indexed not by a cubic system but by a low symmetry system. Thus, the point group of $LaCrO_3$ at 573K is $\bar{3}m$. Possible space groups are $R\bar{3}m$ and $R\bar{3}c$.

Figure (c) shows a CBED pattern of $LaCrO_3$ taken at 573K with an incidence slightly tilted in the [111] direction from the $[1\bar{2}1]$ incidence. ZOLZ reflections of the central part of Fig. (c) are enlarged in Fig. (d). Dynamical extinction lines are seen in hhh (h = odd) ZOLZ reflection disks in Fig. (d), indicating the existence of c-glide planes. Therefore, the space group of $LaCrO_3$ at 573K was determined to be $R\bar{3}c$ (No.167).

References

[a] T. Hashimoto, K. Takagi, K. Tsuda, M. Tanaka, K. Yoshida, H. Tagawa and M. Dokiya: *J. Electrochem. Soc.*, **147** (2000) 4408.

[b] B. F. Buxton, J. A. Eades, J. W. Steeds and G. M. Rackham: *Phil. Trans. R. Soc. London*, **281** (1976) 171.

$LaCrO_3$ [111] T = 573K **100kV**

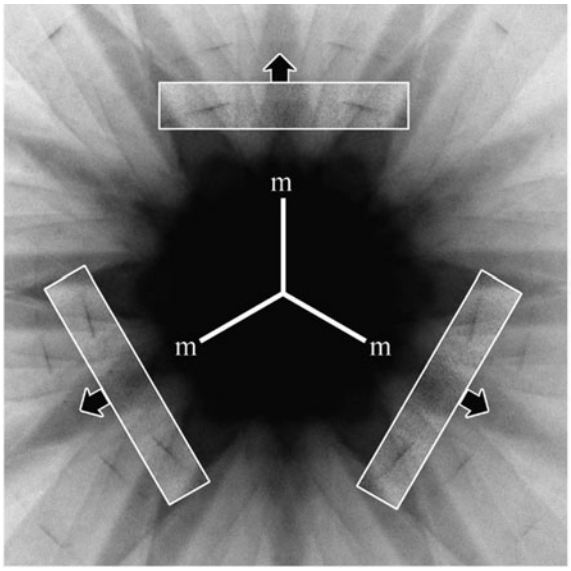

(a)

WP: 3*m*

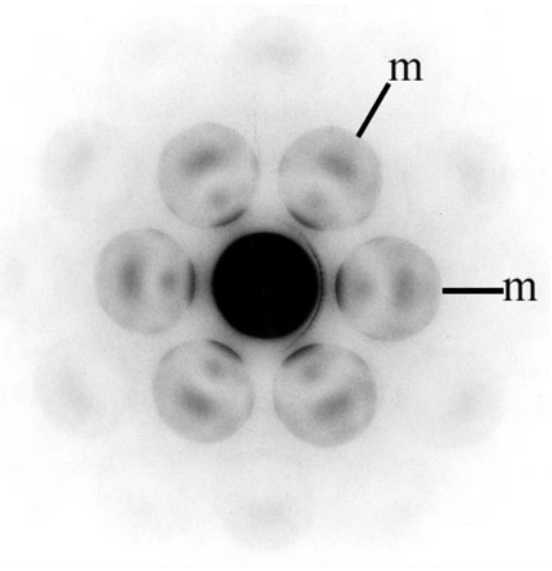

(b)

Proj. WP: 6*mm*

$LaCrO_3$ [1$\bar{2}$1] T = 573K **100kV**

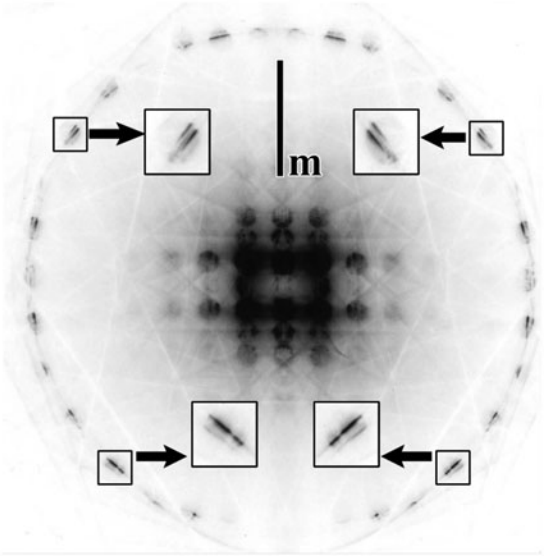

(c)

WP: *m*

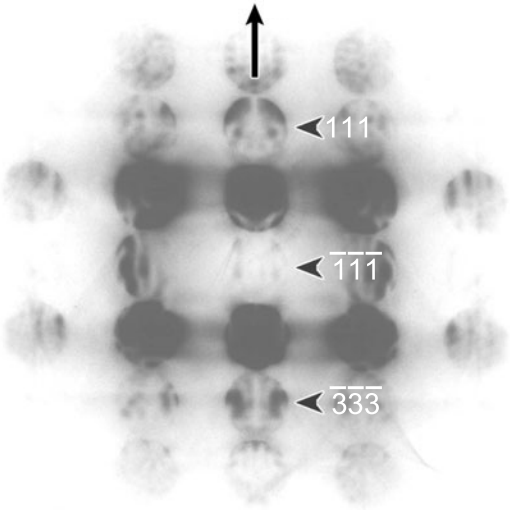

(d)

Dynamical extinction lines in *hhh* (*h* = odd) reflections

Bloch states

Figures (a) and (b) show the projected structure and projected potential of $LaCrO_3$ in the $[11\bar{1}]$ direction, respectively. It is seen that the projected structure consists of the rows of La atoms, the rows of Cr and O atoms and the rows of O atoms. Figures (c), (d) and (e) show the electron density distributions of branches 1, 2 and 5 of the Bloch states, respectively. These were calculated at an accelerating voltage of 100kV using 109 ZOLZ reflections. The electron densities of branches 1 and 2 are concentrated on the rows of La atoms (Fig. (c)) and on the rows of Cr and O atoms (Fig. (d)), respectively. The electron density of branch 5 is concentrated strongly on the rows of O atoms and weakly on the rows of La atoms. Branches 1 and 2 are respectively assigned to the 1*s* states at the La-site and the Cr+O-site. Branch 5 is assigned to the bonding state between the 1*s* state at the O-site and the 2*s* state at the La-site.

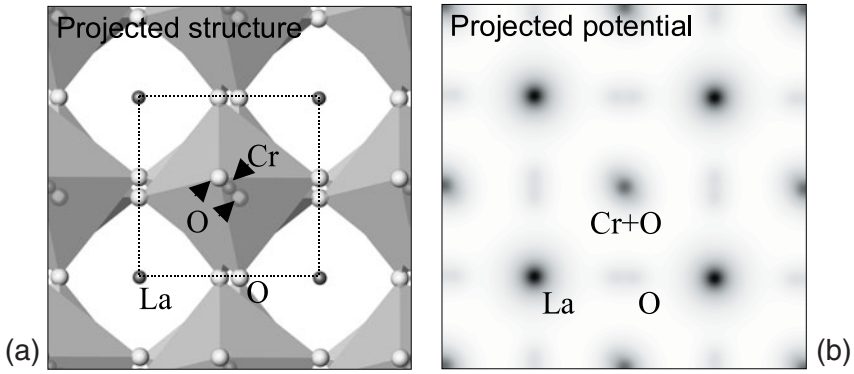

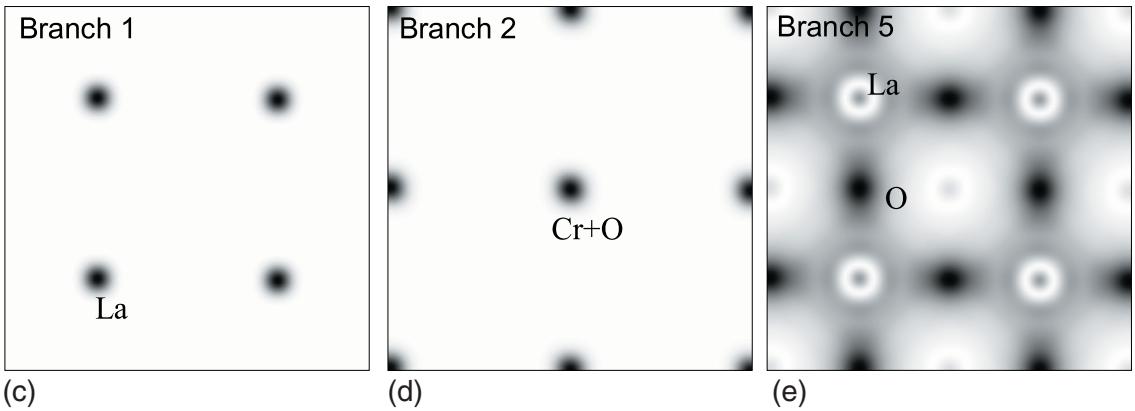

Dispersion surface and excitations of Bloch states

Figures (a) and (b) show a section of the dispersion surface and the excitations of the Bloch states of $LaCrO_3$ in the direction of g_{112} around the $[11\bar{1}]$ incidence. It is seen that branch 5 has the greatest excitation at the zone-axis incidence. Therefore, the CBED patterns taken at the zone-axis incidence are expected to show a high sensitivity to the atom positions and Debye-Waller factors of the O atoms.

$LaCrO_3$

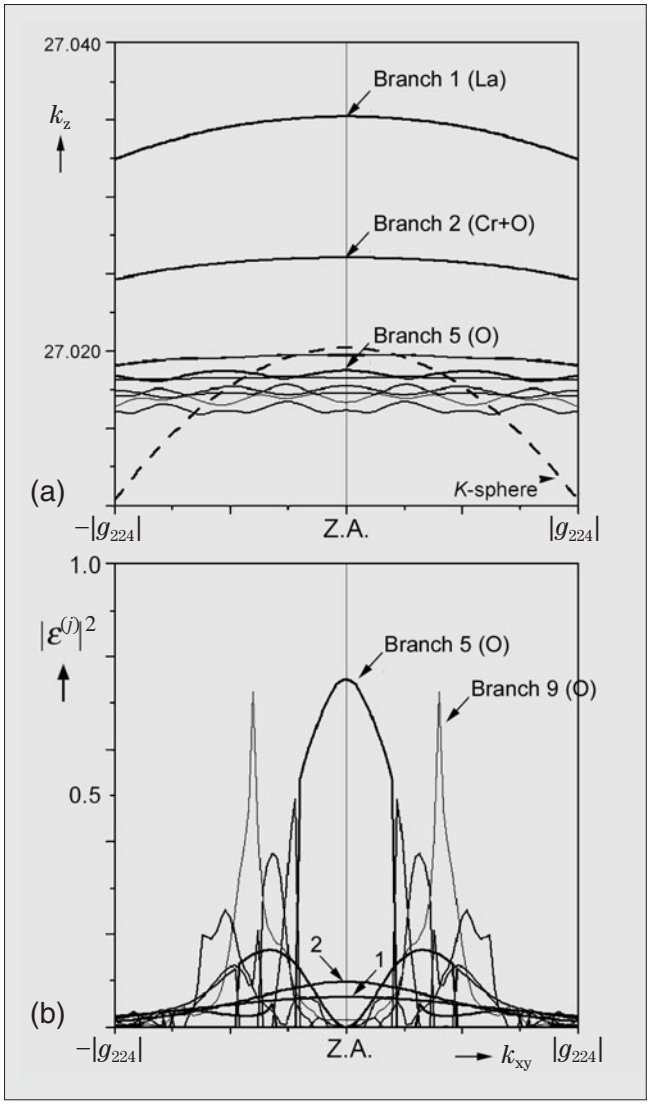

(a) Branches of the dispersion surface and (b) excitations of the Bloch states of $LaCrO_3$ around the $[11\bar{1}]$ incidence.

Dispersion surface and line profiles of HOLZ reflections

$LaCrO_3$

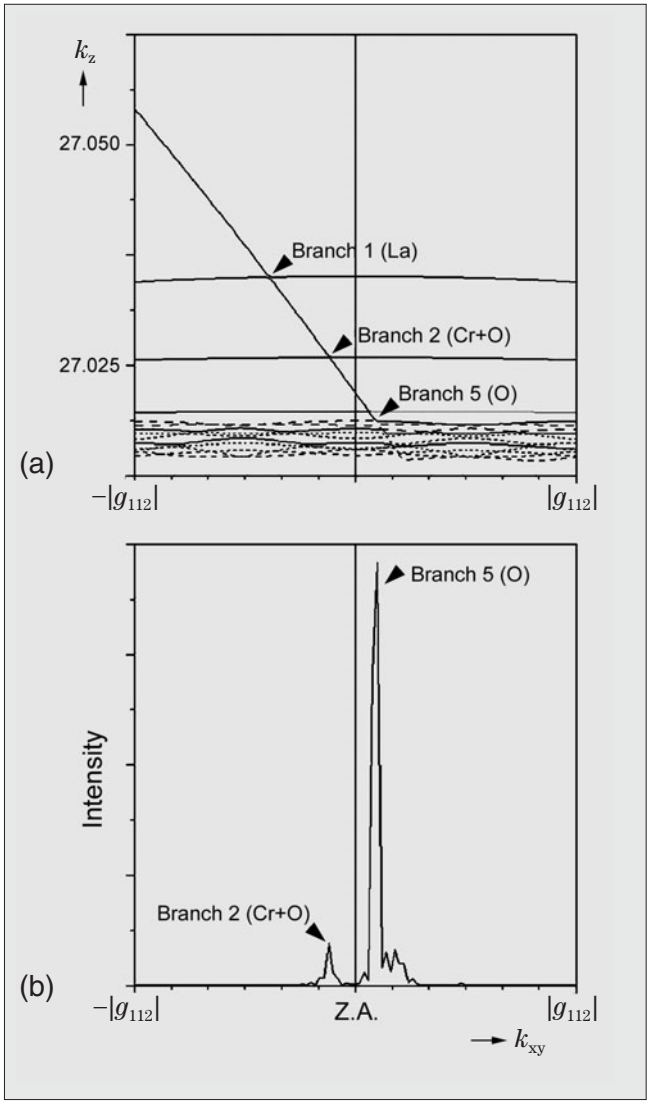

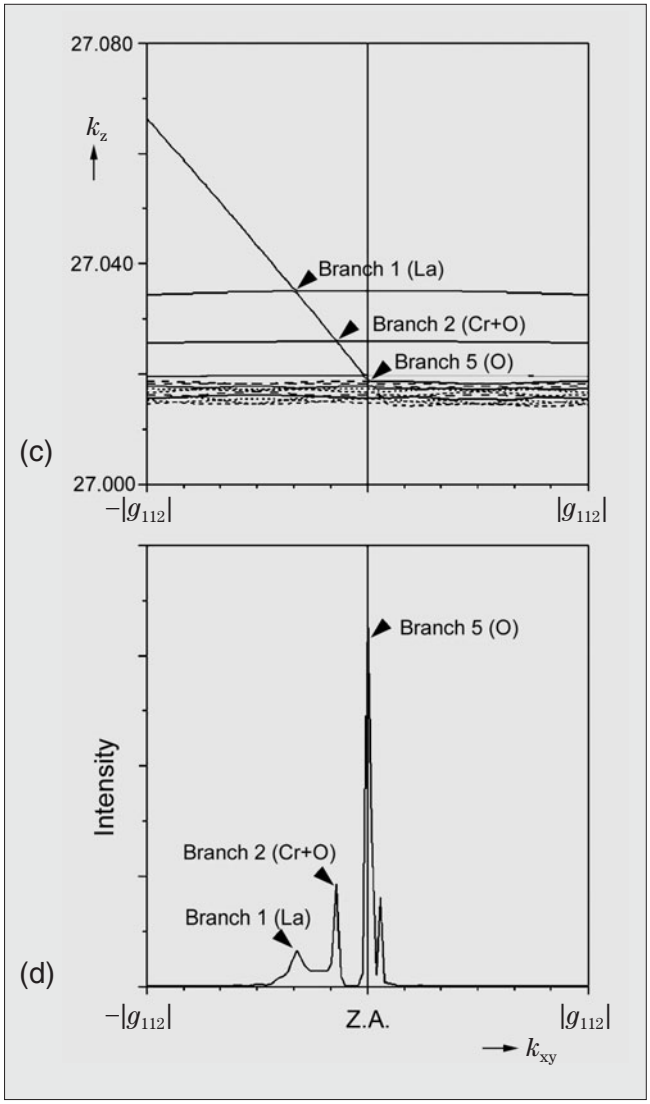

Figure (a) shows a section of the dispersion surface in the direction of g_{112} around the [11$\bar{1}$] incidence. For simplicity, the dispersion surface was calculated using only one 6 9 14 FOLZ reflection and 109 ZOLZ reflections at an accelerating voltage of 100kV. The line profile of the 6 9 14 FOLZ reflection is shown in Fig. (b). Intensity peaks of the FOLZ reflection appear at the intersections between the FOLZ branch and well excited ZOLZ branches.

Similarly, Fig. (c) shows a section of the dispersion surface in the direction of g_{112} around the [11$\bar{1}$] incidence. The line profile of the 9 13 20 SOLZ reflection is shown in Fig. (d). The dispersion surface was calculated using only one SOLZ reflection 9 13 20 and 109 ZOLZ reflections at an accelerating voltage of 100kV. Intensity peaks of the SOLZ reflection appear at the intersections between the SOLZ branch and well excited ZOLZ branches.

Experiments

$LaCrO_3$ [$11\bar{1}$] T = 573K Energy-filtered CBED pattern 100kV

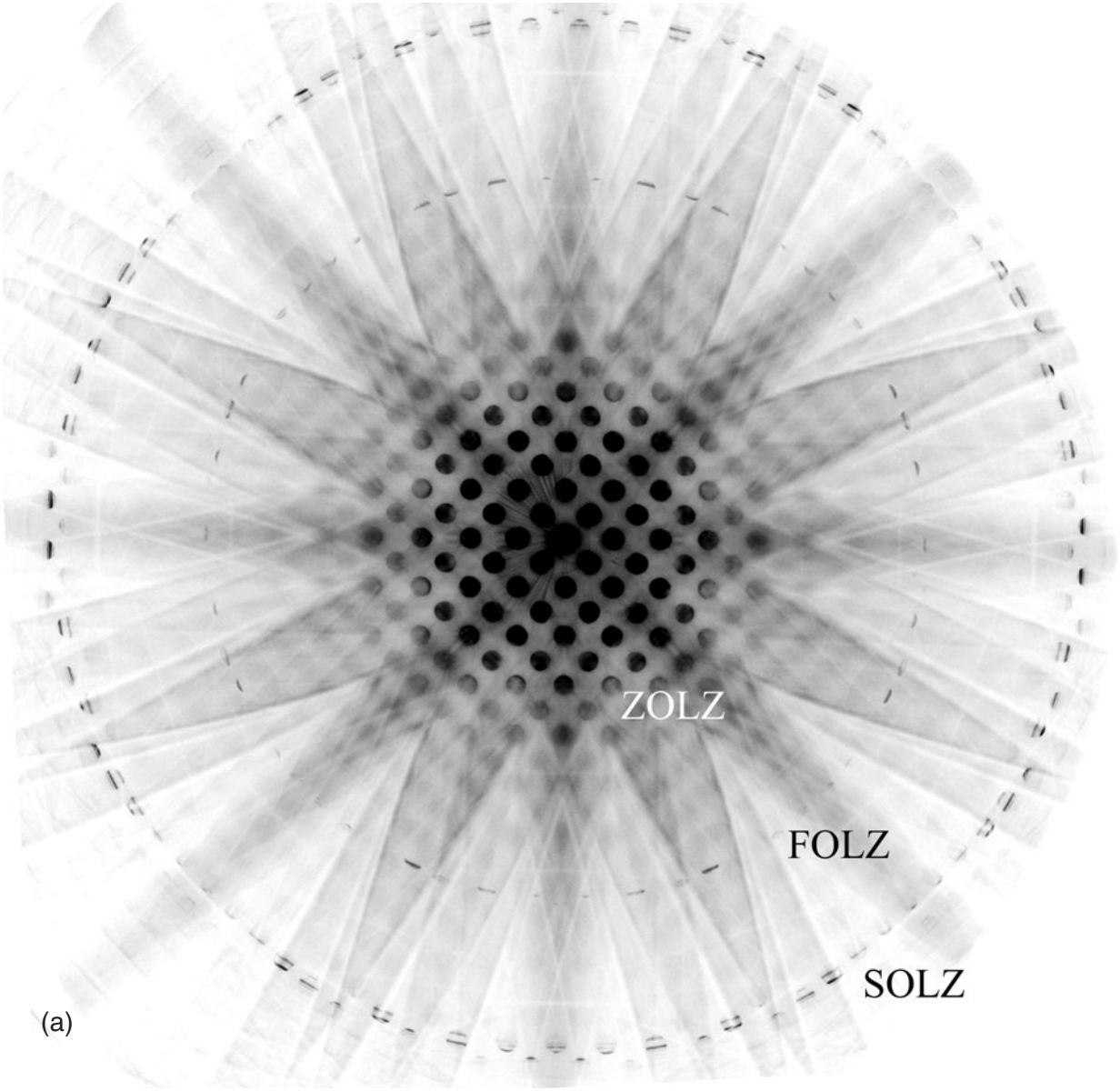

(a)

Photograph (a) shows a CBED pattern taken at 573K with the [$11\bar{1}$] incidence using the JEM-2010FEF energy-filter microscope. The pattern was taken from about a 1nm-diameter area with an acceptance energy of 0±10eV. ZOLZ reflections are seen at the center of the pattern, and FOLZ and SOLZ reflections are seen as rings in the outer part. The central part of Photo (a) is enlarged in Photo (b), which is displayed with a different contrast curve. Since the FOLZ reflections are generated by the rotation of the oxygen octahedra, the FOLZ reflections are sensitive to the positions and Debye-Waller factors of the O atoms.

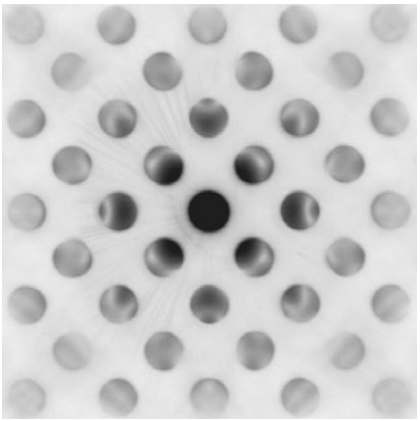

(b)

Data preprocessing: distortion correction and background subtraction

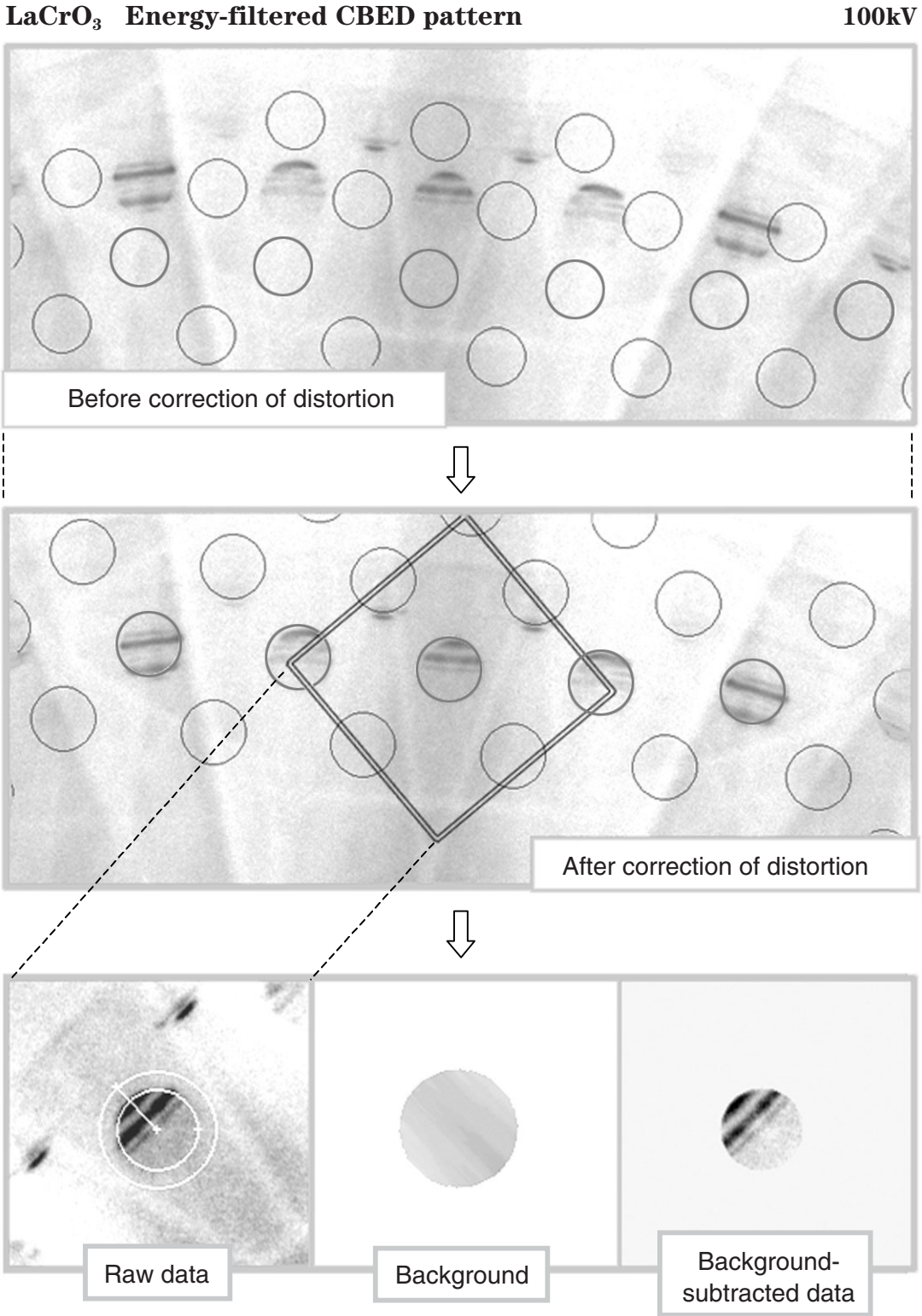

Procedure for distortion correction of a CBED pattern and subtraction of the background due to TDS in $LaCrO_3$.

Fitting

After the distortion correction and background subtraction, two-dimensional intensities of twenty ZOLZ reflections and eighty HOLZ (FOLZ and SOLZ) reflections were taken out of the CBED pattern. The total number of data points in the present pattern was 118466, which consists of 39220 points of ZOLZ reflections and 79246 points of HOLZ reflections.

From the results of the convergence tests of calculated intensities about the number of reflections, 757 reflections were used in the dynamical calculations. 258 weak reflections among the 757 reflections were treated by the GBP method.

The parameters to be refined in the fitting are the coordinate x(O) of the O site, anisotropic Debye-Waller factors of all atoms, U_{11}(La), U_{12}(La), U_{11}(Cr), U_{12}(Cr), U_{11}(O), U_{33}(O), U_{12}(O) and U_{23}(O), low-order structure factors of three ZOLZ reflections F_{101}, $F_{1\bar{1}0}$ and F_{112}, scale factor s, specimen thickness t and 200 geometrical parameters to adjust the positions of reflection disks. The lattice parameters used for the fitting are a_r = 0.547823nm and α_r = 60.6322° [a].

The nonlinear least-squares fitting was performed in the following steps. In the first step, the positional parameter x(O) and anisotropic Debye-Waller factors were refined, where the additional weight factor w_{LZ} to reduce the weight of the ZOLZ reflections was set to 0.002. The values of the low-order structure factors were assumed to be the values calculated from the atomic scattering factors of the neutral atoms. In the second step, the low-order structure factors were refined using the values of the positional parameter and Debye-Waller factors obtained in the first step. The w_{LZ} was set to 0.02 for increasing the weights of ZOLZ reflections, which are sensitive to the low-order structure factors. In the final step, all of the parameters were refined simultaneously.

The final results of the fitting are shown in figures on the following two pages. The patterns in the left, center and right columns respectively show experimental, calculated and difference patterns. The calculated patterns are seen to agree very well with the experimental patterns. The refined values of the structural parameters are given in the table on page 114. The values of R_w and *GOF* were 0.246 and 2.36.

Site	Wyckoff position	Coordinate		
La	2*a*	1/2,	1/2,	1/2
Cr	2*b*	0,	0,	0
O	6*e*	x(O),	$-x$(O)+1/2,	1/4

Atom positions of the rhombohedral phase of $LaCrO_3$.

Reference

[a] K. Oikawa, T. Kamiyama, T. Hashimoto, Y. Shimojyo and Y. Morii: *J. Sol. Stat. Chem.*, **154** (2000) 524.

Fitting results ($LaCrO_3$ [$11\bar{1}$])

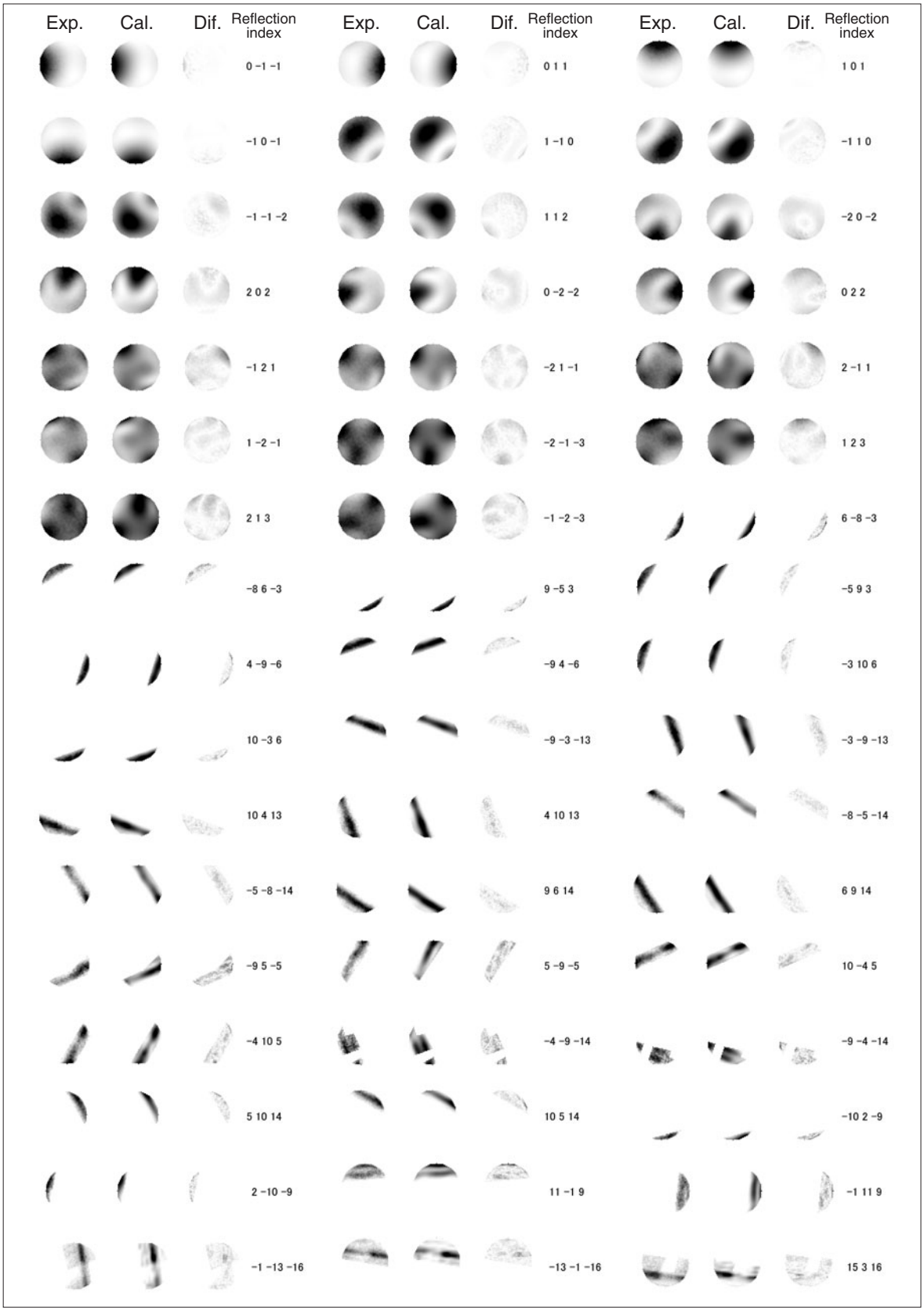

Fitting results (continued) ($LaCrO_3$ [11$\bar{1}$])

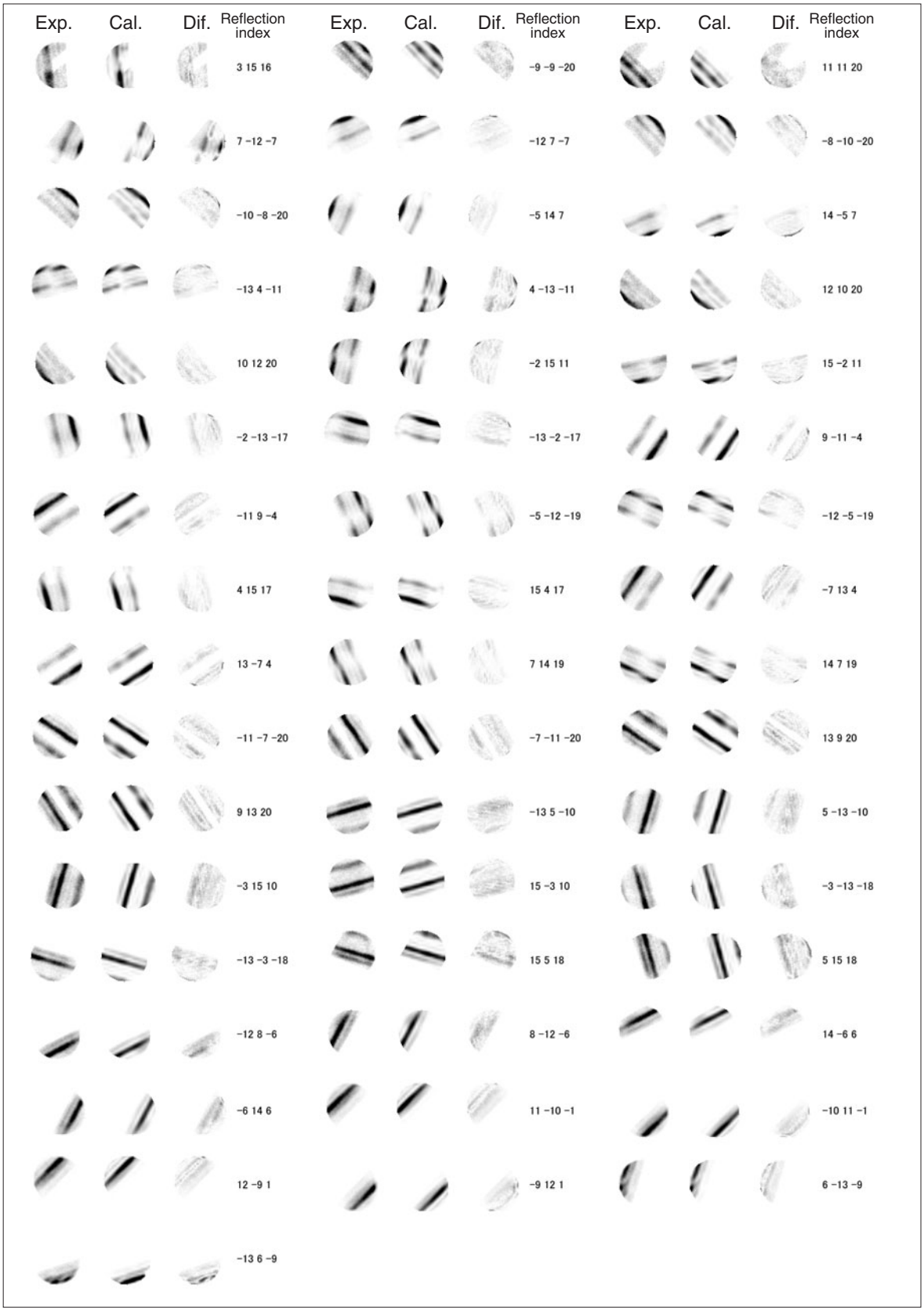

Refined parameters

Table (a) shows the refined values of the positional parameter (fractional coordinate) and anisotropic Debye-Waller factors of $LaCrO_3$. The values obtained by a neutron powder-diffraction experiment using the Rietveld analysis [a], which was conducted based on the space-group determined by us, are shown in the right column for comparison. It is seen that the values agree very well with the CBED values.

Table (b) shows the refined values of the low-order structure factors of $LaCrO_3$. The values calculated from the atomic scattering factors of neutral atoms and ionized atoms are shown for comparison.

(a)

Positional parameter and Debye-Waller factor [Å^2]	CBED (Present result)	Neutron diffraction [a]
x(O)	−0.30621(2)	−0.30589(32)
U_{11}(La)	0.008274(4)	0.0085(6)
U_{12}(La)	−0.002674(2)	−0.0027(4)
U_{11}(Cr)	0.005678(3)	0.0041(10)
U_{12}(Cr)	−0.001871(2)	−0.0010(7)
U_{11}(O)	0.01130(4)	0.0104(6)
U_{33}(O)	0.01456(3)	0.0141(11)
U_{12}(O)	−0.00787(4)	−0.0066(8)
U_{23}(O)	−0.001521(5)	−0.0016(4)

(b)

Low-order structure factor [Å]	Refined	Neutral	Ionized
F_{101}	−7.542(3)	−8.012	−7.238
$F_{1\bar{1}0}$	20.233(3)	19.120	20.761
F_{112}	20.451(2)	19.596	21.009

Reference

[a] K. Oikawa, T. Kamiyama, T. Hashimoto, Y. Shimojyo and Y. Morii: *J. Sol. Stat. Chem.*, **154** (2000) 524.

Atom positions and anisotropic Debye-Waller factors

The crystal structure of $LaCrO_3$ determined by the present fitting is shown in the style of the ORTEP diagram. Anisotropic Debye-Waller factors are displayed as thermal ellipsoids. Figure (a) shows the diagram of the fitting result viewed from the [111] direction. It is seen that the neighboring octahedrons in the [111] direction rotate in directions opposite to each other with respect to the [111] axis. As a result, the O atoms deviate from the positions of the cubic perovskite structure, in which the two atoms overlap in the projection. Figure (b) shows the diagram of the fitting result viewed from the $[\bar{1}\bar{1}2]$ direction. An octahedron in Fig. (b) is enlarged in Fig. (c). It is seen that the thermal ellipsoid is elongated in the directions perpendicular to the bond connecting an O atom at a vertex and the Cr atom at the center of the octahedron. Clear anisotropy of the thermal vibration of the oxygen atom has been found by the CBED method for the first time.

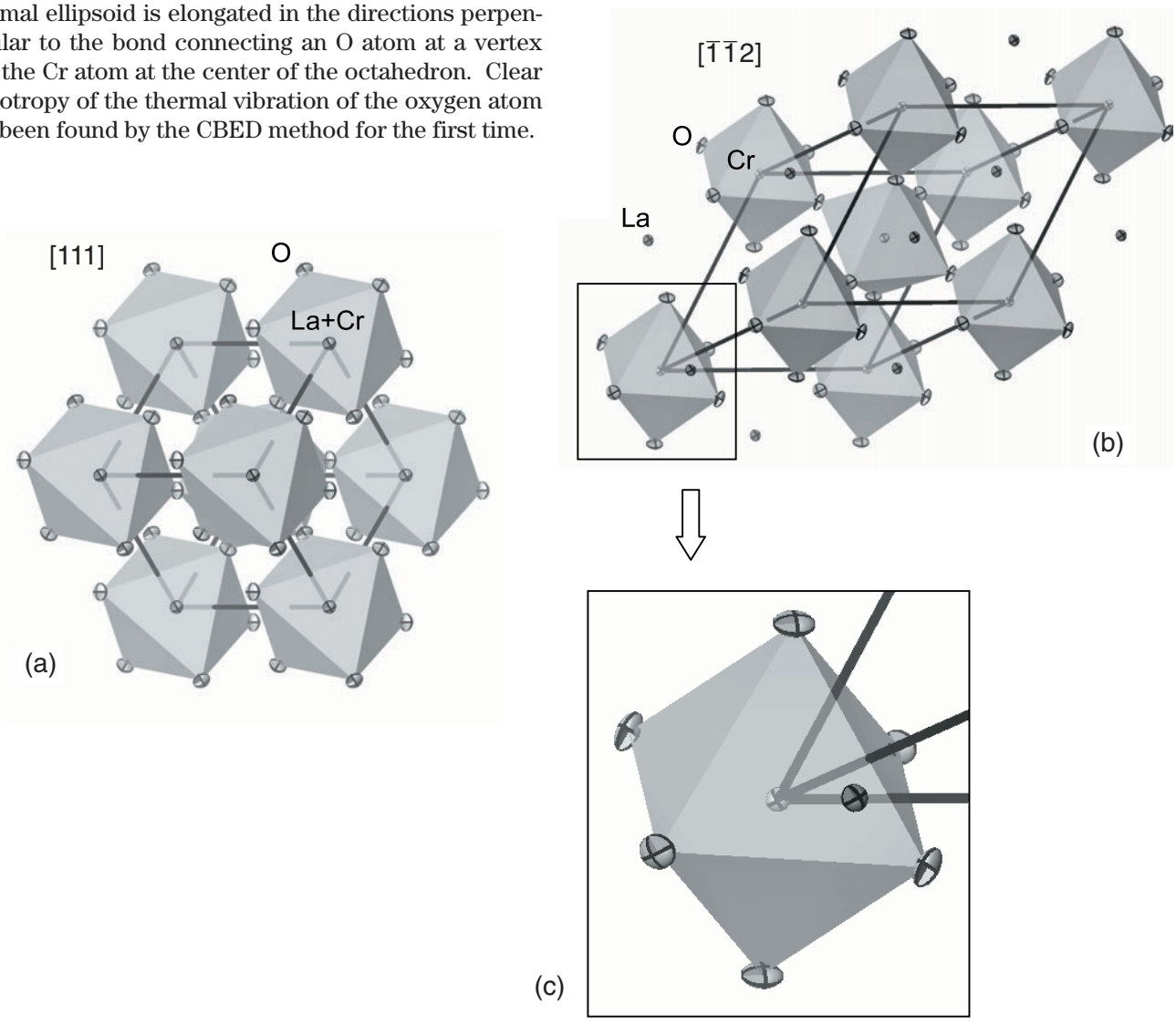

ORTEP diagrams of the fitting result viewed from the [111] direction (a) and the $[\bar{1}\bar{1}2]$ direction (b). An octahedron of Fig. (b) is enlarged in Fig. (c).

Comparison

The structural parameters obtained in the present analysis agree well with those of the neutron diffraction experiments. However, it is easy to see that the calculated patterns using the structural parameters of the neutron diffraction experiments cannot reproduce accurately the experimental CBED patterns. This indicates that the discrepancies between the structural parameters of the present analysis and the neutron diffraction look small but cannot be neglected. It should be emphasized that the CBED method has a high potential to detect such small differences between the structural parameters.

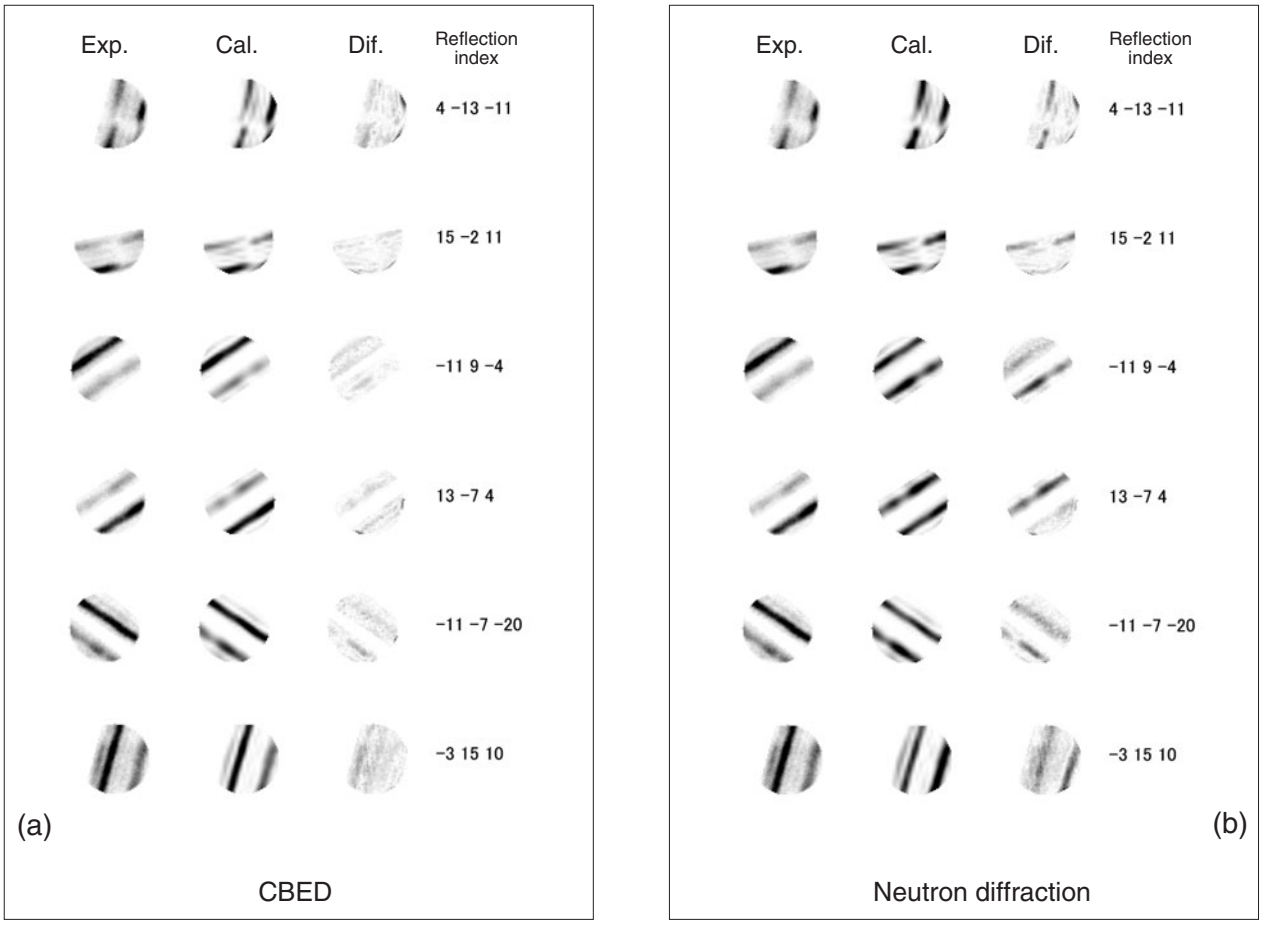

Present result (a) shows small differences between the experiments and the simulations. Considerable differences (b) are seen between the experimental CBED patterns and the patterns simulated by the neutron diffraction data.

Charge-density distributions

Crystal structure factors for X-ray diffraction and electron diffraction

In the present analysis, the low-order crystal structure factors for electron diffraction, which are sensitive to valence electron diffraction, were refined together with the atom positions and Debye-Waller factors. The charge density distribution is obtained using the refined low-order structure factors.

The relation between the crystal structure factors for electron diffraction F_g^e and those for X-ray diffraction F_g^X is given as follows: The structure factors for electrons F_g^e is proportional to the Fourier coefficients of the electrostatic potential V_g as $V_g = F_g^e\, h^2/(8\pi\epsilon_0 m_e e^2\Omega)$, where h, ϵ_0, m_e, e and Ω are Planck's constant, the dielectric constant of vacuum, the rest mass of an electron, the charge of an electron and the volume of the unit cell, respectively. The electrostatic potential $V(\boldsymbol{r})$ is obtained from F_g^e by the Fourier synthesis

$$V(\boldsymbol{r}) = \Sigma_g V_g \exp(2\pi i \boldsymbol{g}\cdot\boldsymbol{r}) = \Sigma_g F_g^e \exp(2\pi i \boldsymbol{g}\cdot\boldsymbol{r})\, h^2/(8\pi\epsilon_0 m_e e^2\Omega).$$

The electrostatic potential $V(\boldsymbol{r})$ can be transformed into the electron density distribution by Poisson's equation

$$\nabla^2 V(\boldsymbol{r}) = -|e|(\rho_n(\boldsymbol{r}) - \rho(\boldsymbol{r}))/\epsilon_0,$$

where the $\rho_n(\boldsymbol{r})$ and $\rho(\boldsymbol{r})$ are the charge distributions of the nuclei and electrons, respectively. The charge density $\rho(\boldsymbol{r})$ is obtained by the Fourier synthesis of the structure factors for X-ray diffraction F_g^X

$$\rho(\boldsymbol{r}) = \Sigma_g F_g^X \exp(2\pi i \boldsymbol{g}\cdot\boldsymbol{r})/\Omega.$$

From Poisson's equation, the relation between F_g^X and F_g^e is derived [a]:

$$F_g^X = \Sigma_i Z_i \exp(-B_i s^2)\exp(-2\pi i \boldsymbol{g}\cdot\boldsymbol{r}) - 8\pi\epsilon_0 h^2 s^2 F_g^e/m_e e^2,$$

where Z_i is the atomic number of the i-th atom and $s = \sin\theta/\lambda = |g|/2$. Using this relation, the structure factors for electrons F_g^e are converted to those for X-rays F_g^X, or the Fourier coefficients of the charge density $\rho(\boldsymbol{r})$.

It should be noted that Debye-Waller factors are contained in the transformation from F_g^e to F_g^X. Thus, the accurate determination of Debye-Waller factors, which can be performed successfully by our refinement method with the use of ZOLZ and HOLZ reflections, is crucial to obtaining high-precision low-order structure factors for X-ray diffraction from the structure factors for electron diffraction.

According to the nature of Poisson's equation, a small change in the low-order structure factors for X-ray diffraction causes a large change in those for electrons. That is, the determination of the low-order F_g^e by the CBED method has an advantage in determining more accurately the low-order F_g^X, compared with the X-ray diffraction method.

Reference

[a] *e.g.* J. C. H. Spence and J. M. Zuo: Electron Microdiffraction, Plenum Press, 1992.

Atomic scattering factors for X-rays and electrons

The crystal structure factors for X-ray diffraction and electron diffraction are expressed as:

$F_g^X = \Sigma_i f_i^X \exp(-B_i s^2)\exp(-2\pi i \boldsymbol{g}\cdot\boldsymbol{r}_i)$ and
$F_g^e = \Sigma_i f_i^e \exp(-B_i s^2)\exp(-2\pi i \boldsymbol{g}\cdot\boldsymbol{r}_i)$,

where f^X and f^e are atomic scattering factors for X-rays and electrons, respectively. f^X and f^e are related by the Mott formula [a]

$$f^e = (Z - f^X)\, m_e e^2 / 8\pi\epsilon_0 h^2 s^2,$$

which is derived from Poisson's equation.

Figure (a) shows the atomic scattering factors of X-rays f^X for neutral and ionized atoms of La, Cr and O as a function of sin θ/λ. The difference of f^X between a neutral atom and an ionized atom is confined in the region in which sin θ/λ is smaller than roughly 0.25Å^{-1}. The difference is the largest at sin θ/λ= 0, where the value of f^X is equal to the total number of electrons Z of the atom. The difference at sin θ/λ = 0 is 25% even for a light element of oxygen and is only about 5% for lanthanum.

Figure (b) shows the atomic scattering factors of electrons f^e for the neutral and ionized atoms. It is seen that the difference between the neutral and ionized atoms is remarkably enhanced in the region of low scattering angles. It is very clear from the two figures that the difference in valence electron distributions is observed more sensitively in the crystal structure factors for electron diffraction than in those for X-ray diffraction.

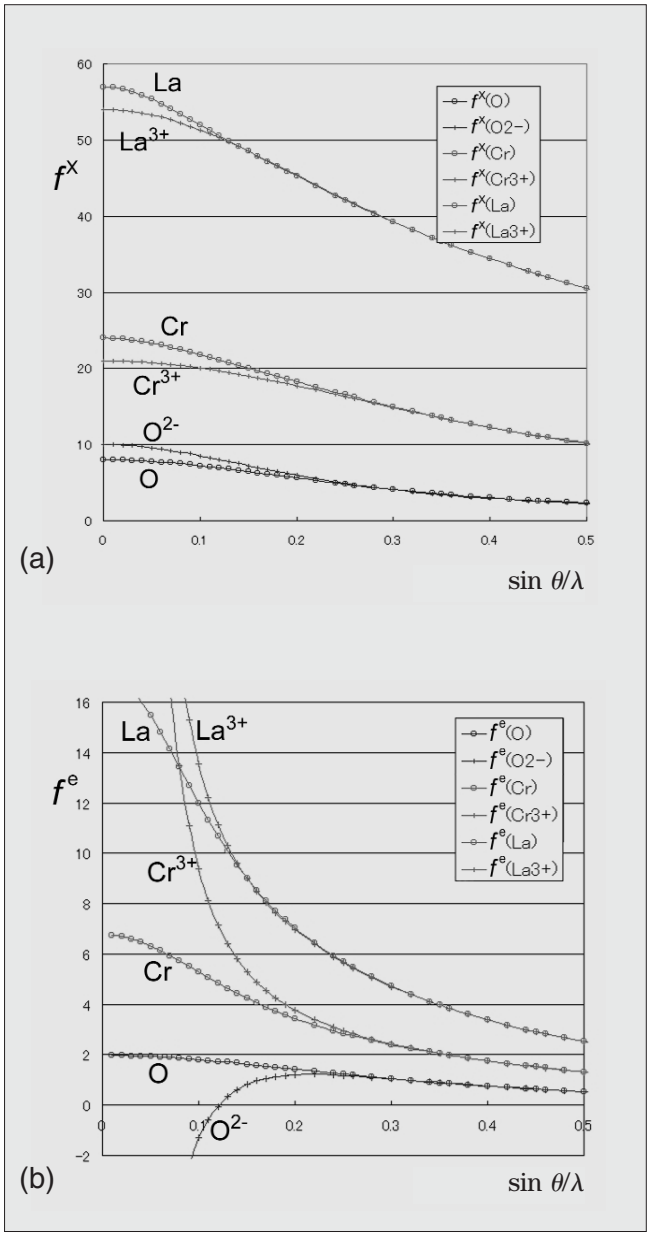

Atomic scattering factors for X-rays (a) and for electrons (b). The differences in the scattering factors between the neutral and ionized atoms at low-scattering angles are noted.

Reference

[a] *e.g.* J. C. H. Spence and J. M. Zuo: Electron Microdiffraction, Plenum Press, 1992.

Error introduced by the Mott formula

From the Mott formula, the following relation is derived for $|\delta f^X/f^X|$:

$$|\delta f^X/f^X| = |\delta f^e/f^e|\ (Z-f^X)/\ f^X,$$

where f^X, f^e, δf^X, δf^e and Z are atomic scattering factors for X-rays and electrons, their estimated errors and the atomic number, respectively. This relation indicates that in the course of the transformation from f^e to f^X, the relative error of f^X is given by the relative error of f^e multiplied by the factor $(Z-f^X)/f^X$. The figure shows the factor $(Z-f^X)/f^X$ for La, Cr and O atoms as a function of sin θ/λ. Thus, if $(Z-f^X)/f^X > 1$, the relative error of f^e is magnified by the transformation to f^X. It is seen that $(Z-f^X)/f^X$ is less than 1 in the region of low scattering angles, at which the atomic scattering factor is sensitive to valence electrons. Therefore, the CBED method can determine the low-order F_g^X more accurately than the X-ray diffraction method.

Since the accuracy of the determination of F_g^X is better than that of F_g^e at high scattering angles, to use the structure factors determined by the X-ray method for high angles and those determined by electron diffraction for low angles is a good method for obtaining high precision charge densities of materials.

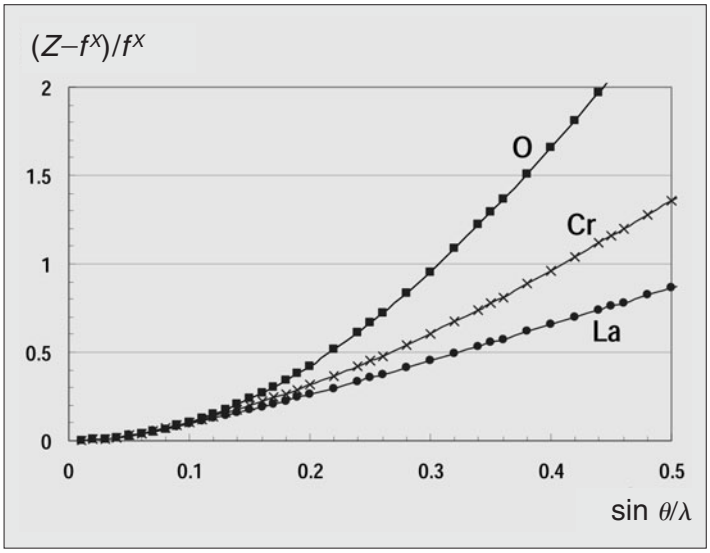

Plot of $(Z-f^x)\ /\ f^x$ as a function of sin θ/λ.

Electrostatic potential and charge density projected in [11$\bar{1}$]

Electrostatic potential and charge density of $LaCrO_3$ projected in the [11$\bar{1}$] direction were calculated with the refined parameters of atom positions, Debye-Waller factors and the low-order structure factors of reflections 101, 1$\bar{1}$0 and 112.

Figure (a) shows the crystal structure of $LaCrO_3$ projected in the [11$\bar{1}$] direction. Figure (b) shows the projected electrostatic potential obtained by using the fitting results. Figure (c) shows the deformation electrostatic potential, or the difference between the electrostatic potential of Fig. (b) and the electrostatic potential calculated with the neutral atoms. It is seen that the potential is increased at the La- and Cr+O-sites and decreased at the O-sites.

Figure (d) shows the projected charge density of the present result. Figure (e) shows the deformation charge density, or the difference between the charge density of Fig. (d) and the charge density calculated with the neutral atoms. The charge transfer from the La and Cr atoms to the O atoms is clearly seen.

Since the nominal valence numbers of La, Cr and O atoms are 3+, 3+ and 2–, respectively, the amount of the transferred charge at the La-site is expected to be larger than that at the Cr+O-site. However, it is seen in Fig. (e) that the peak (negative) of the deformation charge density at the La-site is smaller than the peak at the Cr+O-site. This indicates that the transferred charge is appreciably delocalized for the heavier La atoms but localized for the Cr and O atoms.

(a)

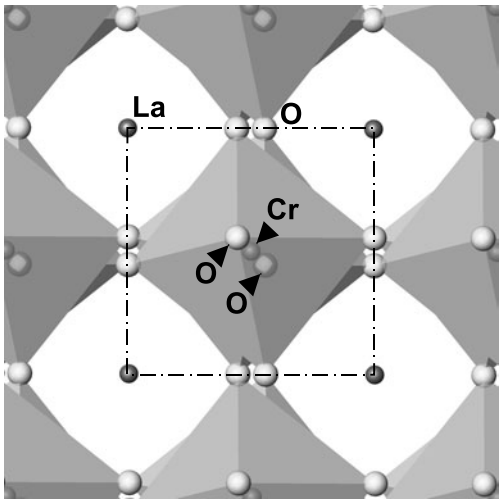

Crystal structure of $LaCrO_3$ projected in the [11$\bar{1}$] direction.

Electrostatic potential

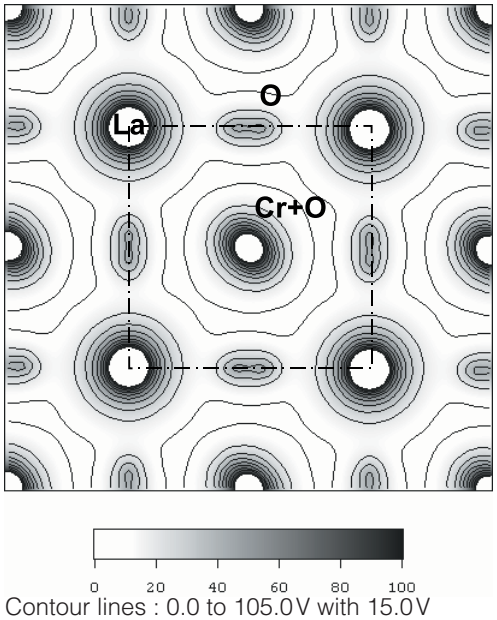

(b)

Contour lines : 0.0 to 105.0V with 15.0V intervals

Deformation potential

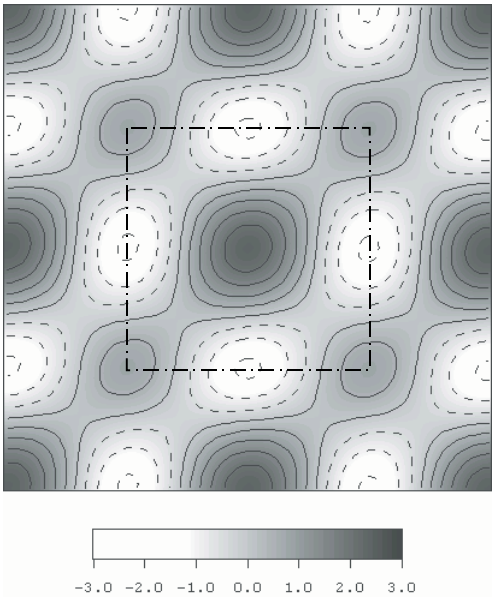

(c)

Contour lines : −3.0 to 3.0V with 0.5V intervals

Charge density

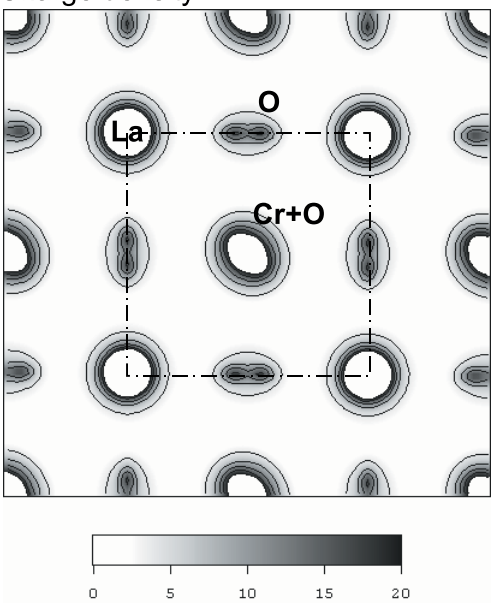

(d)

Contour lines : 0.0 to 20.0eÅ^{-2} with 4.0eÅ^{-2} intervals

Deformation density

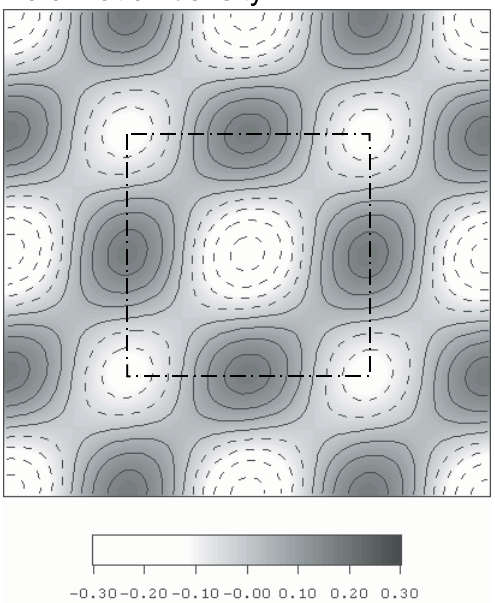

(e)

Contour lines : −0.3 to 0.3eÅ^{-2} with 0.05eÅ^{-2} intervals

Electrostatic potential and charge density projected in the [11$\bar{1}$] direction. The solid lines and dotted lines of the contour maps indicate positive and negative values, respectively.

Three-dimensional distribution of deformation charge density

To obtain three-dimensional distributions of the electrostatic potential and charge density, the low-order structure factors of reflections 201, 200 and 022 were refined using energy-filtered CBED patterns taken at different incidences mentioned below. Photographs (a) and (b) show the CBED patterns of $LaCrO_3$ taken at T = 573K with the 022 Bragg excitation near the [11$\bar{1}$] incidence and with the 200 Bragg excitation near the [010] incidence, respectively, to enhance the intensities of these low-order reflections.

The refined values of the low-order structure factors are shown in the table. The values calculated from the atomic scattering factors of the neutral atoms and ionized atoms are attached for comparison.

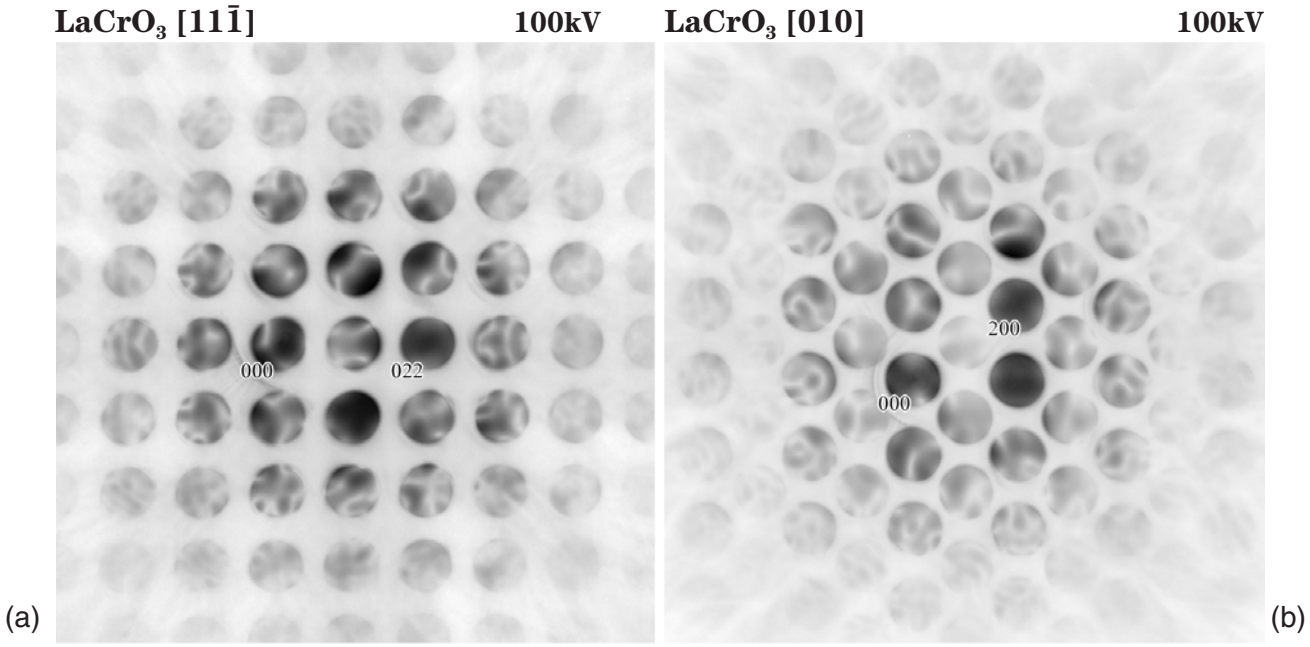

Low-order structure factor [Å]	Refined	Neutral	Ionized
F_{201}	−3.3169(2)	−3.499	−3.175
F_{200}	−11.5847(3)	−12.639	−11.591
F_{022}	21.5340(3)	21.698	21.642

Low-order structure factors refined from the above two CBED patterns.

Using the refined low-order structure factors of the reflections 201, 200 and 022 together with the already refined 101, $1\bar{1}0$ and 112 reflections, the three-dimensional distribution of the charge density of $LaCrO_3$ was constructed. The three-dimensional deformation charge density is visualized in the figure. The charge transfer from the Cr atom to the O atoms is clearly seen.

Since the Cr^{3+} ion in $LaCrO_3$ has three $3d$ electrons which occupy three t_{2g} states, it is expected to form a nearly spherical electron distribution. Thus, the present result is consistent with this conjecture. We have begun the charge-density determination of the orbital-ordering phase of $LaMnO_3$, in which the Mn^{3+} ion has four $3d$ electrons that occupy three t_{2g} states and one e_g state. We already obtained a certain result of the charge density in which the electron distribution is not spherical but extends toward the O-sites. The details will be reported elsewhere.

We are confident that the CBED method can accurately determine the charge densities of materials by making good use of the superb site-selective characteristics of dynamical diffraction.

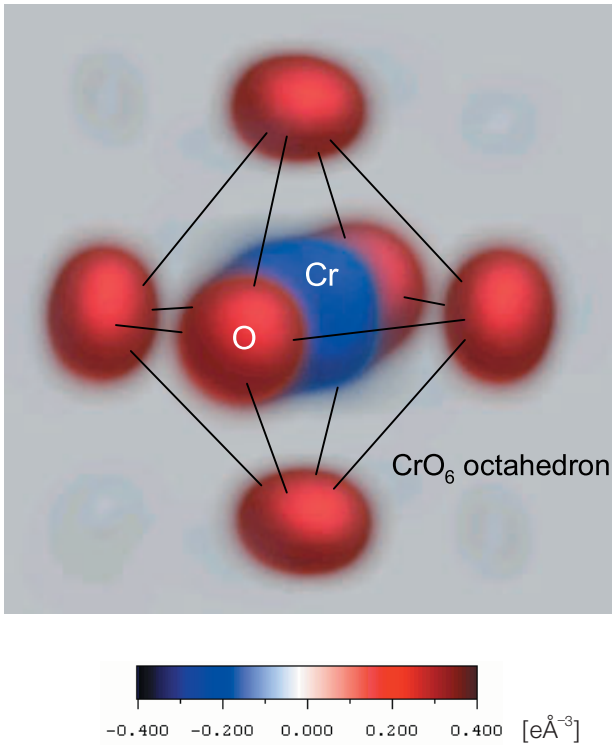

3-D deformation charge density of $LaCrO_3$.

Hexagonal $BaTiO_3$

Atom positions and Debye-Waller factors of the intermediate phase of hexagonal $BaTiO_3$ are refined by our method using energy-filtered two-dimensional HOLZ and ZOLZ CBED patterns.

Hexagonal $BaTiO_3$ is one of the two polymorphic forms of barium titanate; the other is the well known cubic $BaTiO_3$. The hexagonal $BaTiO_3$ at room temperature has six molecular units in the unit cell with lattice parameters of a_h = 0.5735nm and c_h = 1.405nm and belongs to space group $P6_3/mmc$ [a].

Sawaguchi *et al.* [b] found that the hexagonal $BaTiO_3$ undergoes two successive phase transformations at 222K and 74K. Yamamoto *et al.* [c] reported from an X-ray diffraction experiment that the intermediate phase between 222K and 74K belongs to orthorhombic space group $C222_1$. This result was confirmed by us using the CBED method [7]. It was found from Raman [d] and hyper-Raman [e] scattering experiments that the structural phase transformation at 222K is caused by condensation of an E_{2u} phonon mode at the Γ point. Recently, the structural parameters of the intermediate phase and low-temperature phase were refined by neutron powder-diffraction experiments [f], [g].

We selected the intermediate phase of hexagonal $BaTiO_3$ as a test case of our method for simultaneous refinement of many positional parameters.

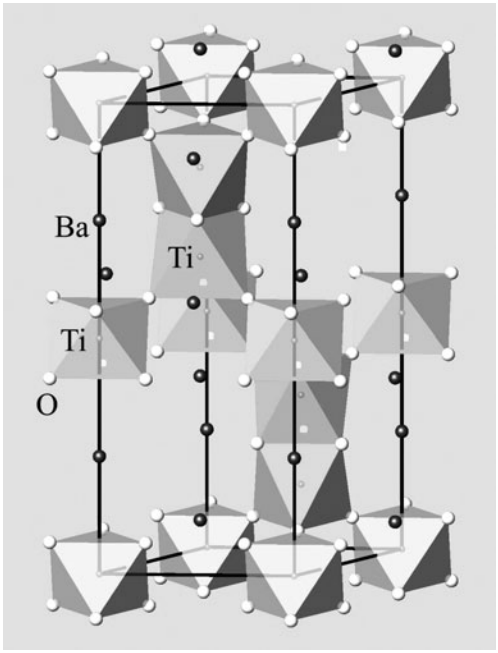

(a)

Crystal structure of hexagonal $BaTiO_3$.

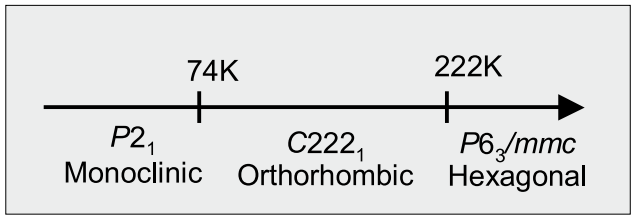

(b)

Sequence of the structural phase transformations of hexagonal $BaTiO_3$.

References

[a] H. T. Evans, Jr. and R. D. Burbank: *J. Chem. Phys.*, **16** (1948) 634; R. D. Burbank and H. T. Evans, Jr.: *Acta Cryst*, **1** (1948) 330.

[b] E. Sawaguchi, Y. Akishige and M. Kobayashi: *J. Phys. Soc. Jpn.*, **54** (1985) 480.

[c] T. Yamamoto, Y. Akishige and E. Sawaguchi: *J. Phys. Soc. Jpn.*, **57** (1988) 3665.

[d] H. Yamaguchi, H. Uwe, T. Sakudo and E. Sawaguchi: *J. Phys. Soc. Jpn.*, **56** (1987) 589.

[e] K. Inoue, A. Hasegawa, K. Watanabe, H. Yamaguchi, H. Uwe and T. Sakudo: *Phys. Rev. B*, **38** (1988) 6352.

[f] Y. Noda, K. Akiyama, T. Shobu, Y. Kuroiwa, H. Nakao, Y. Morii and H. Yamaguchi: *Ferroelectrics*, **217** (1998) 1.

[g] K. Akiyama: *Master Thesis at Chiba University* (1999).

Experiments and fitting

Energy-filtered CBED patterns of the intermediate phase of hexagonal $BaTiO_3$ were taken at 90K with the [001] and [010] incidences using the JEM-2010FEF energy-filter microscope. The acceptance energy was 0±10eV. Two-dimensional intensities of 102 reflections for the [001] data on page 126 and those of 140 reflections for the [010] data on page 129 were extracted from the CBED patterns after distortion correction and background subtraction. The numbers of total data points were 269556 for the [001] data and 182886 for the [010] data.

From the results of the convergence tests of calculated intensities about the number of reflections, 793 reflections were used in the dynamical calculations of the [001] data and 717 reflections for those of [010] data.

The parameters to be refined in the fitting are the positional parameters listed in the table, Debye-Waller factors, low-order structure factors of ZOLZ reflections, scale factor s, specimen thickness t and geometrical parameters to adjust the positions of reflection disks. In the present fitting, a common Debye-Waller factor was used for each element. The lattice parameters used for the fitting are a = 0.5727nm, b = 0.9890nm and c = 1.3942nm [a].

The final results of the fitting are shown in figures on pages 127, 128, 130 and 131. The CBED patterns in the left, center and right columns respectively show experimental, calculated and difference patterns. The calculated patterns are seen to agree very well with experimental patterns. The refined values of the structural parameters are given in the table of page 132.

Site	Wyckoff position	Coordinate
Ba(1)	4*b*	0, y(Ba(1)), 1/4
Ba(2)	8*c*	x(Ba(2)), y(Ba(2)), z(Ba(2))
Ti(1)	4*a*	x(Ti(1)), 0, 0
Ti(2)	8*c*	x(Ti(2)), y(Ti(2)), z(Ti(2))
O(1)	4*b*	0, y(O(1)), 1/4
O(2)	8*c*	x(O(2)), y(O(2)), z(O(2))
O(3)	8*c*	x(O(3)), y(O(3)), z(O(3))
O(4)	8*c*	x(O(4)), y(O(4)), z(O(4))
O(5)	8*c*	x(O(5)), y(O(5)), z(O(5))

Atom coordinates of the intermediate phase of hexagonal $BaTiO_3$.

Reference

[a] Y. Akishige, G. Oomi and E. Sawaguchi: *Sol. Stat. Comm.*, **65** (1988) 621.

Hexagonal $BaTiO_3$ [001] T = 90K Energy-filtered CBED pattern 100kV

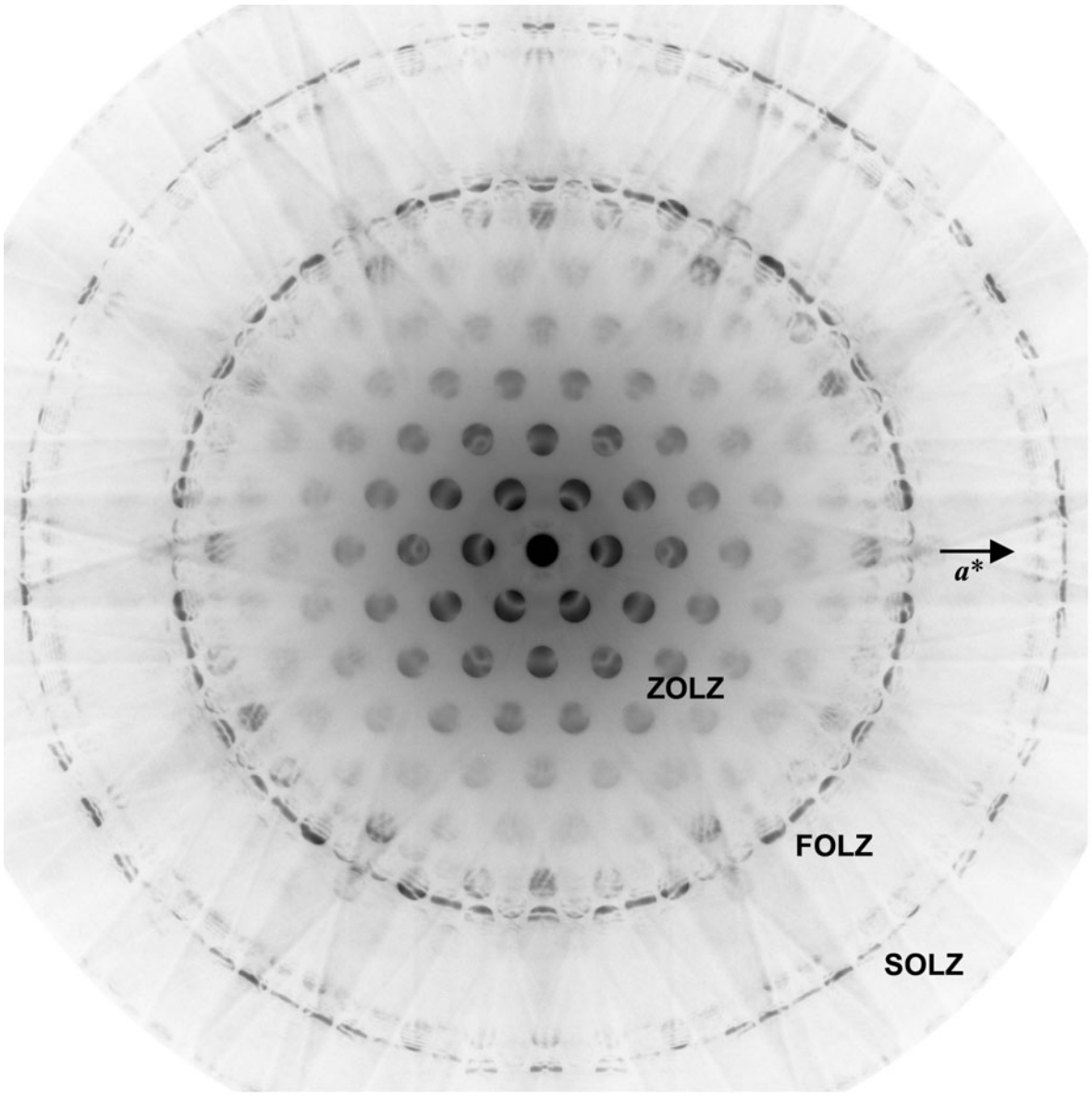

Energy-filtered CBED pattern of the intermediate phase of hexagonal $BaTiO_3$ taken at 90K with the [001] incidence.

Fitting results (hexagonal $BaTiO_3$ [001])

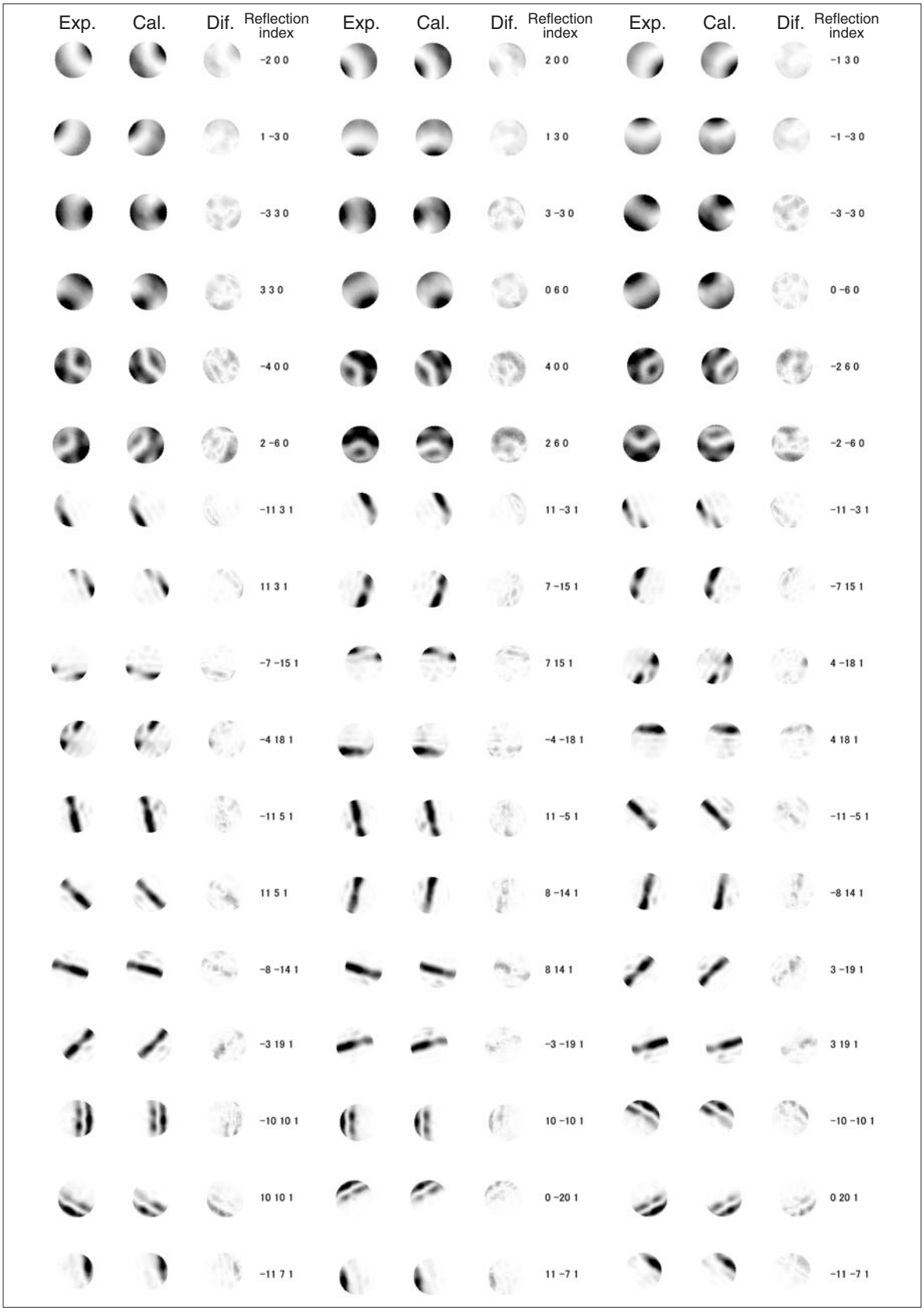

Fitting results (continued) (hexagonal $BaTiO_3$ [001])

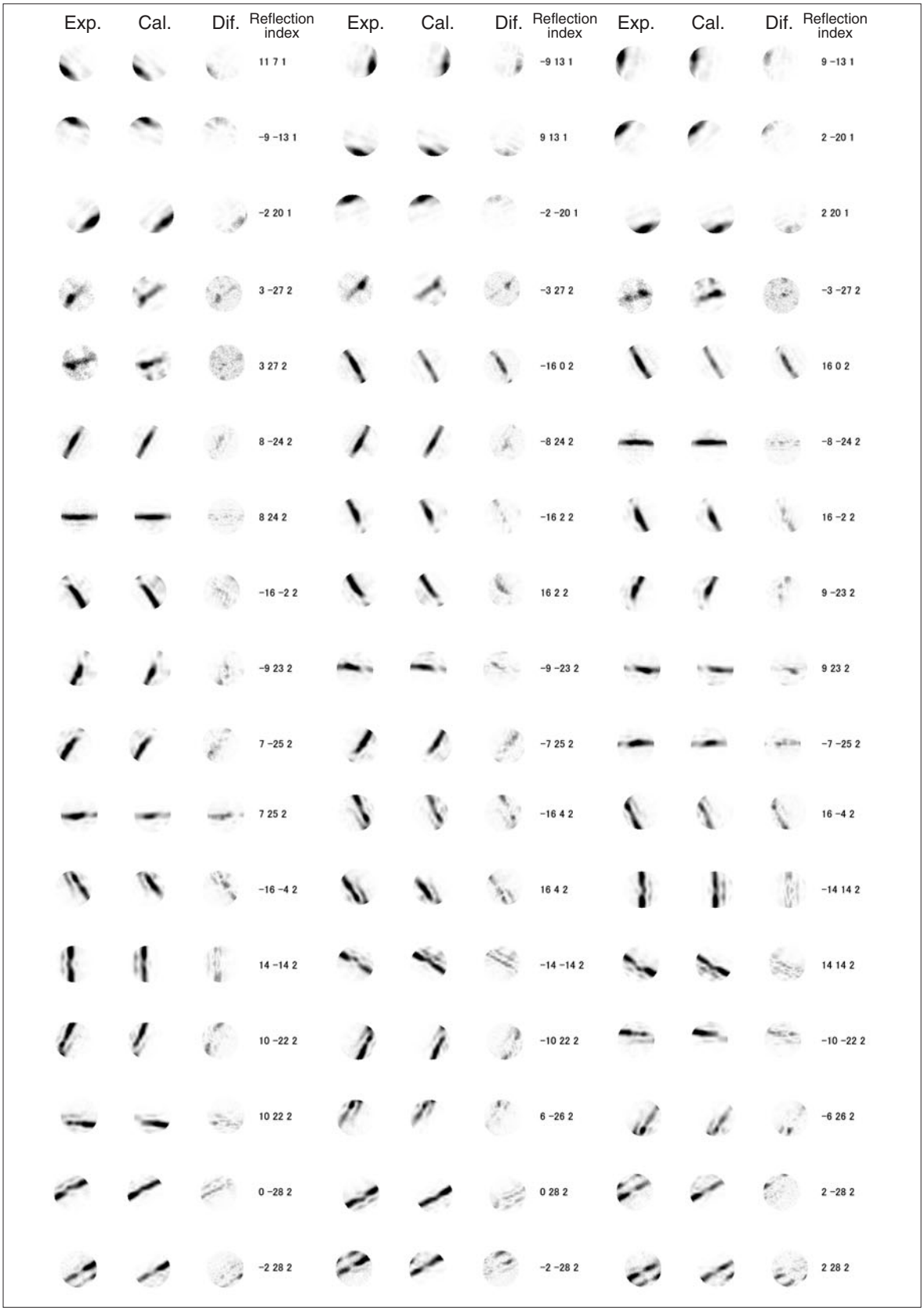

Hexagonal $BaTiO_3$ [010] T = 90K Energy-filtered CBED pattern 100kV

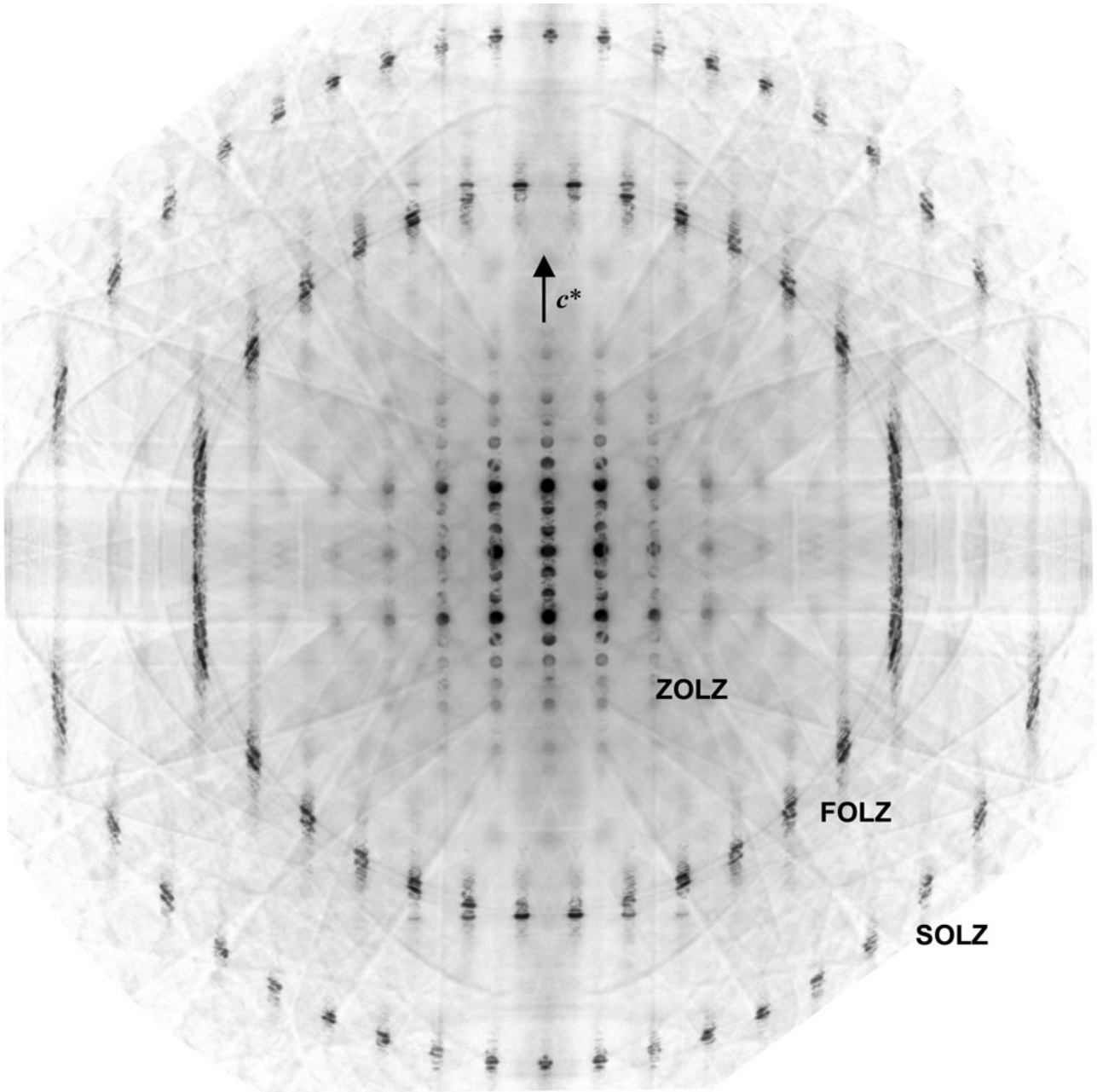

Energy-filtered CBED pattern of the intermediate phase of hexagonal $BaTiO_3$ taken at 90K with the [010] incidence.

Fitting results (hexagonal $BaTiO_3$ [010])

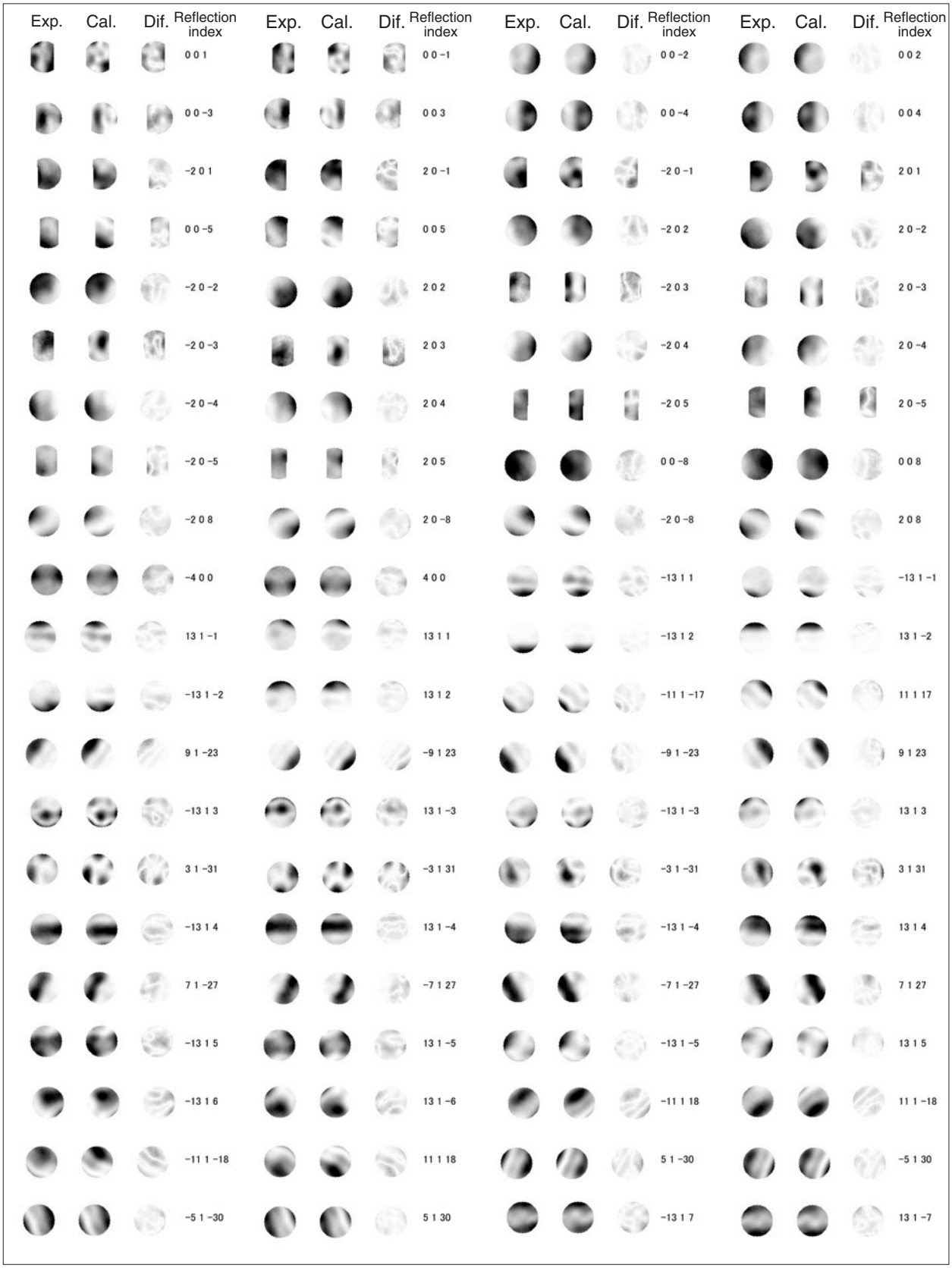

Fitting results (continued) (hexagonal $BaTiO_3$ [010])

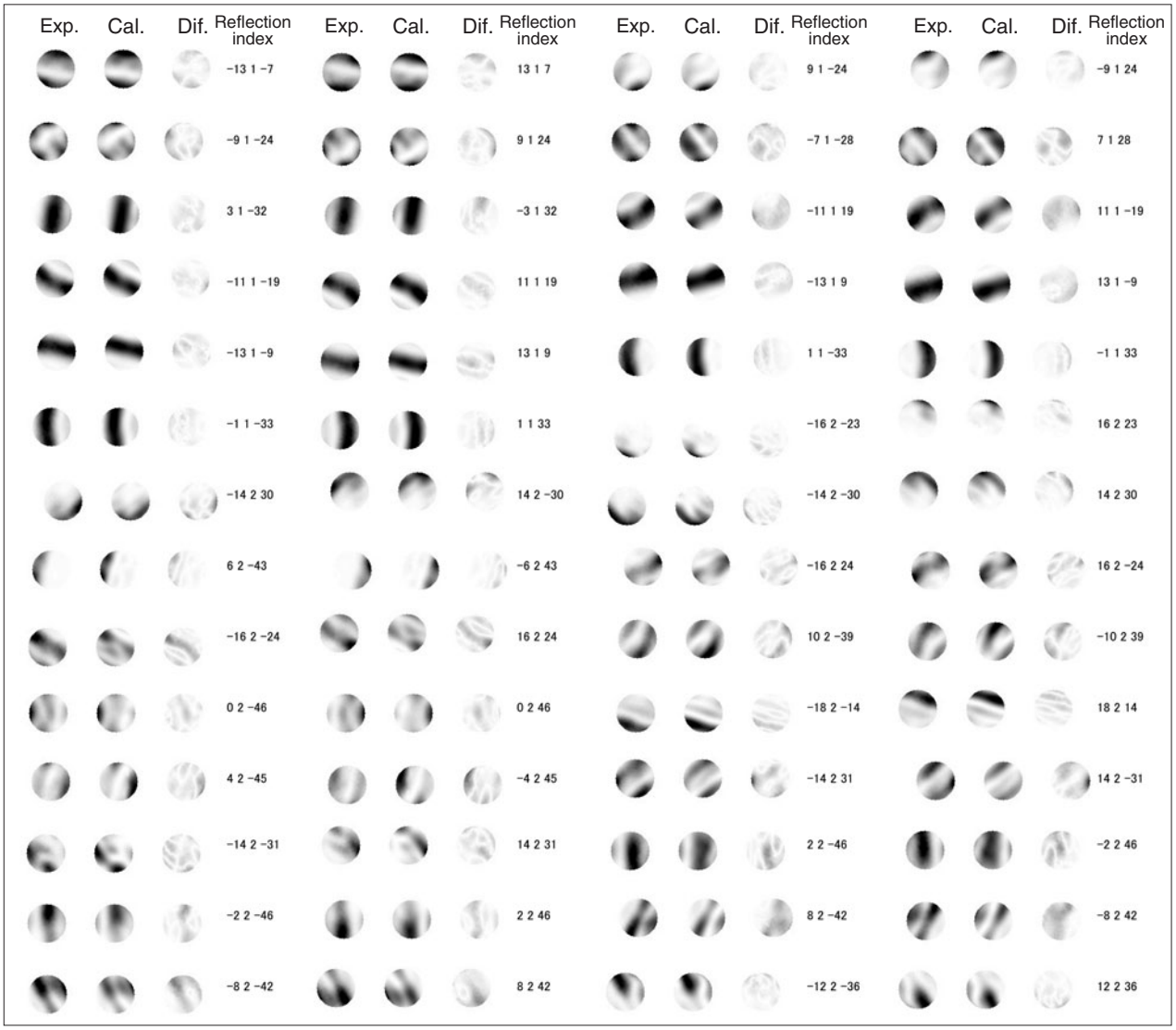

Refined parameters

Table (a) shows the refined values of the positional parameters (fractional coordinates), Debye-Waller factors and low-order structure factors of hexagonal $BaTiO_3$, which were obtained by the combined use of the [001] and [010] CBED patterns. The value of R_w was 0.307. In the present fitting, a common isotropic Debye-Waller factor was used for each element in order to reduce computing time. The better R_w and *GOF* are expected to be obtained by the use of the individual Debye-Waller factor for each atom site. The values of the positional parameters and Debye-Waller factors obtained by a neutron powder-diffraction experiment using the Rietveld analysis [a] are given in Table (b) for comparison. It is seen that the values agree well with the CBED values except some differences in the x coordinates of Ba and Ti though the present R_w is not small enough.

The present CBED method needs enormous time to simultaneously refine many structural parameters, for example, 24 parameters in hexagonal $BaTiO_3$. At present, we refine a set of parameters with other parameters fixed and then refine the next set and so on. We have to utilize parallel computations to refine all structural parameters including anisotropic Debye-Waller factors, by which computing time is expected to be reduced greatly. Furthermore, the parallel computation must be useful for the analysis of local structures of imperfect crystals with the use of a lower symmetry space group and a super-lattice cell.

(a)

	CBED at 90K			
	x	y	z	B
Ba(1)	0	0.000672(3)	0.25	0.28316(5)
Ba(2)	0.009089(2)	0.333576(4)	0.096220(1)	
Ti(1)	0.027159(7)	0	0	0.24284(8)
Ti(2)	0.019561(5)	0.332296(7)	0.846150(1)	
O(1)	0	0.51455(2)	0.25	0.4677(2)
O(2)	0.76979(2)	0.73669(1)	0.253883(5)	
O(3)	0.008169(8)	0.83101(1)	0.081378(3)	
O(4)	0.74480(1)	0.577024(9)	0.077733(5)	
O(5)	0.25380(1)	0.58416(1)	0.079563(4)	

Low-order structure factor [Å]	CBED at 90K
Re [F_{200}]	125.55 (1)
Re [F_{130}]	128.204 (9)
Im [F_{203}]	–4.077 (4)
Re [F_{006}]	–77.547 (3)
Re [F_{204}]	–19.092 (1)

(b)

	Neutron diffraction at 150K (Akiyama *et al.*)			
	x	y	z	B
Ba(1)	0	–0.0008(8)	0.25	0.15(3)
Ba(2)	0.0055(14)	0.3333(6)	0.0969(1)	0.33(2)
Ti(1)	0.0170(20)	0	0	0.42(8)
Ti(2)	0.0130(16)	0.3294(8)	0.8457(2)	0.33(5)
O(1)	0	0.5188(6)	0.25	0.47(7)
O(2)	0.7747(6)	0.7421(4)	0.2484(6)	0.44(4)
O(3)	0.0033(16)	0.8342(5)	0.0801(5)	0.34(5)
O(4)	0.7447(12)	0.5824(9)	0.0822(5)	0.31(10)
O(5)	0.2523(11)	0.5851(9)	0.0794(5)	0.42(10)

Reference

[a] K. Akiyama: *Master Thesis at Chiba University* (1999).

Bloch States

It is demonstrated how the Bloch states formed by incident electrons change with the depth of the projected potential. $SrTiO_3$, $BaTiO_3$, $PbZrO_3$ and $KNbO_3$, which have the cubic perovskite structure with different constituent atoms, are used as examples. On the following pages, projected potentials, electron density distributions of Bloch states, dispersion surface and the excitations of the Bloch states for these materials are shown. These were calculated at the [001] incidence and an accelerating voltage of 100kV using 109 ZOLZ beams.

The cubic perovskite structure consists of the rows of the A-site atoms, the rows of the B-site and O(1)-site (hereafter abbreviated as B+O-site) atoms and the rows of O(2)-site (hereafter abbreviated as O-site) atoms when viewed from the [001] direction.

The Bloch states can be assigned each to an atomic state or a hybridized state. In the case of $SrTiO_3$, the electron densities of branches 1 and 2 are concentrated on the rows of Ti+O (B+O-site) atoms and on the rows of Sr (A-site) atoms, respectively. These states are respectively assigned to the 1*s* state at the Ti+O-site and the 1*s* state at the Sr-site. The electron densities of branches 3 and 4 are on the rows of O-site atoms. These states are respectively assigned to bonding and anti-bonding states of the 1*s* states at the two O-sites. To distinguish the bonding and anti-bonding states, the signs of the wave functions are attached at the density maxima in the figures of the electron density distributions. Branches 5 to 8 are assigned to the hybridized states of the 2*p* states at the Sr-site and the Ti+O-site.

In the case of $PbZrO_3$, it is seen that branch 1 with a large k_z produces the 1*s* state at the Pb-site, and branch 2 forms the 1*s* state at the Zr+O-site contrary to the case of $SrTiO_3$ because the potential of the A-site is deeper than that at the Zr+O-site.

	Atomic number	Lattice parameter
$SrTiO_3$	Sr: 38 Ti+O: 22+8	a = 0.3905nm
$PbZrO_3$	Pb: 82 Zr+O: 40+8	$a \oplus 0.410$nm
$BaTiO_3$	Ba: 56 Ti+O: 22+8	a = 0.40118nm
$KNbO_3$	K: 19 Nb+O: 41+8	a = 0.4007nm

In $SrTiO_3$ and $PbZrO_3$, hybridized states between the 2*p* states at the A-site and the B+O-site are formed because the depths of the potentials at these two sites are not so different for both the materials. On the other hand, the 2*p* states at the A-site and the B+O-site do not form hybridized states in $BaTiO_3$ and $KNbO_3$ because the depths of the potentials at the two sites are much different. The 1*s* states at the two O-sites in the projected unit cell always form hybridized states in all the present cases.

It is seen that the 1*s* bonding states at the O-sites are most strongly excited at the zone-axis incidence. The next strongly excited states are the 1*s* states at the A-sites and the B+O-sites. It should be noted that this fact leads to the high sensitivity of the [001] CBED patterns for the structural parameters of the O-sites. The 2*p* states are not excited at the zone-axis incidence because they are anti-symmetric with respect to the zone axis.

Let us compare the Bloch states on the following pages, taking notice of the relations between the relative values of projected potentials and the sequences of the branches of the dispersion surface.

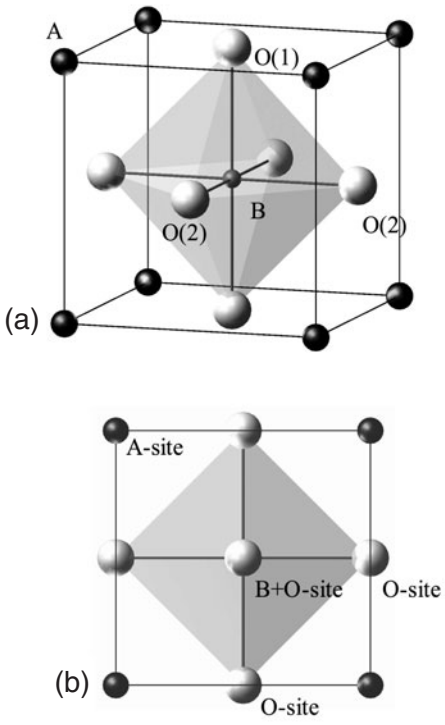

(a) Cubic perovskite structure of ABO_3. (b) The structure projected in the [001] direction.

$SrTiO_3$ [001] Bloch states

100kV

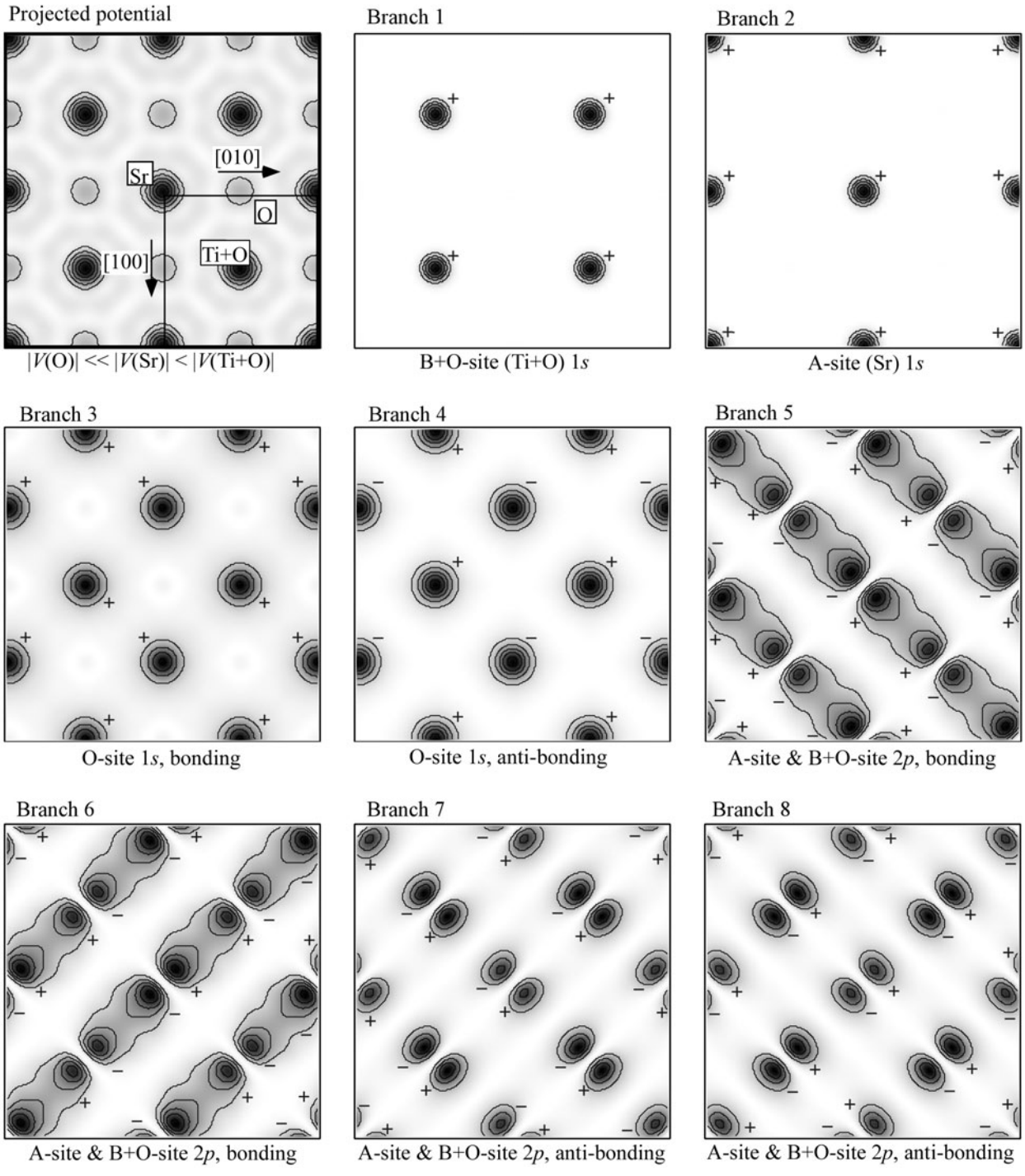

$SrTiO_3$ [001] Dispersion surface and excitations of the branches

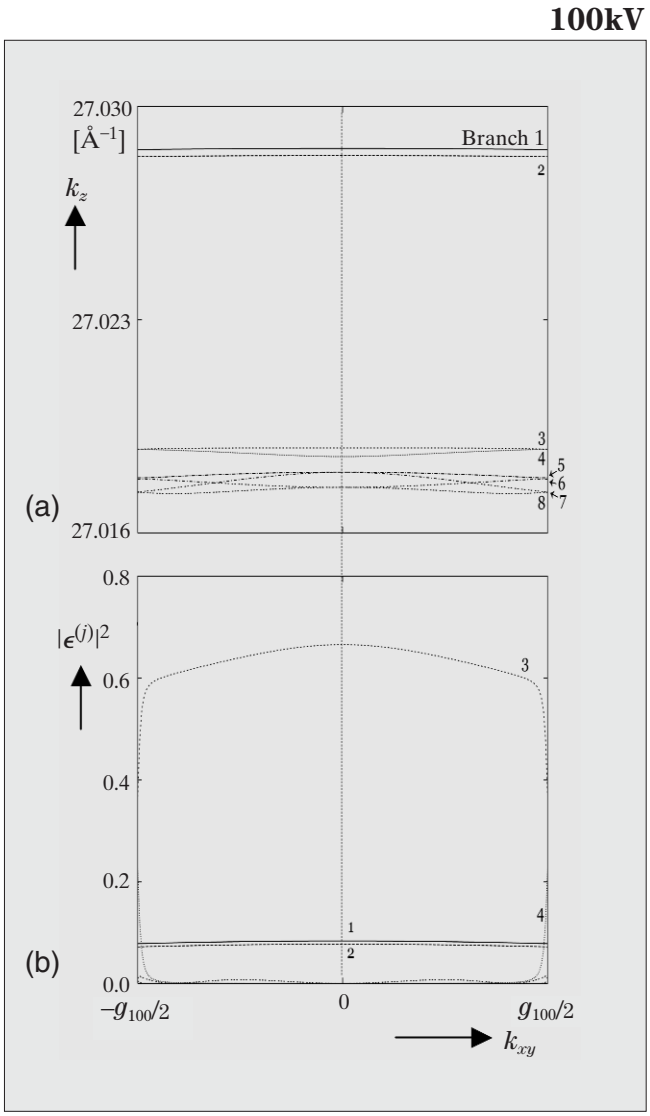

(a) Branches of the dispersion surface of $SrTiO_3$ around the [001] incidence. (b) Excitations of the branches.

Branches 1 and 2 are respectively the 1*s* state of the B+O-site and the 1*s* state of the A-site. Branches 3 and 4 are respectively the bonding and anti-bonding states of the 1*s* states of the O-sites. Since the depths of the potentials of the A-site and the B+O-site are not so different, the 2*p* states of the A-site and the B+O-site form hybridized states. That is, branches 5 and 6 are the bonding states of the hybridized states and branches 7 and 8 are the anti-bonding states of the hybridized states.

	$SrTiO_3$
A-site	Sr
B+O-site	Ti+O
Projected potential	$\|V_O\| \ll \|V_A\| < \|V_{B+O}\|$
Branch 1	B+O 1*s*
Branch 2	A 1*s*
Branch 3	O 1*s* hybrid., bonding
Branch 4	O 1*s* hybrid., anti-bonding
Branch 5	A & B+O 2*p* hybrid., bonding
Branch 6	A & B+O 2*p* hybrid., bonding
Branch 7	A & B+O 2*p* hybrid., anti-bonding
Branch 8	A & B+O 2*p* hybrid., anti-bonding

Assignment of the Bloch states.

$PbZrO_3$ [001] Bloch states

100kV

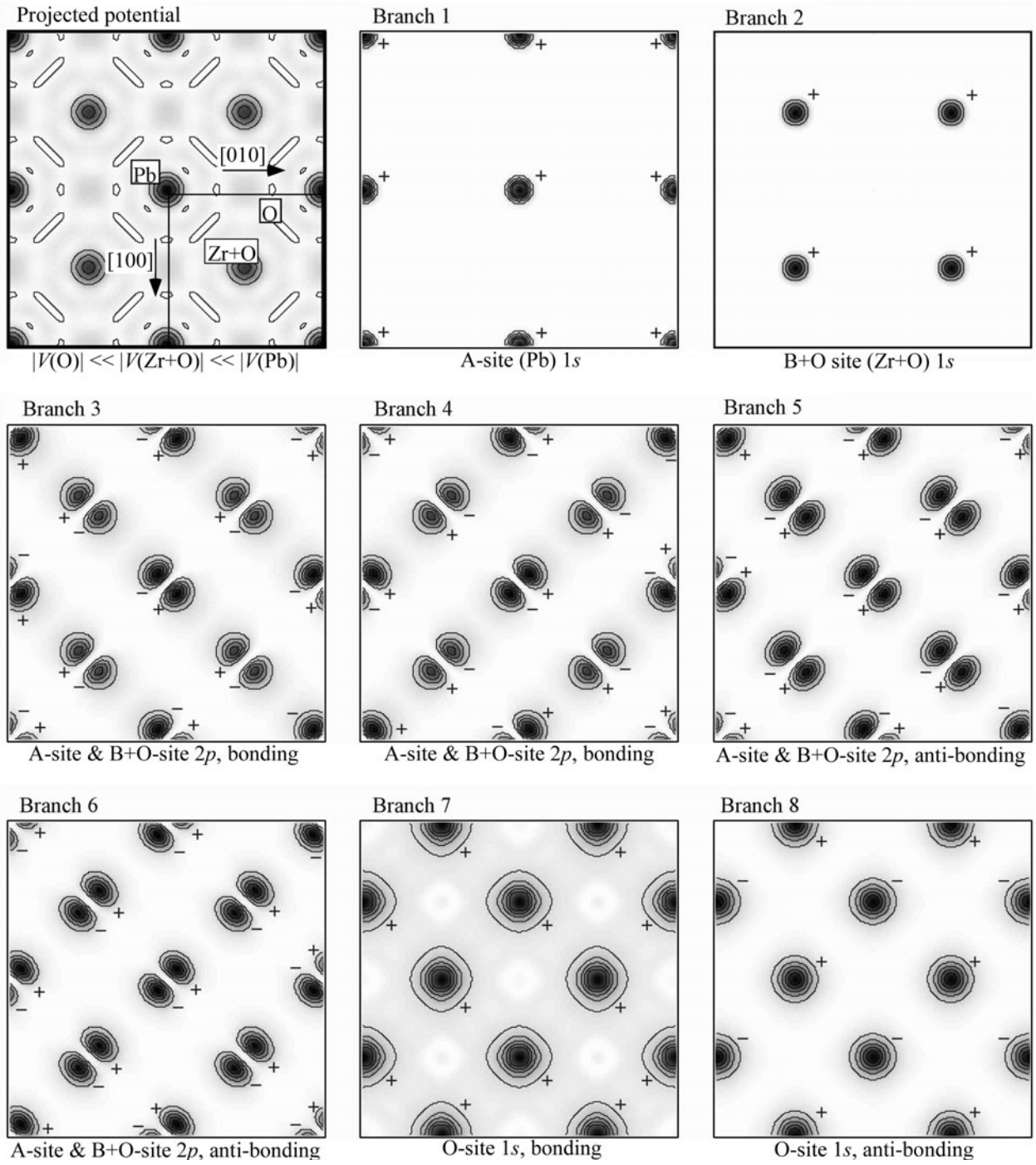

$PbZrO_3$ [001] Dispersion surface and excitations of the branches

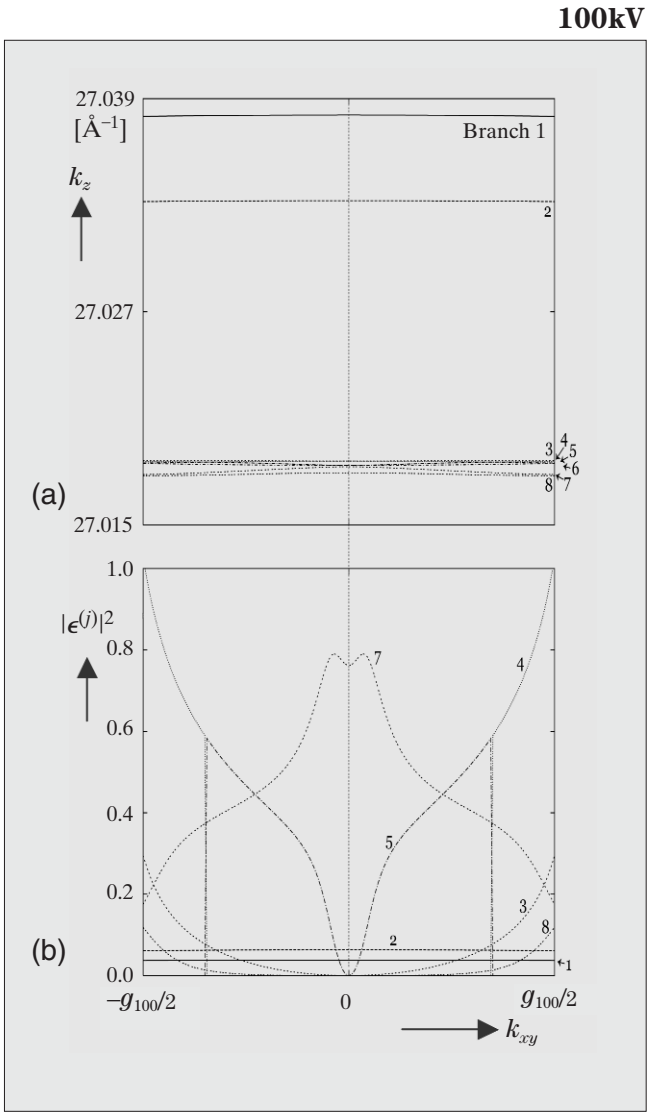

(a) Branches of the dispersion surface of $PbZrO_3$ around the [001] incidence. (b) Excitations of the branches.

Branches 1 and 2 are respectively the 1*s* state of the A-site and the 1*s* state of the B+O-site. Branches 3 to 6 are the hybridized states of the A-site and B+O-site. This is because the depths of the potentials of the A-site and B+O-site are not so different. Branches 7 and 8 are the anti-bonding states of the O-site 1*s* states. In this case, the branches of the 1*s* states of the O-sites appear below the 2*p* states of the A-site and the B+O-site because the potentials of the A-site and B+O-site are much deeper than those of the O-sites.

	$PbZrO_3$
A-site	Pb
B+O-site	Zr+O
Projected potential	$\|V_O\| \ll \|V_{B+O}\| < \|V_A\|$
Branch 1	A 1*s*
Branch 2	B+O 1*s*
Branch 3	A & B+O 2*p* hybrid., bonding
Branch 4	A & B+O 2*p* hybrid., bonding
Branch 5	A & B+O 2*p* hybrid., anti-bonding
Branch 6	A & B+O 2*p* hybrid., anti-bonding
Branch 7	O 1*s* hybrid., bonding
Branch 8	O 1*s* hybrid., anti-bonding

Assignment of the Bloch states.

$BaTiO_3$ [001] Bloch states

100kV

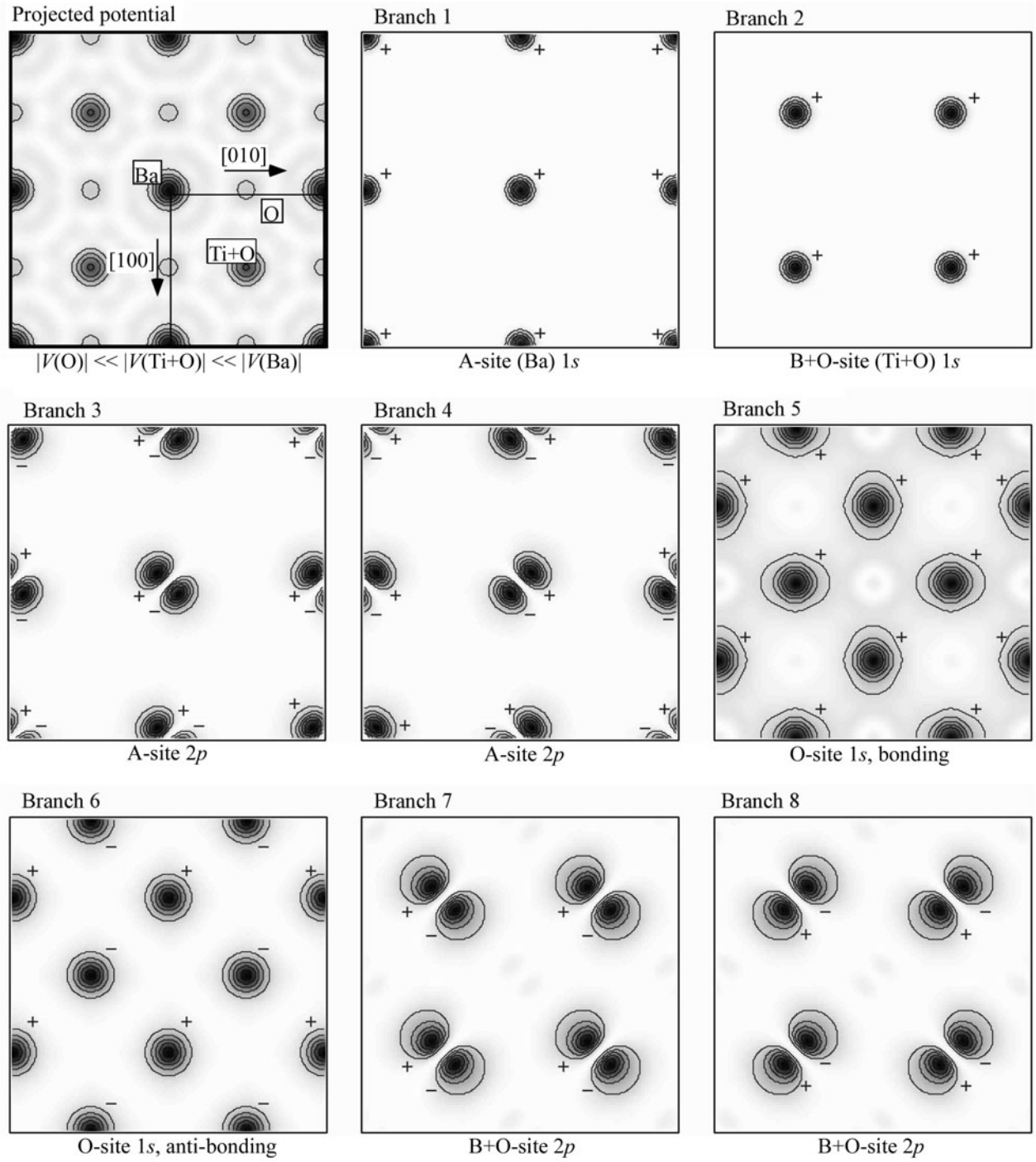

$BaTiO_3$ [001] Dispersion surface and excitations of the branches

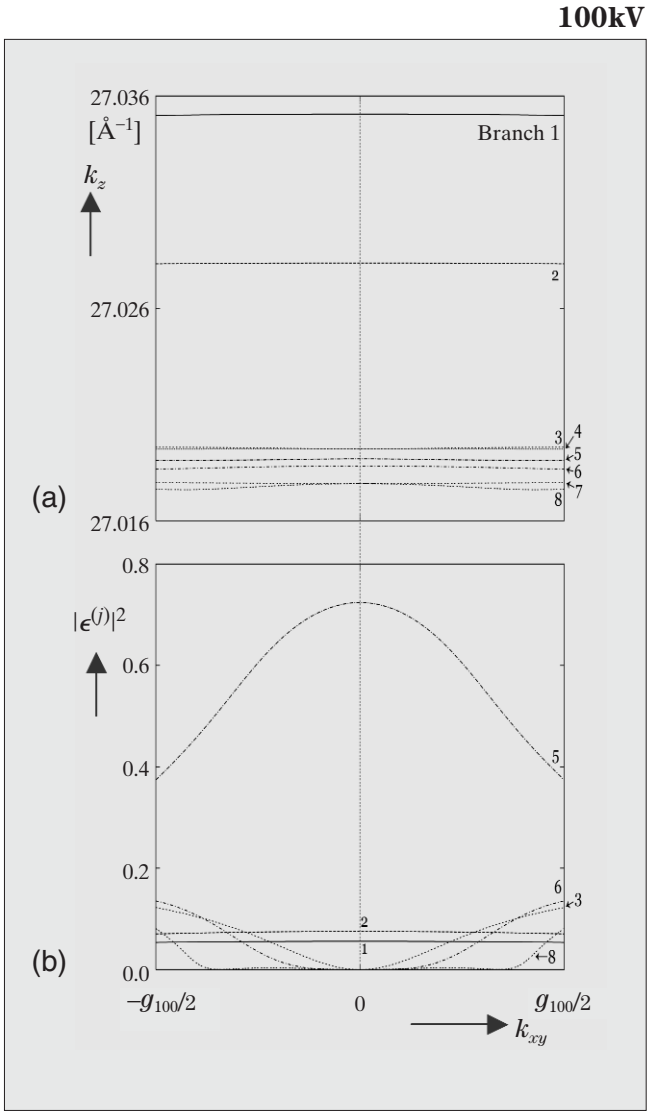

(a) Branches of the dispersion surface of $BaTiO_3$ around the [001] incidence. (b) Excitations of the branches.

Branches 1 and 2 are respectively the 1*s* state of the A-site and the 1*s* state of the B+O-site. This is because the potential of the A-site is deeper than that of the B+O-site in $BaTiO_3$. Branches 3 and 4 are the 2*p* states of the A-site. Branches 5 and 6 are the bonding and anti-bonding states of the 1*s* states of the O-sites. Branches 7 and 8 are the 2*p* states of the B+O-site. The 2*p* states of the A-site and B+O-site do not form hybridized states because the depth of the potential of the A-site is much different from that of the B+O-site in $BaTiO_3$.

	$BaTiO_3$
A-site	Ba
B+O-site	Ti+O
Projected potential	$\|V_O\| \ll \|V_{B+O}\| \ll \|V_A\|$
Branch 1	A 1*s*
Branch 2	B+O 1*s*
Branch 3	A 2*p*
Branch 4	A 2*p*
Branch 5	O 1*s* hybrid., bonding
Branch 6	O 1*s* hybrid., anti-bonding
Branch 7	B+O 2*p*
Branch 8	B+O 2*p*

Assignment of the Bloch states.

$KNbO_3$ [001] Bloch states

100kV

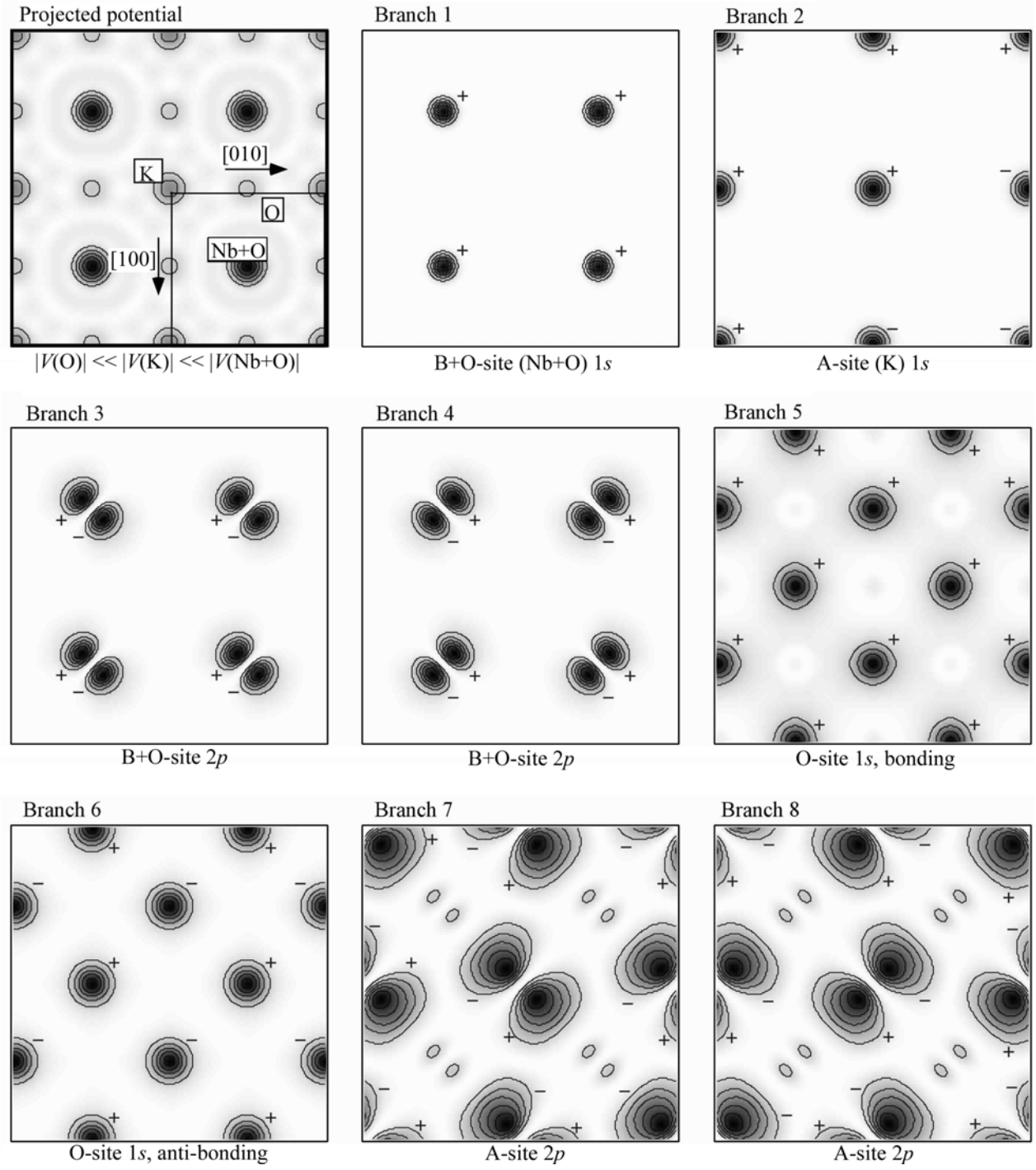

$KNbO_3$ [001] Dispersion surface and excitations of the branches

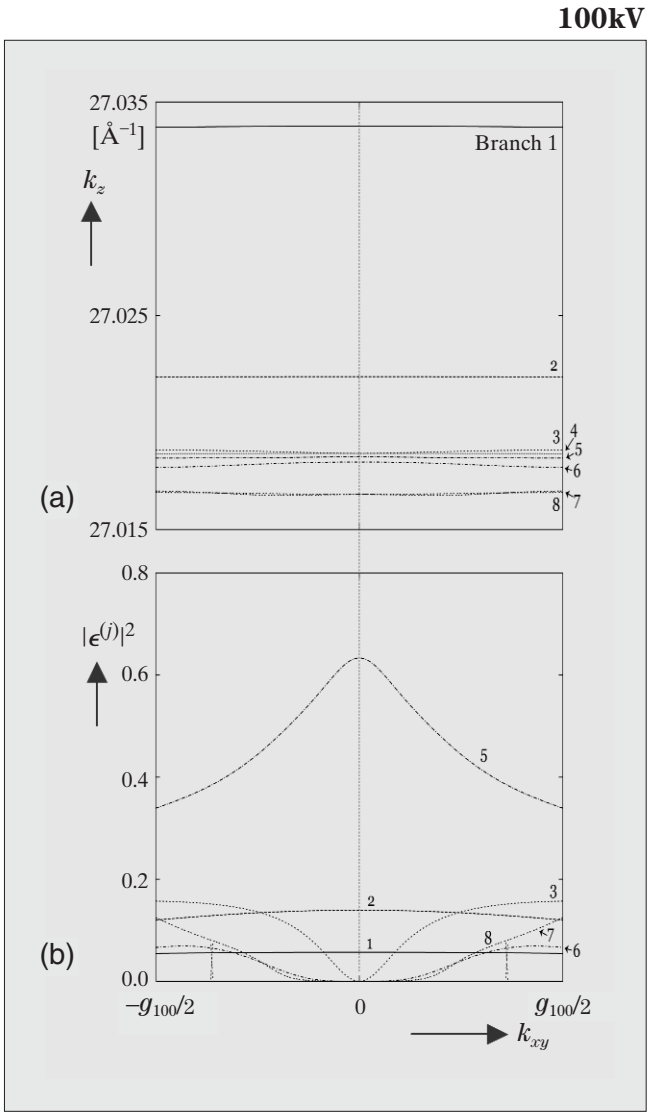

(a) Branches of the dispersion surface of $KNbO_3$ around the [001] incidence. (b) Excitations of the branches.

Branches 1 and 2 are respectively the 1*s* state of the B+O-site and the 1*s* state of the A-site. Branches 3 and 4 are respectively the bonding and anti-bonding states of the 1*s* states of the O-sites. Branches 3 and 4 are the 2*p* states of the B+O-site. Branches 5 and 6 are the bonding and anti-bonding states of the 1*s* states of the O-site. Branches 7 and 8 are the 2*p* states of the A-site. The 2*p* states of the A-site and B+O-site do not form hybridized states because the depth of the potential of the A-site are much different from the B+O-site.

	$KNbO_3$
A-site	K
B+O-site	Nb+O
Projected potential	$\|V_O\| \ll \|V_A\| \ll \|V_{B+O}\|$
Branch 1	B+O 1*s*
Branch 2	A 1*s*
Branch 3	B+O 2*p*
Branch 4	B+O 2*p*
Branch 5	O 1*s* hybrid., bonding
Branch 6	O 1*s* hybrid., anti-bonding
Branch 7	A 2*p*
Branch 8	A 2*p*

Assignment of the Bloch states.

Quasicrystals

Three Types of Decagonal Quasicrystals

At the beginning of discovery of the decagonal quasicrystal, it was simply assumed to belong to space group $P10_5/mmc$. The earlier HREM studies seemed to confirm the assumption. The CBED method brought its capability into full play in revealing the true symmetry of the decagonal quasicrystals. That is, we discovered the noncentrosymmetric decagonal quasicrystals with space group $P\bar{1}0m2$ in Al-Ni-Fe alloys using the CBED method (Type I) [a]. We also found the centrosymmetric ones with space group $P10_5/mmc$ in the same alloy system. A careful HREM study revealed that the basic clusters of 2nm in diameter are the same for both the quasicrystals with the two different space groups. That is, the cluster is noncentrosymmetric or of pentagonal symmetry. In the alloys of space group $P10_5/mmc$, the clusters with opposite senses are intermixed in the scale of a few nm (Type II) [b],[c], whereas in the alloys of space group $P\bar{1}0m2$, the clusters of one sense are arranged to form a domain [d]. It had been believed that there exist decagonal quasicrystals with space group $P10_5/mmc$, which have centrosymmetric clusters or decagonal-symmetry clusters (Type III) [e].

Symmetry of the clusters had long been examined by the HREM method. One has to be very careful about the interpretation of the HREM image because the image is often different from the true projection potential of a specimen crystal due to the lens aberration and strong dynamical diffraction effect. We have recently applied the high-angle annular dark-field (HAADF) method to the investigation of the symmetry of the cluster, or for revealing the positions of the transition metals in the cluster. As a result, we discovered that the decagonal quasicrystals of Type III consist of clusters, which have three transition-metal atoms at the center and have only one mirror symmetry [20]. After our HAADF study, many researchers have used the method in the structural studies of quasicrystals. The characteristic symmetry features of the three types of the decagonal quasicrystals are summarized.

First, selected-area diffraction (SAD) and CBED patterns of the three types of the decagonal quasicrystals are shown. The phase diagrams of the alloy systems, which we have studied so far, are presented later. In this chapter, we describe our recent structural investigations of the decagonal quasicrystals and their crystalline approximants, though those studies have not always used the CBED method. We believe that we will have to come back to the CBED method at the final stage of high-precision structure determination of the quasicrystals.

Type I structure is composed of atom-cluster columns having fivefold-rotation symmetry, which was first revealed by the HREM method and afterwards confirmed by the HAADF method. All the fivefold-symmetry atom-clusters have the same sense of polarity in a domain. The adjacent two domains form an inversion-domain structure. The SAD pattern taken at an incidence along the decagonal (c-) axis shows tenfold-rotation symmetry but the CBED pattern taken at the same incidence shows fivefold-rotation symmetry. The CBED pattern taken at an incidence in direction A (indicated by an arrow in the SAD pattern taken at the c-axis incidence) shows mirror symmetry perpendicular to the c-axis. The CBED pattern taken at an incidence in direction B shows two mirror symmetries parallel and perpendicular to the c-axis. Thus, the space group of the quasicrystal is determined to be noncentrosymmetric $P\bar{1}0m2$.

Type II structure is composed of atom-cluster columns having fivefold-rotation symmetry as well as Type I, but the atom clusters having the opposite sense of polarity to each other are intermixed, which were revealed by HREM studies. As a result, the average structure becomes centrosymmetric. The CBED pattern taken at an incidence along the c-axis shows tenfold-rotation symmetry. The CBED patterns taken at incidences in directions A and B show two mirror symmetries parallel and perpendicular to the c-axis. Thus, the space group of the quasicrystal is determined to be centrosymmetric $P10_5/mmc$.

Type III structure is composed of atom-cluster columns having only one mirror symmetry, which was revealed by the HAADF method. The clusters with mirror symmetry take ten different orientations rotated by $36 \times n$ degrees (n: integer). As a result, the average structure becomes centrosymmetric. The CBED patterns show the same symmetries as those of Type II structure. Thus, the space group is determined to be $P10_5/mmc$.

References

[a] M. Saito, M. Tanaka, A. P. Tsai, A. Inoue and T. Masumoto: *Jpn. J. Appl. Phys.*, **31** (1992) L109.

[b] M. Tanaka, K. Tsuda, M. Terauchi, A. Fujiwara, A. P. Tsai, A. Inoue and T. Masumoto: *J. Non-Cryst. Solids*, **153&154** (1993) 98.

[c] K. Saitoh, K. Tsuda, M. Tanaka, A. P. Tsai, A. Inoue and T. Masumoto: *Philos. Mag.*, **A73** (1996) 387.

[d] K. Tsuda, M. Saito, M. Terauchi, M. Tanaka, A. P. Tsai, A. Inoue and T. Masumoto: *Jpn. J. Appl. Phys.*, **32** (1993) 129.

[e] K. Hiraga, F. J. Lincoln and W. Sun: *Mater. Trans. JIM*, **32** (1991) 308.

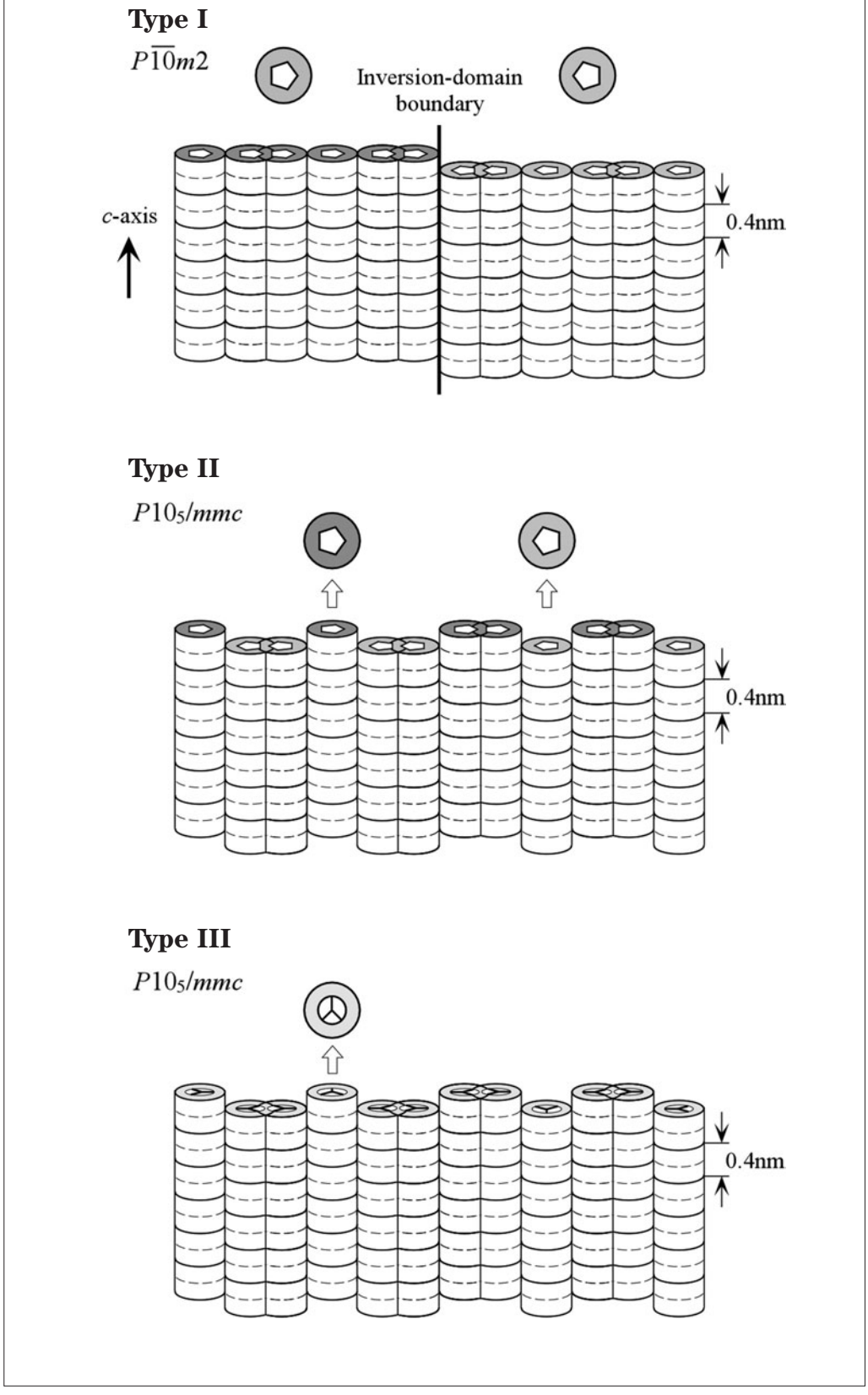
Type I
$P\bar{1}0m2$
Inversion-domain boundary
c-axis
0.4nm
Type II
$P10_5/mmc$
0.4nm
Type III
$P10_5/mmc$
0.4nm

Type I

$Al_{70}Ni_{15}Fe_{15}$ 60kV

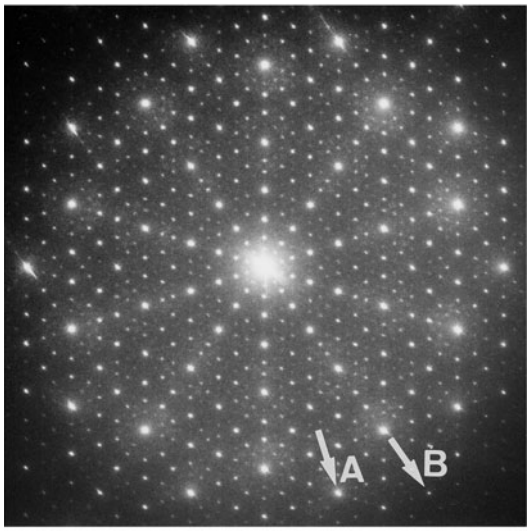

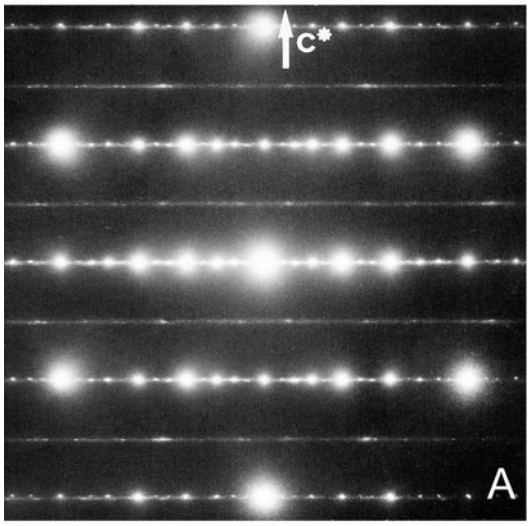

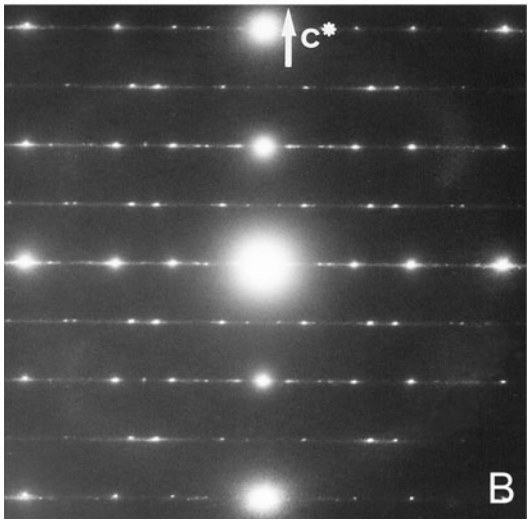

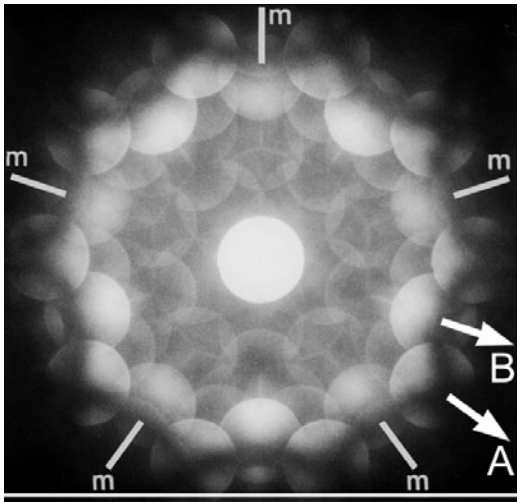

5m

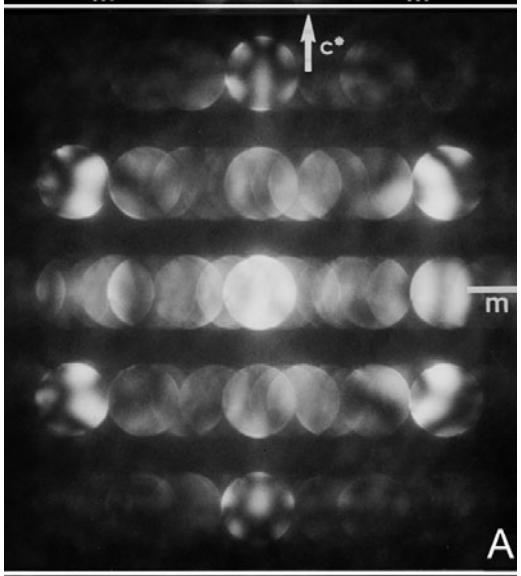

m

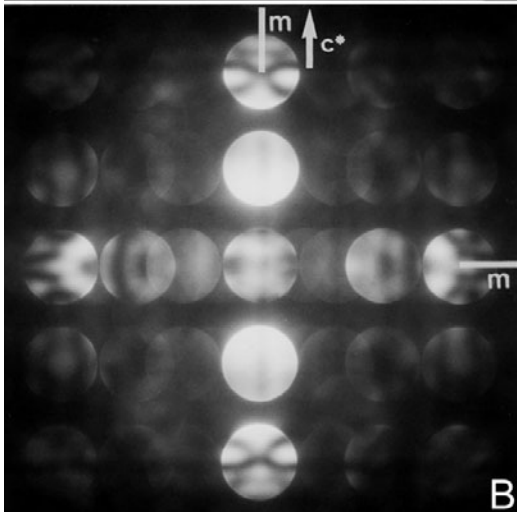

2mm

Type II

$Al_{70}Ni_{20}Fe_{10}$ **100kV**

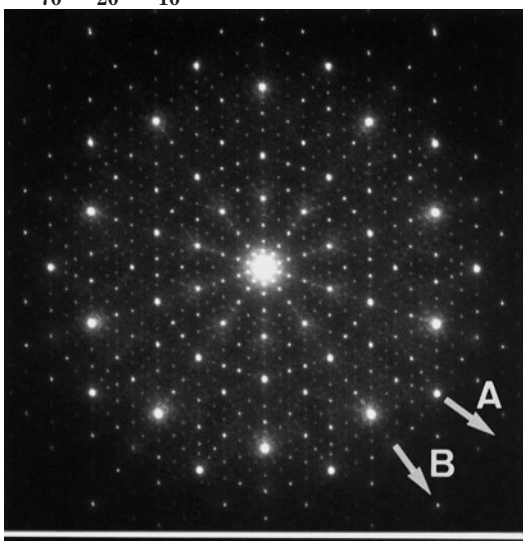

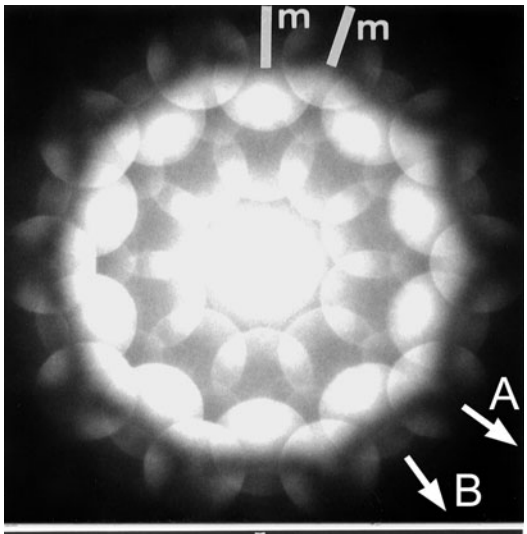

10*mm*

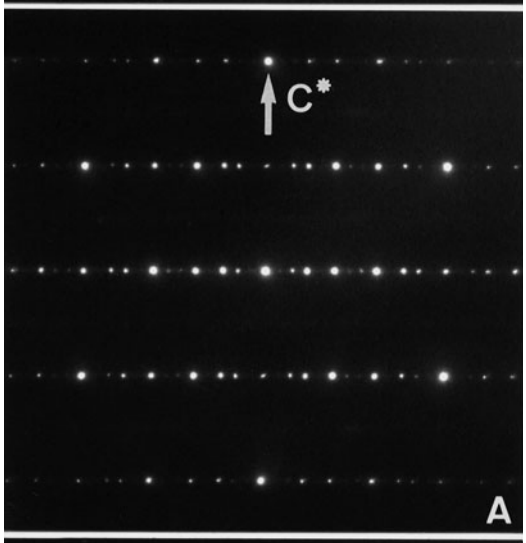

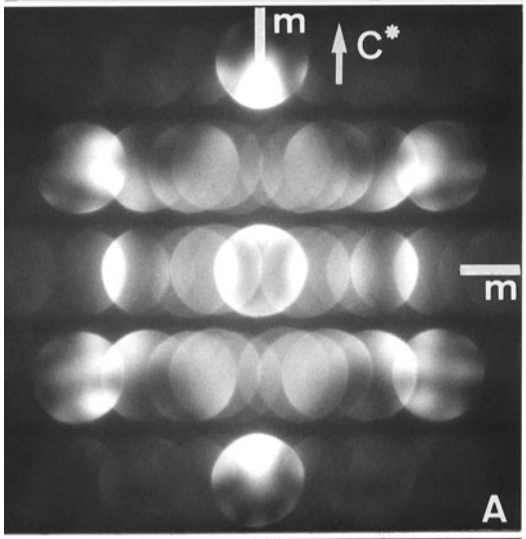

2*mm*

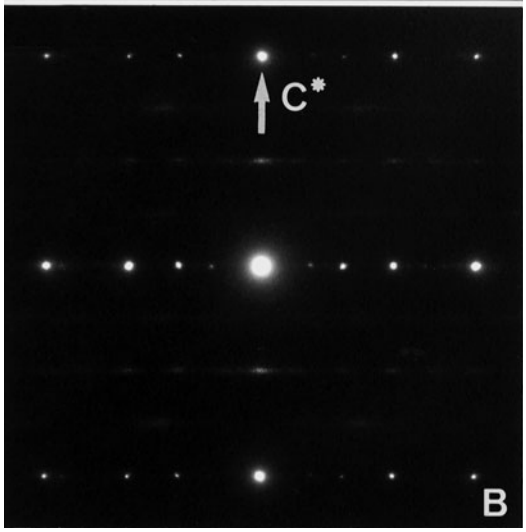

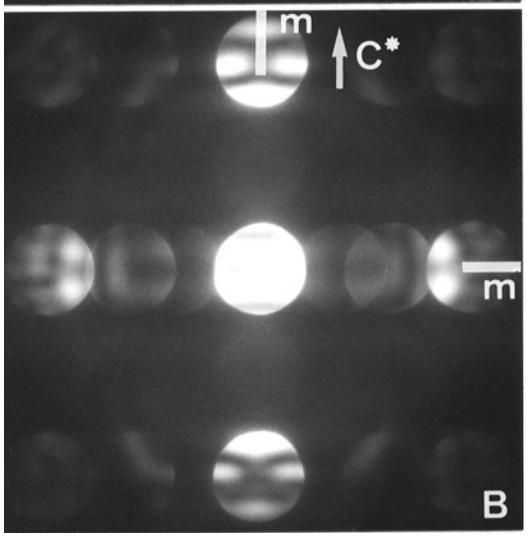

2*mm*

Type III

$Al_{72}Ni_{20}Co_8$ **100kV**

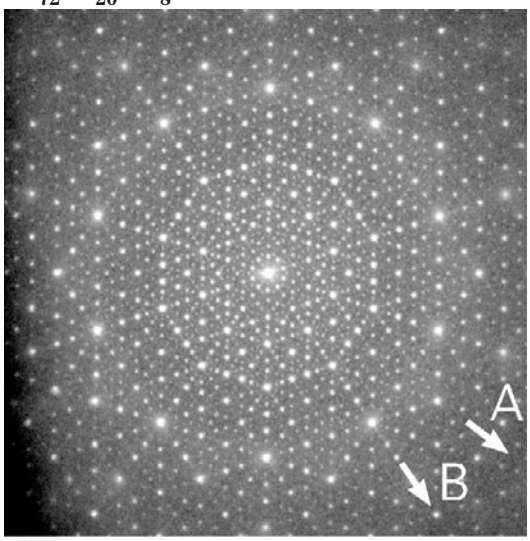

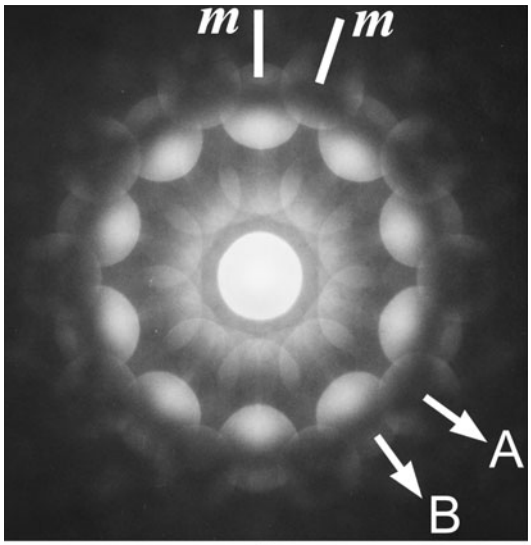

10*mm*

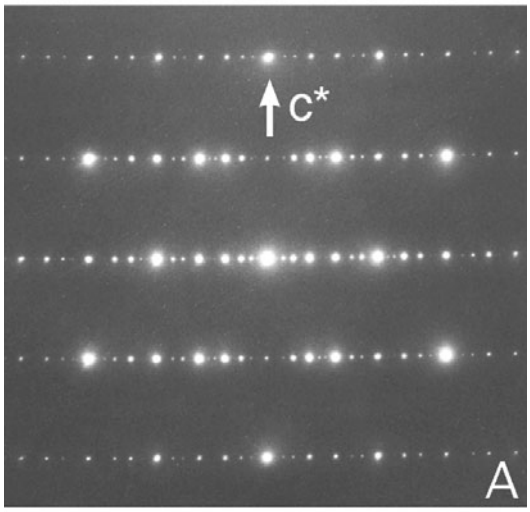

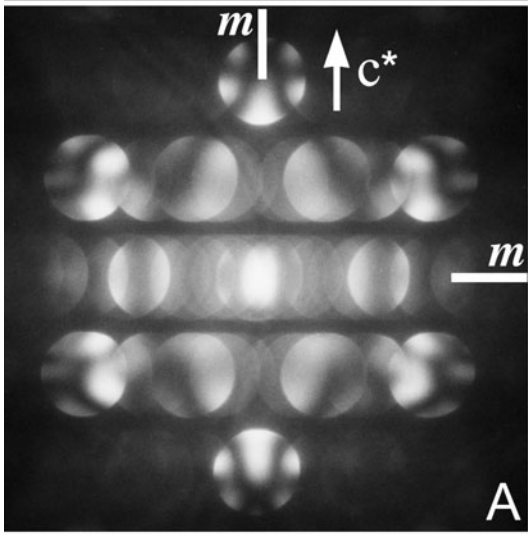

2*mm*

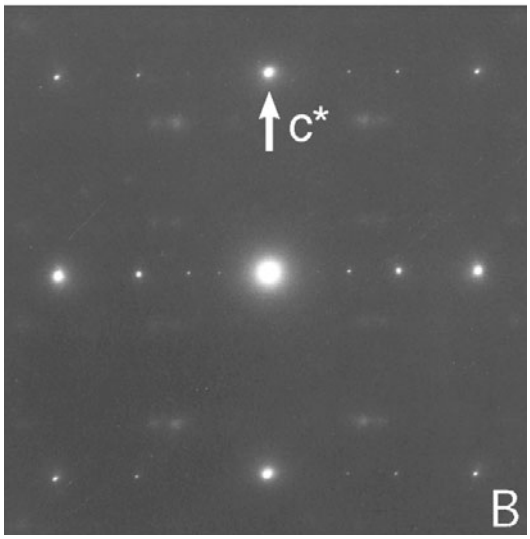

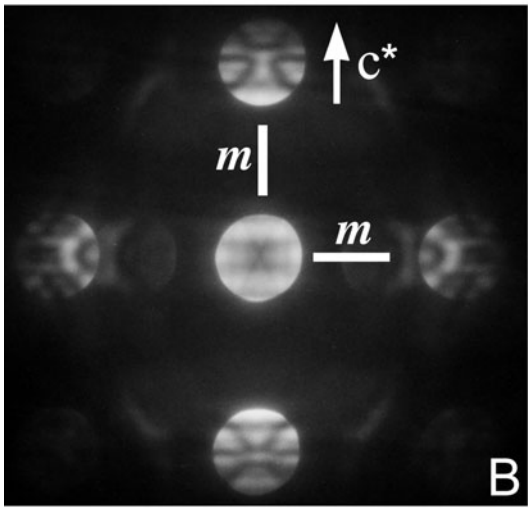

2*mm*

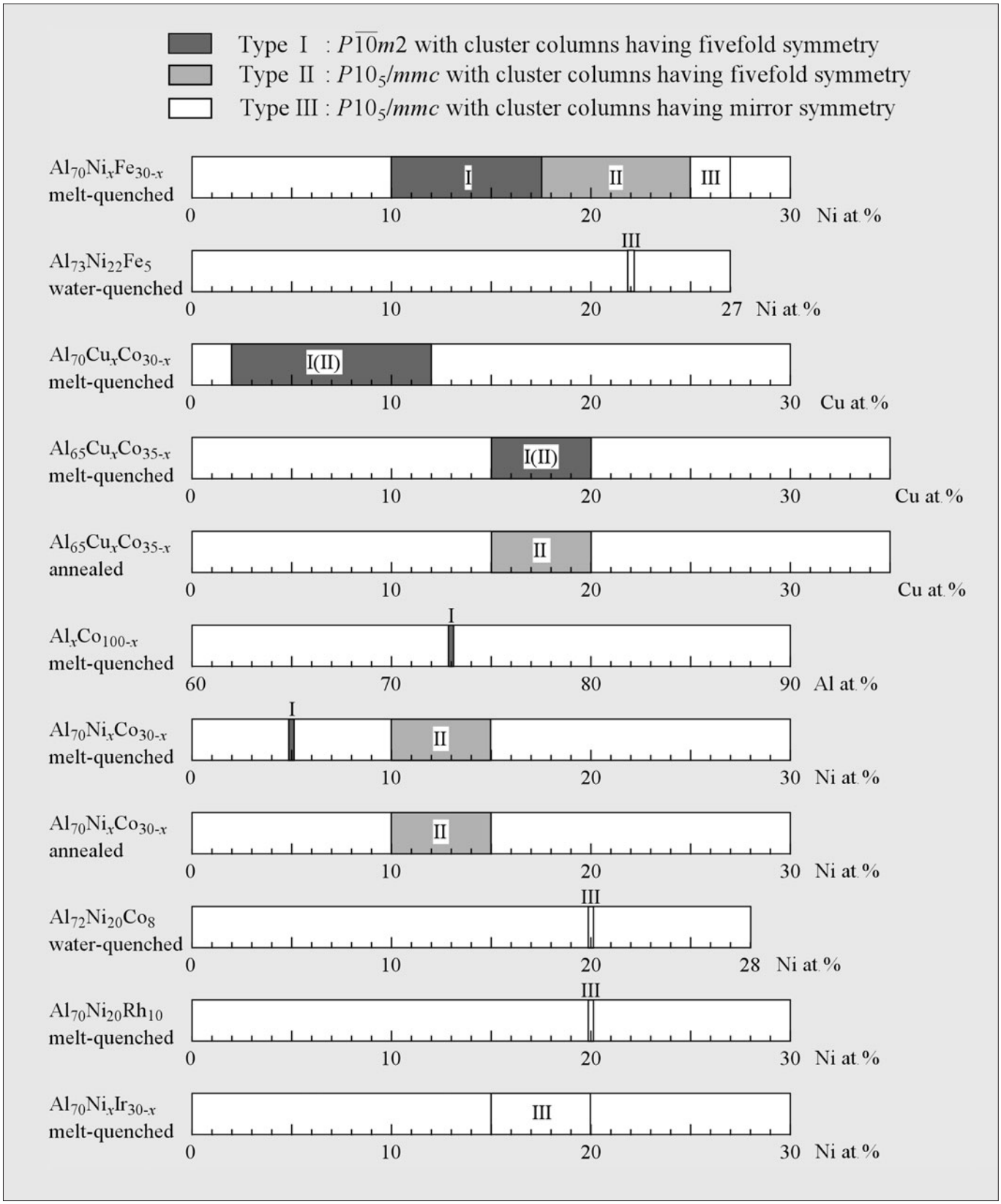

Phase diagrams of aluminum-based alloys, which exhibit decagonal quasicrystalline phases.

HAADF-STEM

The HAADF method provides an atomic resolution image whose intensity is approximately proportional to the square of the atomic number [a]. When the HAADF method is used for an Al-TM (transition metal) alloy, it is expected that the image shows the arrangement of TM atoms selectively. The information on the arrangement of TM atoms gives a breakthrough for revealing the true structure of the decagonal quasicrystals, which has not completely been solved yet. We applied the method to the structural studies of decagonal quasicrystals and their crystalline approximants for the first time and successfully obtained new information about their structures, as shown on the following pages.

The figure shows a schematic diagram of the HAADF-STEM method. The electron beam with accelerating voltages of 100 to 300kV is focused on the specimen and scanned over it. The size of the probe on the specimen, which directly determines the resolution of the image, reached less than 0.2nm by using a field emission gun (FEG). The high-angle scattered electron is collected by an annular dark-field (ADF) detector. The intensities integrated over the detector area are displayed as a function of the probe position. HAADF images were obtained only by using a dedicated scanning transmission electron microscope. Recently, HAADF images can be obtained by an ordinary transmission electron microscope which is equipped with an FEG, a probe scanning unit and an ADF detector.

Reference

[a] S. J. Pennycook and D. E. Jesson: *Ultramicroscopy*, **37** (1991) 14.

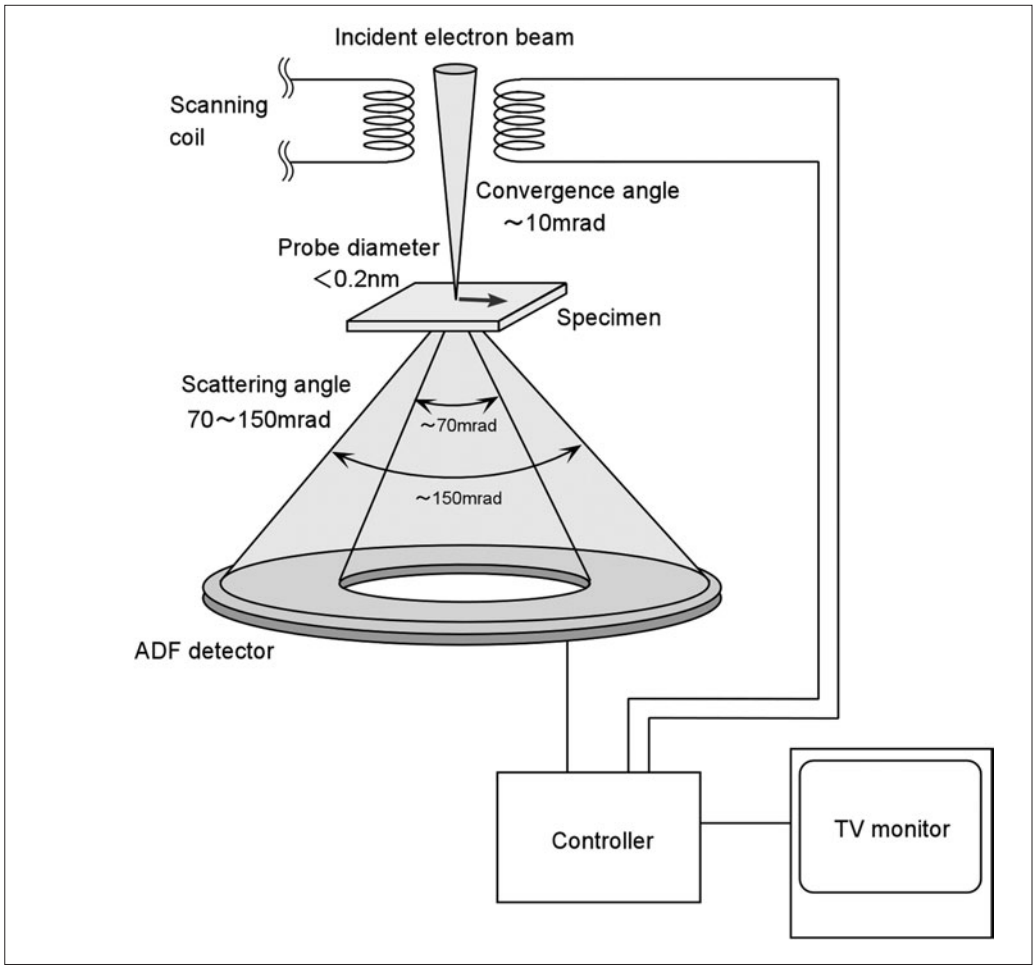

Schematic diagram of HAADF-STEM.

Comparison between the HAADF and HREM methods

Both the HAADF-STEM and HREM methods directly provide atomic arrangements projected in the direction of the incident electron beam. The table shows a comparison between the HAADF-STEM and HREM methods. An HREM image strongly depends on the specimen thickness and defocus amount because of the strong dynamical diffraction effects of low-order reflections and the lens aberration. A true structure image can be obtained only from a very thin specimen under an optimum defocus condition.

On the other hand, the HAADF image is formed mainly by thermal diffuse scattering (TDS) electrons, whose scattering amplitude at a high angle of about 100mrad is approximately proportional to the atomic number Z. The image hardly changes with the specimen thickness because the scattering length of TDS is more than ten times the thickness. It is known that the HAADF intensity is approximately proportional to Z^2. The resolution of the HAADF images is about 0.2nm for 200kV-TEM equipped with a thermal-assisted FEG. A dedicated STEM with a cold-type FEG has a resolution of about 0.1nm [a].

The HAADF method has made it possible to obtain the positions of the constituent transition-metal atoms and symmetries formed by these atoms. The results have reinforced the previous HREM studies on the quasicrystals with $P\bar{1}0m2$ and corrected the widely accepted result obtained by the HREM method. The latter result has opened a new stage of decagonal quasicrystal study [20].

	HAADF	HREM
Intensity	$\sim Z^2$	Electrostatic potential
Spatial resolution	0.2nm	0.17nm (400kV)
Thickness dependence	Weak	Strong
Artifact	None	Present (lens aberration and dynamical diffraction effect)

Comparison between the HAADF and HREM methods.

Reference

[a] P. D. Nellist and S. J. Pennycook: *Inst. Phys. Conf. Ser.*, **161** (1999) 315.

Quasicrystals

$Al_{70}Ni_{15}Fe_{15}$

200kV

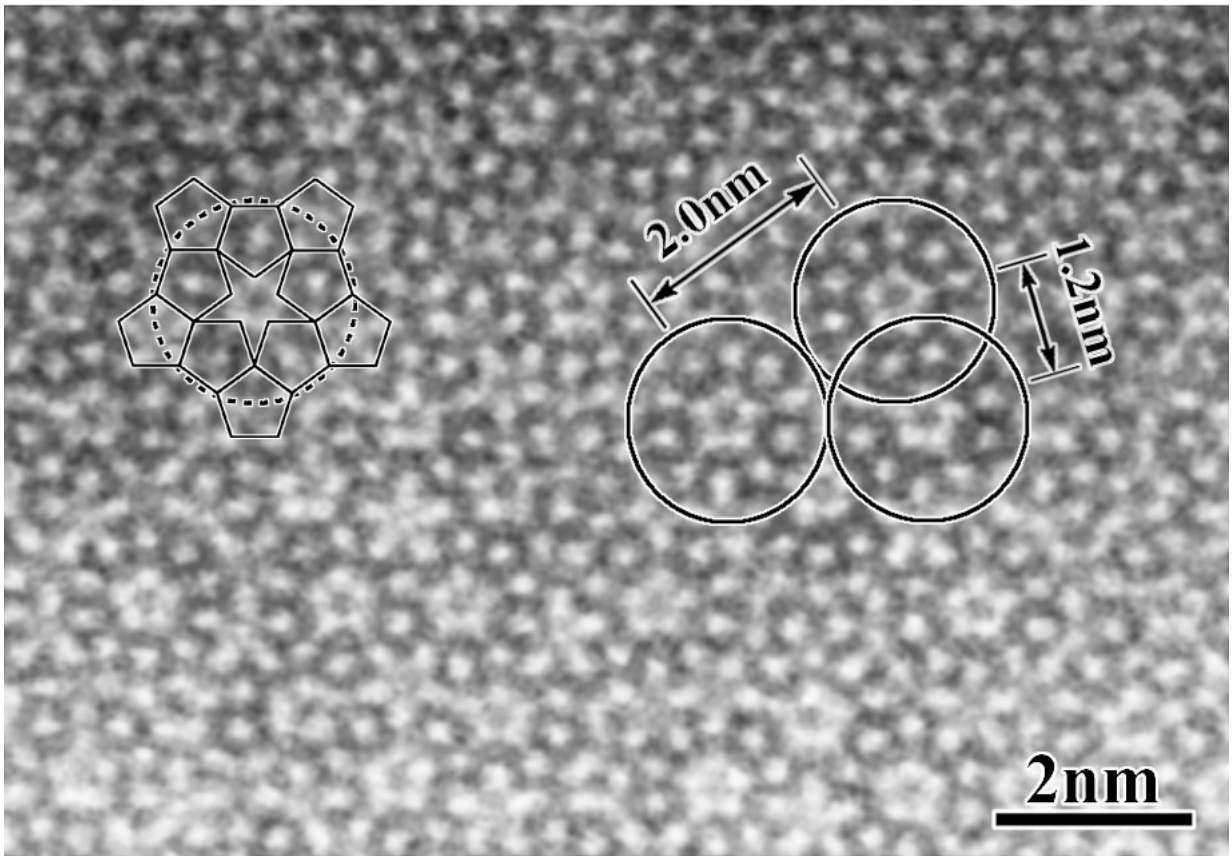

Photograph shows a HAADF image of an $Al_{70}Ni_{15}Fe_{15}$ decagonal quasicrystal taken at an incidence along the decagonal axis [a]. Bright dots correspond to transition-metal (Ni and Fe) atoms. Al atoms are not clearly seen because the intensity from Al is relatively small and the spatial resolution is not high enough. Specific atom-cluster images with a diameter of about 2nm are seen as indicated by the circles. The clusters show fivefold-rotation symmetry due to the bright pentagons around the centers. It should be noted that all the clusters in the image have the pentagons of the same sense of polarity, forming a noncentrosymmetric structure. Two typical intercluster distances of 1.2nm and 2.0nm are seen. The HAADF observation verified the results of HREM and the dark-field microscopy obtained by Tsuda *et al.* [b].

The 2nm atom-cluster is divided into the pentagonal clusters with an edge length of 0.47nm, as seen at the cluster indicated by the dotted circle. The pentagon appears to be similar to that of monoclinic approximants of $Al_{13}Fe_4$ and $Al_{13}Co_4$ (See page 158). Thus, it is considered that the quasicrystal is constructed from the pentagonal clusters, which are close to those of $Al_{13}Fe_4$ and $Al_{13}Co_4$.

References

[a] K. Saitoh, K. Tsuda, M. Tanaka and A. P. Tsai: *Jpn. J. Appl. Phys.*, **38** (1999) L671.

[b] K. Tsuda, M. Saito, M. Terauchi, M. Tanaka, A. P. Tsai, A. Inoue and T. Masumoto: *Jpn. J. Appl. Phys.*, **32** (1993) 129.

Antiphase boundary

Photograph shows a HAADF image of an $Al_{70}Ni_{15}Fe_{15}$ decagonal quasicrystal taken at an incidence perpendicular to the decagonal axis. Two kinds of bright dot arrays A and B are arranged alternately. The dashed line at the center indicates an antiphase-domain boundary. The arrays are shifted at the boundary by a half period in the direction of the decagonal axis. A schematic diagram of the domain structure of $Al_{70}Ni_{15}Fe_{15}$ is shown below. It is the first HAADF observation of the antiphase domains of the quasicrystal.

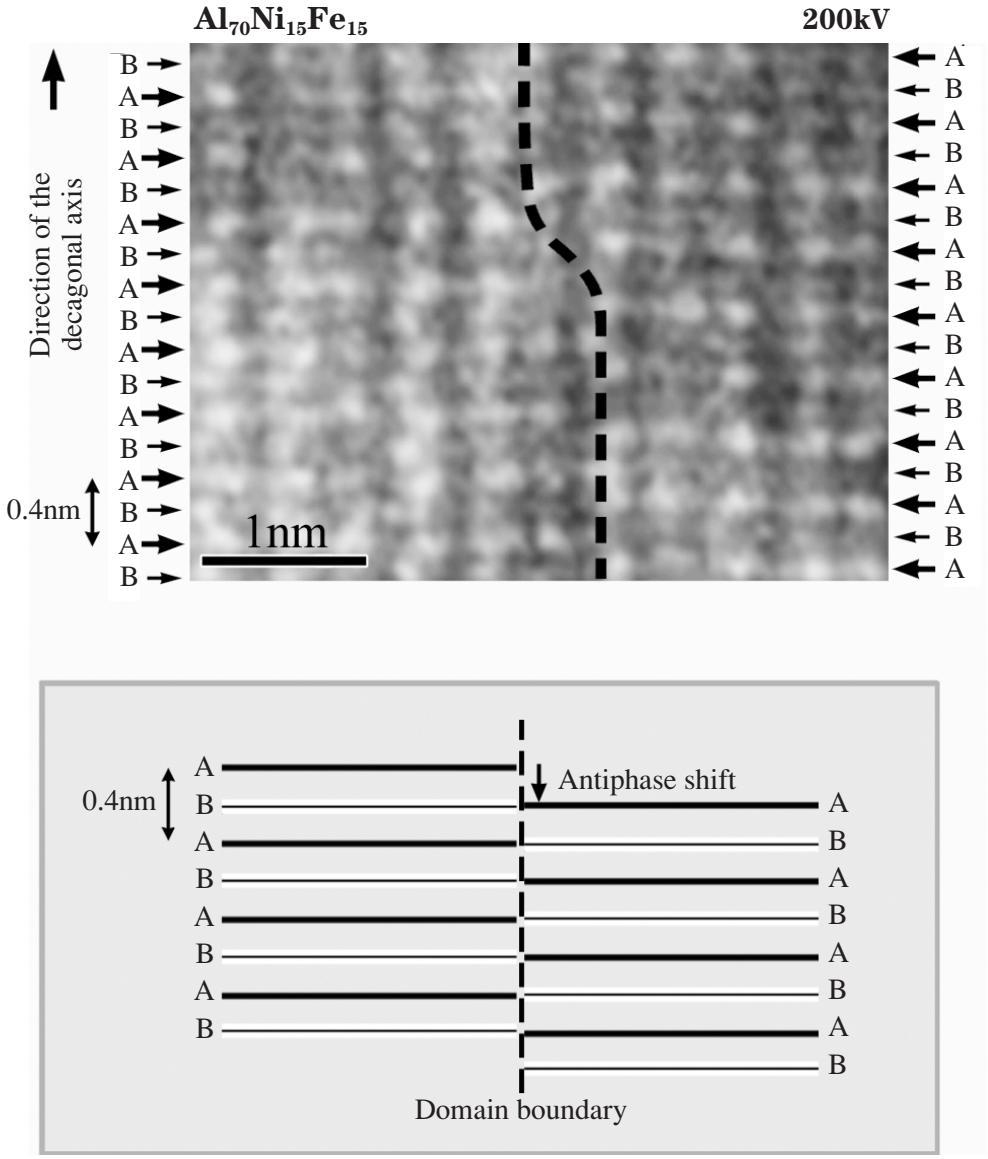

$Al_{72}Ni_{20}Co_8$

200kV

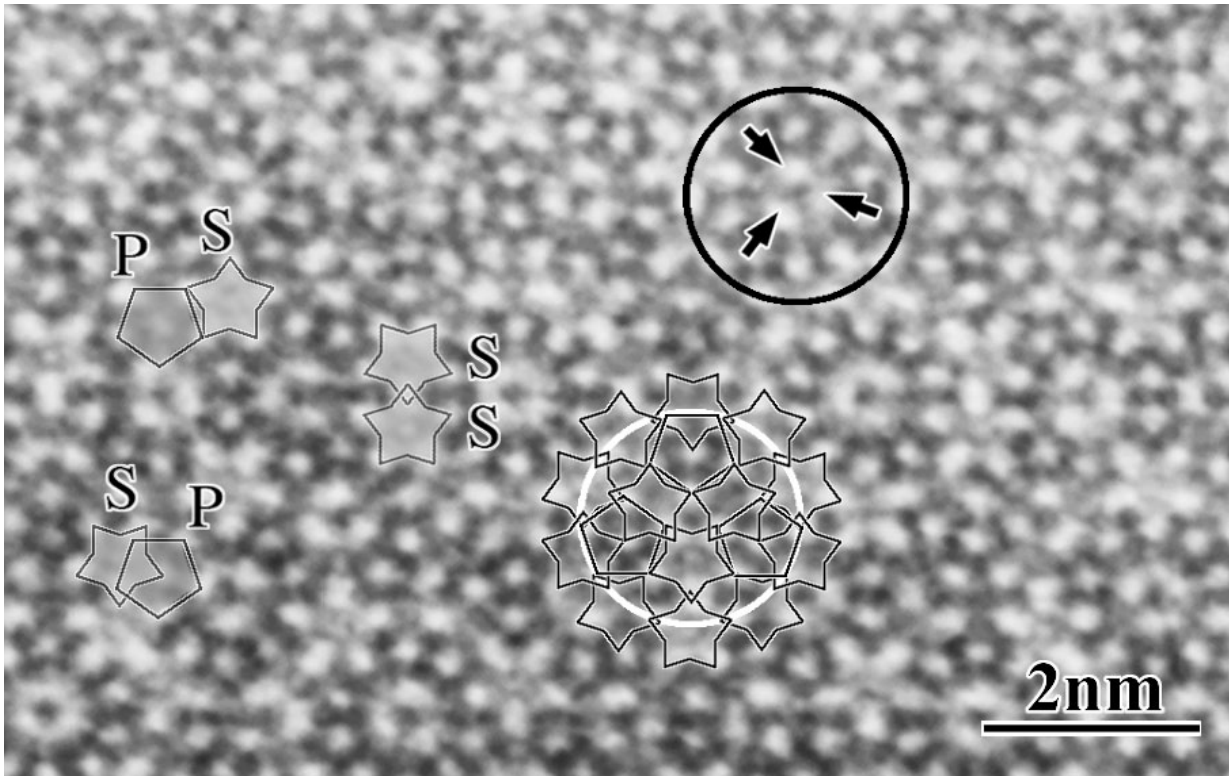

Photograph shows a HAADF image of an $Al_{72}Ni_{20}Co_8$ decagonal quasicrystal taken at an incidence along the decagonal axis [20]. The bright dots correspond to transition-metal (Ni and Co) atoms. The 2nm cluster column indicated by a black circle has three bright dots at the center. This implies that the 2nm cluster column has no decagonal symmetry but only mirror symmetry. The result overthrew what had been believed by the quasicrystal researchers, "the basis or the 2nm diameter cluster of high-quality decagonal quasicrystals with space group $P10_5/mmc$ is of tenfold symmetry".

The 2nm cluster column is divided into more basic cluster columns P and S, which are shown by the pentagons and stars, respectively in the photograph. Structural models of cluster columns P and S are constructed on the basis of the three types of the pentagonal atom clusters of a monoclinic approximant of $Al_{13}Fe_4$ and the HAADF image obtained, as shown in the right figures.

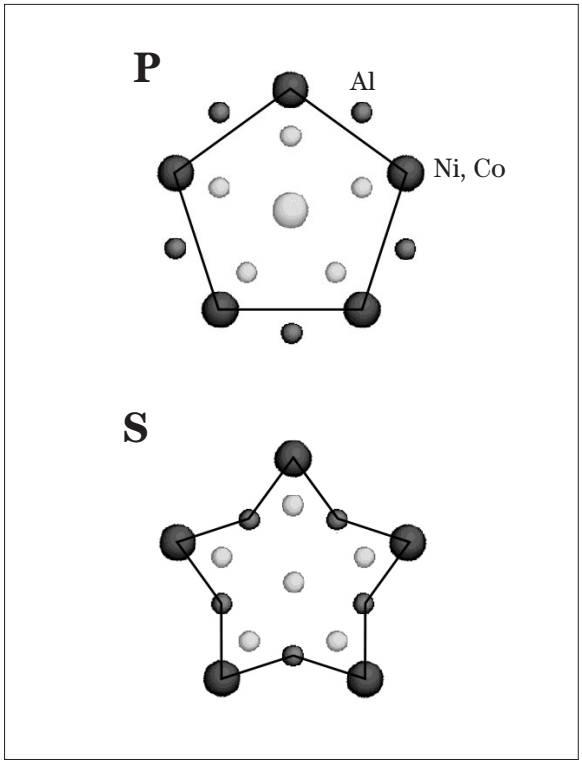

Lattice formed by the cluster columns

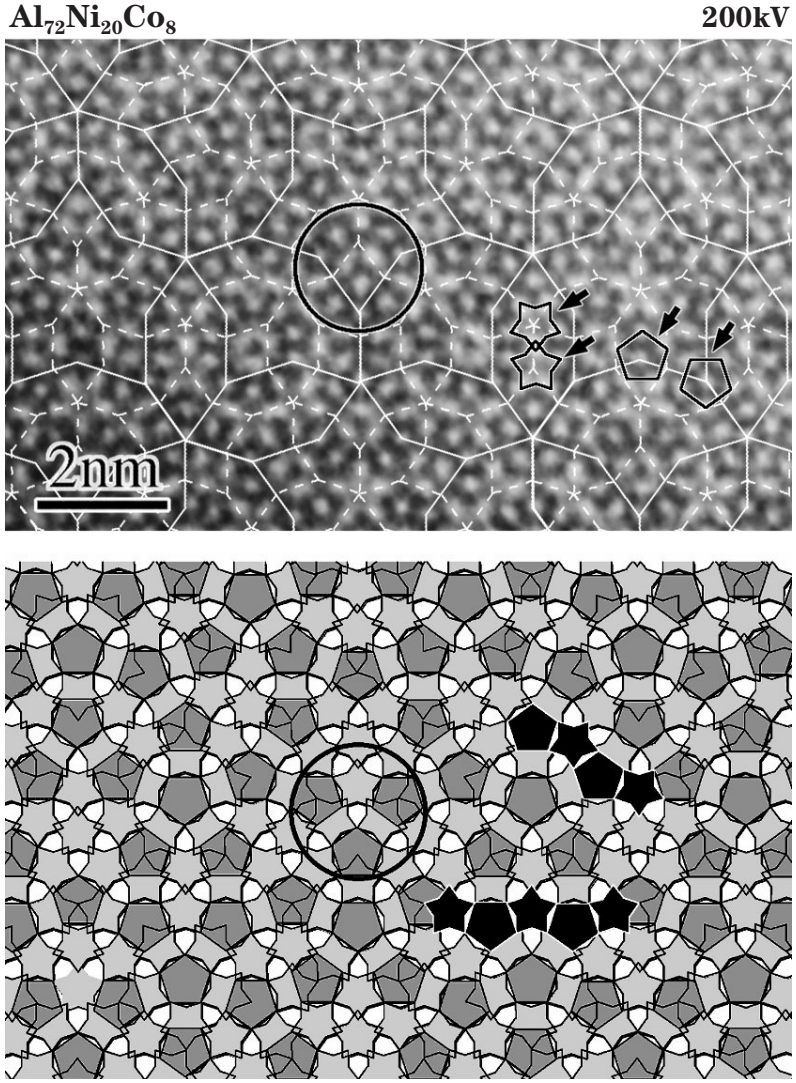

The upper photograph shows a HAADF image of $Al_{72}Ni_{20}Co_8$, where the Penrose lattice is superposed on the image with the white lines. The solid lines indicate a sublattice of the rhombic Penrose-lattice [a], and the dashed lines indicate the complementary sublattice to that of the solid lines. The lattice of the solid lines are τ times as large as those with the dashed lattice. Both the lattices are filled by star, crown and flattened hexagonal tiles. It is seen that the cluster columns P and S are located on the vertices of the solid and dashed lattices, respectively.

The linkage of cluster columns P and S is shown schematically by black pentagons and stars in the lower figure, which is similar, in a short range, to that of the $Al_{13}Fe_4$ approximant.

The tiling of the rhombic Penrose-lattice extends over an area with a diameter more than 50nm. This good quasicrystalline order is confirmed by the fact that reflections with lattice spacings up to about 4nm are observed in electron diffraction patterns.

Reference

[a] R. Penrose: *Bull. Inst. Math Appl.*, **10** (1974) 266.

Approximants

$Al_{13}Co_4$ and $Al_{13}Fe_4$ monoclinic approximants

It is known that many quasicrystals are accompanied by related crystalline phases, which have very close chemical compositions and densities, and display similar diffraction patterns. The related crystalline phases are called "approximants". It is believed that a quasicrystal and its approximant have similar atom-clusters but different arrangements of the clusters, that is, the arrangements in quasicrystals and in approximants are quasiperiodic and periodic, respectively. Structure analysis of the approximant, therefore, plays an important role in revealing and understanding the quasicrystalline structures. Monoclinic $Al_{13}Co_4$ and $Al_{13}Fe_4$ are the most basic approximants of the Al-TM (TM: transition metal) decagonal quasicrystals. It has been considered that they have an isomorphous structure. Structure analyses of $Al_{13}Co_4$ and $Al_{13}Fe_4$ were performed with the assumptions of the space groups of Cm and $C2/m$, respectively [a], [b], [c]. The space group of $Al_{13}Co_4$ was examined by the CBED method [d].

$C2/m$

Photographs show SAD patterns of monoclinic $Al_{13}Co_4$ taken with $[0\bar{1}0]$ and [100] incidences. The $h0l$ reflections with h = odd are absent at the positions indicated by the arrows. The lattice type is determined to be C-centered. Photographs on the right-side page show CBED patterns of monoclinic $Al_{13}Co_4$ taken with $[0\bar{1}0]$ and [100] incidences. The $[0\bar{1}0]$ CBED pattern shows 2-fold-rotation symmetry. Thus, possible point groups are limited to 2 or $2/m$. The [100] CBED pattern shows mirror symmetry perpendicular to the b^*-direction. Thus, the point group of monoclinic $Al_{13}Co_4$ is determined to be $2/m$. Dynamical extinction lines are not seen in the [100] CBED pattern. Thus, the space group is determined to be $C2/m$. It was revealed that $Al_{13}Co_4$ does not belong to Cm but to the same space group as $Al_{13}Fe_4$.

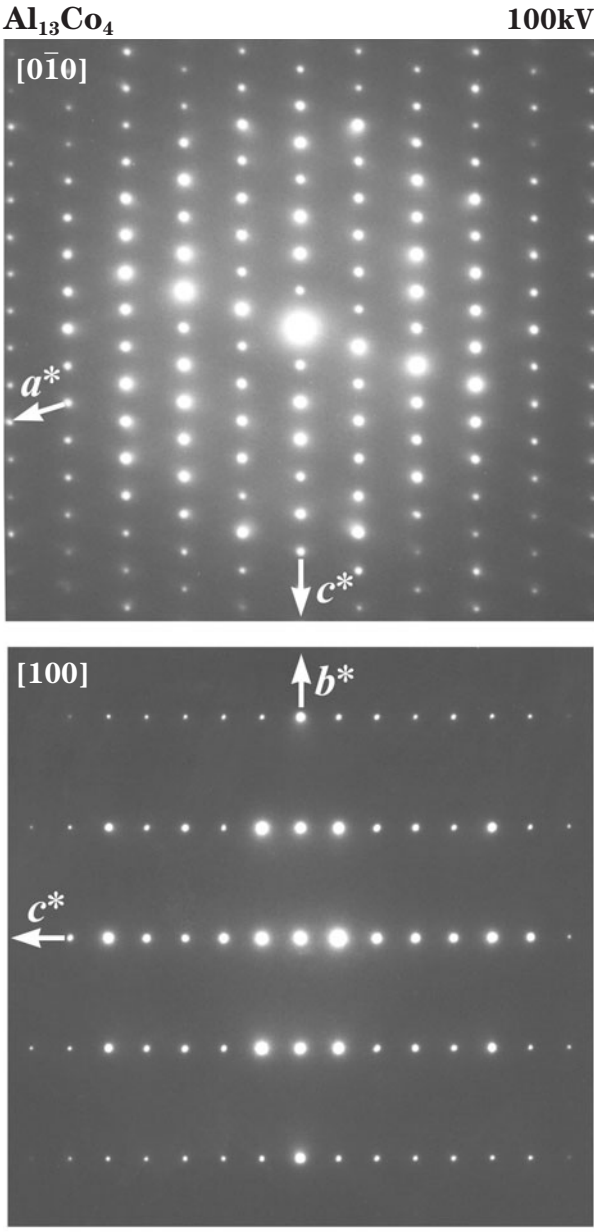

References

[a] R. C. Hudd and W. H. Taylor: *Acta Cryst.*, **15** (1962) 441.

[b] P. J. Black: *Acta Cryst.*, **8** (1955) 43.

[c] P. J. Black: *Acta Cryst.*, **8** (1955) 175.

[d] T. Yokosawa, K. Saitoh, M. Tanaka and A. P. Tsai: *J. Phys. Soc. Jpn.*, **69** (2000) 1586.

$Al_{13}Co_4$ **100kV**

[$0\bar{1}0$]

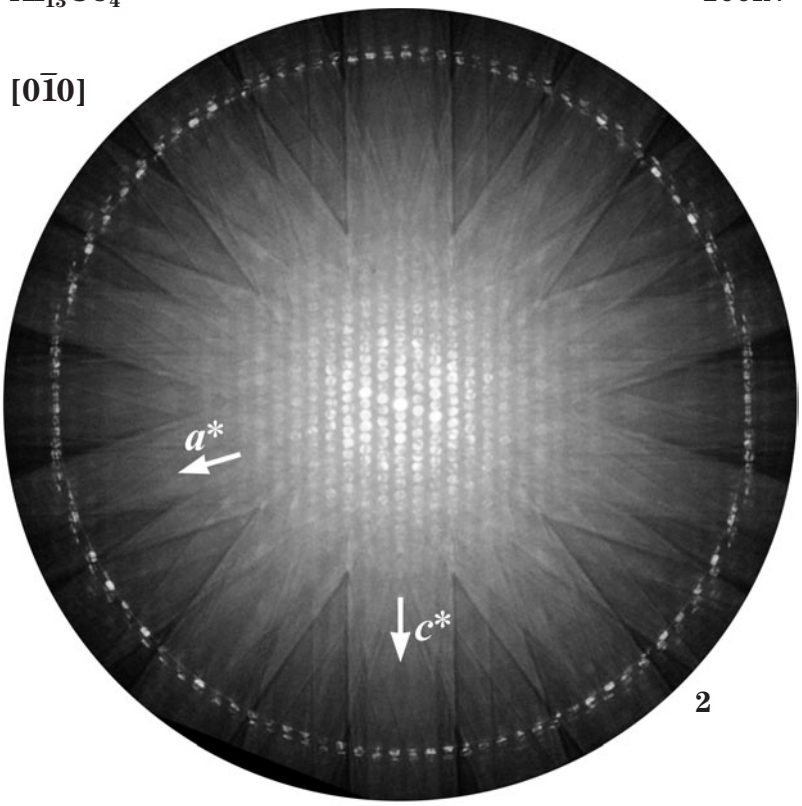

2

[100]

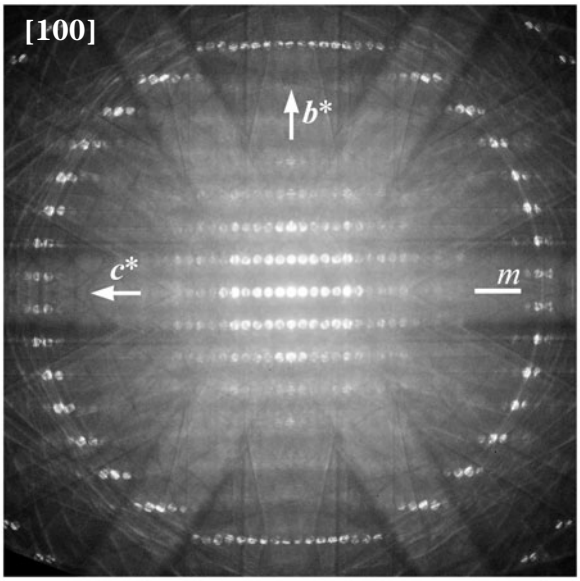

m

$Al_{13}Fe_4$ **200kV**

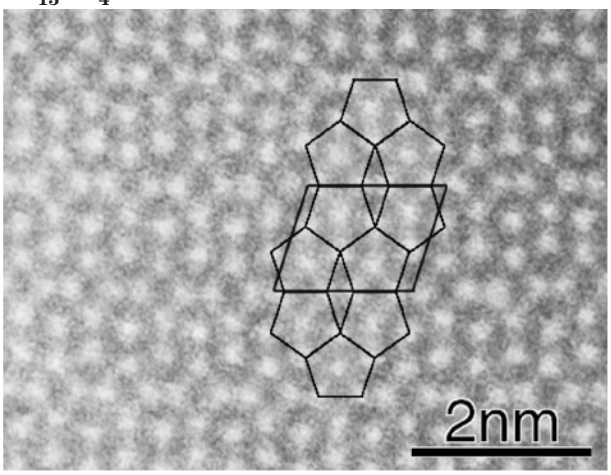

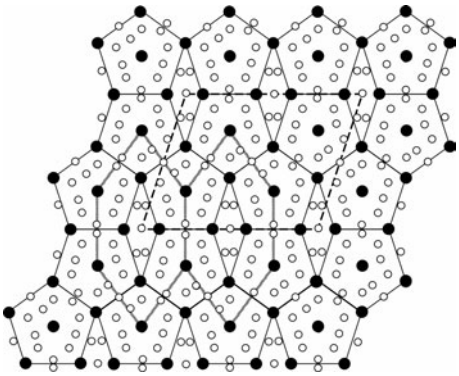

The photograph shows a HAADF image of monoclinic $Al_{13}Fe_4$ taken at an incidence along the *b*-axis, in place of that of $Al_{13}Co_4$ because of image quality. The bright spots correspond to Fe atoms. Al atoms are not clearly seen because the intensity from Al is relatively low and the spatial resolution is not high enough. A pentagon formed by six Fe atom columns, one at the center and five at the vertices of the pentagon, is seen as indicated by the black lines. The neighboring pentagons have an opposite sense of polarity to each other and share two Fe atoms or an edge of the pentagon. The unit cell indicated by the parallelogram contains the four pentagons.

The figure shows the atomic arrangement of $Al_{13}Fe_4$ projected along the *b*-axis, where the atom positions determined by Black were used [a]. The black and white circles show Fe and Al atoms, respectively. It is seen that the HAADF image displays Fe atoms selectively.

Reference

[a] P. J. Black: *Acta Cryst.*, **8** (1955) 43.

τ^2-inflated $Al_{13}Co_4$ monoclinic approximant

The family of monoclinic approximants whose lattice parameters a and c are τ^n (n=2, 3, 4) times as large as those of monoclinic $Al_{13}Co_4$ were found by Ma *et al.* in the Al-Co alloy system [a]. They found on the basis of HREM observation that the τ^n-inflated approximants have pentagonal atom-clusters inflated by τ^n-times as large as the TM-pentagon with a 0.47nm edge length of monoclinic $Al_{13}Co_4$. The unit cells of all the inflated phases are composed of four inflated pentagonal clusters, which are arranged in the same manner as the pentagonal clusters of monoclinic $Al_{13}Co_4$. Atom-cluster columns with a 2nm diameter were not observed in their HREM images because the defocus amount might not be optimum. The structure of τ^2-$Al_{13}Co_4$ has not been solved yet.

The photographs on this page show SAD patterns of τ^2-inflated $Al_{13}Co_4$ taken at incidences along [010] and [100] axes. The [010] pattern shows the $h0l$ (h=odd) reflection spots, which are forbidden for the C-centered monoclinic lattice, as indicated by arrows. Thus, the alloy is identified to have a primitive lattice. However, since the reflection spots specific to the primitive lattice are weak, the deviation from the C-centered structure is small. The [100] pattern shows reflection spots at a height of 1/0.8nm^{-1} in the b^*-direction. Thus, the periodicity along the b-axis is the same as that of monoclinic $Al_{13}Co_4$, implying that τ^2-$Al_{13}Co_4$ has the same layer structure as that of monoclinic $Al_{13}Co_4$.

The photographs on page 160 show CBED patterns of τ^2-$Al_{13}Co_4$ taken at the same incidences as those of the SAD patterns. In the [010] CBED pattern, the arrowheads of the same shapes show a pair of first-order Laue-zone reflection disks which are related with 2-fold-rotation operation. From the examination of the symmetry of the reflections, it is confirmed that the pattern shows 2-fold-rotation symmetry. Thus, possible point groups are limited to 2 and 2/m because the alloy belongs to the monoclinic system. The [100] CBED pattern shows mirror symmetry perpendicular to the b^*-axis. Thus, the point group is determined to be 2/m. No dynamical extinction lines are observed in the CBED patterns. Therefore, the space group is determined to be $P2/m$ [b].

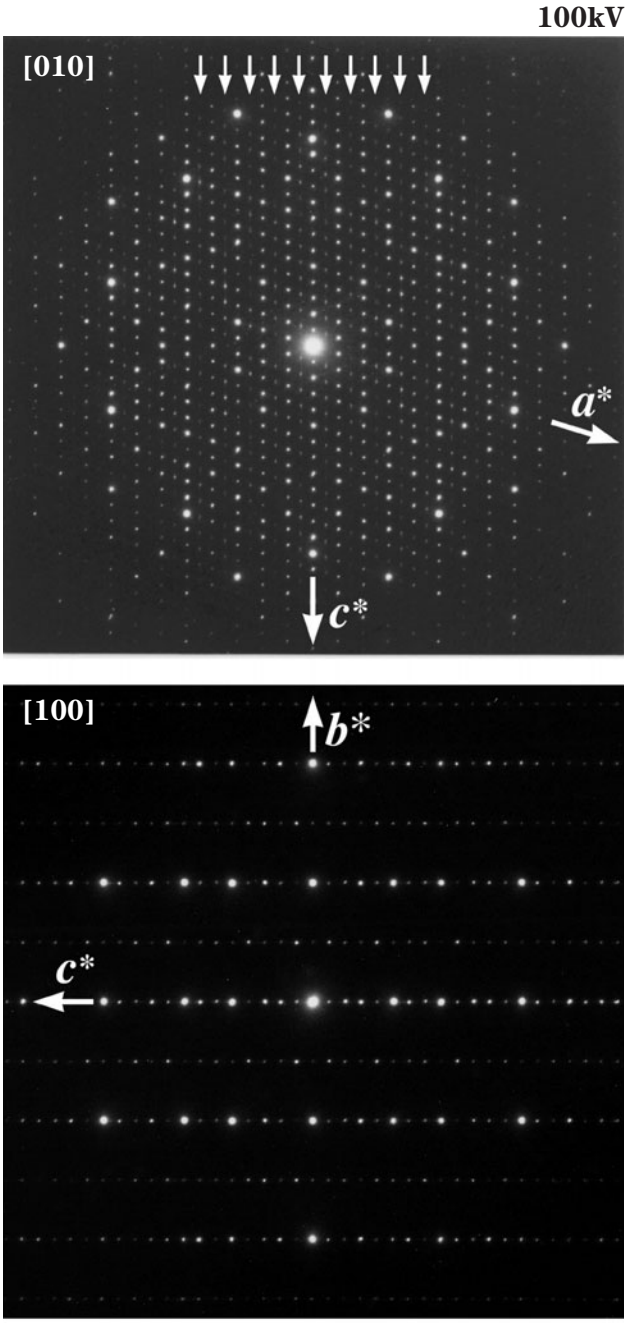

References

[a] X. L. Ma, X. Z. Li and K. H. Kuo: *Acta Cryst.*, **B51** (1995) 36.

[b] K. Saitoh, T. Yokosawa, M. Tanaka and A. P. Tsai: *J. Electron Microsc.*, **48** (1999) 105.

τ^2-$Al_{13}Co_4$ 100kV

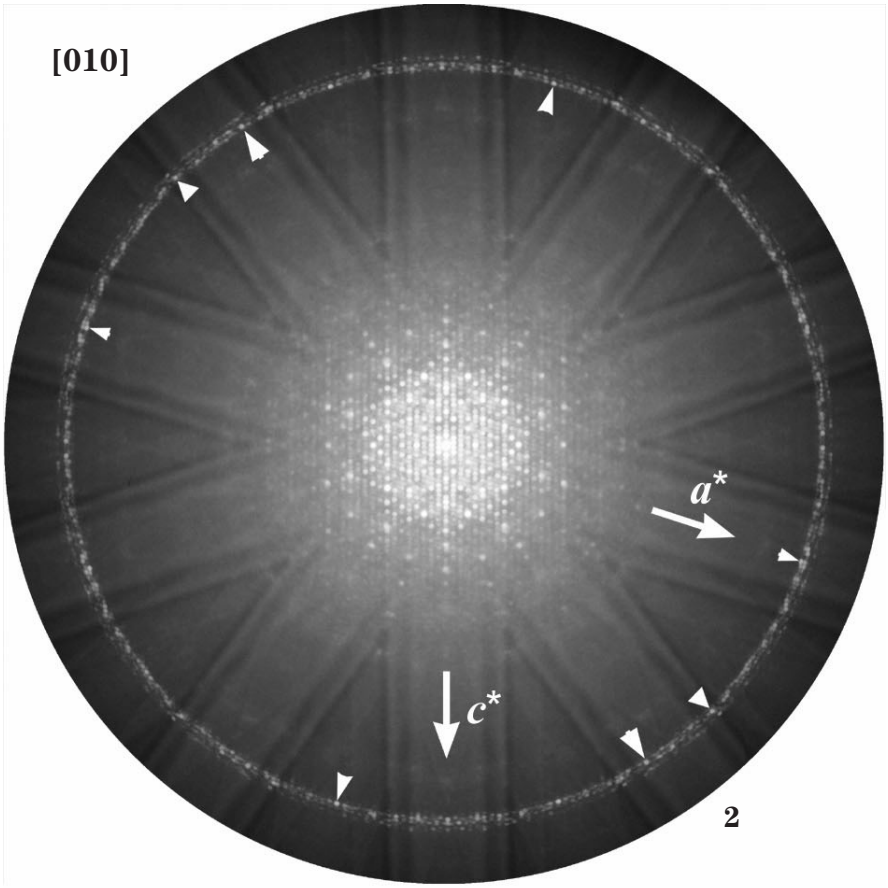

2

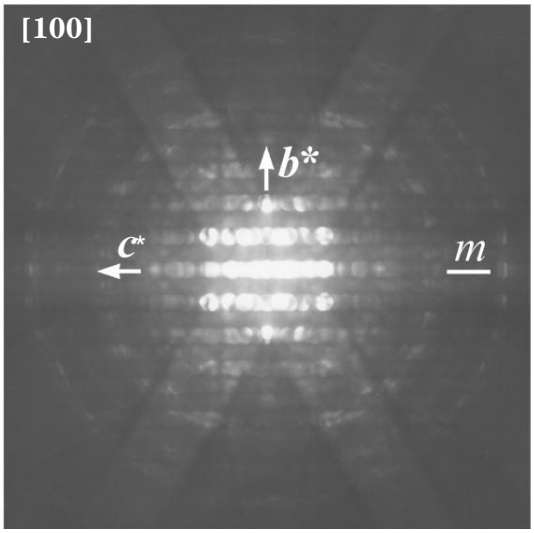

m

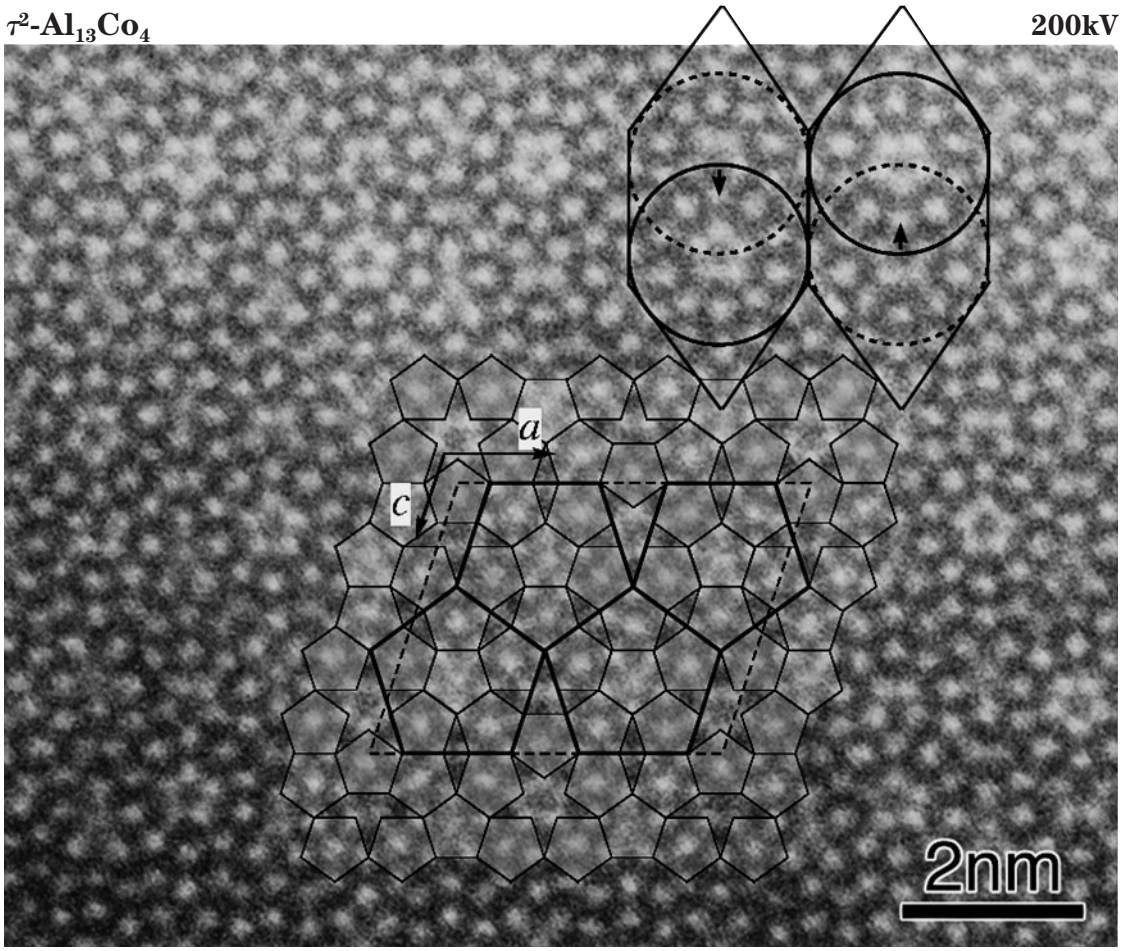

Photograph shows a HAADF image of monoclinic τ^2-inflated $Al_{13}Co_4$ taken at an incidence along the *b*-axis, where the bright dots correspond to Co atoms. The TM-pentagon clusters similar to those of $Al_{13}Fe_4$ are clearly seen as indicated by the thin lines. Similarly to the case of $Al_{13}Fe_4$, the neighboring TM-pentagons share two Co atoms. The six TM-pentagons form a τ^2-inflated pentagon indicated by the thick lines. The unit cell indicated by the dashed parallelogram contains the four inflated pentagons.

A specific fivefold-symmetry atom-cluster with a 2nm diameter is seen as indicated by the black circle. The cluster is composed of a dark dot at the center, five bright dots around the center, a dark ring surrounding the dots, ten bright dots around the ring and a dark ring surrounding the ten dots. This feature is quite similar to that of the fivefold-symmetry cluster column with a 2nm diameter of $Al_{70}Ni_{15}Fe_{15}$. Thus, it is considered that the 2nm fivefold-symmetry clusters of the quasicrystals already appear in the approximant.

Another type of a 2nm cluster, which has almost the same configuration as the fivefold-symmetry cluster, is seen as indicated by the dashed circle. We call the cluster the pseudo-fivefold-symmetry cluster hereafter. In the pseudo-fivefold-symmetry cluster, one of the five bright dots around the center is slightly shifted toward the overlapping fivefold-symmetry cluster as indicated by the arrows. The shifted bright dots take a regular position of the overlapping fivefold-symmetry cluster. The two types of the 2nm clusters are overlapped with an intercluster distance of 1nm in the direction perpendicular to the *c*-plane. The fivefold-symmetry cluster and pseudo-fivefold-symmetry cluster appear alternately in the *a*-direction. The former cluster contacts the latter with two bright dots shared. As a result, the intercluster distance is 2nm. The sense of the bright pentagon at the center of each 2nm cluster is the same in all the clusters lined up in the *a*-direction.

Stacking Sequence of Atom Clusters

All the decagonal quasicrystals we show in this chapter are considered to be formed by the atom clusters based on the three types of the atom clusters of the $Al_{13}Co_4$ ($Al_{13}Fe_4$) approximant, or atom clusters A, B and C as shown in the top figure. The transition metal (TM) positions in clusters A and B form almost regular pentagons (solid lines). On the other hand, the Al positions in clusters A, B and C are displaced from a regular pentagon (dashed lines). We assume that pentagonal clusters in the quasicrystals have regular pentagonal symmetry for high symmetry of the quasicrystalline structures. The modified clusters A', B' and C' are shown in the middle figure, where all the clusters have perfect pentagonal symmetry. On the right-side page, the stacking sequences of atom clusters in the two types of decagonal quasicrystals are drawn schematically and compared with those of the approximant phases.

The approximant phases of $Al_{13}Co_4$, $Al_{13}Fe_4$ and τ^2-$Al_{13}Co_4$ have one type of a pentagonal atom-cluster column with an edge length of 0.47nm as seen in the HAADF images, and have a periodicity of approximately 0.8nm in the *b*-axis or the pseudo-decagonal axis as seen in the diffraction pattern on the right-side page. The atom cluster column has a stacking sequence of ACBC... with an interval of approximately 0.2nm.

On the other hand, $Al_{72}Ni_{20}Co_8$ has the two types of the atom-cluster columns, or the pentagonal (P) and star-shaped (S) atom-cluster columns with an edge length of 0.47nm as seen in the HAADF image. The periodicity along the decagonal axis is approximately 0.4nm as seen in the diffraction pattern on the right-side page. It is considered that atom-cluster columns P and S are constructed by the basic clusters A', B' and C' with stacking sequences of A'C'A'C'... and B'C'B'C'..., respectively, at an interval of approximately 0.2nm. It should, however, be noted that the central atoms in model clusters P and S (in the bottom figure) are modified on the basis of the HAADF images from those constructed by simple combinations of clusters A', B' and C'.

A decagonal quasicrystal of $Al_{70}Ni_{15}Fe_{15}$ has the pentagonal atom-cluster columns with an edge length of 0.47nm as seen in the HAADF image. The periodicity along the decagonal axis is approximately 0.4nm. We consider that the atom clusters with an edge length of 0.47nm stack with a sequence of XC'XC'... at an interval of approximately 0.2nm, where X takes A' or B' randomly. It should be noted that the diffuse streaks perpendicular to the decagonal axis are always seen at heights corresponding to a spacing of 0.8nm in the diffraction pattern on the right-side page, whereas $Al_{72}Ni_{20}Co_8$ exhibits no diffuse streaks. The diffuse scattering can be explained by a random distribution of small volumes of the ordered structure of a 0.8nm periodicity with a stacking sequence of A'C'B'C'... .

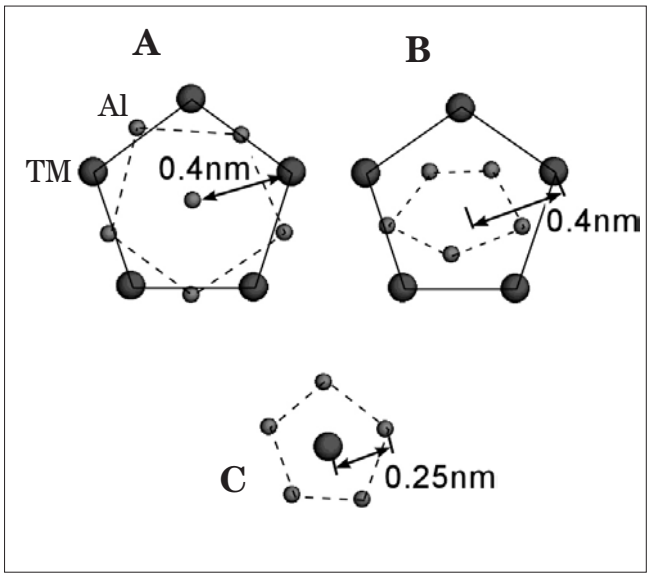

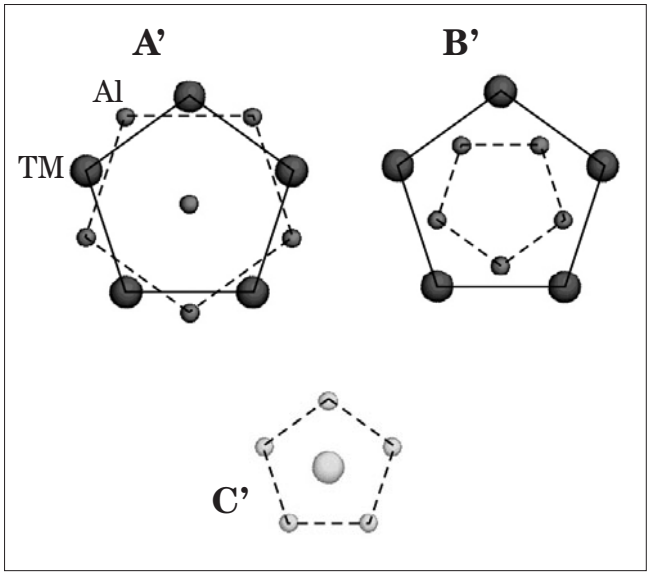

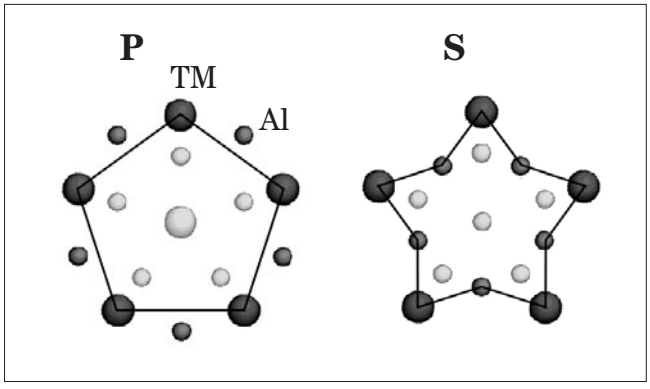

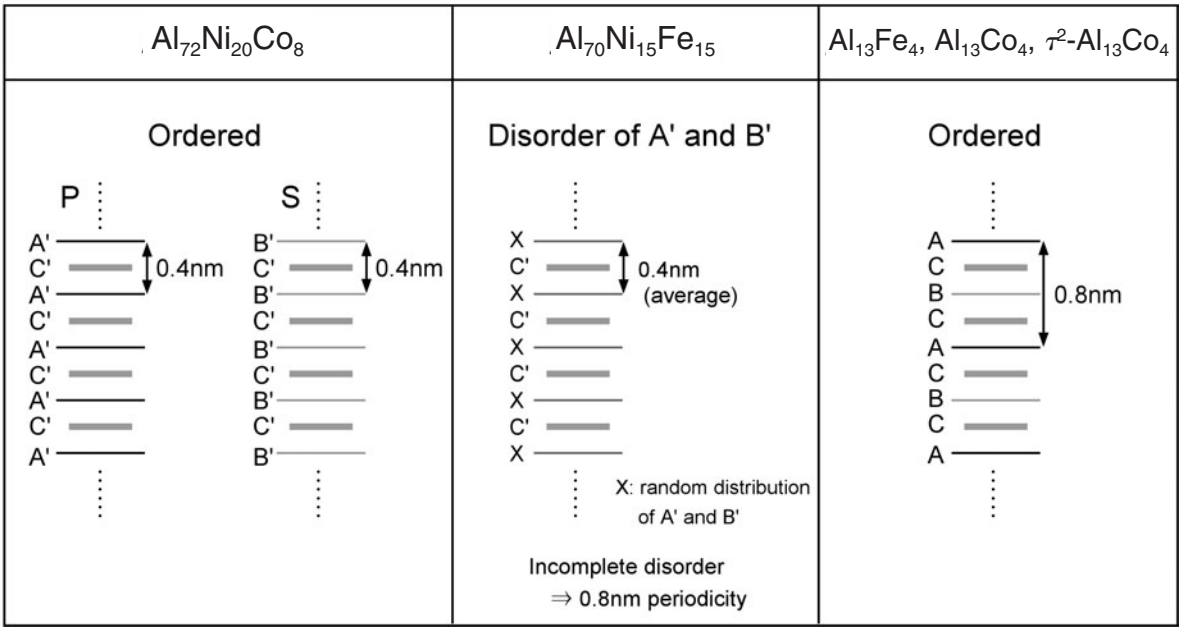

Schematic drawings of stacking sequences of atom clusters in decagonal quasicrystals of $Al_{72}Ni_{20}Co_8$ and $Al_{70}Ni_{15}Fe_{15}$ and monoclinic approximants of $Al_{13}Fe_4$, $Al_{13}Co_4$ and τ^2-$Al_{13}Co_4$

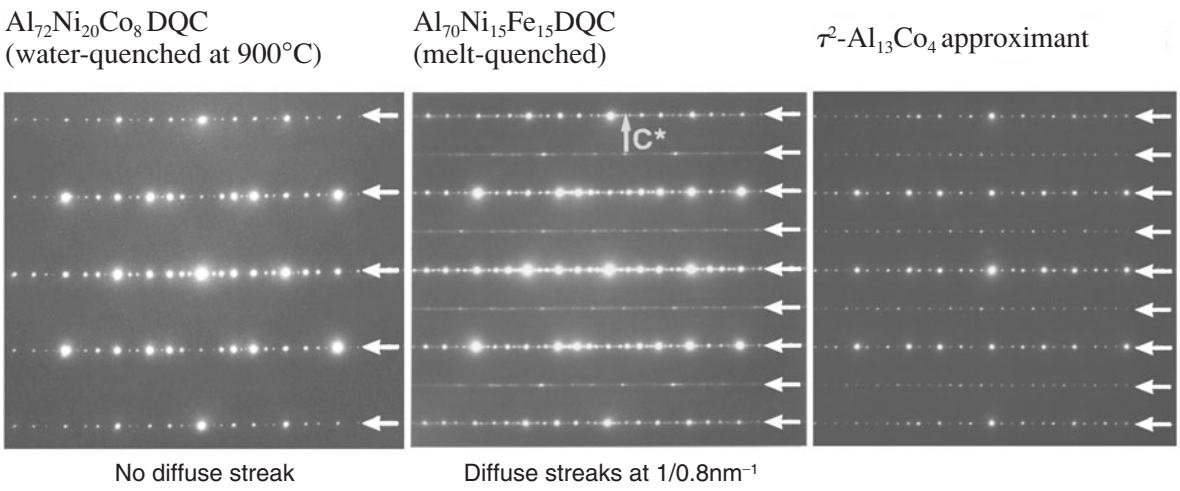

Selected-area diffraction patterns of decagonal quasicrystals of $Al_{72}Ni_{20}Co_8$ and $Al_{70}Ni_{15}Fe_{15}$ and a monoclinic approximant of τ^2-inflated $Al_{13}Co_4$.

Formation of a Decagonal Quasicrystal from an Approximant

We have investigated how the quasicrystal is formed from its approximant. We observed HREM images of an $Al_{73}Co_{27}$ alloy, which contained both approximant and quasicrystalline grains intermixing together.

The upper photograph on the right-side page shows an HREM image of a melt-quenched $Al_{73}Co_{27}$ decagonal quasicrystal taken at an incidence along the decagonal axis. The circles indicate 2nm diameter atom-cluster columns projected along the decagonal axis. The column has fivefold-rotation symmetry due to the dark pentagon at the center. The senses of the pentagons of all the columns are the same. The intercolumnner distances are 1.2nm and 2.0nm. The bonds between the columns take five orientations, each separated by $72\times n$ degrees. Star- and crown-shaped arrangements of the columns are seen, which are characteristic of the decagonal quasicrystal.

The lower photograph on the right-side page shows an HREM image of the monoclinic τ^2-$Al_{13}Co_4$ approximant. The solid and dashed circles indicate the fivefold-symmetry columns and the pseudo-fivefold-symmetry columns, respectively. These two columns are connected with an intercolumnar distance of 1.0nm. We assume an elongated hexagonal tile, which contains a column pair with a 1nm distance, as indicated by the white lines. The unit cell of τ^2-$Al_{13}Co_4$ is shown by the dotted line, which contains four elongated hexagonal tiles. It should be noted that the orientation of the hexagonal tiles or of the bond between the fivefold-symmetry columns and pseudo-fivefold-symmetry columns is of mono-sense.

Al-Co alloys form crystalline approximant phases and quasicrystalline phases by slow solidification and rapid quenching, respectively. Thus, a coexisting state of an approximant and a quasicrystal is expected to be formed by cooling at an appropriate speed. We found specimen areas which contain both the decagonal and the τ^2-$Al_{13}Co_4$ phases. The photograph on page 166 shows an HREM image of such an area of the alloy. The image shows the 1nm column pairs, which was already shown in the lower photograph on the right-side page. The tiling of the elongated hexagons is drawn with the white lines. On the left side of the image, the hexagonal tiles take the mono-orientational arrangement of the τ^2-$Al_{13}Co_4$ approximant. On the right side, the mono-orientational arrangement of the tiles breaks down, but the hexagonal tiles with five different orientations are seen to intermix by sharing their edges with other tiles. It is important to understand the formation of a quasicrystal to see how the star(S)- and crown(C)-shaped arrangements are formed in the $Al_{73}Co_{27}$ alloy.

Furthermore, we found a new approximant in the $Al_{73}Co_{27}$ alloy consisting of the Penrose's skinny- and fat-rhombus tiles, which are characteristic arrangements of quasicrystals. Thus, it can be said that this approximant is closer to a quasicrystal than monoclinic τ^2-$Al_{13}Co_4$. The new approximant contains rocket- and butterfly-shaped arrangements, which are composed of three and four 1nm column pairs, respectively. We found that the skinny- and fat-rhombus tiles are also constructed from the 1nm column pairs as well as the star-, crown-, rocket- and butterfly-shaped tiles. Therefore, solving the structure of the 1nm column pair is an important key to revealing the true structure of the quasicrystal.

$Al_{73}Co_{27}$

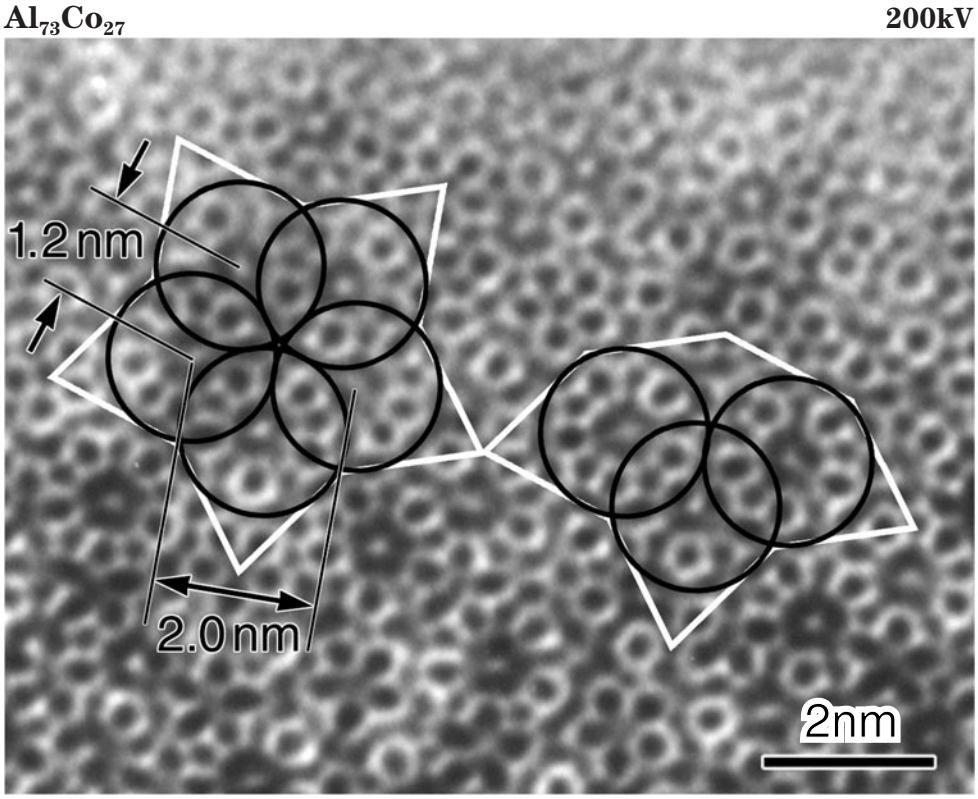
Al73Co27
200kV
1.2 nm
2.0 nm
2nm

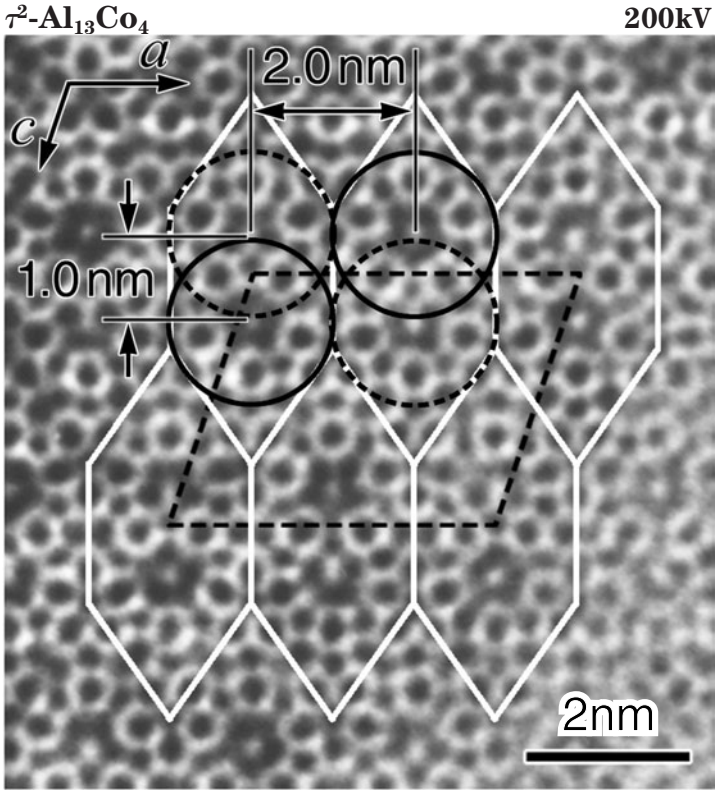
τ2-Al13Co4
200kV
a
c
2.0 nm
1.0 nm
2nm

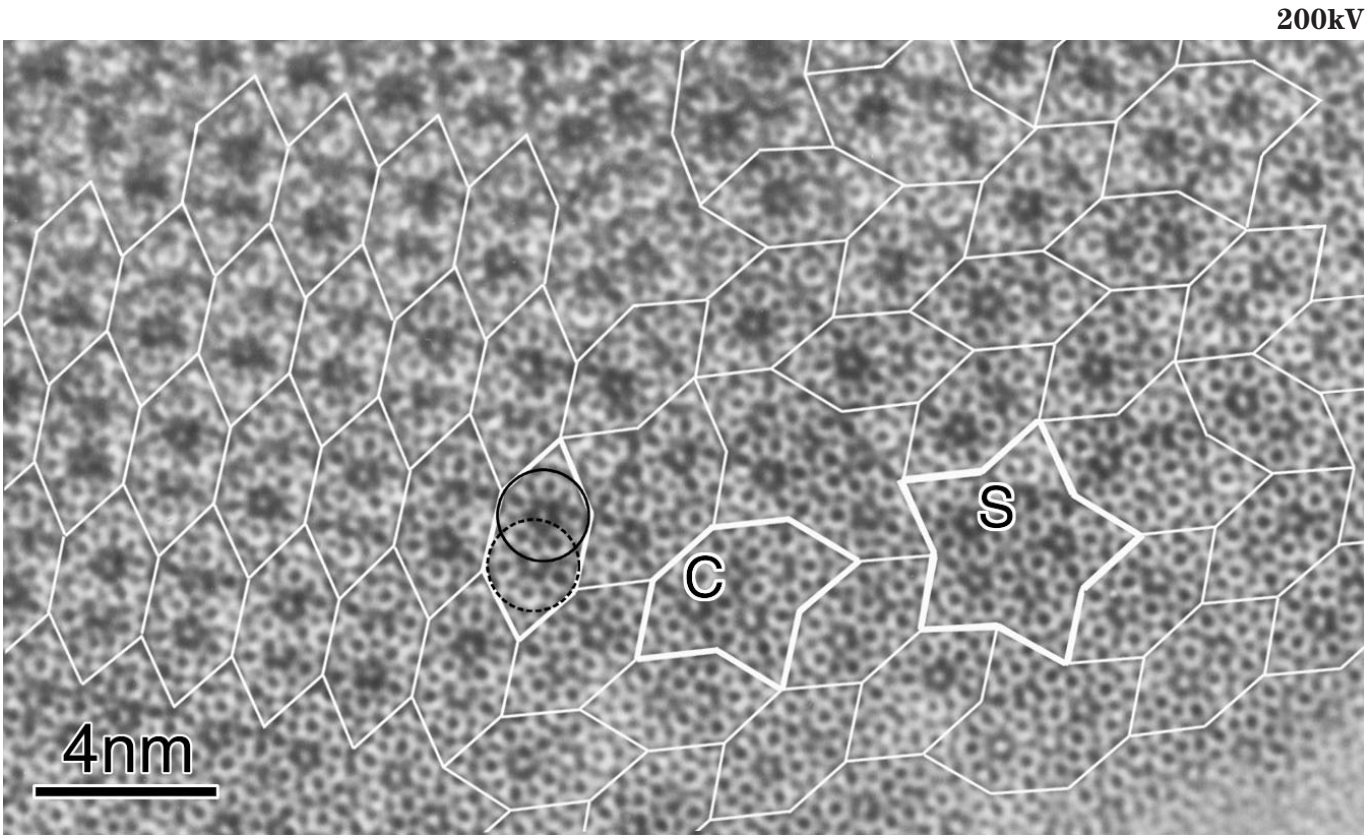

Tiling of the τ^2-$Al_{13}Co_4$ approximant (on the left) and the star- and crown-tiles characteristic of the decagonal quasicrystal (on the right) coexisting in a $Al_{73}Co_{27}$ alloy.

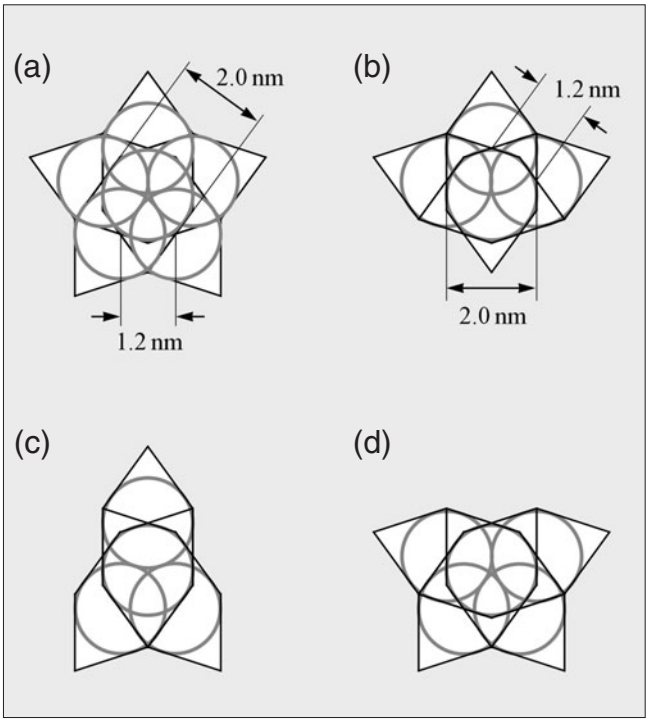

Four examples of the combinations of the elongated hexagons or the 1nm column pairs. The star tile (a) and crown tile (b) are seen in the HREM image on the previous page. The rocket tile (c) and butterfly tile (d) often appear in the decagonal quasicrystal as well as (a) and (b).

Combination of column pairs with a 1nm intercolumnar distance

(a)

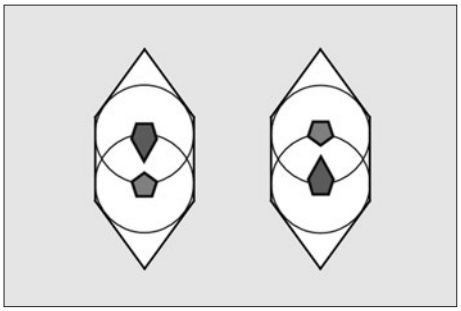

(b)

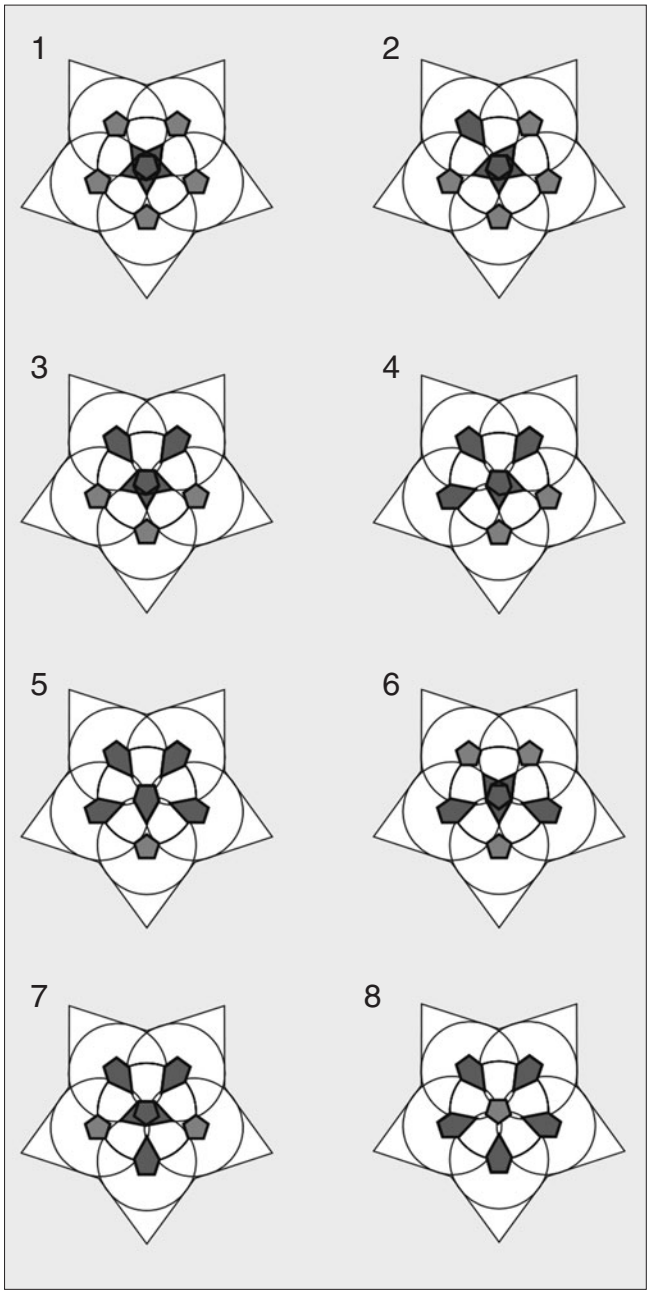

The elongated hexagon is composed of a fivefold-symmetry cluster column and a pseudo-fivefold-symmetry cluster column, and thus the hexagon is polar. Figure (a) shows two possible occupations of the columns in the hexagon. In the star tile, eight combinations of the hexagons are possible according to the two senses of the hexagons. All of them are schematically shown in Fig. (b). It is noted that the only combinations 1 and 8 exhibit true fivefold symmetry. It appears from experiments that there is no specific preference in the eight combinations for the formation of the star-arrangements.

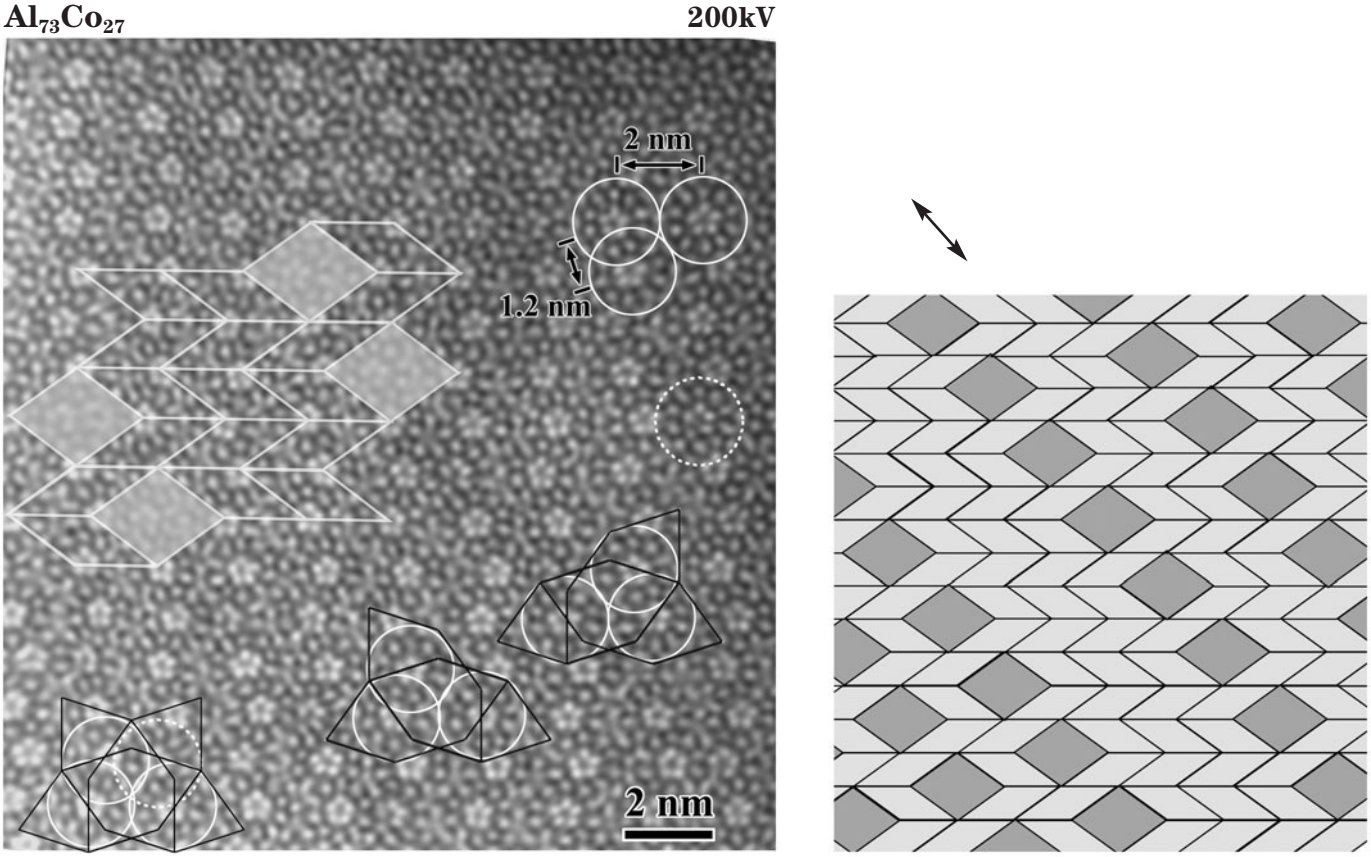

Photograph shows a HAADF image taken from a different specimen area of the same alloy as shown on the previous pages. Fivefold-symmetry atom-clusters and pseudo-fivefold-symmetry atom-clusters with a 2nm diameter are seen as indicated by the solid and dashed circles, respectively. The arrangement of the clusters forms a lattice composed of two types of the rhombi, or the Penrose's fat and skinny rhombi, as is shown in the right figure. The fivefold-symmetry clusters are located on the vertices of the two rhombi.

The arrangement of both the tiles is perfectly periodic in the direction of the arrow, but show an imperfect periodicity in the direction perpendicular to the arrow. Thus, the alloy in this area forms a crystalline approximant consisting of the Penrose's tiles, which contains a disorder in one direction. The 1nm column pair is not clearly seen in the image, but combinations of the pairs (c) and (d) on page 166, or "rocket" and "butterfly", which are respectively composed of three and four 1nm column pairs, are seen as indicated by the black lines on the lower side of the image.

The rockets and butterflies always appear at the skinny and fat tiles, respectively (see the next page), and cover the specimen area by allowing their overlapping. This indicates that the specimen area can also be interpreted to be composed of the rockets and butterflies as well as the skinny- and fat-rhombus tiles. It is considered that the structure of the specimen area is closer to a quasicrystal than to monoclinic τ^2-$Al_{13}Co_4$ due to the formation of the rocket and butterfly tiles.

Photograph (a) shows an enlarged HAADF image of an area which is composed of two skinny tiles and one fat tile. 2nm fivefold-symmetry cluster columns p_1 to p_7 are occupied on the vertices of the two rhombi as indicated by the solid circles. 2nm pseudo-fivefold-symmetry cluster columns d_1 to d_4 are located inside the rhombi, as indicated by the dashed circles. The pairs (p_1, d_1), (p_2, d_1), (p_3, d_1), (p_4, d_3), ..., are the 1nm column pairs. It is seen that the combination of the three 1nm column pairs (p_1, d_1), (p_2, d_1) and (p_3, d_1) forms a rocket as shown in Photo (b). Similarly, the pairs (p_4, d_3), (p_5, d_3) and (d_2, d_3) form another rocket, whose orientation is different by 108 degrees counterclockwise from the rocket shown in Photo (b). A butterfly is formed by the pairs (p_6, d_4), (p_3, d_4), (d_2, d_4) and (p_7, d_4) as shown in Photo (c).

We emphasize that the skinny- and fat-rhombus tiles seen in the quasicrystals already appear in the present $Al_{73}Co_{27}$ approximant. We have seen that the skinny- and fat-rhombus tiles as well as the star-, crown-, rocket- and butterfly-shaped tiles are all constructed from the 1nm column pairs. Therefore, to solve the structure of the 1nm column pair is an important key to revealing the true structure of the quasicrystal.

(a)

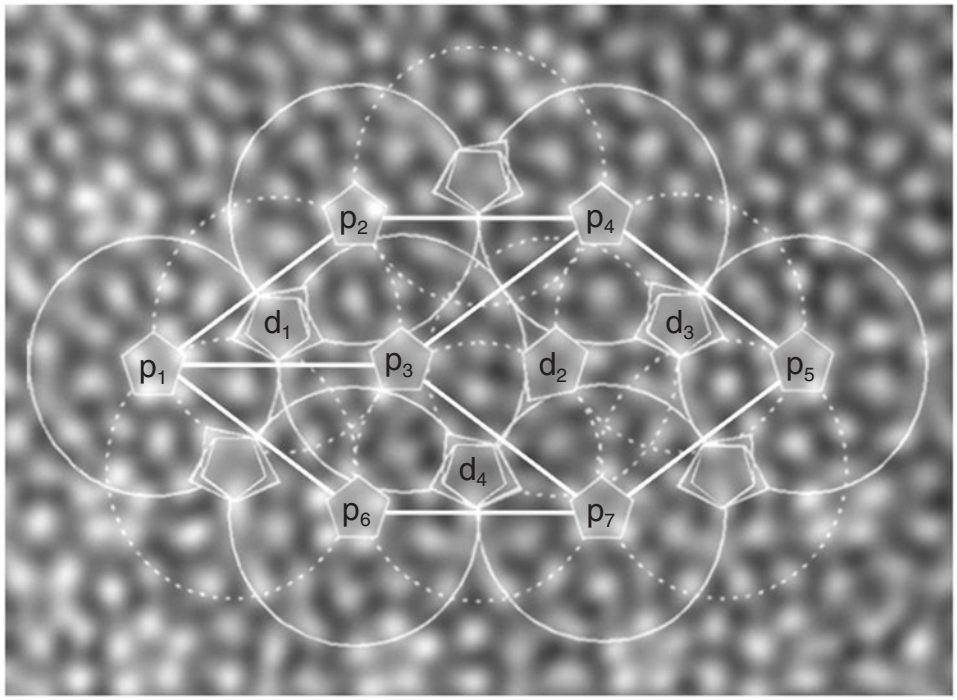

(b)

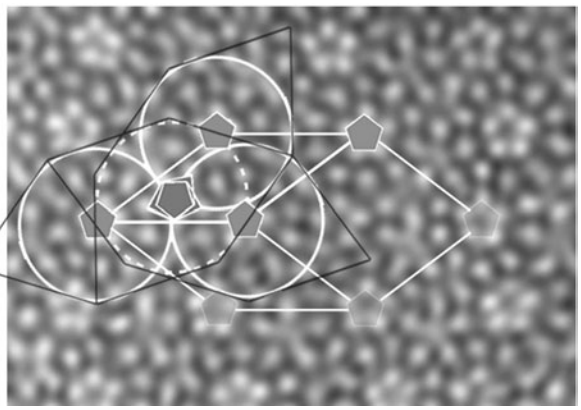

(c)

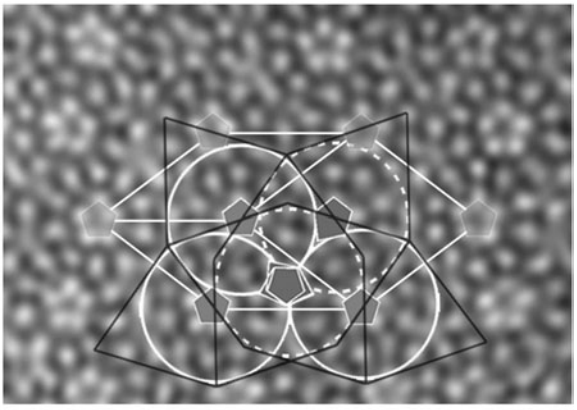

Chemical Disorder

ALCHEMI

Atom location by channeling-enhanced microanalysis (ALCHEMI) is a technique that allows determination of the site occupation of different atoms [a]. The original ALCHEMI method required characteristic X-ray emissions obtained under two different diffraction (or channeling) conditions. The angular-scanning technique of the incident electron beam, which displays a two-dimensional channeling pattern, was introduced in the ALCHEMI method [b], [c]. Rossouw *et al.* [d] described that the angular-scanning ALCHEMI patterns around low-index zone-axes provide more reliable and accurate results about the site occupation than the original method because a number of intensity data (~5000 data) are available due to angular scanning and the axial channeling (better localization) takes place due to the zone-axis incidence. Rossouw *et al.* [e] remarked that the channeling pattern is so sensitive that visual inspection of the pattern can detect impurity atoms with one atomic percent, which preferentially occupy a particular site.

Decagonal quasicrystals are usually composed of three elements, for example, aluminum and two transition metals. It has long been a question whether two transition metals take an ordered or a disordered arrangement. Actually, the recent model proposed by Steinhardt *et al.* [f] takes an ordered structure of two kinds of the transition metals. We applied the ALCHEMI method to decagonal quasicrystals to reveal the role of the second transition metal.

References

[a] J. Taftø and J. C. H. Spence: *Ultramicroscopy*, **9** (1982) 243.

[b] T. A. Bielicki: *Inst. Phys. Conf. Ser.*, **68** (1984) 67.

[c] K. K. Christenson and J. A. Eades: *Inst. Phys. Conf. Ser.*, **93** (1988) 15.

[d] C. J. Rossouw, P. S. Turner, T. J. White and A. J. O'Connor: *Philos. Mag. Lett.*, **60** (1989) 225.

[e] C. J. Rossouw, C. T. Forwood, M. A. Gibson and P. R. Miller: *Philos. Mag.*, **A74** (1996) 77.

[f] P. J. Steinhardt, H.-C. Jeong, K. Saitoh, M. Tanaka, E. Abe and A. P. Tsai: *Nature*, **396** (1998) 55.

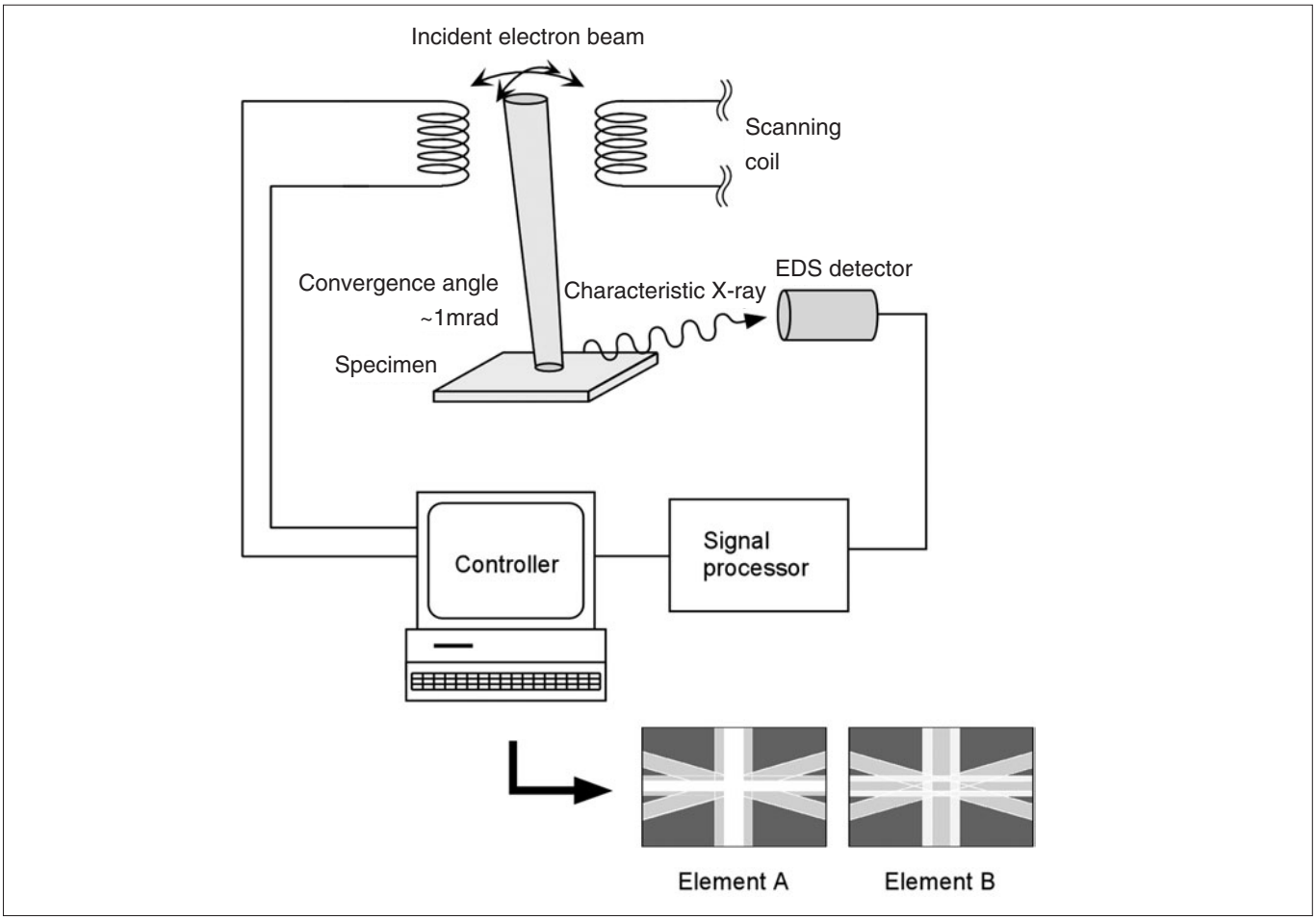

$Al_{72}Ni_{20}Co_8$

The upper photographs show channeling patterns from an $Al_{72}Ni_{20}Co_8$ decagonal quasicrystal near the decagonal zone-axis, showing characteristic X-ray emissions from Al (a), Ni (b) and Co (c) [24]. Intensity-ratio patterns of Ni/Al, Co/Al and Co/Ni are shown in Photos (d), (e) and (f). The pattern of Al signals (Photo (a)) is clearly different from those of transition-metal signals (Photos (b) and (c)). The differences are clearly seen in the ratio patterns of Photos (d) and (e). Only very faint contrast above noise exists in Photo (f). This indicates that Ni and Co are distributed randomly across the same set of sublattice sites (disordered).

The lower photographs show channeling patterns of the quasicrystal taken by tilting it to the [10010] direction from the decagonal zone-axis, showing X-ray emissions from Al (g), Ni (h) and Co (i). Intensity-ratio patterns of Ni/Al, Co/Al and Co/Ni are shown in Photos (j), (k) and (l). The two types of bands perpendicular to the <10000> and <10010> directions are seen as denoted by 1 and 2, respectively. The pattern of Al signals differs from those of TM signals. Only extremely faint contrast above noise is seen in Photo (f). These clearly indicate chemical disorder between Ni and Co.

We have found that the two kinds of transition metals are arranged in disorder. This implies that the second element varies the electron-atom ratio and thus the quasicrystal is a Hume-Rothery compound [a].

Reference

[a] A. P. Tsai, A. Inoue and T. Masumoto: *Mater. Trans. JIM*, **30** (1989) 463.

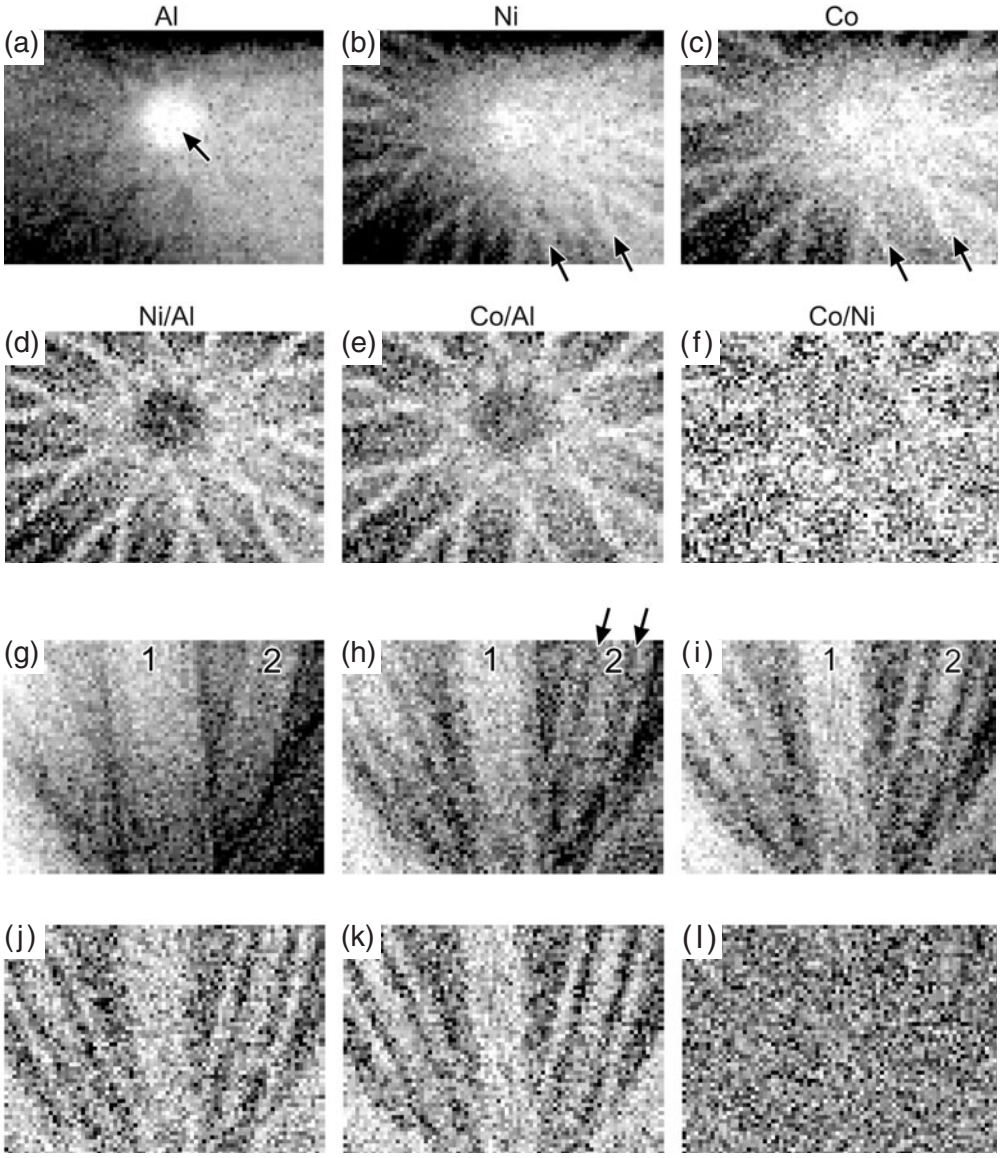

Inelastic Scattering

Theoretical

Since the energy filtering technique for electron microscopy was established, it has already been a common sense that rocking curves of diffraction patterns (CBED patterns) formed by elastically scattered electrons are reproduced very well by the dynamical calculations of electron diffraction. It is high time to study inelastic scattering quantitatively. There exist three major fundamental inelastic scattering processes: plasmons (5 to 30eV), core-excitations (> 50eV) and phonons (thermal diffuse scattering, TDS) (< 0.1eV). The cross section of the core-excitations is small but that of plasmons is very large. Inelastic scattering due to plasmons is harmful to the quantitative analysis of the rocking curves of the diffraction patterns. Owing to the development of the energy-filtering technique, inelastic scattering due to plasmons and core-excitations can be removed. However, inelastic (quasi-elastic) scattering due to phonons (TDS) is difficult and impractical to remove at present. TDS is known as the major origin of the anomalous absorption effect. In contrast to plasmon scattering, TDS extends to large scattering angles and forms Kikuchi bands and Kikuchi lines, which are impedimental to the accurate analysis of the rocking curves of CBED patterns.

Omoto, our student, derived a comprehensive theoretical expression for inelastic scattering of fast transmission electrons from a perfect crystal [31]. His expression includes both elastic and inelastic multiple scatterings and is regarded as an extended form of Fujimoto's expression for elastic scattering [a]. When the approximation of single inelastic scattering is applied to the expression, it becomes equivalent to the formula of Rez *et al.* [b]. When TDS is considered with the use of the Einstein model or the scattering factor for TDS given by Hall and Hirsch [29], the expression of Rossouw and Bursill [30] is derived. This expression is used here in computer simulations of TDS intensity distributions (Kikuchi patterns). We will show many results of the simulations for MgO, Al and TiO_2 and compare them with experimental results.

Before showing the simulation results of Kikuchi patterns, we describe a brief flow of the studies of inelastic scattering with special emphasis on TDS. After that, we quote the important equations, which are the basis of the present calculations.

The fundamental theory that describes inelastic scattering of fast electrons in a crystal was investigated by Kainuma [28] on quantum mechanical basis. The characteristic intensity distribution of Kikuchi patterns was qualitatively explained by his theory. Following Kainuma's work, Yoshioka [c] investigated the effect of inelastic scattering on elastic scattering. He showed that the effect gives rise to an additional imaginary part of the crystal potential. A set of coupled differential equations or Yoshioka's equation has been a guide to the study of inelastic scattering of high-energy electrons. TDS was first studied in dynamical diffraction by Takagi [27], who derived the transition matrix elements between Bloch waves for single phonon excitations under the assumption of single inelastic scattering. He obtained for TDS the same azimuthal angular dependence of Kikuchi patterns (Kikuchi-band profiles) as that of Kainuma [28]. However, he ignored the cross terms of the transition probabilities between the different Bloch waves, thereby the thickness dependence of the intensity distribution having been absent. Howie [d] investigated plasmon scattering on the basis of Yoshioka's equation by assuming the solution to be a Bloch wave with a depth (z)-dependent amplitude. He clarified that only intra-branch transitions are allowed for plasmon scattering. This result explains that the electron microscope images formed by both elastically and inelastically (plasmon) scattered electrons show similar thickness-inclination fringes. His work provided the basis for the following studies. Humphreys and Whelan [e] applied Howie's theory [d] to single electron excitations and showed that inelastic scattering due to single electron excitations at very small angles causes mainly intra-branch transitions, thus giving rise to the preservation of diffraction contrast as in the case of plasmon excitations. Using the theories of Howie [d] and Humphreys and Whelan [e], Rez *et al.* [f] gave a general formulation of the dynamical intensity distribution for single phonon excitations. In contrast to Takagi's theory [27], they took account of the cross terms of the transition probabilities between different Bloch waves completely, and thus obtained the thickness dependent angular distribution of the intensity scattered by single phonon excitations. They carried out computer simulations of the diffuse intensities due to single acoustic phonon excitations for the systematic reflection cases of three crystals. They obtained strong peaks at the low-order Bragg spots and diffuse intensities monotonically decreasing with the deviation from the spots. Although they gave a complete formula of the thickness dependent intensity distribution for single inelastic scattering, the transition matrix elements were still approximated to the first order or single phonon excitations as is the case of Takagi's treatment. Their approximation breaks down at large scattering angles, where the contribution of multiphonon excitations becomes large.

In contrast to the theory of single phonon excitations, a semiclassical theory of TDS using the Einstein model developed by Hall and Hirsch [29] takes account

of multiphonon excitations implicitly. Thus, the theory is applicable to the interpretation of TDS intensity at large scattering angles. Assuming that the incident Bloch waves are transferred to the plane waves by TDS under the two-beam approximation, they gave the expression of the scattering cross section of TDS. The expression contains the scattering factor for TDS, which is a very important factor for the calculations of TDS. They integrated each component of the cross section over the whole scattering angles and obtained the normal and anomalous absorption coefficients for many crystals and their temperature dependence. They showed that TDS is the major source of the anomalous absorption. Okamoto *et al.* [g] carried out numerical calculations of line profiles of Kikuchi bands and Kikuchi lines for the excitations of valence electrons, core electrons and phonons using the two-beam dynamical theory. They adopted the independent Bloch-wave approximation and the Einstein model for phonons. They explained the formation of the defect Kikuchi band. Rossouw and Bursill [30] extended the theory of Hall and Hirsch [29] to a many beam dynamical formulation, where they assumed that both the incident and scattered electrons form Bloch waves. They presented an expression for the TDS intensity distribution in the manner of full dynamical diffraction. They performed computer simulations of the TDS diffuse intensity for TiO_2 using a nine-beam approximation, and compared them with an experimental observation. The agreement between the simulations and the experiments was unfortunately unsatisfactory presumably due to the small number of beams used for the simulations.

The theories we mentioned above are based on the Bloch-wave theory. Meanwhile, a multislice theory of inelastic scattering has been developed by Wang [h]. He applied the theory to simulations of angular distributions of electrons scattered by phonon, plasmon and single electron excitations [i]. He took account of the lattice dynamics of atomic vibrations instead of the Einstein model for the calculations of TDS for Si and Mo. The calculated streak patterns qualitatively explained the experimental observations but the detailed comparison was not carried out. It is noted that his calculations aim to explain sharp streak patterns but not the Kikuchi pattern over large scattering angles.

It should be noted that even for single inelastic scattering, quite a big computing power is needed to obtain an accurate simulation pattern because elastic scattering occurring before and after inelastic scattering should be taken into account. Those simulations have been getting realistic to a level where they can be compared with experiments, due to the advance of the performance of computers. Recently, Muller *et al.* [j] has performed the computer simulations of TDS and CBED patterns of Si using the multislice method under the frozen phonon approximation. Their simulations appear to show good agreement with the experiments on the whole, but the detailed profiles of the Kikuchi pattern especially at low angle areas cannot be compared because they are hidden by the CBED disks. Instead, the Kikuchi patterns should be compared with an ordinary selected area diffraction (SAD) pattern. If reliable theoretical calculations of diffuse TDS patterns over a large angular range become possible, they can be used to subtract the quasi-elastic TDS background from energy-filtered CBED patterns in order to improve the precision of quantitative analysis of CBED patterns.

Omoto developed a Bloch-wave method [31] of simulating Kikuchi patterns, which can give a clear physical interpretation and simultaneously calculate the patterns of different specimen thicknesses in contrast to the multislice method. He has performed many computer simulations of TDS intensities and quantitative comparison with experimental SAD patterns.

References

[a] F. Fujimoto: *J. Phys. Soc. Jpn.*, **14** (1959) 1558.
[b] P. Rez, C. J. Humphreys and M. J. Whelan: *Phil. Mag.*, **35** (1977) 81.
[c] H. Yoshioka: *J. Phys. Soc. Jpn.*, **12** (1957) 618.
[d] A. Howie: *Proc. Roy. Soc.*, **A 271** (1963) 268.
[e] C. J. Humphreys and M. J. Whelan: *Phil. Mag.*, **20** (1969) 165.
[f] P. Rez, C. J. Humphreys and M. J. Whelan: *Phil. Mag.*, **35** (1977) 81.
[g] K. Okamoto, T. Ichinokawa and Y. H. Ohtsuki: *J. Phys. Soc. Jpn.*, **30** (1971) 1690.
[h] Z. L. Wang: *Acta Cryst.*, **A45** (1989) 636.
[i] Z. L. Wang: *Acta Cryst.*, **A48** (1992) 674.
[j] A. D. Muller, B. Edward, E. J. Kirkland and J. Silcox: *Ultramicroscopy*, **86** (2001) 371.

A comprehensive expression of the scattering amplitude for elastic and inelastic scattering of fast transmission electrons from a perfect crystal is given as

$$|\phi(t)\rangle = \exp[it\hat{M}]|a_0\rangle|\boldsymbol{O}\rangle, \tag{1}$$

where $|a_0\rangle$ and $|\boldsymbol{O}\rangle$ are the initial states of the crystal and the incident plane wave of an electron, $\hat{M}$ is the elastic and inelastic scattering operator and t is the thickness of a specimen.

The scattering amplitude in direction $\boldsymbol{K}_i + \boldsymbol{G}$ to excite the crystal from the 0th state to the ith state, where $\boldsymbol{G}$ is the reciprocal lattice vector, is obtained by multiplying (1) by $\langle\boldsymbol{G}|\langle a_i|$ from the left side.

$$\langle\boldsymbol{G}|\langle a_i|\phi(t)\rangle = \langle\boldsymbol{G}|\langle a_i|\exp[it\hat{M}]|a_0\rangle|\boldsymbol{O}\rangle \tag{2}$$

If we consider only elastic scattering ($i = 0$), eq.(2) is reduced to

$$\langle\boldsymbol{G}|\langle a_i|\phi(t)\rangle^{(0)} = \langle\boldsymbol{G}|\exp[it\hat{M}_{00}]|\boldsymbol{O}\rangle, \tag{3}$$

where the superscript (0) implies elastic scattering. The expression (3) is exactly Fujimoto's equation. Thus, equation (1) including inelastic scattering is regarded as a natural extension of Fujimoto's equation.

The amplitude of single inelastic scattering $\langle\boldsymbol{G}|\langle a_i|\phi(t)\rangle^{(1)}$ is expressed in the following way,

$$\langle\boldsymbol{G}|\langle a_i|\phi(t)\rangle^{(1)} = \int_0^t \langle\boldsymbol{G}|\underbrace{\exp[i(t-\xi)\hat{M}_{ii}]}_{3}\underbrace{i\,d\xi\hat{M}_{i0}}_{2}\underbrace{\exp[i\,\xi\hat{M}_{00}]}_{1}|\boldsymbol{O}\rangle. \tag{4}$$

As illustrated in Fig. (a) on the right-side page, the incident electron is scattered elastically in slice 1 of thickness ξ, scattered inelastically in slice 2 of infinitely small thickness $d\xi$ and again scattered elastically in slice 3 of thickness $(t - \xi)$.

Let us consider only thermal diffuse scattering (TDS). When the atom vibrations are approximated by the Einstein model, the intensity of TDS electrons in direction $\boldsymbol{p} + \boldsymbol{G}$ per a solid angle is expressed as

$$\frac{dI_p^G}{d\Omega} = t\sum_{\lambda\lambda'}\sum_{\mu\mu'}\langle\boldsymbol{G}|\,p\lambda\rangle\langle p\lambda'|\boldsymbol{G}\rangle\langle 0\mu|\boldsymbol{O}\rangle\langle\boldsymbol{O}|0\mu'\rangle \times T_{\mu\mu'}^{\lambda\lambda'}\frac{\exp[it\gamma_{p\lambda\lambda'}] - \exp[it\gamma_{0\mu\mu'}]}{it(\gamma_{p\lambda\lambda'} - \gamma_{0\mu\mu'})}, \tag{5}$$

where

$$T_{\mu\mu'}^{\lambda\lambda'} = \sum_{gh}\sum_{g'h'}\langle p\lambda|\boldsymbol{g}\rangle\langle\boldsymbol{g}'|p\lambda'\rangle T(\boldsymbol{Q},\boldsymbol{Q}')\langle\boldsymbol{h}|0\mu\rangle\langle 0\mu'|\boldsymbol{h}'\rangle, \quad \boldsymbol{Q}=\boldsymbol{p}+\boldsymbol{g}-\boldsymbol{h},\ \boldsymbol{Q}'=\boldsymbol{p}+\boldsymbol{g}'-\boldsymbol{h}' \tag{6}$$

$\gamma_{p\lambda\lambda'} = \gamma_{p\lambda} - \gamma^*_{p\lambda'}$ and γ and μ denote indices of the Bloch states. $T_{\mu\mu'}^{\lambda\lambda'}$ stands for inelastic scattering and other terms stand for elastic scattering. $T(\boldsymbol{Q},\boldsymbol{Q}')$ is the following function

$$T(\boldsymbol{Q},\boldsymbol{Q}') = \frac{1}{V_c}\sum_{\alpha} f_\alpha(\boldsymbol{Q})f_\alpha(\boldsymbol{Q}')\exp[-i(\boldsymbol{Q}-\boldsymbol{Q}')\cdot\boldsymbol{r}_\alpha] \times\{\exp[-W_\alpha(\boldsymbol{Q}-\boldsymbol{Q}')] - \exp[-W_\alpha(\boldsymbol{Q}) - W_\alpha(\boldsymbol{Q}')]\}, \tag{7}$$

which is the TDS scattering factor given by Hall and Hirsch. $T(\boldsymbol{Q},\boldsymbol{Q}')$ for MgO is shown in Fig. (b).

In the limiting case $t \to \infty$, only the terms $\lambda = \lambda'$ and $\mu = \mu'$ remain, the TDS intensity or eq.(5) becomes

$$\lim_{t\to\infty}\frac{1}{t}\frac{dI_p^G}{d\Omega} = \sum_{\lambda\mu}|\langle\boldsymbol{G}|p\lambda\rangle|^2\,T_\mu^\lambda|\langle 0\mu|\boldsymbol{O}\rangle|^2, \tag{8}$$

where

$$T_\mu^\lambda = T_{\mu\mu'}^{\lambda\lambda'} = \sum_{gh}\sum_{g'h'}\langle p\lambda|\boldsymbol{g}\rangle\langle\boldsymbol{g}'|p\lambda\rangle T(\boldsymbol{Q},\boldsymbol{Q}')\langle\boldsymbol{h}|0\mu\rangle\langle 0\mu|\boldsymbol{h}'\rangle. \tag{9}$$

This is equivalent to Takagi's expression. In this expression, the cross terms of the transition probabilities (Fig. (c)) are omitted and the absorption effect in the elastic scattering process cannot be taken into account. As a result, the thickness dependence, the asymmetry features, the accurate intensity distribution along the band, the accurate incidence-orientation dependence and the interference fringes of Kikuchi patterns cannot be discussed.

First, simulated Kikuchi patterns of MgO, Al and TiO_2 at zone-axis incidences are shown. The thickness dependence, the incidence-orientation dependence and B-factor dependence of zone-axis Kikuchi patterns are displayed. Simulated Kikuchi patterns are compared with experimental patterns. Second, the Kikuchi patterns of MgO were calculated at the exact 020 excitation under the two-beam approximation using Takagi's independent Bloch-wave treatment. Excess and defect Kikuchi bands are analyzed in terms of the transitions between the branches of the dispersion surface. The thickness dependence, the asymmetry features, the accurate intensity distribution along the band, the accurate incidence-orientation dependence and the interference fringes of the Kikuchi patterns are shown, which were calculated using eq.(5). The experimental Kikuchi patterns of MgO at systematic reflection cases are compared with the simulated patterns.

(a)

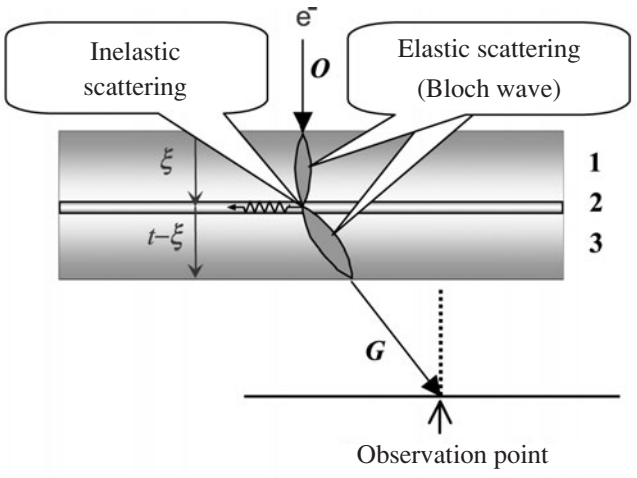

From page 178, it is firstly shown how the [100] zone-axis Kikuchi patterns of MgO change with the specimen thickness. Kikuchi patterns are weak and vague for thin specimens. As the thickness increases, clear Kikuchi bands appear and fine interference fringes are created. The line profiles at three different positions in the [001] direction are shown for the different specimen thicknesses. A similar series of patterns are shown for the [100] zone-axis Kikuchi patterns of Al.

(b)

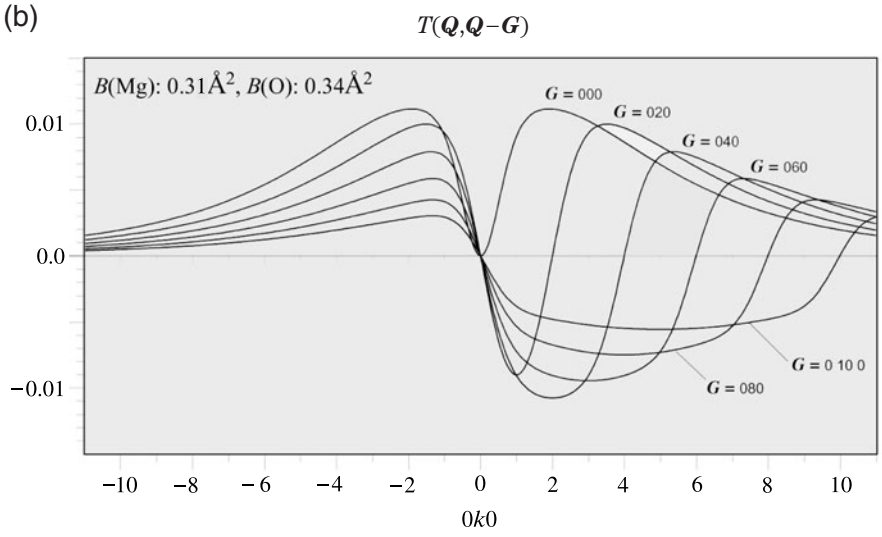

(c)

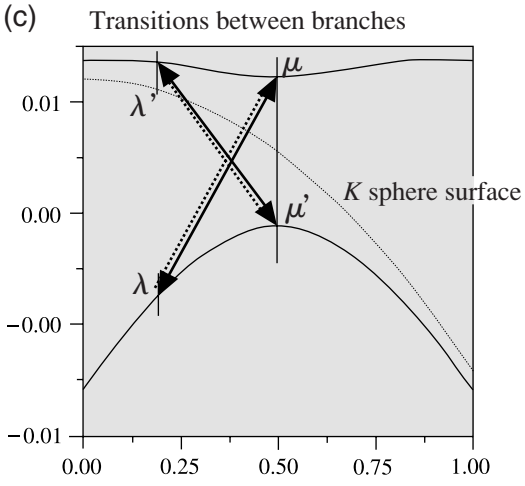

Simulations of Kikuchi Patterns (Zone-Axis Cases)

Thickness dependence

MgO [100]

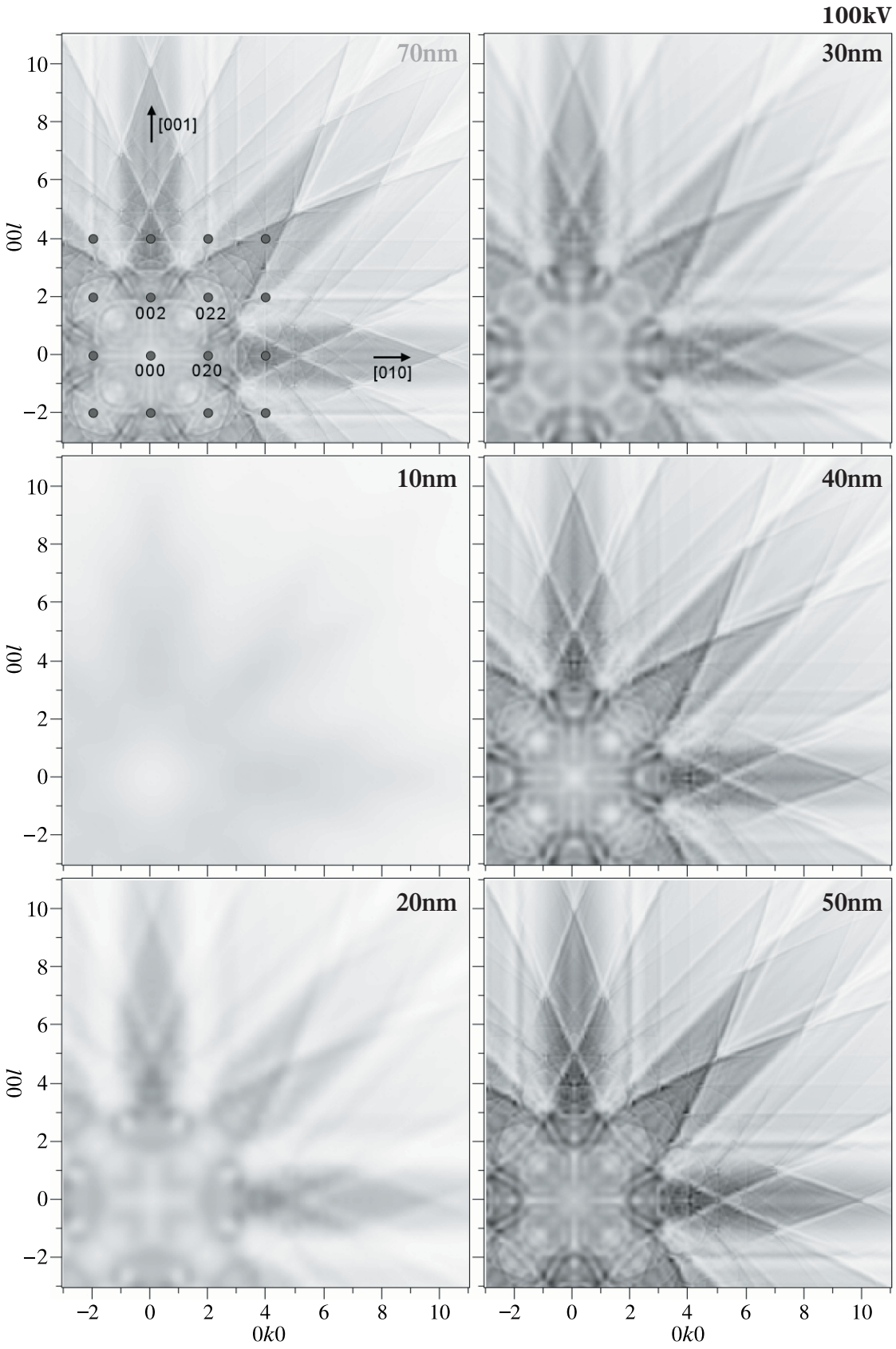

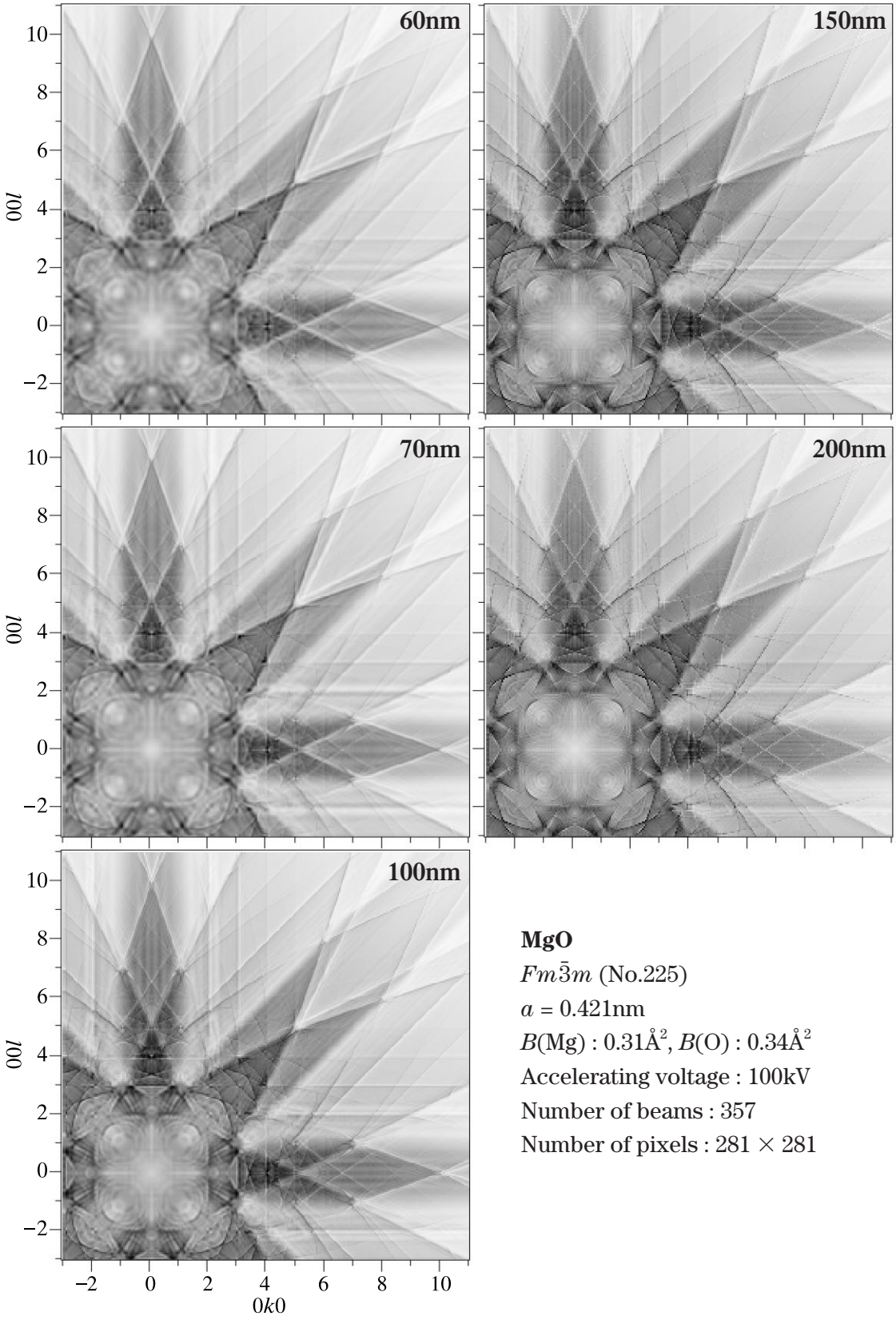

MgO

$Fm\bar{3}m$ (No.225)

a = 0.421nm

B(Mg) : 0.31Å^2, B(O) : 0.34Å^2

Accelerating voltage : 100kV

Number of beams : 357

Number of pixels : 281 × 281

Line profiles in the [010] direction passing through the position of 001

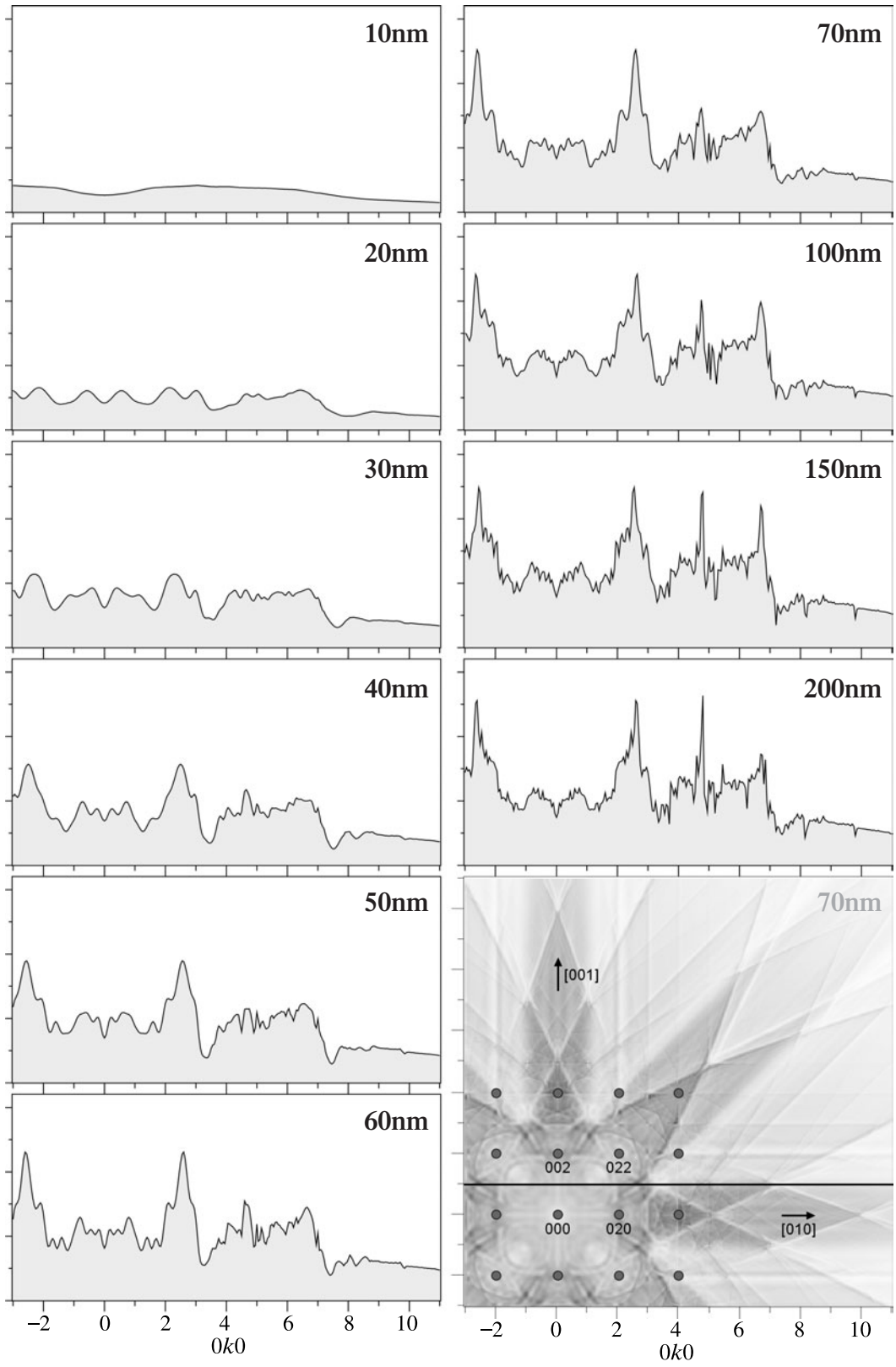

Line profiles in the [010] direction passing through the position of 005

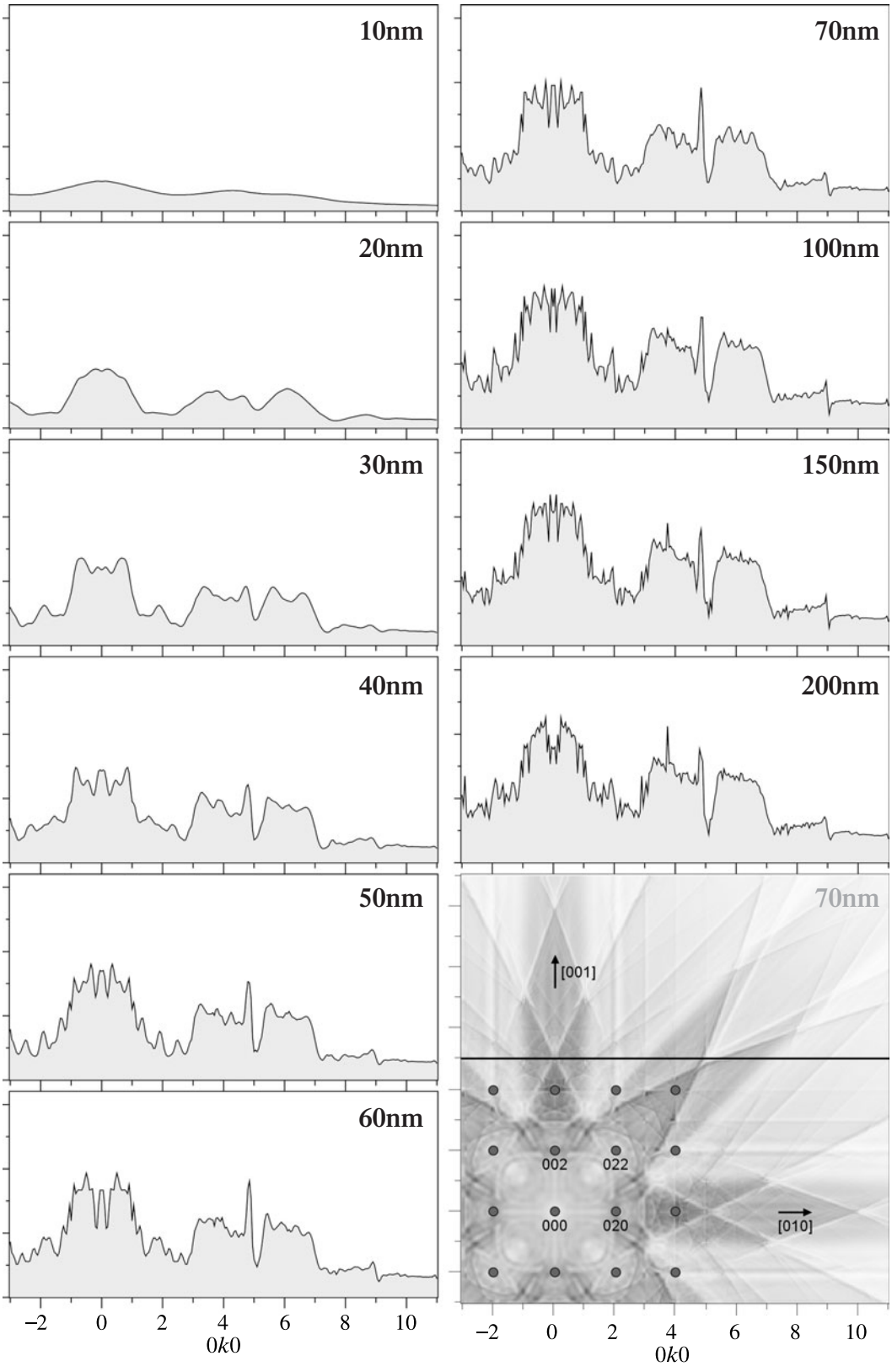

Line profiles in the [010] direction passing through the position of 009

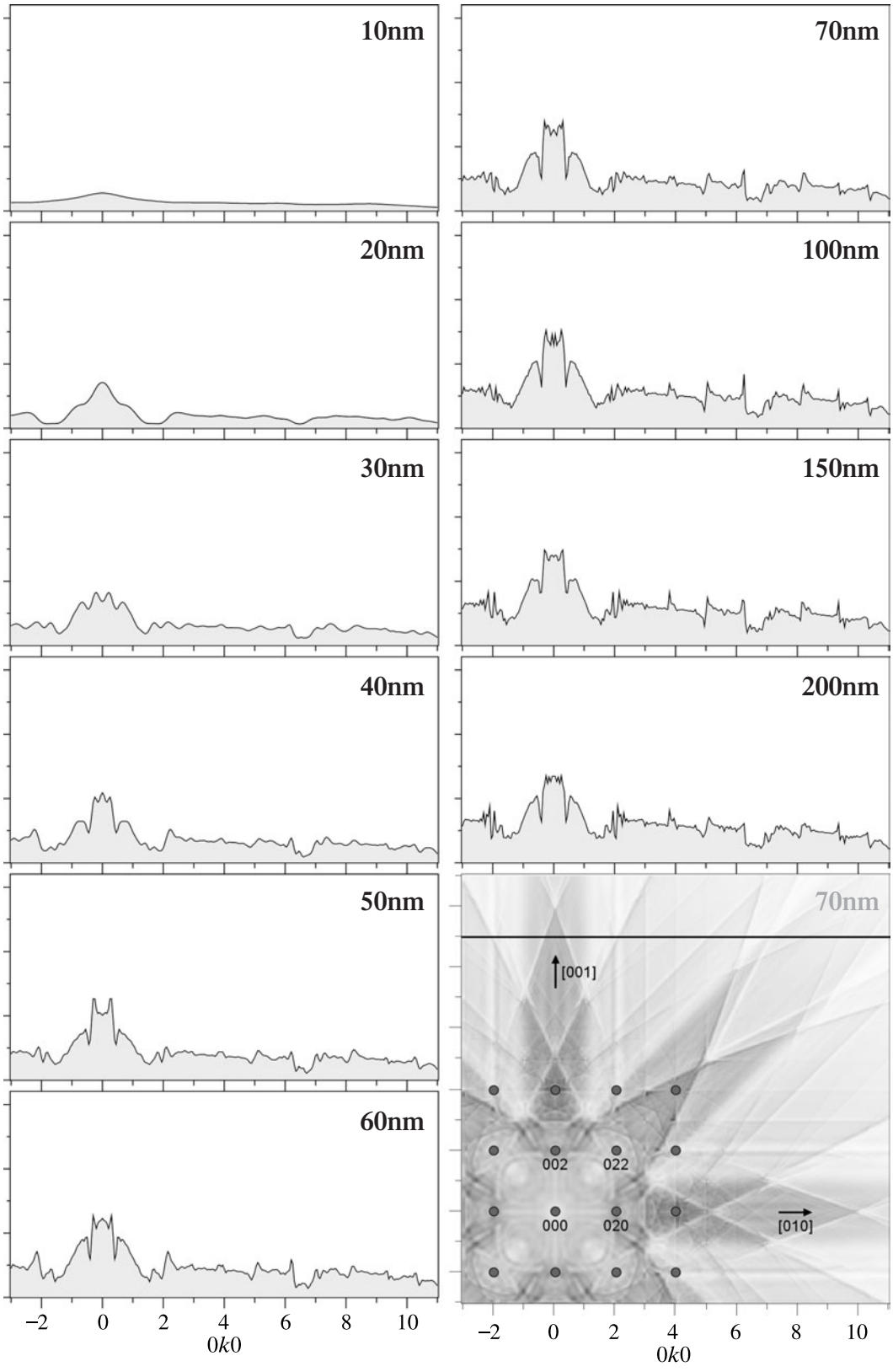

Al [100]

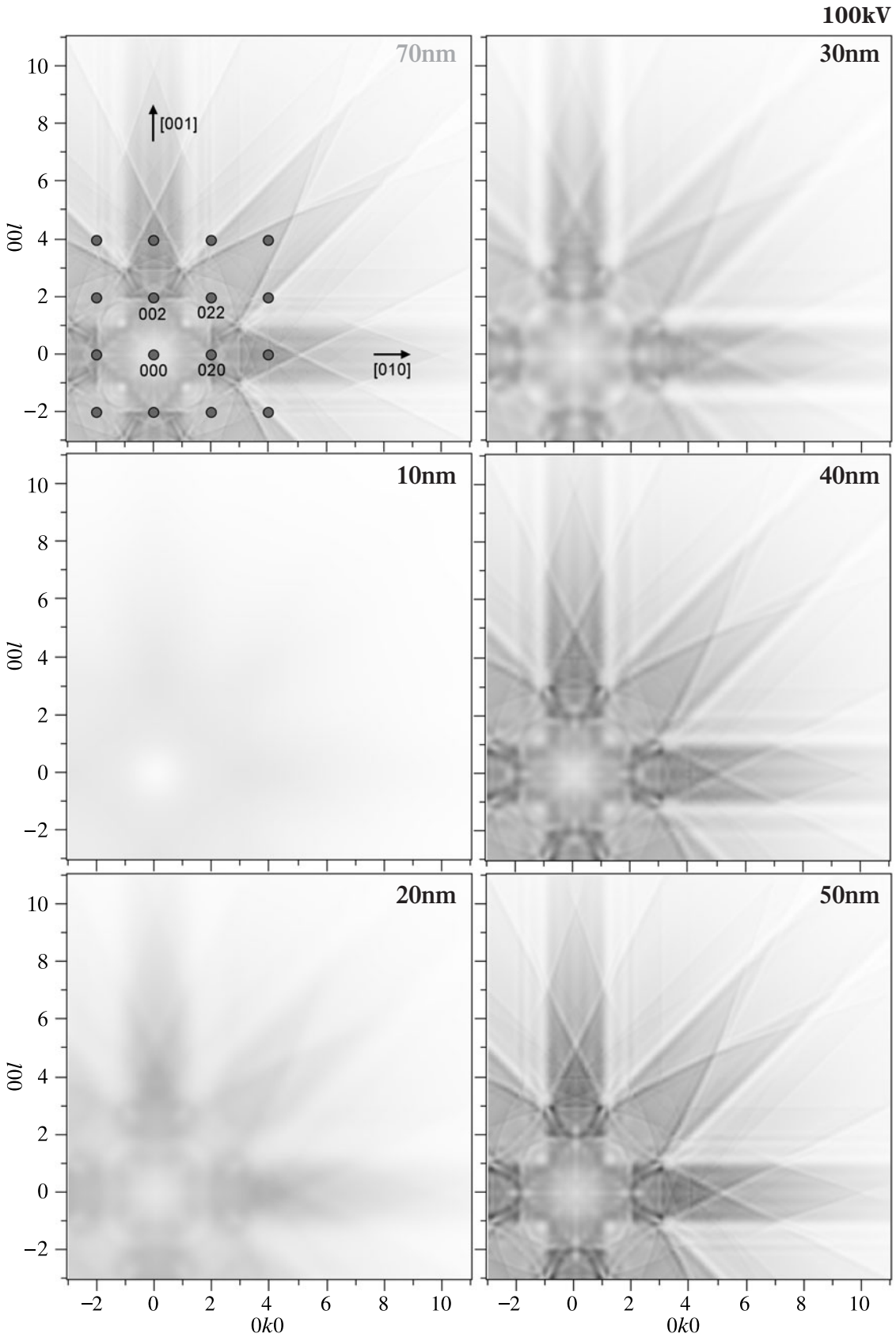
100kV
70nm
30nm
10nm
40nm
20nm
50nm
[001]
[010]
002
022
000
020
00l
0k0

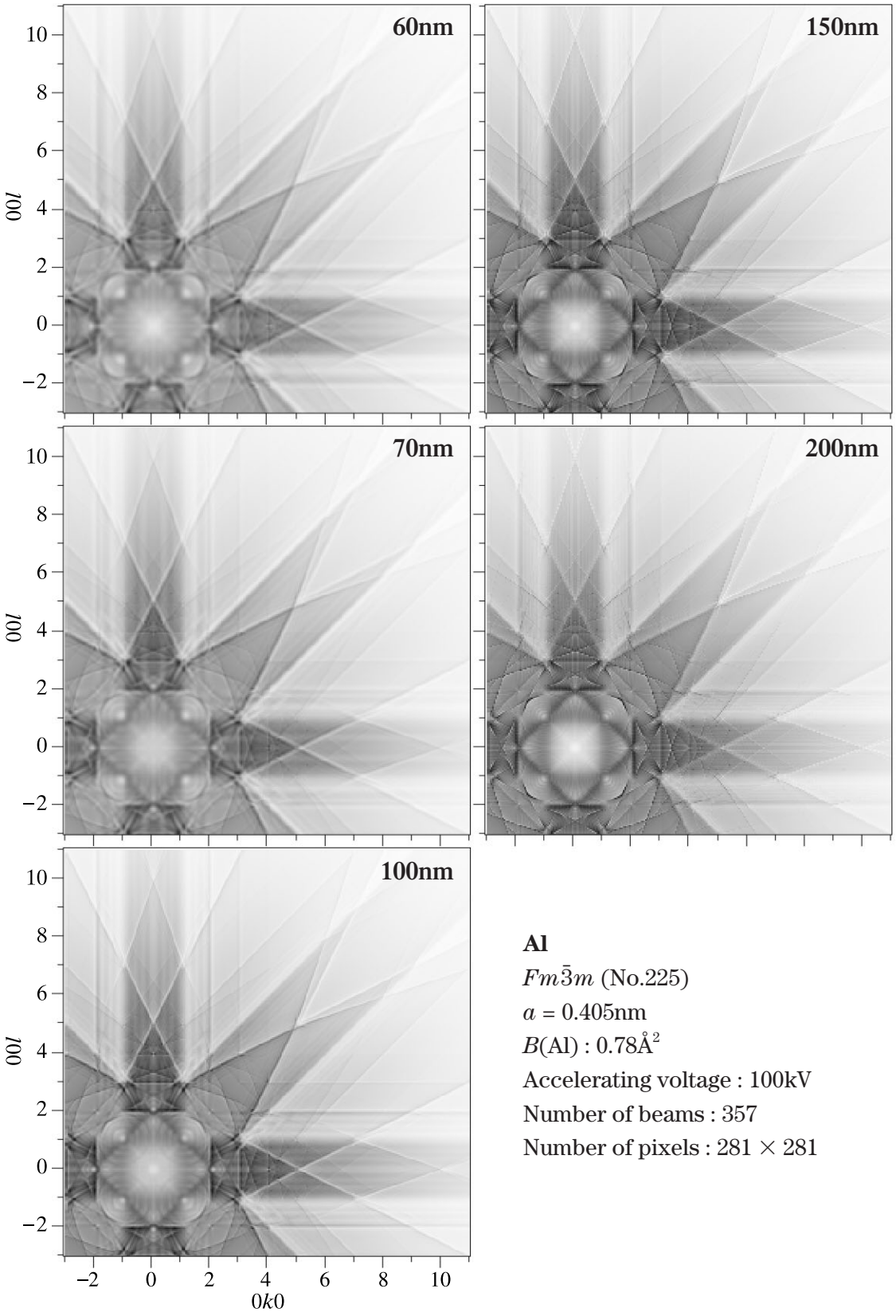

Al

$Fm\bar{3}m$ (No.225)

a = 0.405nm

B(Al) : 0.78Å^2

Accelerating voltage : 100kV

Number of beams : 357

Number of pixels : 281 × 281

Line profiles in the [010] direction passing through the position of 001

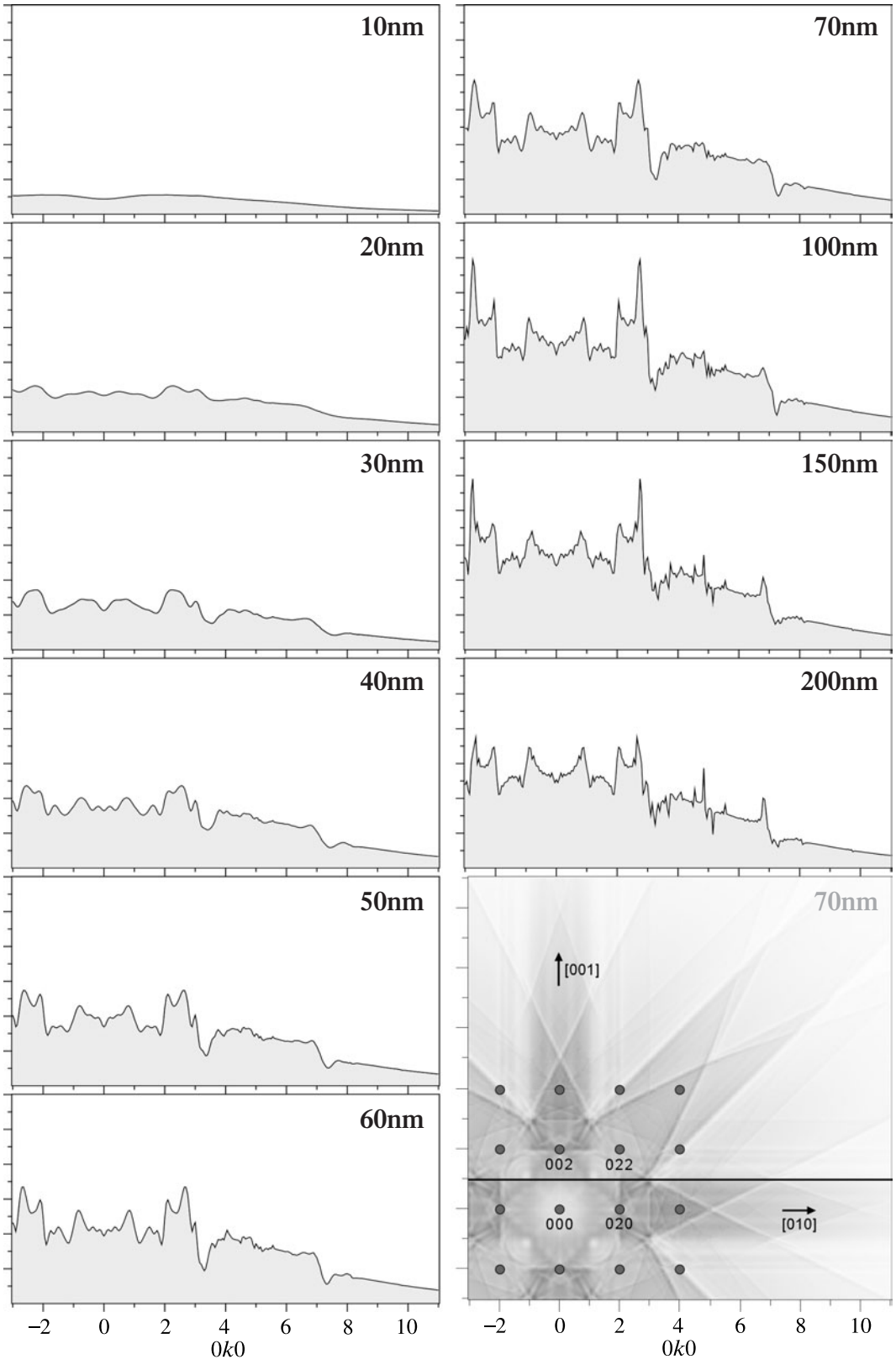

Line profiles in the [010] direction passing through the position of 005

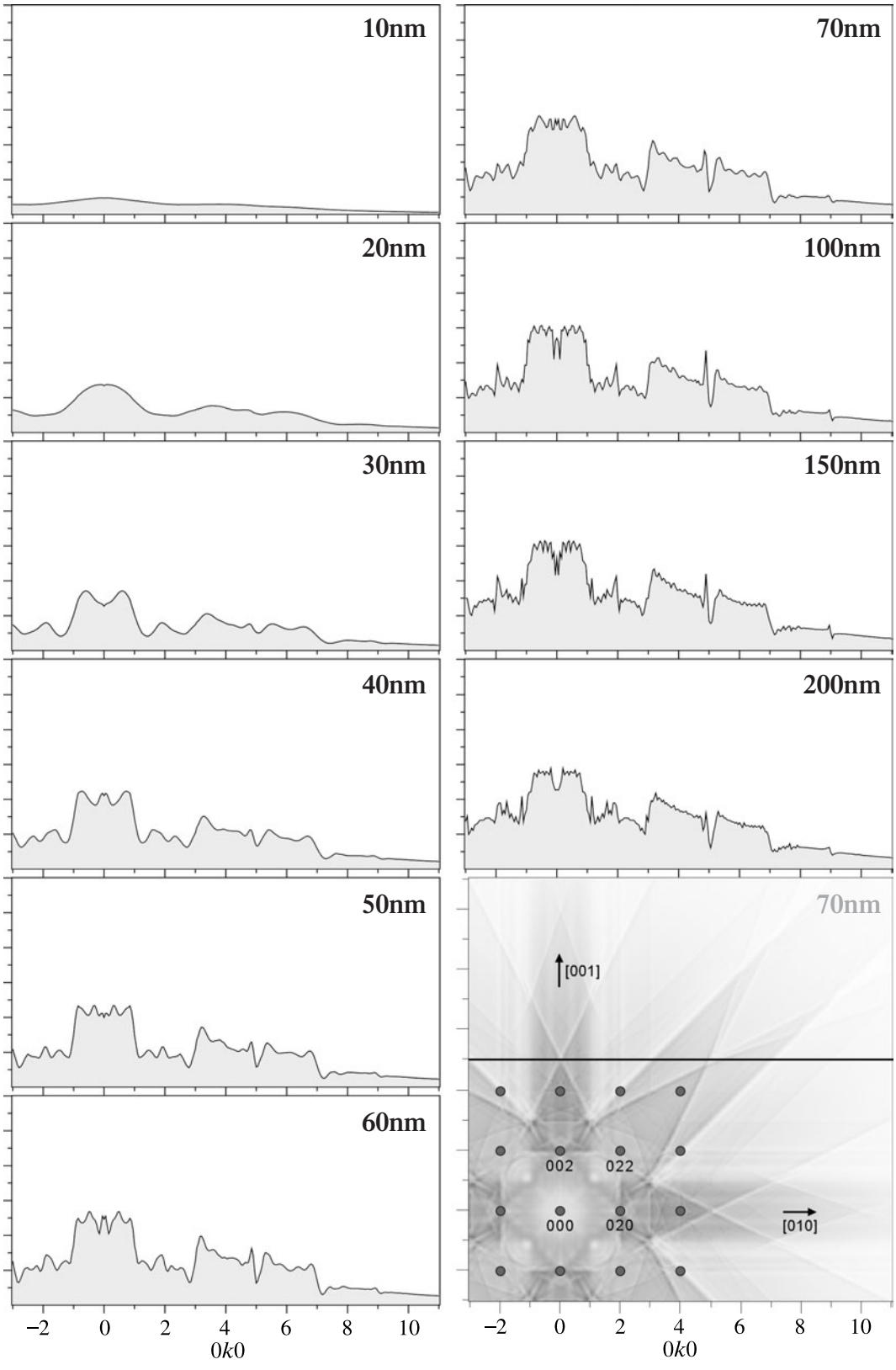

Line profiles in the [010] direction passing through the position of 009

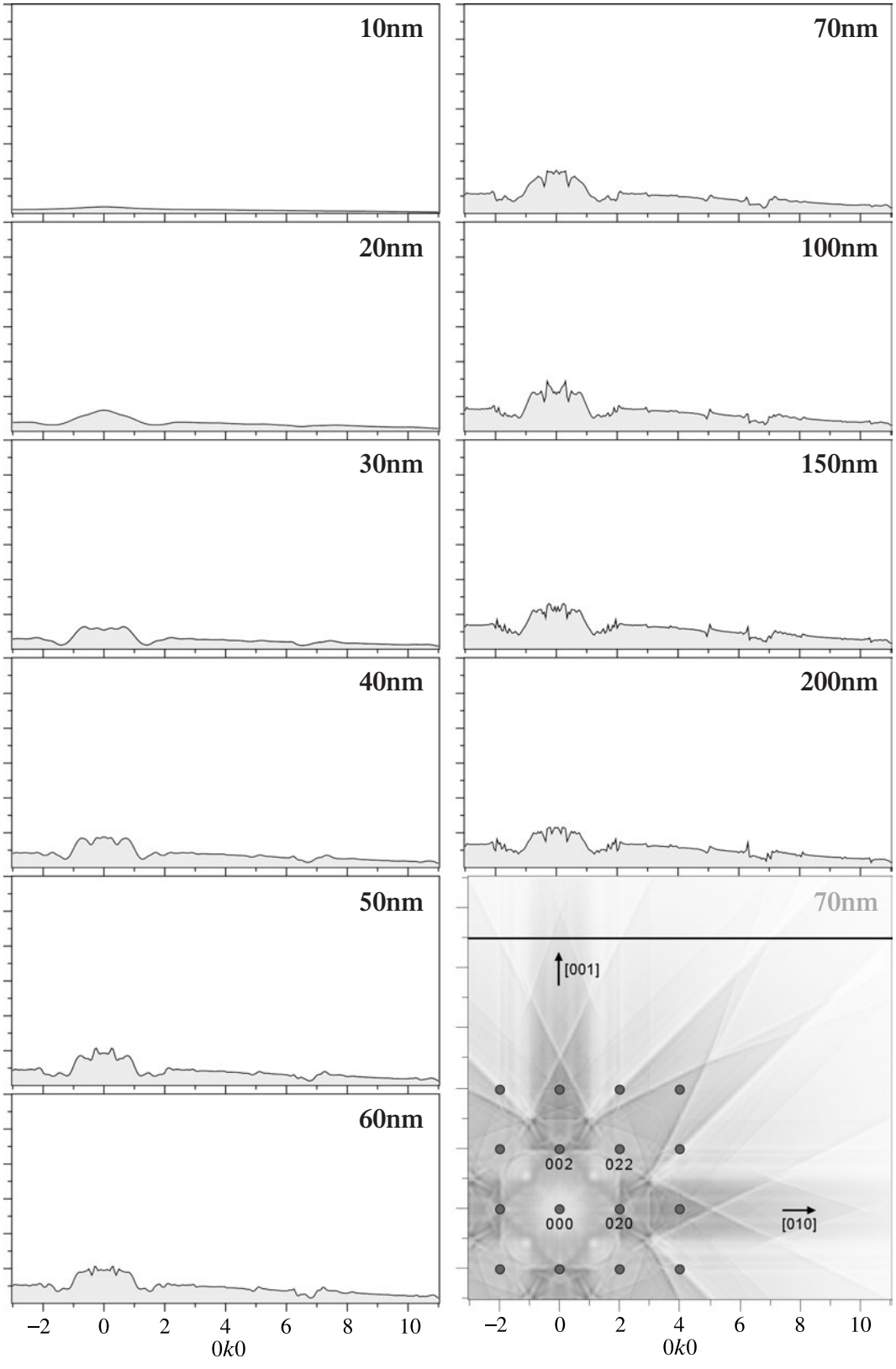

Incidence-orientation dependence

It is shown how the Kikuchi patterns of MgO at the [100] zone-axis incidence change with the orientation of the incident beam. The incidence orientation is changed from (a) (zone axis) to (f) in the [010] direction as shown in the figure. The simulations were carried out at an accelerating voltage of 100kV with 357 beams for B(Mg) = 0.31Å^2 and B(O) = 0.34Å^2, the number of pixels being 281 × 281. All the patterns on the right-side page are similar but their intensities decrease with the increase of the tilt angle from the zone axis. This is understood by the fact that the excitation of branch 1 of the Bloch states, from which most part of the Kikuchi band is originated, decreases with the tilt angle. The line profiles at different positions in the [001] direction are shown (l = 0.0 to 2.0).

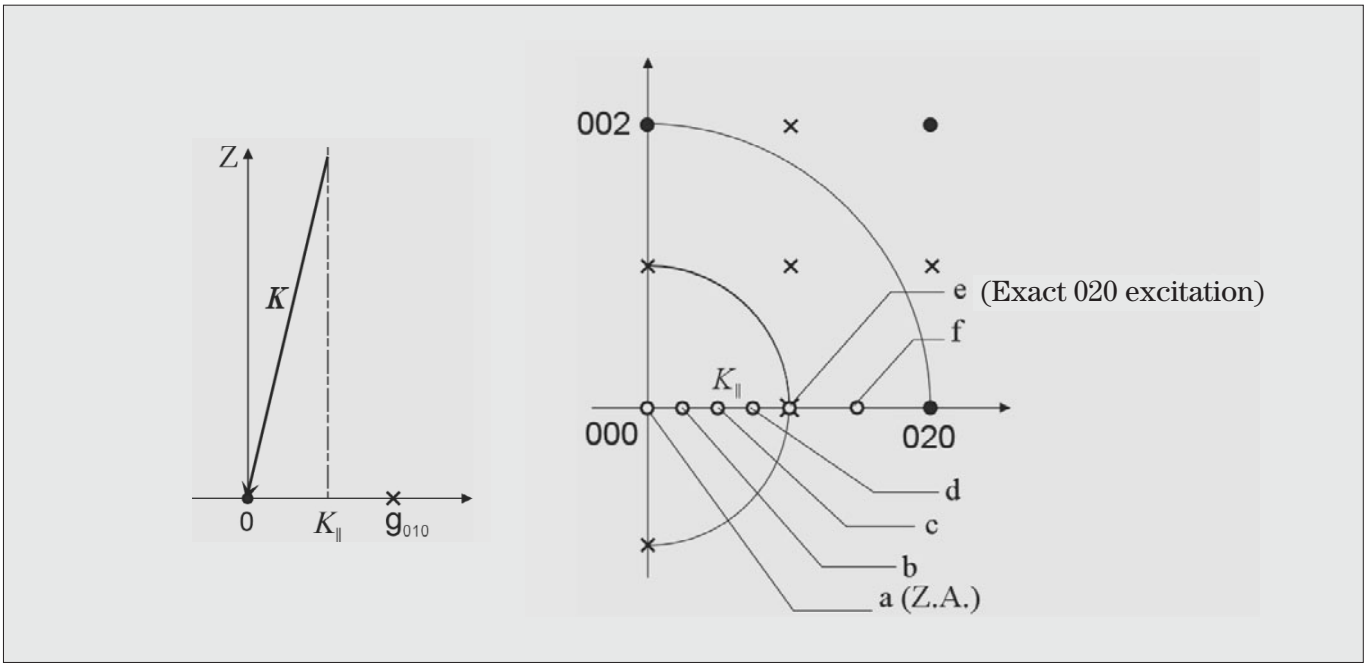

MgO [100]

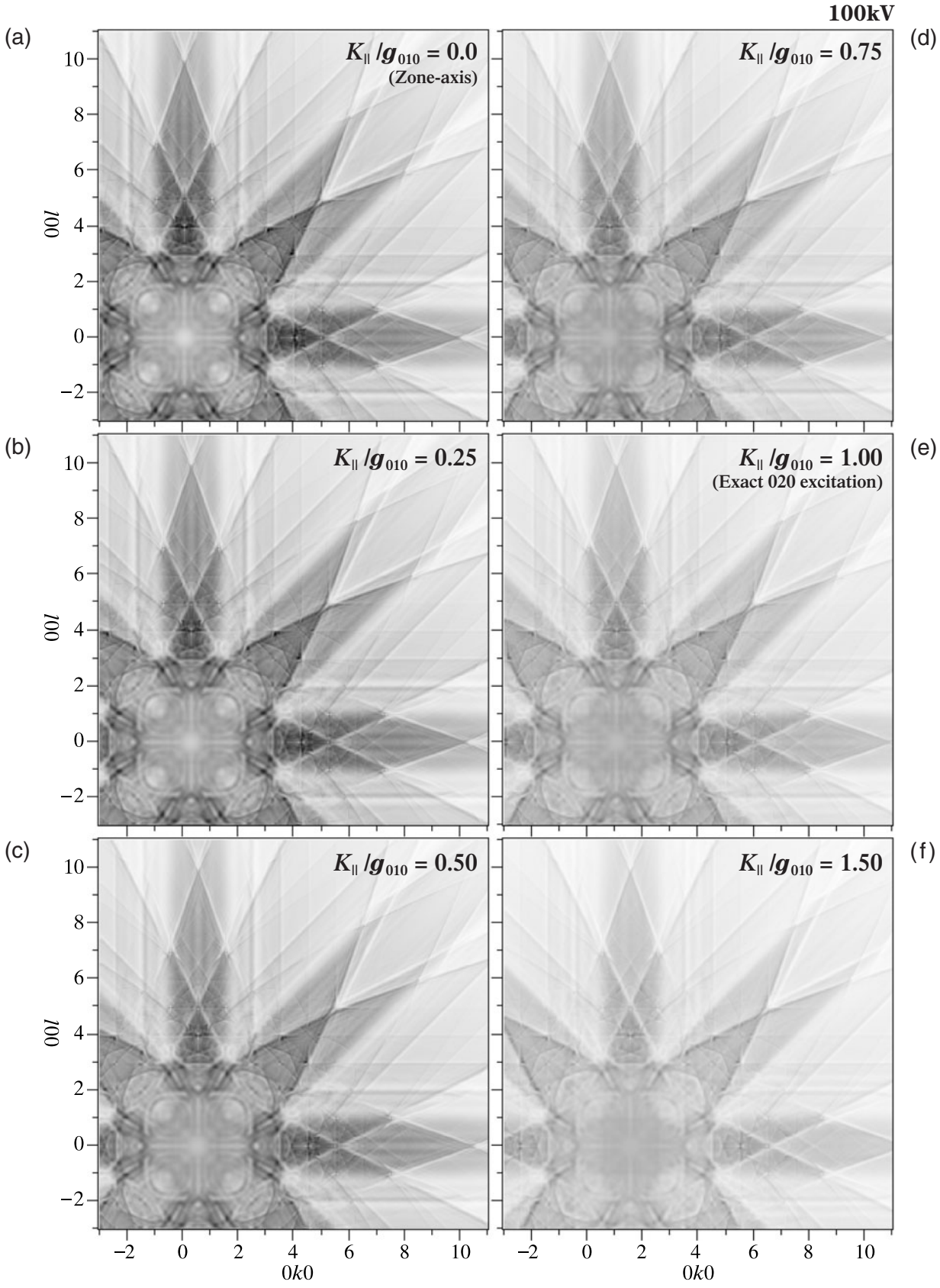
100kV
(a)
$K_{\parallel}/g_{010}$ = 0.0
(Zone-axis)
(b)
$K_{\parallel}/g_{010}$ = 0.25
(c)
$K_{\parallel}/g_{010}$ = 0.50
(d)
$K_{\parallel}/g_{010}$ = 0.75
(e)
$K_{\parallel}/g_{010}$ = 1.00
(Exact 020 excitation)
(f)
$K_{\parallel}/g_{010}$ = 1.50
100
0k0
10
8
6
4
2
0
−2

Line profiles

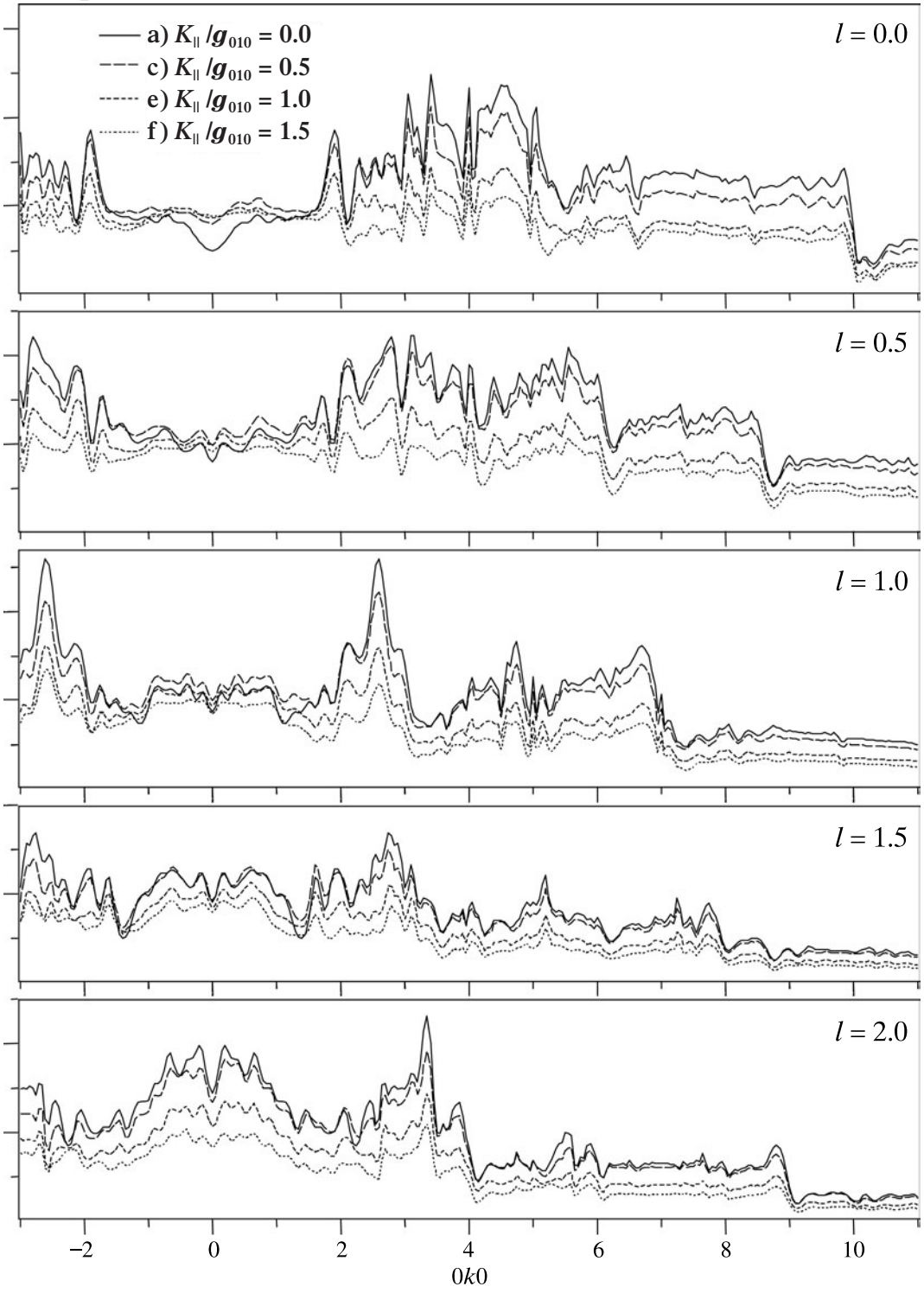

B-factor dependence

It is shown how the Kikuchi patterns of MgO at the [100] zone-axis incidence change with the Debye-Waller factors (*B* factors). Simulations were performed for five cases (a to e). The values of the *B* factors and the corresponding TDS scattering factors $T(\boldsymbol{Q},\boldsymbol{Q})$ are given in the figure. The line profiles of the patterns at different positions in the [001] direction are shown. It is seen that the intensities of the Kikuchi patterns increase with the increase of the *B* factors, or with the increase of the thermal motions of atoms.

Plots of TDS scattering factor $T(\boldsymbol{Q},\boldsymbol{Q})$ (Einstein model)

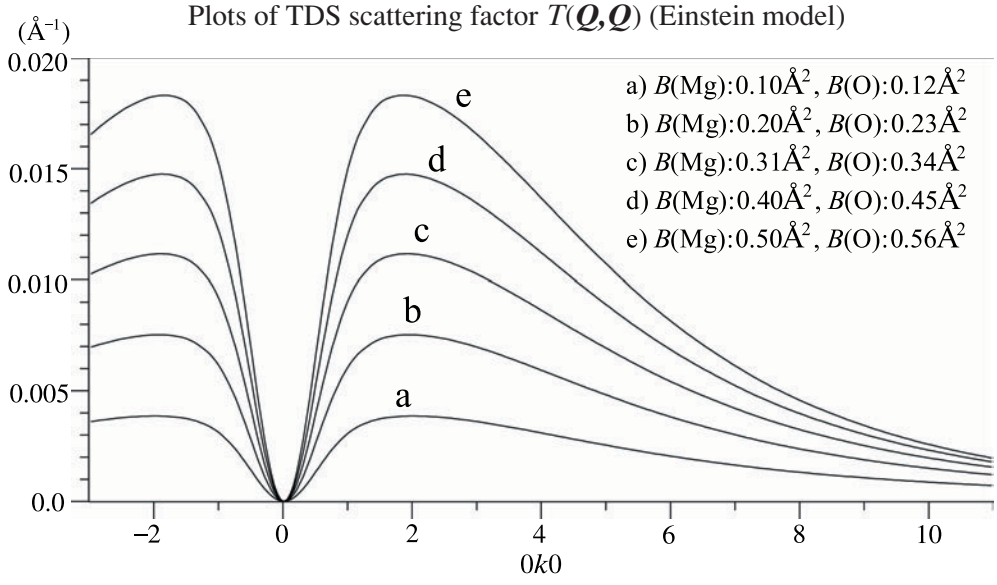

MgO [100]

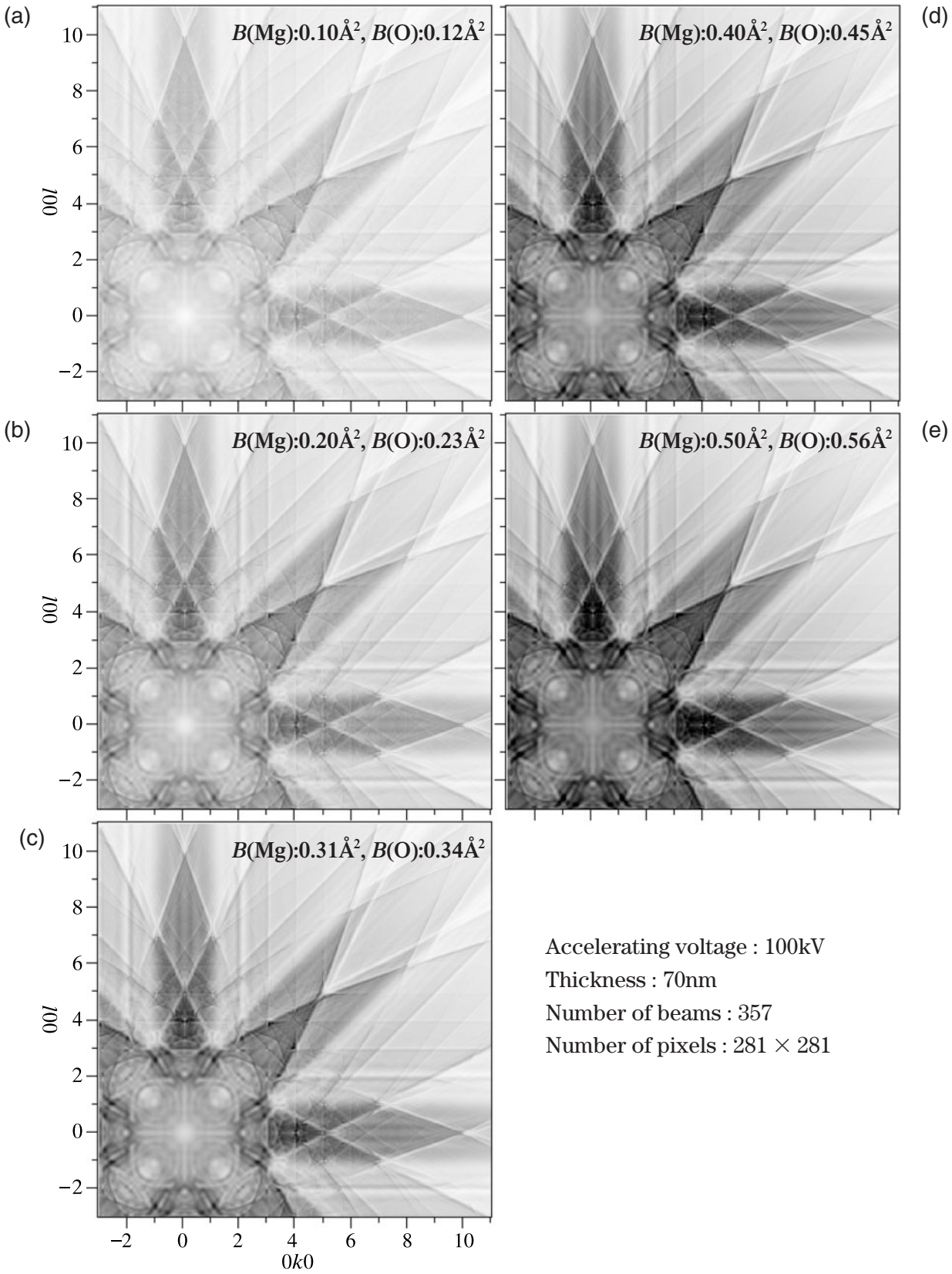

Accelerating voltage : 100kV
Thickness : 70nm
Number of beams : 357
Number of pixels : 281 × 281

Line profiles

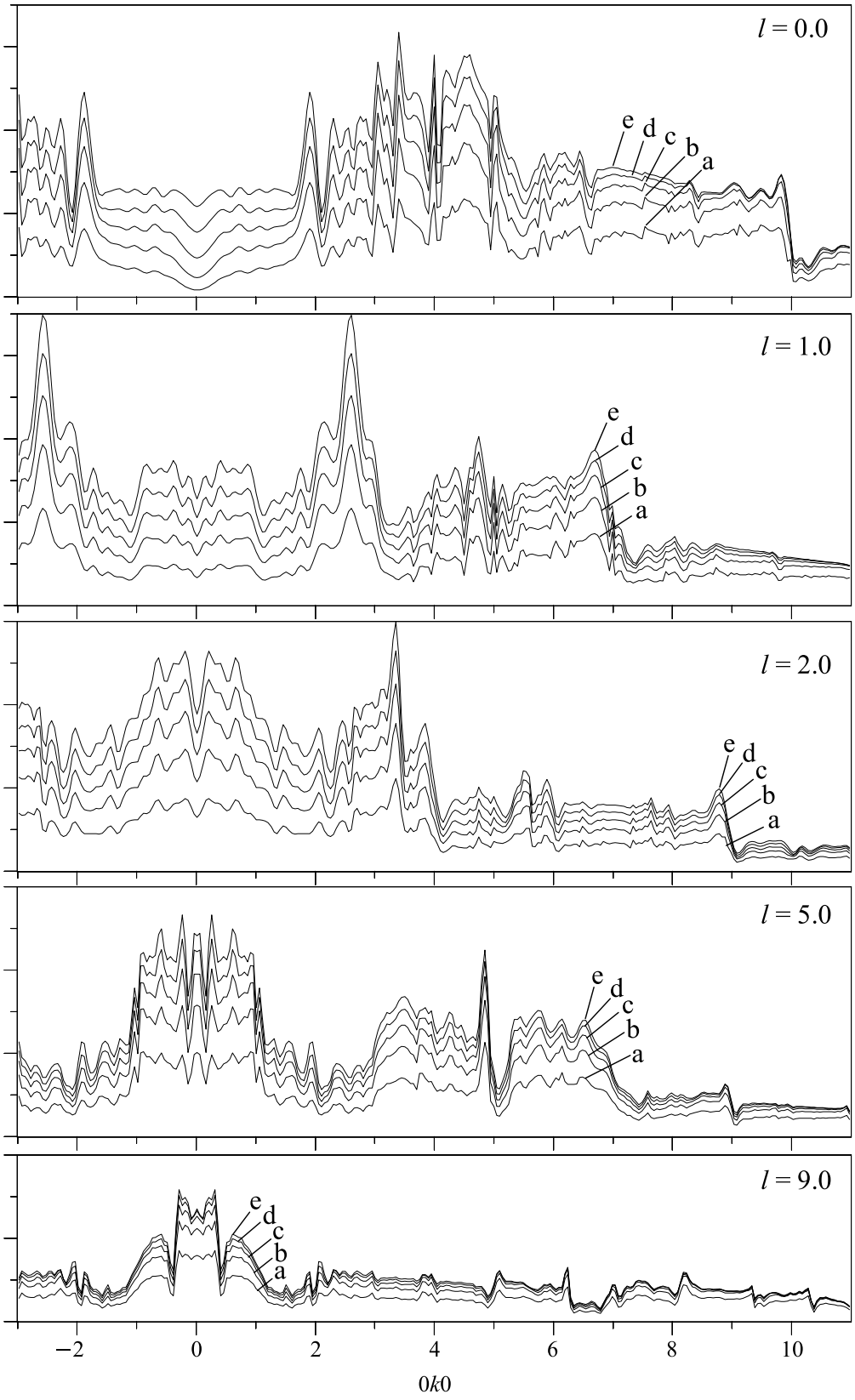

Contributions from constituent elements

MgO [100]

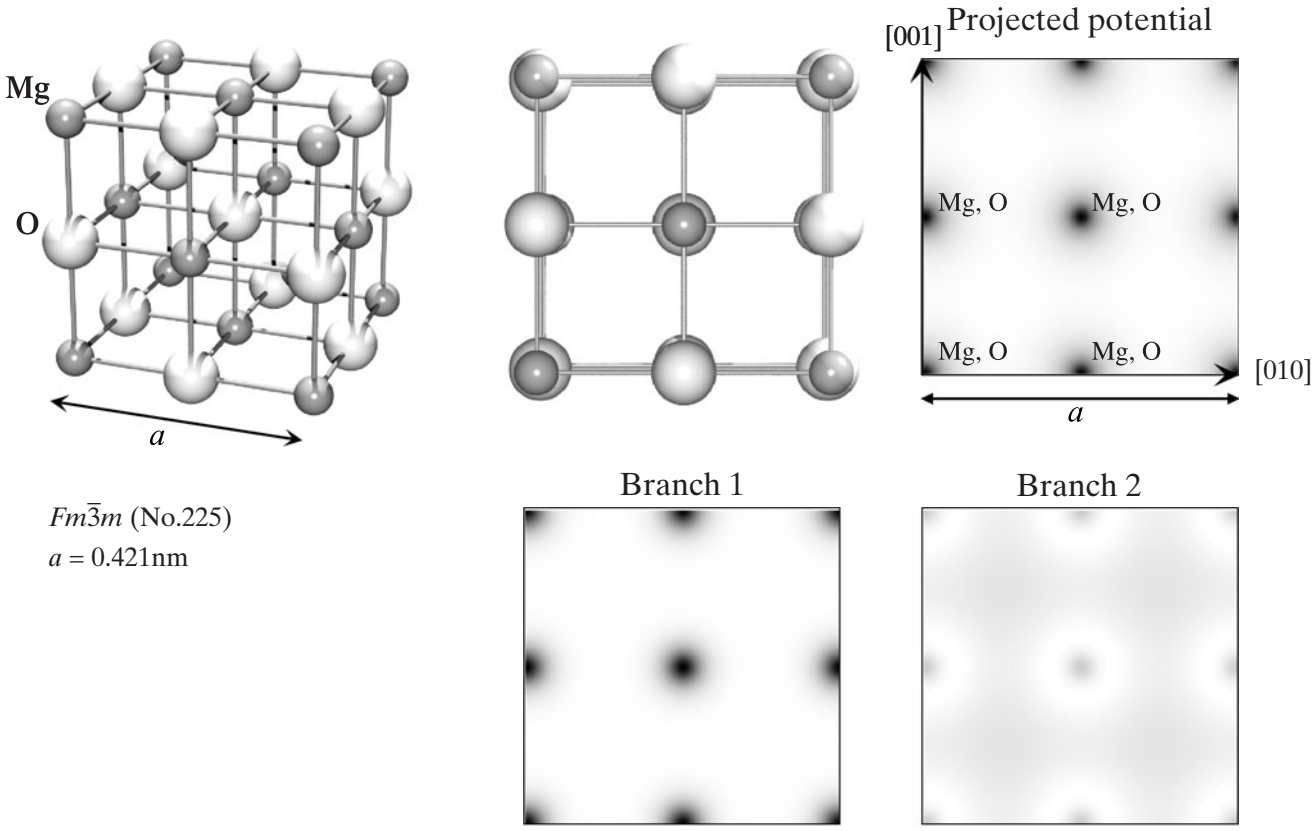

$Fm\bar{3}m$ (No.225)

a = 0.421nm

Branch	Excitation ratio
1	0.43
2	0.56

$T(\boldsymbol{Q},\boldsymbol{Q}')$ contains the sum of atom species. If summation is carried out only for a definite atom species, the contributions from different atom species can be separately calculated. A similar simulations can also be carried out by selecting a definite branch of the initially excited Bloch states because a Bloch state often forms its intensity maximum at the rows consisting of atoms of one kind.

In the case of the [100] incidence for MgO, Mg atoms are located on top of O atoms. Thus, the Kikuchi patterns produced by both atoms are the same but their intensities are different according to the difference of their atomic scattering factors. In the case of the [110] incidence for MgO, the branches 1 and 2 form high electron concentrations on Mg and O atom rows, respectively. The Kikuchi bands running in the upper-right direction have different intensity distributions between the patterns of Mg and O. That is, owing to the difference of the excitations of the branches (the sites of inelastic scattering) concerned, the innermost band is weaker than the next band in the pattern of O but the innermost band is stronger than the next band in the pattern of Mg.

In the case of the [001] incidence for TiO_2, the branches 1 and 5 form high electron concentrations on Ti and O atom rows, respectively. Since these two Bloch states are very different, the Kikuchi patterns formed by Ti and O atom rows appear very different. In the case of the [110] incidence for TiO_2, the result is similar to that of the MgO [110] case.

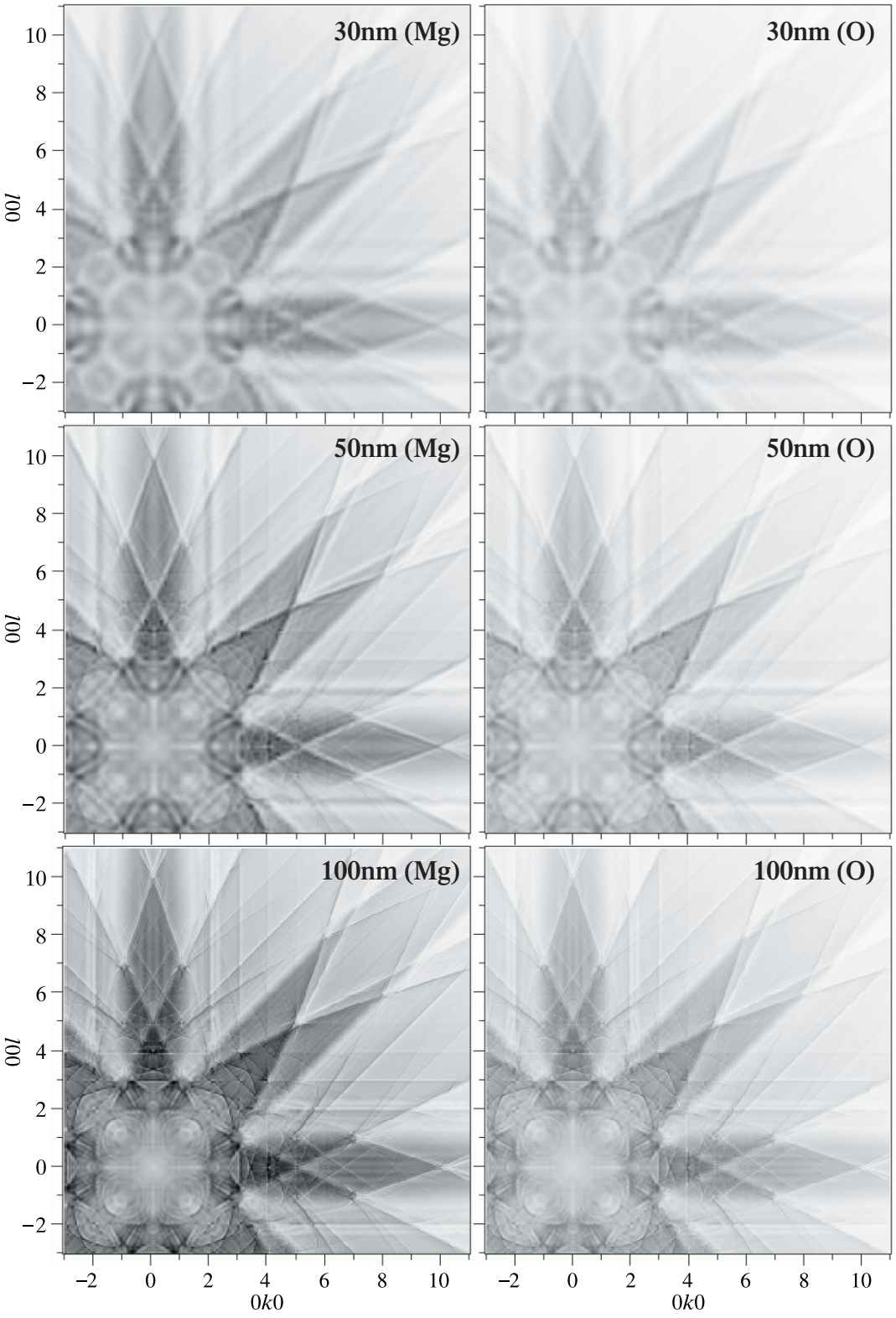

Accelerating voltage : 100kV
B(Mg) : 0.31Å^2, B(O) : 0.34Å^2

Number of beams : 357
Number of pixels : 281 × 281

MgO [110]

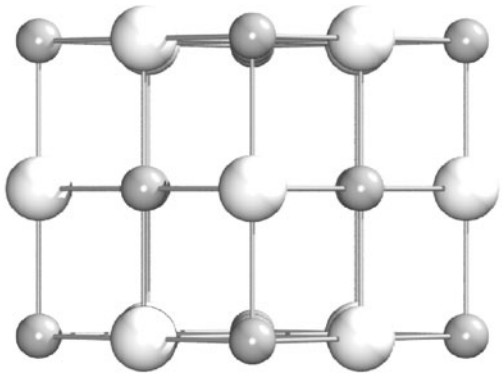

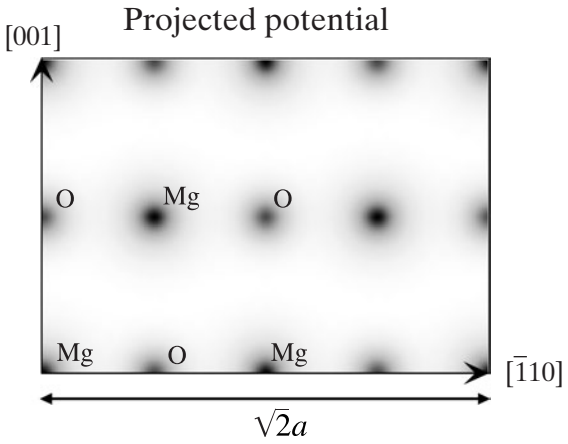

Branch 1

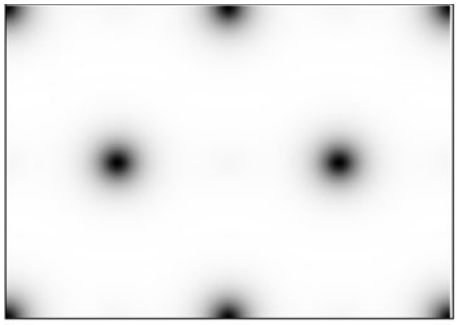

Branch 2

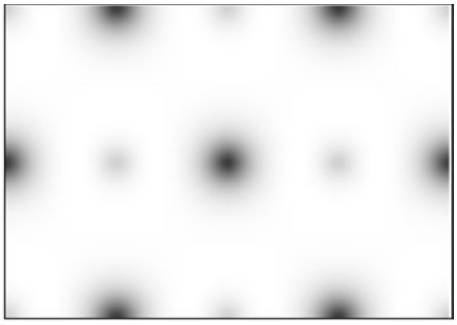

Branch 4

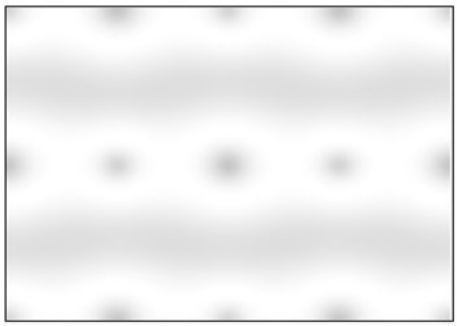

Branch 8

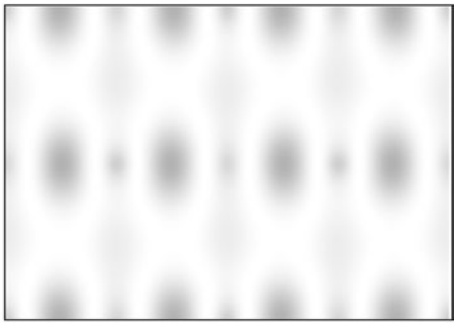

Branch	Excitation ratio
1	0.54
2	0.23
4	0.22
8	0.01

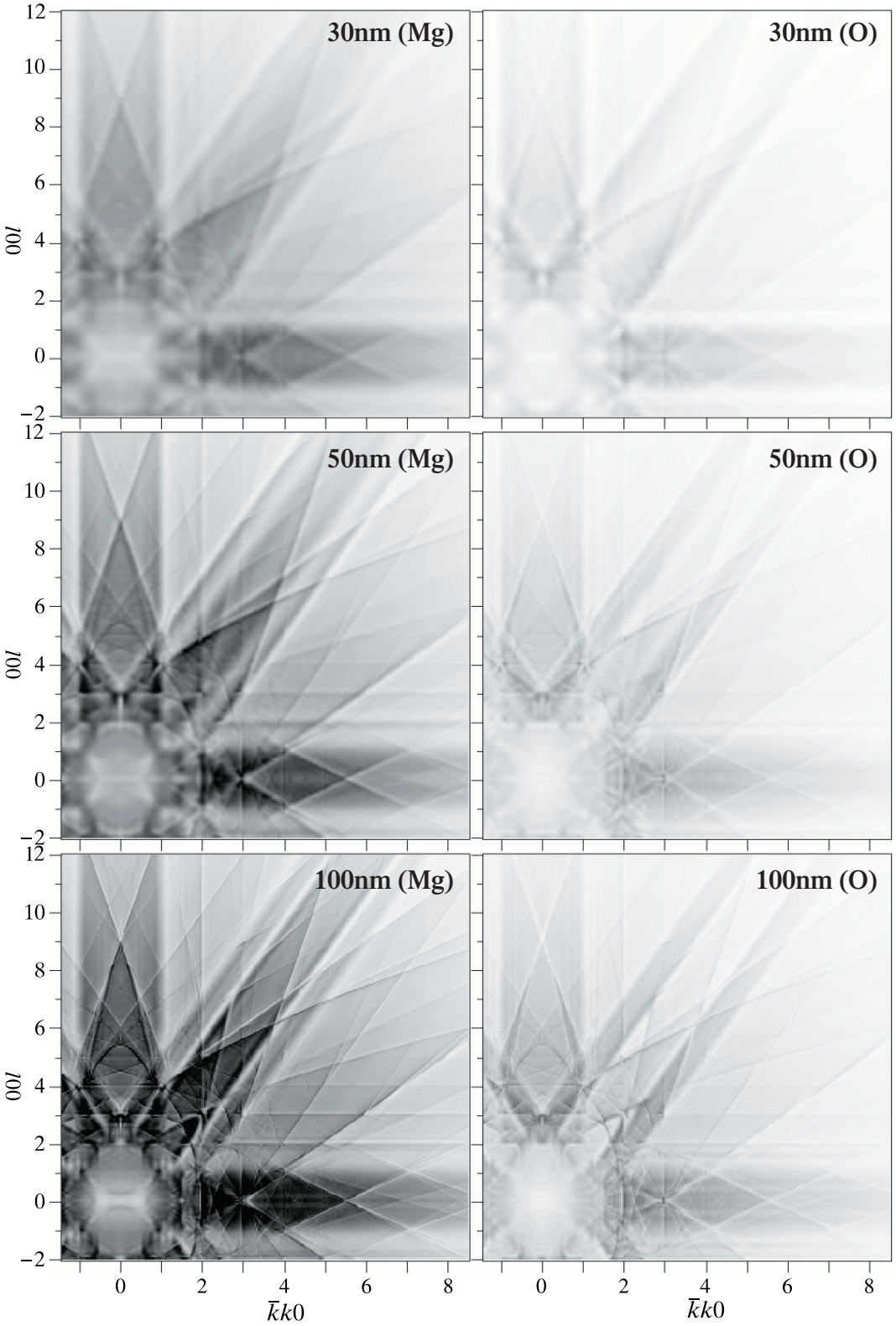

Accelerating voltage : 100kV
B(Mg) : 0.31Å^2, B(O) : 0.34Å^2

Number of beams : 315
Number of pixels : 279 × 281

TiO_2 [001]

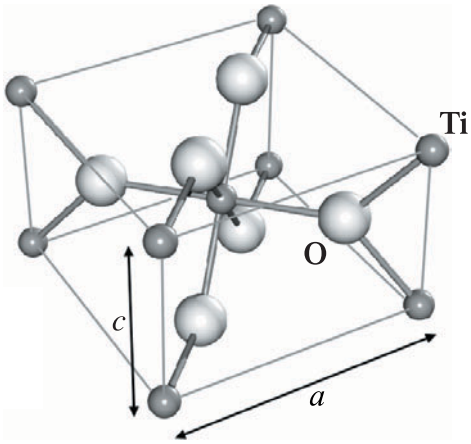

$P4_2/mnm$ (No.136)
a = 0.459nm
c = 0.296nm

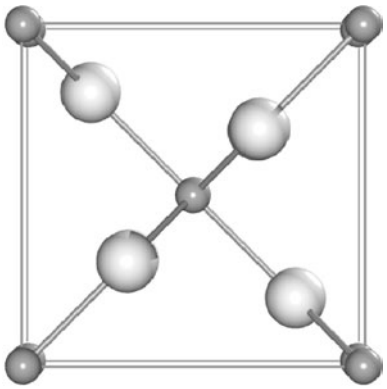

[010] Projected potential

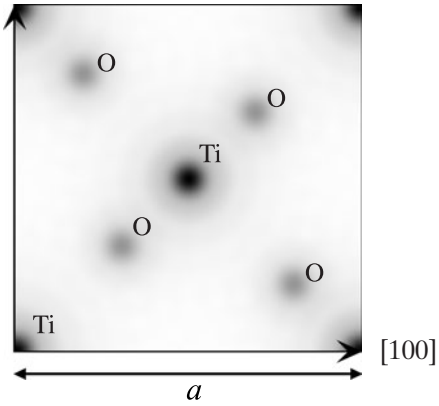

Branch 1

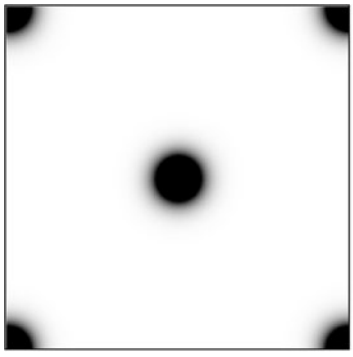

Branch 5

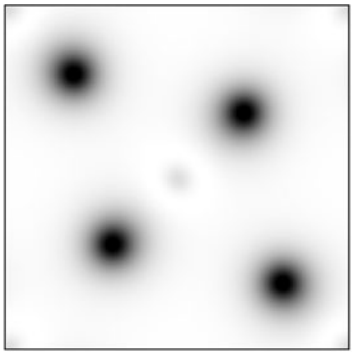

Branch 13

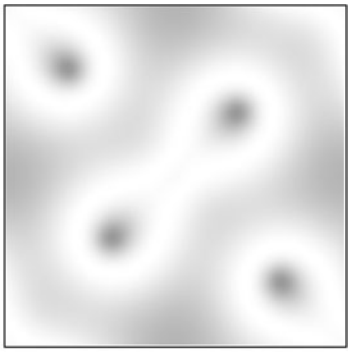

Branch	Excitation ratio
1	0.12
5	0.56
13	0.30

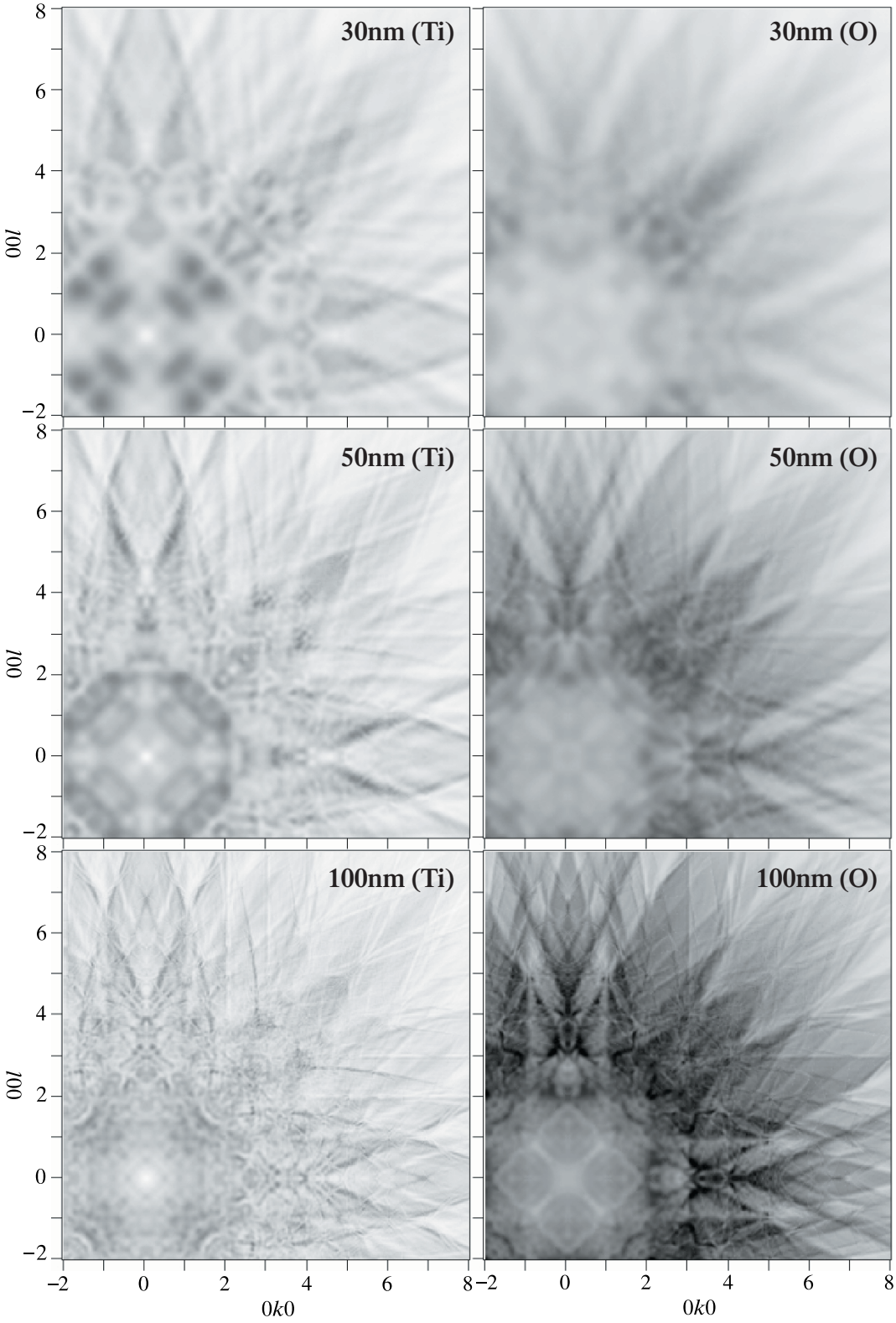

Accelerating voltage : 100kV
B(Ti) : 0.35Å^2, B(O) : 0.44Å^2

Number of beams : 553
Number of pixels : 301 × 301

TiO_2 [110]

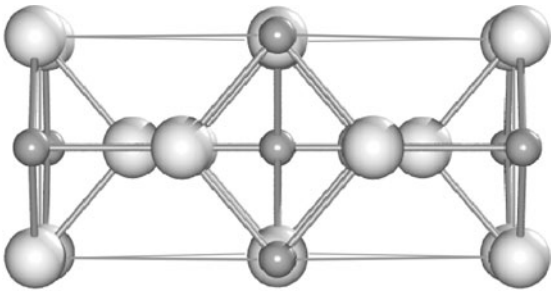

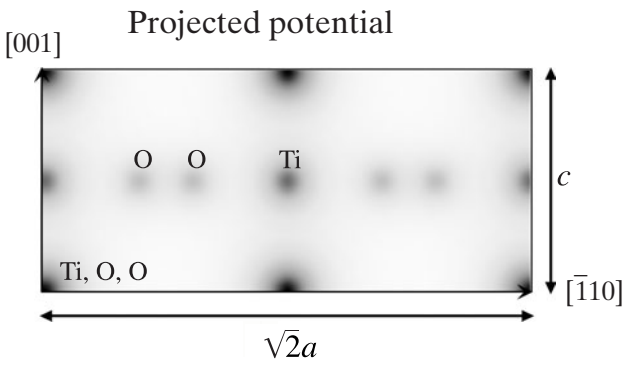

Branch 1

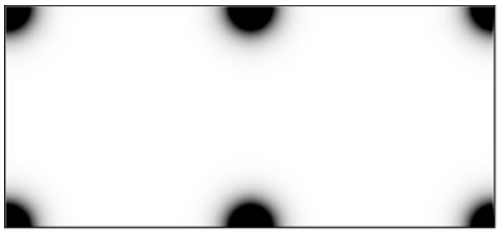

Branch 2

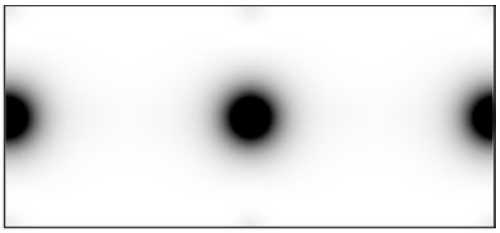

Branch 3

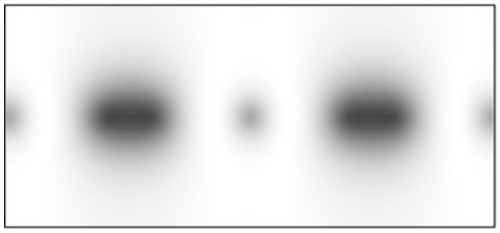

Branch 6

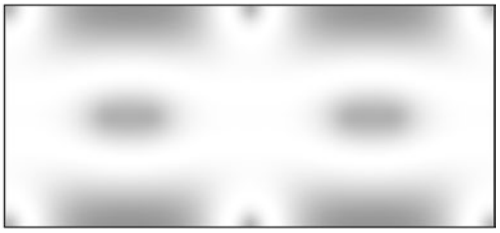

Branch	Excitation ratio
1	0.16
2	0.34
3	0.34
6	0.14

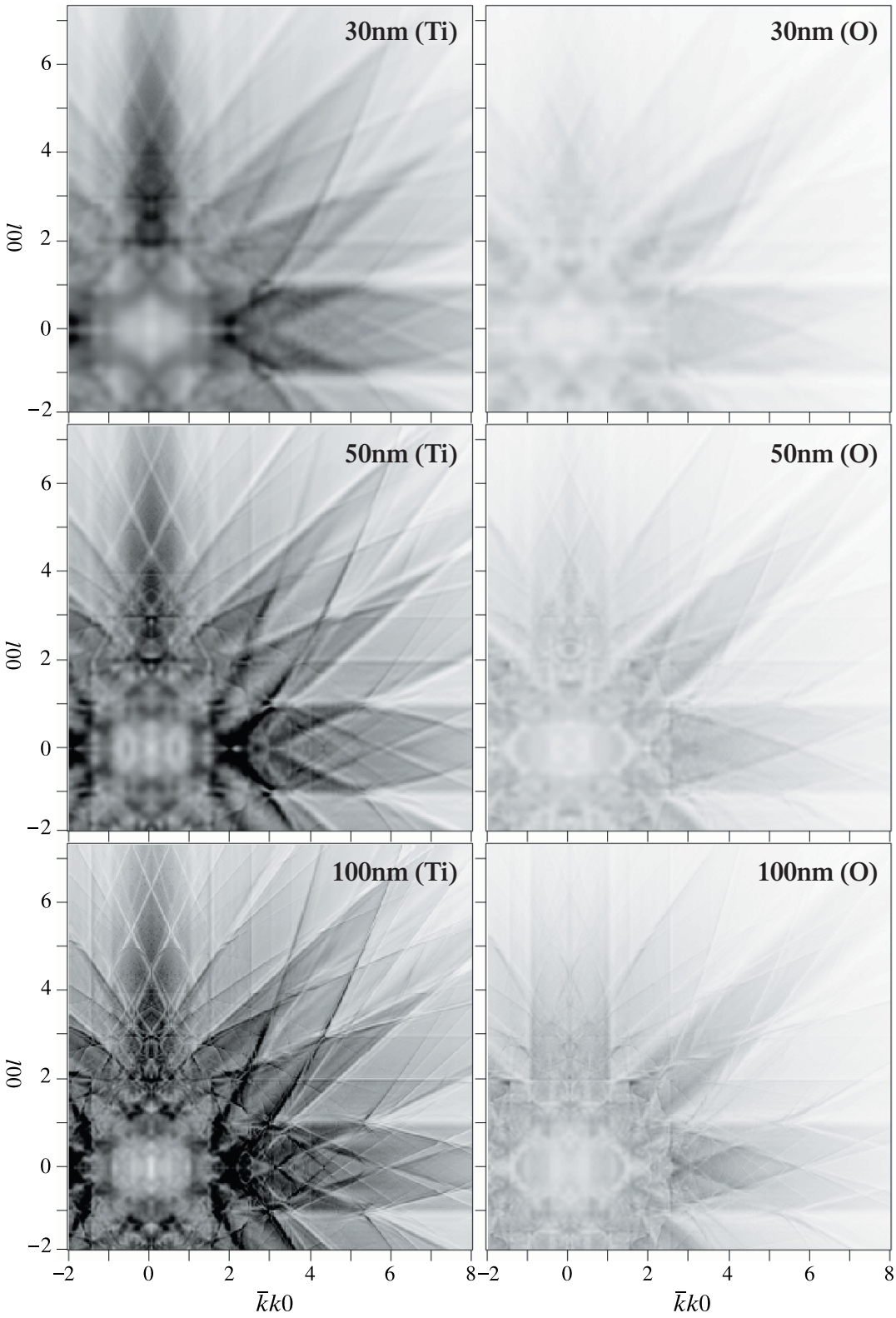

Accelerating voltage : 100kV
B(Ti) : 0.35Å^2, B(O) : 0.44Å^2

Number of beams : 315
Number of pixels : 301 × 295

Beam-number dependence

MgO [100]

It is shown how the simulation areas of the Kikuchi patterns extend with the increase of the beam number and how the precision of the pattern is improved with the beam number.

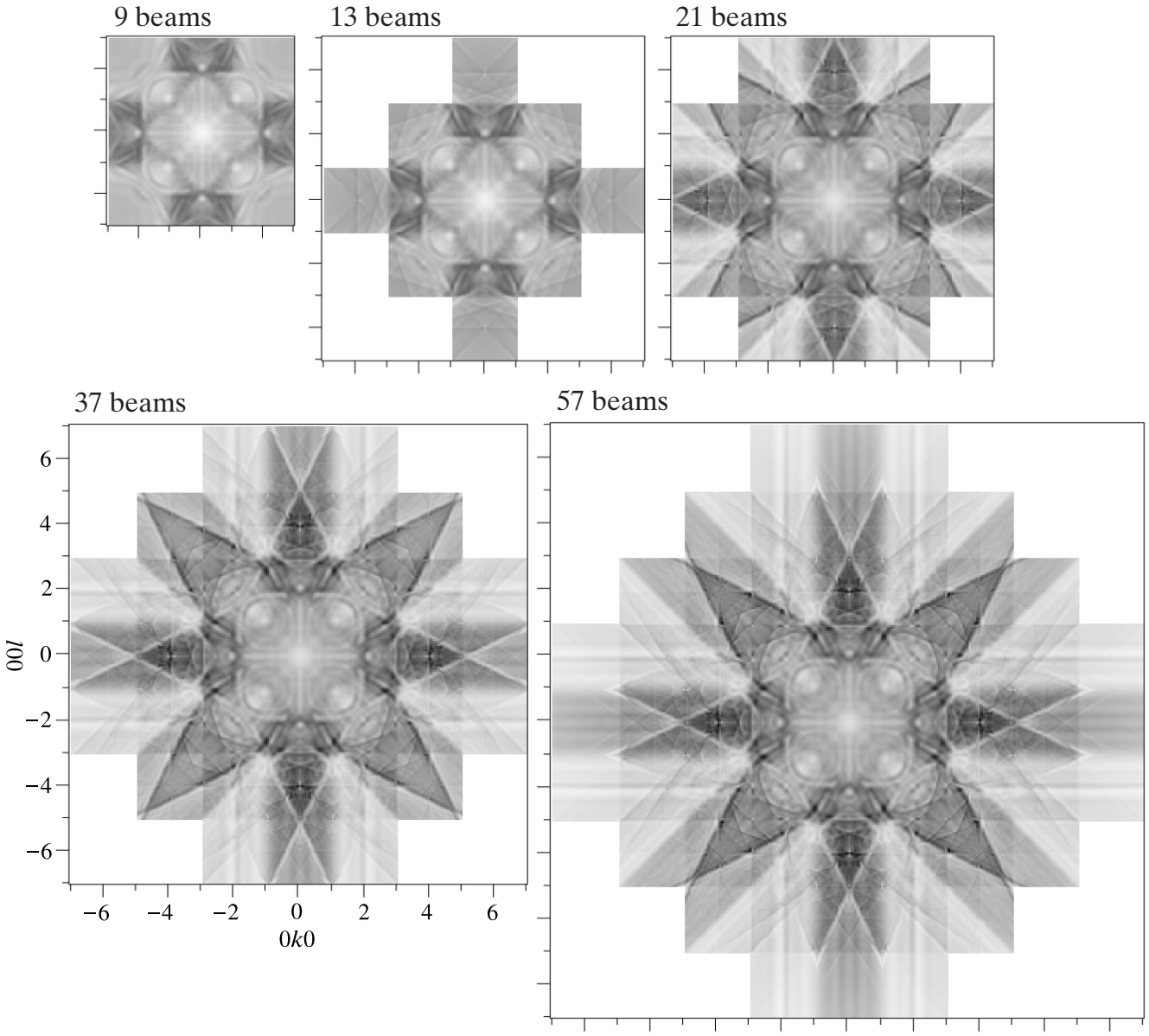

Enlargements of the central parts

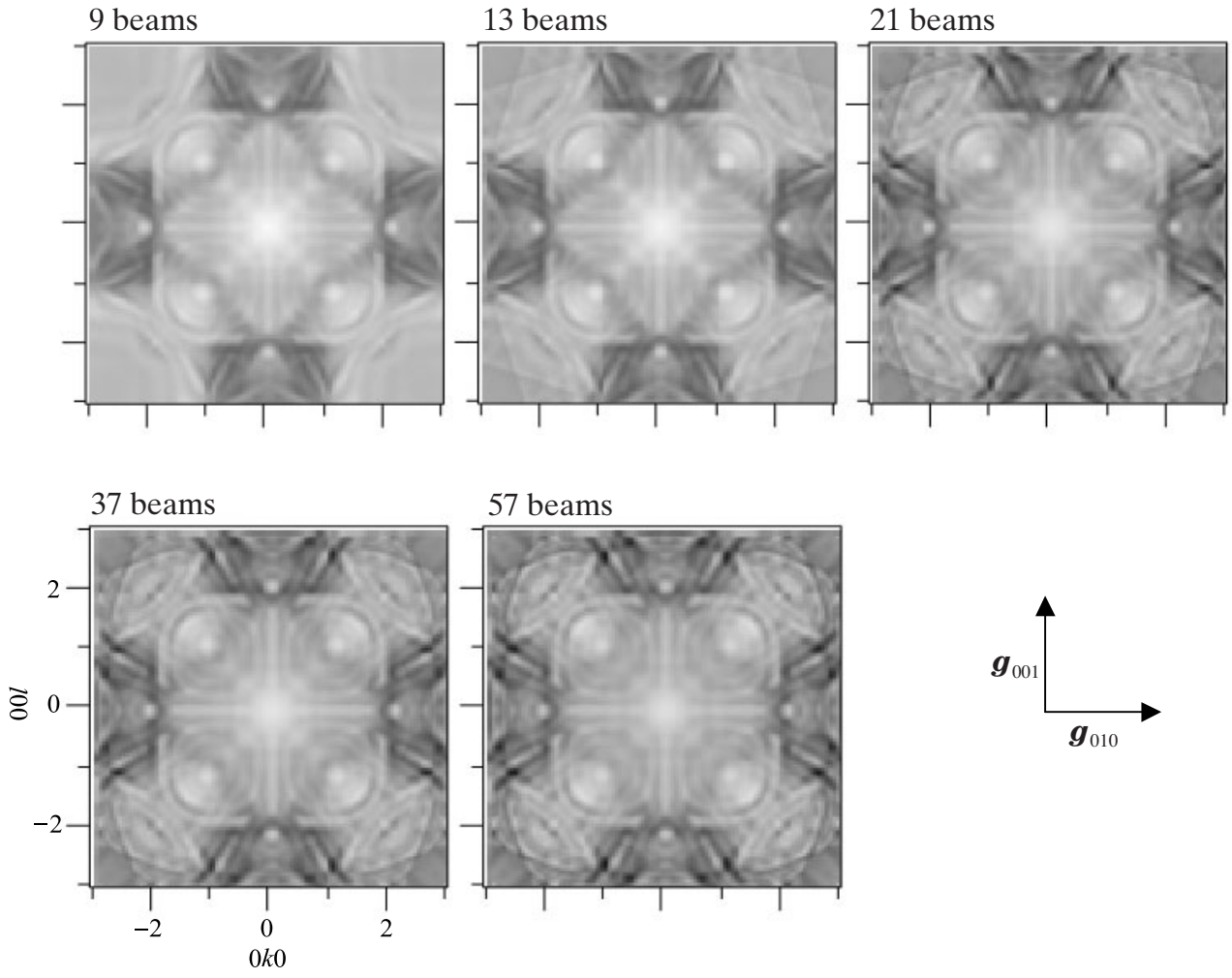

Details are clearly seen with the increase in the beam number.

Precision of the patterns

The central parts of the Kikuchi patterns of MgO at the [100] zone-axis incidence simulated with 37, 57 and 69 beams are displayed in the left column of the figures. Differences between those patterns and the pattern simulated with 357 beams are shown in the middle column. The difference patterns enhanced by 4 times in intensity are shown in the right column.

On the right-side page, the Kikuchi patterns extending to high angles are displayed, which are simulated with 357, 277 and 221 beams. The differences between the latter two patterns and the pattern with 357 beams are shown on the right. The difference patterns are enhanced by 32 times in intensity.

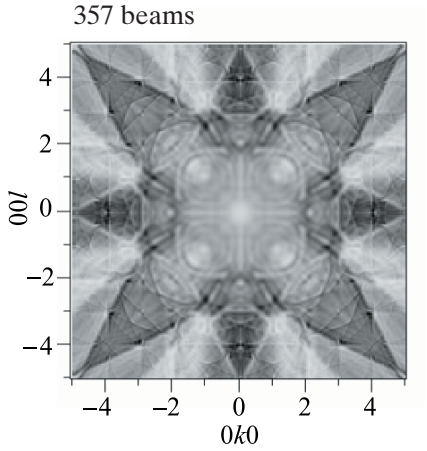

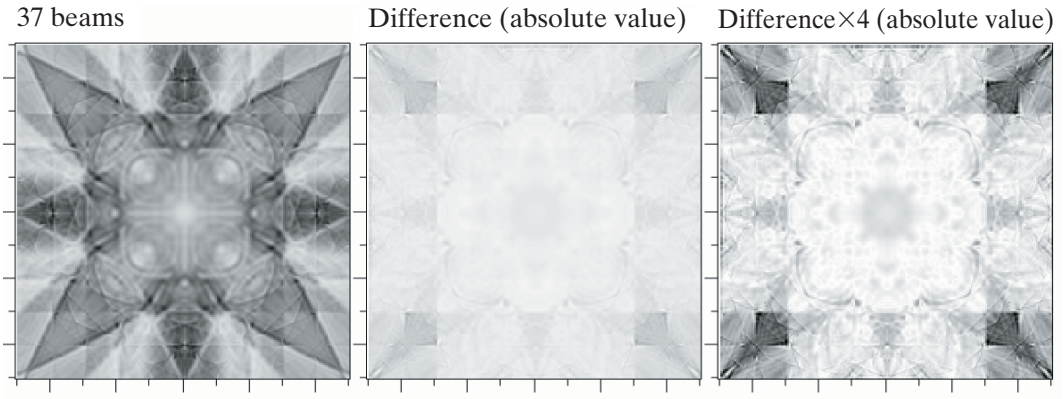

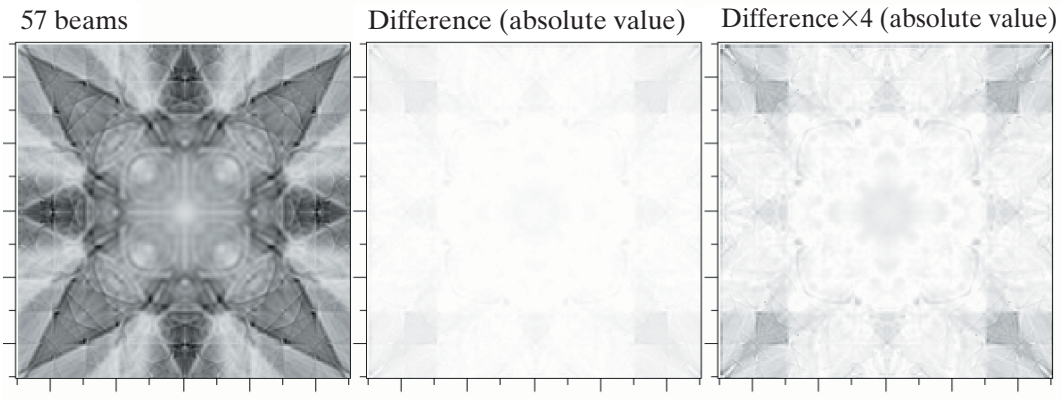

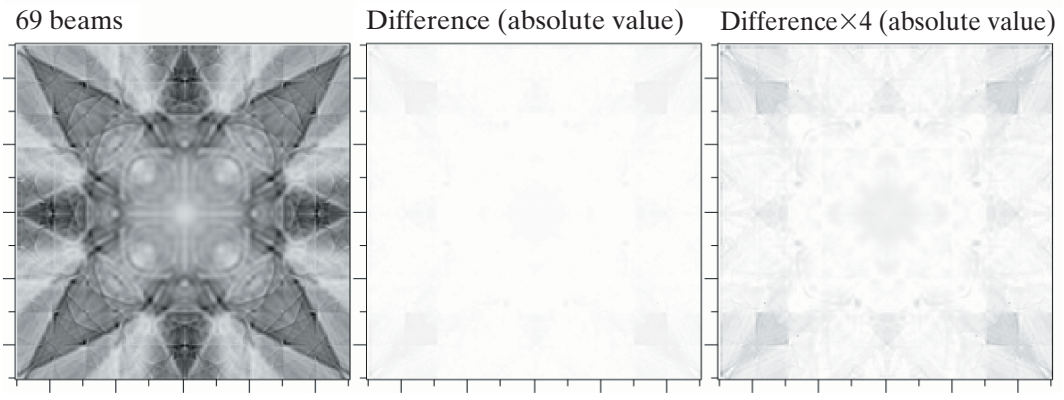

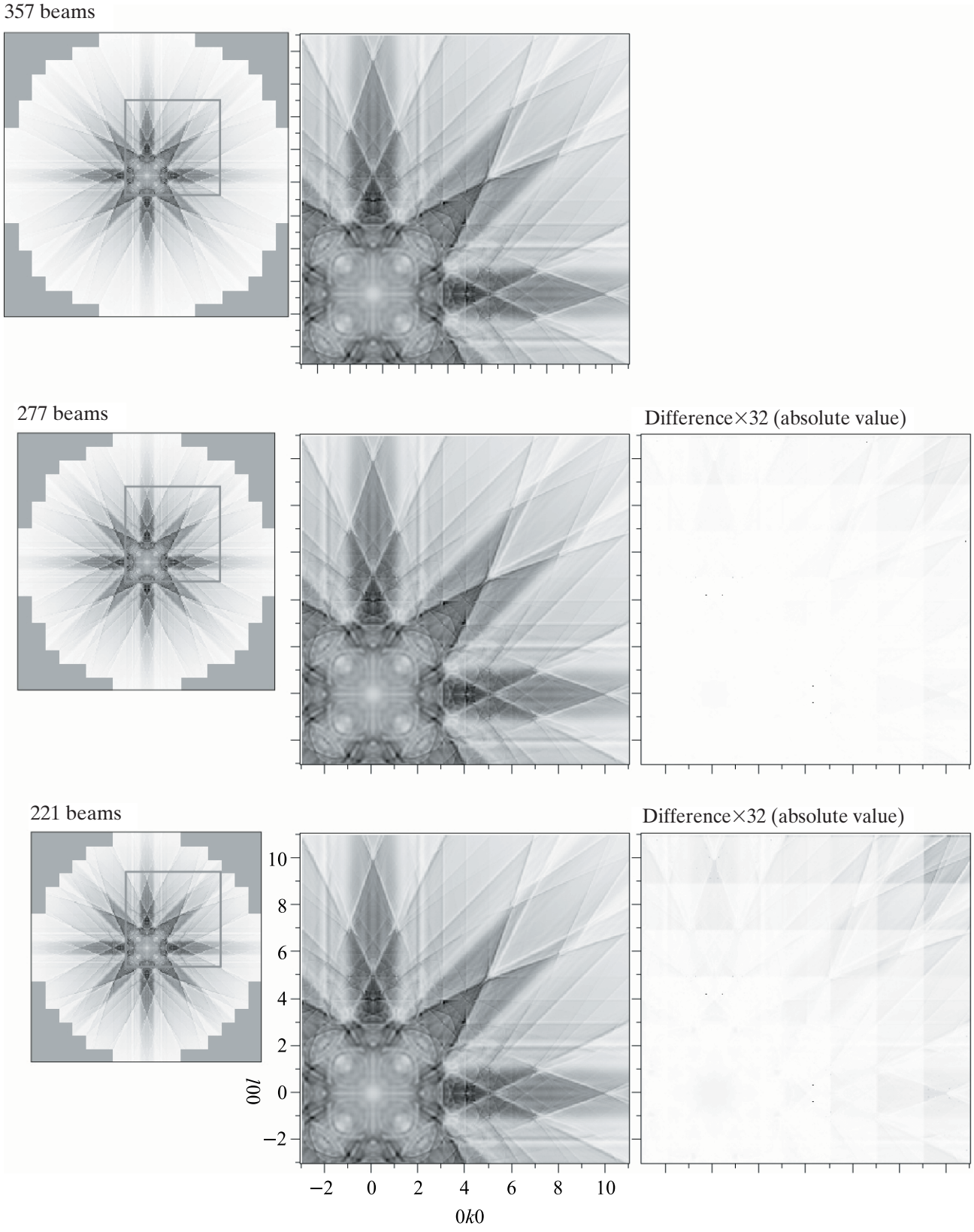
357 beams
277 beams
Difference×32 (absolute value)
221 beams
Difference×32 (absolute value)
10
8
6
4
2
0
−2
h00
−2
0
2
4
6
8
10
0k0

Comparison Between Experimental and Simulated Patterns (Zone-Axis Cases)

Simulated zone-axis Kikuchi patterns are compared with experimental patterns for MgO [100], MgO [110], Al [100] and TiO_2 [111]. All the experimental diffraction patterns are energy-filtered zero-loss patterns taken with the JEM-2010FEF at an accelerating voltage of 100kV. The simulations agree very well with the experiments. That is, not only the Kikuchi lines and bands at high angles but also the detailed patterns at the central area are reproduced very well. It is seen that the thickness dependence and incidence-orientation dependence are also reproduced well by the simulations. Only some intensity differences in the vicinity of the incident beam exist between experiments and simulations, which may be attributed to other origins.

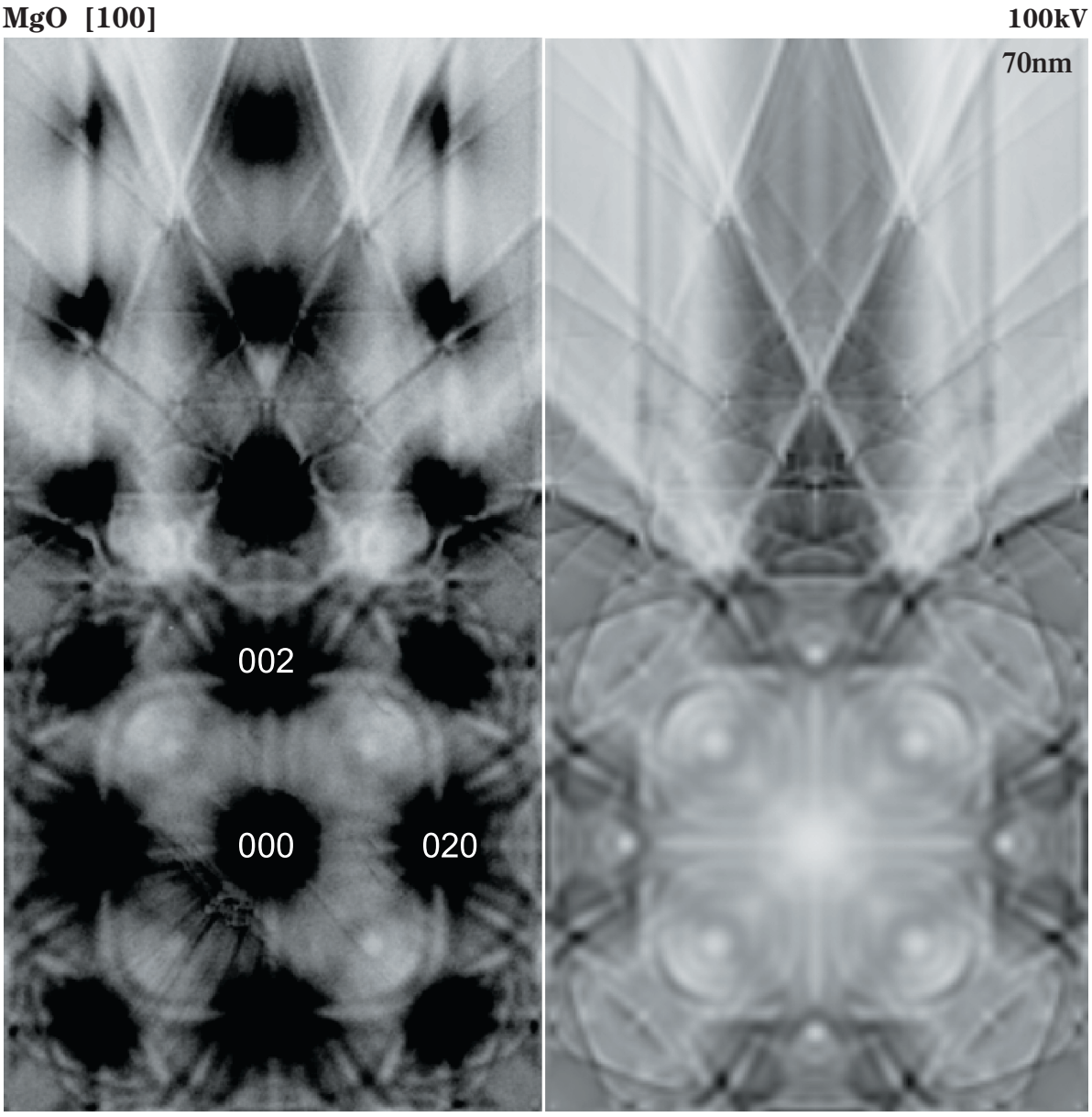

Experiment Simulation

MgO [100]

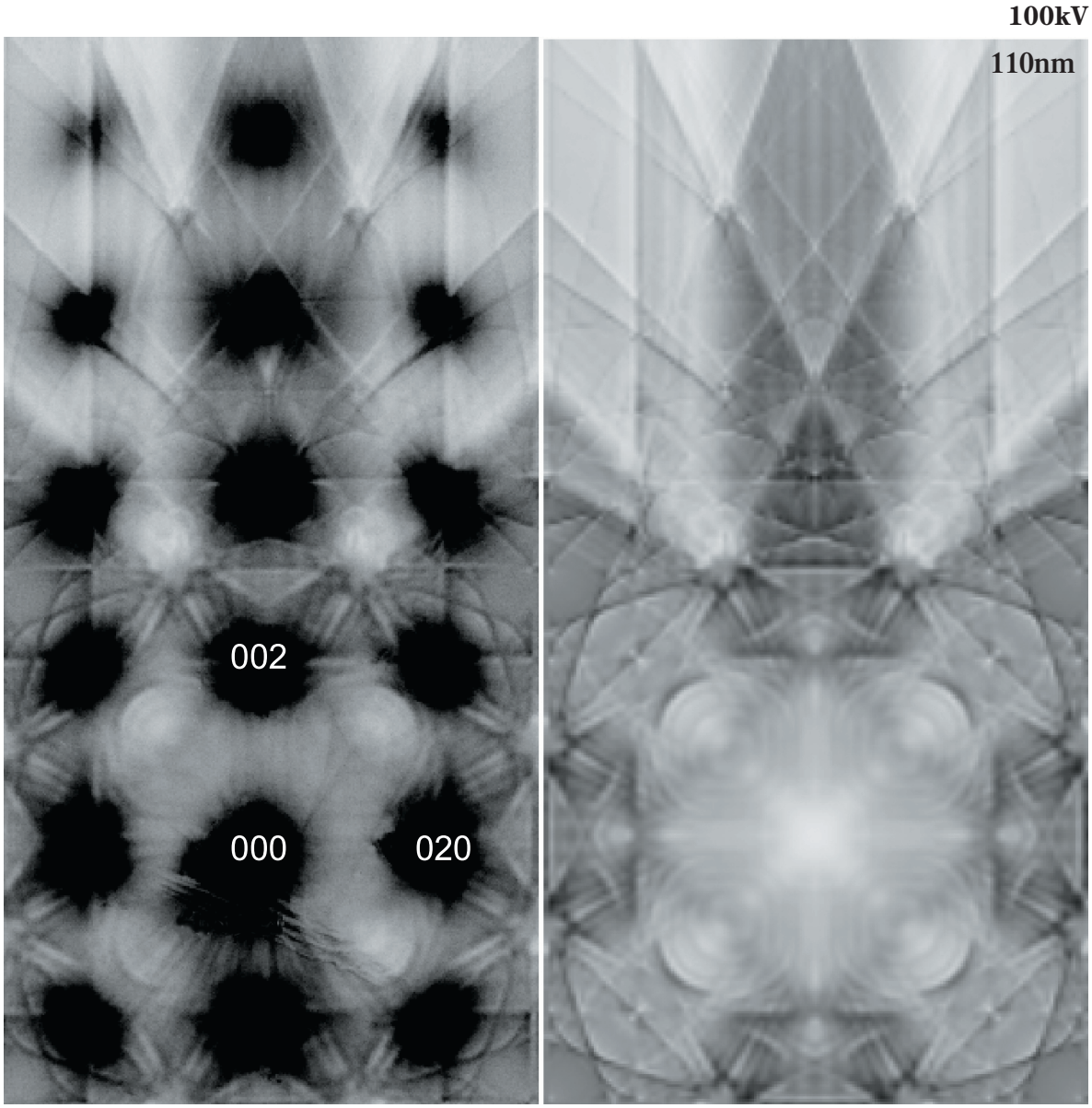

Experiment Simulation

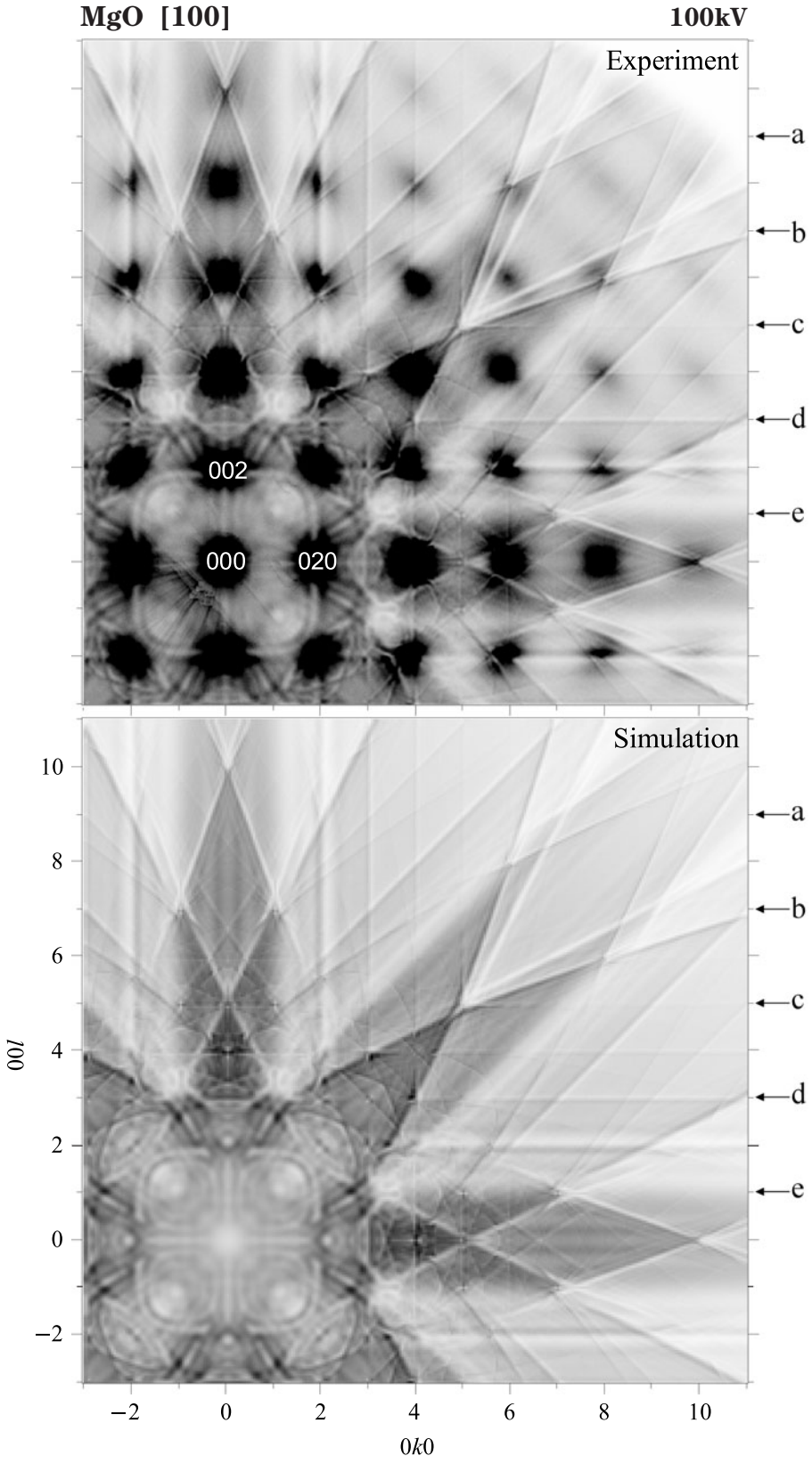
MgO [100]
100kV
Experiment
a
b
c
d
e
002
000
020
Simulation
a
b
c
d
e
10
8
6
4
2
0
−2
00l
−2
0
2
4
6
8
10
0k0

Line profiles

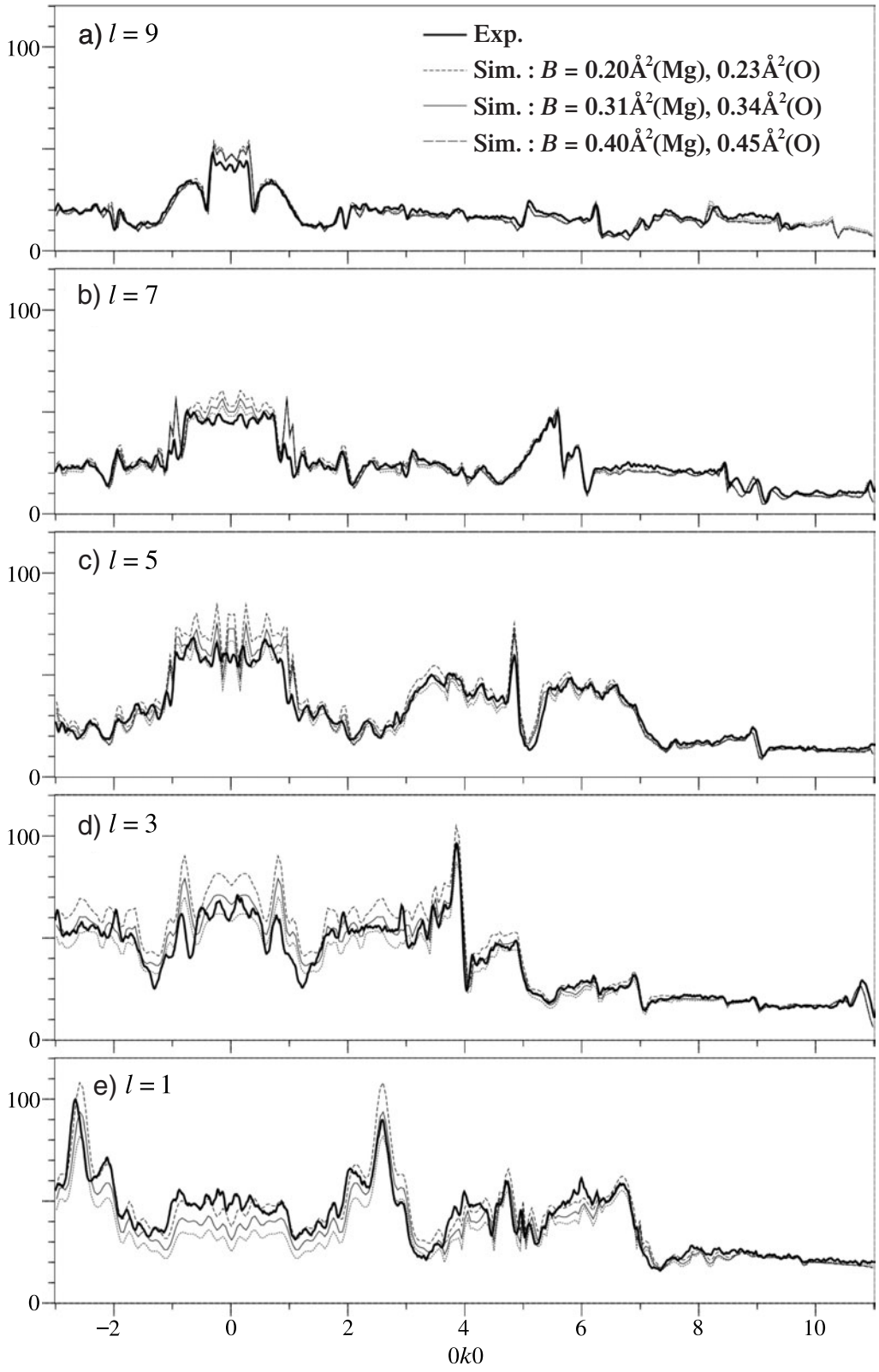

Thickness dependence

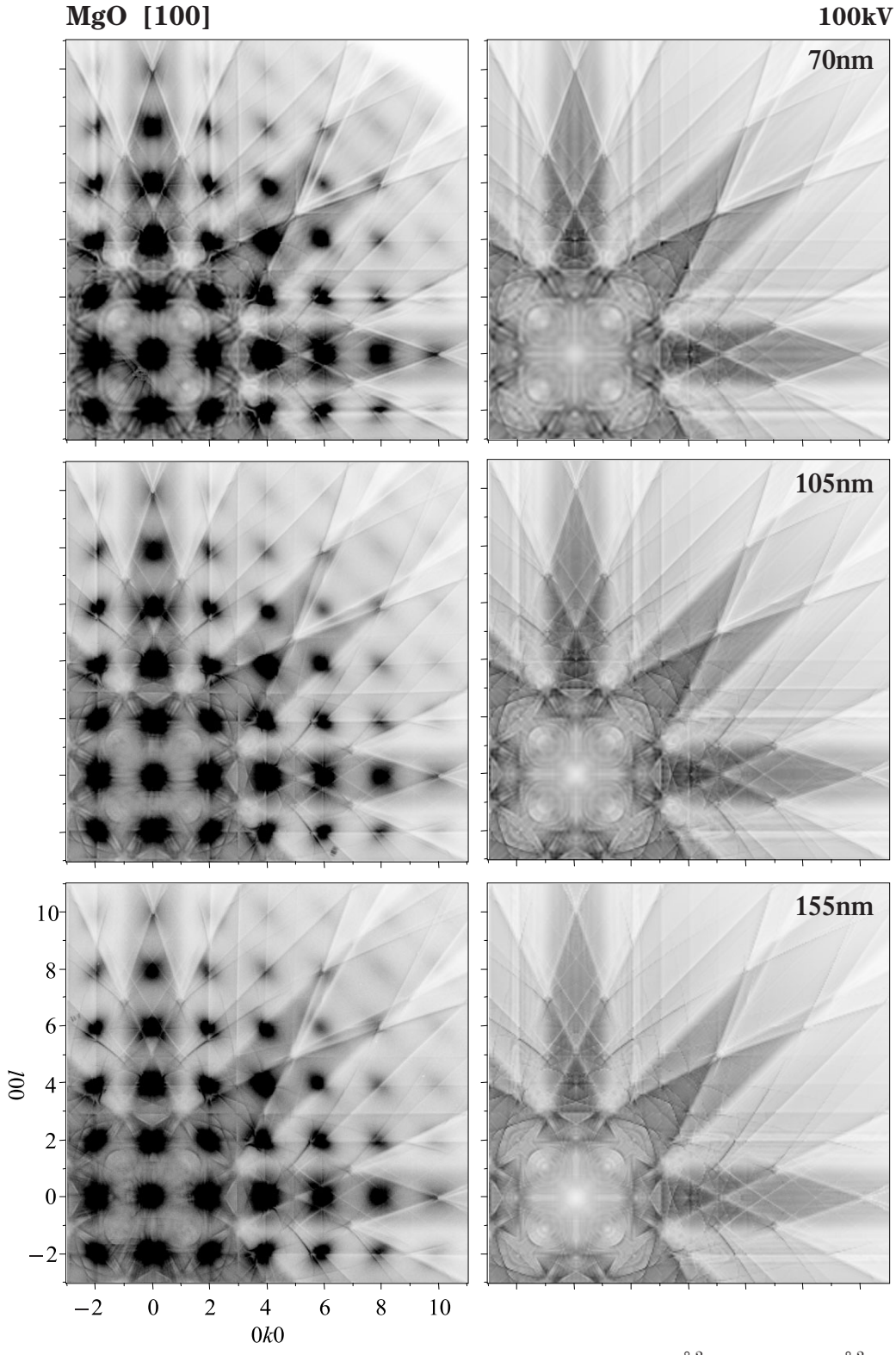

B(Mg) : 0.31Å^2, B(O) : 0.34Å^2
Number of beams : 277
Number of pixels : 281 × 281

Incidence-orientation dependence

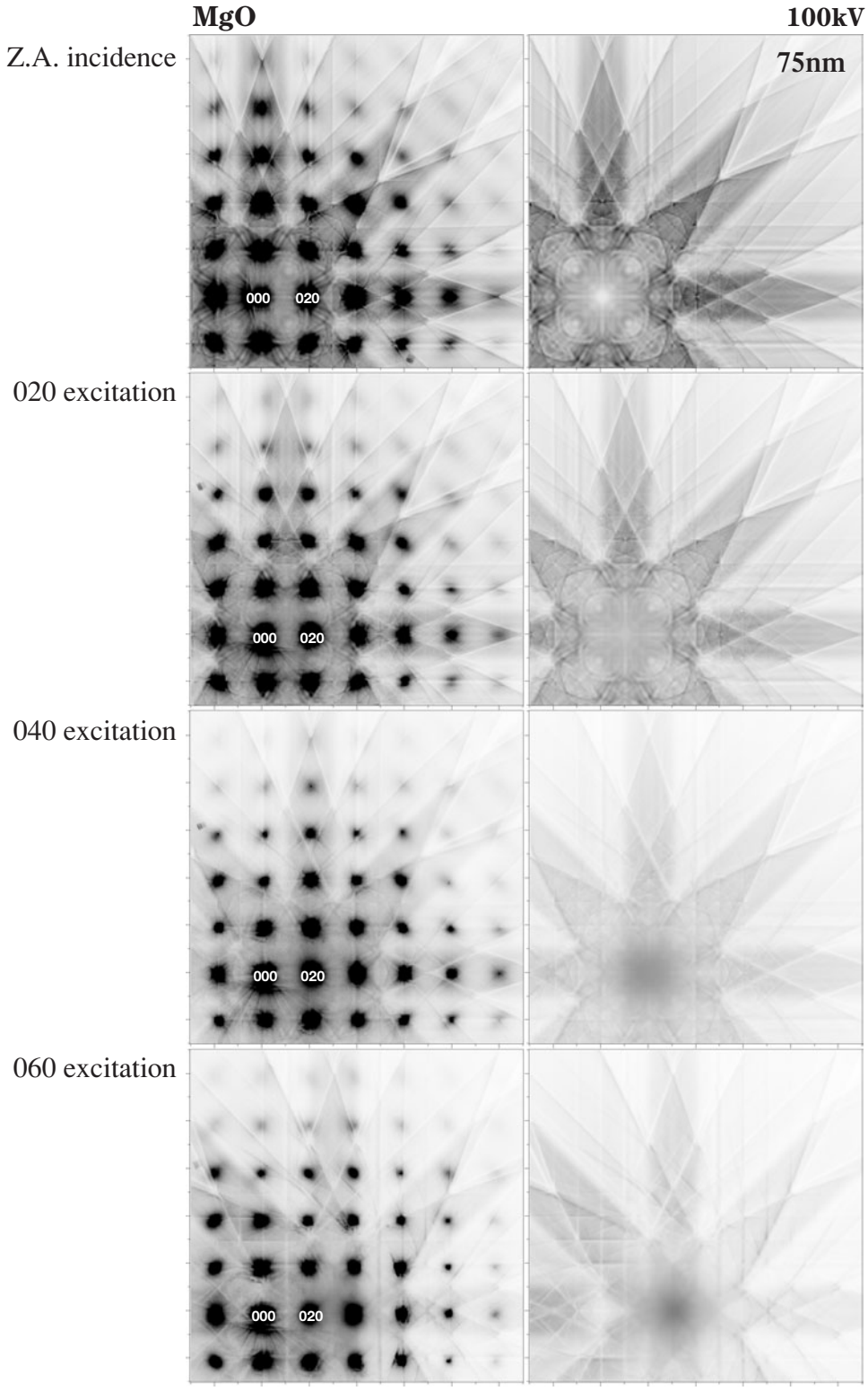

B(Mg) : 0.31Å^2, B(O) : 0.34Å^2
Number of beams : 277
Number of pixels : 281 × 281

CBED patterns

Figure (a) shows an experimentally obtained energy-filtered zero-loss CBED pattern and Fig. (b) shows a simulated CBED pattern superposed on a Kikuchi pattern, where the B factors were assumed to be 0.31Å^2 for Mg and 0.34Å^2 for O. The simulated Kikuchi pattern is constructed by a weighted average of the intensities for five different incidences $K_{\parallel}/\boldsymbol{g}_{010}$ = 0.0 (Z.A.), 0.2, 0.4, 0.6 and 0.8. The both patterns are displayed by $(I/I_{max})^{\gamma}$, where I_{max} is the maximal value of the intensity in the pattern and γ = 0.15. Overall, the agreement appears good. Since the detailed profiles around the cross center of the Kikuchi bands are hidden by the CBED disks, the CBED pattern is not appropriate for the detailed examination of the simulation of the Kikuchi pattern.

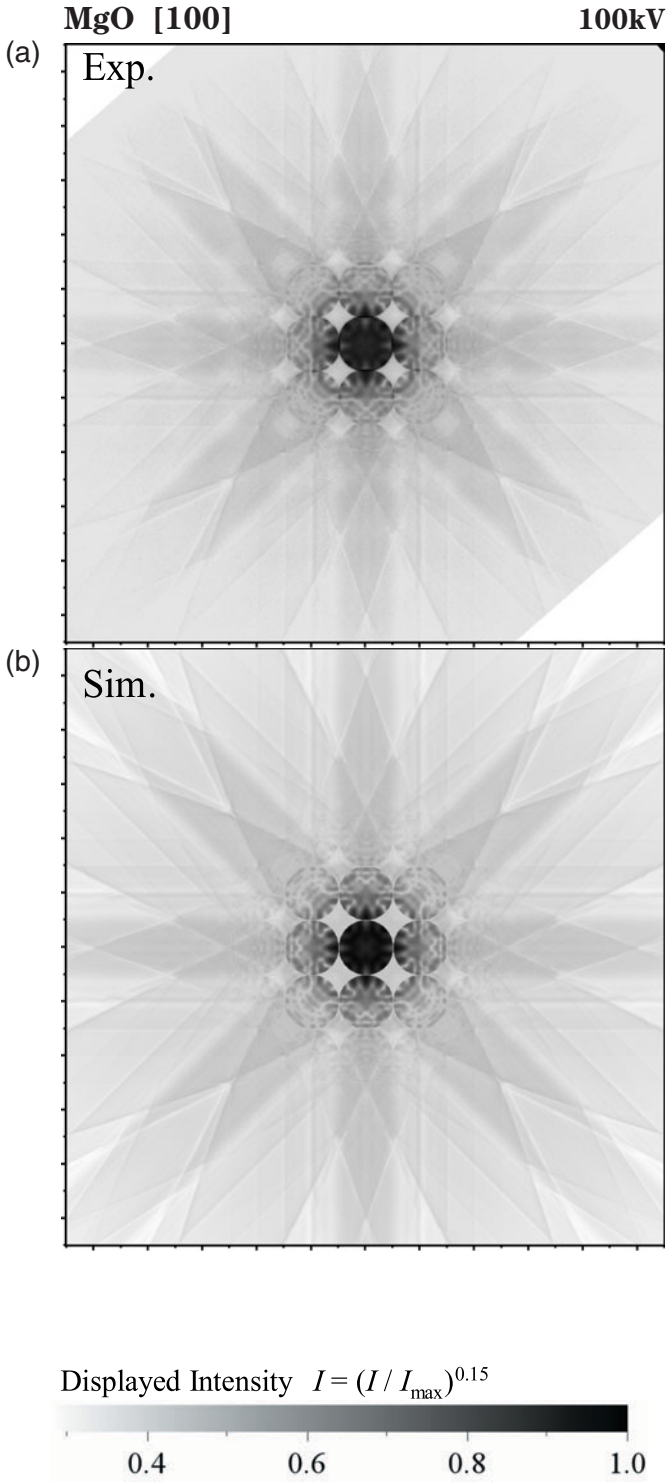

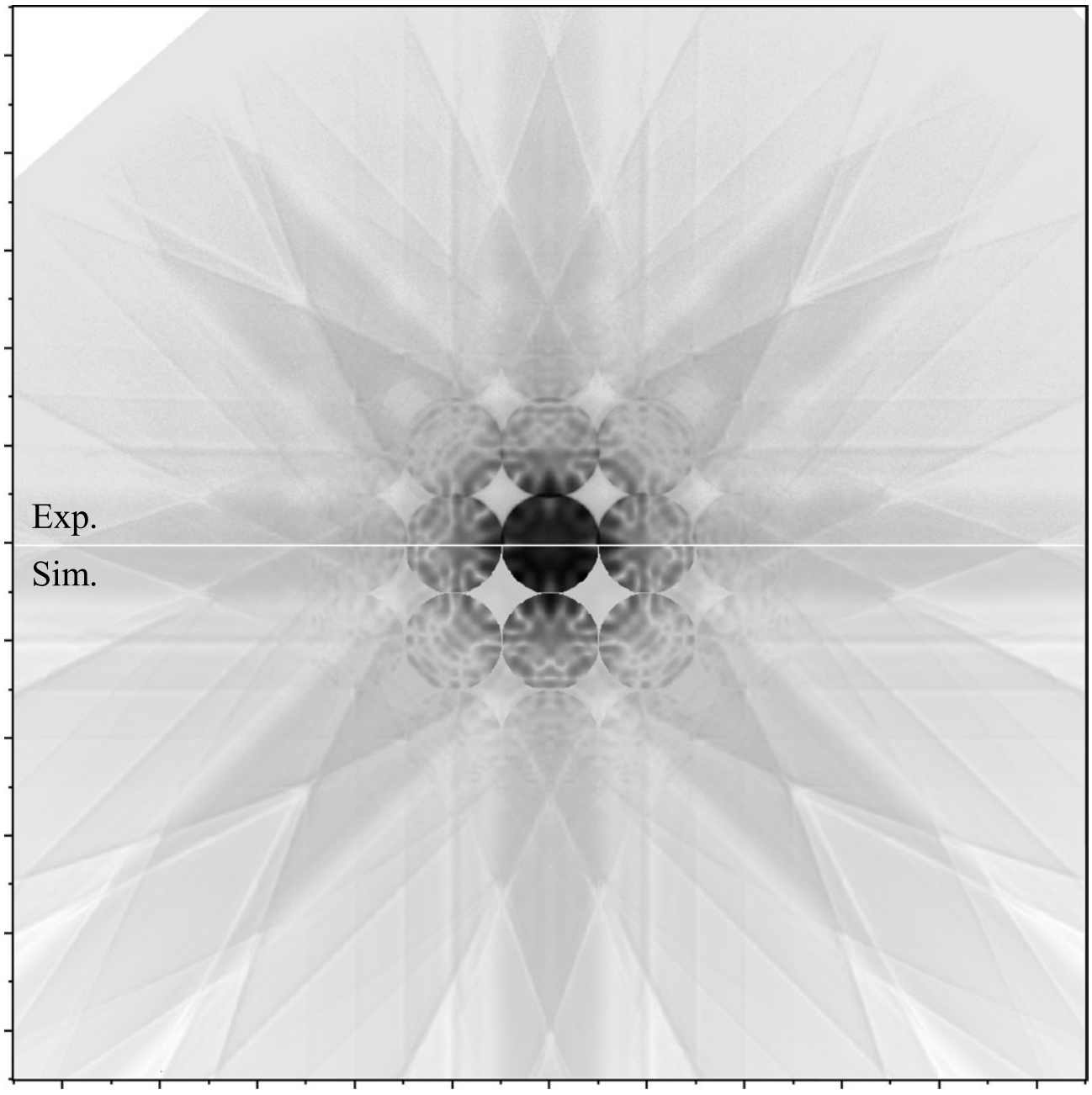

The upper half of the experimental pattern is displayed with the lower half of the simulated pattern. A high-precision reproduction of the experimental pattern by the simulation is noted.

MgO [110]

Thickness dependence

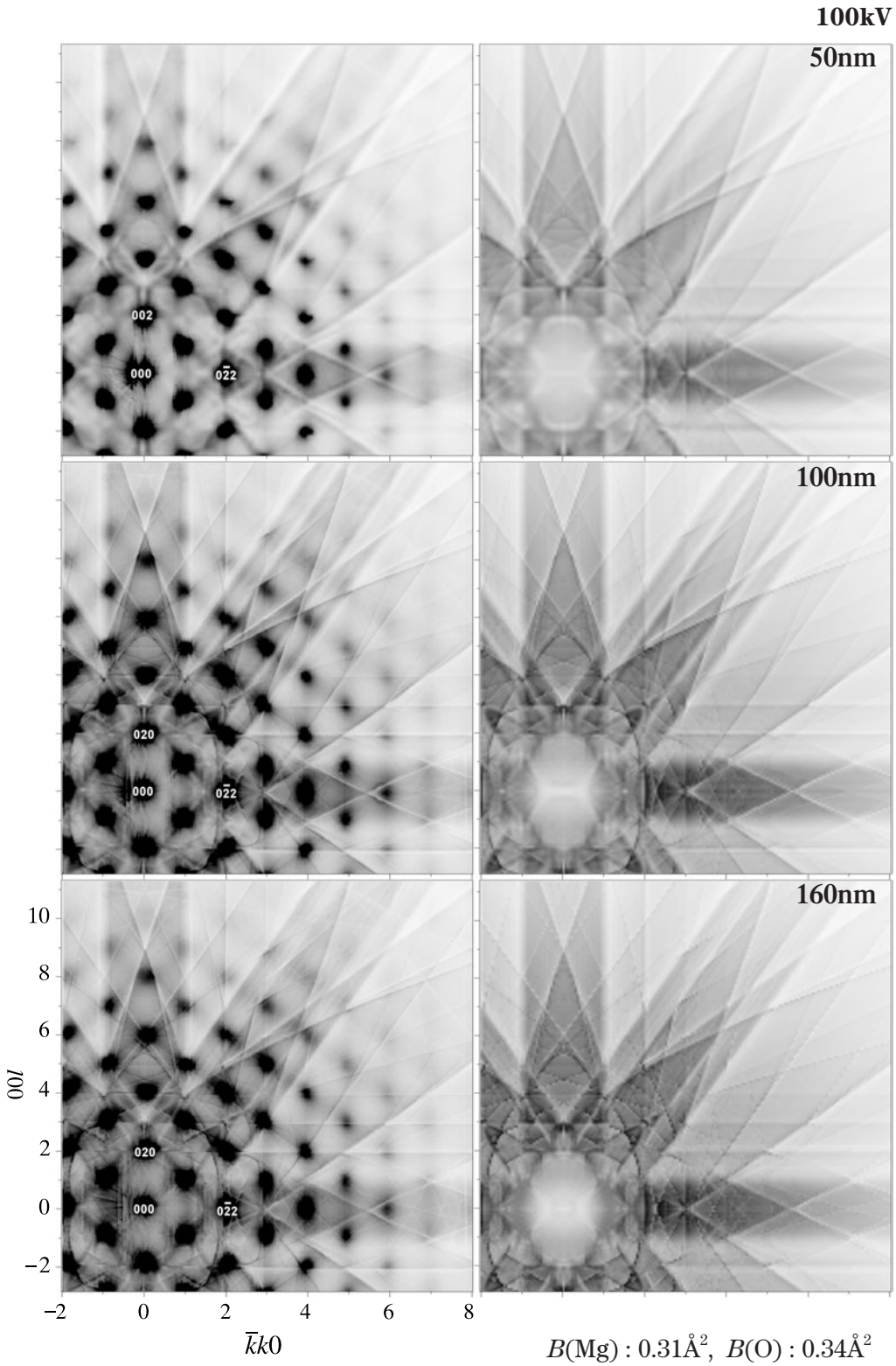

B(Mg) : 0.31Å^2, B(O) : 0.34Å^2
Number of beams : 315
Number of pixels : 201 × 200

Incidence-orientation dependence

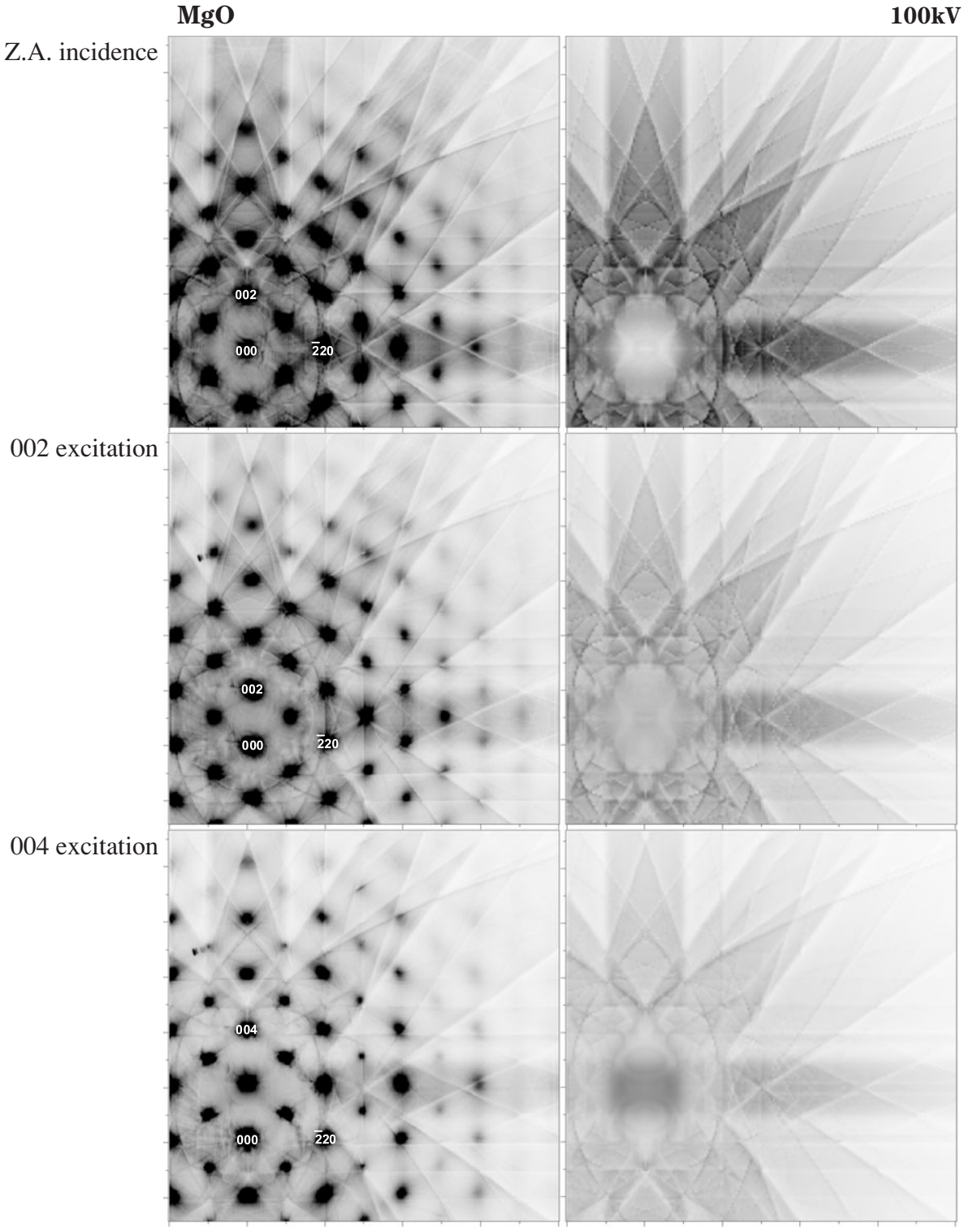

B(Mg) : 0.31Å^2, B(O) : 0.34Å^2
Thickness : 160nm
Number of beams : 315
Number of pixels : 201 × 200

Al [100]

100kV

105nm

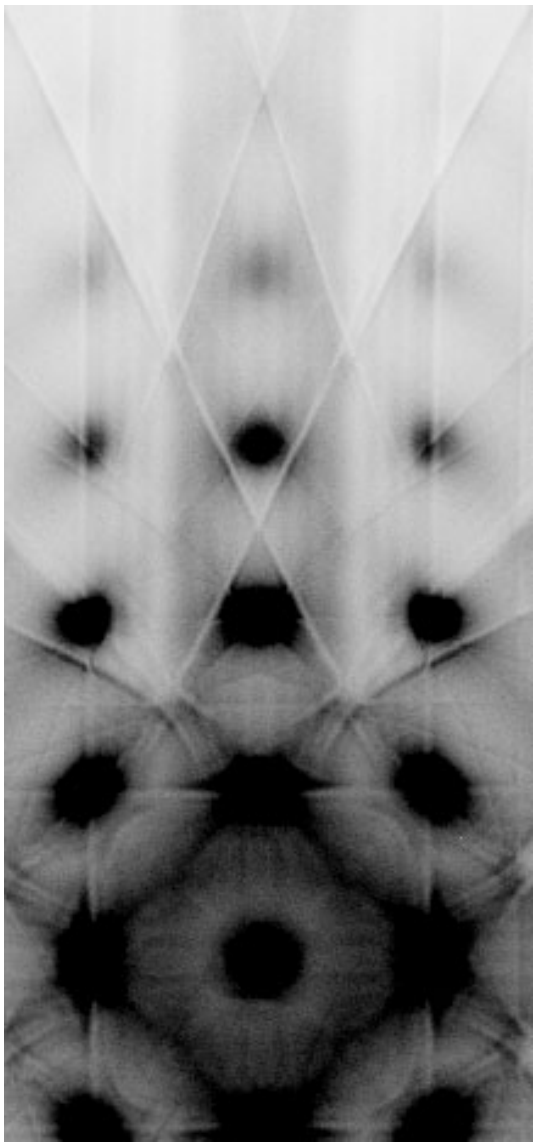

Experiment

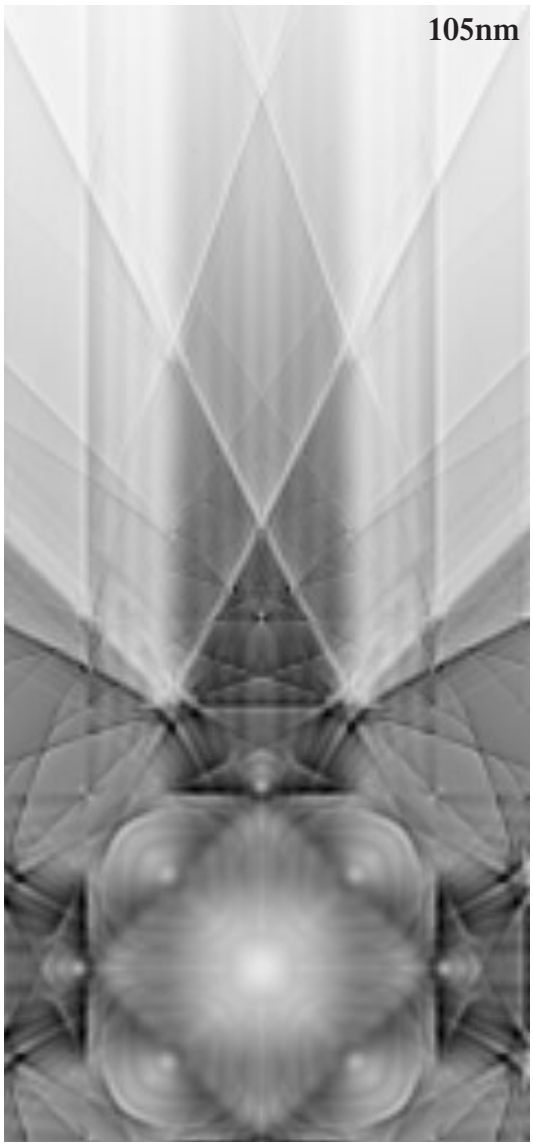

Simulation

Thickness dependence

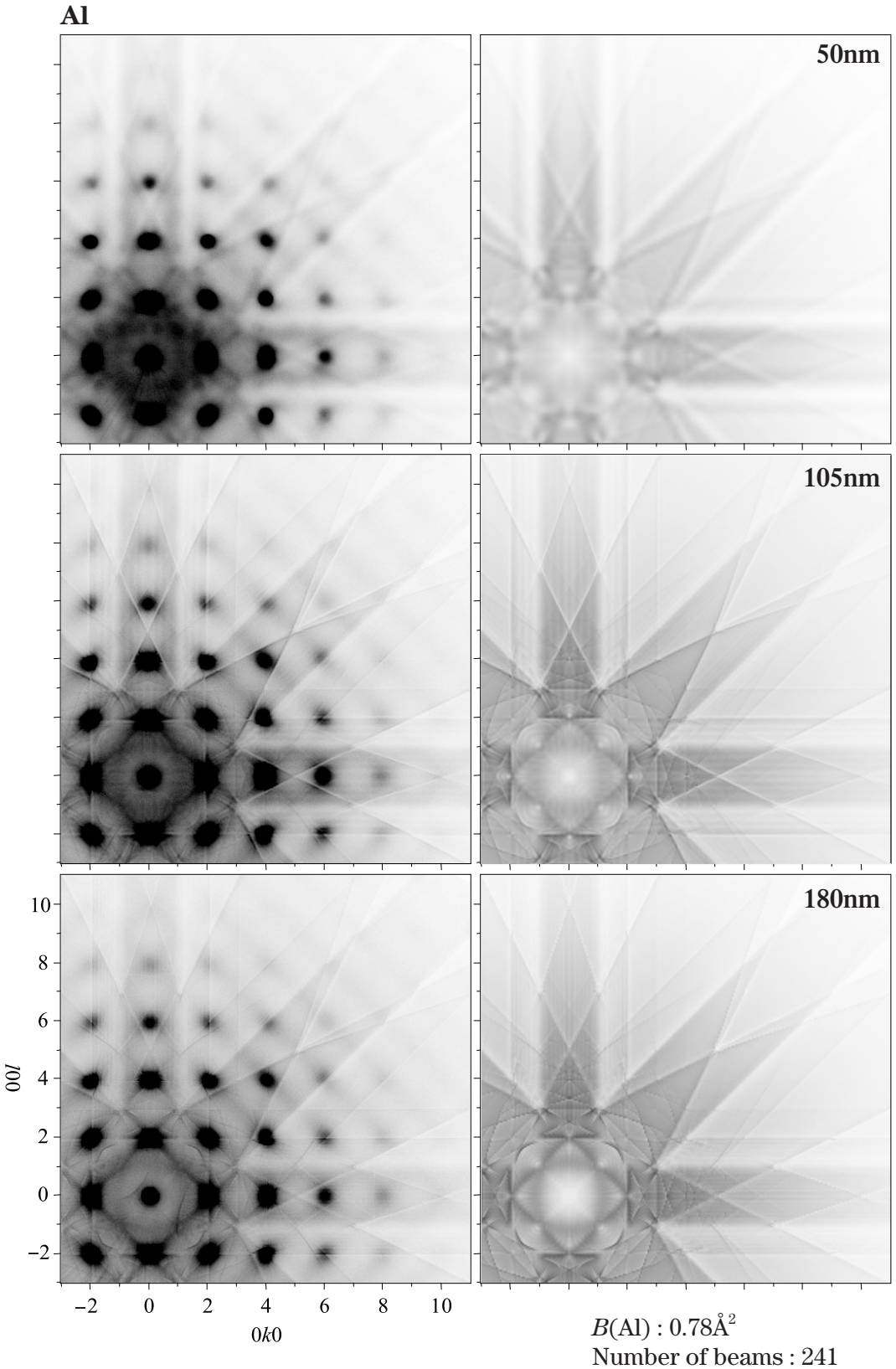

B(Al) : 0.78Å^2
Number of beams : 241
Number of pixels : 281 × 281

TiO_2 [111]

100kV

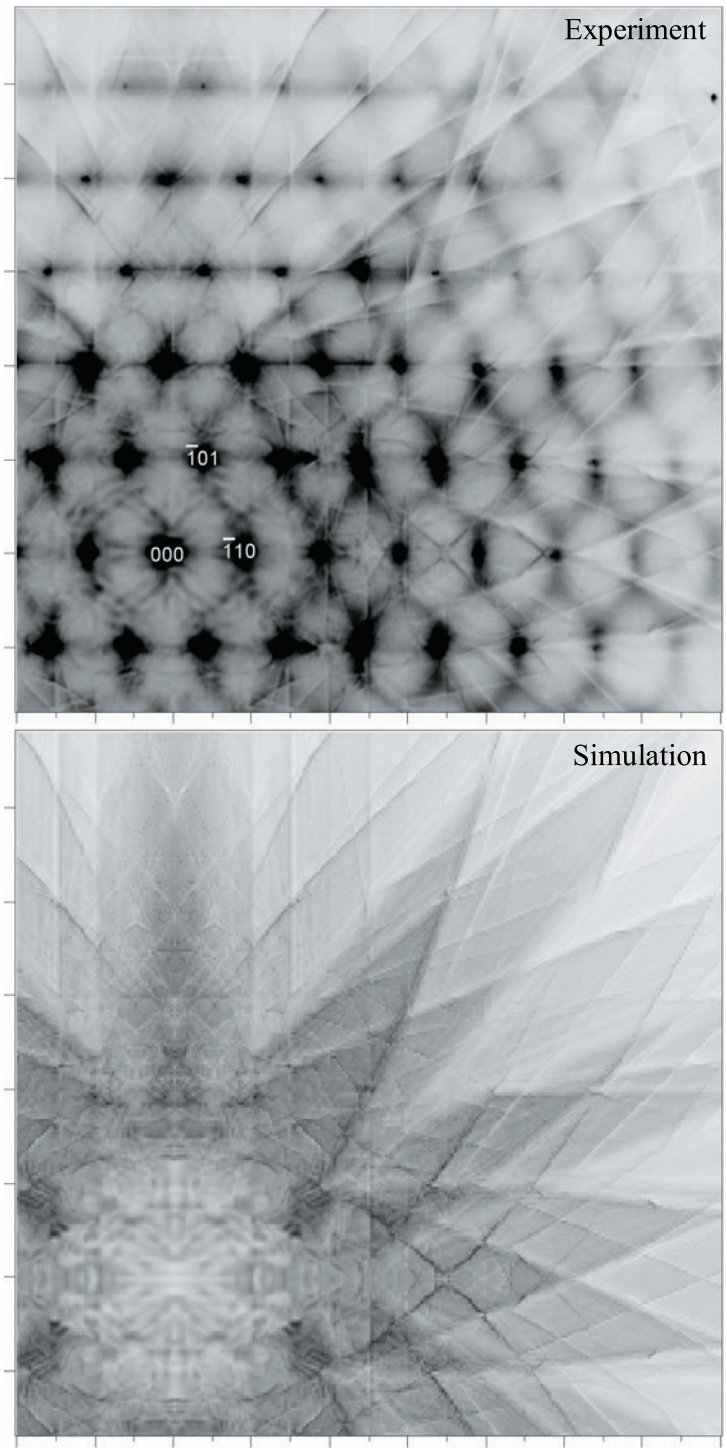

B(Ti) : 0.35Å^2, B(O) : 0.44Å^2
Thickness : 150nm
Number of beams : 427
Number of pixels : 271 × 270

Enlargements of three parts

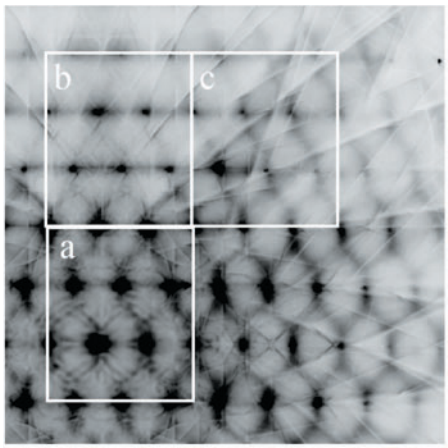

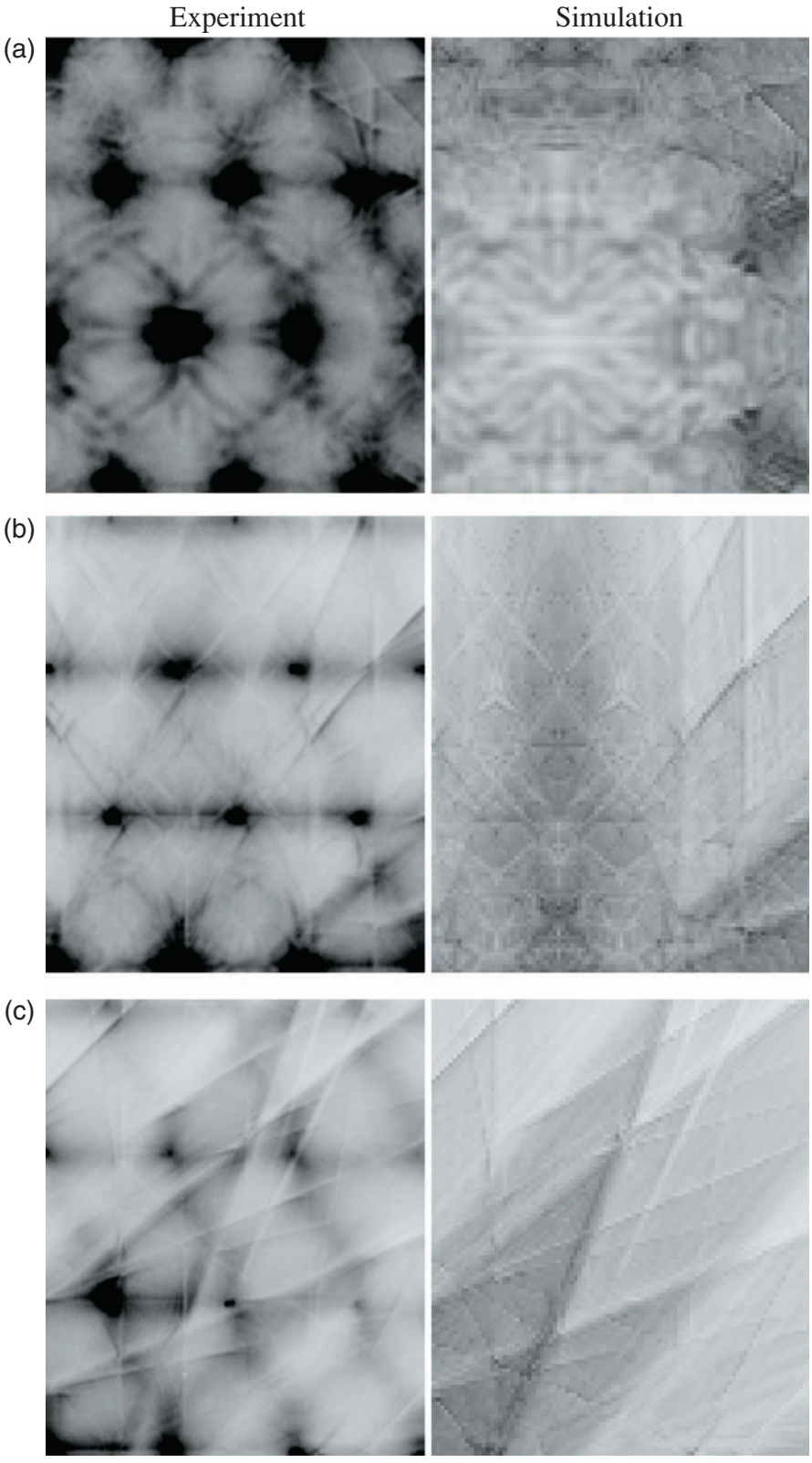

Simulations of Kikuchi Patterns (Systematic Reflection Cases)

We have shown that the Kikuchi patterns taken at zone-axis incidences are reproduced very well by the simulations based on Omoto's theoretical derivation. In this section, the Kikuchi patterns in systematic reflection cases are displayed and discussed. Kainuma [28] and Takagi [27] gave theoretical intensity profiles of the Kikuchi line and band using the two-beam dynamical theory. Takagi's independent Bloch-wave treatment is valid for thick specimens. Unfortunately, even Takagi did not give detailed explanations of the formation of Kikuchi bands in terms of the transitions between the Bloch waves. Furthermore, since Takagi neglected the cross terms of the transition probabilities between the Bloch waves, the detailed features of the Kikuchi bands cannot be discussed.

However, Takagi's treatment is useful to understand the outline of the formation of Kikuchi bands in terms of the transitions between the Bloch waves. We show simulations of the Kikuchi patterns of MgO on page 223, which were calculated at the 020 excitation under the two-beam approximation using eq.(8) on page 176, equivalent to Takagi's expression. In the present simulations, however, transition probabilities $T(\boldsymbol{Q},\boldsymbol{Q}')$ based on the Einstein model given by Hall and Hirsch [29] were used instead of the transition probabilities of single phonon scattering used in Takagi's original paper [27].

The intensity distribution of the Kikuchi bands of MgO is separated into the contributions of transitions from the two Bloch waves initially excited. Furthermore, the contribution from each Bloch wave is separated into the normal and anomalous absorption terms. The excess and defect features of the 020 (lowest-order) Kikuchi band are explained in terms of the sum of the anomalous absorption terms ($T(\boldsymbol{Q},\boldsymbol{Q}-\boldsymbol{G})$, $\boldsymbol{G}$ = 020) [28],[27],[a]. It is also shown that the constructive and destructive additions of the normal and anomalous absorption terms of the transition 1→1 are important for the formation of the excess band and defect band, respectively.

A similar interpretation is given for the case of the symmetric incidence of MgO, where three beams instead of two beams are taken into account. In addition, we show systematic many-beam simulations for the 020 excitation of MgO. The basic feature of the 020 band is the same as that of the two-beam calculation. Furthermore, the Kikuchi bands due to 040, 060, … reflections are reproduced. It is seen that the defect band area extends as the order of reflection becomes high.

Beyond Takagi's treatment (eq.(8)), we have used a more accurate expression eq.(5) on page 176, in which the cross terms of the transition probabilities and the absorption effect in the elastic scattering process are taken into account. The thickness dependence, the asymmetry features, the accurate intensity distribution along the band, the accurate incidence-orientation dependence and the interference fringes of the Kikuchi bands have been obtained. Such behaviors have been actually observed in experimental Kikuchi patterns. Finally, systematic many-beam simulations are compared with the experimental Kikuchi patterns.

It has been confirmed that Kikuchi patterns are reproduced very well by the simulations based on the recent theory with the use of the Einstein model.

Reference

[a] K. Okamoto, T. Ichinokawa, Y. H. Ohtsuki: *J. Phys. Soc. Jpn.*, **30** (1971) 1690.

Transition probability in the independent Bloch-wave treatment

$$T_{\mu}^{\lambda} = T_{\mu\mu}^{\lambda\lambda} = \sum_{gh}\sum_{g'h'} \langle p\lambda|\boldsymbol{g}\rangle\langle\boldsymbol{g}'|p\lambda\rangle T(\boldsymbol{Q},\boldsymbol{Q}')\langle\boldsymbol{h}|0\mu\rangle\langle 0\mu|\boldsymbol{h}'\rangle$$

$$\boldsymbol{Q}=\boldsymbol{p}+\boldsymbol{g}-\boldsymbol{h},\ \boldsymbol{Q}'=\boldsymbol{p}+\boldsymbol{g}'-\boldsymbol{h}'$$

Plots of $T(\boldsymbol{Q},\boldsymbol{Q}-\boldsymbol{G})$

The scattering factor of TDS given by Hall and Hirsch, $T(\boldsymbol{Q},\boldsymbol{Q}-\boldsymbol{G})$, is plotted as a function of $\boldsymbol{Q}$ for MgO. $T(\boldsymbol{Q},\boldsymbol{Q}-\boldsymbol{G})$ is negative in the circle with a radius of $|\boldsymbol{G}/2|$ centered at $\boldsymbol{G}/2$. The areas where $T(\boldsymbol{Q},\boldsymbol{Q}-\boldsymbol{G})$ is negative give the defect Kikuchi band. The areas where $T(\boldsymbol{Q},\boldsymbol{Q}-\boldsymbol{G})$ is positive give the excess band. As is seen in Figs. (a) to (c), the defect area extends in the [001] direction as the order of reflection becomes high.

$$T(\boldsymbol{Q},\boldsymbol{Q}-\boldsymbol{G}) = \frac{1}{V_c}\sum_{\alpha} f_\alpha(\boldsymbol{Q}) f_\alpha(\boldsymbol{Q}-\boldsymbol{G})\exp[-i\boldsymbol{Q}\cdot\boldsymbol{r}_\alpha] \times\{\exp[-W_\alpha(\boldsymbol{G})] - \exp[-W_\alpha(\boldsymbol{Q}) - W_\alpha(\boldsymbol{Q}-\boldsymbol{G})]\}$$

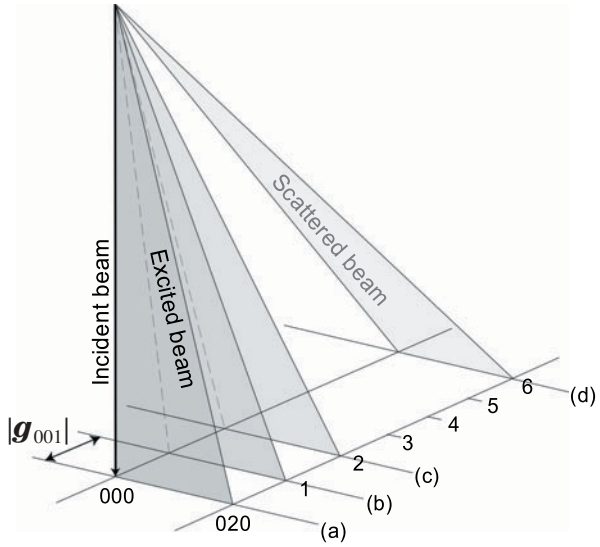

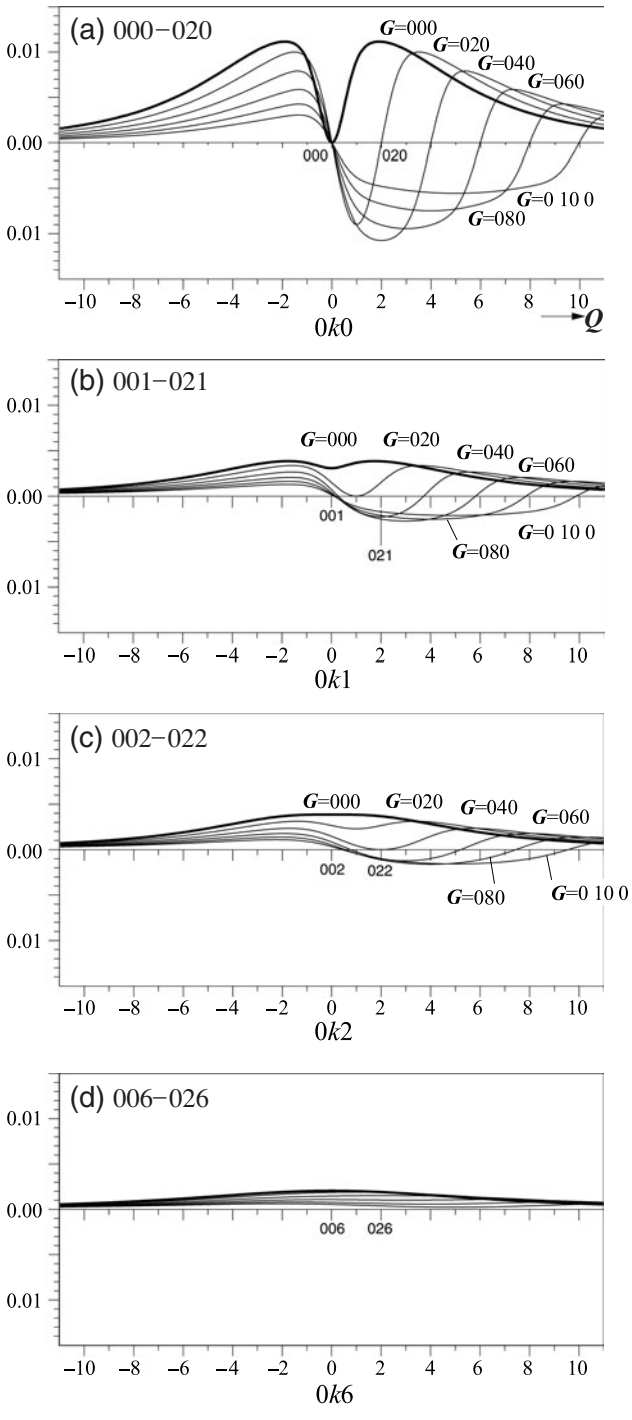

B(Mg): 0.31Å^2
B(O): 0.34Å^2

Interpretation of Kikuchi bands by the transitions between Bloch waves

Two-beam simulations (MgO 020 excitation)

The initial Bloch waves μ = 1 and 2 have the same excitation probability at the 020 excitation for the two-beam case. Due to TDS, the initial Bloch waves are transferred to the final Bloch waves λ = 1 and 2 in a different direction, $-\boldsymbol{p}$ (See Fig. (a)). To obtain the intensities of a Kikuchi band, the transition probabilities should be multiplied by the wave densities of the final states (λ) (Fig. (b)).

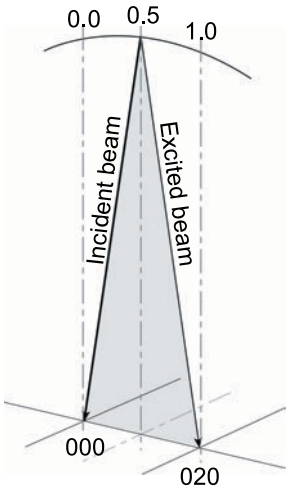

Incident-beam condition.

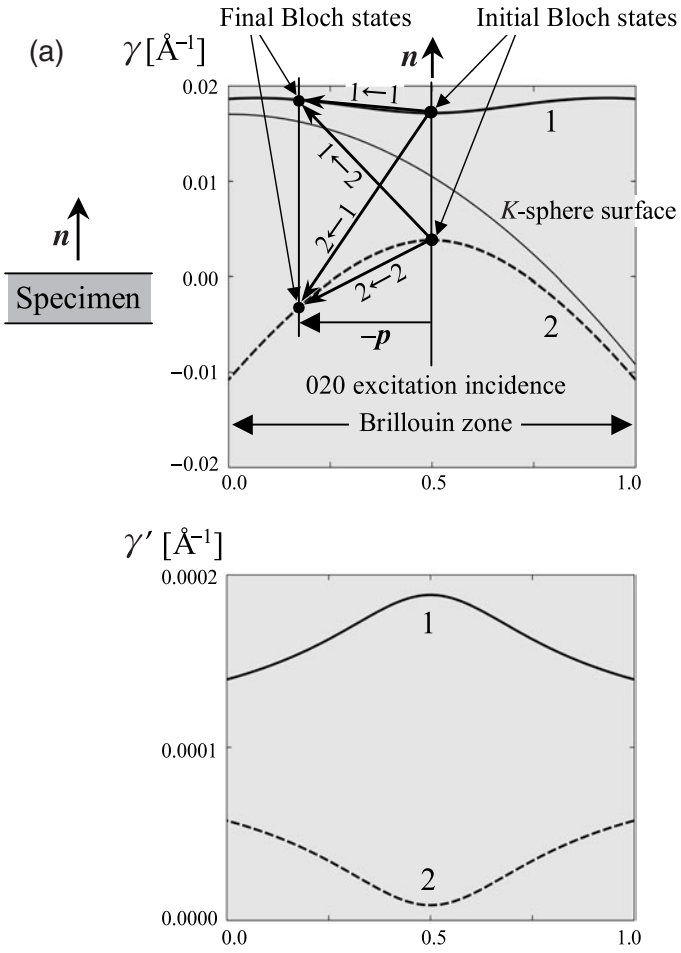

Real (γ) and imaginary (γ') parts of the dispersion surface.

Branch	Excitation
1	0.50
2	0.50

Absolute squares of excitation amplitudes at the 020 excitation incidence.

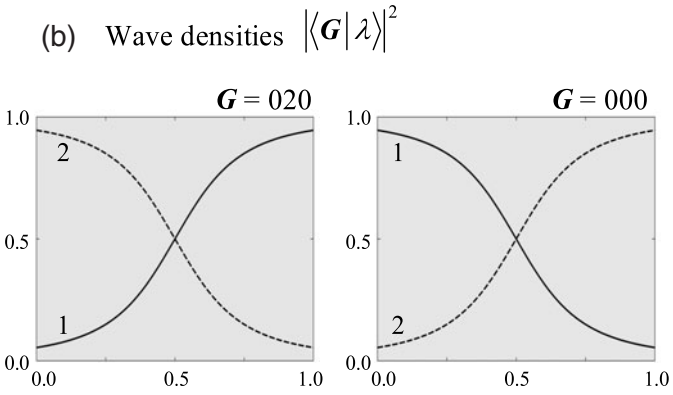

Absolute squares of the component-wave amplitudes of the Bloch waves.

Kikuchi band calculated by the independent Bloch-wave treatment (Takagi's treatment)

$$\lim_{t\to\infty}\frac{1}{t}\frac{dI_p^G}{} = \sum_{\lambda\mu}\left|\langle \boldsymbol{G}|p\lambda\rangle\right|^2 T_\mu^\lambda \left|\langle 0\mu|\boldsymbol{O}\rangle\right|^2$$

The intensity distribution and bird's-eye views of the Kikuchi band of MgO at the 020 excitation are shown, which were calculated by the independent Bloch-wave treatment (Takagi's treatment) with the use of the transition probabilities $T(\boldsymbol{Q},\boldsymbol{Q}-\boldsymbol{G})$ given by Hall and Hirsch. The excess band dominates most part of the Kikuchi band but the defect band appears at low scattering angles.

The definitions of "excess" and "defect" are that the intensity of a Kikuchi band is greater and smaller than the intensity just outside the band, respectively.

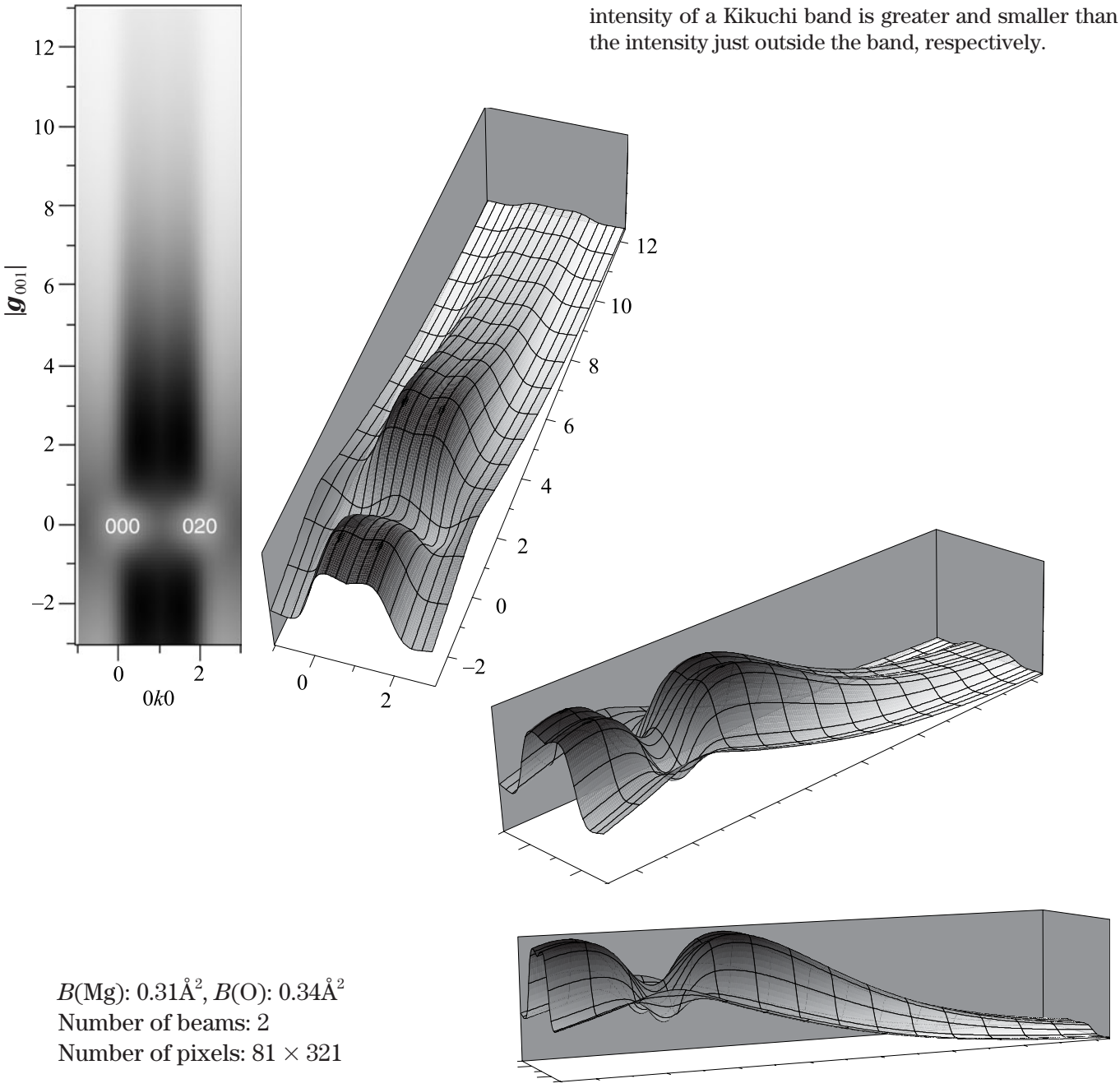

B(Mg): 0.31Å^2, B(O): 0.34Å^2
Number of beams: 2
Number of pixels: 81 × 321

Intensity contributions from branches 1 and 2

The intensity distribution of the Kikuchi band of MgO at the 020 excitation is separated into the contributions of the transitions from the two Bloch waves initially excited. The major part of the contributions to the excess Kikuchi band comes from the transition 1→1. At low scattering angles, the transitions 1→1 and 1→2 form the defect band though the contribution from the transition 2→1 cannot be neglected.

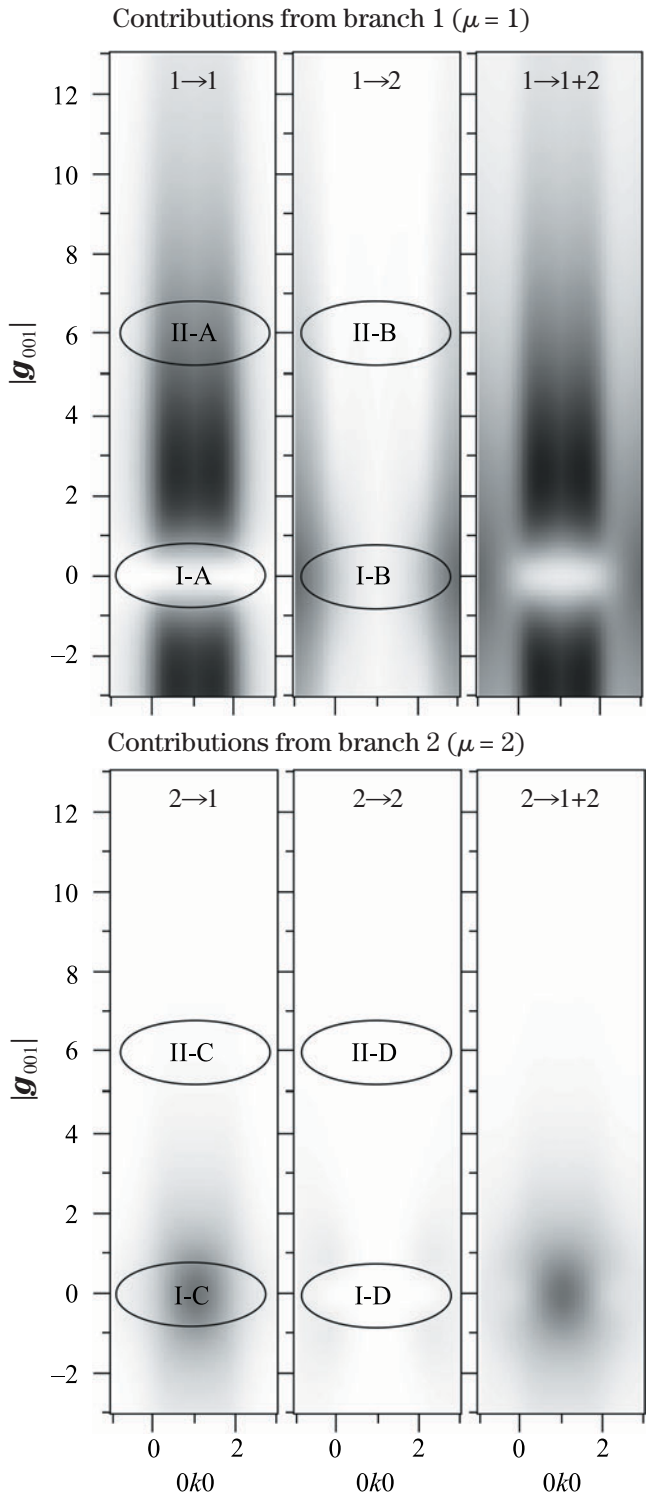

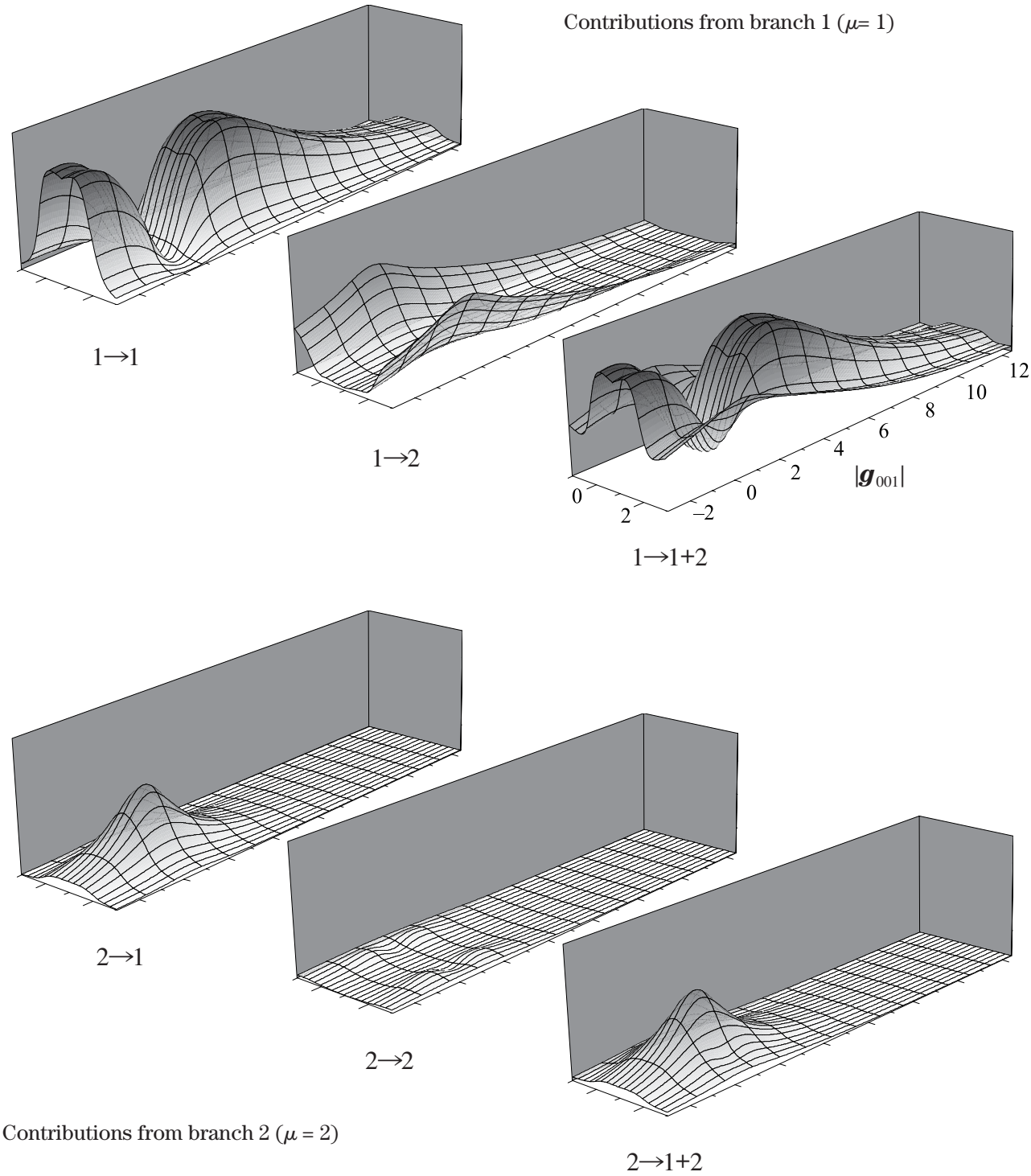

Bird's-eye views of the contributions from the two branches.

Probability densities of the transitions from branches 1 and 2

Probability densities of the transitions 1→1, 1→2, 2→1 and 2→2 on the 006 − 026 row due to TDS multiplied by $|\langle \boldsymbol{O}|\mu\rangle|^2$ are shown in Fig. (a). The wave densities $|\langle \boldsymbol{G}|\lambda\rangle|^2$ for branches 1 and 2 are drawn in Fig. (b). The intensity contributions (intensity profiles) from the transitions on the 006 − 026 row are shown in Fig. (c). It is seen that the excess Kikuchi band is created from the transition 1→1. The symbols II-A, II-B, II-C and II-D to assign the 006 − 026 row are referred to the figure on page 224.

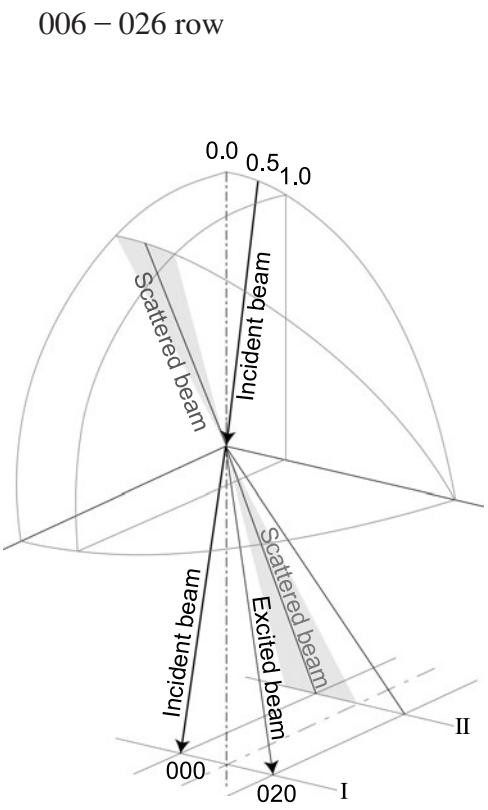

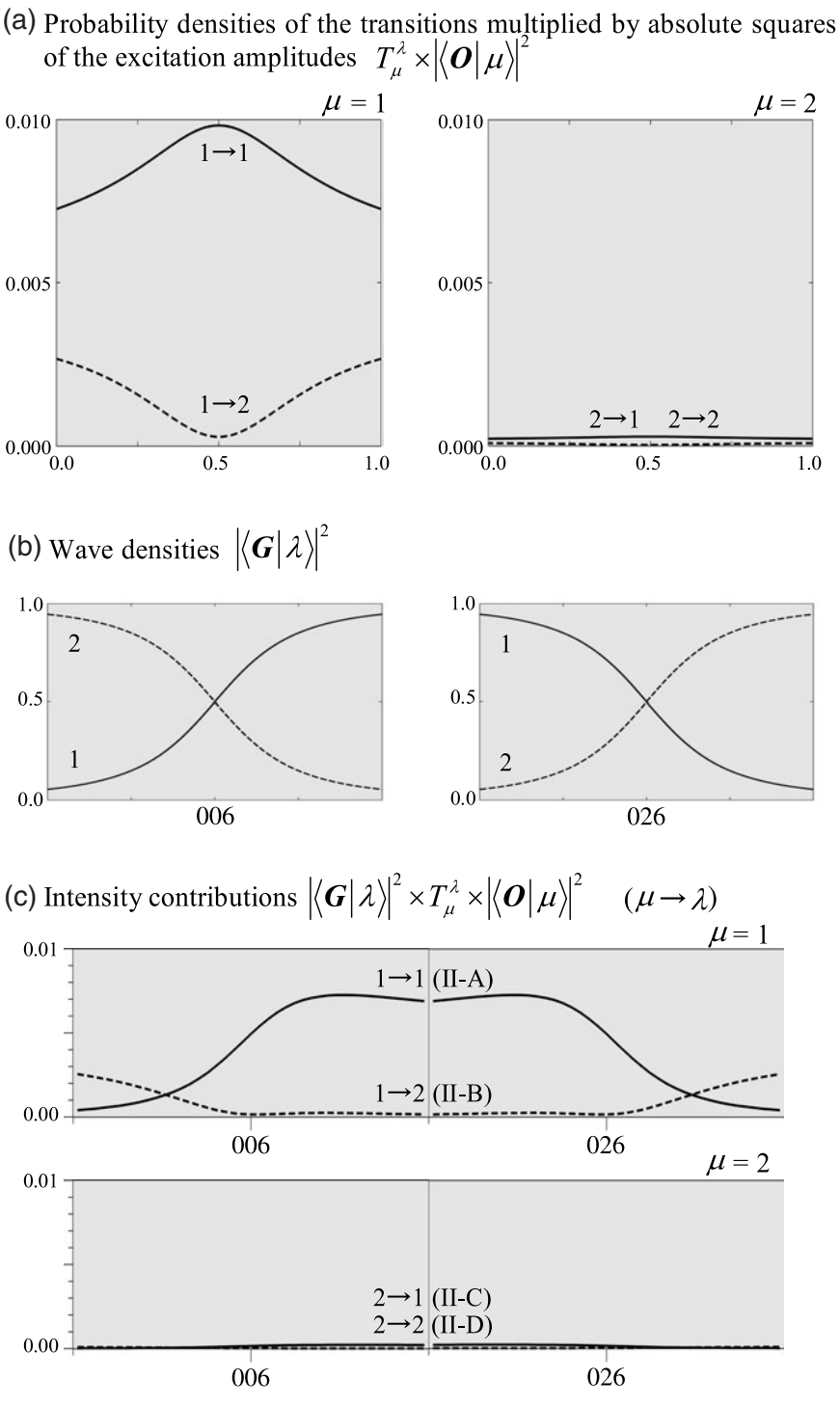

Probability densities of the transitions 1→1, 1→2, 2→1 and 2→2 on the 000 − 020 row due to TDS multiplied by $|\langle \boldsymbol{O}|\mu\rangle|^2$ are shown in Fig. (a). The wave densities $|\langle \boldsymbol{G}|\lambda\rangle|^2$ are drawn for branches 1 and 2 in Fig. (b). The intensity contributions (intensity profiles) from the transitions on the 000 − 020 row are shown in Fig. (c). The important point for the formation of the defect Kikuchi band is that there exists nearly no intensity contribution from the transition 1→1.

From Fig. (c), it is seen that the defect band is created by the inter-branch transition 1→2, though the contribution from the transition 2→1 exists. The symbols I-A, I-B, I-C and I-D to assign the 000 − 020 row are referred to the figure on page 224.

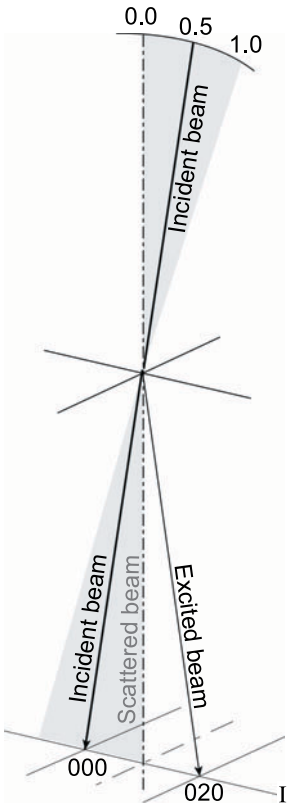

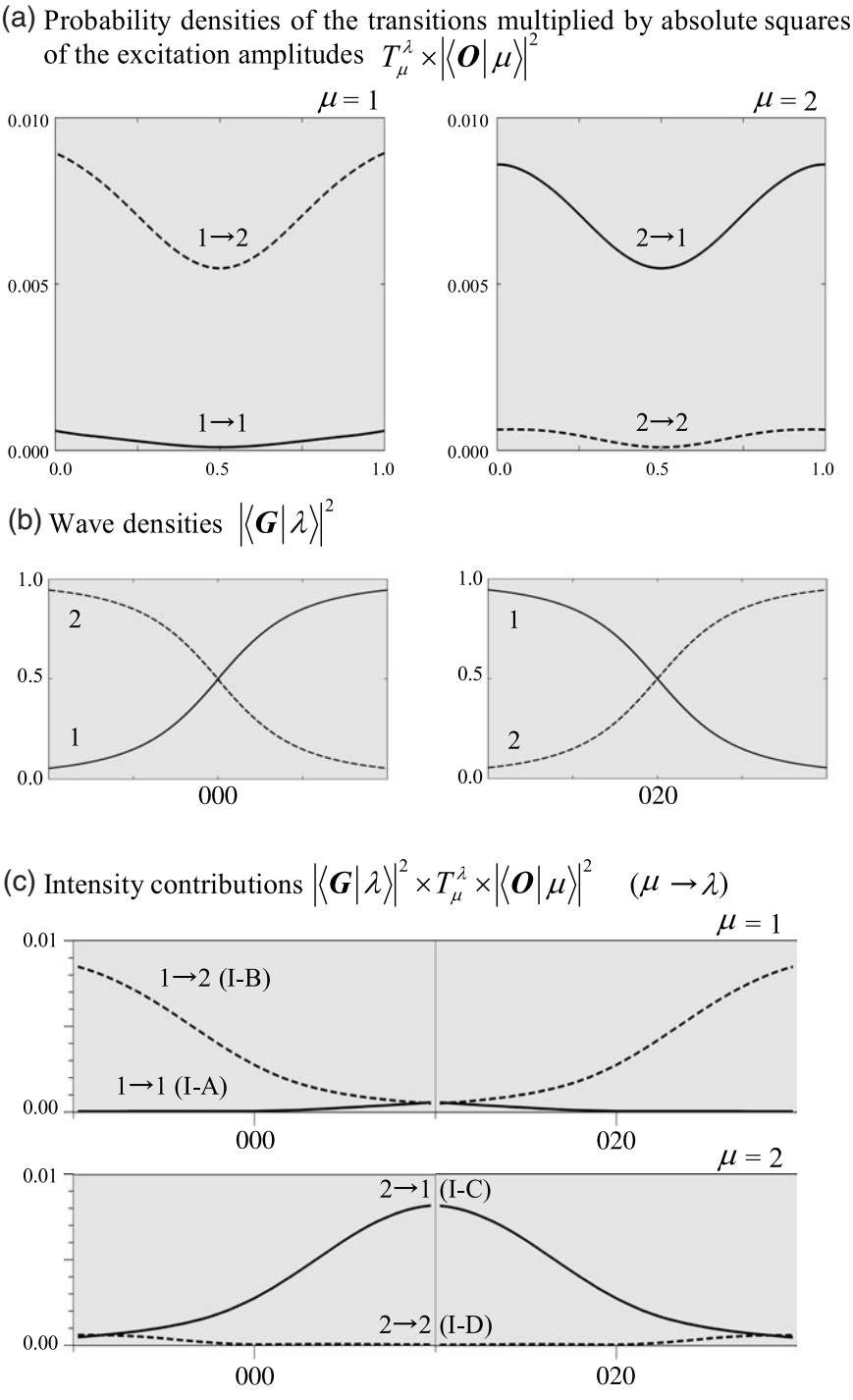

Contributions of normal and anomalous absorptions

Intensity contributions from the two branches are further separated into the contributions from the normal and anomalous absorption terms, which are produced by the transition probabilities $T(\boldsymbol{Q},\boldsymbol{Q})$ and $T(\boldsymbol{Q},\boldsymbol{Q}-\boldsymbol{G})$ ($\boldsymbol{G}$ = 020 in this case), respectively. The angular distributions of the intensity contributions from normal and anomalous absorption terms are shown in the figures below. Integrations of the distributions produce the normal and anomalous absorptions in the elastic scattering part.

The excess and defect features of the 020 Kikuchi band are created by the anomalous absorption terms of the transitions 1→1 and 1→2. The sum of the normal absorption terms gives no contribution to form the Kikuchi band. The normal absorption terms create the Kikuchi line except around the symmetric incidence.

Let us see the relation between the normal and anomalous absorption terms in the formation of the Kikuchi band. The excess Kikuchi band is created by the contribution mainly from the transition 1→1, where the contributions from both the normal and anomalous absorption terms are added constructively. For the formation of the defect Kikuchi band at low scattering angles, the contribution from the transition 1→1 is important, where the negative contribution of the anomalous absorption term cancels the contribution from the corresponding normal absorption term. The transition 1→2 gives the strong positive contribution outside the band edge to form the defect band. It is noted that the transition 2→1 gives the positive contribution so as to create the excess band.

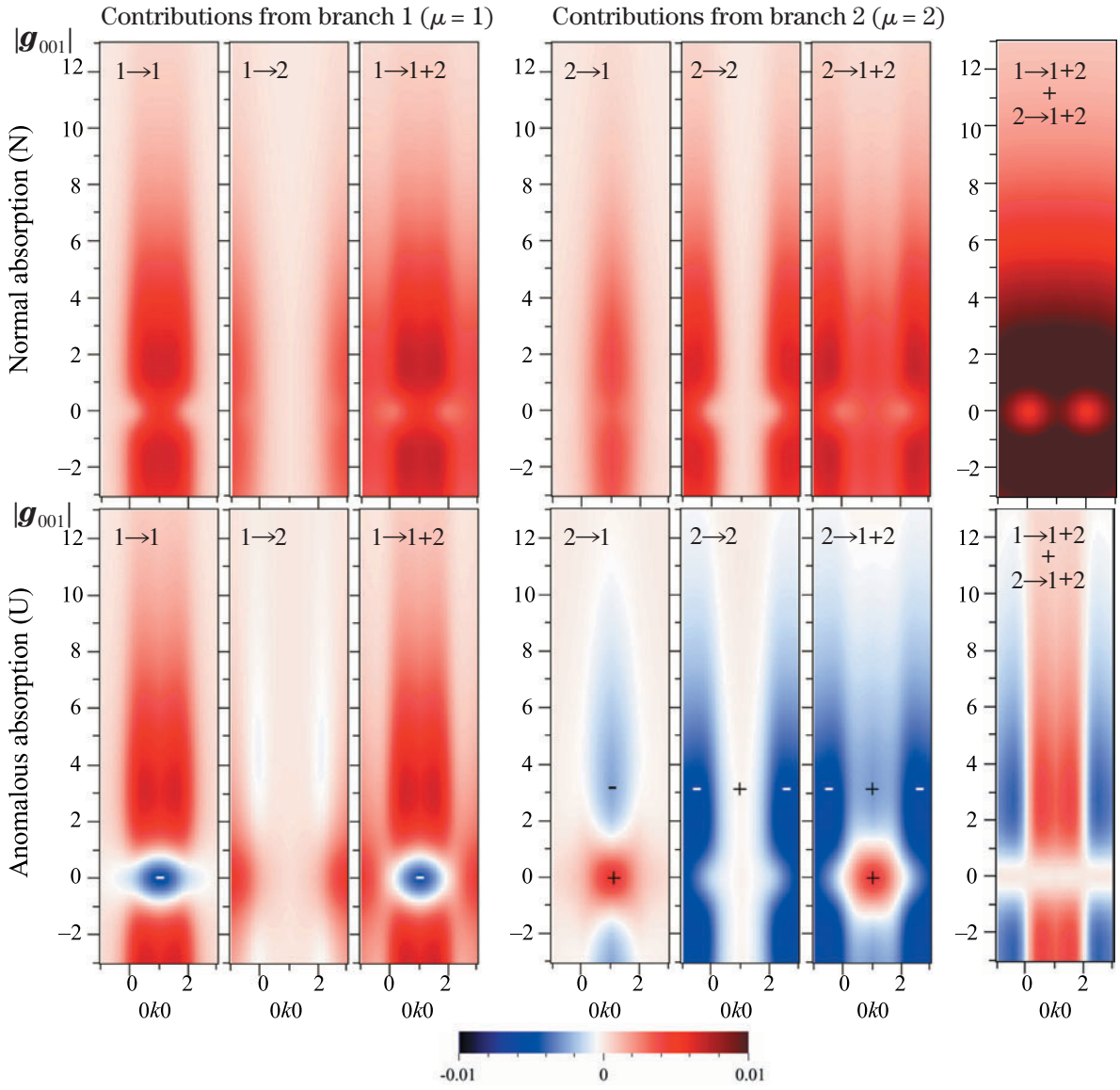

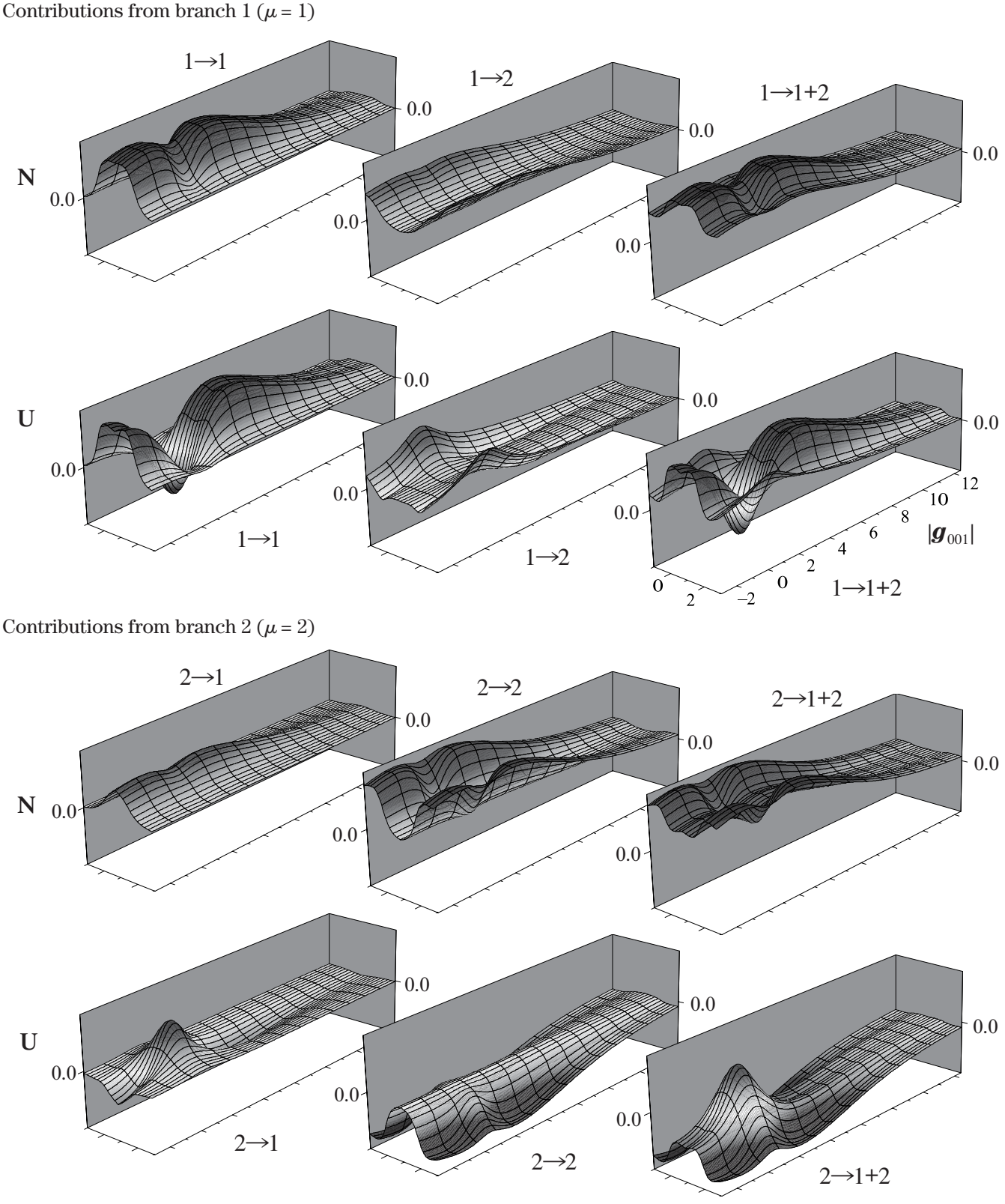

Bird's-eye views of the contributions from the normal and anomalous absorptions.

Probability densities of the transitions from branches 1 and 2 – Contributions of normal and anomalous absorptions –

Probability densities of the transitions from branches 1 and 2 on the 006 − 026 row and 000 − 002 row are separated into the contributions of the normal and anomalous absorptions. The formation of the Kikuchi band is roughly understood by the behavior of the probability densities of the transitions because the initial Bloch waves 1 and 2 have the same excitation probability in the present case. On the 006 − 026 row, the normal absorption terms (N) of the transitions 2→1 and 2→2 are almost canceled by the corresponding anomalous absorption terms (U). The sum of the normal and anomalous contributions of the transition 1→2 is small. Thus, the transition 1→1 creates the excess band.

On the other hand, on the 000 – 020 row, the terms N of the transitions 1→1 and 2→2 are almost canceled by the corresponding terms U. Thus, the transitions 1→2 and 2→1 form the defect band. However, the probability densities of the transitions 1→2 and 2→1 are not sufficient to discuss the intensity contributions of the transitions because the wave densities of the final states play an important role (See Fig. (c) on page 227).

(a) 006 − 026 row

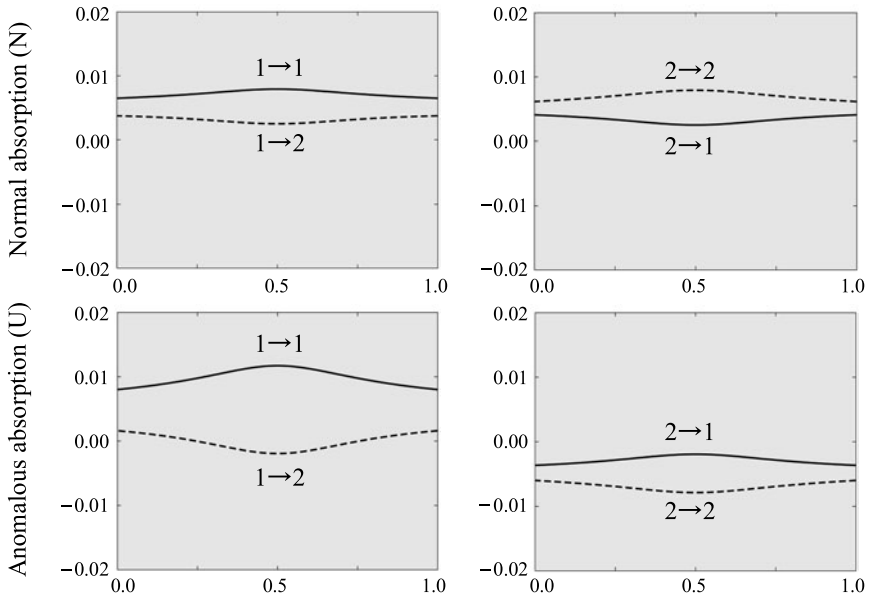

(b) 000 − 020 row

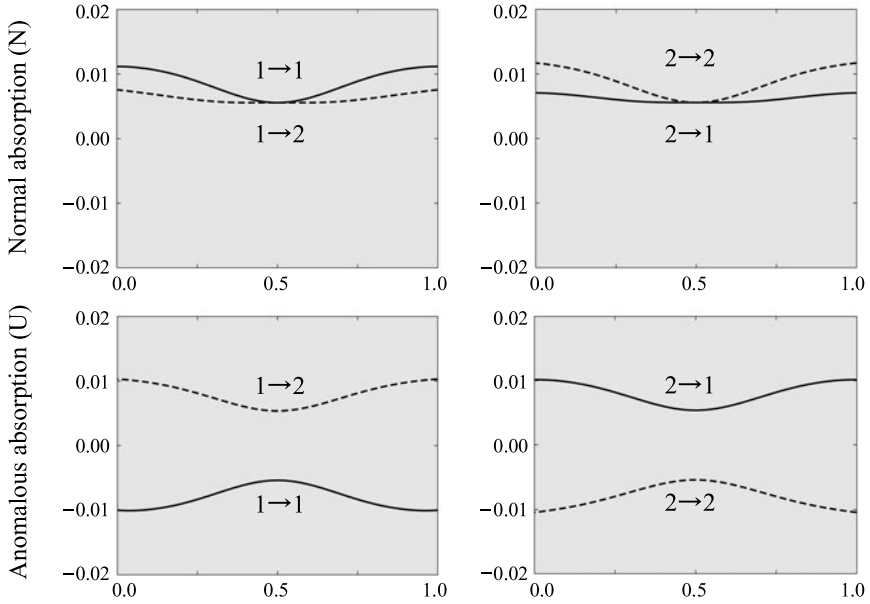

Three-beam simulations (MgO symmetric incidence)

The absolute squares of the excitation amplitudes of the initial states (μ) at the symmetric incidence are given by the table below. As is seen in the table, the major excitation is limited to the first branch of the Bloch states. Thus, the Kikuchi band is created mostly by the transitions from Bloch wave 1. The transitions due to TDS in a different direction, $-\boldsymbol{p}$, are shown in Fig. (a). The wave densities of the final states (λ) are displayed in Fig. (b).

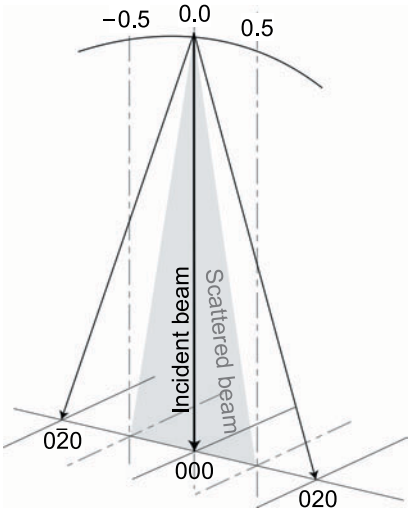

Initial incident-beam condition.

Branch	Excitation
1	0.89
2	0.11
3	0.00

Absolute squares of excitation amplitudes at the symmetric incidence.

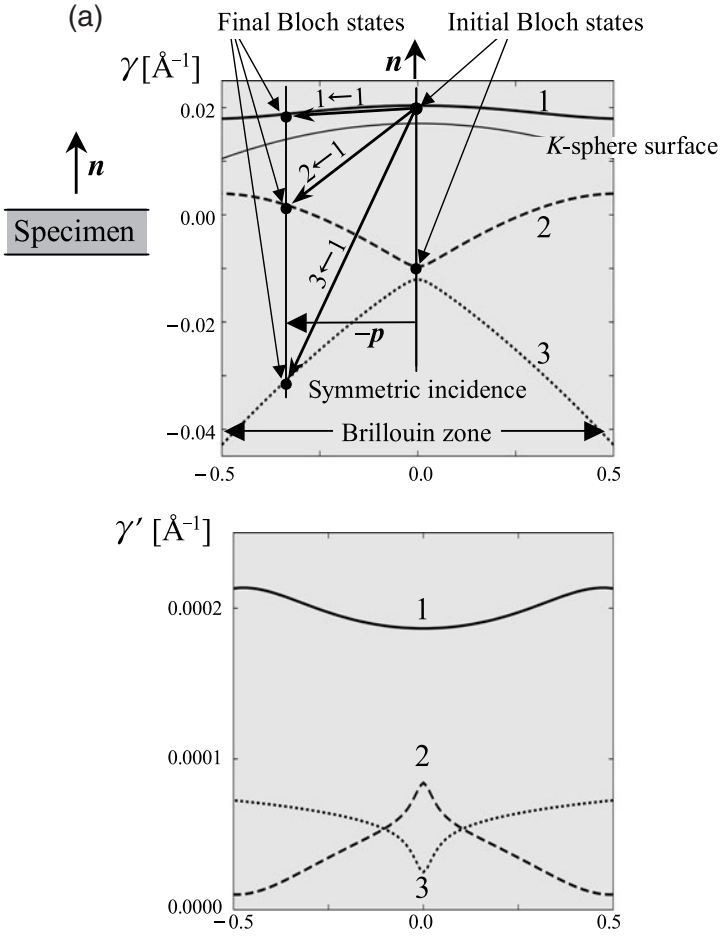

Real (γ) and imaginary (γ') parts of the dispersion surface.

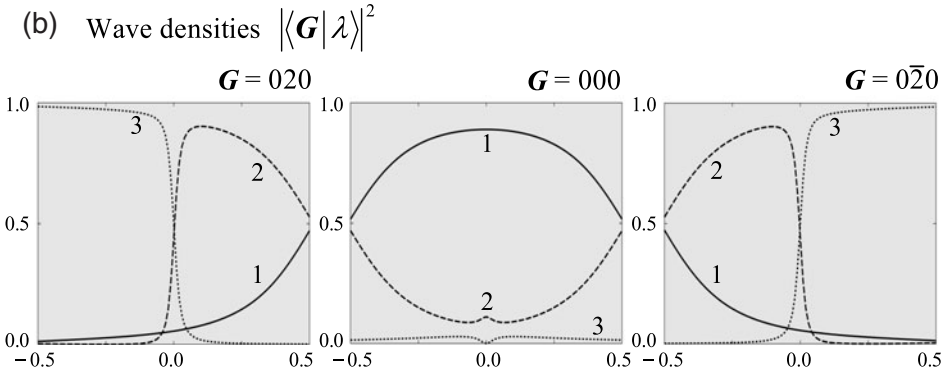

Absolute squares of the component wave-amplitudes of the Bloch waves.

Kikuchi band calculated by the independent Bloch-wave treatment (Takagi's treatment)

$$\lim_{t\to\infty}\frac{1}{t}\frac{dI_p^G}{d\Omega}=\sum_{\lambda\mu}\left|\langle \boldsymbol{G}|p\lambda\rangle\right|^2 T_\mu^\lambda\left|\langle 0\mu|\boldsymbol{O}\rangle\right|^2$$

The intensity distribution and bird's-eye views of the Kikuchi band of MgO at the symmetric incidence are shown, which were calculated by the independent Bloch-wave treatment (Takagi's treatment) with the use of the transition probabilities $T(\boldsymbol{Q},\boldsymbol{Q}-\boldsymbol{G})$ given by Hall and Hirsch. The excess band dominates most part of the Kikuchi band but the defect band appears at low scattering angles. The excess and defect features are seen not only at the 020 band but also at the 040 band.

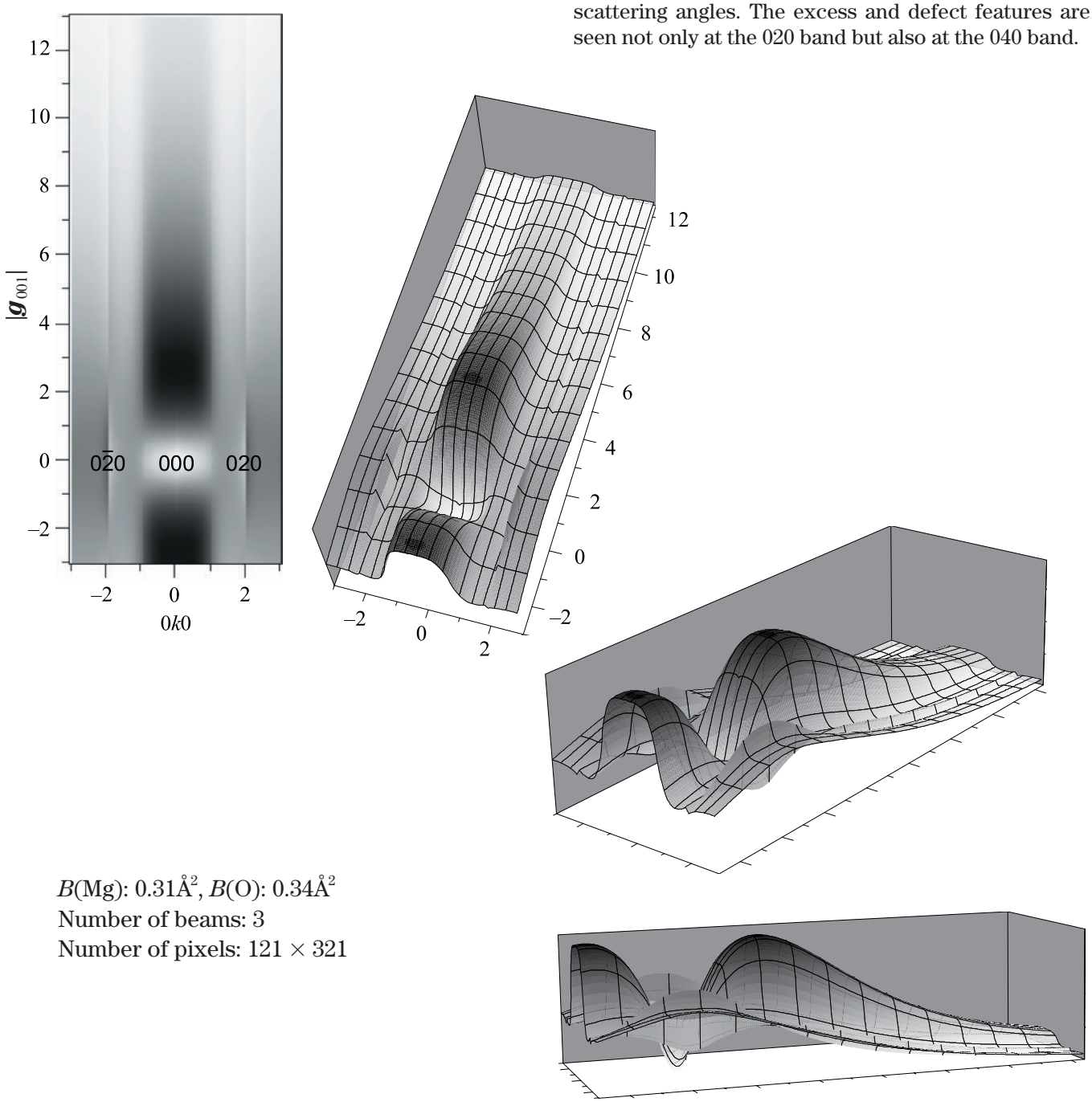

B(Mg): 0.31Å^2, B(O): 0.34Å^2
Number of beams: 3
Number of pixels: 121 × 321

Intensity contributions from branch 1

The intensity distribution of the Kikuchi band of MgO at the symmetric incidence is almost interpreted in terms of the contributions from the transitions of branch 1. The excess and defect features of the 020 Kikuchi band are explained by the contribution from the transitions 1→1 and 1→2. The excess and defect features of the 040 Kikuchi band are formed according to the relative strength between the transitions 1→2 and 1→3.

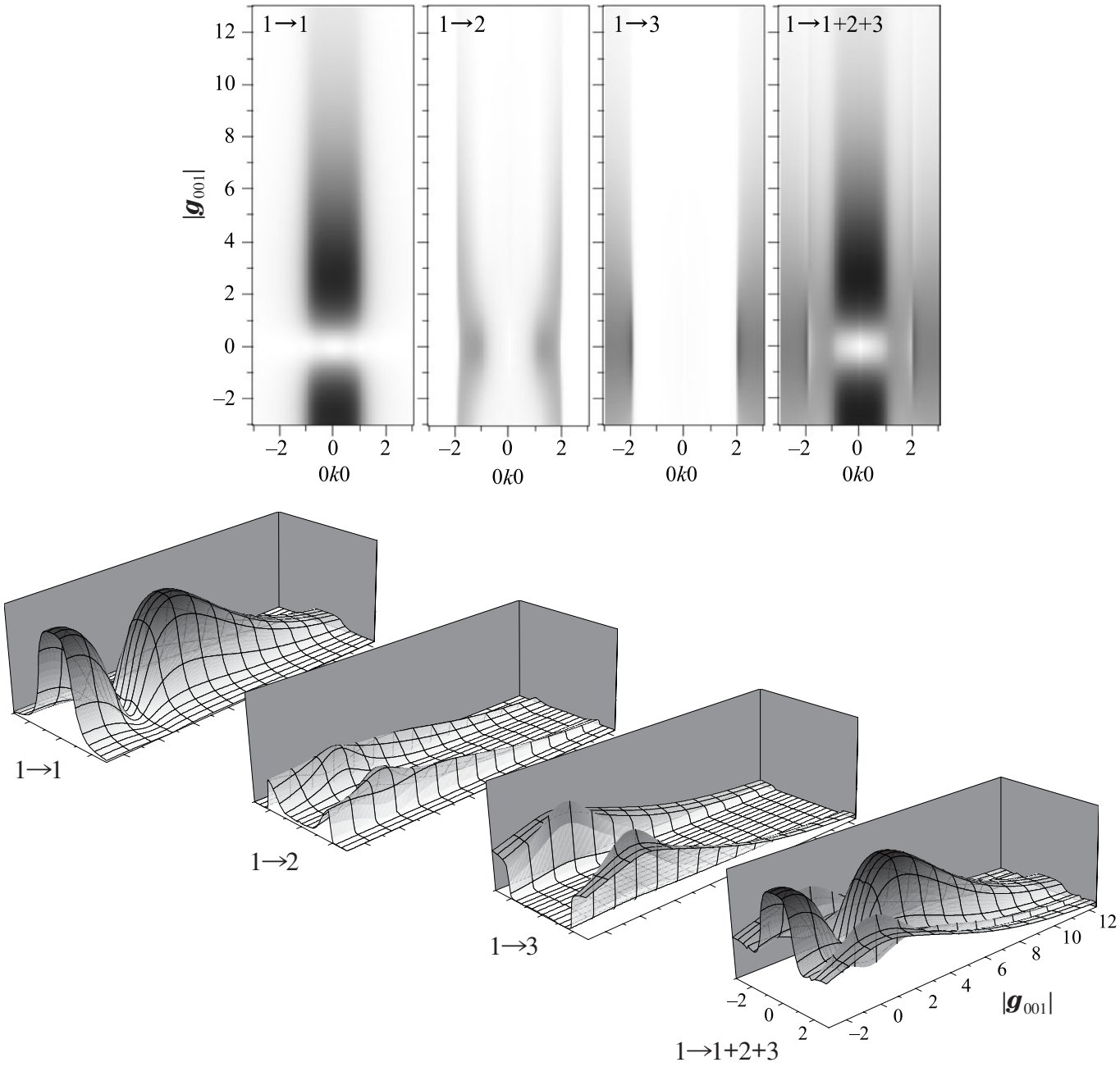

Bird's-eye views of the contributions from branch 1.

Probability densities of the transitions from branches 1 and 2

Probability densities of the transitions from branches 1 and 2 to branches 1, 2 and 3 on the $0\bar{2}6 - 026$ row multiplied by $|\langle \boldsymbol{O}|\mu\rangle|^2$ are shown in Fig. (a). The wave densities $|\langle \boldsymbol{G}|\lambda\rangle|^2$ are drawn for branches 1, 2 and 3 in Fig. (b). The intensity contributions (intensity profiles) from the transitions on the $0\bar{2}6 - 026$ row are shown in Fig. (c).

It is seen that the 020 excess Kikuchi band is created by the transition 1→1. The excess feature of the 040 Kikuchi band is seen to be created by the contributions from the transitions from 1→2 and 1→3.

$0\bar{2}6$ – 026 row

(a) Probability densities of the transitions multiplied by absolute squares of the excitation amplitudes $T_\mu^\lambda \times \left|\langle \boldsymbol{O}|\mu\rangle\right|^2$

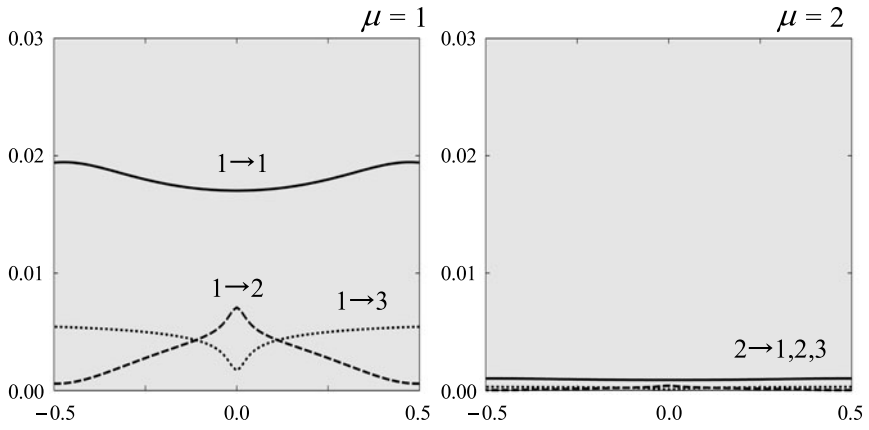

(b) Wave densities $\left|\langle \boldsymbol{G}|\lambda\rangle\right|^2$

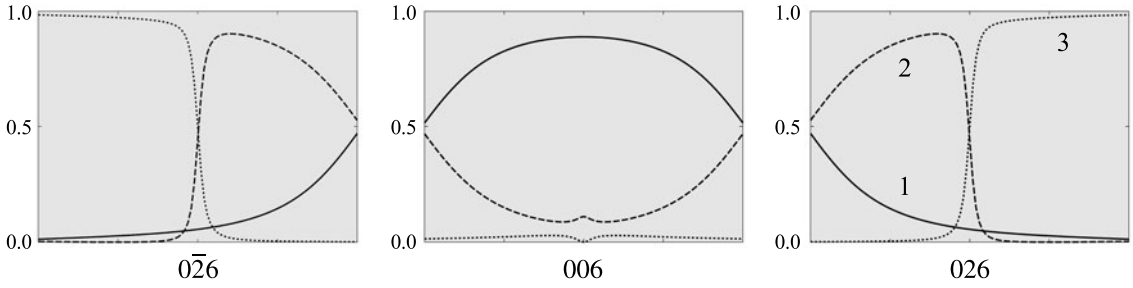

(c) Intensity contributions $\left|\langle \boldsymbol{G}|\lambda\rangle\right|^2 \times T_\mu^\lambda \times \left|\langle \boldsymbol{O}|\mu\rangle\right|^2$ $(\mu \rightarrow \lambda)$

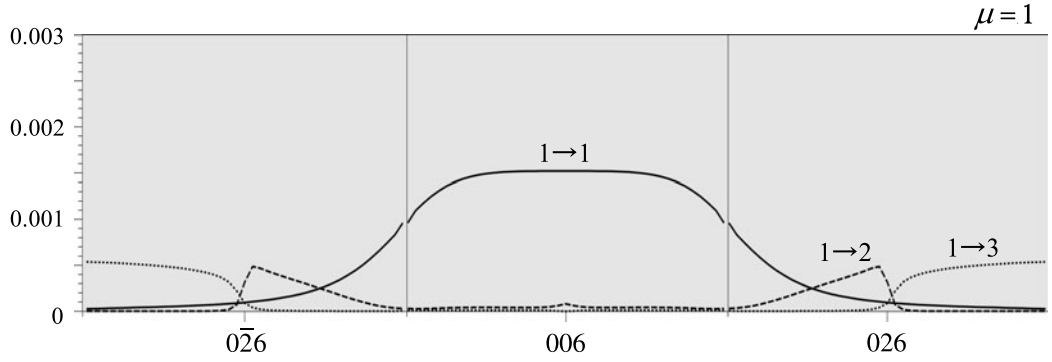

Probability densities of the transitions from branches 1 and 2 to branches 1, 2 and 3 multiplied by $|\langle \boldsymbol{O}|\mu\rangle|^2$ are shown on the $0\bar{2}0 - 020$ row in Fig. (a). The wave densities $|\langle \boldsymbol{G}|\lambda\rangle|^2$ are drawn for branches 1, 2 and 3 in Fig. (b). The intensity contributions (intensity profiles) from the transitions on the $0\bar{2}0 - 020$ row are shown in Fig. (c).

The important point for the formation of the 020 defect Kikuchi band is that there exists nearly no intensity contribution from the transition 1→1. From Fig. (c), it is seen that the defect band is created by the inter-branch transition 1→2. The defect feature of the 040 Kikuchi band is seen to be created by the contributions from the transitions 1→2 and 1→3.

$0\bar{2}0 - 020$ row

(a) Probability densities of the transitions multiplied by absolute squares of the excitation amplitudes $T_\mu^\lambda \times \left|\langle \boldsymbol{O}|\mu\rangle\right|^2$

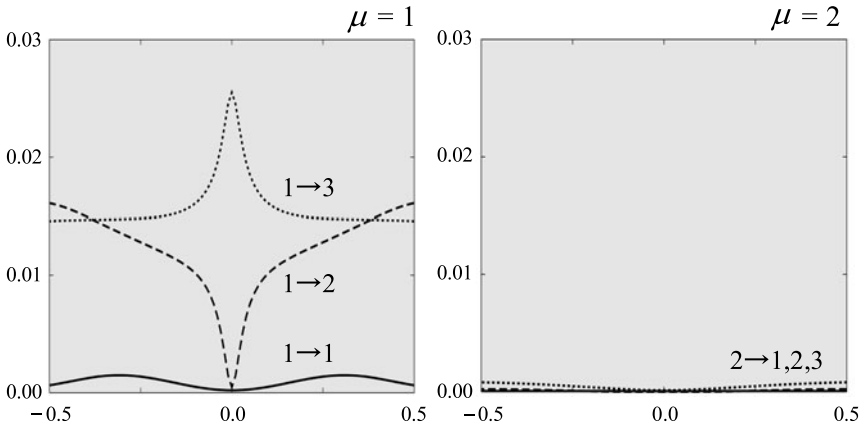

(b) Wave densities $\left|\langle \boldsymbol{G}|\lambda\rangle\right|^2$

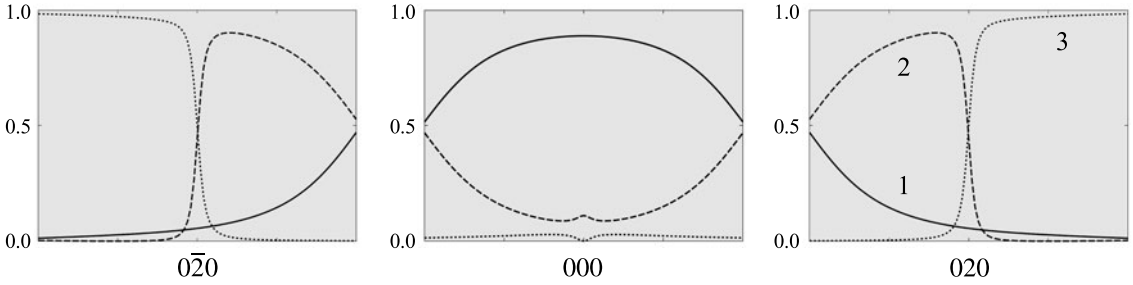

(c) Intensity contributions $\left|\langle \boldsymbol{G}|\lambda\rangle\right|^2 \times T_\mu^\lambda \times \left|\langle \boldsymbol{O}|\mu\rangle\right|^2 \quad (\mu \rightarrow \lambda)$

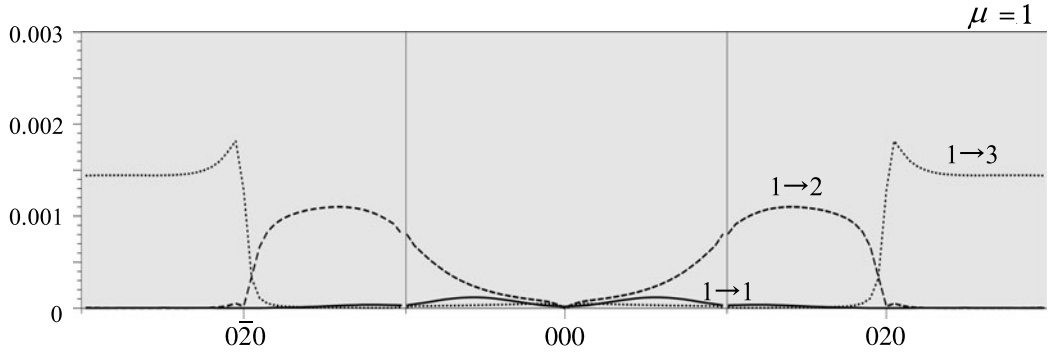

Contributions of normal and anomalous absorptions

Intensity contributions from branch 1 are further separated into the contributions from the normal and anomalous absorption terms.

The excess and defect features of the 020 Kikuchi band are created by the anomalous absorption term of the transitions 1→1 and 1→2. It is seen that the sum of the normal absorption terms forms a Kikuchi band with low contrast.

Let us see the relation between the normal and anomalous absorption terms in the formation of the Kikuchi band. The 020 excess Kikuchi band is created by the contribution mainly from the transition 1→1, where the contributions from both the normal and anomalous absorption terms are added constructively. For the formation of the defect Kikuchi band at low scattering angles, the contributions from the transition 1→1 are important, where the negative contribution of the anomalous absorption term cancels the contribution from the corresponding normal absorption term. The transition 1→2 gives positive contributions outside the band edge to form the defect band.

The excess and defect features of the 040 Kikuchi band are created by the anomalous absorption terms of the transitions 1→2 and 1→3.

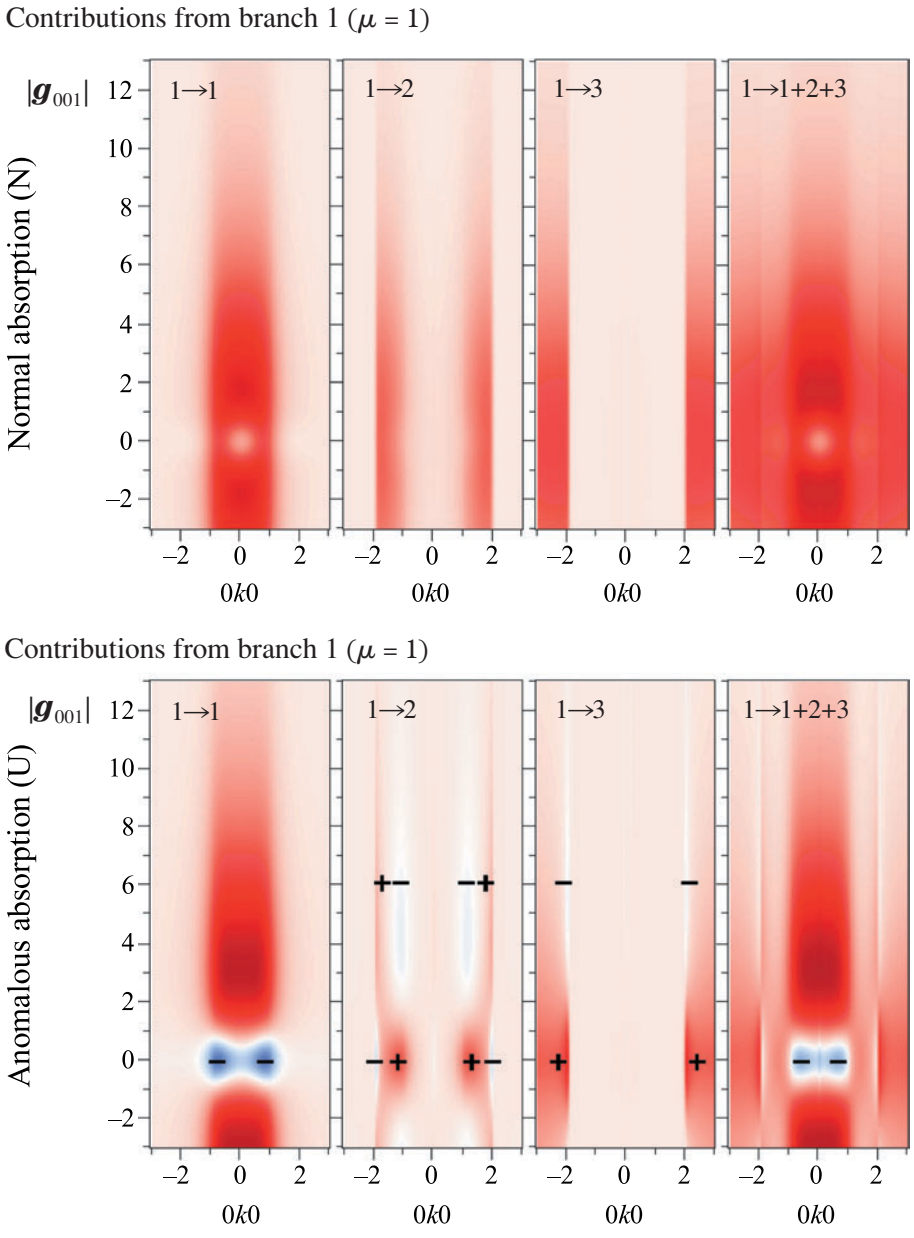

Contributions from branch 1 ($\mu = 1$)

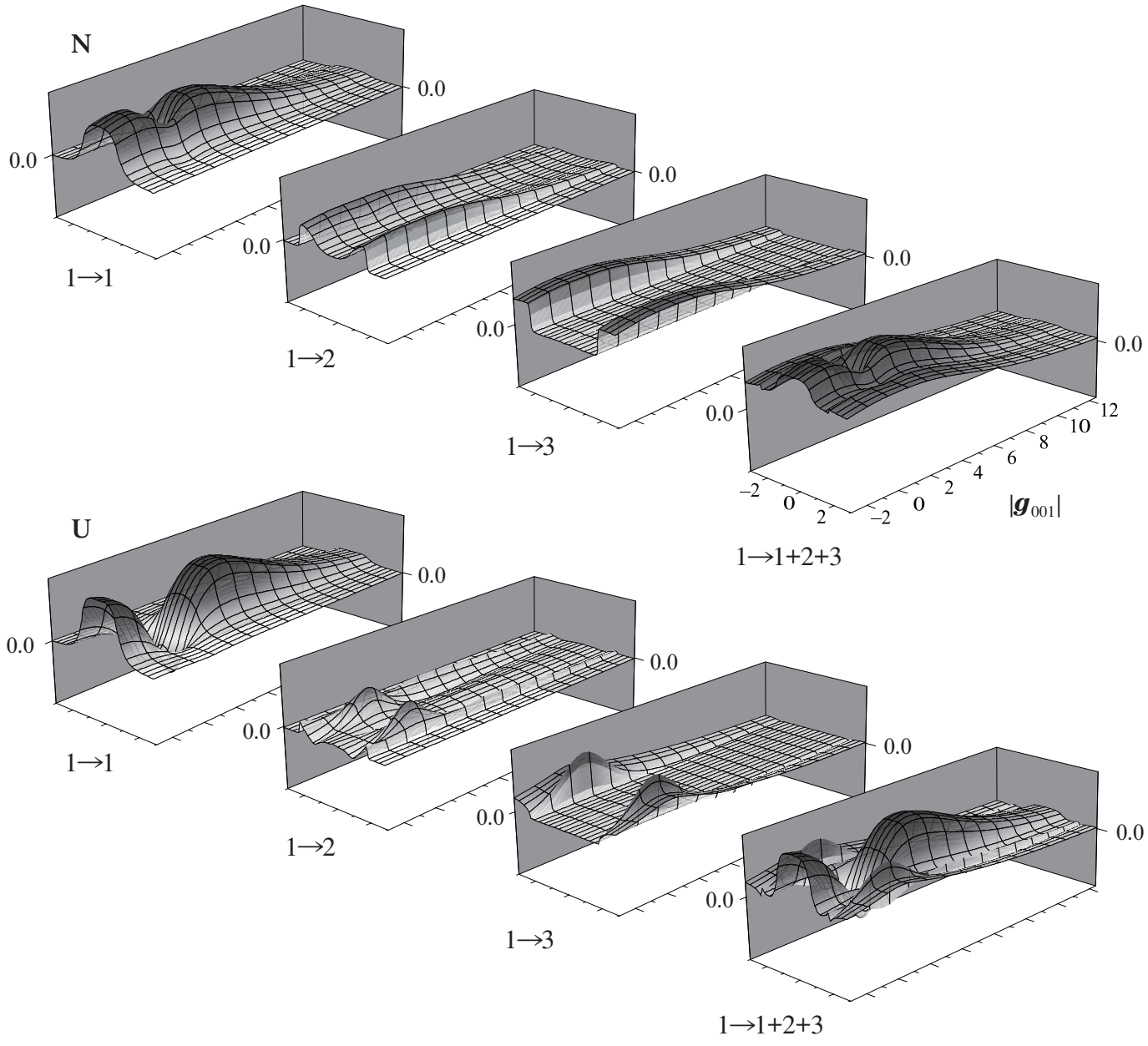

N: Normal absorption U: Anomalous absorption

Bird's-eye views of the contributions from the normal and anomalous absorptions.

Probability densities of the transitions from branches 1 and 2 – Contributions of normal and anomalous absorptions –

Probability densities of transitions from branches 1 and 2 on the $0\bar{2}6 - 026$ row and $0\bar{2}0 - 020$ row (on the right-side page) are separated into the contributions of the normal and anomalous absorptions. The behaviors of the probability densities of the transitions are helpful to understand the formation of the Kikuchi band though the excitation probabilities of the initial and final states have to be considered in this case. On the $0\bar{2}6 - 026$ row, the excess band is created almost by the transition 1→1 because the transitions 1→2 and 1→3 are small and the transitions from branch 2 are negligible due to small $|\langle \boldsymbol{O}|\mu\rangle|^2$, $\mu = 2$.

On the other hand, on the $0\bar{2}0 - 020$ row, the normal absorption term (N) of the transition 1→1 is almost canceled by the anomalous absorption term (U). Although the term U of the transition 1→3 is large in the incident beam direction, the intensity contribution is small due to small $|\langle \boldsymbol{G}|\lambda\rangle|^2$, $\lambda = 3$. As a result, the defect band is formed by the transition 1→2 (See Fig. (c) on page 235).

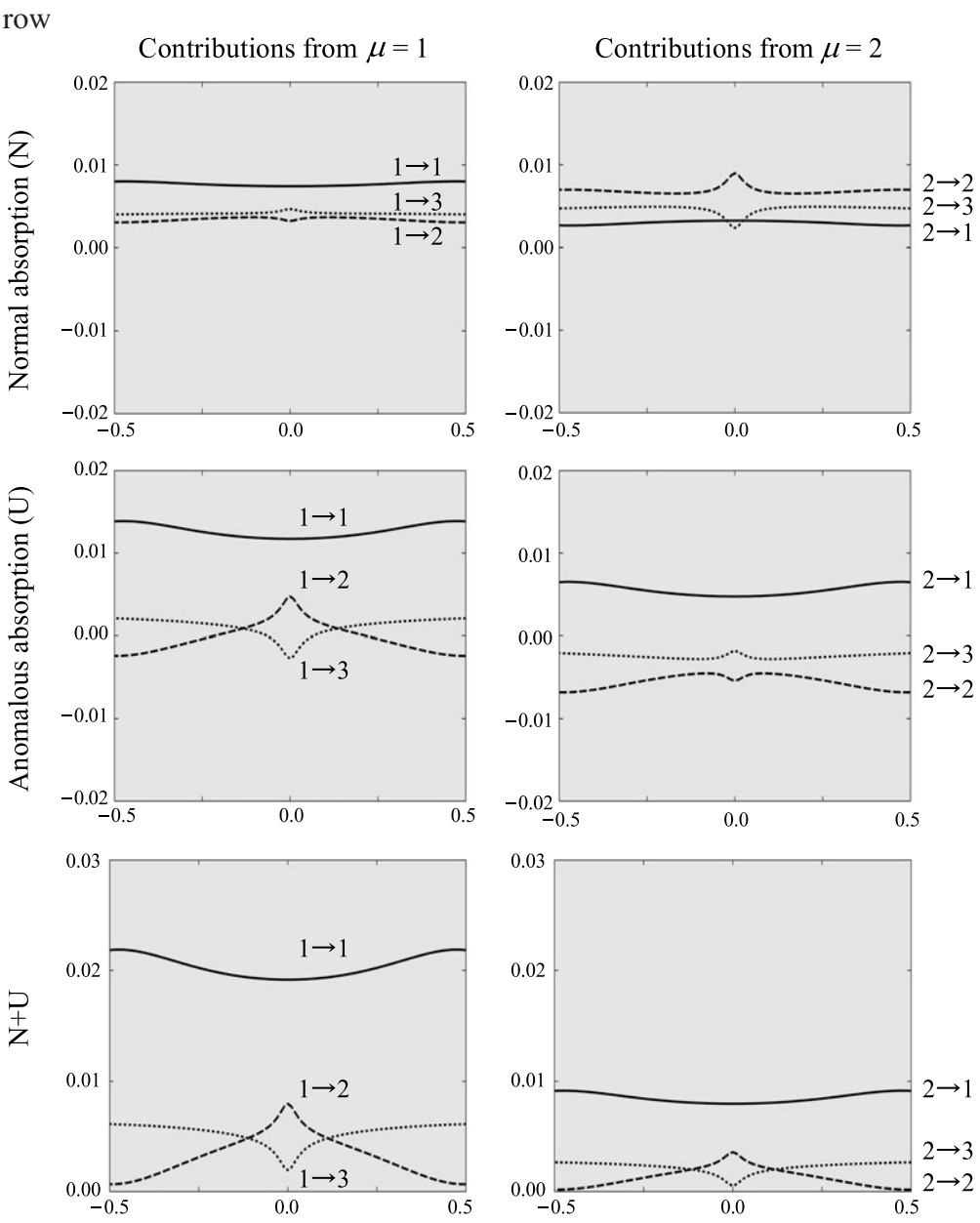

$0\bar{2}0$ – 020 row

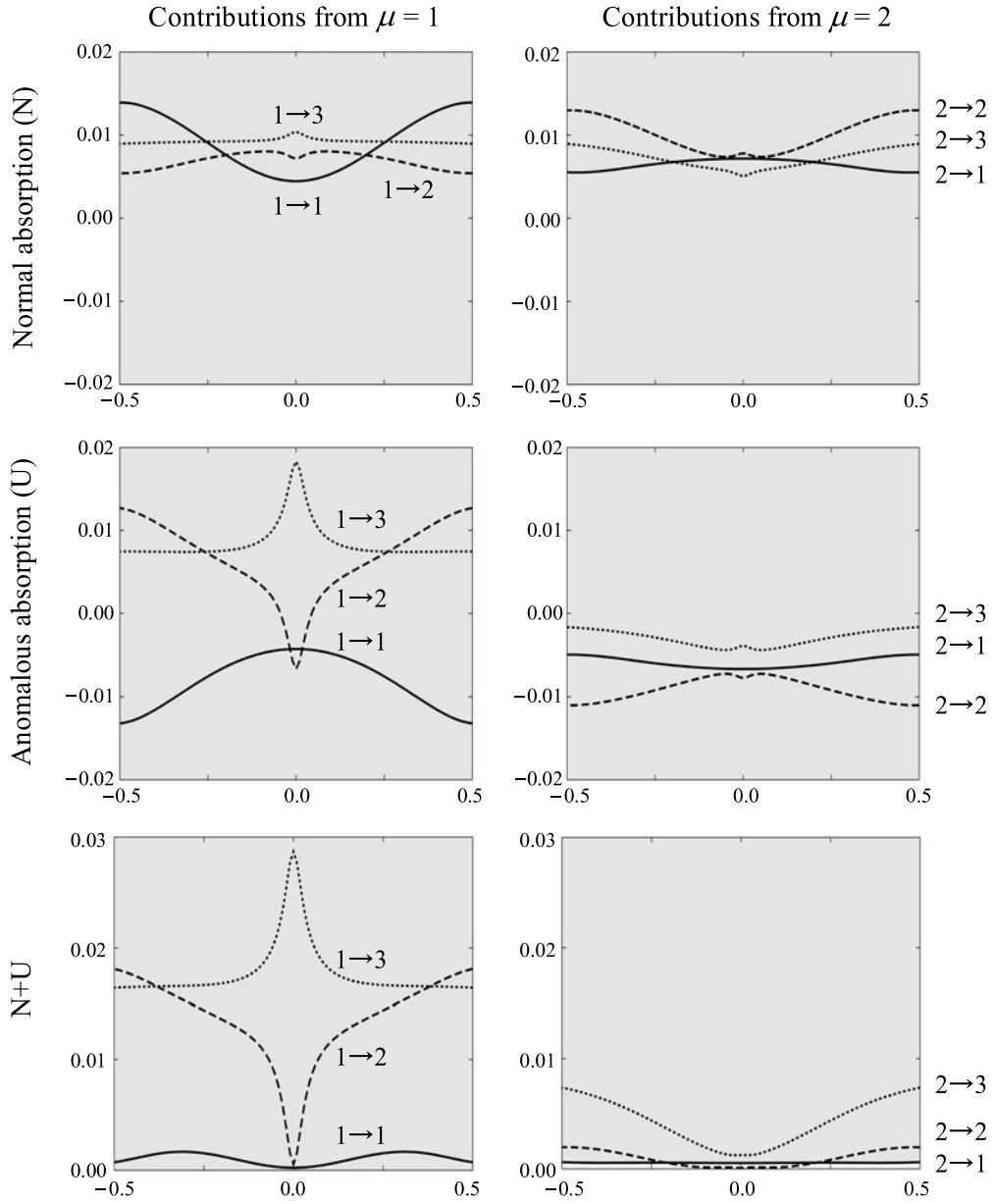

Many-beam simulations (MgO 020 excitation)

The initial Bloch waves 1 and 2 of MgO occupy an excitation of 98% of the whole Bloch waves at the 020 excitation incidence in a calculation with ten systematic beams. The real and imaginary parts of the branches of the dispersion surface are shown in Fig. (a). The wave densities of the final states are displayed in Fig. (b).

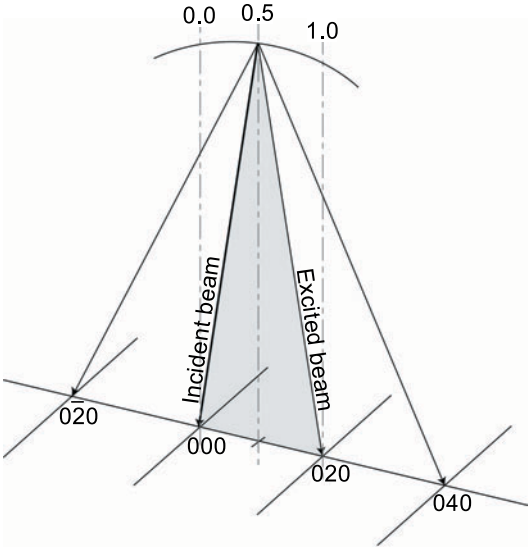

Incident-beam condition.

Branch	Excitation
1	0.48
2	0.50
3	0.014
4	0.0034
:	:

Absolute squares of excitation amplitudes at the 020 excitation incidence.

(a)

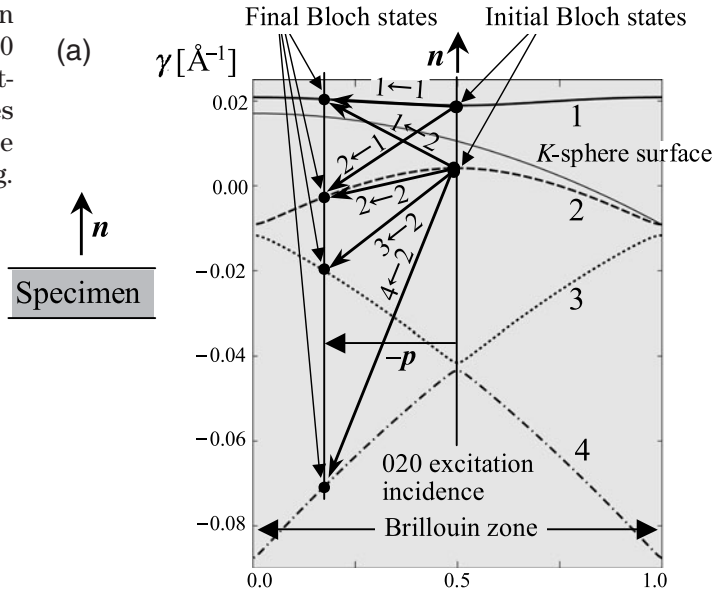

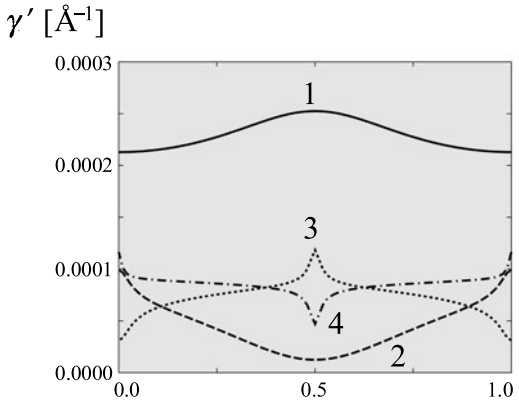

Real (γ) and imaginary (γ') parts of the dispersion surface.

(b) Wave densities $\left|\langle \boldsymbol{G} | \lambda \rangle\right|^2$

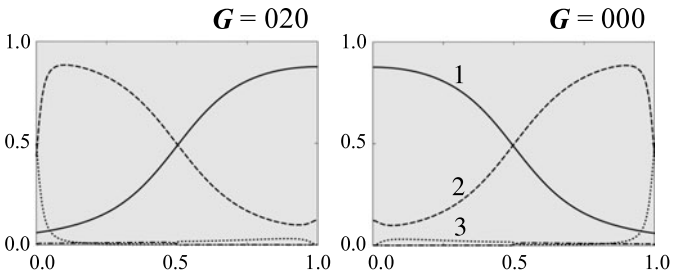

Absolute squares of the component-wave amplitudes of the Bloch waves.

Kikuchi bands calculated by the independent Bloch-wave treatment (Takagi's treatment)

Due to the increase of the beam number of the calculation, the Kikuchi bands of high-order reflections are well reproduced. The basic feature of the 020 (central) band is the same as that of the two-beam calculation. It should be noted that the defect band area extends as the order of reflection becomes high (See page 221).

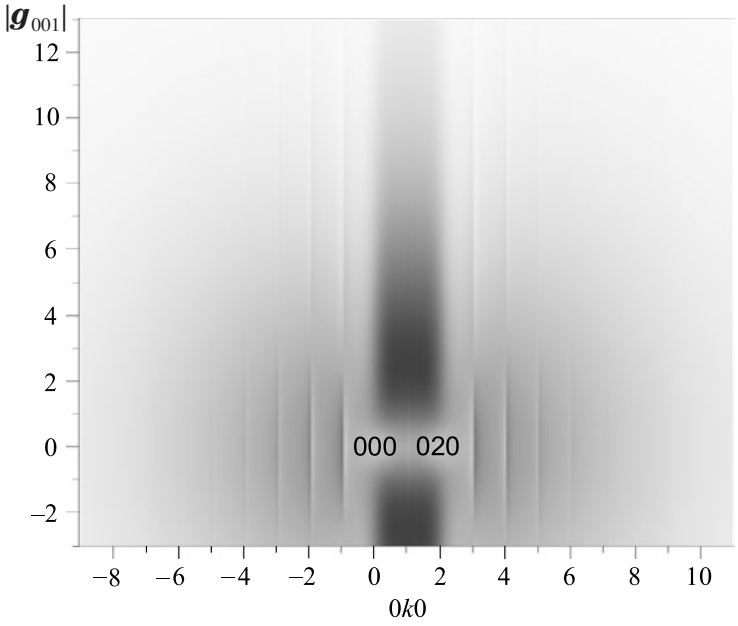

B(Mg): 0.31Å^2, B(O): 0.34Å^2
Number of beams: 10
Number of pixels: 401 × 321

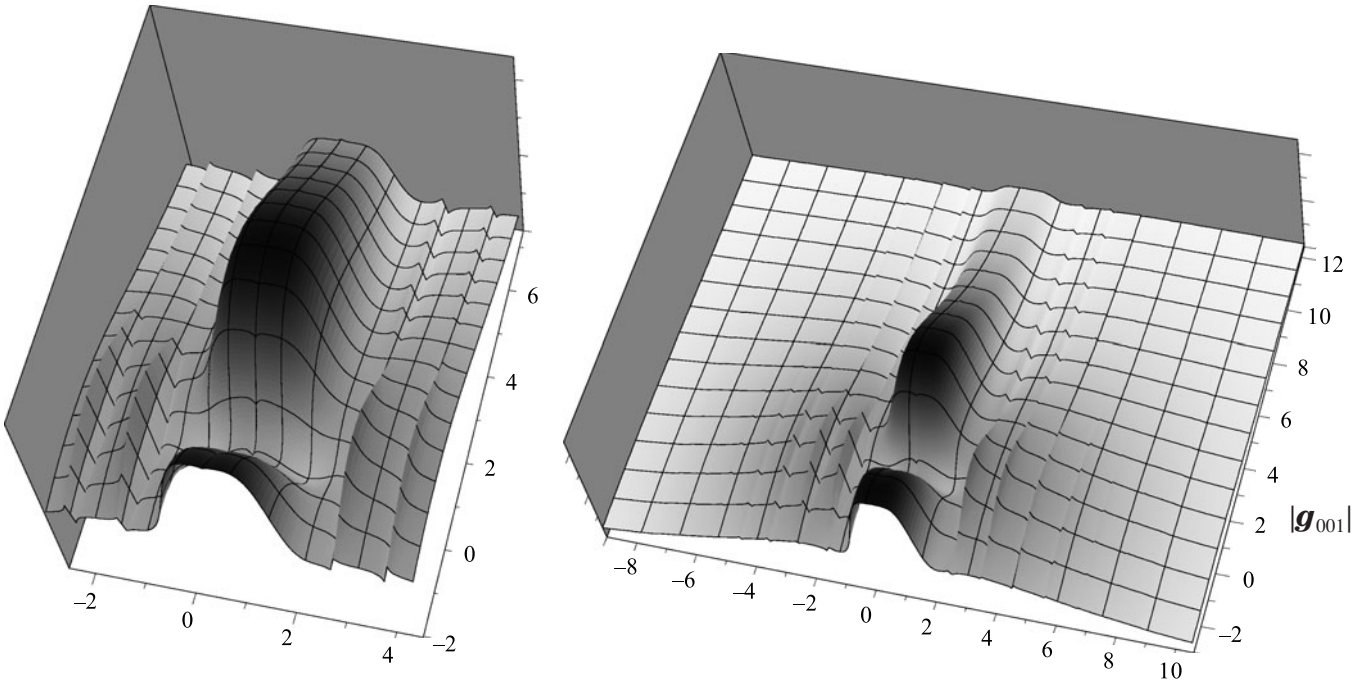

Effects of the cross terms of the transitions between the Bloch waves

Beyond Takagi's treatment (eq.(8)), we have used a more accurate expression eq.(5) on page 176, in which the cross terms of the transition probabilities and the absorption effect in the elastic scattering process are taken into account. The thickness dependence, the asymmetry features, the accurate intensity distribution along the band, the accurate incidence-orientation dependence and the interference fringes of the Kikuchi bands have been obtained.

For the two-beam case, in which a Bragg reflection is exactly excited, the Kikuchi band is asymmetric with respect to the center of the band. The degree of asymmetry is strong at thicknesses of n and $(n+1/2)$ times the extinction distance ξ_g of the excited reflection, but weak at thicknesses of $(n+1/4)$ and $(n+3/4)$ times ξ_g. This indicates a strong Pendelloesung effect of the dynamical diffraction on the Kikuchi band. The asymmetry is strong for thin specimens and weak for thick specimens. It is noted that the Kikuchi band is symmetric with respect to the band center for the case of the symmetric incidence.

In the case of Takagi's treatment, the intensity distribution across the Kikuchi band is featureless but the Kikuchi bands calculated with eq.(5) shows the interference fringes parallel to the band edge. In the case of Takagi's treatment, the excess band near the defect band has a strong intensity and forms a hump (Fig. (a)), but the intensity calculated with eq.(5) is weak and the intensity distribution along the band is more gradual with a small hump (Fig. (b)). This is roughly explained in terms of the strong absorption of the branch 1 in the elastic scattering process.

These behaviors are really observed in the experimental Kikuchi patterns of MgO. It is emphasized that these phenomena can be explained not by Takagi's independent Bloch-wave treatment but only by the sophisticated treatment of eq.(5).

(a) Without the cross terms (Takagi's treatment)

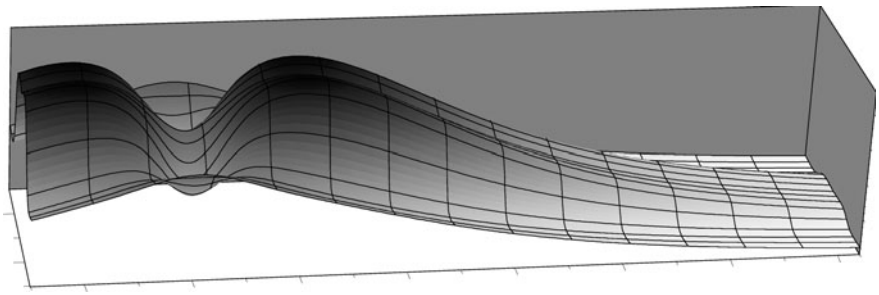

(b) With the cross terms

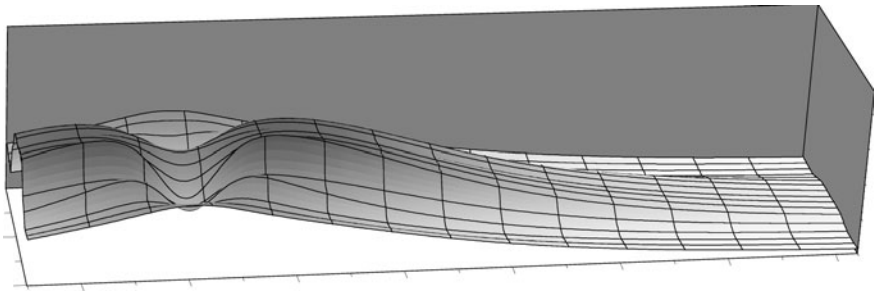

B(Mg): 0.31Å^2, B(O): 0.34Å^2
Number of beams: 2
Number of pixels: 81 × 321

Thickness dependence of the Kikuchi band (MgO 020 excitation)

The figures show the thickness dependence of the Kikuchi band of MgO which were calculated at the 020 excitation under the two-beam approximation using eq.(5) on page 176. The Kikuchi bands are weak and vague for thin specimens. As the thickness increases, the Kikuchi bands and their asymmetry become clear.

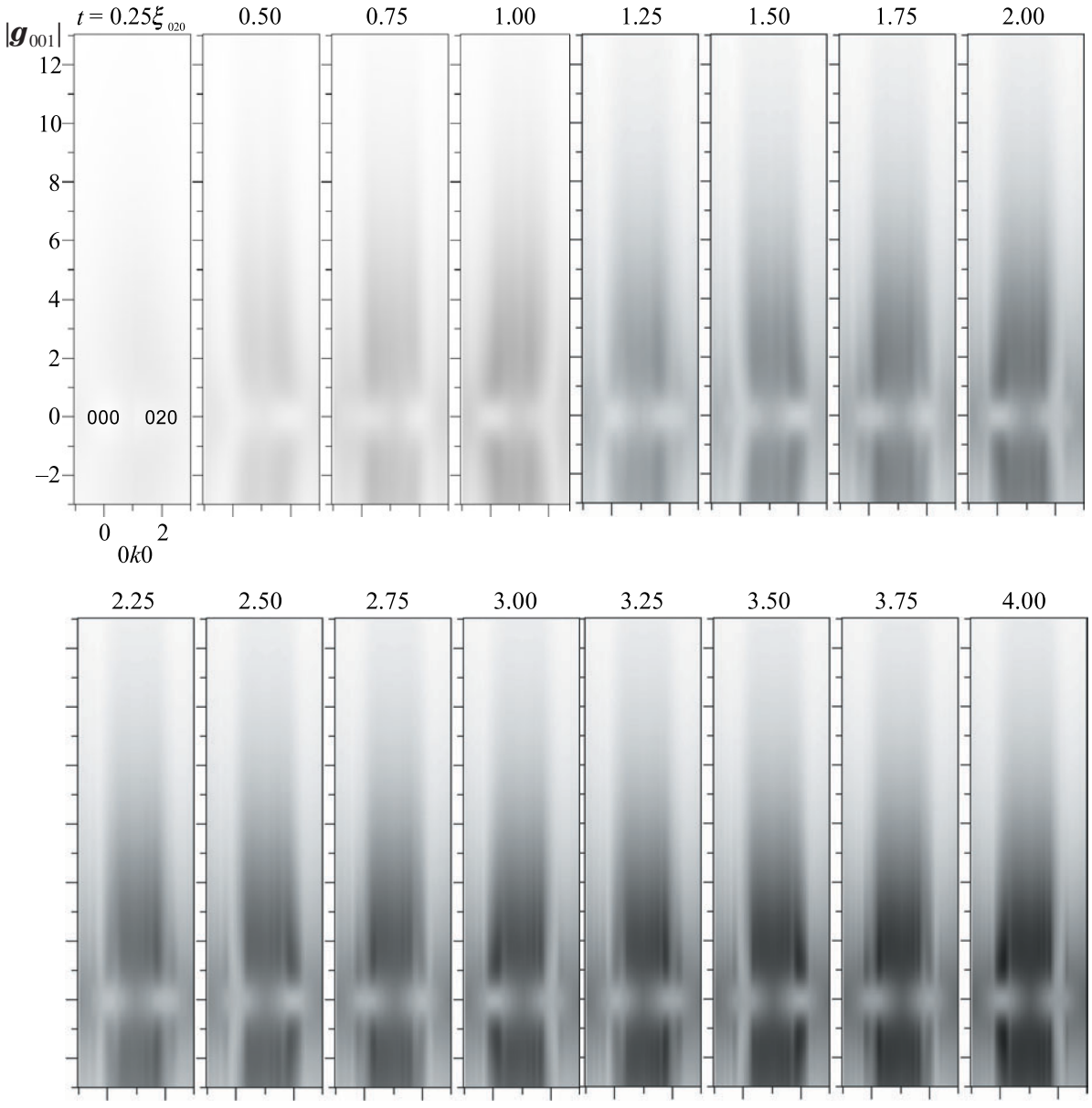

B(Mg): 0.31Å^2, B(O): 0.34Å^2
Number of beams: 2
Number of pixels: 81 × 321
Extinction distance ξ_{020}: 42.5nm

Thickness dependence of the Kikuchi band of MgO, where the thickness is given in the unit of the extinction distance of the reflection ξ_{020} (= 42.5nm).

Asymmetry of the Kikuchi band (MgO 020 excitation)

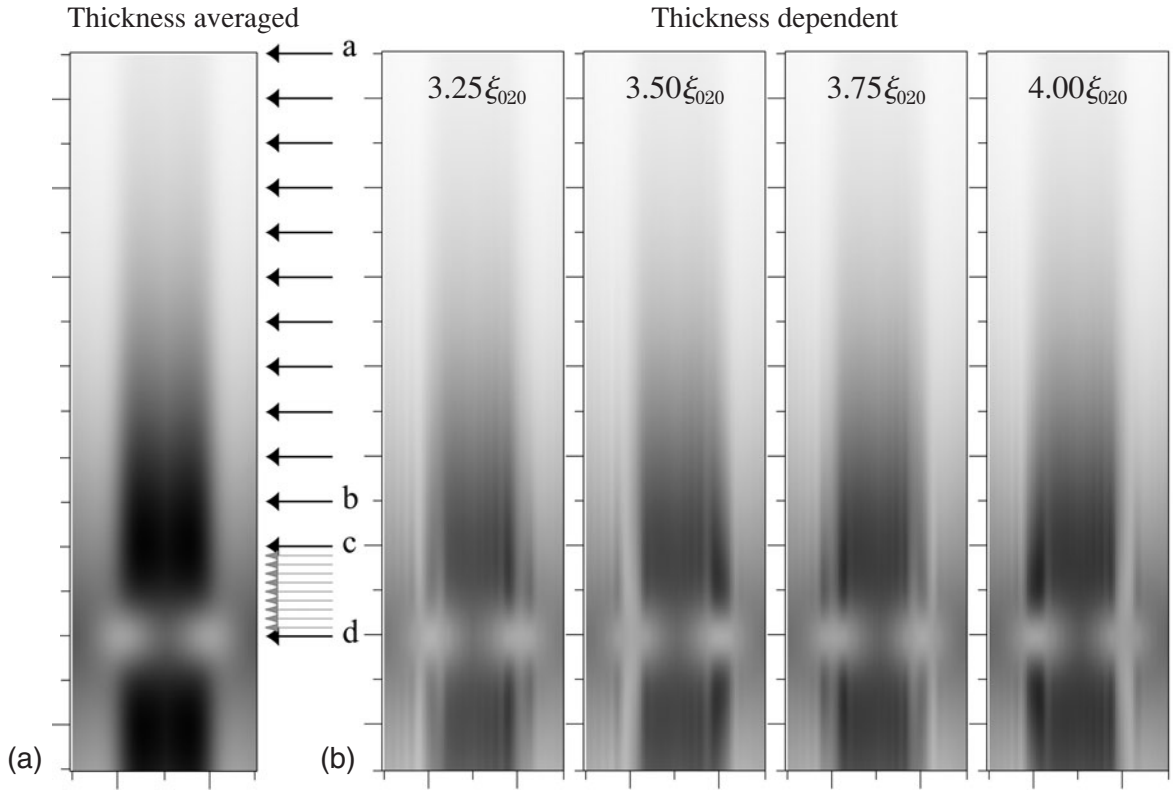

Line profiles

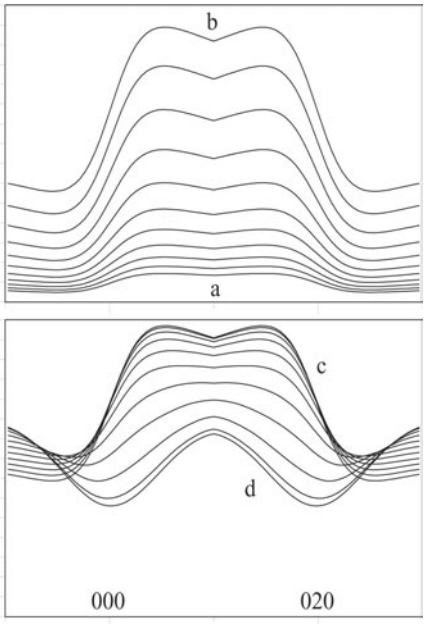

Four simulated Kikuchi bands of Fig. (b), which are shown on the last page, are compared with the band calculated by Takagi's treatment (Fig. (a)). The line profiles of Figs. (a) and (b) at the positions indicated by arrows and letters at the right side of Fig. (a) are displayed on this page and the next page, respectively. The profiles calculated by Takagi's treatment are symmetric with respect to the center of the band and show no fringes. The profiles calculated by eq.(5) are asymmetric with respect to the center of the band, and show the interference fringes. The asymmetry is strong at thicknesses of n and (n+1/2) times the excitation distance ξ_{020}, but weak at thickness of (n+1/4) and (n+3/4) times ξ_{020}.

Line profiles

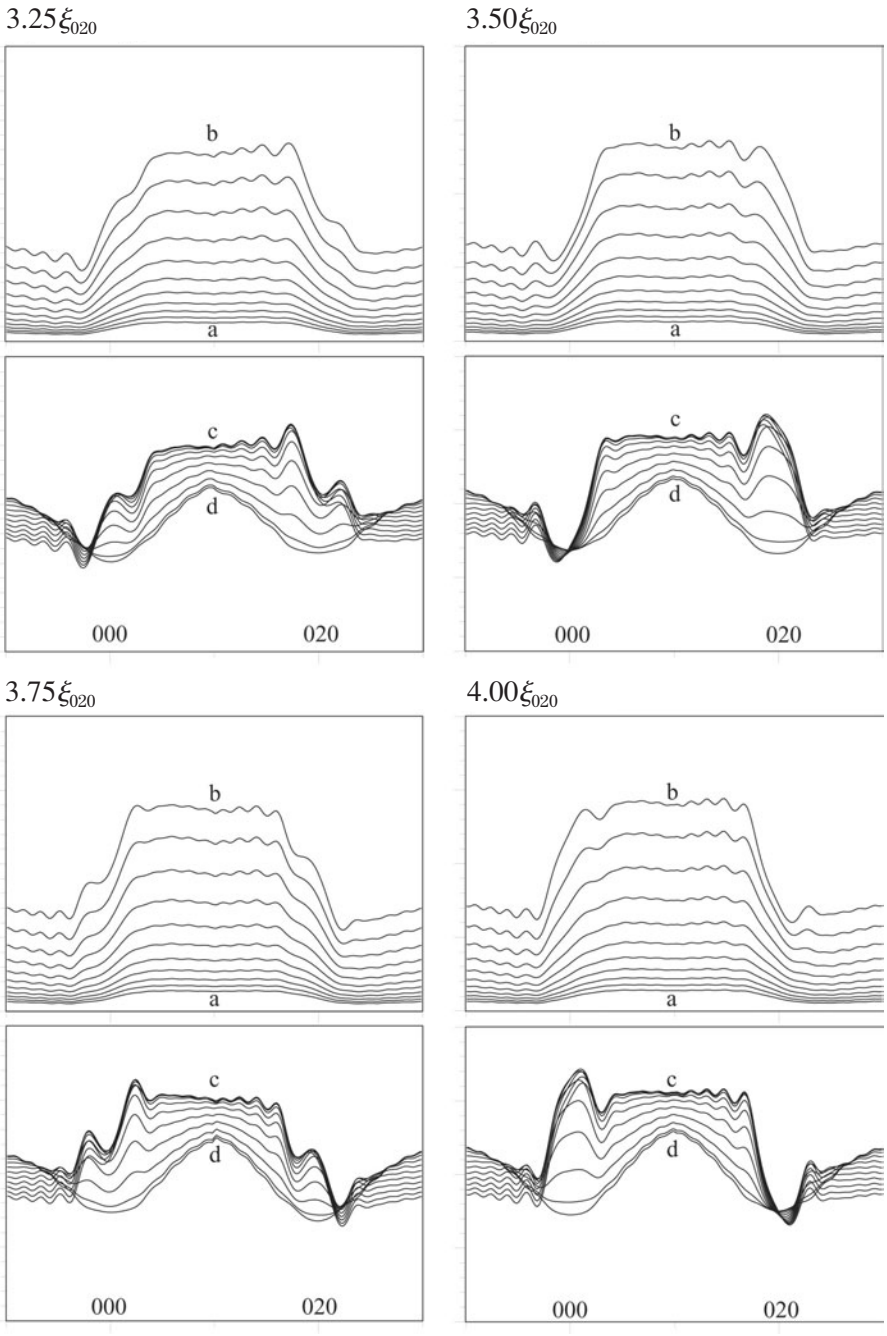

Thickness dependence of the Kikuchi band (MgO symmetric incidence)

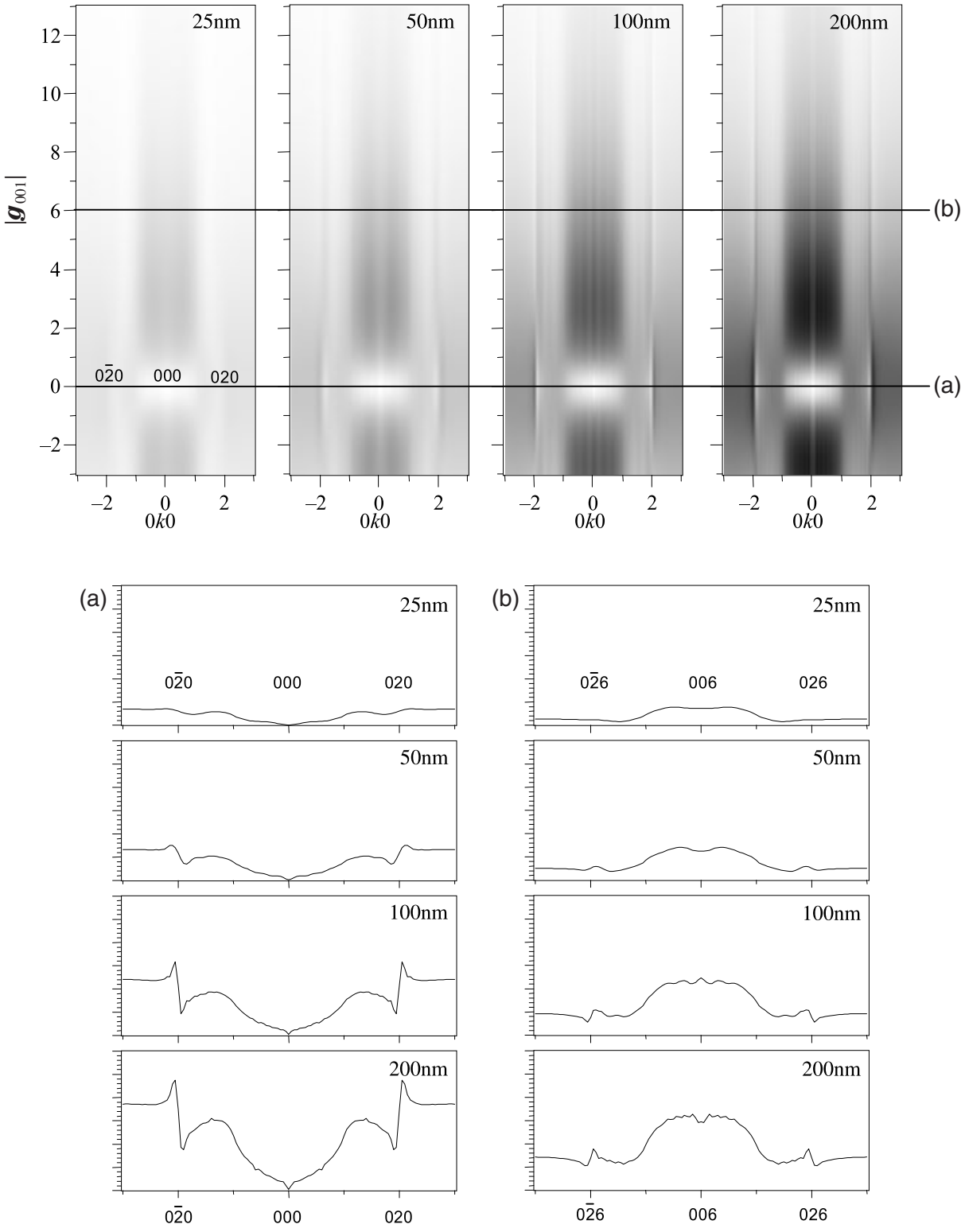

The Kikuchi bands simulated at the symmetric incidence condition with three 0*k*0 systematic reflections. The intensity profiles on lines (a) and (b) in the upper figures at thicknesses of 25nm, 50nm, 100nm and 200nm are displayed in the lower figures. The profiles are symmetric with respect to the 000 and 006 positions in contrast to the profiles at the 020 excitation.

Incidence-orientation dependence of the Kikuchi band

It was examined how the Kikuchi bands of MgO change with the incidence orientation using eq.(8) (Takagi's treatment) (Figs. (a) to (c)) and eq.(5) (with cross terms) (Figs. (d) to (f)). Simulations were carried out with 13 beams at an accelerating voltage of 100kV for three incidences of symmetric, 040 excitation and 080 excitation. The line profiles were taken from the positions indicated by the dotted lines given at the simulations.

Let us examine the 040 and 060 Kikuchi bands. Figure (a), which was calculated by eq.(8) without the cross terms, is similar to Fig. (d), which was calculated by eq.(5) with the cross terms, except the interference fringes already mentioned. When the incident beam is tilted, the 040 and 060 Kikuchi bands of Figs. (b) and (c) are still symmetric with respect to the center of the 020 Kikuchi band, but those of Figs. (e) and (f) are already asymmetric. The intensity profiles of the dispersion type are seen at Kikuchi band edges in both Figs. (b) and (c). However, Fig. (e) shows profiles which are transitional from Kikuchi bands to Kikuchi lines and Fig. (f) nearly shows profiles of Kikuchi lines. Actually, not Kikuchi band but Kikuchi lines are seen in the bottom Photo on page 211, which was taken at the incidence of the 060 excitation of MgO.

In the case of Takagi's treatment, Kikuchi bands change to Kikuchi lines more slowly with the tilt of the incident beam than in the case of eq.(5). From these simulations, it was found that the cross terms play an important role in calculating the accurate incidence-orientation dependence of the Kikuchi band.

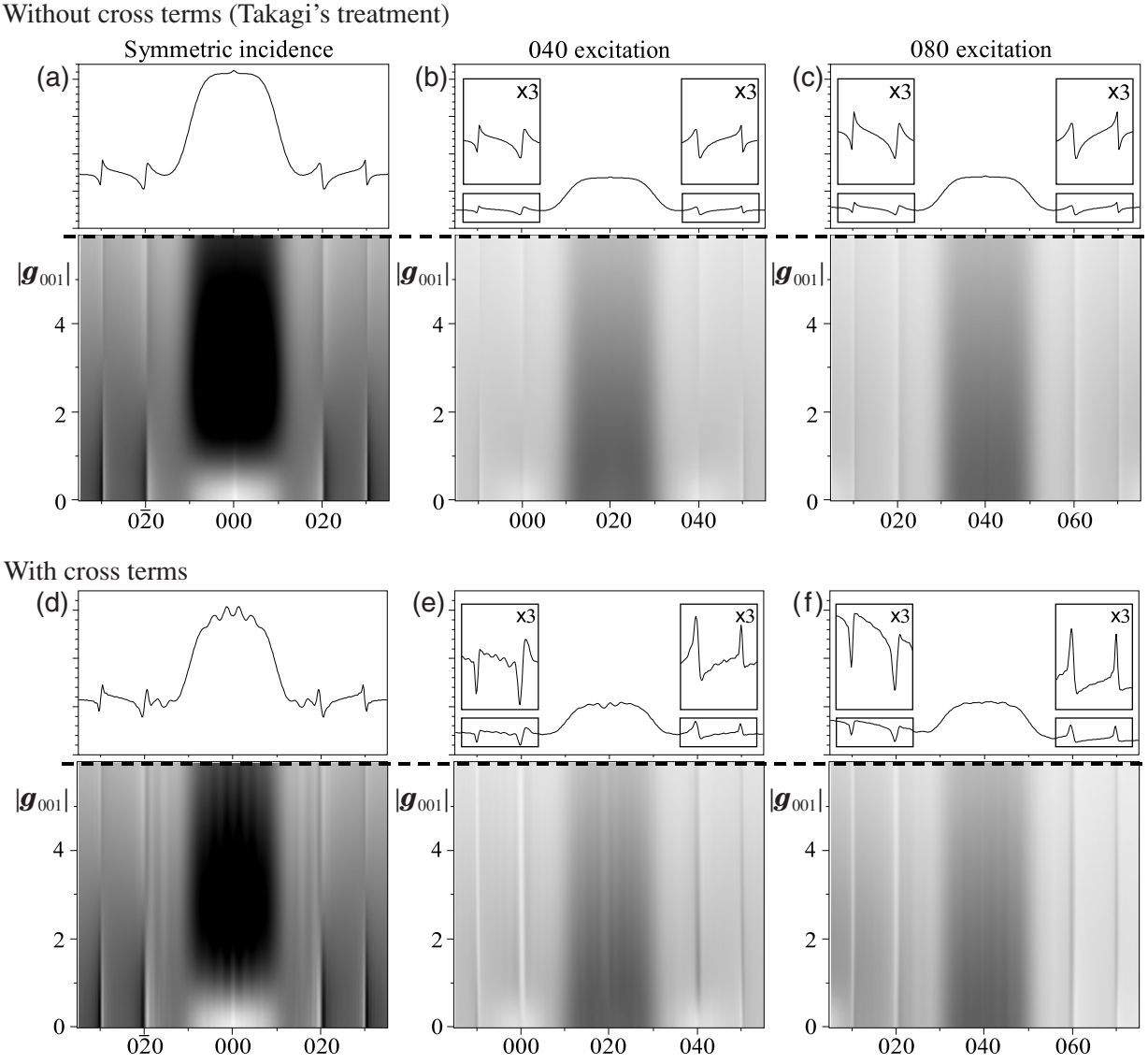

Change from Kikuchi bands to Kikuchi lines

Let us see the change from Kikuchi bands of the 040 and 060 reflections to Kikuchi lines with the tilt of the incident beam using the contributions of the normal and anomalous absorption terms. For qualitative understanding, simulations were carried out with the use of Takagi's treatment. At the symmetric incidence, there exist Kikuchi bands or the definite contribution from the anomalous absorption term but exist no Kikuchi lines or only a little contribution to the band from the normal absorption term. It is clearly seen that the intensities from the normal absorption term or the Kikuchi lines increase with the tilt of the incident beam, but the intensities from the anomalous absorption term or the Kikuchi bands decrease.

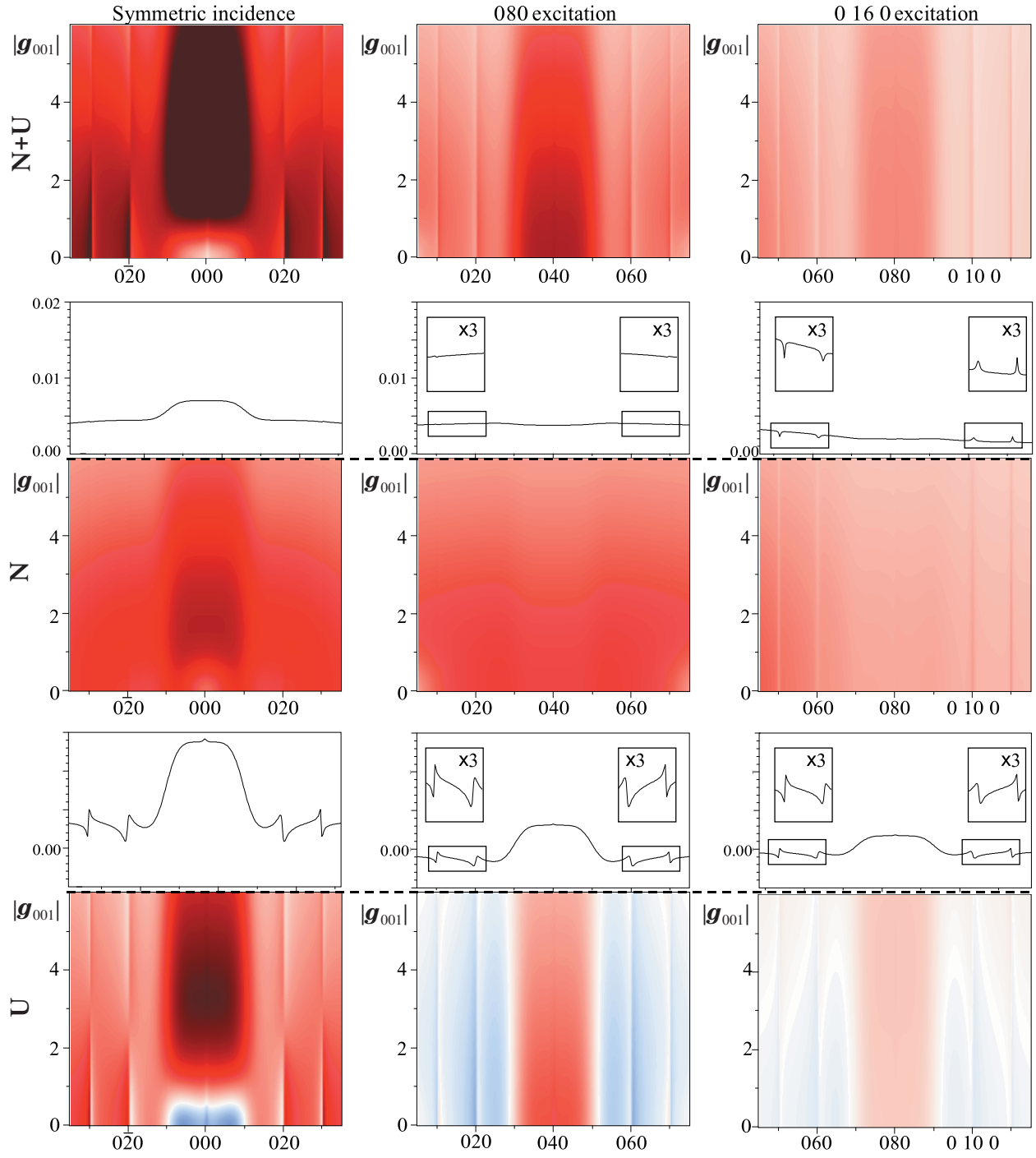

Comparison Between Experimental and Simulated Patterns (Systematic Reflection Cases)

Experimental Kikuchi patterns of MgO taken at the systematic reflection conditions are compared with experimental ones. All the experimental diffraction patterns are energy-filtered zero-loss patterns taken by the JEM-2010FEF at an accelerating voltage of 100kV with an energy window of $\varnothing E = \pm 5$eV. The Kikuchi lines due to the accidental reflections cannot be avoided in the experiments. The thicknesses of the experimental patterns were separately determined by the CBED method but there may be a variation of about 5nm in thickness in the illuminated areas where the Kikuchi patterns were taken. The simulations were carried out using eq.(5) on page 176, where ten systematic beams for the 020 excitation and eleven beams for the symmetric incidence are taken but the accidental reflections were not used to elucidate the systematic interaction.

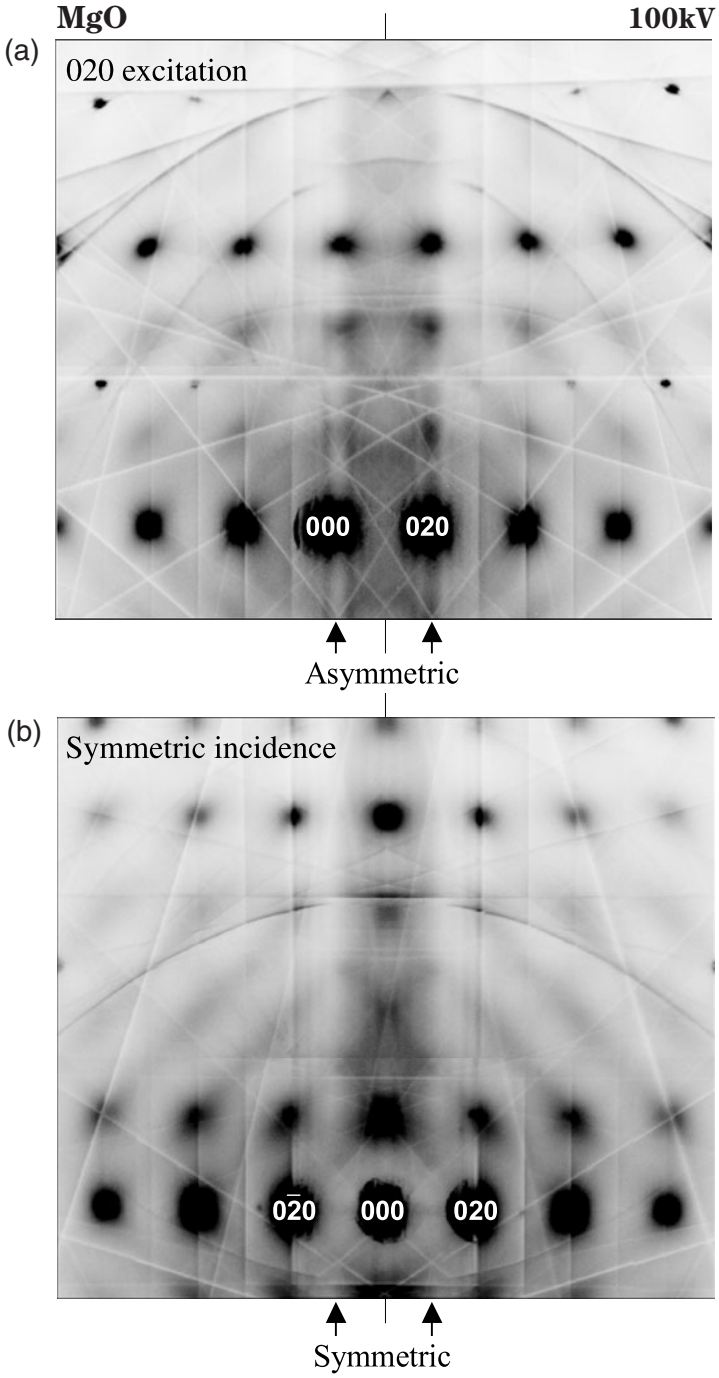

MgO 020 excitation

For the 020 excitation, experimental patterns taken at six different thicknesses are shown and corresponding simulations are displayed. Simulations were carried out with ten systematic beams using eq.(5) on page 176. The overall intensity distributions of the Kikuchi bands and the asymmetric features are well reproduced by the simulations. It is seen that the defect band area extends as the order of a reflection becomes high.

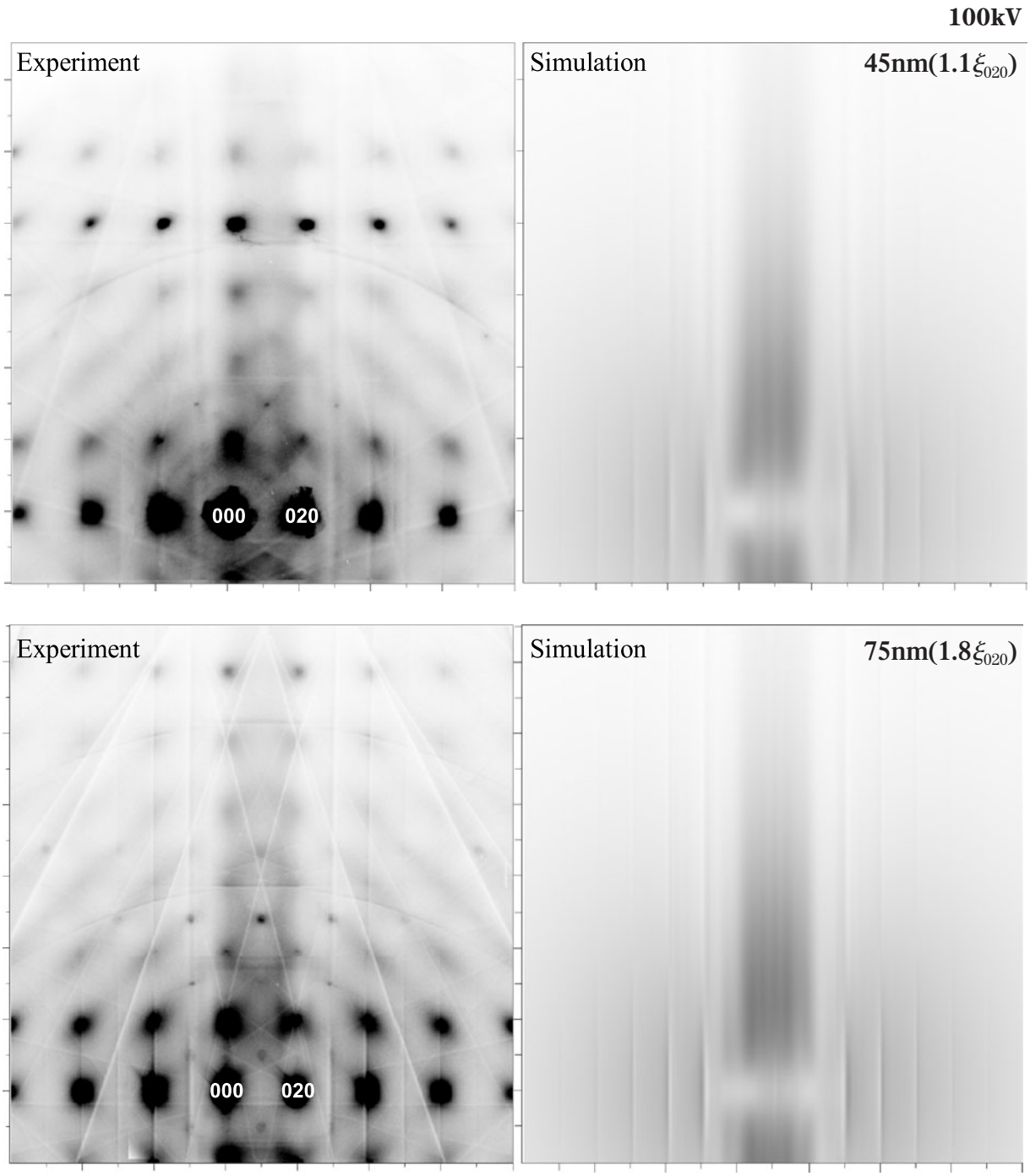

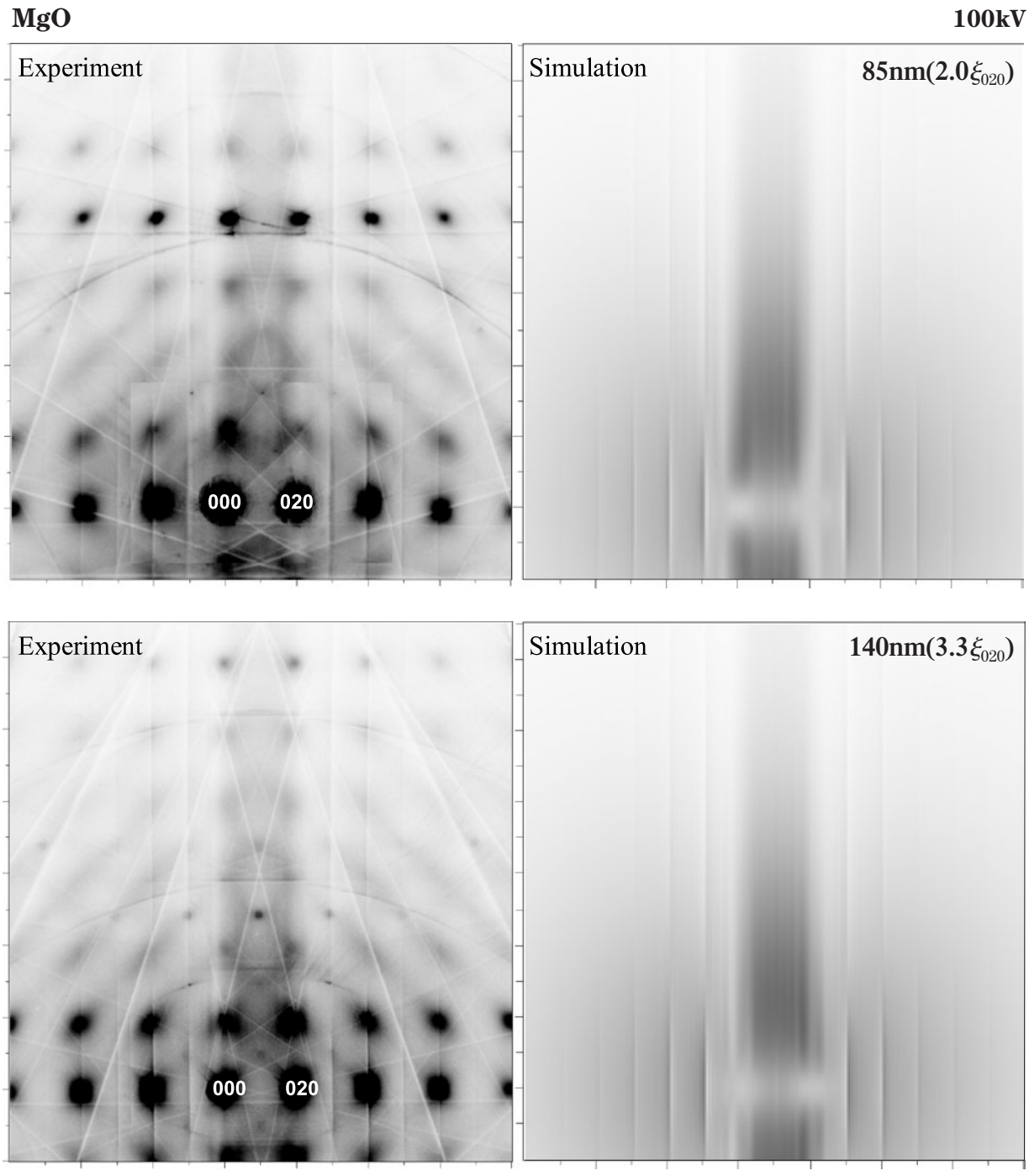

B(Mg): 0.31Å^2, B(O): 0.34Å^2
Number of beams: 210

Number of pixels: 281 × 321
Extinction distance ξ_{020}: 42.5nm

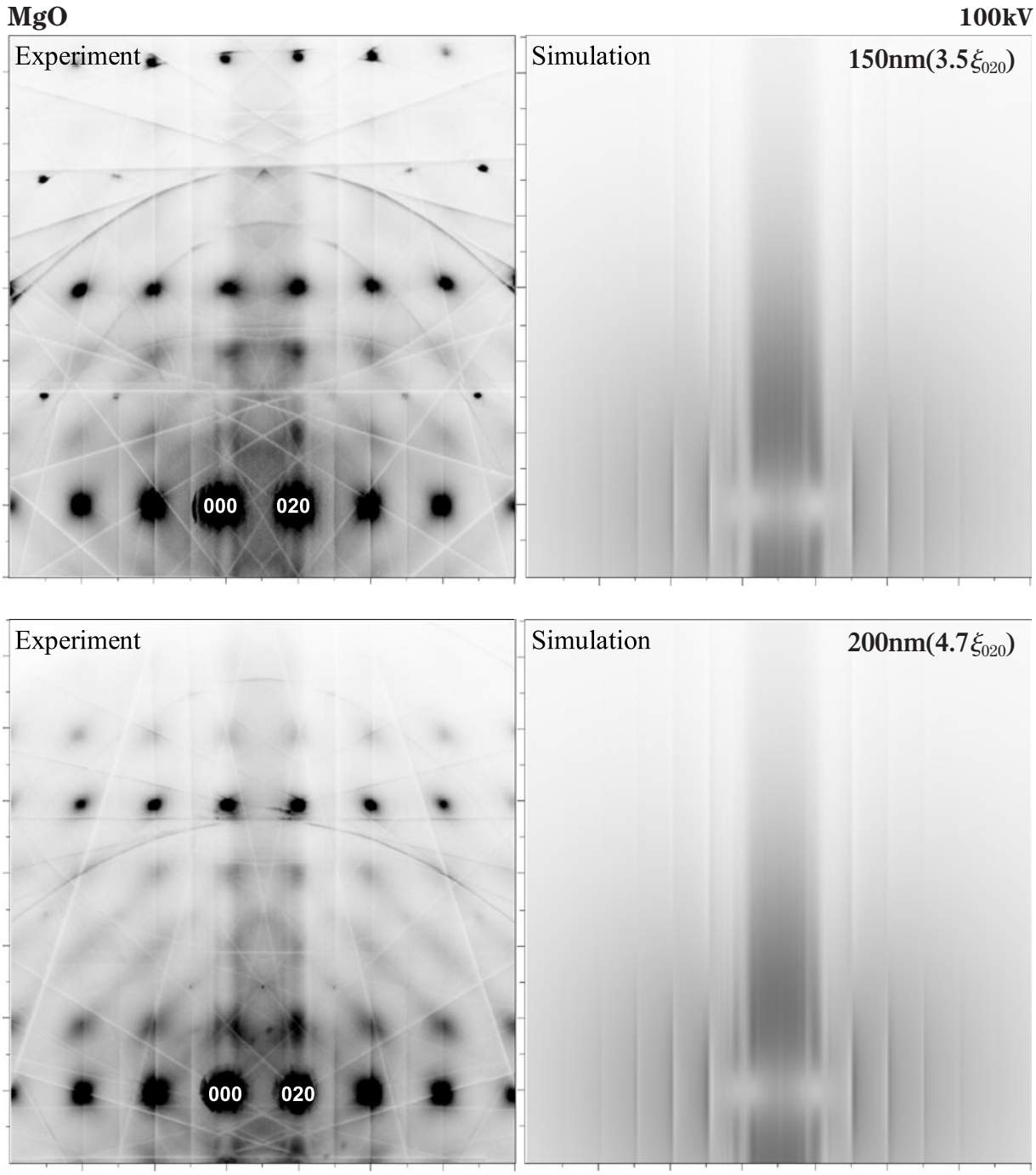
MgO
100kV
Experiment
Simulation
150nm(3.5ξ_{020})
000
020
Experiment
Simulation
200nm(4.7ξ_{020})
000
020

MgO symmetric incidence

For the symmetric incidence, two experimental patterns are shown and the corresponding simulations are displayed. The simulations were carried out by eleven systematic beams using eq.(5) on page 176. The overall intensity distributions and the symmetric features are well reproduced.

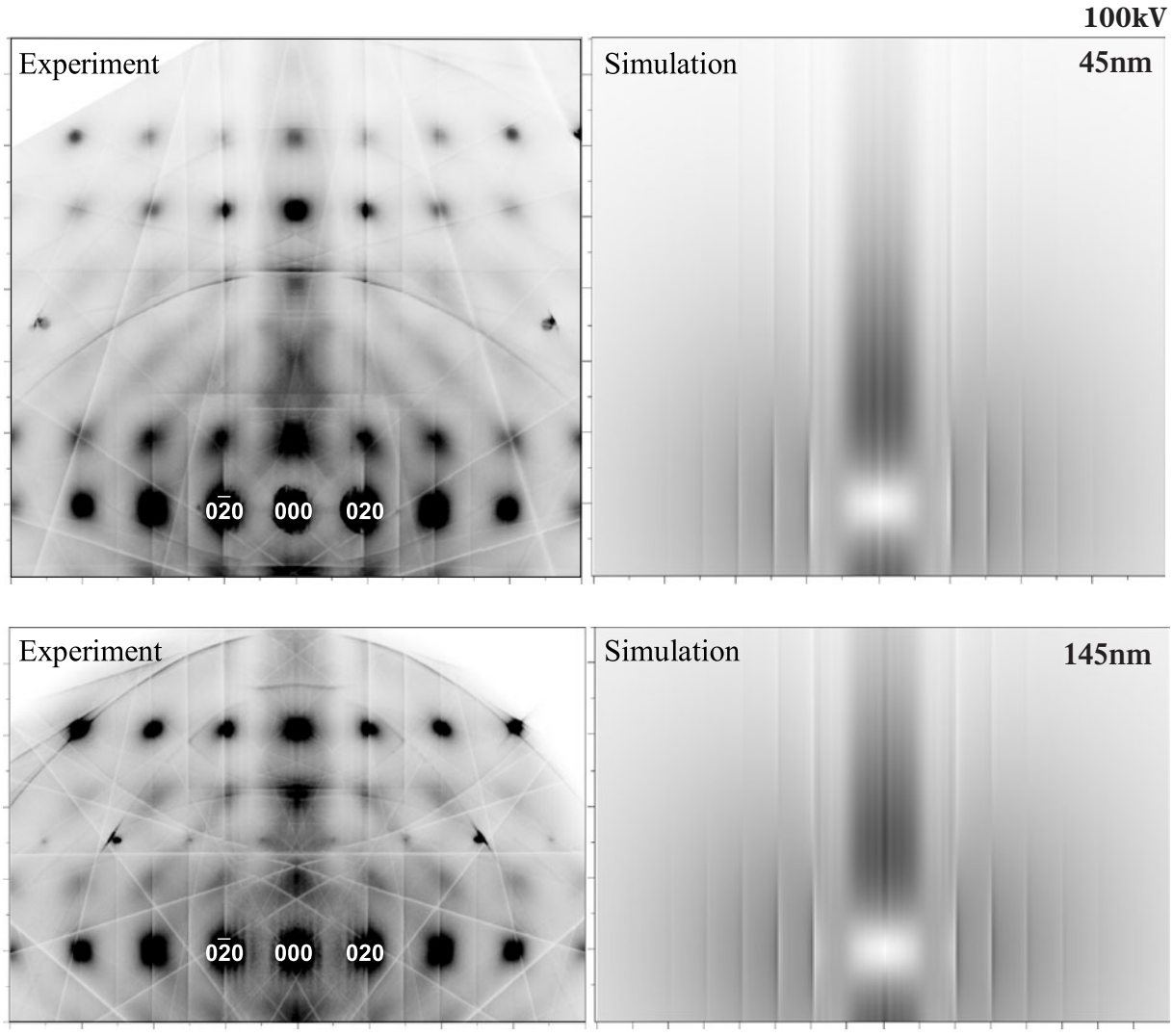

B(Mg): 0.31Å^2, B(O): 0.34Å^2
Number of beams: 11
Number of pixels: 321 × 301 (top)
321 × 221 (bottom)

Interface Analysis

Determination of Displacement Vectors

We already reported on a general method for determining the shift vector of a stacking fault using the defocus CBED method [a],[38],[7]. We cite here the essential part of the method with a view to understanding the following part.

When a defocus convergent-beam illuminates a specimen area containing a stacking fault with a displacement vector $\boldsymbol{R}$ oblique to the specimen surface, a continuous change of the intensity profile of a reflection line is observed across the fault as illustrated in the upper figure on the right-side page. Phase shift α is expressed by

$$\alpha_i = 2\pi \boldsymbol{g}_i \cdot \boldsymbol{R} = \alpha_i' + 2\pi n_i, \tag{1}$$

where the suffix i specifies the reflection index, α_i' takes a value between $-\neq$ and $\neq$, and n_i is an integer. $\boldsymbol{g}_i$ is (h_i, k_i, l_i) and $\boldsymbol{R} = {}^t(u, v, w)$. For three arbitrary reflections, eq. (1) is written as

$$\begin{aligned} 2\pi \boldsymbol{g}_1 \cdot \boldsymbol{R} &= \alpha_1' + 2\pi n_1 \\ 2\pi \boldsymbol{g}_2 \cdot \boldsymbol{R} &= \alpha_2' + 2\pi n_2 \\ 2\pi \boldsymbol{g}_3 \cdot \boldsymbol{R} &= \alpha_3' + 2\pi n_3. \end{aligned} \tag{2}$$

When we define G, A and N as

$$G = \begin{pmatrix} \boldsymbol{g}_1 \\ \boldsymbol{g}_2 \\ \boldsymbol{g}_3 \end{pmatrix}, \quad A = \begin{pmatrix} \alpha'_1/2\pi \\ \alpha'_2/2\pi \\ \alpha'_3/2\pi \end{pmatrix} \quad \text{and} \quad N = \begin{pmatrix} n_1 \\ n_2 \\ n_3 \end{pmatrix},$$

eq. (2) is written as

$$G\boldsymbol{R} = A + N.$$

By multiplying G^{-1} from left, we obtain

$$\boldsymbol{R} = G^{-1} A + G^{-1} N.$$

To determine $\boldsymbol{R}$, we have to know both the values of A and N. The values of A are determined by experiments using the curves of the lower figure on the right-side page, but the values of N cannot be found from the experiments. Thus, $\boldsymbol{R}$ cannot be determined by a set of three linearly independent reflections. However, from the translational symmetry of crystals, the components of $\boldsymbol{R}$ are limited to values in ranges of $-1/2 < u < 1/2$, $-1/2 < v < 1/2$ and $-1/2 < w < 1/2$. Application of the conditions enables us to obtain allowed sets of values of n_i or a finite number of possible displacement vectors $\boldsymbol{R}$. We have the values of $2\pi \boldsymbol{g}_i \cdot \boldsymbol{R}$ for the reflections from the 4th on and compare the values with the experimental ones. The displacement vector $\boldsymbol{R}$ is unambiguously determined to be the vector whose phase shifts calculated for the reflections from the 4th on are in good agreement with the experimental values.

Reference

[a] M. Tanaka, S. Yamada and M. Terauchi: 5th Asia-Pacific Electron Microscopy Conference, Electron Microscopy I, World Scientific (1992) 154.

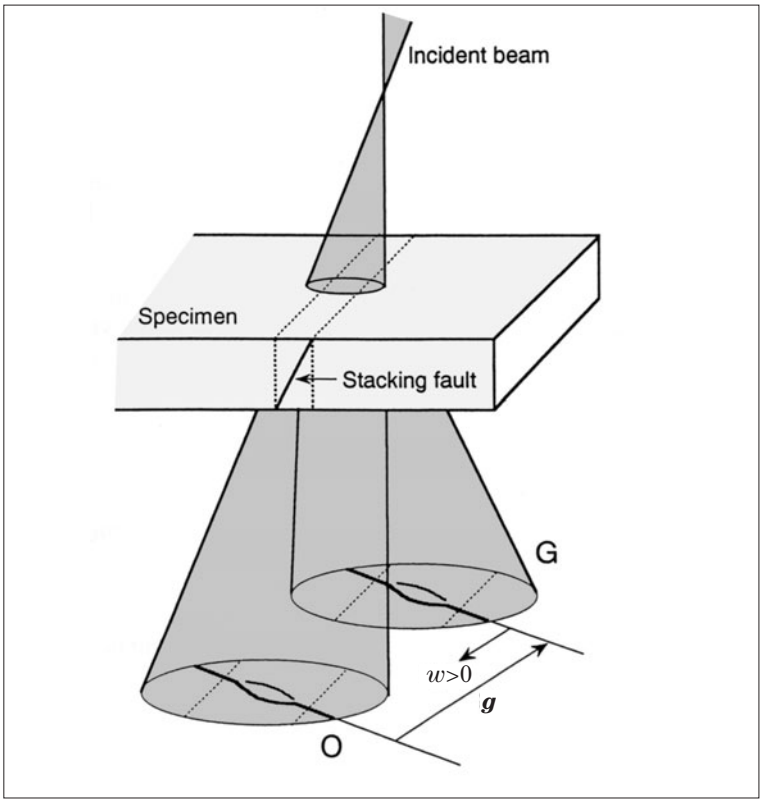

Defocused convergent-beam illumination for an area containing a stacking fault oblique to the specimen surface and expected reflection line profiles.

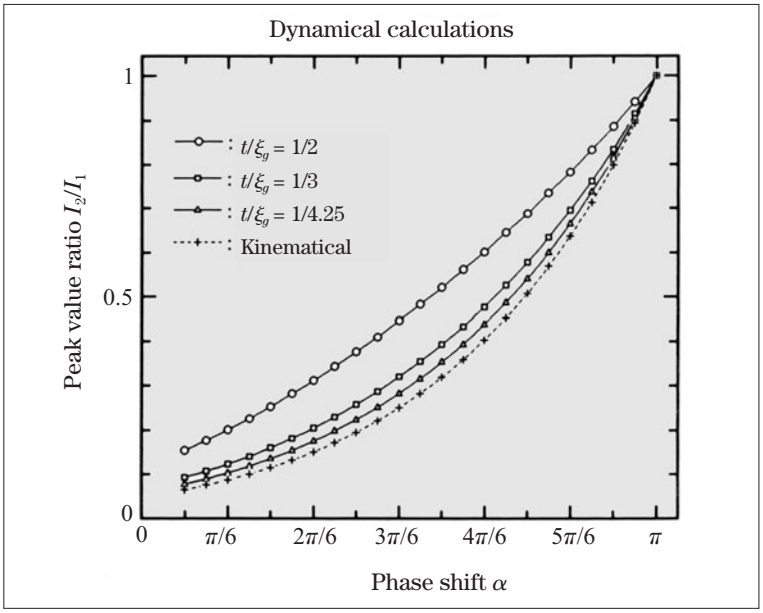

Peak value ratio between the principal and subsidiary peaks I_2/I_1 as a function of the phase shift α for different values of t/ξ_g, where t and ξ_g are the specimen thickness and the extinction distance of reflection $\boldsymbol{g}$.

Stacking fault of TiO_2

Determination of the displacement vector

The upper photograph shows a bright-field image of TiO_2 taken from an area where stacking faults are contained. The lower photograph shows a defocus CBED pattern of a stacking fault of TiO_2 taken from an area of about 200nm in diameter at an electron incidence tilted by about 8 degrees from the [110] direction. The dotted lines correspond to the top and bottom edges of the stacking fault. The specimen thicknesses measured at positions A and B using the CBED method [33] were 37.5nm and 50.7nm, respectively. The six reflections of $10\bar{3}$, $\bar{2}21$, $\bar{5}52$, $\bar{4}42$, $\bar{4}5\bar{1}$ and $5\bar{5}0$ have been used for the determination of the displacement vector.

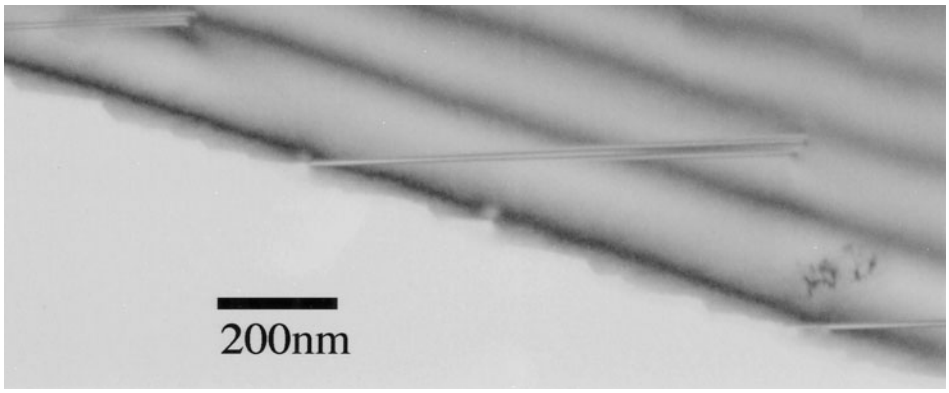

Bright-field image of TiO_2 containing stacking faults.

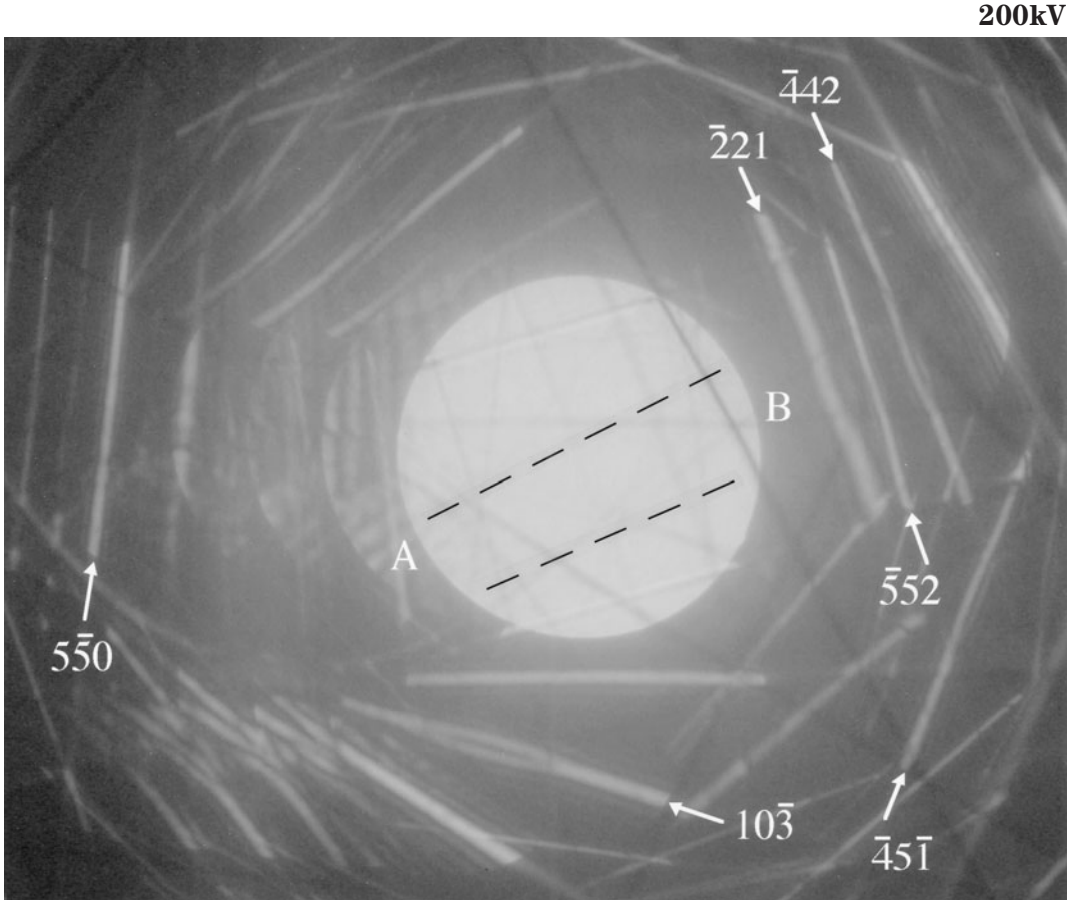

Defocus CBED pattern taken from an area containing a stacking fault of TiO_2.

The table shows the extinction distances ξ_g of the reflections, the specimen thicknesses t in the middle of the fault on the reflection lines and the ratios t/ξ_g. The specimen thicknesses on reflection lines were determined by interpolation provided that thickness changes linearly from positions A to B. The right figures show intensity profiles of the $10\bar{3}$, $\bar{2}21$, $\bar{5}52$, $\bar{4}42$ and $\bar{4}5\bar{1}$ reflections at a depth of the fault of $t/2$. The background intensity was subtracted by using a Lorentz curve, whose maximum is at the incident beam, as shown with the dotted line.

$\boldsymbol{g}$	$10\bar{3}$	$\bar{2}21$	$\bar{5}52$	$\bar{4}42$	$\bar{4}5\bar{1}$	$55\bar{0}$
ξ_g (nm)	278.5	269.2	242.0	306.2	336.0	205.6
t (nm)	41.8	47.0	39.5	43.7	46.4	39.5
t/ξ_g	1/6.7	1/5.7	1/6.1	1/7.0	1/7.2	1/5.2

Extinction distances ξ_g, specimen thicknesses t and their ratios t/ξ_g for the six reflections.

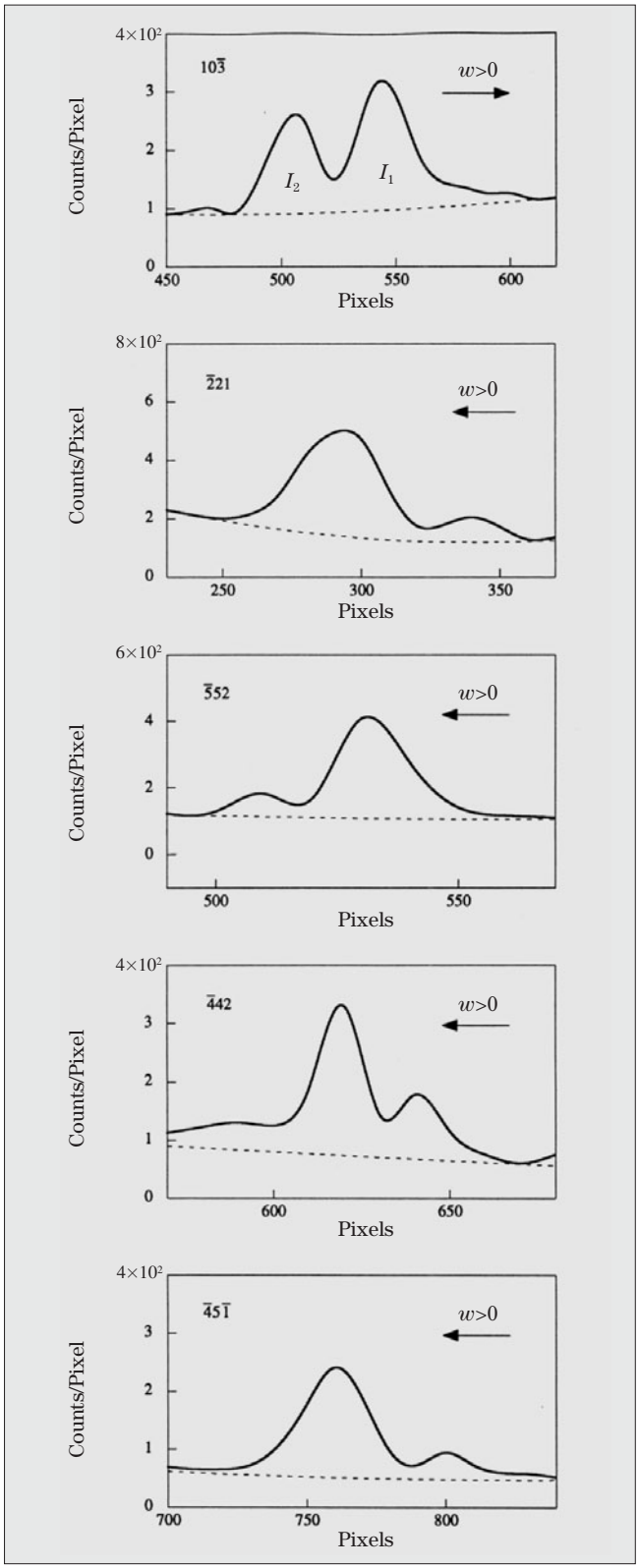

Measured intensity profiles of the five reflections with the background approximated by a Lorentz curve.

The phase shift α is determined from the peak value ratio I_2/I_1 between the principal I_1 and subsidiary I_2 peaks by referring to the curves shown in the right figures. The sign of α is positive (negative) when the subsidiary peak appears at an angular position of a positive (negative) excitation error w, which is positive at the direct beam side of the principal peak of a reflection line. The lower table shows the intensity ratios I_2/I_1 of those reflections and their phase shifts α. Since the fault had almost no influence on the intensity profile of the $5\bar{5}0$ reflection line, the phase shift was assumed to be zero. The displacement vector $\boldsymbol{R}$ is determined as shown on the next page by the method described at the beginning of this chapter.

$\boldsymbol{g}$	$10\bar{3}$	$\bar{2}21$	$\bar{5}52$	$\bar{4}42$	$\bar{4}5\bar{1}$	$5\bar{5}0$
I_2/I_1	0.81	0.18	0.22	0.44	0.23	—
α	-0.917π	-0.364π	0.437π	-0.688π	-0.460π	~0

Intensity ratios I_2/I_1 between the principal I_1 and subsidiary I_2 peaks and the phase shifts obtained from the ratios for the six reflections.

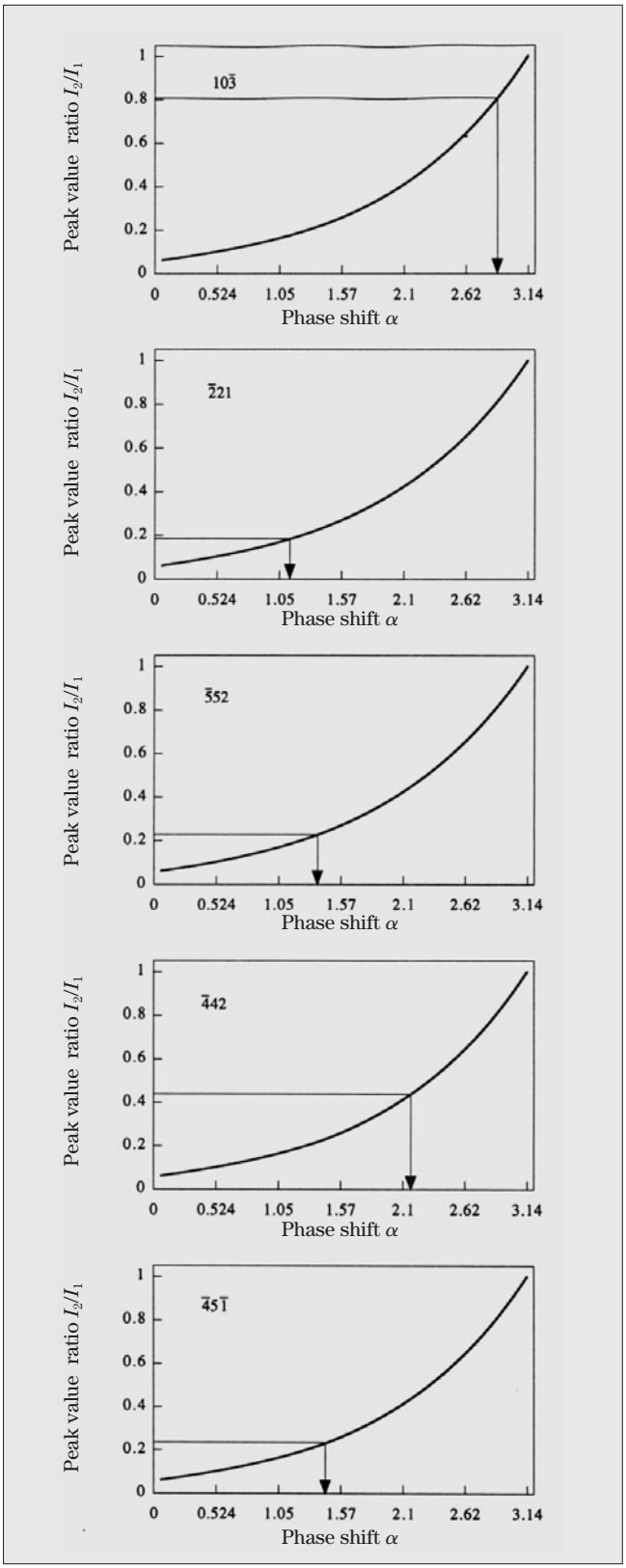

Peak value ratio I_2/I_1 as a function of the phase shift α for the thickness given in the table on the last page. From the measured values of I_2/I_1, the phase shifts are determined.

Through the use of the three $5\bar{5}0$, $10\bar{3}$ and $\bar{4}5\bar{1}$ reflections,

$$\boldsymbol{R}=\begin{pmatrix} u \\ v \\ w \end{pmatrix} = \begin{pmatrix} 5 & \bar{5} & 0 \\ 1 & 0 & \bar{3} \\ \bar{4} & 5 & \bar{1} \end{pmatrix}^{-1} \begin{pmatrix} 0 \\ -0.917\pi/2\pi \\ -0.460\pi/2\pi \end{pmatrix} + \begin{pmatrix} 5 & \bar{5} & 0 \\ 1 & 0 & \bar{3} \\ \bar{4} & 5 & \bar{1} \end{pmatrix}^{-1} \begin{pmatrix} n_1 \\ n_2 \\ n_3 \end{pmatrix}.$$

Using conditions for u, v and w,

$$\begin{aligned} -\frac{1}{2} &< \frac{6.72}{14\pi} + \frac{(15n_1-5n_2+15n_3)}{10} \le \frac{1}{2} \\ -\frac{1}{2} &< \frac{5.60}{14\pi} + \frac{(13n_1-5n_2+15n_3)}{10} \le \frac{1}{2} \\ -\frac{1}{2} &< \frac{23.5}{14\pi} + \frac{(5n_1-5n_2+15n_3)}{10} \le \frac{1}{2}. \end{aligned}$$

From the inequalities, ten sets of n_1, n_2 and n_3 are obtained. Substitution of the sets of n_1, n_2 and n_3 into the above equation yields the following ten possible displacement vectors.

n_1	n_2	n_3	$\boldsymbol{R}$
–3	0	3	$\boldsymbol{R}_1 = [\overline{0.11}\ \ 0.49\ \ 0.11]$
–2	0	2	$\boldsymbol{R}_2 = [\overline{0.11}\ \ 0.29\ \ 0.11]$
–1	0	1	$\boldsymbol{R}_3 = [\overline{0.11}\ \ 0.09\ \ 0.11]$
0	0	0	$\boldsymbol{R}_4 = [\overline{0.11}\ \ \overline{0.11}\ \ 0.11]$
0	2	1	$\boldsymbol{R}_5 = [0.39\ \ 0.39\ \ \overline{0.39}]$
1	0	–1	$\boldsymbol{R}_6 = [\overline{0.11}\ \ \overline{0.31}\ \ 0.11]$
1	2	0	$\boldsymbol{R}_7 = [0.39\ \ 0.19\ \ \overline{0.39}]$
2	2	–1	$\boldsymbol{R}_8 = [0.39\ \ \overline{0.01}\ \ \overline{0.39}]$
2	2	–2	$\boldsymbol{R}_9 = [0.39\ \ \overline{0.21}\ \ \overline{0.39}]$
4	2	–3	$\boldsymbol{R}_{10} = [0.39\ \ \overline{0.41}\ \ \overline{0.39}]$

We calculate the values of $\alpha_n = 2\pi \boldsymbol{g}_{\bar{4}42} \cdot \boldsymbol{R}_n$ (n = 1 to 10) for the 4th reflection $\bar{4}42$. The table at the bottom shows the values of α_n. When we compare the values with the experimental value of $\alpha_{exp} = -0.688\pi$, possible displacement vectors are limited to $\boldsymbol{R}_1$ and $\boldsymbol{R}_8$. For the 5th reflection $\bar{2}21$, the experimental phase shift is $\alpha_{exp} = -0.364\pi$ and the calculated ones are $\alpha_1 = 2\pi \boldsymbol{g}_{\bar{2}21} \cdot \boldsymbol{R}_1 = 0.629\pi$ and $\alpha_8 = 2\pi \boldsymbol{g}_{\bar{2}21} \cdot \boldsymbol{R}_8 = -0.371\pi$. Therefore, the displacement vector of the stacking fault is determined to be $\boldsymbol{R}_8$.

$\boldsymbol{R}$	$\boldsymbol{R}_1$	$\boldsymbol{R}_2$	$\boldsymbol{R}_3$	$\boldsymbol{R}_4$	$\boldsymbol{R}_5$
α_n	-0.761π	-0.342π	0.058π	0.439π	0.458π
$\boldsymbol{R}$	$\boldsymbol{R}_6$	$\boldsymbol{R}_7$	$\boldsymbol{R}_8$	$\boldsymbol{R}_9$	$\boldsymbol{R}_{10}$
α_n	0.858π	0.837π	-0.742π	0.360π	0.040π

Phase shifts α_n of the $\bar{4}42$ reflection calculated for ten possible displacement vectors.

$\boldsymbol{R}$	Initial combinations of three reflections	S
$[0.39\ \ \overline{0.01}\ \ \overline{0.38}]$	$5\bar{5}0\ \ \bar{4}5\bar{1}\ \ \bar{2}21$	0.043
$[0.40\ \ \overline{0.01}\ \ \overline{0.38}]$	$10\bar{3}\ \ 5\bar{5}0\ \ \bar{2}21$	0.056
$[0.43\ \ 0.03\ \ \overline{0.37}]$	$10\bar{3}\ \ \bar{4}5\bar{1}\ \ \bar{2}21$	0.060
$[0.39\ \ \overline{0.01}\ \ \overline{0.39}]$	$10\bar{3}\ \ 5\bar{5}0\ \ \bar{4}5\bar{1}$	0.061
$[0.37\ \ \overline{0.03}\ \ \overline{0.39}]$	$10\bar{3}\ \ 5\bar{5}0\ \ \bar{5}52$	0.074

Displacement vectors $\boldsymbol{R}$ and their reliability factors S calculated for five different initial sets of three reflections.

Slightly different values for the displacement vector were obtained by choosing different initial combinations of reflections. A reliability factor $S = \Sigma|\alpha_{exp} - \alpha_{cal}| / \Sigma\ |\alpha_{exp}|$ is calculated for each combination, where summation is carried out for the reflections other than three reflections chosen for the initial combination. The table on the top shows the values of $\boldsymbol{R}$ for different initial combinations of three reflections and their reliability factors obtained. The displacement vector $\boldsymbol{R}$ which gives the largest S value includes the $\bar{5}52$ reflection. The detailed inspection shows that a fine line crosses the $\bar{5}52$ reflection at the measurement position. Thus, this displacement vector is discarded. The final result is obtained by averaging the four values of the displacement vectors given in the table, which exhibit good reliability factors. The value obtained is

$\boldsymbol{R}$ = [0.40±0.02, 0.00±0.02, –0.38±0.01],

S = 0.055.

The displacement vector has never been reported. Using electron microscope images and selected area diffraction patterns, the index of the fault plane was determined to be $(1\bar{1}2)$ by tilting the specimen to the fault plane parallel to the incident beam. It should be noted that the displacement vector is not parallel to the fault plane but has a component perpendicular to the plane.

We have shown that inelastically scattered electrons due to plasmon excitation are very harmful for quantitative CBED studies. In the present case, the contribution of the inelastically scattered electrons was subtracted in a form of smooth background from the raw intensity, but unsmooth background due to plasmon-loss electrons still exists at the peak positions. The present experiment has been nevertheless conducted by choosing as thin a specimen area as possible to avoid the effect of inelastically scattered electrons.

Structural model

It is well known that Magneli phases exist in Ti_nO_{2n-1} [a]. The phases are derived from the mother structure of TiO_2 by periodically subtracting oxygen ion planes and operating shear displacements. Thus, the stacking fault found in TiO_2 is naturally considered to be formed by an oxygen deficiency and a shear displacement.

Figure (a) on the right-side page shows the perfect crystal structure projected in the [110] direction, where the circles are drawn proportional to the ion radii of Ti^{+4} (0.068nm) and O^{-2} (0.140nm) ions. The rhombi which connect oxygen ions show the projection of the oxygen octahedra. Let us consider a $(1\bar{1}2)$ plane that intersects only oxygen ions, which are denoted by *a*, *b*, *c*, *d*, *e* and *f*, and equivalent ones. We remove oxygen ions *a* to *e* but do not remove ion *f* (Fig. (b)), because the former ions overlap with other ions when the displacement vector $\boldsymbol{R}$ obtained by the present experiment is operated, but the latter ion *f* is not overlapped. Removal of the oxygen ions (Fig. (b)) causes the breakdown of oxygen octahedra to oxygen pentagons (pyramids 1 and 2 shown by thick solid lines) and the formation of large deformed octahedra (parallelograms shown by thick broken lines) at the fault.

g	$\boldsymbol{R} = 0$	$\boldsymbol{R} = \boldsymbol{R}_{//}$	$\boldsymbol{R} = \boldsymbol{R}_{//} + \boldsymbol{R}_{\perp}$
AB	0.280	0.365	0.341
AC	0.450	0.378	0.344
AD	0.503	0.380	0.340

Distances of oxygen ions AB, AC and AD for three displacements of $\boldsymbol{R} = 0$ (perfect), $\boldsymbol{R} = \boldsymbol{R}_{//}$ and $\boldsymbol{R} = \boldsymbol{R}_{//} + \boldsymbol{R}_{\perp}$

Figure (c) shows the structure of the stacking fault derived by operating the vector $\boldsymbol{R}$ to Fig. (b). Rotation and deformation of the pentagon (pyramid 1) and the octahedron (the parallelogram) are caused by the operation of the vector $\boldsymbol{R}$.

We consider the distances between oxygen A above the fault plane and three oxygens **B**, **C** and **D** below the fault. The table at the bottom shows the O-O distances for three cases of the displacements;

1) no displacement $\boldsymbol{R} = 0$ (perfect),

2) $\boldsymbol{R} = \boldsymbol{R}_{//}$ and

3) $\boldsymbol{R} = \boldsymbol{R}_{//} + \boldsymbol{R}_{\perp}$,

where $\boldsymbol{R}_{//}$ and $\boldsymbol{R}_{\perp}$ are the parallel and perpendicular components to the $(1\bar{1}2)$ plane of the displacement vector obtained by the present experiment. It should be noted that the three distances AB, AC and AD after operating the displacement $\boldsymbol{R}_{//} + \boldsymbol{R}_{\perp}$ take nearly the same value. This oxygen arrangement appears to be more balanced than that for $\boldsymbol{R} = \boldsymbol{R}_{//}$. The distances between titanium ion α and two titanium ions β and γ are respectively 0.358nm and 0.296nm for a perfect crystal. The distances changed to 0.241nm and 0.264nm, respectively, after operating the displacement vector $\boldsymbol{R} = \boldsymbol{R}_{//} + \boldsymbol{R}_{\perp}$. These values are respectively 33% and 11% smaller than those for the perfect crystal. It is known in the Magneli phases that the Ti-Ti distance at the shear plane undergoes a decrease down to 30% of the distance for the perfect crystal. The present values appear to be acceptable, when the values are compared with that for Magneli phases.

Reference

[a] K. Kosuge: Chemistry of Non-stoichiometric Compounds, Oxford Univ. Press, 1994.

(a) Perfect crystal structure of TiO_2 projected in the [110] direction. Large open circles and small black circles represent O^{-2} and Ti^{+4} ions, respectively. The rhombi show the linkage of oxygen octahedra. (b) Oxygen ions *a* to *e* are removed. Breakdown of oxygen octahedra to pyramids (thick solid lines) and formation of deformed octahedron (dotted lines) are noted. (c) Structure of the stacking fault on the $(1\bar{1}2)$ plane of TiO_2 derived by removing oxygen ions and operating the displacement vector. Rotation and deformation of the pyramid and octahedron occur due to the operation of the vector.

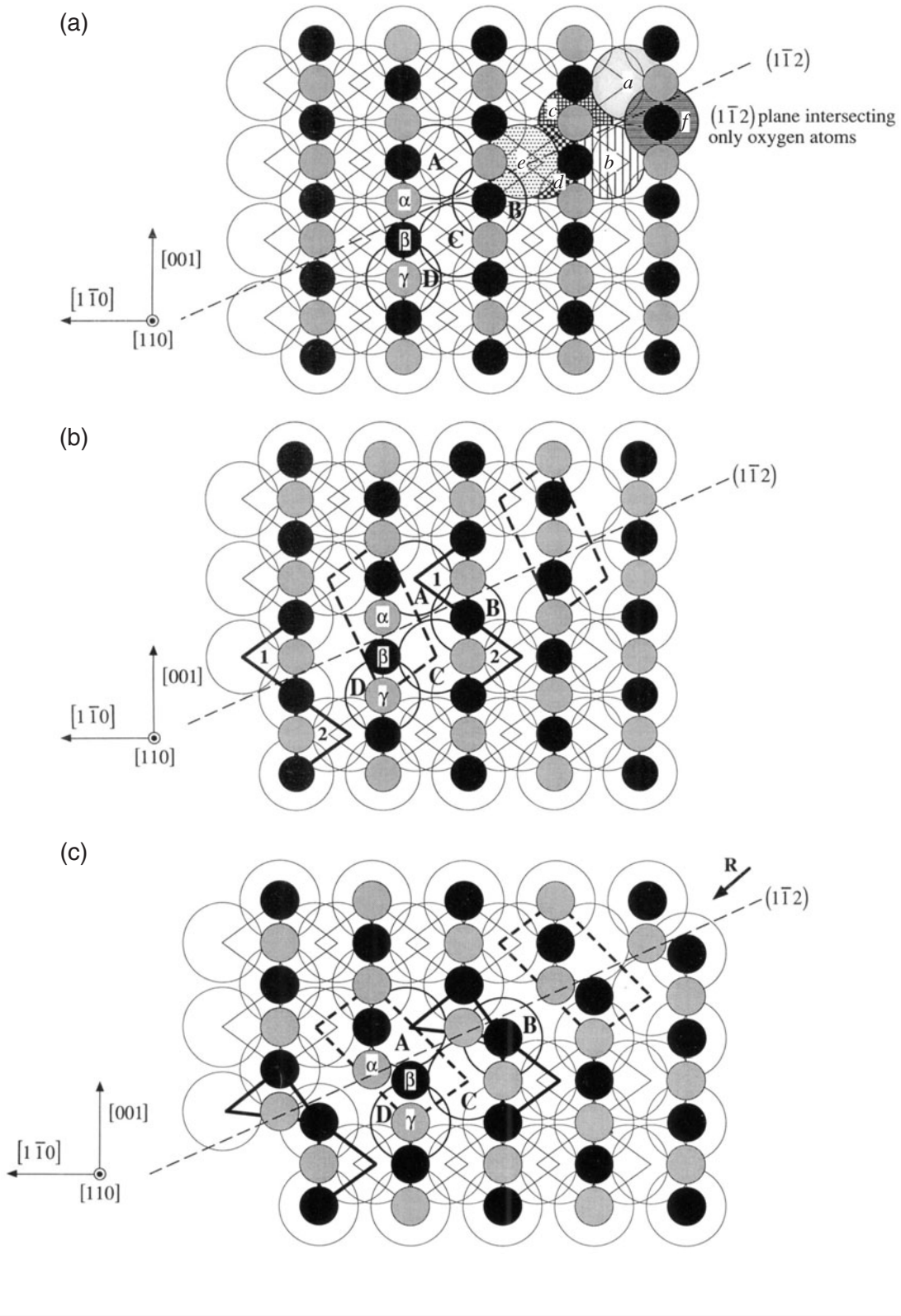
(a)
(1$\bar{1}$2)
(1$\bar{1}$2) plane intersecting only oxygen atoms
a
b
c
d
e
f
A
B
C
D
α
β
γ
[001]
[1$\bar{1}$0]
[110]
(b)
(1$\bar{1}$2)
1
2
[001]
[1$\bar{1}$0]
[110]
(c)
R
(1$\bar{1}$2)
[001]
[1$\bar{1}$0]
[110]

Inversion domain boundary of AlN

Aluminum nitride (AlN) is an attractive material in the electronics industry owing to its good mechanical, thermal and electronic properties. It possesses the non-centrosymmetric wurtzite crystal structure, which belongs to the space group $P6_3mc$ with lattice parameters of a = 0.311nm and c = 0.498nm. In sintered AlN, extended defects have been frequently observed by transmission electron microscopy (TEM) and have attracted considerable attention. Two distinct morphologies of the extended defects have been found; a flat variant, which lies on the basal plane (0001), and a curved variant, which usually does not possess specific habit planes. They often join to form so-called dome-like defects. The extended defect was first observed by Hagege, Ishida and Tanaka [a]. It has been interpreted as a stacking fault, an antiphase domain boundary (APB) or as an inversion domain boundary (IDB) [b], [c]. The last interpretation is now known to be correct. It is known that the presence of impurities, mainly oxygen atoms, in AlN is detrimental to the electronic and thermal properties of AlN. The IDB was found to be associated with oxygen atoms [b], [d].

It has been found that the IDB in AlN is accompanied by an additional displacement [b]. Thus, the IDB was characterized by a mirror operation and a displacement. Harris *et al.* [d] proposed the interfacial model for the flat IDB based on Pauling's electrostatic valence rule. The model contains a single Al-O octahedron layer. They reported that the displacement vector for the flat variant is $\boldsymbol{R}_F$ = (1/3) [10$\bar{1}$0] + (1/3) [0001]. Using the α-fringe method, Westwood *et al.* [e] determined the displacements respectively at the flat and the curved IDB to be $\boldsymbol{R}_F$ = (1/3) [10$\bar{1}$0] + 0.3897 [0001] and $\boldsymbol{R}_c = x[0001] + \epsilon$, where the value x is in a range 0.05 to 0.43 and ϵ expresses a small additional displacement vector lying on the basal plane. Using the weak-beam method, Berger [f] determined the displacement vectors respectively at the flat and the curved IDB to be $\boldsymbol{R}_F$ = (1/3) [$\bar{1}$100] + x[0001], where the value x was not determined, and $\boldsymbol{R}_c = x[0001]$, where $x = n + 0.18$ and n is an integer.

It should be noted that the measured phase shift is the total phase shift, which is composed of the phase shift due to the mirror operation and the phase shift due to the lattice displacement. To determine the displacement, the phase shift due to the mirror operation must be subtracted from the measured phase shift. This subtraction was not made in the determination by Westwood *et al.* [e] but was made in the determination by Berger [f]. All the studies to date for the determination of $\boldsymbol{R}$ have been conducted by the electron microscope image methods. These methods are difficult to determine the displacements accurately because only low-order reflections are utilized for the analysis. The use of the weak-beam technique is limited because it requires a large wedge-shaped specimen with a definite wedge angle and without bending. Thus, it is needed to determine accurately the displacement vectors at the IDBs by using a more powerful technique for understanding the structure of the IDBs.

Yan, Terauchi and Tanaka [40] studied the structures of IDBs in sintered AlN ceramics using convergent-beam electron diffraction and high-resolution electron microscopy. The displacement vectors at a flat and a curved IDB were determined to be $\boldsymbol{R}_F$ = (0.11±0.02)<0001> + ϵ_F, where ϵ_F = (0.02±0.05)<1$\bar{1}$00>, respectively. An interfacial model was derived for the flat IDB. The model contains a single Al-O(N) octahedron layer. An HREM study supported the model.

References

[a] S. Hagege, Y. Ishida and S. Tanaka: *J. Phys., Paris*, **49** (1988) C5-189.

[b] A. D. Westwood and M. R. Notis: *J. Am. Ceram. Soc.*, **74** (1991) 1226.

[c] A. Berger: *J. Am. Ceram. Soc.*, **74** (1991) 1148; *Ibid.*, **78** (1995) 153.

[d] J. H. Harris, R. A. Youngman and R. G. Teller: *J. Mater. Res.*, **5** (1990) 1763.

[e] A. D. Westwood, R. A. Youngman, M. R. McCartney, A. N. Cormack and R. Notis: *J. Mater. Res.*, **10** (1995) 1270; *Ibid.* 10 (1995) 1287.

[f] A. Berger: *J. Am. Ceram. Soc.*, **78** (1995) 153.

Inversion domains

A $3\bar{3}01$ dark-field image of AlN containing flat and curved faults is shown in Photo (a), where the letters P and C indicate a flat fault and a curved fault respectively. When the specimen was tilted so that the incident beam is parallel to the (0001) plane, the flat defects were observed with edge on. Thus, the habit plane of the flat defects is the basal plane (0001). No specific habit plane exists for the curved defects. Photographs (b) and (c) show CBED patterns taken from positions A and B respectively at either side of the flat fault P in Photo (a) with the incident beam of the $[11\bar{2}0]$ direction. At this crystal setting, the flat defects are observed with edge on. Each CBED pattern has mirror symmetry with respect to the c^*-axis. There is no mirror symmetry with respect to the line which is perpendicular to the c^*-axis and passes through the center of the 0000 disk. This indicates that the c axis is the polar axis. The two CBED patterns coincide with each other by mirror operation with respect to the line which is perpendicular to the c^*-axis and passes through the center of the 0000 disk. Two domains are proved to have opposite senses.

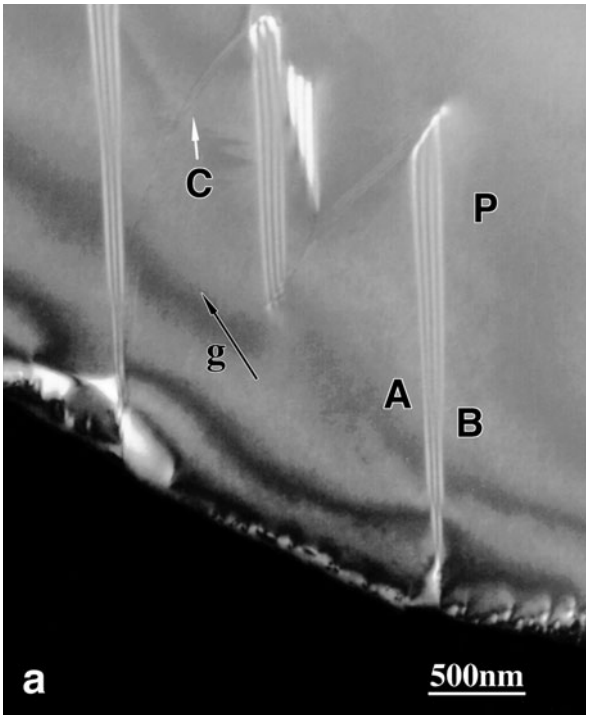

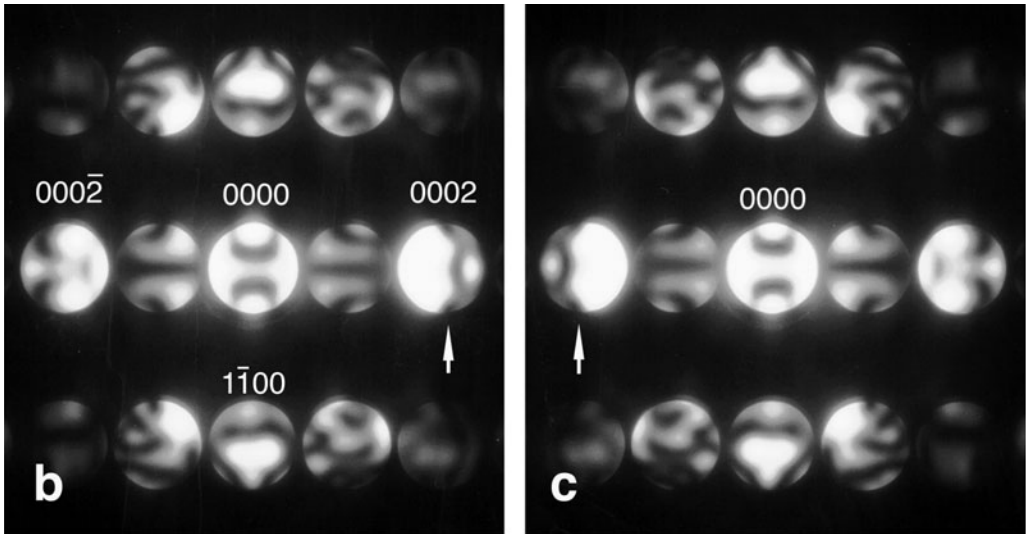

(a) $3\bar{3}01$ dark-field image of the inversion domain boundaries in sintered AlN. (b) and (c) the $[11\bar{2}0]$ zone-axis CBED patterns taken respectively from (b) position A and (c) position B in Photo (a).

Whether or not the two domains are related by inversion operation was examined by comparing the ±**G** dark-field CBED patterns. Photographs (a) and (b) show a pair of $\pm 3\bar{3}01$ dark-field CBED patterns taken at either side of the flat fault P in Photo (a) on the last page. The $3\bar{3}01$ dark-field pattern coincides with the $\bar{3}30\bar{1}$ dark-field pattern when the former is superposed on the latter with a translation of $-2\boldsymbol{G}$ ($\boldsymbol{G} = 3\bar{3}01$). This symmetry 2_R proves that inversion symmetry does exist between two sides of the flat fault. Therefore, the flat fault is a boundary where two adjacent domains satisfy mirror and inversion operations. The coexistence of the mirror and inversion symmetries between two domains is understood by the fact that a twofold axis, which is a symmetry of AlN itself, exists perpendicular to the mirror symmetry; the twofold axis and the mirror symmetry perpendicular to the axis automatically create an inversion symmetry. The same result was also obtained for the curved defect. The CBED patterns taken from the two domains adjoining to the flat IDBs always showed the same sense of polarity as exhibited in Photos (b) and (c) on the last page or a head-to-head configuration, but the curved IDBs have opposite senses of polarity or a tail-to-tail configuration. This implies that the flat and curved IDBs have different interfacial structures.

100kV

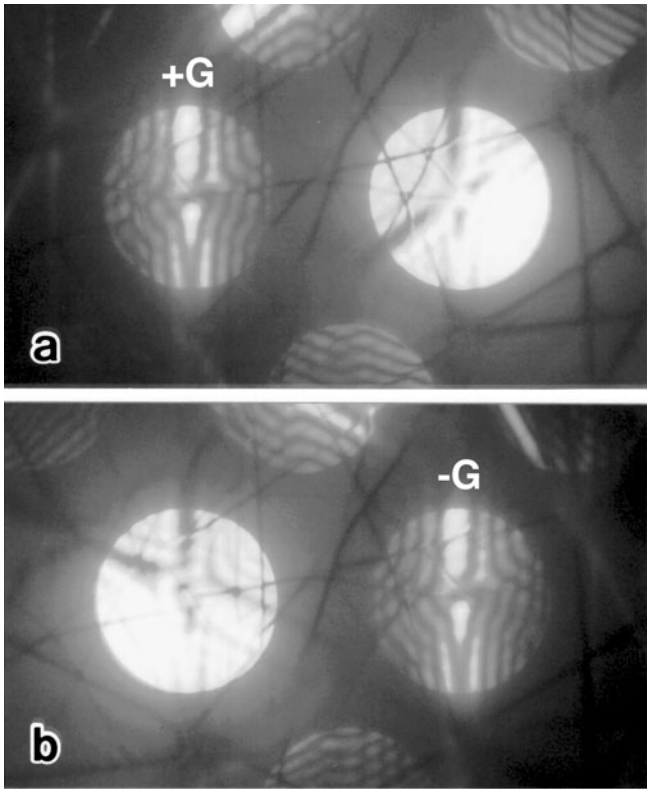

(a) $3\bar{3}01$ and (b) $\bar{3}30\bar{1}$ dark-field CBED patterns taken on either side of the flat fault P in Photo (a) on the last page.

Determination of the displacement vector

Photograph shows a defocus CBED pattern taken from an area of about 200nm diameter containing a flat IDB at 100kV. The broken lines indicate the top and bottom edges of the IDB. The specimen thicknesses measured at two sides of the IDB using the CBED method were 57.2 and 60.1nm. The specimen thickness t in the middle of the IDB is interpolated to be 58.6nm. The intensity profiles of four reflections $22\bar{4}\bar{2}$, $31\bar{4}5$, $\bar{2}\bar{1}3\bar{3}$ and $\bar{3}\bar{2}5\bar{3}$ show continuous changes across the IDB. The IDB or phase shift has no influence on the reflections $\bar{3}\bar{3}60$ and $\bar{4}\bar{4}80$.

100kV

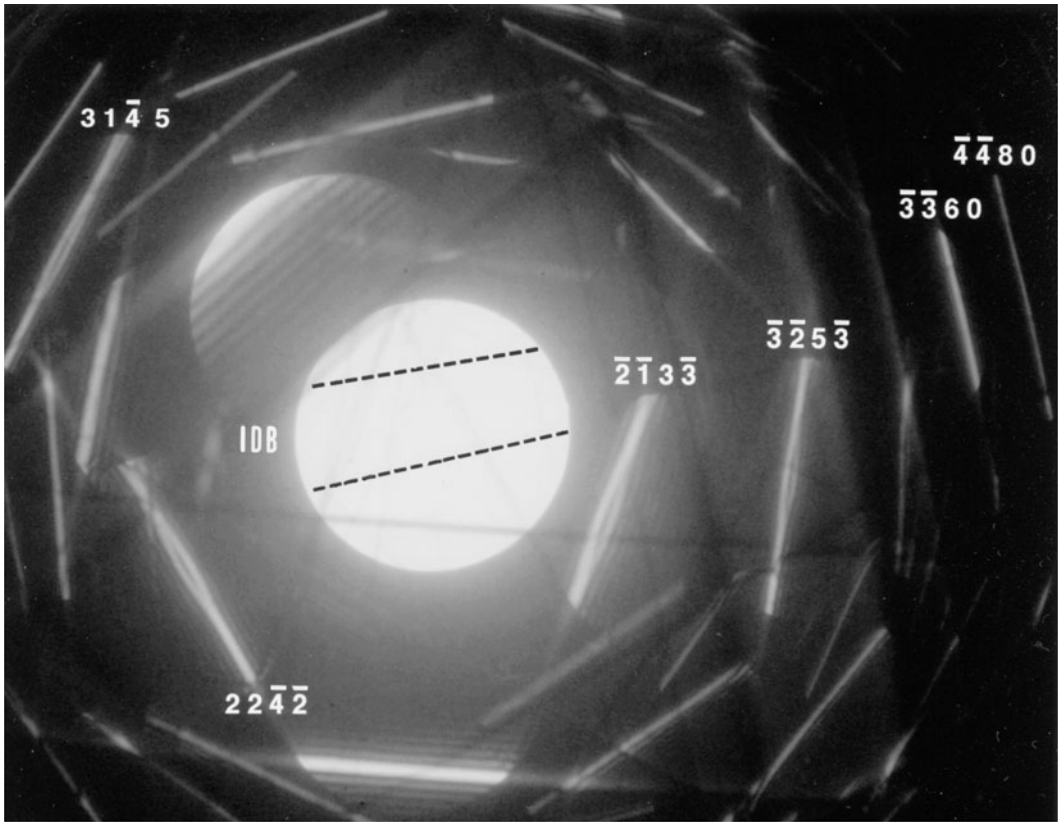

Figure (a) shows the intensity profile (rocking curve) of the $22\bar{4}\bar{2}$ reflection measured at a depth of the fault of $t/2$. The background intensity due to inelastic scattering electrons was subtracted using a Lorentz curve (dotted curve), whose maximum is at the incident beam. The intensity ratio I_2/I_1 between the two peaks was measured to be 0.62.

Figure (b) shows the calculated curves of the intensity ratio I_2/I_1 against the absolute value of the phase shift for four values of t/ξ_g ($\boldsymbol{g}$ = $22\bar{4}\bar{2}$, $31\bar{4}5$, $\bar{2}\bar{1}3\bar{3}$ and $\bar{3}\bar{2}5\bar{3}$). The sign of α is determined from the sign of w at the subsidiary maximum. The phase shift α_{meas} of the $22\bar{4}\bar{2}$ reflection was determined to be -0.802π.

Table shows ξ_g, the ratios t/ξ_g, the measured intensity ratios I_2/I_1 and the phase shifts α_{meas} for five reflections of $\bar{3}\bar{3}60$, $22\bar{4}\bar{2}$, $31\bar{4}5$, $\bar{2}\bar{1}3\bar{3}$ and $\bar{3}\bar{2}5\bar{3}$.

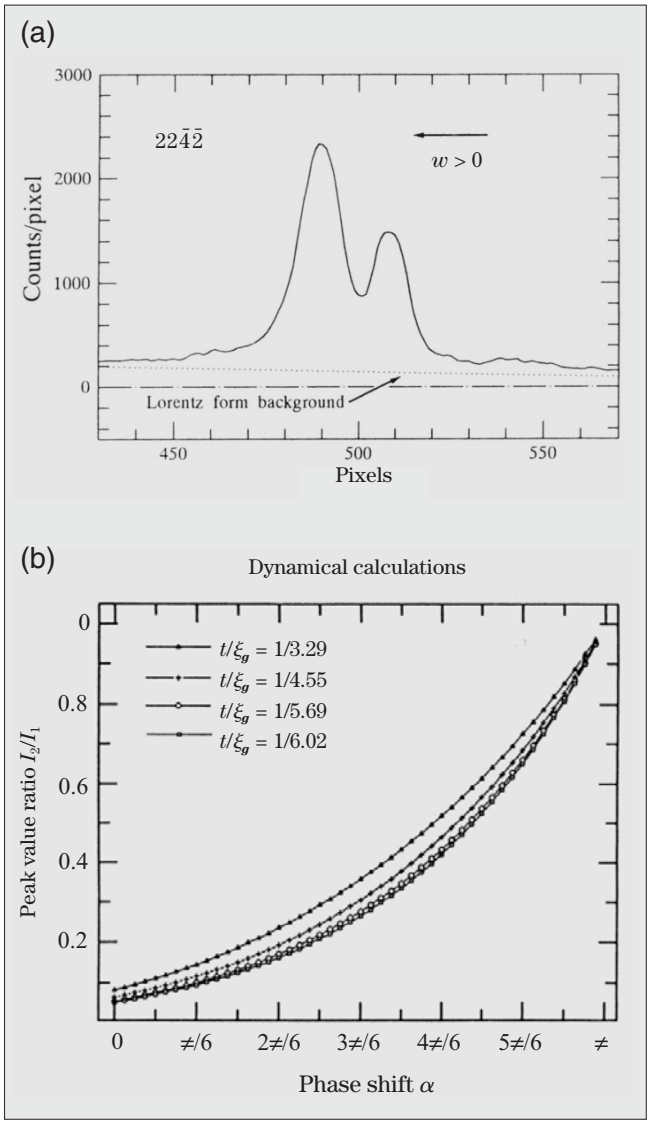

Peak value ratios I_2/I_1 as a function of the absolute value of the phase shift α for four values of t/ξ_g ($\boldsymbol{g}$ = $22\bar{4}\bar{2}$, $31\bar{4}5$, $\bar{2}\bar{1}3\bar{3}$ and $\bar{3}\bar{2}5\bar{3}$), where t and ξ_g are the specimen thickness and the extinction distance of reflection $\boldsymbol{g}$.

$\boldsymbol{g}$	ξ_g (nm)	t/ξ_g	I_2/I_1	α_{meas} ($\neq$)
$\bar{3}\bar{3}60$	183.4	1/3.09	0	0
$22\bar{4}\bar{2}$	269.7	1/4.55	0.62	–0.802
$31\bar{4}5$	337.7	1/5.69	0.90	0.958
$\bar{2}\bar{1}3\bar{3}$	195.2	1/3.29	0.62	–0.780
$\bar{3}\bar{2}5\bar{3}$	356.7	1/6.02	0.58	–0.802

The reflection indices, the extinction distances ξ_g, the ratios t/ξ_g, the intensity ratios I_2/I_1 and the phase shifts obtained from the intensity ratios of the five reflections in Photo (a) on the previous page.

The phase shift α_{meas} is the total phase shift, which is composed of the phase shift α_{IB} due to the lattice inversion and the phase shift α_R due to the lattice displacement $\boldsymbol{R}$, where $\alpha_R = 2\pi \boldsymbol{g}\cdot\boldsymbol{R}$. The phase shift α_{IB} is calculated from the crystal structure-factor. The phase shift α_R is thus obtained by subtracting α_{IB} from α_{meas}. Table shows the values of α_{IB} and α_R of the five reflections for the flat IDB and those of the four reflections for the curved IDB, the latter being separately studied. The displacement vector is unambiguously determined by solving the equations $2\pi \boldsymbol{g}_i\cdot\boldsymbol{R}_i = \alpha_{R_i} + 2n_i\pi$, where the suffix i specifies the reflection index and n_i is an integer. From the phase shifts α_{R_i}, the displacement vectors at the flat and curved IDBs are determined to be $\boldsymbol{R}_F = (0.11 \pm 0.02)[0001] + \epsilon_F$, where $\epsilon_F = (0.02 \pm 0.05)[1\bar{1}00]$ and $\boldsymbol{R}_c = (0.17 \pm 0.02)[0001] + \epsilon_c$, where $\epsilon_c = (0.03 \pm 0.01)[\bar{1}100]$, respectively. The major displacements are in the c-direction and the minor components ϵ are in the basal plane.

The displacement vector $\boldsymbol{R}_F = (1/3)[\bar{1}100] + x[0001]$ (where x is a non-integer) at the flat IDB reported by Berger [a] has not only a component along the c-axis but also a large basal component of $(1/3)[\bar{1}100]$. The difference between his result and the present result is attributed to the fact that Berger assumed the IDB to be a mirror domain boundary. The detailed discussion should be referred to a reference [40]. It is noted that the displacement parallel to the c-axis is similar to that of Westwood *et al.* [b] in terms of magnitude, but has a different sign from theirs.

		$\alpha_R = (\alpha_{meas} - \alpha_{IB})\ (\pi)$	
$\boldsymbol{g}$	$\alpha_{IB}\ (\pi)$ calculated	Flat IDB	Curved IDB
$\bar{3}\bar{3}60$	0	0	0
$22\bar{4}\bar{2}$	–0.325	–0.477	—
$31\bar{4}5$	–0.226	–0.816	–0.468
$\bar{2}\bar{1}3\bar{3}$	–0.096	–0.684	–0.936
$\bar{3}\bar{2}5\bar{3}$	–0.115	–0.687	–0.927

Calculated values of α_{IB} and α_R of the five reflections for the flat IDB and those of the four reflections for the curved IDB (the values of α_R are defined between $-\pi$ and π).

Displacement vectors determined

$\boldsymbol{R}_F = (0.11 \pm 0.02)[0\ 0\ 0\ 1] + (0.02 \pm 0.05)[1\ \bar{1}\ 0\ 0]$

$\boldsymbol{R}_c = (0.17 \pm 0.02)[0\ 0\ 0\ 1] + (0.03 \pm 0.01)[\bar{1}\ 1\ 0\ 0]$

References

[a] A. Berger: *J. Am. Ceram. Soc.*, **74** (1991) 1148; *Ibid.* **78** (1995) 153.

[b] A. D. Westwood, R. A. Youngman, M. R. McCartney, A. N. Cormack and R. Notis: *J. Mater. Res.*, **10** (1995) 1270; *Ibid.* **10** (1995) 1287.

Structural model

By comparing the experimental and simulated CBED patterns, the polarity of each domain was determined so that the two domains have a head-to-head configuration. (the sense of the *c*-axis is defined as indicated by the arrows in the figures). The flat IDB was characterized by the lattice inversion and a displacement of $\boldsymbol{R}_F = (0.11 \pm 0.02)[0001] + \epsilon_F$, $\epsilon_F = (0.02 \pm 0.05)[1\bar{1}00]$.

Let us neglect the small component ϵ_F for the sake of simplicity. The $[11\bar{2}0]$ projection of the interfacial structure of the ideal lattice inversion without displacement is shown in Fig. (a), where the head-to-head configuration is satisfied. The interface is assumed to terminate on an Al atom plane according to previous studies. Each aluminum atom at the interface is surrounded by six nitrogen atoms, which form a distorted octahedron as indicated by the dotted lines. It was experimentally found that the IDBs are associated with oxygen impurities. We also detected an increase of oxygen content at the boundary using EDS. Thus, it is feasible that the replacement of nitrogen atoms with oxygen atoms at the interface takes place. We consider that all nitrogen atoms at the interface are replaced with oxygen atoms and that the tetrahedral Al-O bonds have the same length as that of the tetrahedral Al-N bonds, 0.191nm. The interface contains a single distorted Al-O octahedron layer. Such a displacement that makes the distorted octahedron to recover the regular one is energetically favorable for the structure. Figure (b) shows the $[11\bar{2}0]$ projection of the structure with the displacement. The dotted lines in this figure indicate a regular octahedron, in which the Al-O bond length is 0.220nm. The displacement vector is calculated to be 0.173 [0001], which is larger than the displacement vector of (0.11 ± 0.02) [0001] experimentally determined. The difference can be due to the fact that all nitrogen atoms were replaced with oxygen atoms at the interface and that the tetrahedral Al-O bond length is taken to be the same as the tetrahedral Al-N bond length. Figure (c) shows the $[11\bar{2}0]$ projection of a structure with the single Al-O(N) octahedron layer. The Al-O and Al-N bond lengths at the interface are indicated in the figure. The displacement for this interfacial structure becomes 0.083 [0001], which is closer to the experimental displacement of (0.11 ± 0.02) [0001].

The presence of nitrogen atoms at the interface can cause a relaxation or a distortion of the regular octahedral configuration of aluminum and oxygen atoms. The small component of ϵ lying on the basal plane in the displacement vectors determined may be due to this relaxation.

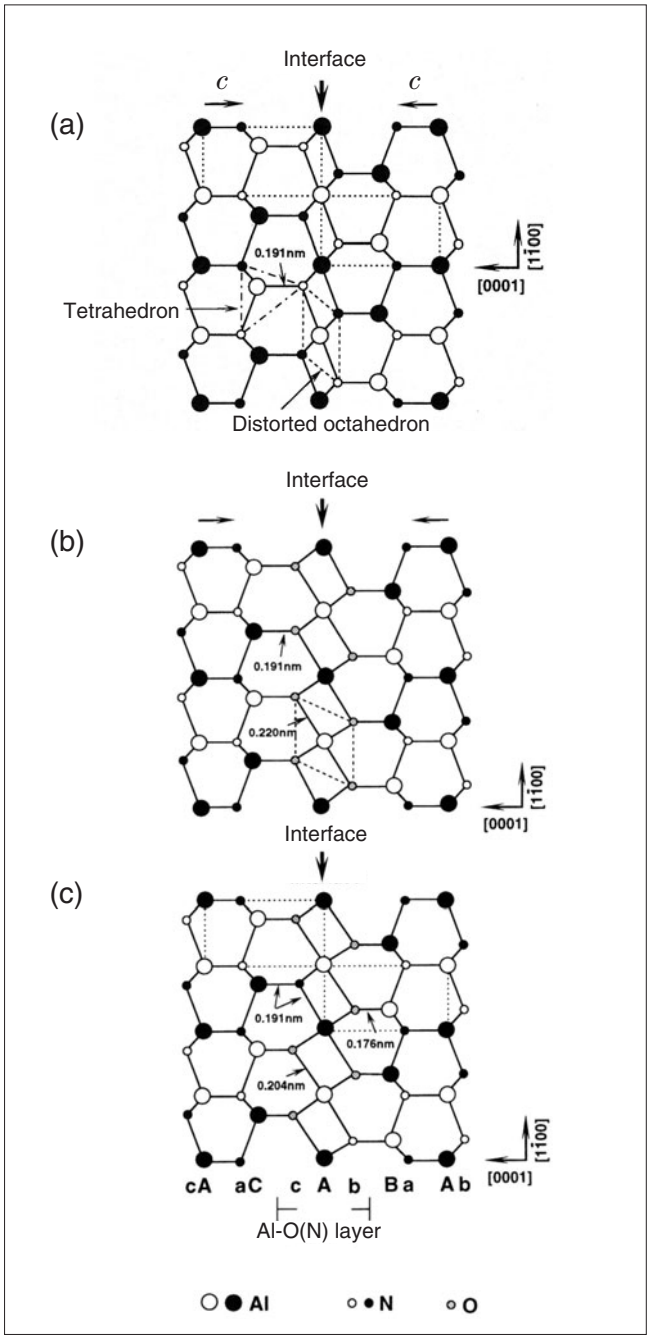

$[11\bar{2}0]$ projections of the atomic structures. (a) An ideal IDB. (b) The interfacial model containing an Al-O octahedron layer at the interface. (c) The interfacial model containing the refined Al-O(N) octahedron layer at the interface.

The photograph shows an HREM image of a flat IDB taken at the [11$\bar{2}$0] zone-axis electron incidence. The position of the interface is indicated by the thick arrow. The zigzag streaks in the [0001] direction indicated by two black lines show a shift in the [1$\bar{1}$00] direction at the interface. The streaks adjacent to the interface in either side of the interface run in the same direction.

The inset on the photograph is the simulated image of the present interfacial model of Fig. (c) on the left-side page for a thickness of 2nm. It shows that not only the positions and shapes of the bright spots but also the direction of the streaks are in excellent agreement with those of the experimental image. This evidence strongly supports the interfacial model derived from the result obtained by the defocus CBED method.

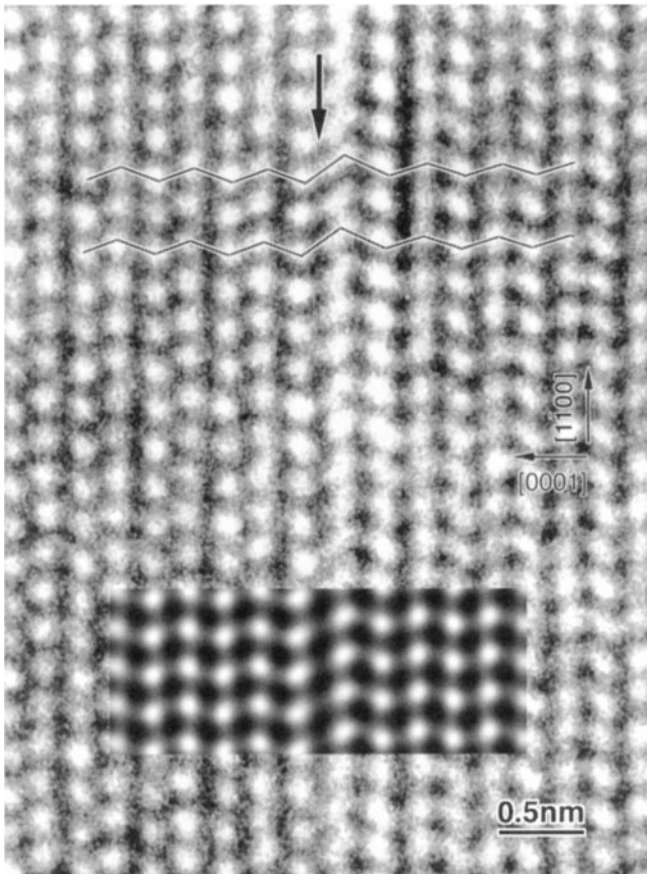

[11$\bar{2}$0] zone-axis HREM image of a flat IDB taken with a defocus of –37nm. The inset is the simulated image of the present interfacial model of Fig. (c) on the left-side page.

Determination of Lattice Parameters

Interface of SiC

The lattice parameters of thin epitaxial SiC films on 6H-SiC substrates were determined by comparing the experimental HOLZ line patterns with many-beam dynamical simulations [42].

Two investigated specimens were grown by molecular beam epitaxy at different substrate temperatures of 1300˚C (specimen 1) and 1050˚C (specimen 2). Photographs (a) to (d) on the right-side page show the bright- and dark-field images of specimens 1 and 2 taken with a JEM-2010 operated at 200kV. Twins marked T and stacking faults were occasionally found in both specimens. Hillocks of Si single crystals, marked H, were observed only in specimen 2. The table shows the growth conditions and the characteristic features of specimens 1 and 2.

CBED experiments were carried out at defect-free positions in the middle of the layers at room temperature and liquid N_2 temperature. To improve the reliability of the results, experiments were carried out at two zones [320] and [331]. The microscope was operated at about 100kV for the CBED studies. Prior to the lattice parameter determination of the grown layers, the accelerating voltage of the electron microscope was determined by comparing an experimental HOLZ line pattern of Si [111] with dynamical simulations.

Specimen 1

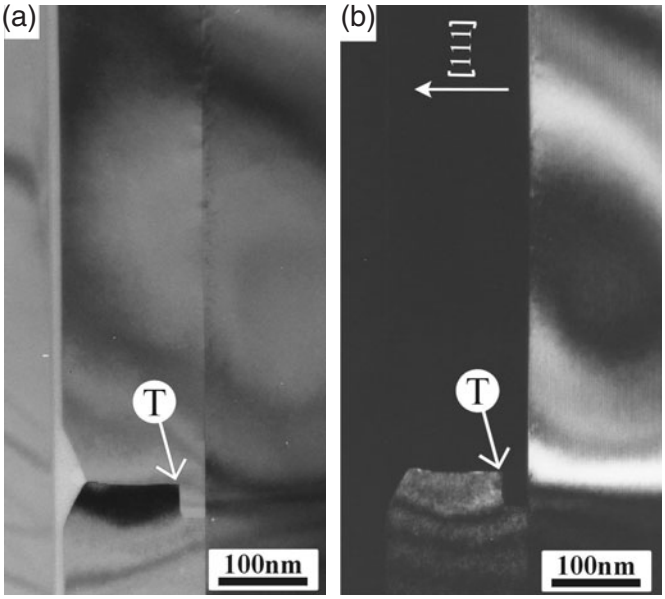

Specimen 2

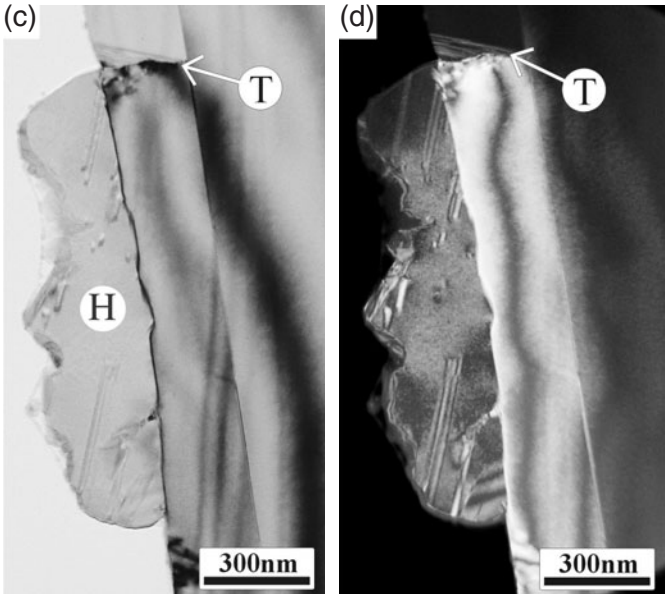

	Specimen 1	Specimen 2
Substrate	Hexagonal (6H)	Hexagonal (6H)
Growth temperature	1300°C	1050°C
Growth mode	Intermittent supply of C with constant Si flow	Simultaneous supply of C and Si with high Si excess
Thin film	Cubic Few defects	Rhombohedral Many defects, Si hillocks

Growth conditions and characteristic features of the thin film specimens 1 and 2.

3C-SiC: specimen 1 (cubic symmetry)

The underlaid bright-field image of specimen 1 shows the 3C-SiC layer and the 6H-SiC substrate on both sides of the glue. The position of the electron probe for the CBED patterns is indicated by a mark ⊗ on the layer. Overlaid on the bright-field image are the Kikuchi map of 3C-SiC and the experimental CBED patterns, which give the relation between the directions of the [320] and [331] zones and the edge direction of the layer. The straight edge is noted.

Figures on the right-side page show calculated CBED patterns at the [320] (a) and [331] (c) zone axes, together with their schematic drawings of HOLZ lines (b) and (d). The distances between the cross points of the HOLZ lines are measured and the ratios between the distances, R1, R2 and R3, are used for the determination of the lattice parameters. The suffix of each reflection denotes the order of Laue zone of the reflection.

Specimen 1

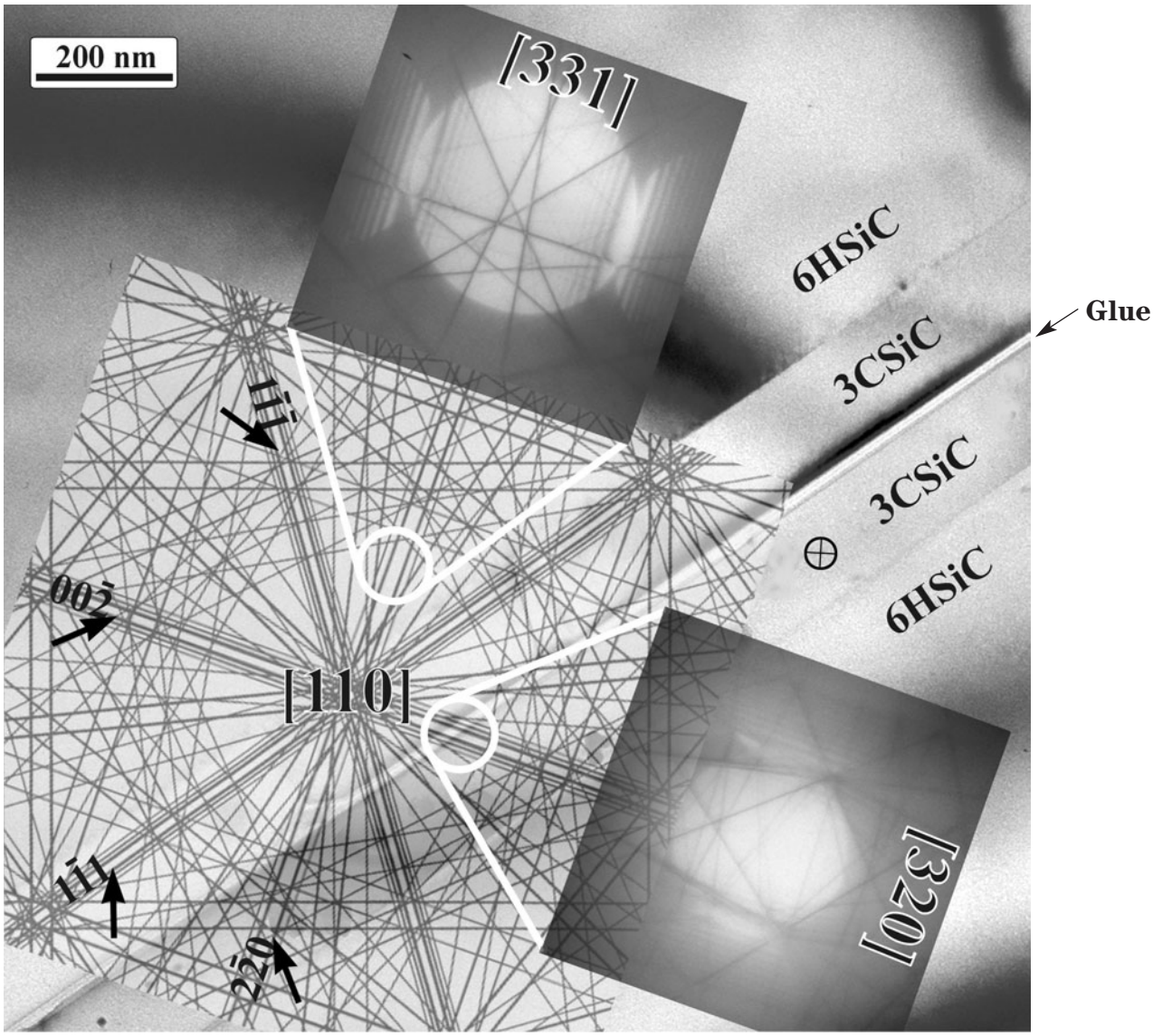

CBED patterns and a Kikuchi map of 3C-SiC are overlaid on the bright-field image of specimen 1. Relation of orientations between the [320] and [331] zones and the edge direction of the layer is seen.

[320]

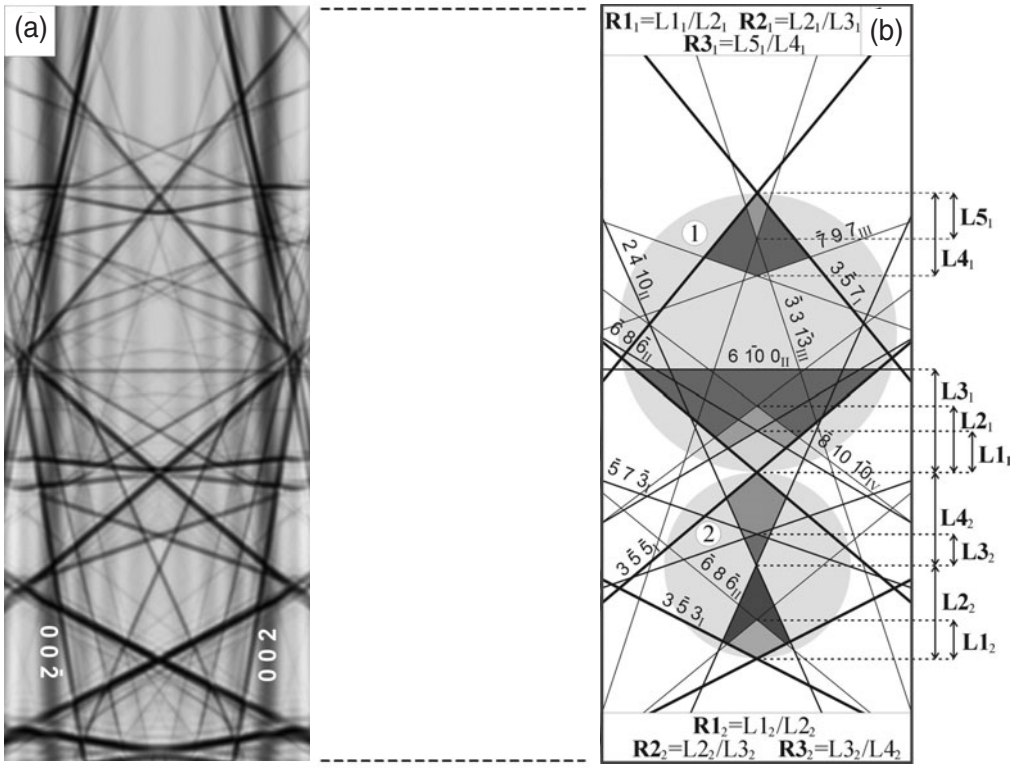

[331]

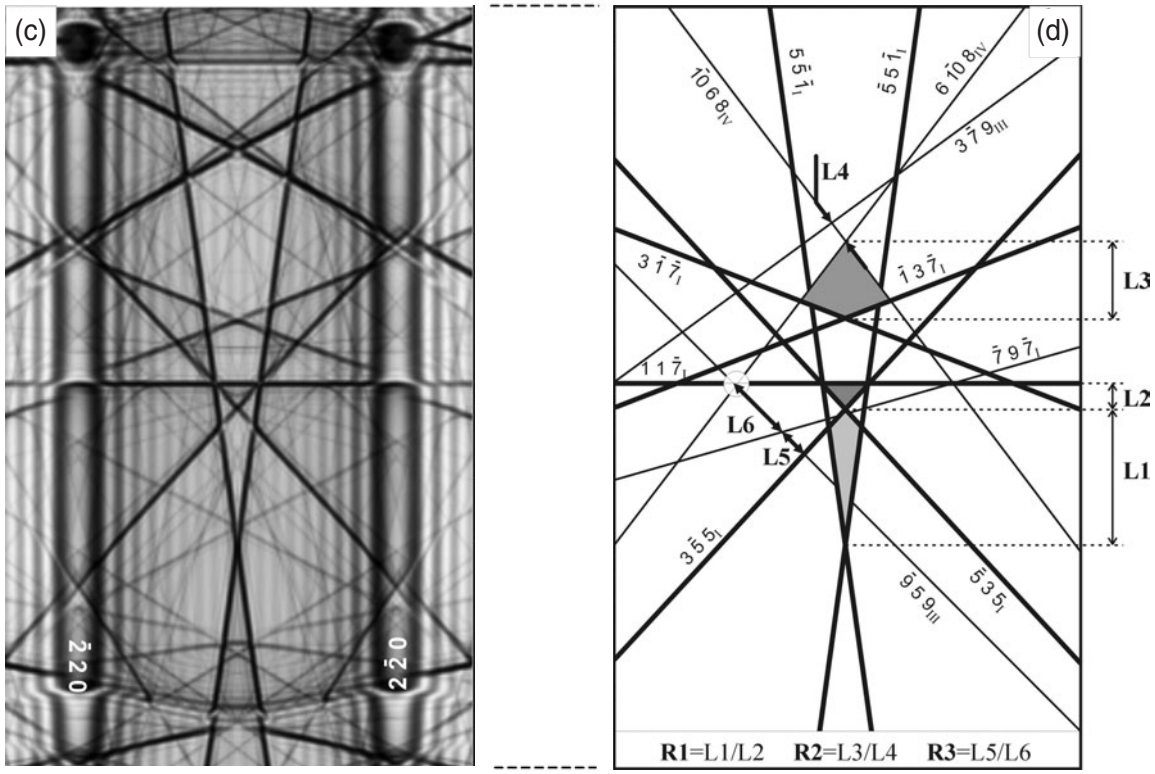

Simulated CBED patterns of cubic SiC at the [320] and [331] zone axes together with the schemes of HOLZ lines. The HOLZ lines are indexed and the suffix shows the order of Laue zone reflections.

Photograph (a) shows an experimental CBED pattern of specimen 1 at the [320] zone. The pattern is fully symmetric with respect to the central vertical line as is expected from the cubic symmetry.

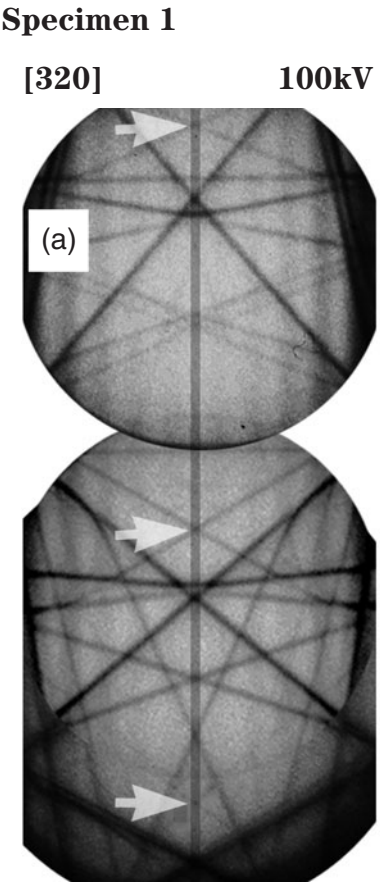

Symmetric

The values of the ratios R1, R2 and R3 for specimen 1 obtained from the experimental [320] and [331] zone-axis patterns at room temperature and liquid N_2 temperature are drawn as the horizontal lines marked ① in the figures on the right-side page. The width of the lines indicates the maximum error of the ratio measurement. The inclined lines in the figures show the ratios R1, R2 and R3 as a function of the lattice parameter, which were obtained from the simulated CBED patterns, the dots in the lines being the calculated points. The actual lattice parameters of specimen 1 were determined from the crossing points between the experimental and simulated lines R1, R2 and R3 for the two temperatures. The values were determined to be a = 0.4374±0.0001nm for room temperature and 0.4369±0.0001nm for liquid N_2 temperature. As a result of careful and repeated measurements, the accuracy mentioned was achieved. It should be noted that it is possible to see such a small change of 0.0005nm simply by visual inspection.

The value determined at room temperature is 0.34% larger than the reported value of a = 0.4359nm for the bulk 3C-SiC.

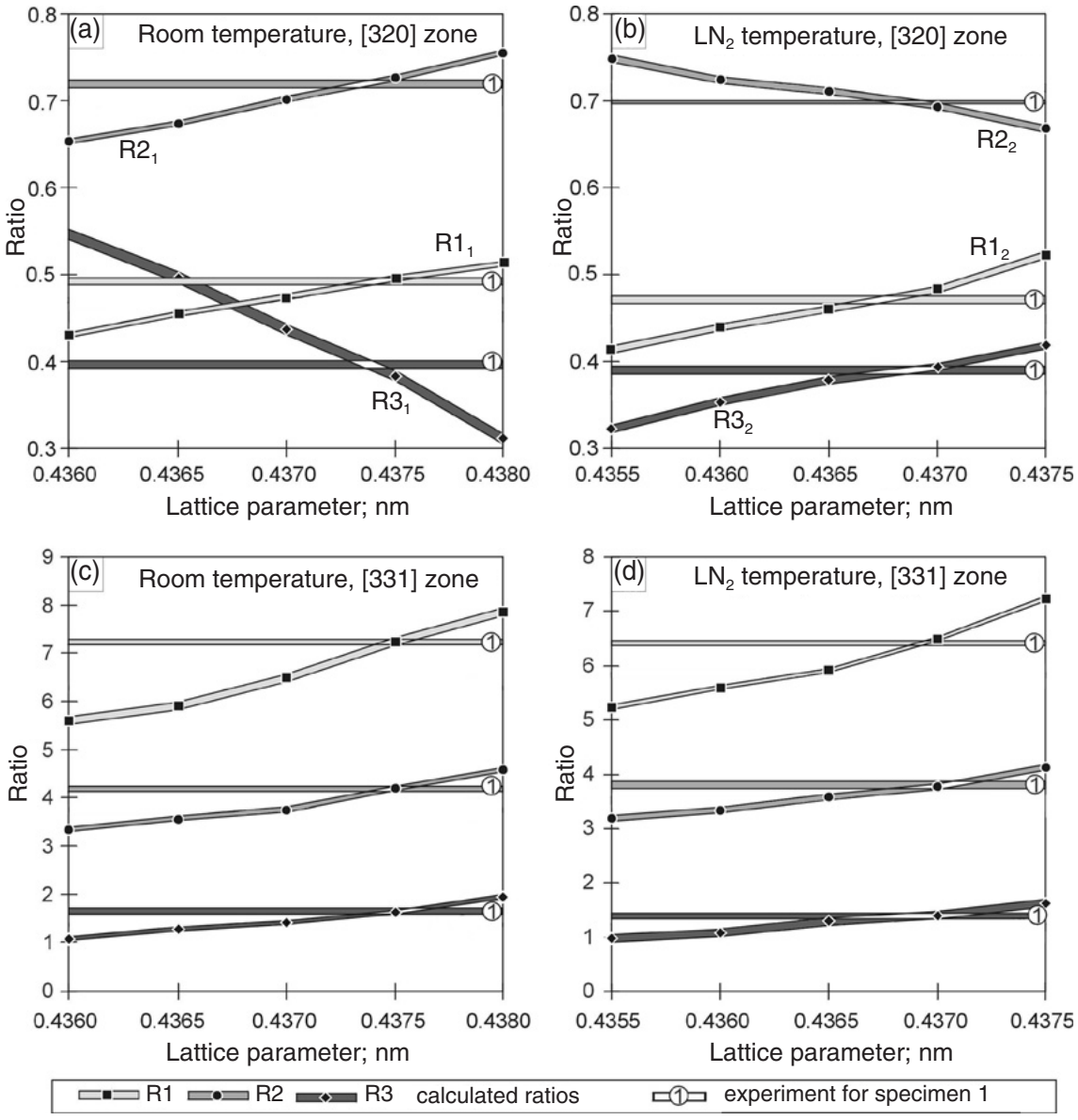

The ratios R1 (square), R2 (sphere) and R3 (rhombus) (defined on page 275) as a function of the lattice parameter obtained from simulated CBED patterns of 3C-SiC for the [320] and [331] zone axes at room temperature and liquid N_2 temperature. The three horizontal lines show the experimental values of R1, R2 and R3. The width of the lines corresponds to the maximum standard deviation.

3C-SiC: Specimen 2 (with rhombohedral distortion)

The underlaid bright-field image of specimen 2 shows the 3C-SiC layer and the 6H-SiC substrate on both sides of the glue. The position of the electron probe for the CBED patterns is indicated by a mark ⊗ on the layer. Overlaid on the bright-field image are the Kikuchi map of 3C-SiC and the experimental CBED patterns, which give the relation between the directions of the [320] and [331] zones and the edge direction of the layer. The formation of hillocks are noted.

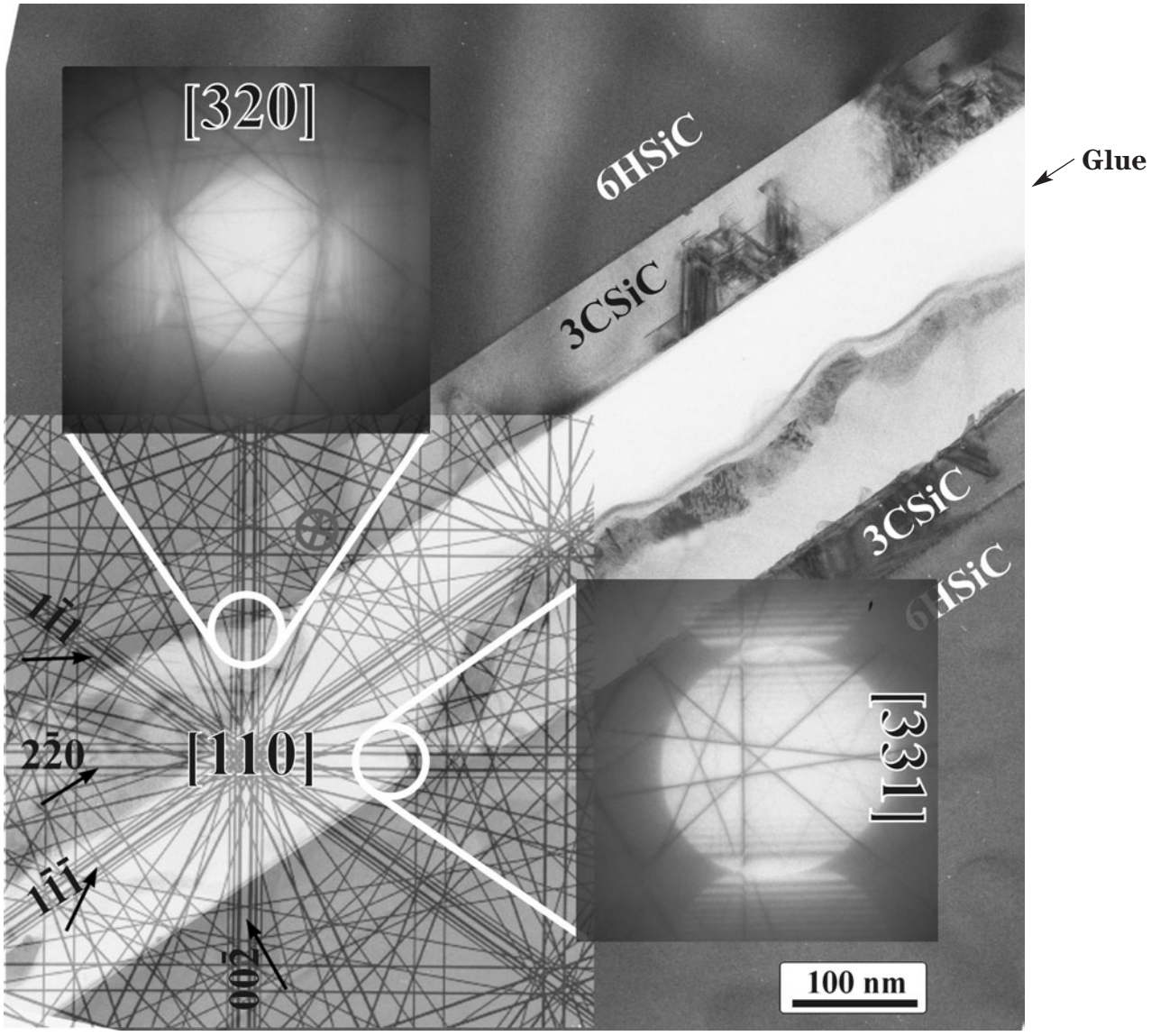

CBED patterns and a Kikuchi map of 3C-SiC are overlaid on the bright-field image of specimen 2. Relation of orientations between the [320] and [331] zones and the edge direction of the layer is seen.

Symmetry breakdown of HOLZ line patterns due to a rhombohedral distortion

Photograph (a) shows an experimental CBED pattern obtained at the [320] zone for specimen 2. In contrast to the symmetric CBED pattern taken from specimen 1 (See page 276), HOLZ lines in Photo (a) are asymmetric with respect to the central vertical line. At the [331] zone of Photo (b), the CBED pattern of specimen 2 remains symmetric as shown by the arrows pointing to the cross points of HOLZ lines on the central vertical line.

These behaviors at the [320] and [311] zones of specimen 2 are explained by a rhombohedrally strained cell shrinked in the [111] direction. At the [320] and [331] zone-axis incidences, [001] & [$2\bar{3}0$] and [$1\bar{1}0$] & [$11\bar{6}$] are the pairs of the base vectors, respectively. That is, the rhombohedral distortion causes the breakdown of the mirror symmetry perpendicular to the [001] direction, which is along the vertical line in Photo (a), and holds the mirror symmetry perpendicular to the [$1\bar{1}0$] direction, which is also along the vertical line in Photo (b). The formation of Si hillocks on top of the layer should be the origin of a compressive stress in the [111] direction, which causes the transformation from cubic to rhombohedral symmetry.

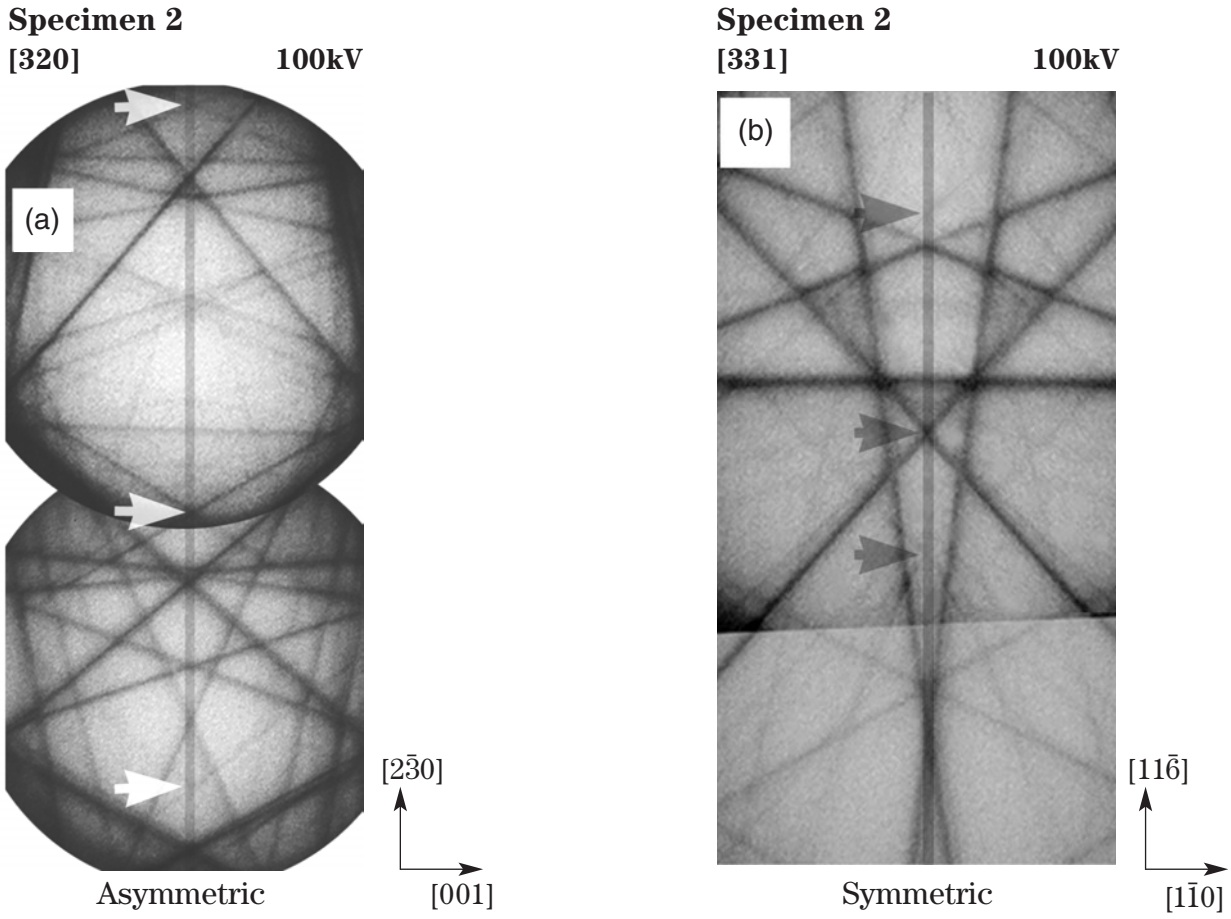

Experimental CBED pattern of specimen 2 taken at the [320] zone axis (a), showing asymmetry with respect to the central vertical line inserted. Asymmetry is seen from the shifts of the cross points of the HOLZ reflections as marked. The experimental CBED pattern taken at the [331] zone axis (b) is symmetric with respect to the vertical line inserted.

3C-SiC: Specimen 2 (with a rhombohedral distortion)

[320] CBED patterns were simulated for different rhombohedral angles of (a) 90.00°, (b) 89.90°, (c) 89.85° and (d) 89.50° with a lattice parameter of a = 0.4364nm, which was determined by a comparison of Photo (a) on the last page and simulated patterns. The experimental [320] CBED pattern obtained at liquid N_2 temperature is overlaid on the simulated patterns. The enlarged insets make clear the fitting between the experimental and simulated HOLZ lines. As is seen in the photographs, the best fit was obtained with a rhombohedral angle of α = 89.90°. It should be pointed out that a difference in the angle of 0.05° is detectable by visual inspection.

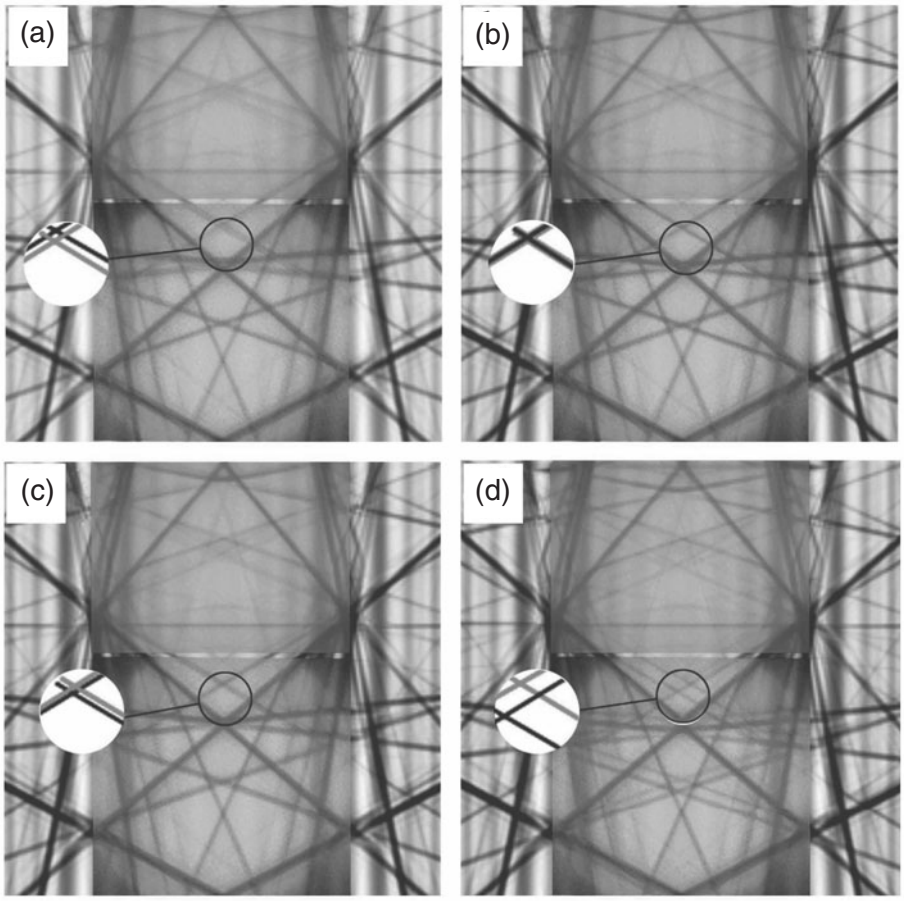

Simulated (gray) CBED patterns of specimen 2 calculated for a cubic cell (a) and for rhombohedral cells (b) 89.90˚, (c) 89.85˚ and (d) 89.50˚ with a = 0.4364nm are overlaid by the experimental (light gray) CBED pattern obtained at liquid N_2 temperature. As seen from the enlarged insets, the best fit is achieved with a rhombohedral angle of α = 89.90˚.

Interface of GaAs

As another example of determining lattice parameters, we deal with a layer material of InAs grown on a GaAs substrate. A defect of about 20nm in radius was found at the substrate side of the interface as shown in Photo (a) on the right-side page. We examined the lattice strains at two positions of about 100nm below the flat interface (position 1) and the defect (position 2). CBED patterns were taken from the positions with the [210] zone-axis incidence at about 100kV. Using a pattern at a bulk area, the accelerating voltage was determined by fitting the distances between the cross points of HOLZ lines indicated in Photo (b) on the right-side page with kinematical and dynamical simulations. The pattern showed the best fit with the kinematical and dynamical simulations at 100.9kV and 101.2kV, respectively.

A CBED pattern from position 1 showed good agreement with the simulated patterns of the bulk lattice parameter a = 0.56537nm. A CBED pattern from the strained area, position 2, is shown in Photo (c). The lattice parameters of position 2 were first determined by fitting the HOLZ line pattern with kinematical simulations and afterwards examined by dynamical simulations.

Photograph (d) on the following page shows an enlarged pattern of Photo (c). The positions of the HOLZ lines are drawn by dotted lines as shown in Photo (e), where the curved experimental lines are approximated by straight dotted lines. A pattern (full lines) kinematically simulated using the bulk lattice parameter (a = 0.56537nm) at the kinematically determined accelerating voltage (100.9kV) is overlaid on the pattern of Photo (e) as shown in Photo (f). It is seen that the dotted lines do not agree with the full lines nor have mirror symmetry with respect to the central vertical line, showing the lowering of the symmetry of the strained area.

In advance of the fitting, we examined what HOLZ lines are sensitive to the changes of lattice parameters a, b, c, α, β, and γ. It was found that the breaking of the mirror symmetry takes place only through the changes of the parameters α and β. The horizontal positions of the cross points of the HOLZ lines were best fitted by changing α and β by $\Delta\alpha = 0.076^\circ$ and $\Delta\beta = 0.258^\circ$ as shown in Photo (g), where an enlargement is attached.

It was found that the HOLZ lines indicated by black arrows in Photo (h) are insensitive to the change of the parameter b. Thus, the parameters a, c, and γ were simultaneously refined using these lines. The parameters obtained were Δa = 0.0008nm, Δc = 0.0007nm and $\Delta\gamma = 0.229^\circ$. Finally, the parameter b was determined by the fitting of the HOLZ lines, which intersect with the lines indicated by the black arrows. The lattice parameter b was determined to be Δb = –0.0019nm. Photograph (i) shows almost good agreement between the experimental HOLZ lines (dotted lines) and the simulated lines (full lines) using the refined lattice parameters. However, some lines at the lower part of the photograph show insufficient agreement. This disagreement can be due to the use of kinematical simulations. The dynamical simulation was carried out using the lattice parameters determined by the kinematical simulations and an accelerating voltage of 101.2kV. The simulation is overlaid by the experimental dotted lines (Photo (j)). Occasionally, the agreement between the experimental and theoretical lines is fairly good without any readjustment of the lattice parameters in the present case.

It is noted that the Hough transform is conveniently utilized in an automated procedure for detecting the positions of HOLZ lines [a], [36]. When the Hough transform is used, the position (the slope and intersect) of a HOLZ line is transformed into a point in the Hough space.

Reference

[a] S. Kraemer, J. Mayer: *J. Microscopy*, **194** (1999) 2.

GaAs

(a)

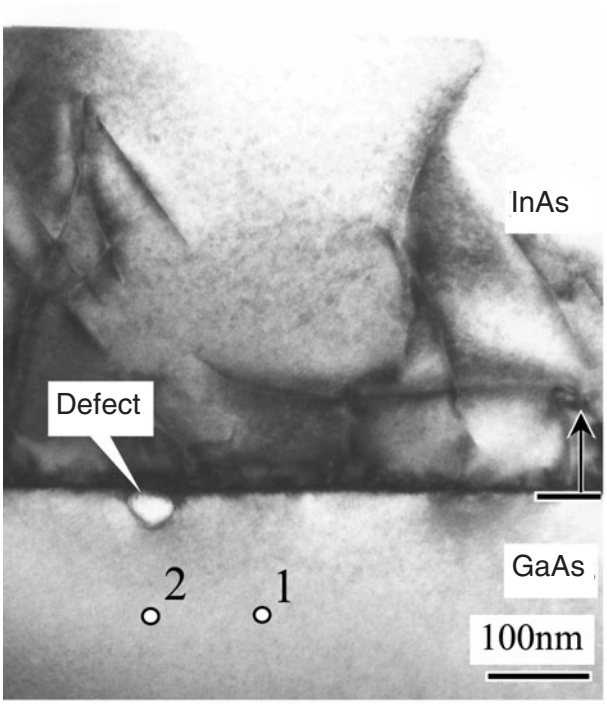

A layer material of InAs grown on a GaAs substrate

[210] bulk area, unstrained ~100kV

(b)

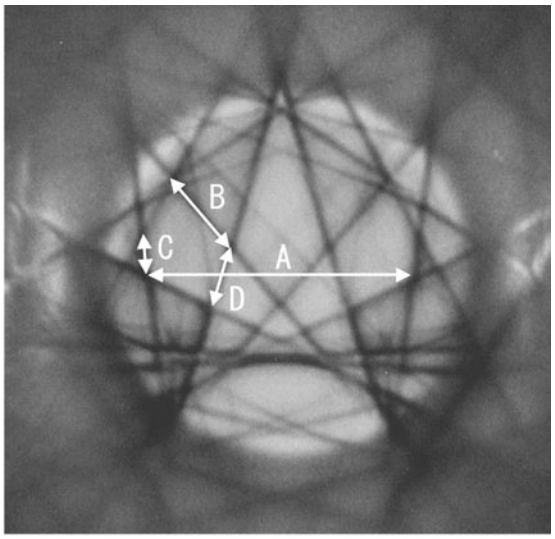

Kinematical: 100.9kV, Dynamical: 101.2kV

[210] position 2, strained ~100kV

(c)

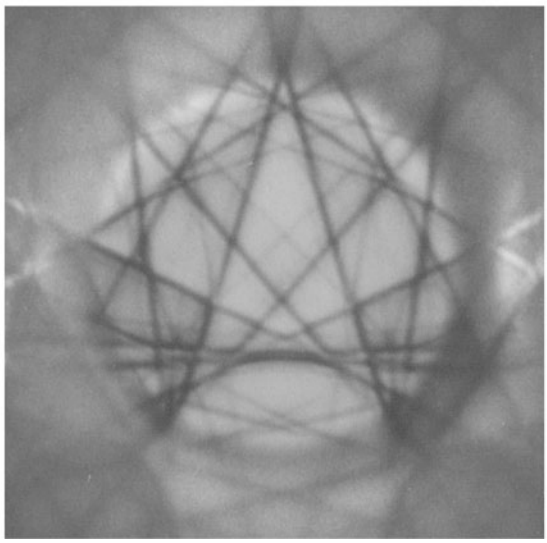

Step 1: Comparison with kinematical simulations

GaAs [210] **~100kV**

(d)

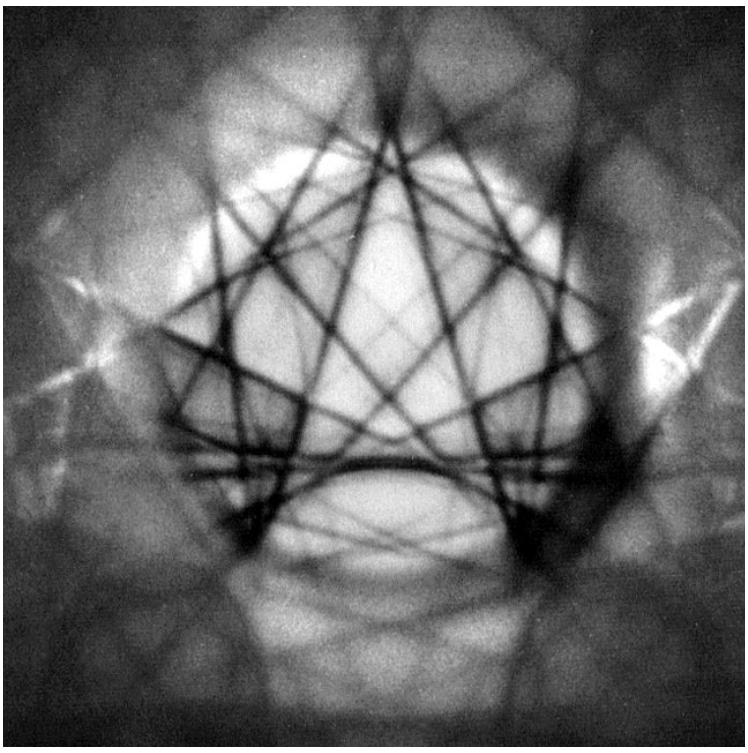

Experimental pattern
from position 2 (strained)

(e)

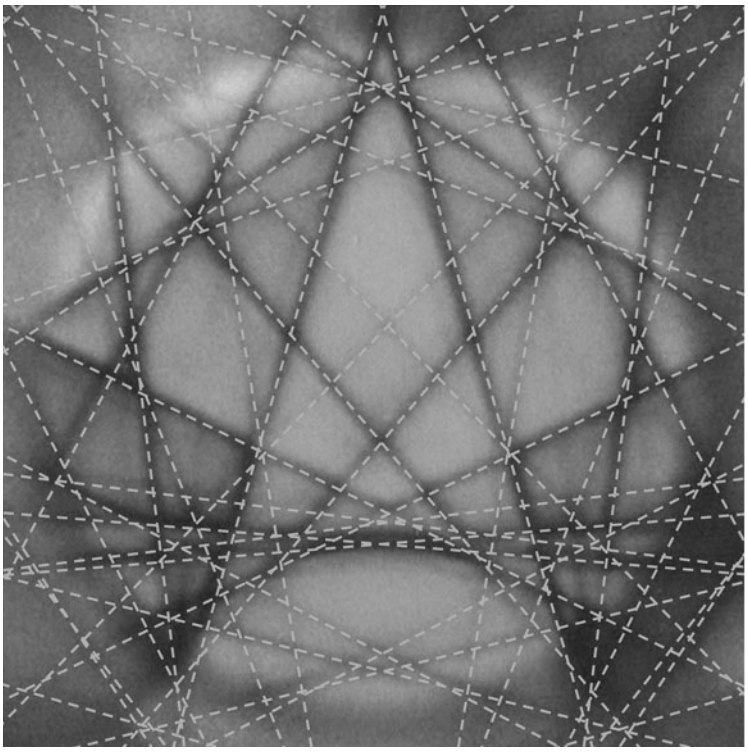

Determination of HOLZ line
positions (dotted lines)

GaAs [210] **~100kV**

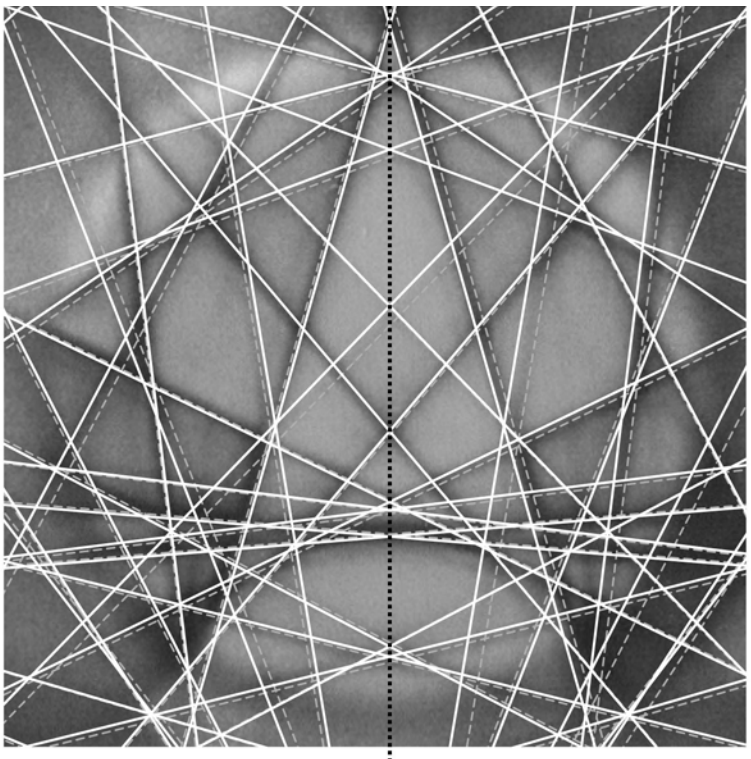

a= 0.56537nm
$\Delta a=\Delta b=\Delta c$=0nm
$\Delta\alpha=\Delta\beta=\Delta\gamma=0°$
Accelerating voltage for
kinematical simulation: 100.9kV

simulation
experiment

(f)

$\Delta\alpha$ and $\Delta\beta$

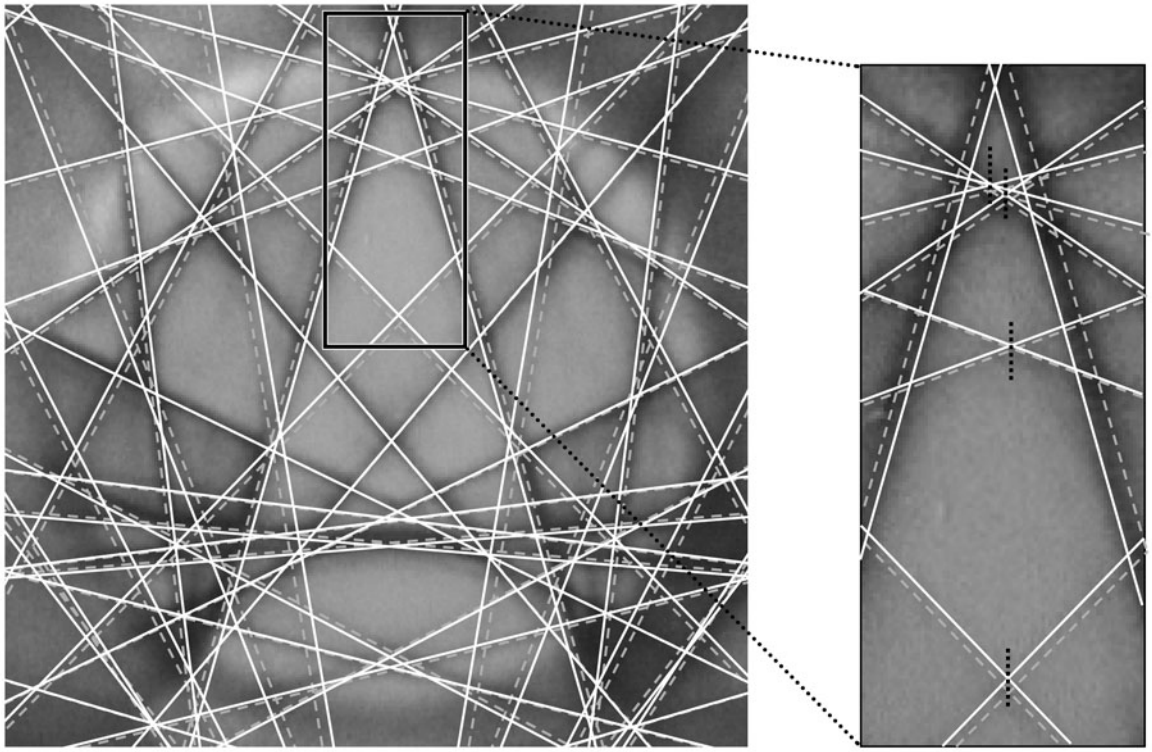

(g)

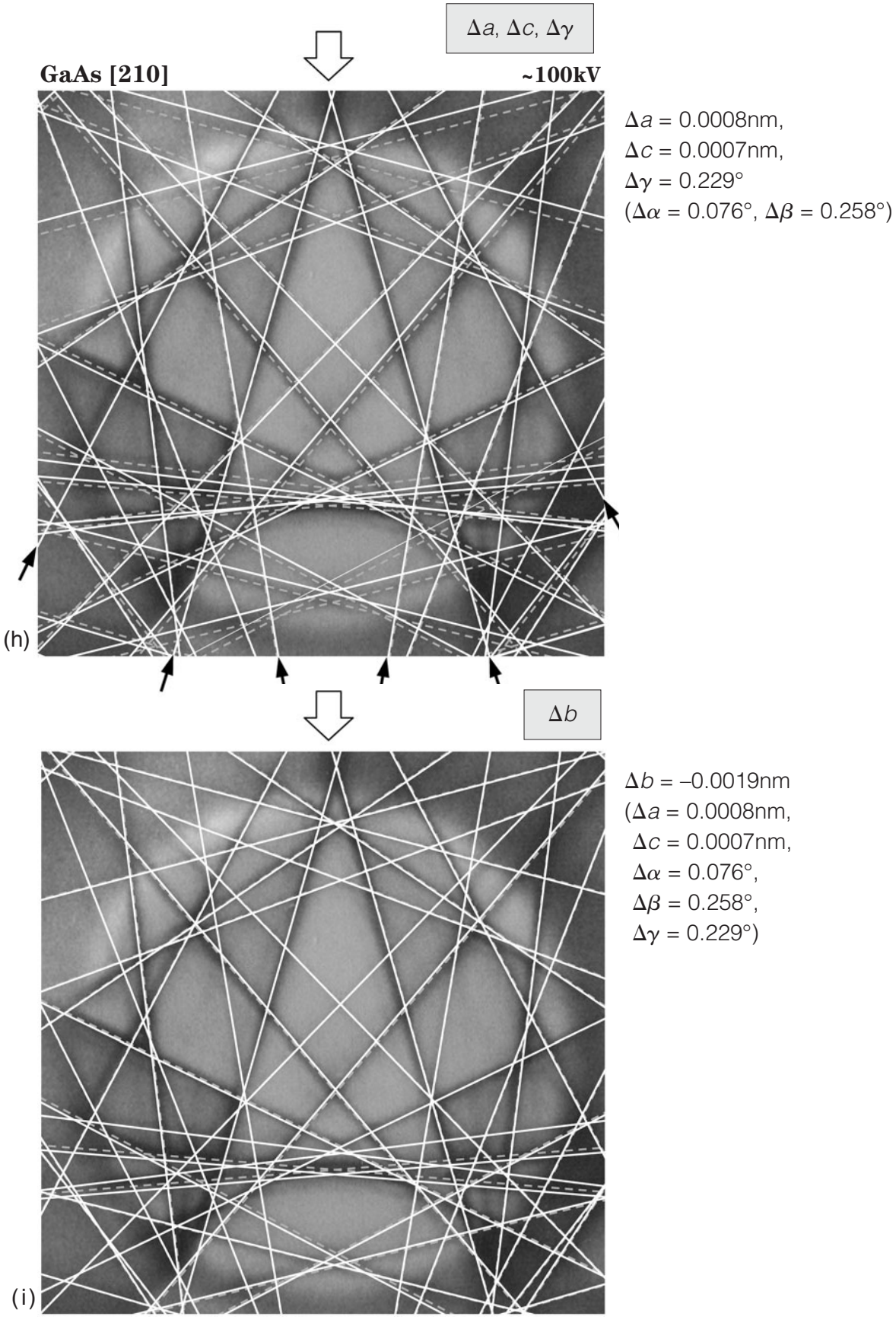
Δa, Δc, Δγ
GaAs [210]
~100kV
Δa = 0.0008nm,
Δc = 0.0007nm,
Δγ = 0.229°
(Δα = 0.076°, Δβ = 0.258°)
(h)
Δb
Δb = –0.0019nm
(Δa = 0.0008nm,
Δc = 0.0007nm,
Δα = 0.076°,
Δβ = 0.258°,
Δγ = 0.229°)
(i)

Step 2: Comparison with dynamical simulation

(j)

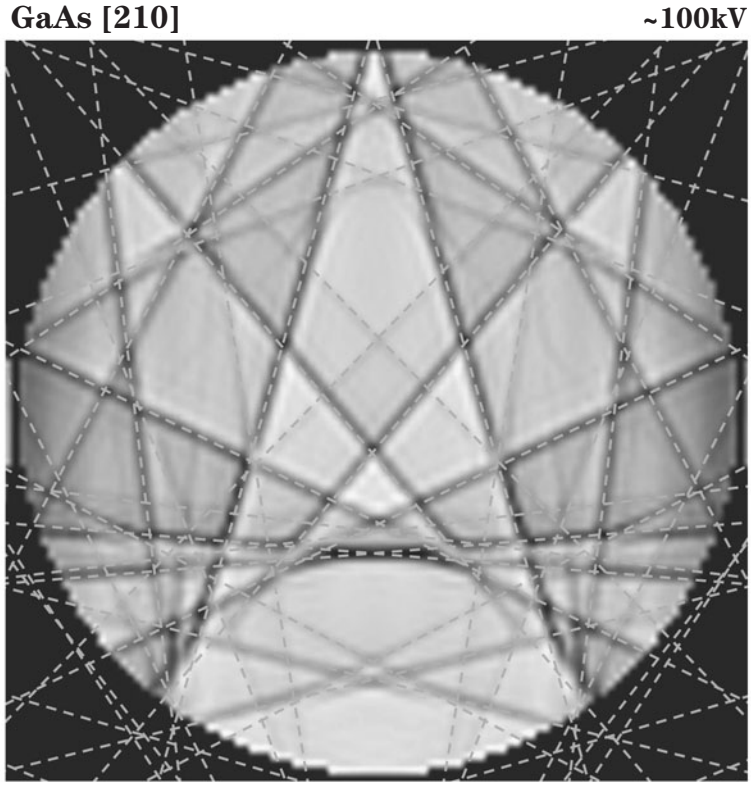

Δa = 0.0008nm,
Δb = −0.0019nm,
Δc = 0.0007nm,
$\Delta \alpha$ = 0.076°,
$\Delta \beta$ = 0.258°,
$\Delta \gamma$ = 0.229°
Accelerating voltage for dynamical simulation: 101.2kV

Present result	Bulk
a = 0.5662(4)nm b = 0.5635(4)nm c = 0.5661(2)nm α = 90.076(37)° β = 90.258(55)° γ = 90.229(18)°	$a = b = c$ = 0.56537nm $\alpha = \beta = \gamma = 90°$

Effects of Surfaces on Defocus CBED Patterns

Dislocations

Defocus illumination allows observing the whole strained area and identifying the Burgers vector of a dislocation. The defocus CBED pattern shows n nodes at the crossing region between a reflection line $\boldsymbol{g}$ and a dislocation line with a Burgers vector $\boldsymbol{b}$ when $\boldsymbol{g}\cdot\boldsymbol{b} = n$ as shown in Fig. (a). When the relative sign of $\boldsymbol{g}\cdot\boldsymbol{b}$ is correctly determined, the Burgers vector is identified using three linearly independent reflections [7].

Photograph (b) shows an electron micrograph of a Si specimen containing a dislocation. Defocus CBED patterns (c) and (d) were obtained respectively from specimen areas A and B in Photo (b). The Burgers vector $\boldsymbol{b}$ of the dislocation was determined to be $[01\bar{1}]/2$. The size of illuminated specimen areas A and B were the same. The specimen thicknesses of the areas A and B were determined to be 180nm and 98nm by CBED, respectively. Intensity profiles of the reflections of Photo (c) agree well with the simulated patterns, which are calculated by using the strain field for an isotropic bulk material, but those of Photo (d) are not well reproduced.

Specific features of reflection lines observed in thin specimen areas are described. A strain field model is given taking account of surface relaxation. Simulations of the intensity distribution of a reflection line based on the model are presented.

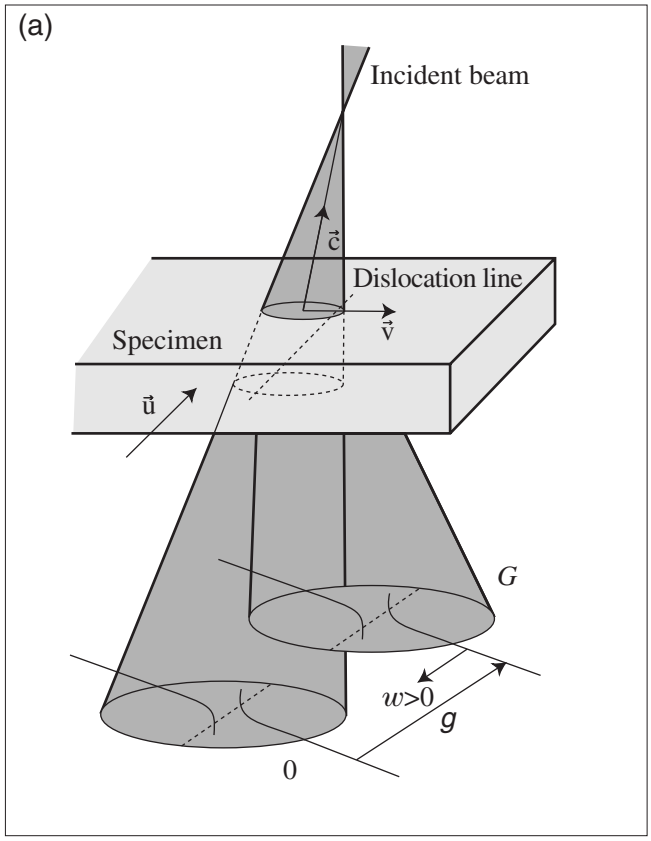

Defocus CBED pattern from a dislocation in the case of $\boldsymbol{g}\cdot\boldsymbol{b} = 1$.

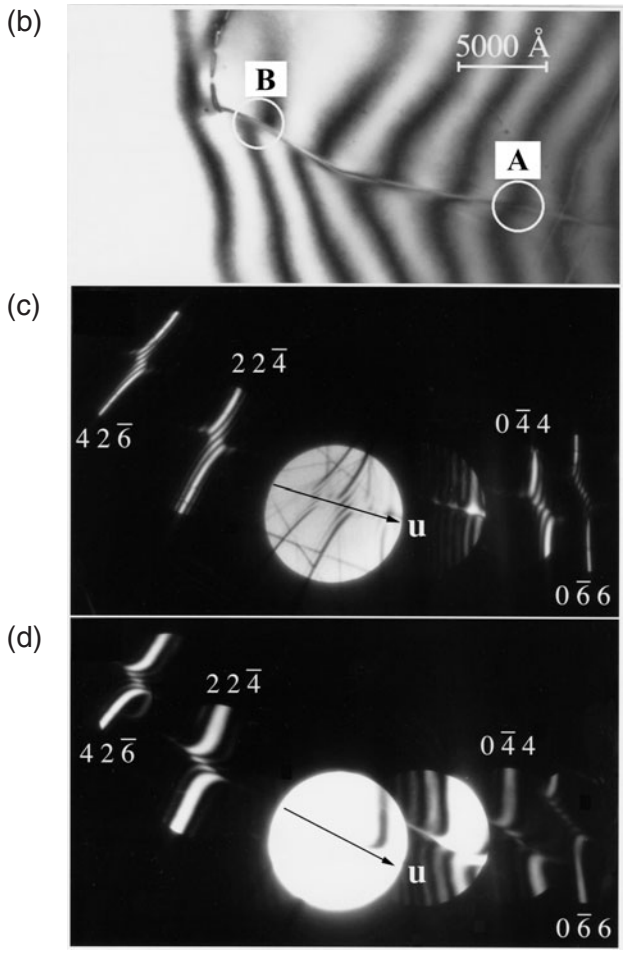

Photographs (e) and (f) show the $22\bar{4}$ reflection lines of Photos (c) and (d), respectively. An arrow labeled u in each photo denotes the position and the direction of the dislocation. Both reflection lines show three nodes.

The reflection profile of Photo (f) has the following two different features compared with that of Photo (e).

(1) The principal peak of Photo (f) shows a stronger bend near the dislocation than the bend of Photo (e).

(2) The bend of the reflection line in Photo (f) is confined in a smaller range along the reflection line than the bend of Photo (e).

The feature (1) is reproduced by a simulation by using a strain field for a bulk material. Since largely strained regions near the dislocation occupy the major part of the specimen thickness for thin specimens, the stronger bend of the reflection line is expected. However, the feature (2) cannot be reproduced by using a strain field for a bulk material. Since Photos (c) and (d) on the left-side page were obtained from specimen areas of the same size, the feature (2) indicates that the strained area in a thin specimen is more localized along the dislocation line than in a thick specimen. This indicates that the strain field in a thin specimen is relaxed more rapidly than in a thick specimen.

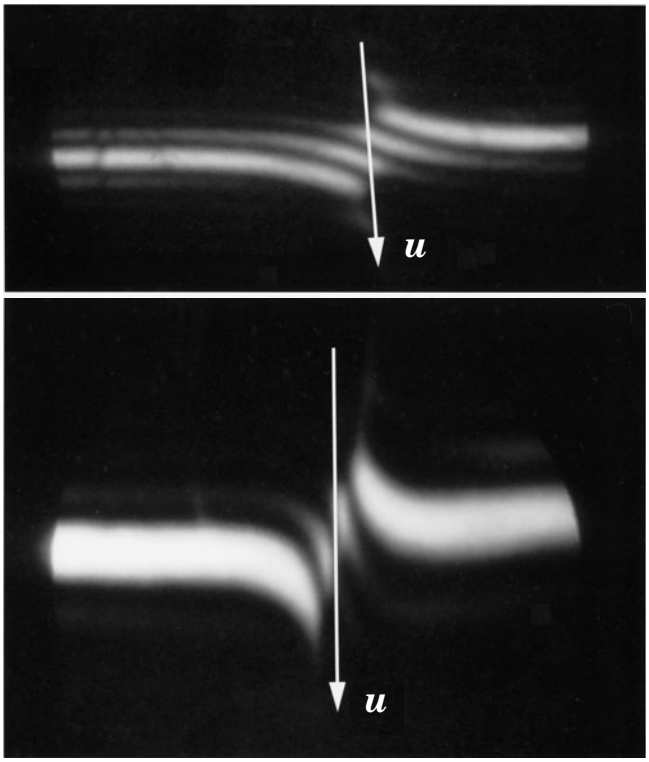

Figure (a) shows a model for a thick specimen containing a screw dislocation at the center of the specimen. In this model, surfaces are assumed to be far from the dislocation. Thus, the surfaces are free from the strain due to the dislocation. Therefore, simulations of reflection profiles using a strain field for a bulk specimen well reproduce the experimental reflection profiles.

In the case of a thin specimen containing a screw dislocation at the center (Fig. (b)), surfaces of the specimen exist too near the dislocation to neglect the effect of surface relaxation. If we consider only the dislocation, the strain remains at the surfaces. Since the surfaces should be free from strains, image dislocations are needed for thin specimens to keep free surfaces. Figure (b) shows an array of image dislocations [a], which causes the strain-free surfaces, where ◉ and ⊗ denote the opposite senses of the screw dislocations.

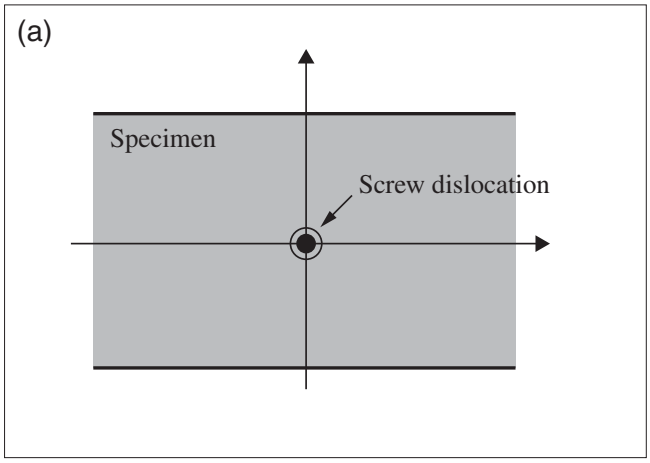

Model for a thick specimen.

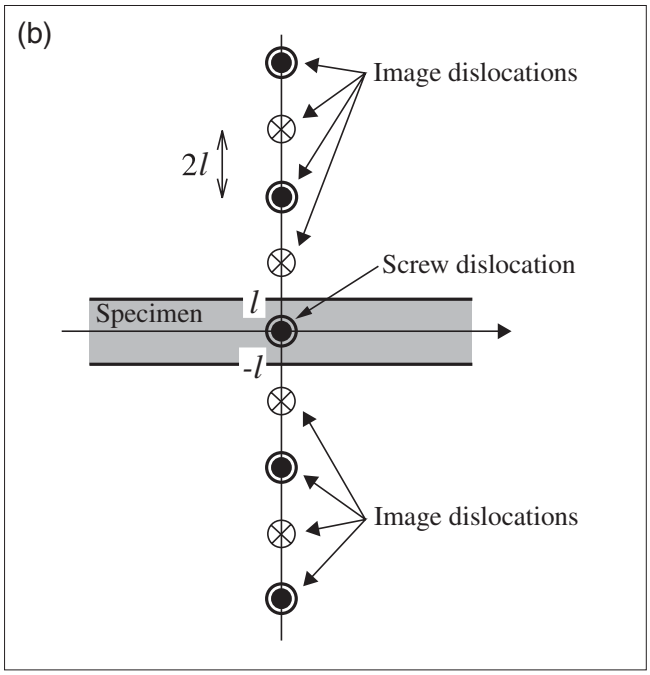

Model for a thin specimen.

Reference

[a] J. P. Hirth and J. Lothe: Theory of dislocations, McGraw-Hill, New York, 1968.

Figures (c) and (d) are simulated profiles of a reflection, which crosses a screw dislocation at right angle with $\boldsymbol{g}\cdot\boldsymbol{b} = 4$, by using model (a) on the left-side page. Specimen thicknesses of Figs. (c) and (d) are assumed to be 100nm and 54nm, respectively. Figure (d) shows a stronger bend of the reflection line near the dislocation than Fig. (c). This explains the feature (1) written on the page 289. However, the distance of the bend along the reflection line is almost the same as for Figs. (c) and (d).

Figures (e) and (f) are reflection profiles simulated by using model (b) on the left-side page. Figure (f) shows a smaller distance of bend of the reflection line than Fig. (e). This qualitatively agrees with the feature (2) on the pege 289. The model (b) on the opposite page may be an ideal one. Experimental results appear in-between the models (a) and (b). It should be noted that an effect of surface relaxation is clearly observed in a CBED pattern.

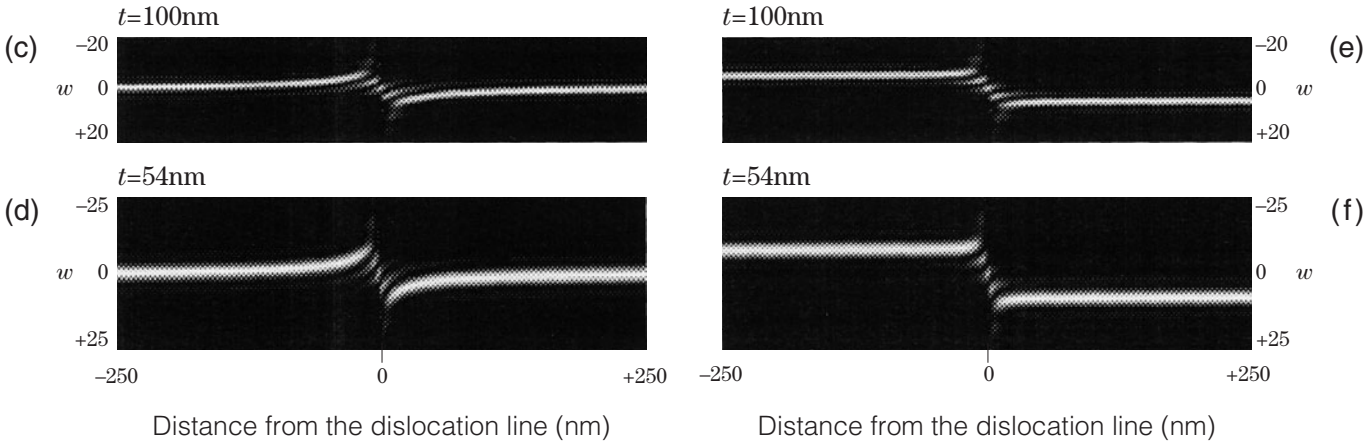

Stacking faults

When a defocused convergent beam illuminates a specimen containing a stacking fault, a reflection line $\boldsymbol{g}$ across the fault with a shift vector $\boldsymbol{R}$ shows a continuous change of the reflection profile depending on the phase shift of $\alpha = 2\pi\boldsymbol{g}\cdot\boldsymbol{R}$ in such a way as illustrated in Fig. (a). A simulated pattern of a reflection line across a stacking fault at right angle is shown in Fig. (b). The rocking curve of the reflection clearly changes in the positions and intensities of the principal peak and the first subsidiary peak at the crossing region with the stacking fault. The intensity ratio of the two peaks depends on the phase shift of $\alpha = 2\pi\boldsymbol{g}\cdot\boldsymbol{R}$ [7].

It should be noted that the reflection profile of Fig. (b) is symmetric with respect to the horizontal line through the center, where the fault plane exists at the center of the specimen. Asymmetric reflection profiles are observed together with symmetric reflection profiles in defocus CBED patterns taken from areas containing stacking faults of Si.

The asymmetric features of the observed reflection lines and a possible explanation are given on the following pages.

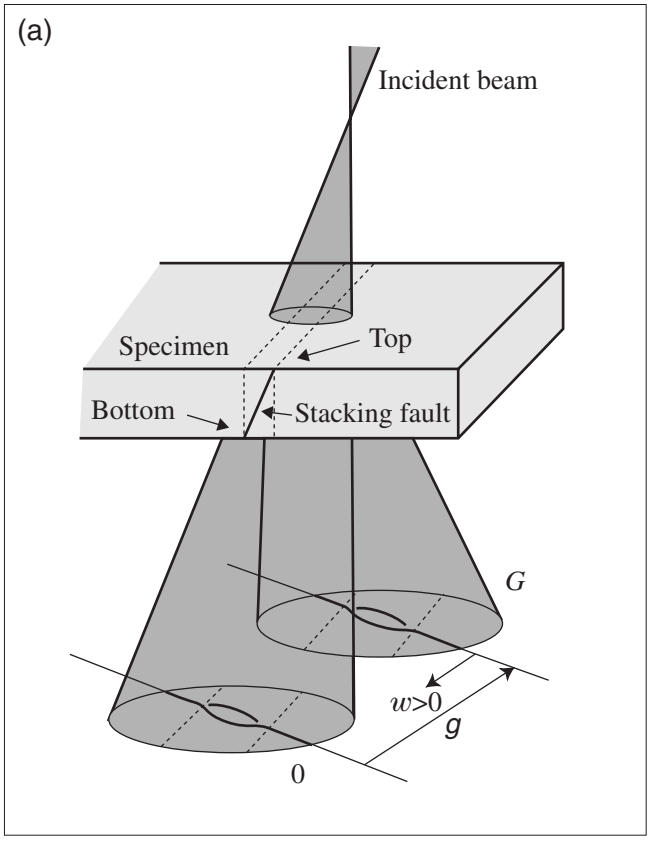

Defocus CBED pattern from a stacking fault.

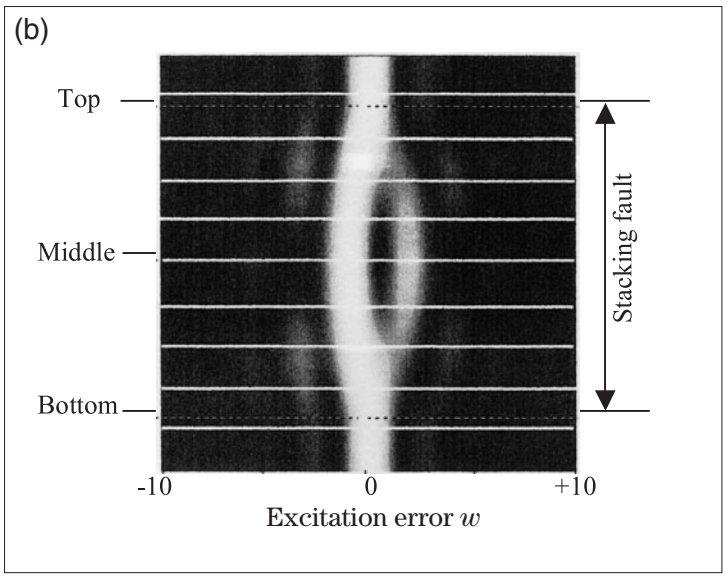

Simulation of a reflection line across a stacking fault for $\alpha=2\pi/3$.

Photographs (a) and (b) show $35\bar{1}$ and $6\bar{4}\bar{2}$ reflection lines in one defocus CBED pattern obtained from a stacking fault of Si. The reflection profile of Photo (a) is symmetric with respect to the center but the profile of Photo (b) is clearly asymmetric. The asymmetric behavior always appears at one end of the stacking fault, where the stacking fault meets with the top or bottom surface of the specimen.

(a)

$35\bar{1}$ reflection

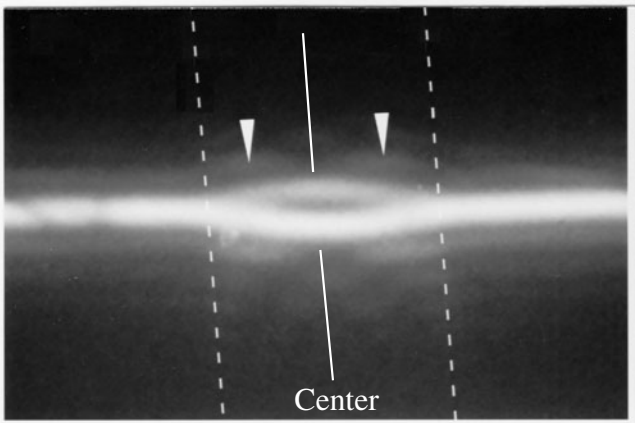

Symmetric intensity distribution.

$6\bar{4}\bar{2}$ reflection

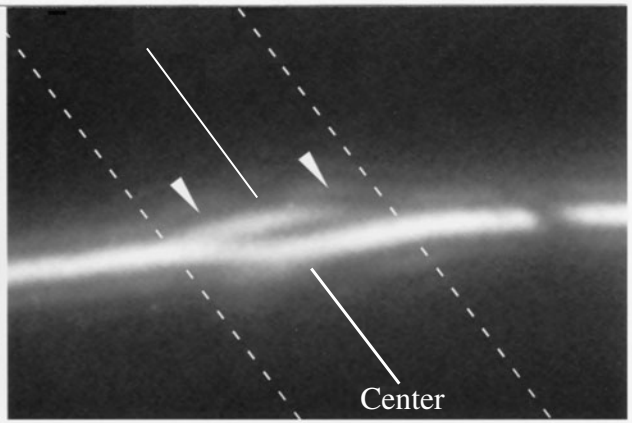

Asymmetric intensity distribution.

(b)

Photographs (a), (b) and (c) show reflection profiles obtained from the same stacking fault in Si but from different specimen areas with different thicknesses. The asymmetry of the profiles appears more conspicuous in thinner specimen areas. This indicates that the asymmetry is not due to an absorption effect, which is essential for the interpretation of the electron microscope images of a stacking fault in thick specimens [a].

Simulations of the reflection profile using the known shift vector of the [111]/3 type for the stacking fault cannot provide the asymmetric profile, even if the micro twin structure is taken into account [b].

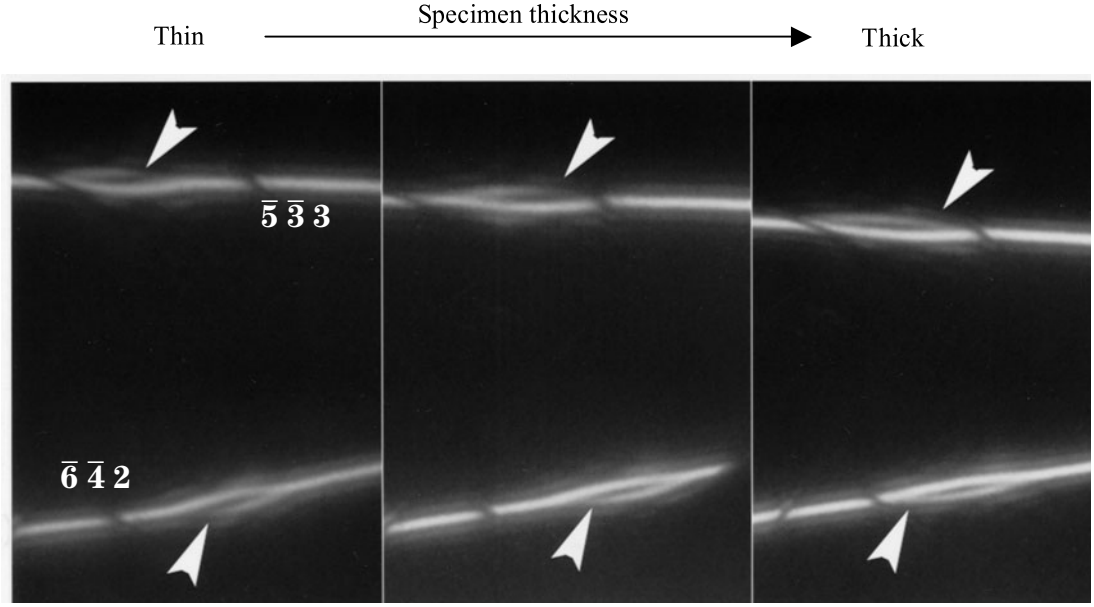

$\bar{6}\,\bar{4}\,2$ reflection : $\alpha = +2\pi/3$
$\bar{5}\,\bar{3}\,3$ reflection : $\alpha = -2\pi/3$

References

[a] P. B. Hirsch, A. Howie, R. B. Nicholson, D. W. Pashley and M. J. Whelan: Electron microscopy of thin crystals, Butterworths, London, 1965.

[b] O. L. Krivanek and D. M. Maher: *Appl. Phys. Lett.* **32** (1978) 451.

One possible model of a stacking fault, which gives asymmetric reflection profiles, is shown in Fig. (a). The stacking fault has a usual shift vector $\boldsymbol{R} = [11\bar{1}]/3$ in the middle of the specimen but has an additional shift vector $\pm\Delta\boldsymbol{R}$ at the top and the bottom regions of the specimen. The shift vector $\Delta\boldsymbol{R}$ was approximately determined to be $[5\bar{3}0]/100$ from the phase shifts α by measuring intensity ratios of the principal peak and the subsidiary peak [7] at the top and the bottom regions.

Figure (b) shows three reflection profiles simulated by using the model in Fig. (a). Additional phase shifts $\Delta\alpha = 2\pi\boldsymbol{g}\cdot\Delta\boldsymbol{R}$ were -0.32π for $\bar{5}\bar{3}\bar{1}$, 0.60π for $95\bar{1}$ and 0.08π for $22\bar{4}$. The $\bar{5}\bar{3}\bar{1}$ and $95\bar{1}$ reflections clearly show asymmetric reflection profiles but the $22\bar{4}$ reflection is almost symmetric. This implies that strong asymmetry is expected for reflections which have large values of $2\pi\boldsymbol{g}\cdot\Delta\boldsymbol{R}$.

Simulations of reflection profiles for different specimen thicknesses by using the model in Fig. (a) showed that the asymmetry appears more conspicuously in thinner specimens. These results are consistent with the experimental results on the opposite page. The asymmetry of the reflection profiles has also been observed in rutile [7] and copper. It should be noted that CBED can detect a small structural change of the stacking fault near the specimen surfaces.

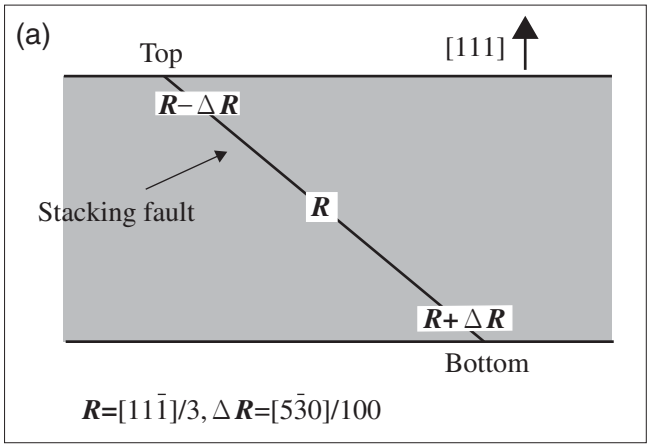

Model for a stacking fault with an additional shift.

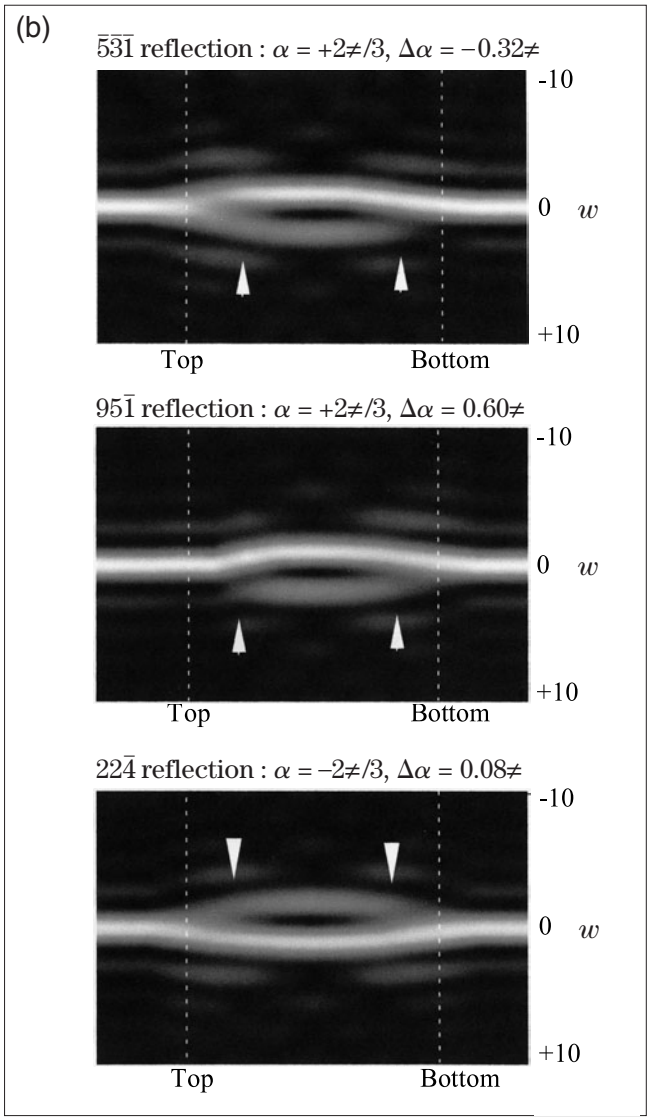

Simulations for the model shown in Fig. (a).

Future Trend of Transmission Electron Microscopes

As already described, we manufactured an Ω-filter electron microscope (JEM-2010FEF) [14], which enables us to perform precise crystal structure analysis at a sub-nanometer scale using the CBED method. CBED is a successful method for the characterization of materials with the combination of diffractometry and microscopy.

We know that microscopy, diffractometry and spectroscopy are three important functions of electron microscopes and have made a great contribution to materials research. In this chapter, we describe the future trend of TEM other than CBED.

In the near future, the combined use of spectroscopy and diffractometry as well as spectroscopy and microscopy will be a weighty subject for the nanometer scale characterization of materials, which includes studies of the momentum dependence of electron energy-loss spectra and the spatial variation of electronic structures. For this purpose, better energy resolutions of electron energy-loss spectroscopy (EELS) and X-ray emission spectroscopy (XES) are required.

The electronic structures have been studied by analyzing the spectra of inelastically scattered electrons, the method being called EELS. The electron energy-loss near-edge fine structure (ELNES) gives the partial density of states (DOS) of the conduction band. The valence-electron excitation spectrum is transformed to the dielectric function (ϵ) by the Kramers-Kronig analysis. The imaginary part of the dielectric function is proportional to the joint DOS (J_{DOS}) of the valence and conduction bands multiplied by transition probabilities.

Conventional EELS instruments attached to a TEM take EELS spectra with an energy resolution of about 1eV from a nanometer-scale specimen area. To reveal the details of electronic structures, a better energy resolution, namely 0.2eV, is necessary. We have developed a high energy-resolution EELS microscope (JEM-HREA80) [43], which is equipped with an Wien-filter monochromator and analyzer. Its energy resolutions are as high as 50meV to 0.2eV but its spatial resolution is unfortunately 30 to 100nm in diameter. The Ω-filter microscope JEM-2010FEF can take EELS spectra from a sub-nanometer specimen area. However, the energy resolution of its spectra remains at about 1eV. Thus, analytical electron microscopes, which permit us to study both the crystal structures and the electronic structures at a nanometer scale with an energy resolution of 0.2eV, are necessary for the development of materials science and nanotechnology. The design of our new microscope is described below.

Together with the DOS of the conduction band (unoccupied states), the DOS of the valence band (occupied states) is required for the understanding of the whole electronic structure. Unfortunately, the DOS of the valence band cannot be reached directly by EELS. A partial DOS of the valence band can be obtained by XES. An EDS device attached to a TEM is a tool for taking XES spectra. However, since the energy resolution of the conventional EDS device is about 130eV, it is insufficient for the study of the electronic structures. An energy resolution of about 1eV is a target resolution for the time being for the study of the DOS of the valence band. We have constructed a grazing-incidence soft-X-ray spectrometer. Its design and the results of its applications are given below.

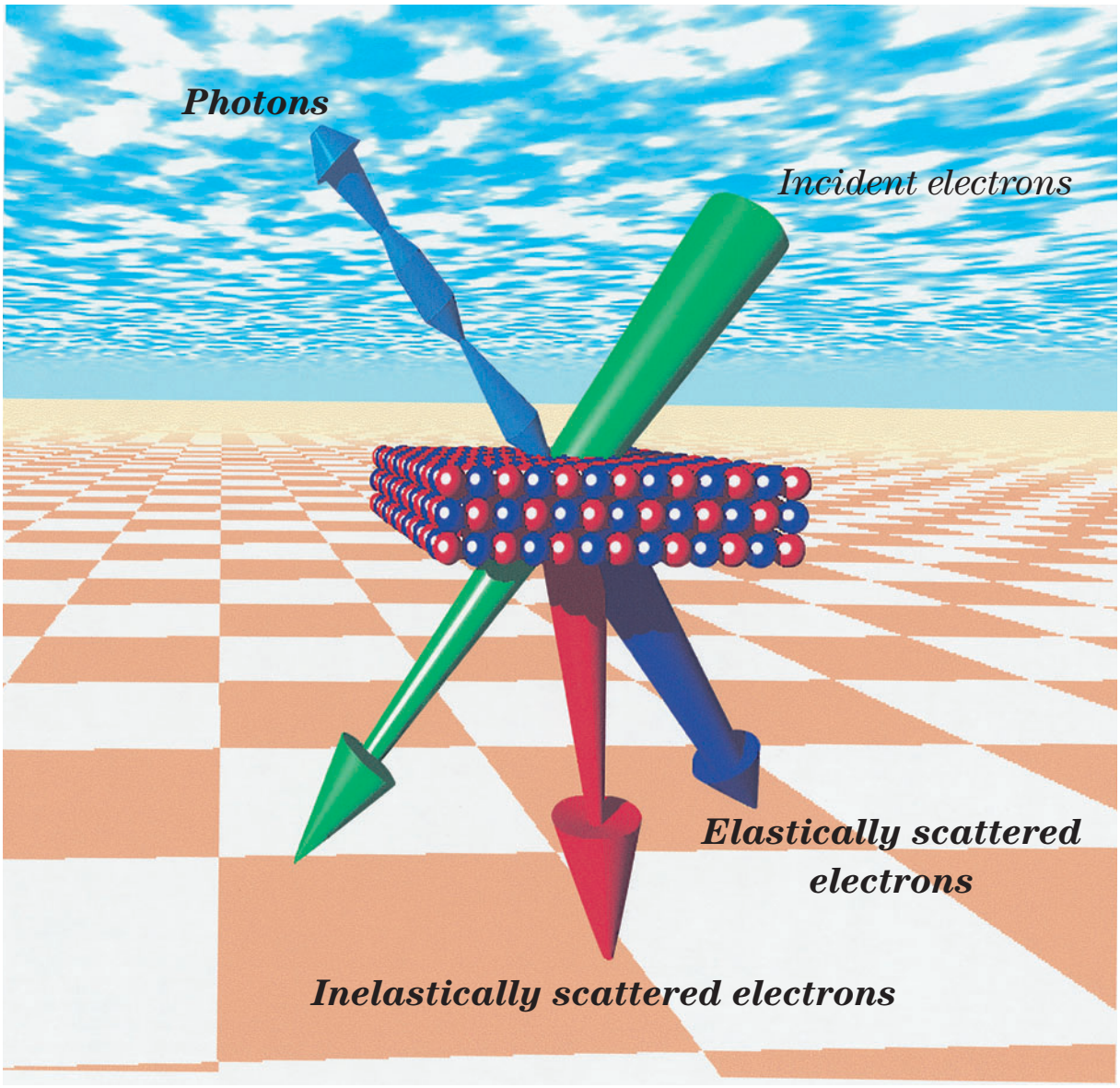
Photons
Incident electrons
Elastically scattered electrons
Inelastically scattered electrons

Two Important Electron Microscopes Already Developed

Ω-filter electron microscope

We again show a photograph of the column part of our JEM-2010FEF and a schematic ray-path of the microscope. The details of the performance are referred to the chapter on energy filtering. An example of energy filtering is given on the right-side page.

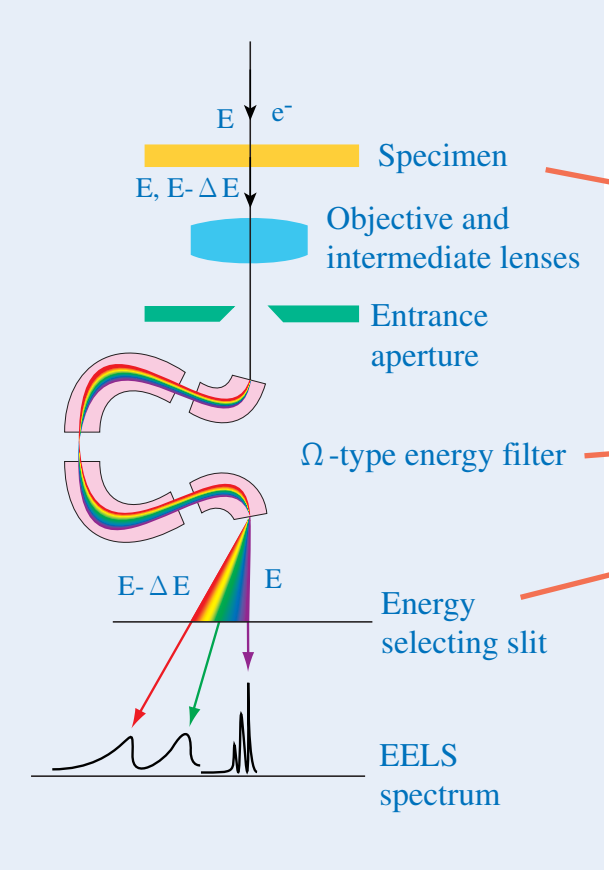

JEM-2010FEF

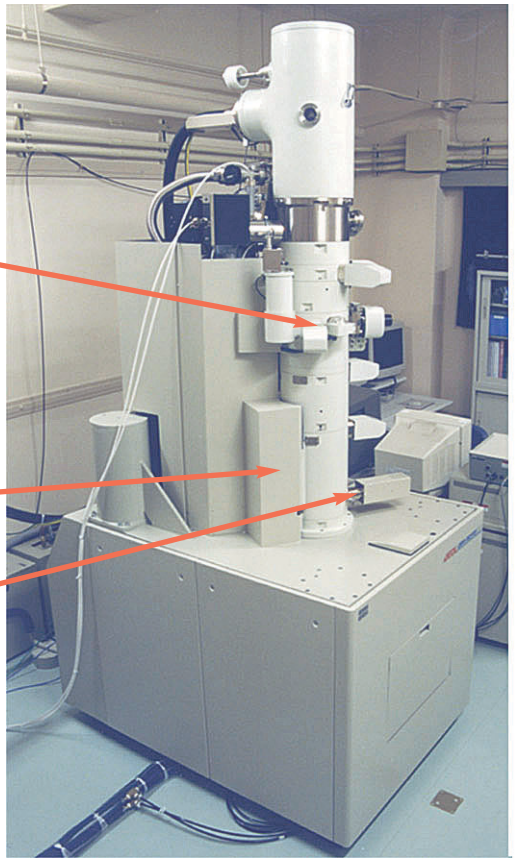

Effect of energy filtering on CBED patterns

Diamond [111]

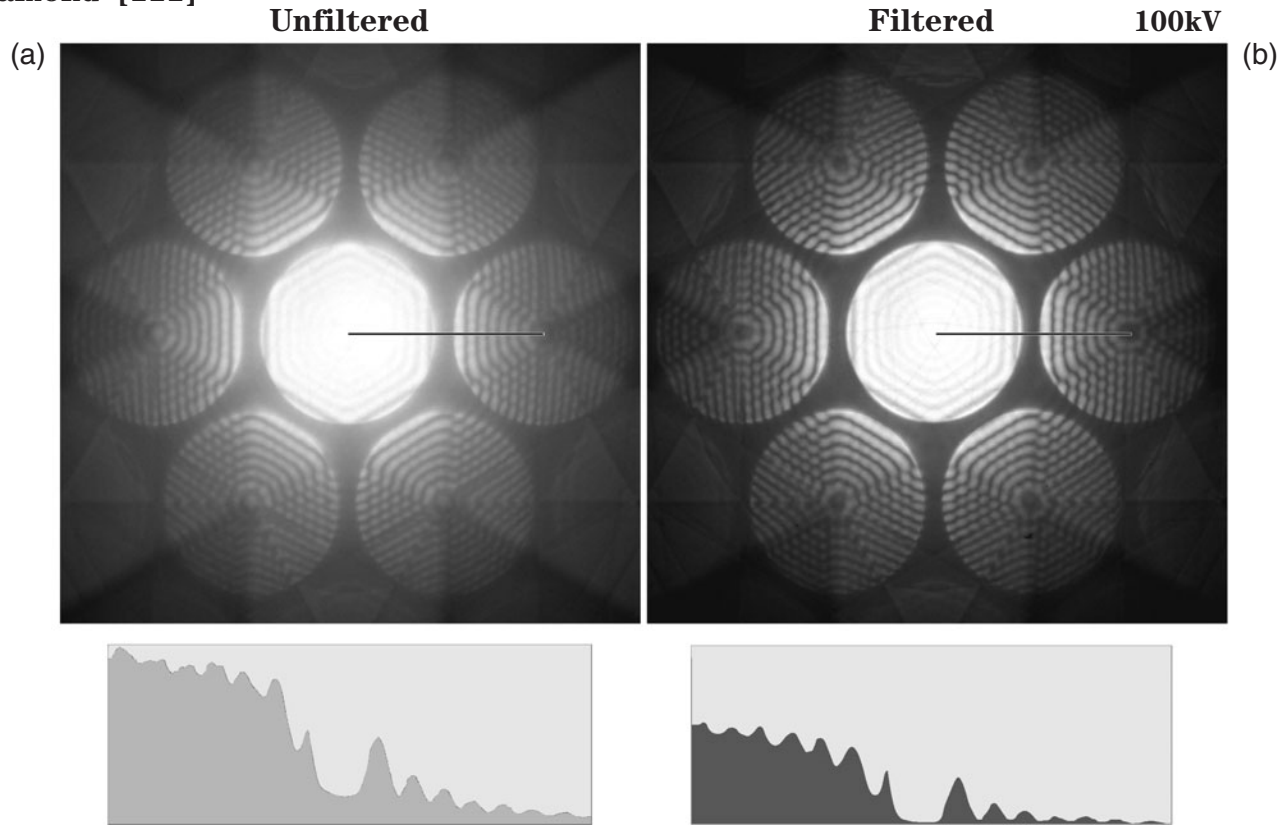

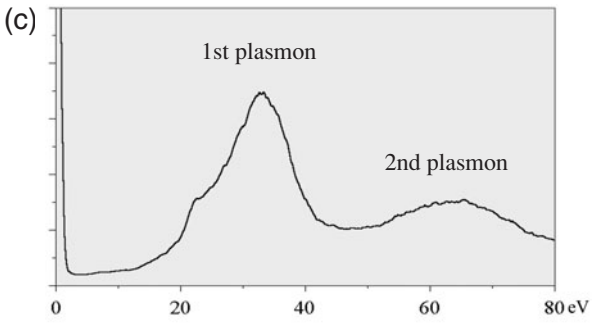

Photographs (a) and (b) show unfiltered and zero-loss filtered CBED patterns of diamond [111] taken at 100kV with $\Delta E = \pm 8$eV. Intensity line-profiles along the black lines in Photos (a) and (b) are shown below the patterns. It is seen that the pattern became clear by removing the plasmon-loss intensity. Figure (c) shows the energy-loss spectrum of the specimen. It is seen that the plasmon-loss intensities can be fully removed by setting the width of the energy-selecting slit at $\Delta E = \pm 8$eV.

High energy-resolution EELS microscope

We developed a high energy-resolution EELS microscope, JEM-HREA80, under a Joint Research with Industry project (1985–1990) supported by a Grant-in-Aid of the Ministry of Education, Science, Sports and Culture of Japan. It is equipped with Wien filters as the monochromator and the analyzer [43]. The Wien filters are set at a potential of HT–U_0 (HT = 60kV, U_0 = 15 to 2000V) to achieve a large energy dispersion. High potentials (HT) for the electron gun and the Wien filters are supplied from one HT tank to cancel out instability and drift of the high potential. For the illumination-lens system, the specimen goniometer and the imaging-lens system of the EELS microscope, the column part of a JEM-1200EX transmission electron microscope is utilized.

The EELS spectra are detected by a CCD camera. The microscope is operated at energy resolutions of 50meV to 0.2eV for routine measurements. The best resolutions for cases without and with a specimen are 12meV and 25meV, respectively. Spatial and momentum resolutions are 30 to 100nm in diameter and 3nm^{-1} in diameter, respectively. This instrument has been applied to the studies of electronic structures of fullerenes, quasicrystals, metal-insulator transitions of vanadium oxides and many other materials [44].

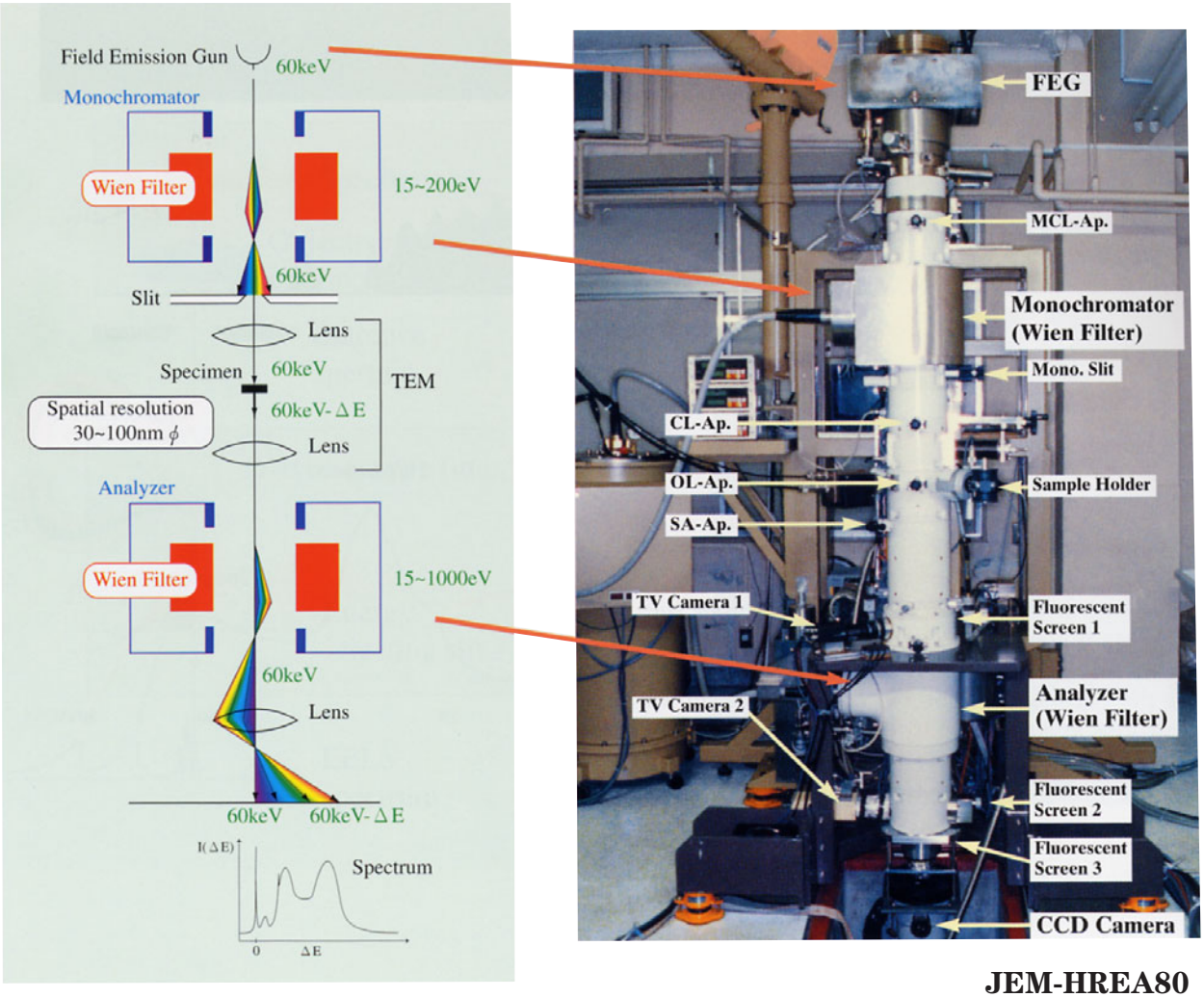

JEM-HREA80

The best energy resolution and an application to α-boron

Figure (a) shows the energy spread of the zero-loss beam without a specimen, which was obtained by setting the monochromator and analyzer at U_0 = 15V. The full width at half maximum (FWHM) of the peak was measured to be 12meV using a reference peak of an energy difference of 200meV. The reference peak was obtained by changing the retarding potential U_0 of the analyzer by an amount of 200meV.

Figure (b) shows boron *K*-edge spectra of α-boron in an energy range from 185eV to 200eV. The top spectrum was obtained by a conventional field-emission transmission electron microscope with an energy resolution of about 1eV. It does not show any fine peaks. The middle spectrum was obtained by our EELS microscope with an energy resolution of 0.17eV. It shows fine peaks, which indicate that there are peak structures in the density of states (DOS) of the conduction band [a]. The bottom one is a DOS of the conduction band of this material obtained by a recent *ab initio* calculation [b]. The comparison between the high energy-resolution boron *K*-edge spectrum (middle) and the theoretical one (bottom) shows good agreement. These show that a high energy-resolution of about 0.2eV is necessary for the detailed comparison between inner-shell excitation spectra and calculated DOS of conduction bands.

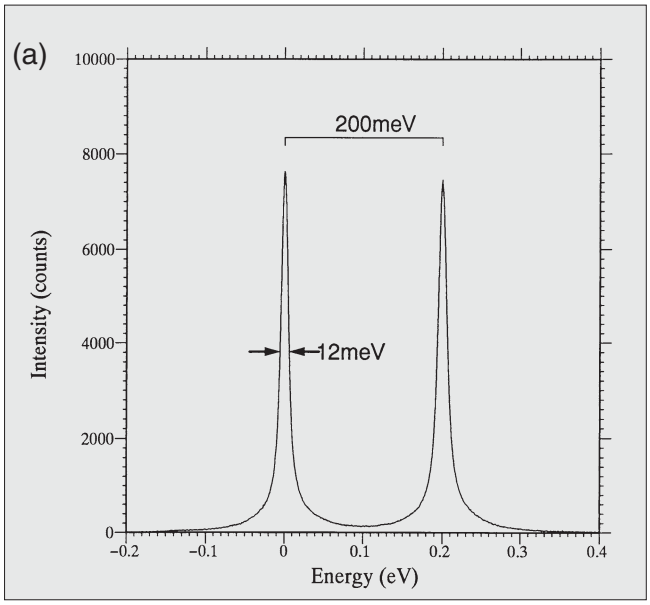

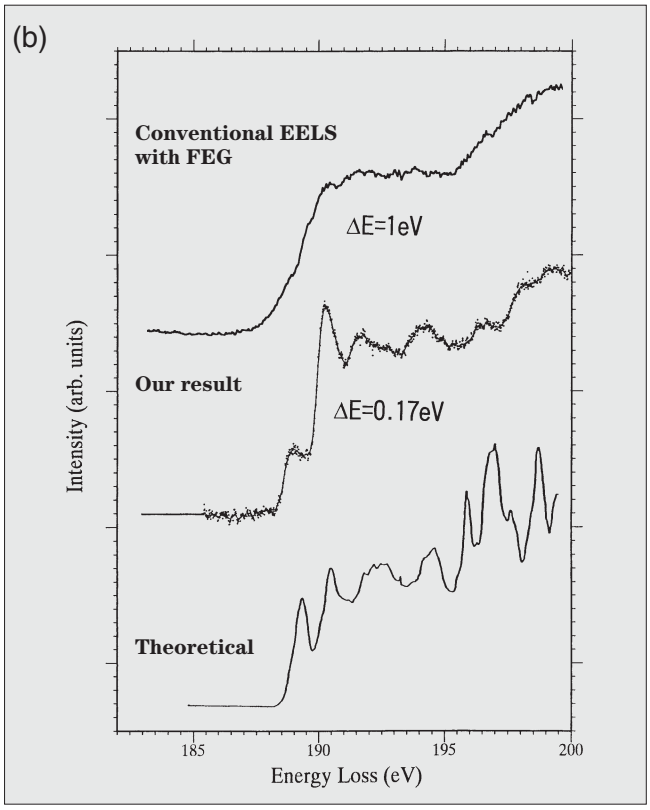

References

[a] M. Terauchi, Y. Kawamata, M. Tanaka, M. Takeda and K. Kimura: *J. Solid State Chem.*, **133** (1997) 156.

[b] S. Gunji and H. Kamimura: *Phys. Rev. B*, **54** (1996) 13665.

MIRAI 21 Electron Microscope

Analytical transmission electron microscopes, which permit us to study both the crystal structures and the electronic structures at a nanometer scale, are strongly expected to appear on the market. Since 1999, we have started to manufacture such a new electron microscope under a project named “MIRAI 21” of Japan Science and Technology Corporation (JST) [49]. MIRAI means “Future” in Japanese and is the abbreviation of “Microscope for Innovative Research and Advanced Investigation”.

The microscope is of an accelerating voltage of 200kV and has a spatial resolution of 0.19nm and an energy resolution of 0.2eV at a probe size on a specimen of less than 2nm in diameter. It should be noted that a better energy resolution is attainable for a larger probe size. The microscope is constructed based on the JEM-2010FEF, but equipped with a double Wien-filter monochromator and an improved | -filter analyzer. A new and the most important element is the Wien-filter monochromator, which requires a high stability of the accelerating voltage of better than 5×10^{-7}. Specification of MIRAI 21, JEM-2010FEF and JEM-HREA80 are given for comparison.

Specifications

	MIRAI 21	JEM-2010FEF	JEM-HREA80
Accelerating voltage	200kV	200kV	60kV
Energy resolution	0.2eV	1eV	0.012eV
Probe size	2nm	0.5nm	30nm
Spatial resolution	0.19nm	0.19nm	2nm
Year	2003	1997	1994

MIRAI=未来=Future

JEM-2010FEF

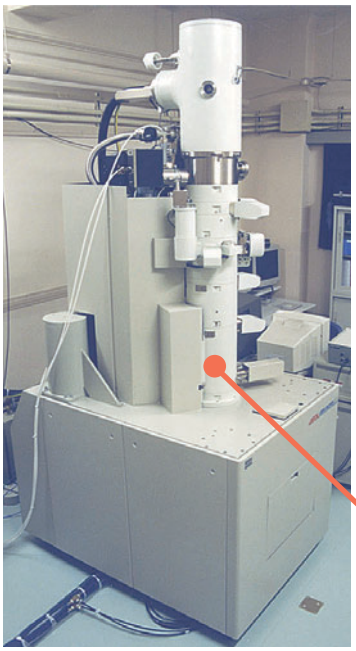

JEM-HREA80

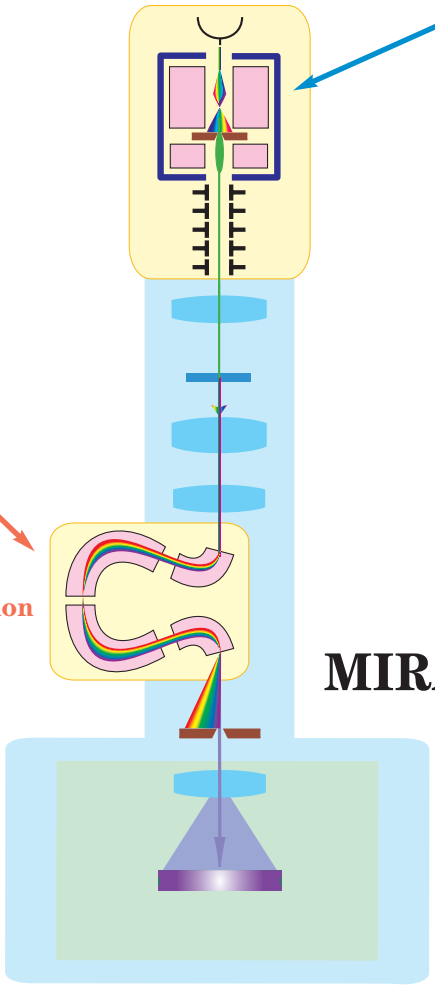

Fundamentals of MIRAI 21
Monochromator

Figure (a) shows a schematic diagram of the electron gun which includes a monochromator. The monochromator is located below the extraction anode of the field-emission gun (FEG) and above the acceleration tube. The filter is composed of two Wien filters. The energy-selection slit is inserted between the two Wien filters. The mechanical dimensions of filters I and II are 4cm and 1cm in length, respectively. The ratio of the dimensions is chosen to form an achromatic image below filter II. Astigmatic focus as seen in the electron trajectories (Fig. (b)) is adopted to reduce the Boersch effect. The electron beam does not form a spot above the accelerating tube but forms it only below the condenser lens to reduce the Boersch effect. The double Wien-filter is operated under an incident electron-beam energy of less than 1keV. The energy dispersion of the filter is expected to be about 17μm/eV at an electron-beam energy of 800eV.

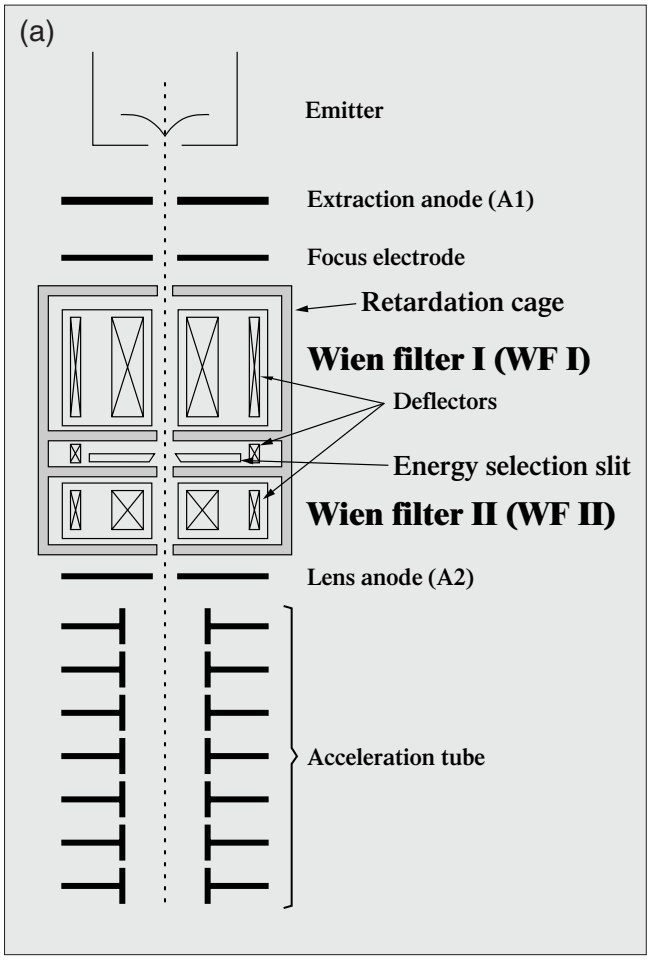

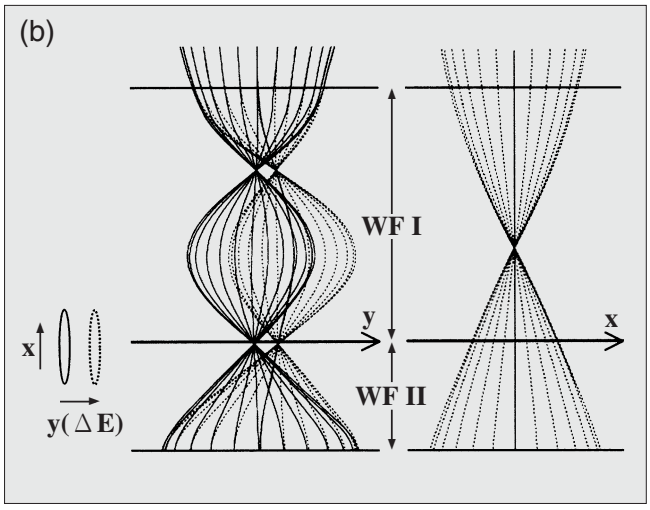

Stability of the accelerating voltage

The monochromator is set at the high potential of the accelerating voltage of the incident electrons but the analyzer at the ground potential. Thus, the fluctuation of the accelerating voltage causes a lowering of the energy resolution of the EELS spectra. To obtain an energy resolution of 0.2eV at an accelerating voltage of 200kV, the stability of the voltage must be better than 5×10^{-7} ($200kV\times5\times10^{-7}= 0.1V$). The feedback circuit used to accurately detect the fluctuation of the accelerating voltage is set in a separate tank (Feedback tank), which is specially designed to exclude electric and electromagnetic noise. To reduce the drift of the accelerating voltage, special attention is paid to controlling the temperature of the feedback circuit.

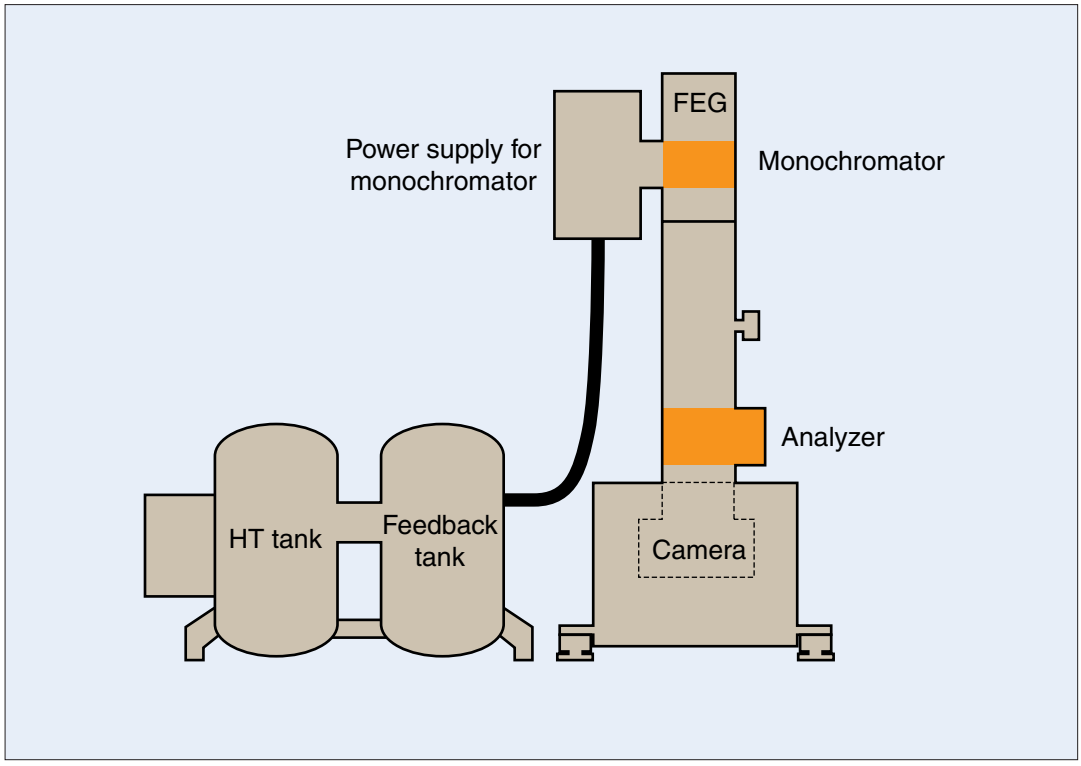

High Energy-Resolution XES

Density of states of valence bands

The electron energy-loss near-edge fine structure (ELNES) gives the partial density of states (DOS) of the conduction band. Together with the DOS of the conduction band, CB (unoccupied states), the DOS of the valence band, VB (occupied states), is needed to understand the whole electronic structure. Unfortunately, the DOS of VB cannot be reached directly by EELS. The partial DOS of VB can be obtained by X-ray emission spectroscopy (XES).

A conventional EELS instrument attached to a TEM usually takes spectra with an energy resolution of about 1eV, by which the DOS of CB has been studied by ELNES until now. Thus, at least a similar energy resolution is necessary also for the spectra of the DOS of VB. Our present target is to achieve a resolution of about 1eV for XES in a TEM, though an energy resolution of about 0.2eV will be required in the future to study the fine structures of the DOS of VB.

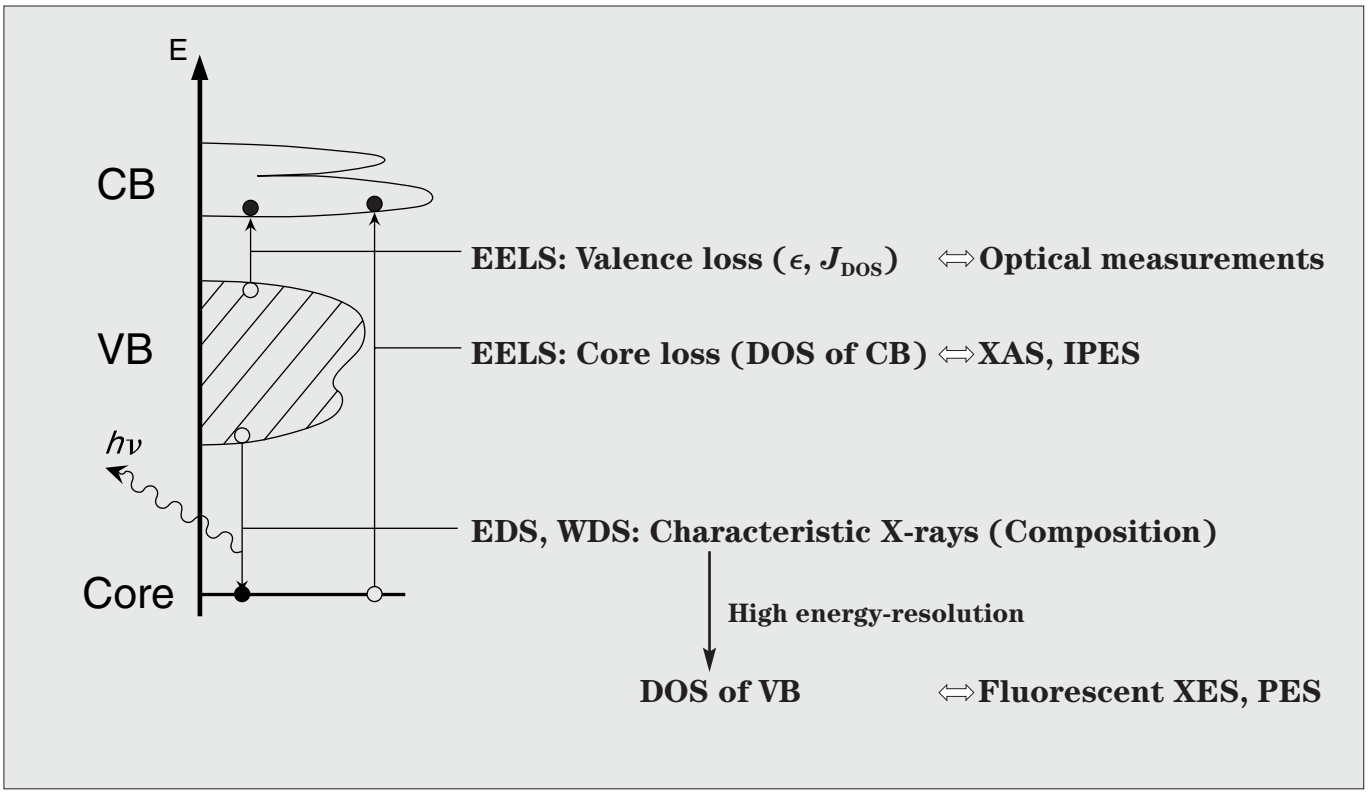

Soft-X-ray spectrometer for a transmission electron microscope

We constructed a flat-field grazing-incidence soft-X-ray spectrometer [53] using an aberration-corrected concave grating proposed by Kita *et al.* [a]. The spectrometer is composed of the grating and a CCD detector. The grating was designed for diffracted X-rays to focus not on the Rowland circle but on a plane nearly normal to the rays. The smaller energy dispersion of the grating compared to the dispersion of an ordinary concave grating has the advantage of detecting a wider energy range for a CCD detector of a certain size, while the larger dispersion of an ordinary grating needs a movable detector along the Rowland circle to detect a spectrum over a wide energy range. The present grating is of 1200grooves/mm and a $50\times30\text{mm}^2$ ruled area. The incidence angle α of X-rays emitted from a specimen to the grating was set to be 87 degrees. The size of the CCD is $26.4\times7.9\text{mm}^2$ with one pixel size of $24\times24\,\mu\text{m}^2$. The longer side of the rectangular CCD was set to be parallel to the direction of energy dispersion of X-rays. The distance from the specimen position to the CCD detector is about 47cm. The collection angle of the present spectrometer is 1.85×10^{-4}sr. Figure shows a schematic diagram of the spectrometer. A sputter-ion pump (SIP) and a turbo-molecular pump (TMP) combined with a rotary pump (RP) were used to evacuate the spectrometer chamber. A gate valve was placed between the spectrometer and the column of the TEM to separate the vacuums of the two. The energy resolution of the spectrometer was estimated to be about 0.6eV at the energy of boron *K*-emission. Since our spectrometer is making progress in its performance, the latest information on our development should be referred to our papers in the proceedings of the related conferences.

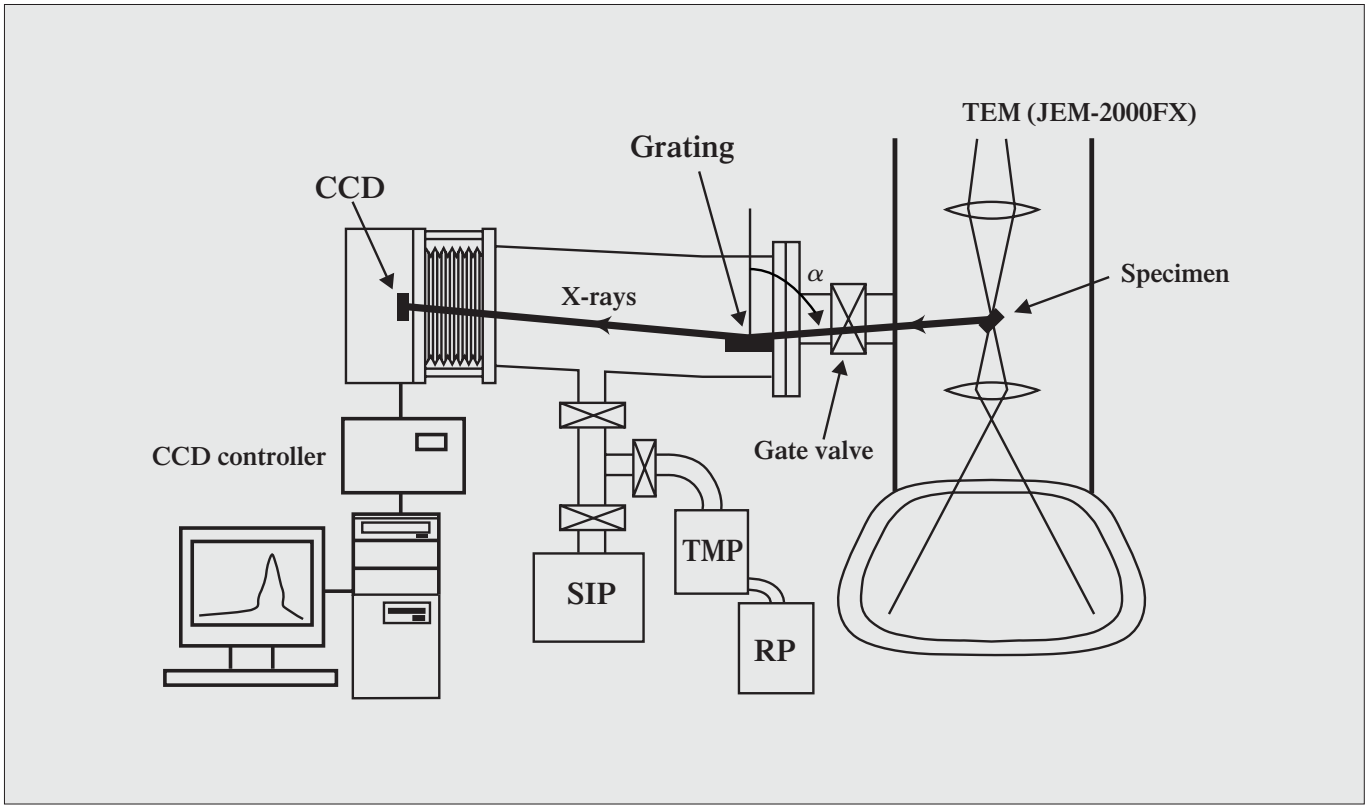

Reference

[a] T. Kita, T. Harada, N. Nakano and H. Kuroda: *Appl. Optics*, **22** (1983) 512.

DOS of valence bands
Hexagonal boron nitride

Figure (a) shows a spectrum of boron *K*-emission obtained from a specimen area of 1μm in diameter of a single crystal of hexagonal boron nitride (*h*-BN) with a probe current of about 180nA [53]. The acquisition time of the spectrum was 1 hour. The horizontal axis represents the channel number of the CCD. The dominant peak is located at about channel 670, which is accompanied by two shoulders indicated by vertical solid and dotted lines. The end of the peak at the right side indicated by an arrowhead corresponds to the top of the valence band. The smaller peak appears at about channel 635, which has one shoulder as shown by a vertical solid line. These features of the spectrum are very similar to those of the spectrum reported by Tegeler *et al.* [a] as shown by the solid line in Fig. (b). The spectrum was obtained from a specimen of powder *h*-BN by using synchrotron orbital radiation with an energy resolution of 0.2eV. The dotted lines in Fig. (b) show a theoretically calculated DOS of the valence band [b]. The spectrum in Fig. (a) is well fitted by a sum of five gaussian peaks as shown in Fig. (c). The peak labeled (1), which corresponds to the shoulder indicated by the dotted line in Fig. (a), is assigned to the $\neq$ component of the valence band by referring to the theoretically calculated DOS shown in Fig. (b). The peaks labeled (2) to (5), which correspond to two peaks and two shoulders indicated respectively by arrows and vertical solid lines in Fig. (a), are assigned to the σ component of the valence band by referring to the theoretically calculated DOS shown in Fig. (b).

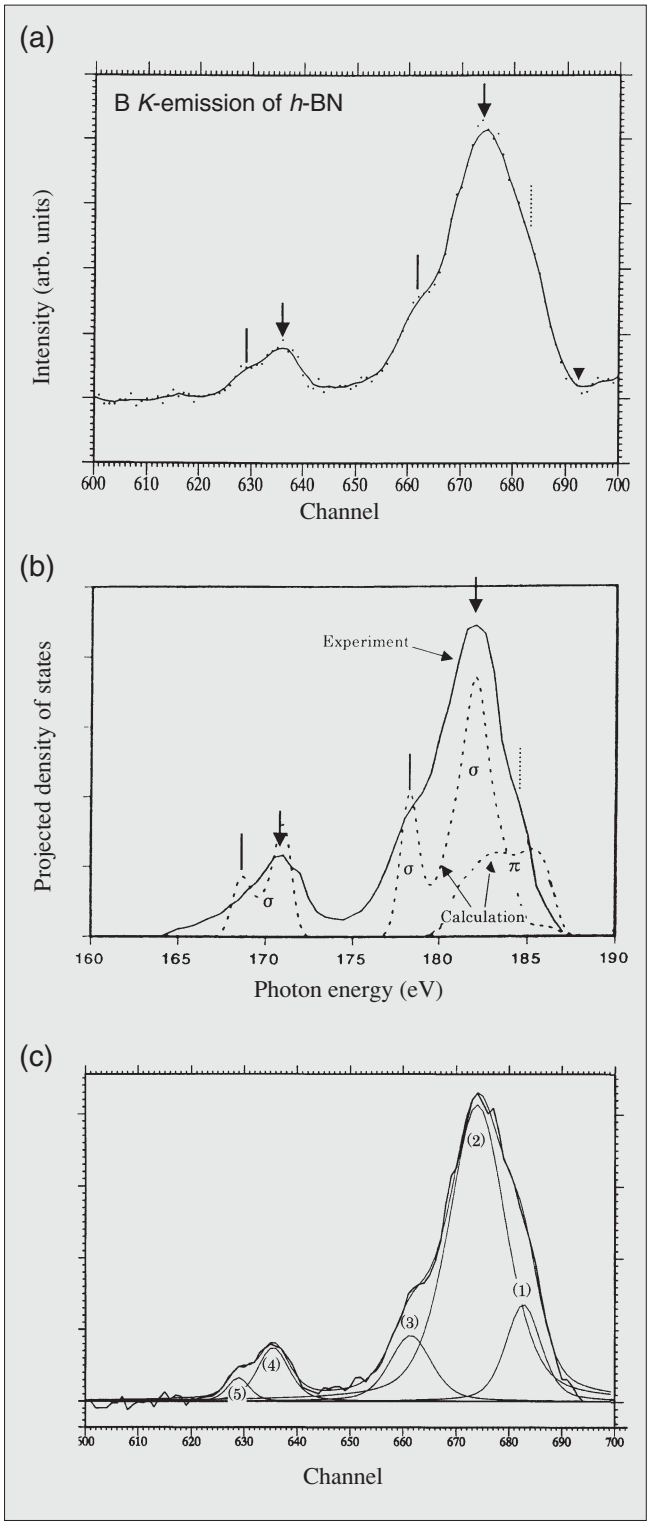

References

[a] E. Tegeler, N. Kosuch, G. Wiech and A. Faessler: *Phys. Stat. Sol. (b)*, **91** (1979) 223.

[b] H. Ma, S. H. Lin, R. W. Carpenter, P. Rice and O. F. Sankey: *J. Appl. Phys.*, **73** (1993) 7422.

β-boron

Silicon

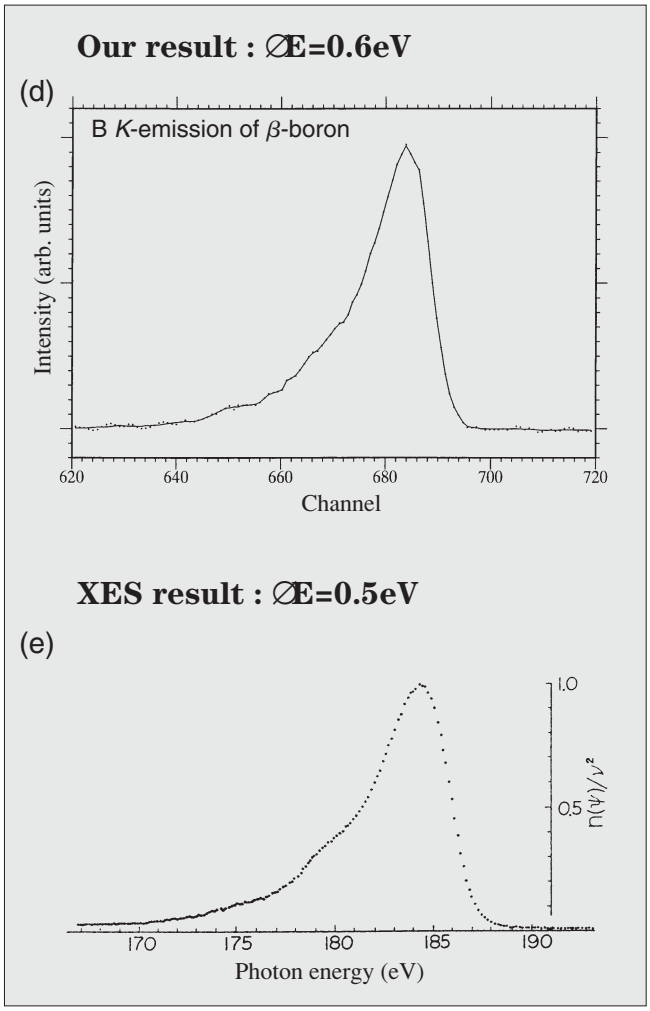

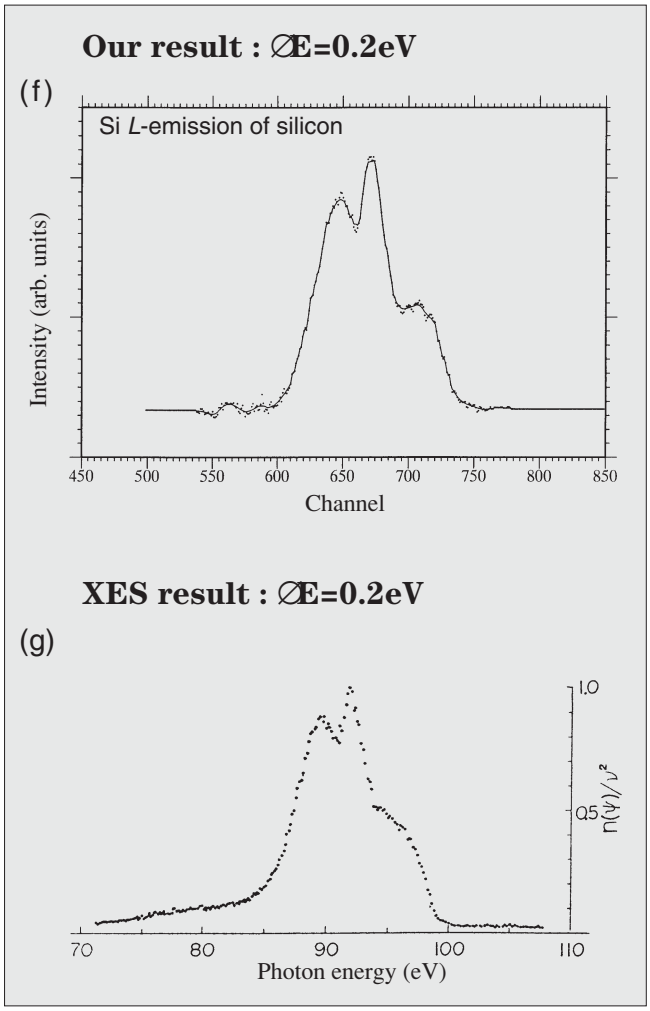

Figures (d) and (f) respectively show a *K*-emission spectrum of β-boron and an *L*-emission spectrum of silicon obtained by using our soft-X-ray spectrometer attached to a JEM-2000FX. Both the spectra were taken from specimen areas of about 600nm in diameter. Probe currents were 53nA for (d) and 66nA for (f). The acquisition times of the spectra were 2 hours [a].

Figures (e) and (g) show earlier data of a *K*-emission spectrum of β-boron and an *L*-emission spectrum of silicon, respectively. The spectra were obtained by illuminating specimen areas of about 1cm in size with an electron beam with a beam current of 5μA using a Rowland-mount spectrometer and a serial-detection system [b].

It should be noted that spectra similar to the XES spectra, which were taken by an earlier instrument [b] from specimens of about 1cm in size with an acquisition time of several days, have recently been obtained by a modern TEM from specimen areas of about 600nm in diameter at an acquisition time of 2 hours [a]. This progress has been achieved by a combination of a TEM, which incorporates an illumination-lens system capable of producing a small electron beam with a high current density, and the present soft-X-ray spectrometer equipped with a parallel-detection system using a CCD.

References

[a] H. Yamamoto, M. Terauchi and M. Tanaka: *Meeting Abstracts of the Phys. Soc. Jpn.*, **56** (2001) 684.

[b] O. Aita and T. Sagawa: *J. Phys. Soc. Jpn.*, **27** (1969) 164.

Atlas of CBED Symmetries

CBED, based fully upon dynamical diffraction, can distinguish polar crystals from nonpolar crystals, thus allowing the unique identification of all point groups by inspecting the symmetries appearing in CBED disks [a], [33]. The two-dimensional symmetry elements of 1, 2, 3, 4, 6 and m exhibit their symmetries in CBED patterns taken at the electron incidence parallel to the symmetry elements. The three-dimensional symmetries of 2', m', i and $\bar{4}$, which are illustrated in the right figure, appear in an excited dark-field disk or a set of excited dark-field disks.

Furthermore, CBED enables us to reveal the presence of 2_1-screw axes and glide planes through a conspicuous dynamical diffraction effect. When a crystal has these axes or planes, special extinction lines appear in kinematically forbidden reflections, the lines being called dynamical extinction lines.

Here, we present, as the atlas of CBED symmetries, the symmetries of zone-axis patterns, dark-field patterns and the dynamical extinction lines obtained by computer simulations. To display clear symmetries, a little unfamiliar materials were used as specimens in some cases.

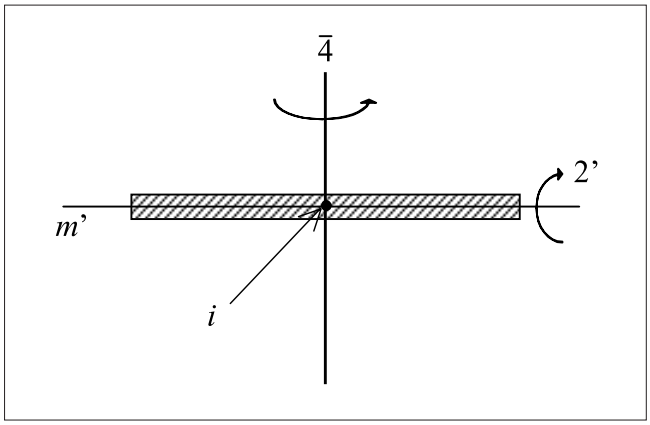

Symmetry elements 2', m', i and $\bar{4}$ of an infinitely extended parallel-sided specimen.

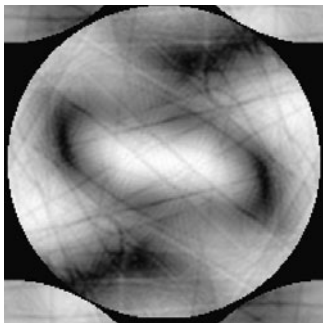
2

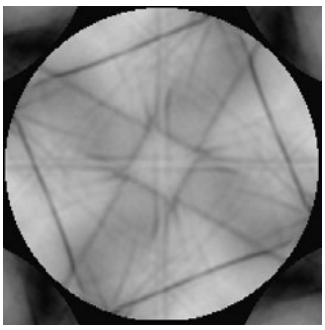
4

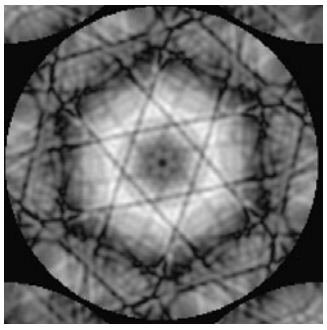
6

Reference

[a] B. F. Buxton, J. A. Eades, J. W. Steeds and G. M. Rackham: *Phil. Trans. R. Soc. London*, **281** (1976) 171.

Symmetries of Bright-Field and Whole Patterns

Simulations of the symmetries of zone-axis patterns (bright-field and whole patterns) of 1, 2, 3, 4, 6, m, $2mm$, $3m$, $4mm$ and $6mm$ are presented. The specimen name, space group, lattice parameters, crystal orientation and accelerating voltage are given at each simulated pattern.

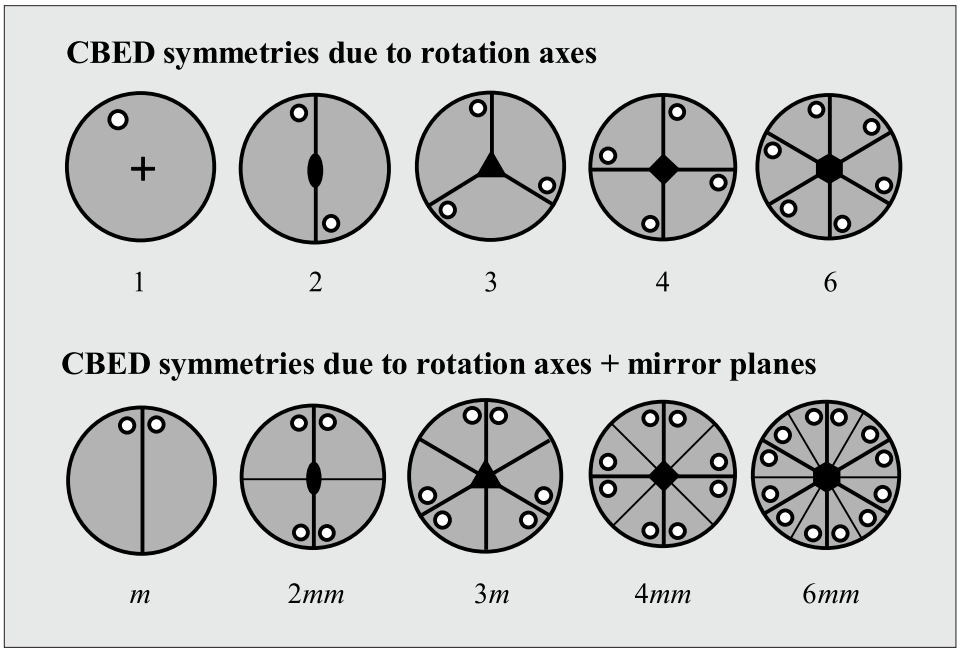

CBED symmetries due to rotation axes and mirror planes.

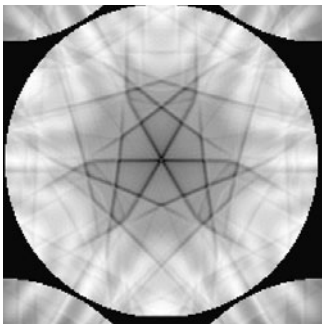

$3m$

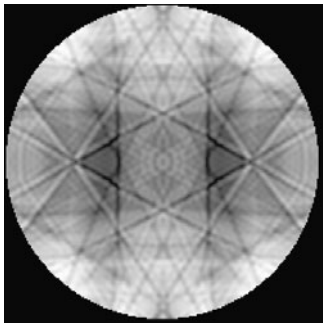

$2mm$

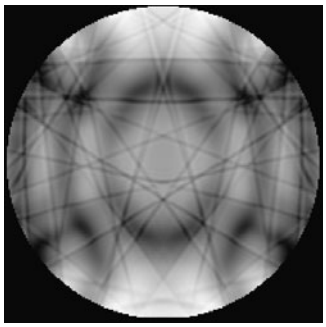

m

Symmetry 1

Ti_5O_9 [001] *Cm* **100kV**

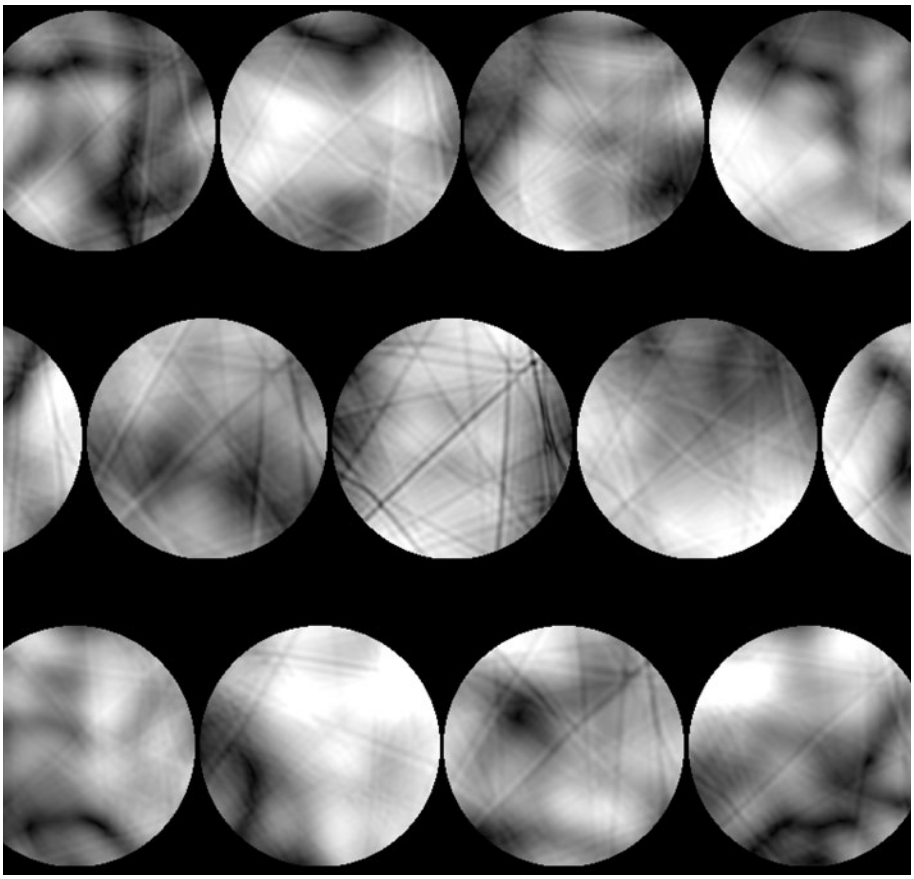

a = 0.557nm, *b* = 0.712nm, *c* = 0.887nm, α = 97.3°, β = 112.2°, γ = 108.3°.

	2D (projection)		3D	
	BP	WP	BP	WP
Symmetry	2	1	1	1

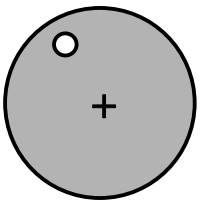

WP symmetry 1

Symmetry 2

MoO_2 [010] $P2_1$ **40kV**

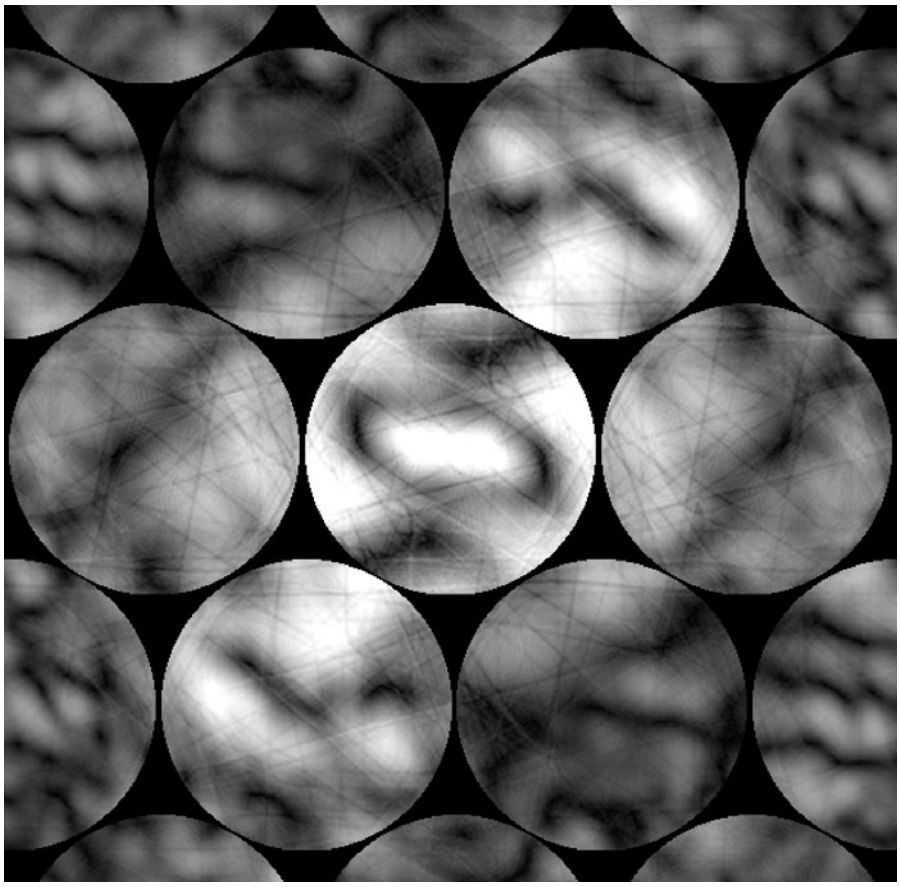

a = 0.558nm, b = 0.484nm, c = 0.561nm, α = 90°, β = 120.6°, γ=90°.

	2D (projection)		3D	
	BP	WP	BP	WP
Symmetry	2	2	2	2

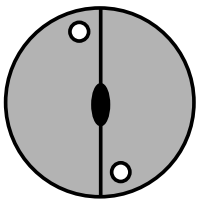

WP symmetry 2

Symmetry 3

B_2O_3 [0001] $P3_1$ **60kV**

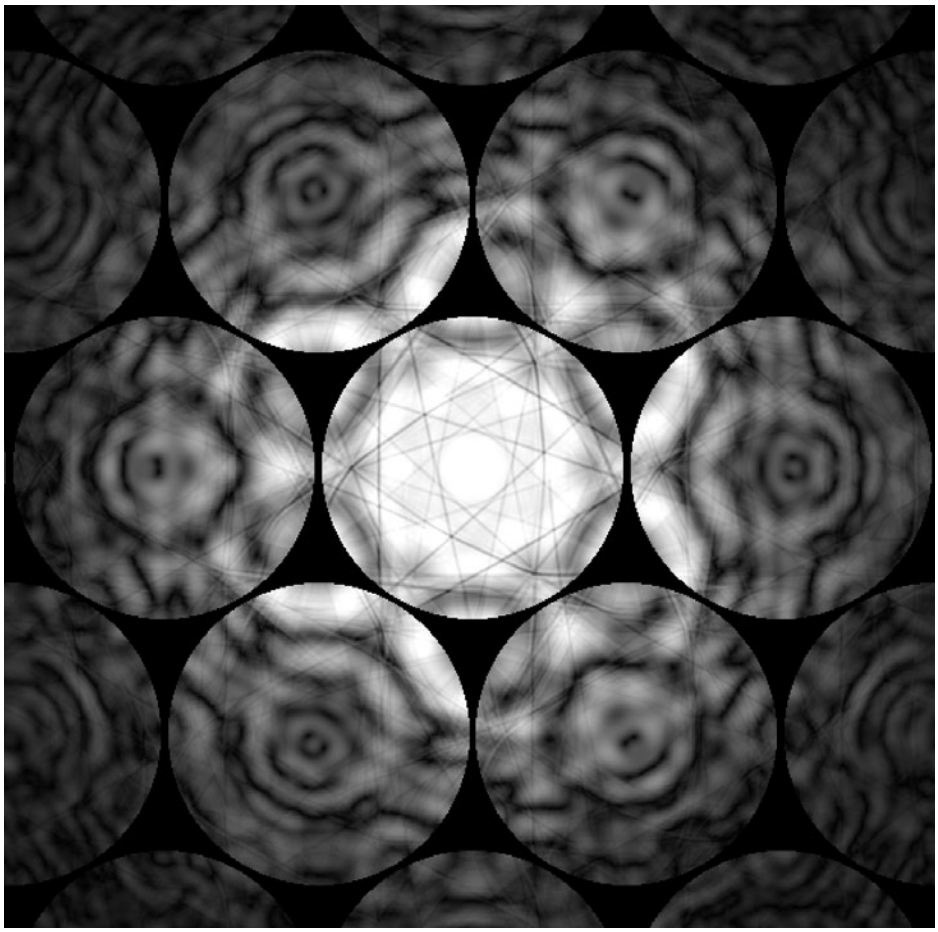

$a = b = 0.433$nm, $c = 0.832$nm, $\alpha = \beta = 90°$, $\gamma = 120°$.

	2D (projection)		3D	
	BP	WP	BP	WP
Symmetry	6	3	3	3

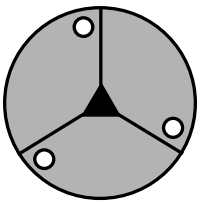

WP symmetry 3

Symmetry 4

Ti_5Te_4 [001] *I4/m* **40kV**

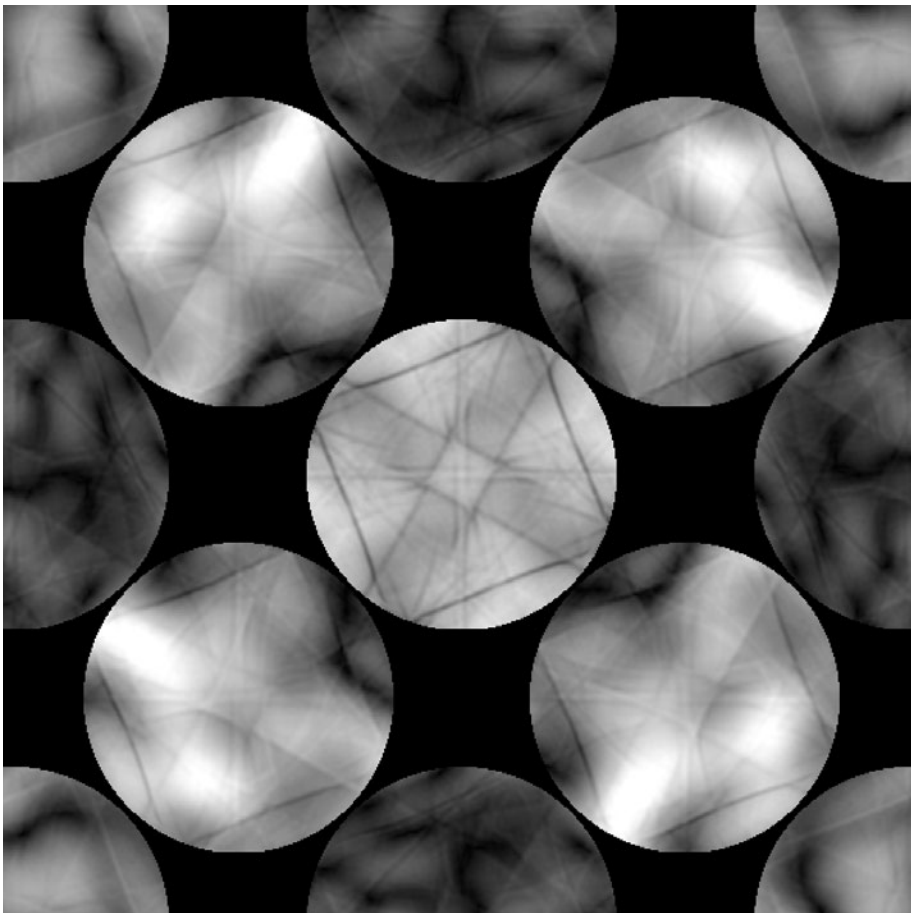

a = *b* = 1.016nm, *c* = 0.377nm, $\alpha = \beta = \gamma = 90°$.

	2D (projection)		3D	
	BP	WP	BP	WP
Symmetry	4	4	4	4

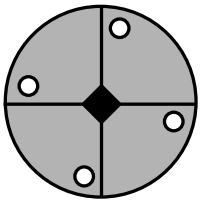

WP symmetry 4

Symmetry 6

PI_3 [0001] $P6_3$ **80kV**

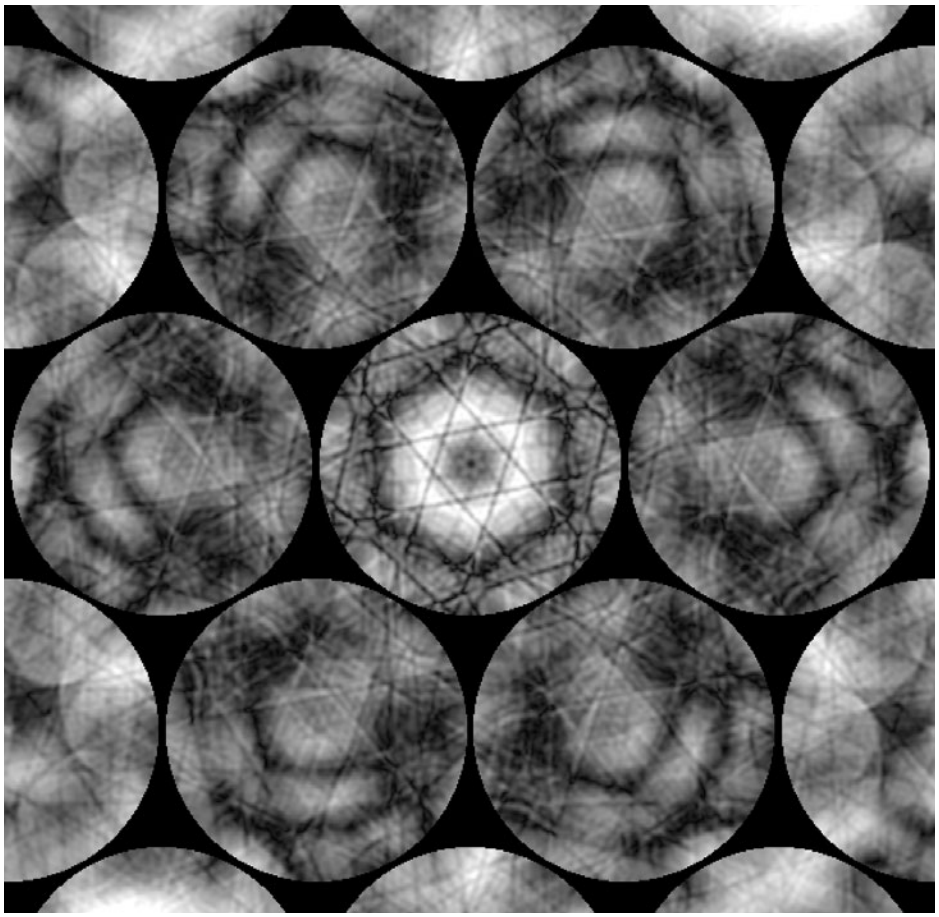

$a = b = 0.711$nm, $c = 0.727$nm, $\alpha = \beta = 90°$, $\gamma = 120°$.

	2D (projection)		3D	
	BP	WP	BP	WP
Symmetry	6	6	6	6

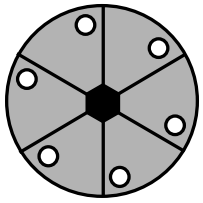

WP symmetry 6

Symmetry *m*

KNO_2 [100] *Cm* **100kV**

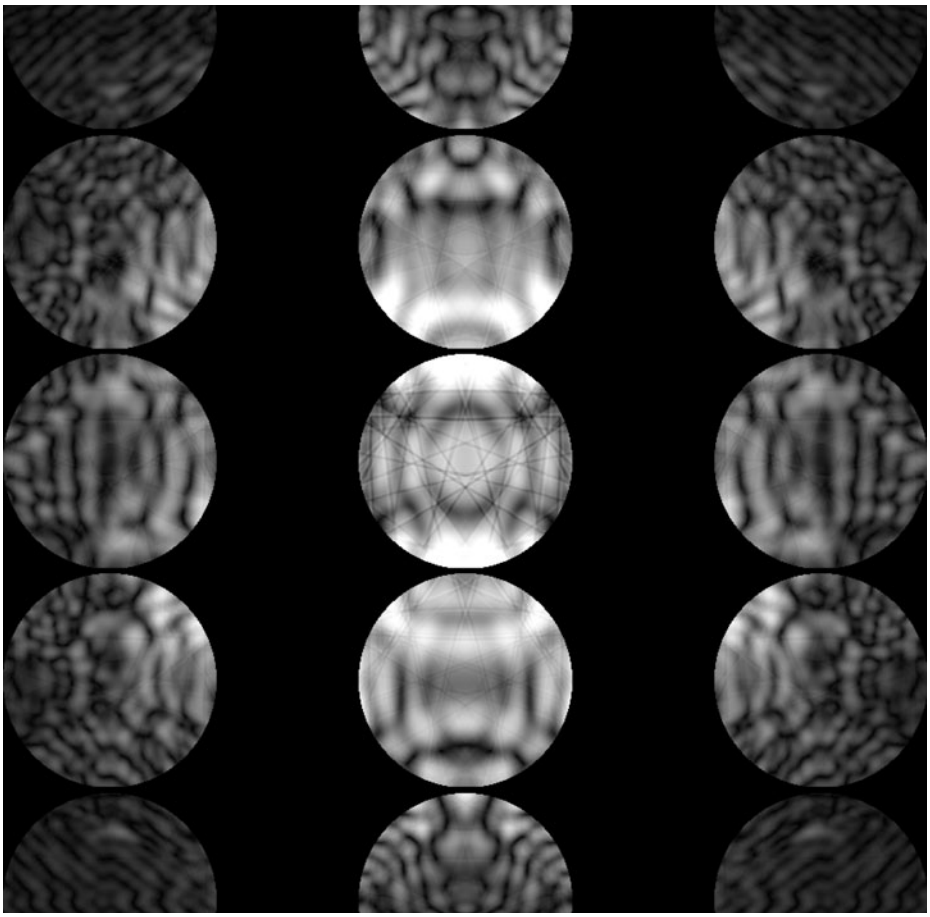

a = 0.731nm, *b* = 0.499nm, *c* = 0.445nm, $\alpha = \gamma = 90°$, $\beta = 114.8°$.

	2D (projection)		3D	
	BP	WP	BP	WP
Symmetry	2*mm*	*m*	*m*	*m*

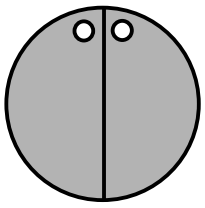

WP symmetry *m*

Symmetry 2*mm*

Ti_2CaO_4 [001] *Cmcm* **80kV**

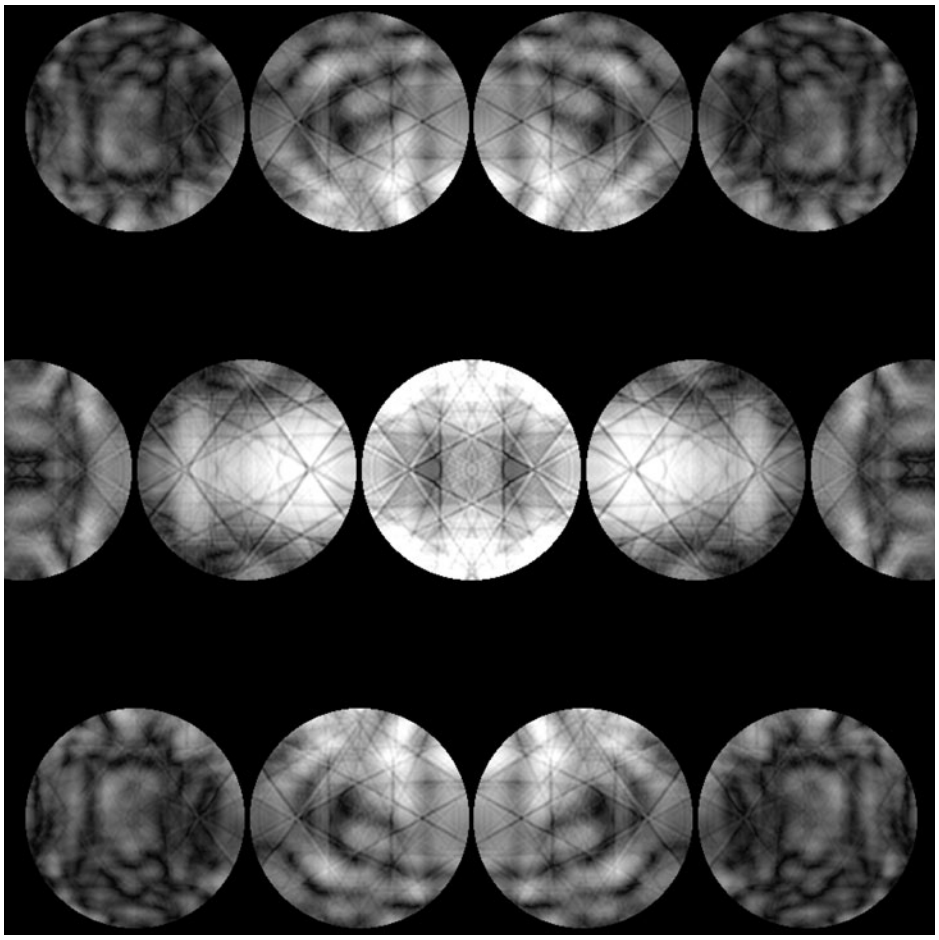

a = 0.314nm, b = 0.973nm, c = 0.998nm, $\alpha = \beta = \gamma = 90°$.

	2D (projection)		3D	
	BP	WP	BP	WP
Symmetry	2*mm*	2*mm*	2*mm*	2*mm*

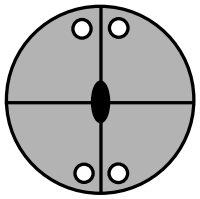

WP symmetry 2*mm*

Symmetry $3m$

InAs [111] $F\bar{4}3m$ **100kV**

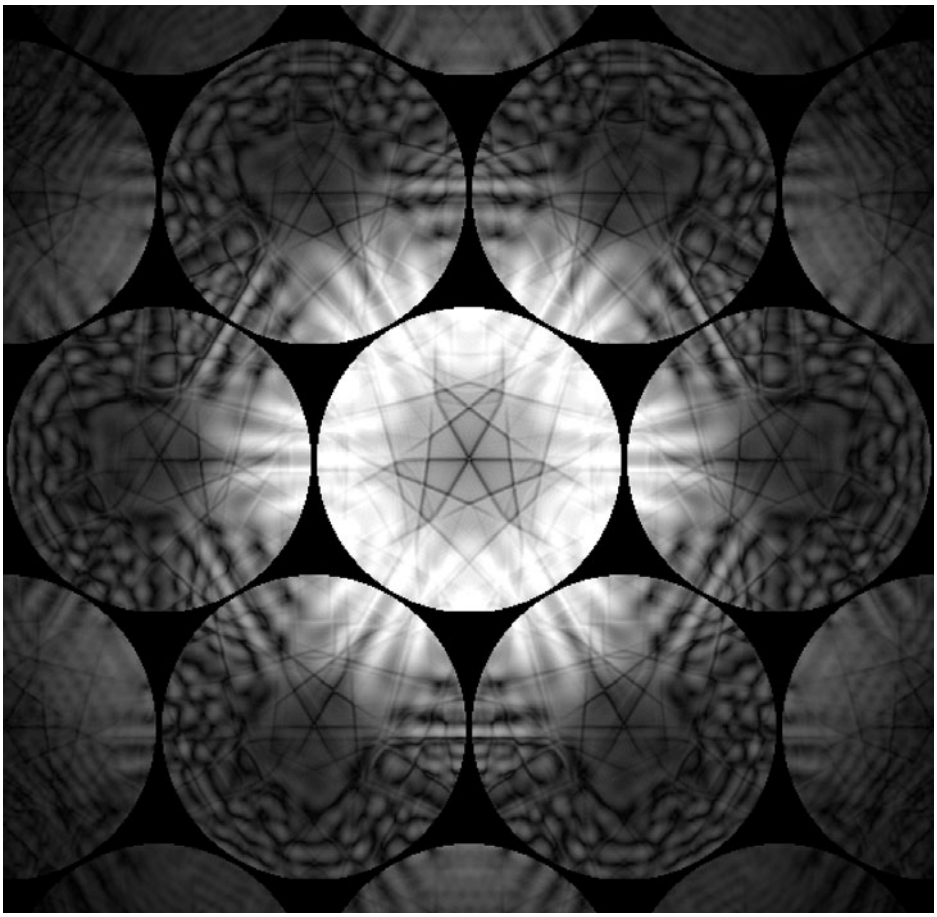

$a = b = c = 0.604$nm, $\alpha = \beta = \gamma = 90°$.

	2D (projection)		3D	
	BP	WP	BP	WP
Symmetry	$6mm$	$3m$	$3m$	$3m$

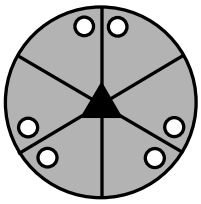

WP symmetry $3m$

Symmetry 4*mm*

Ge [001] $Fd\bar{3}m$ **60kV**

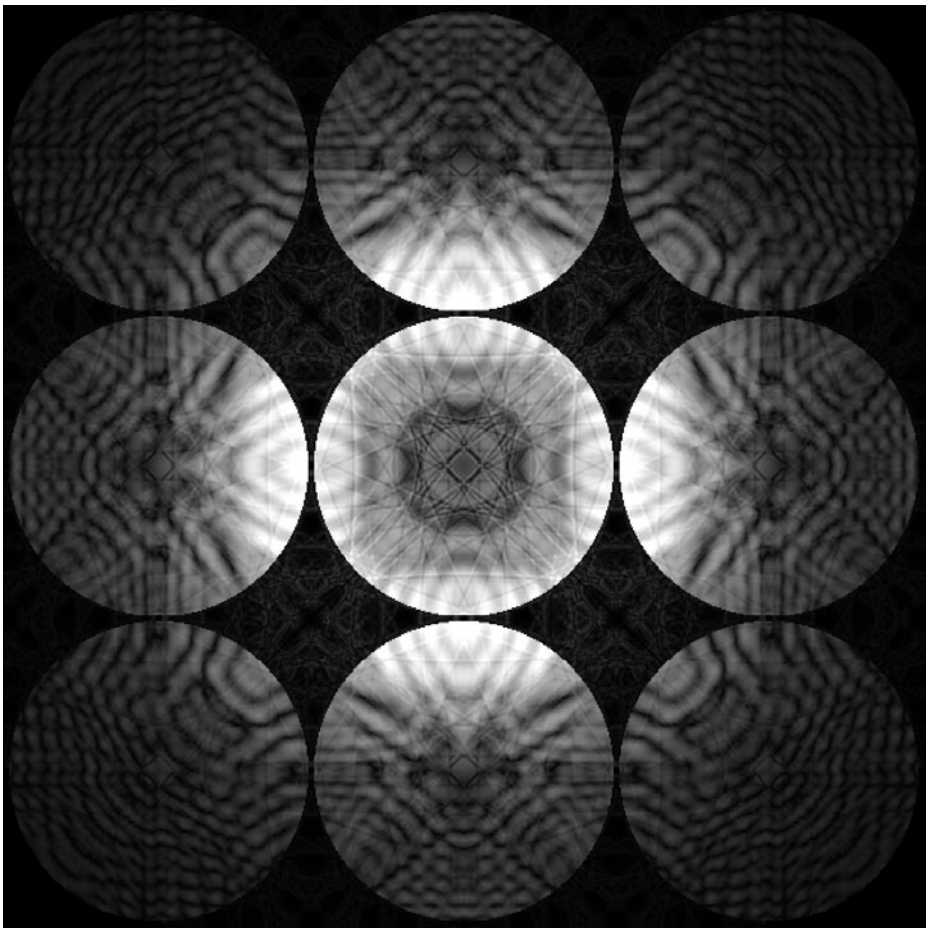

$a = b = c = 0.566$nm, $\alpha = \beta = \gamma = 90°$.

	2D (projection)		3D	
	BP	WP	BP	WP
Symmetry	4*mm*	4*mm*	4*mm*	4*mm*

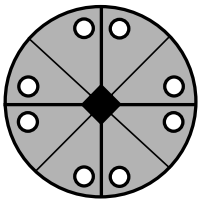

WP symmetry 4*mm*

Symmetry 6*mm*

Graphite [0001] $P6_3/mmc$ **80kV**

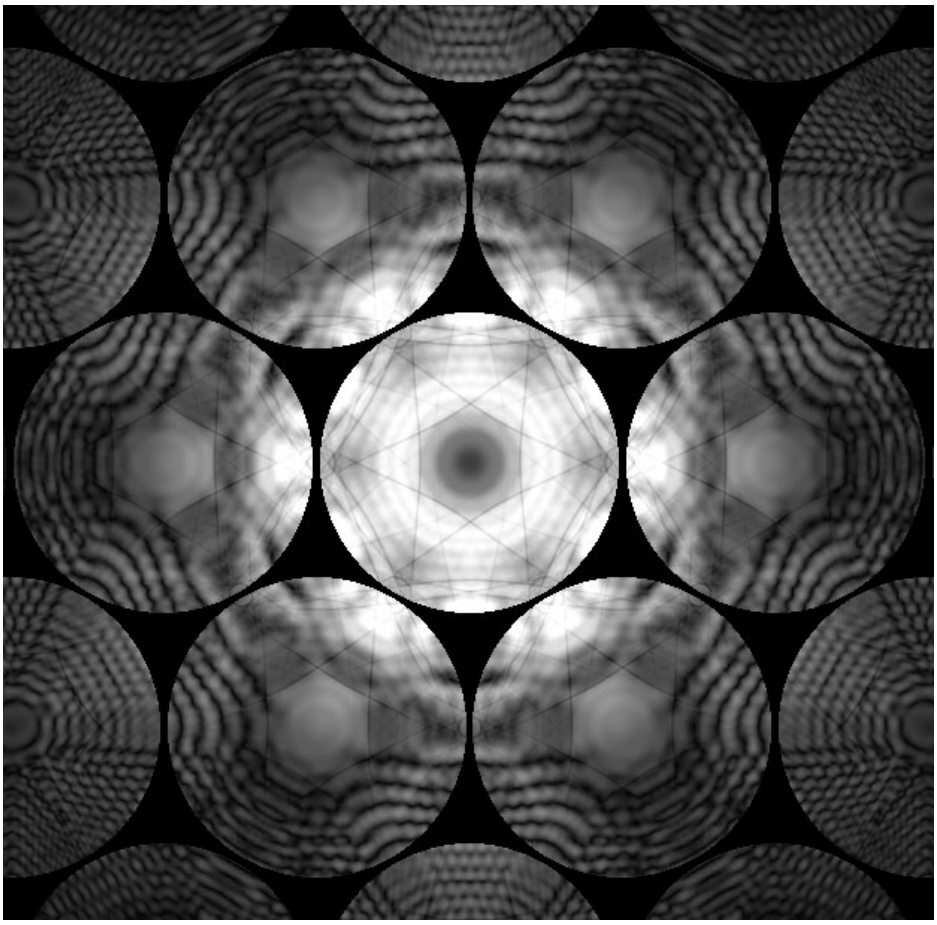

$a = b = 0.246$nm, $c = 0.670$nm, $\alpha = \beta = 90°$, $\gamma = 120°$.

	2D (projection)		3D	
	BP	WP	BP	WP
Symmetry	6*mm*	6*mm*	6*mm*	6*mm*

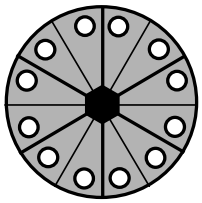

WP symmetry 6*mm*

Symmetries of Dark-Field Patterns

The schematic patterns of the three-dimensional symmetries of 1_R, m_2, 2_R and 4_R appearing in CBED patterns are shown in the figures from (a) to (d), respectively. The derivation of the patterns of 1_R, m_2 and 2_R is given on the following two pages. Simulations of each symmetry are presented with the specimen name, space group, lattice parameters, crystal orientation and accelerating voltage.

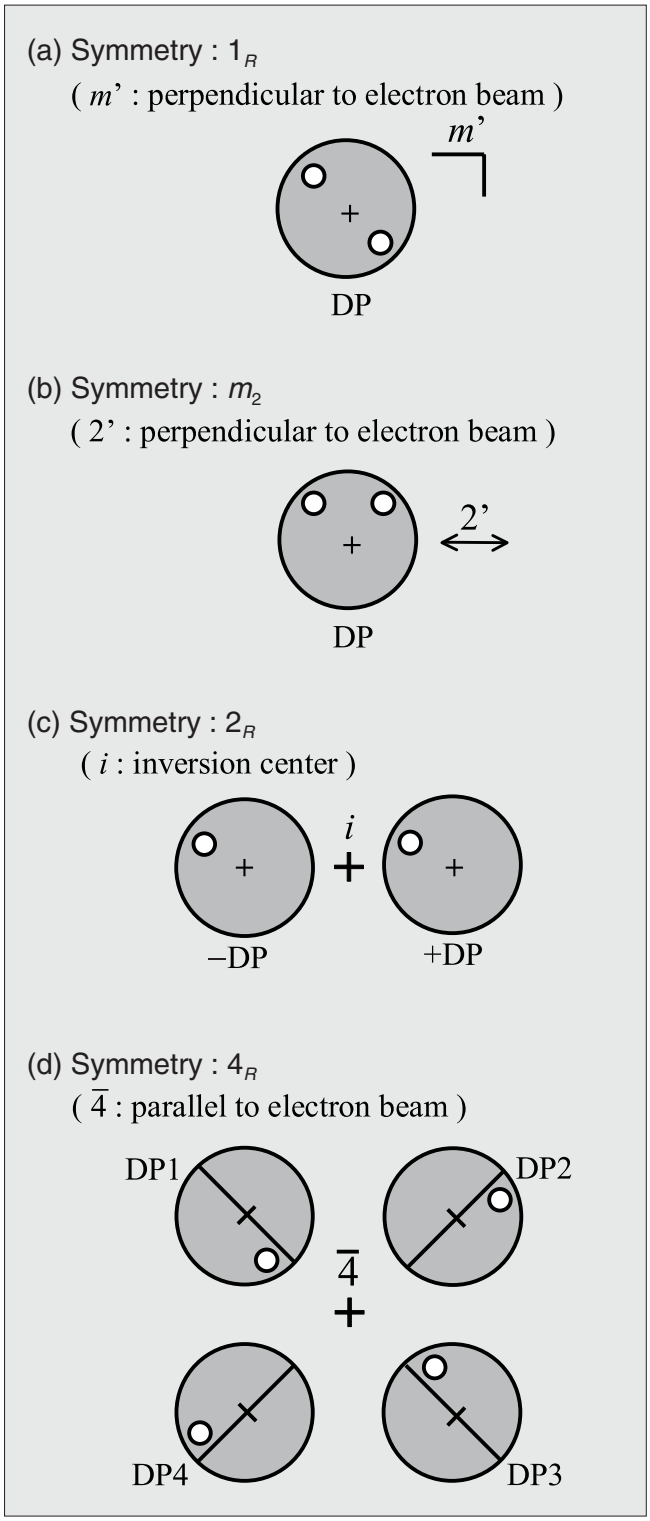

Derivation of patterns of 1_R, m_2 and 2_R

The derivation of the pattern of dark-field symmetry 1_R due to the mirror symmetry m' perpendicular to the electron beam is shown in Fig. (a). The left figure (1) shows a convergent incident-beam onto a specimen, a transmitted-beam disk (O) and an exactly excited diffracted-beam disk (DP). An incident electron beam, whose direction is designated by a cross x, transmits the specimen and comes to the open circle ○ in O. The diffracted beam comes to the direction indicated by the filled circle ● in DP. The middle figure (2) is obtained by applying the symmetry operation m' to the incident-, transmitted- and diffracted-beams in (1) with respect to the specimen position. Then, the incident-beam comes from the underside of the specimen in (2). The transmitted- and diffracted-beams are formed at the upper side of the specimen. The right figure (3) is created by applying the reciprocity theorem (R-T) (shown in Fig. (b)) to (2). The incident convergent beam of (3) retrieves the same situation as that of (1), and the DP disks in (1) and (3) are the same excited disk. Thus, the two filled circles, which give the same intensity, are obtained in the diffraction disk as shown in the bottom figure. Therefore, the intensity distribution of the excited disk has 2-fold rotational symmetry with respect to the exact Bragg position, which we call symmetry 1_R.

(a) Symmetry 1_R

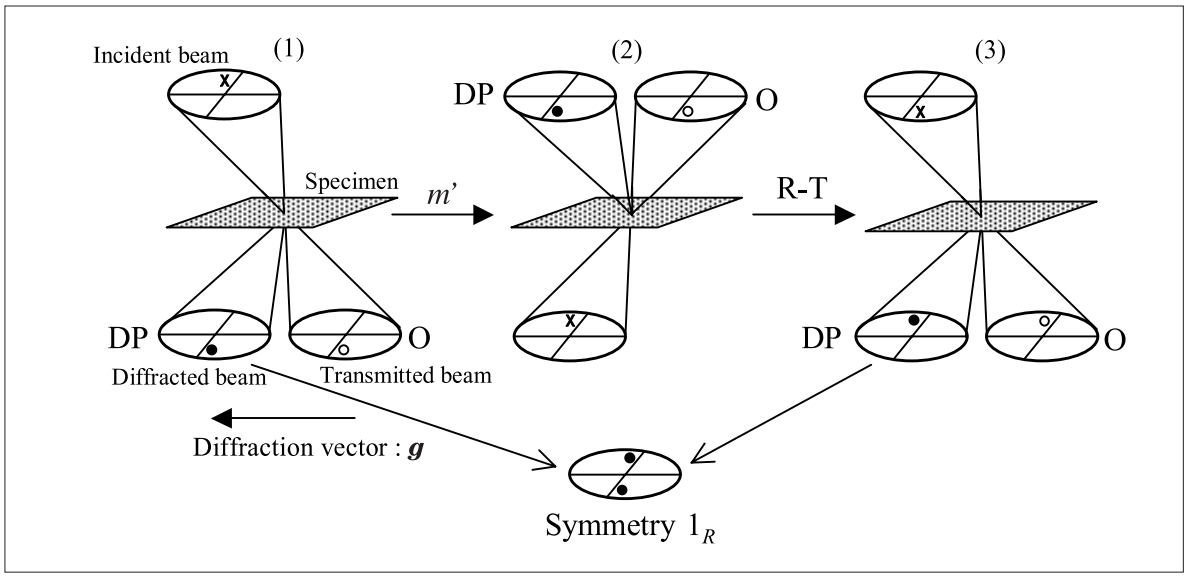

(b) Reciprocity

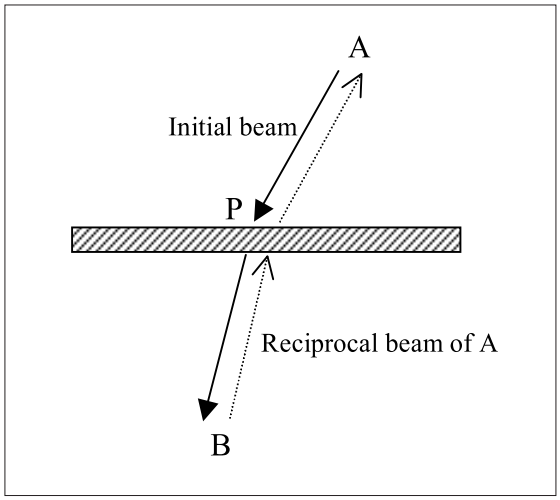

Diagram to illustrate the reciprocity in optics. The amplitude of a wave at B, which is emitted from a source at A and scattered by a specimen P, is equal to the amplitude at A, which is emitted from the same source placed at B and scattered by P.

(c) Symmetry m_2

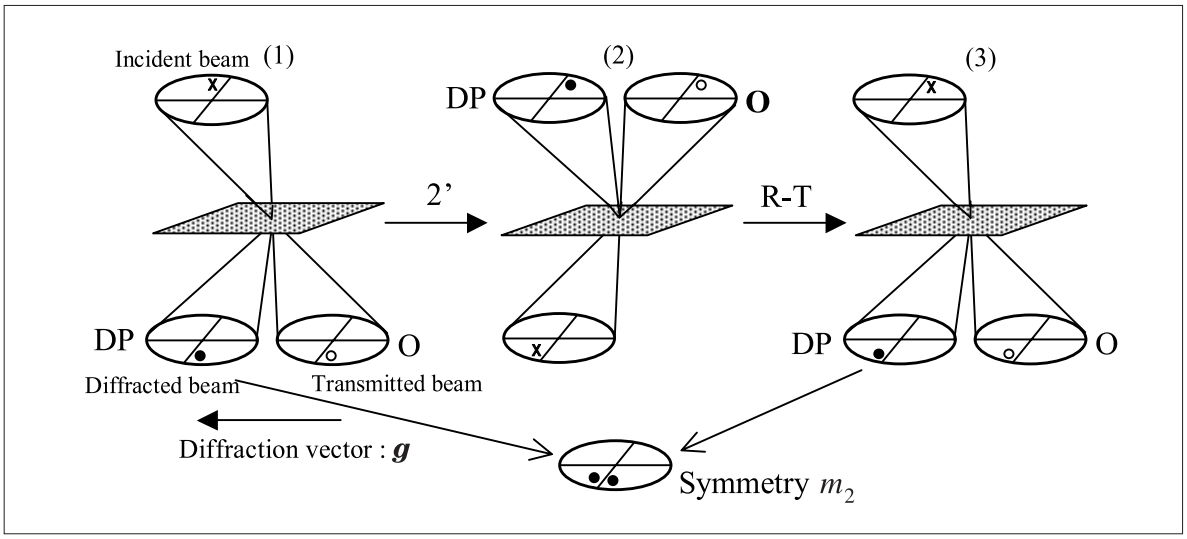

The left figure (1) shows a convergent incident beam, a transmitted-beam disk (O) and an exactly excited diffracted-beam disk (DP). The middle figure (2) is obtained by applying the symmetry operation 2' to the incident-, transmitted- and diffracted-beams in (1). The right figure (3) is created by applying the reciprocity theorem (R-T) to (2). As a result, the two filled circles, which give the same intensity, are obtained in the diffraction disk as shown in the bottom figure. Thus, the intensity distribution of the excited diffraction disk has mirror symmetry, which is perpendicular to the diffraction vector with respect to the exact Bragg position. The symmetry is called m_2.

(d) Symmetry 2_R

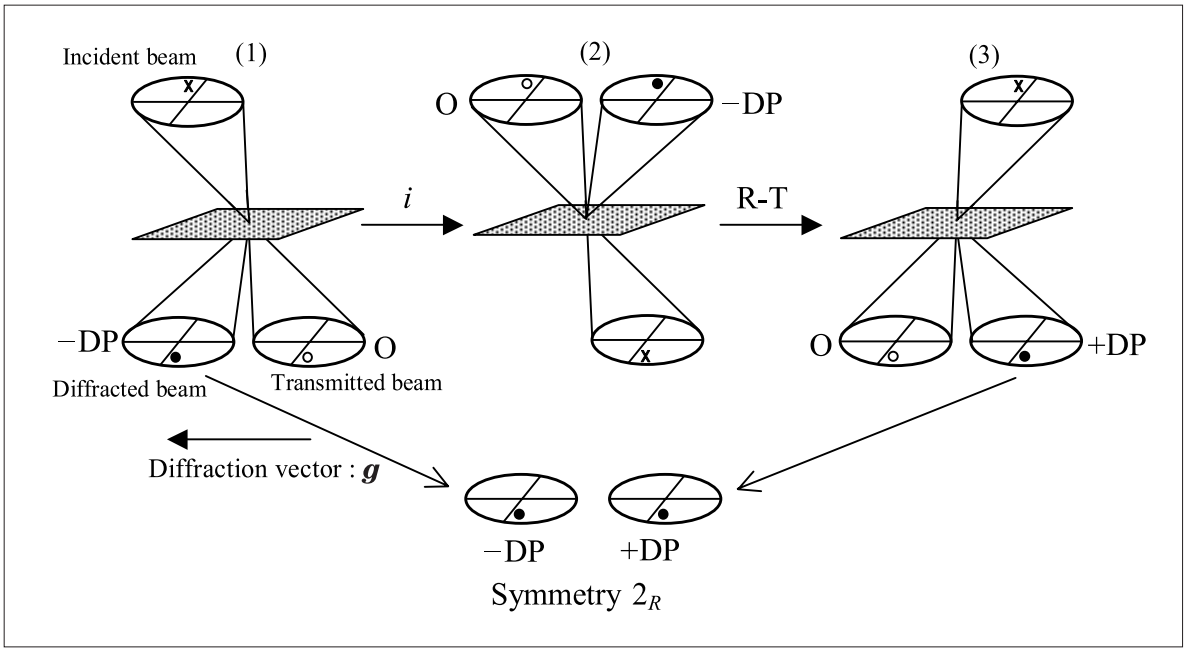

The left figure (1) shows a convergent incident beam, a transmitted beam disk (O) and an exactly excited diffracted-beam disk (−DP). The middle figure (2) is obtained by applying the symmetry operation *i* to the incident-, transmitted- and diffracted-beams in (1). The right figure (3) is created by applying the reciprocity theorem (R-T) to (2). The incident beam of (3) excites the diffraction +DP opposite to diffraction −DP of (1). As a result, the intensity of the filled circle in the diffraction disk of −DP is equivalent to that of the filled circle in the diffraction disk +DP. Thus, the intensity distributions of +DP and −DP coincide with each other through a translational operation parallel to the diffraction vector. The symmetry is called 2_R or translational symmetry.

Symmetry 1_R

KNO_2 [010] *Cm* **40kV**

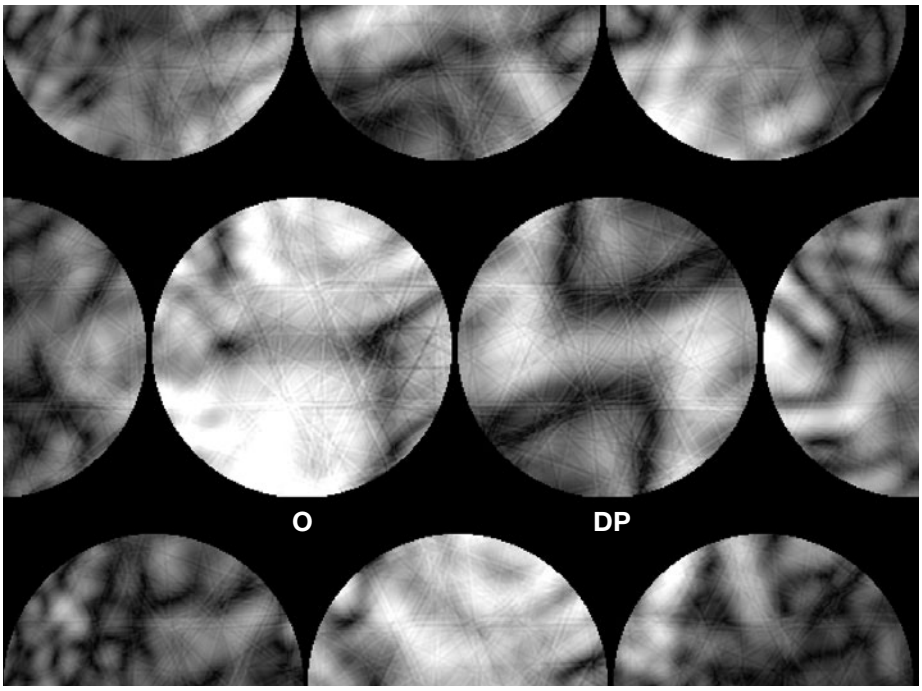

a = 0.731nm, b = 0.499nm, c = 0.445nm, $\alpha = \gamma = 90°$, β = 114.8°.

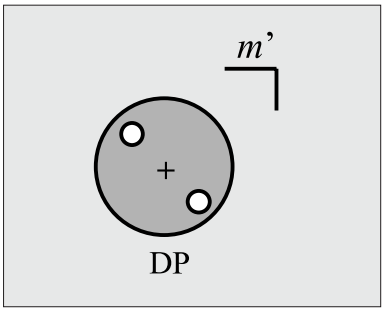

Symmetry 1_R

Symmetry m_2

Si [111] $Fd\bar{3}m$ **100kV**

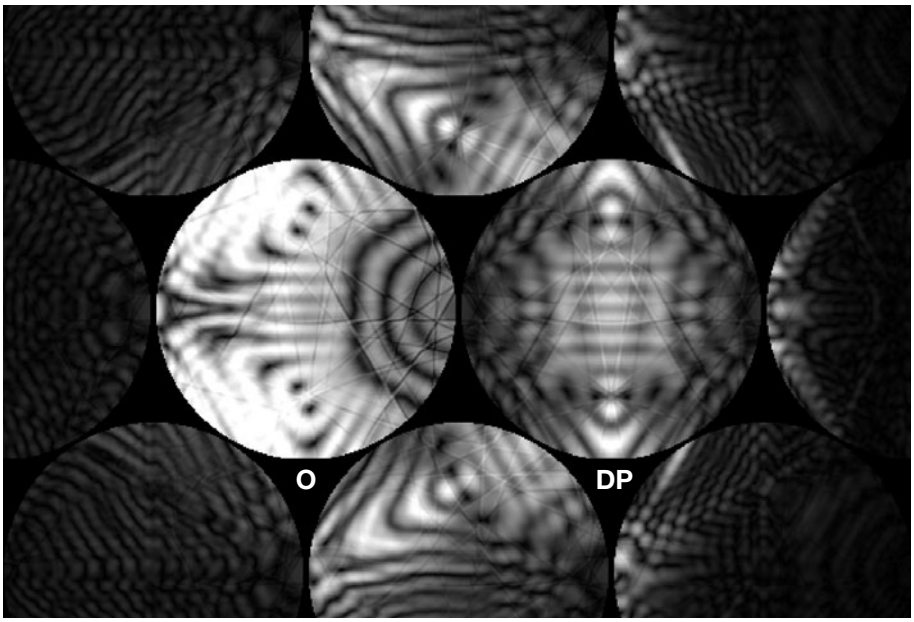

$a = b = c = 0.543$nm, $\alpha = \beta = \gamma = 90°$.

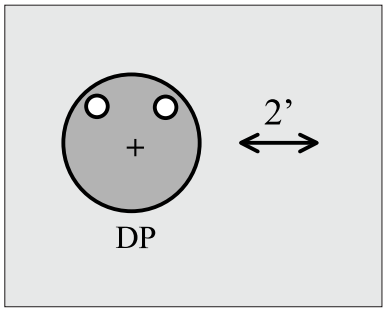

Symmetry m_2

Symmetry 2_R

Ti_5Te_4 [101] *I4/m* **120kV**

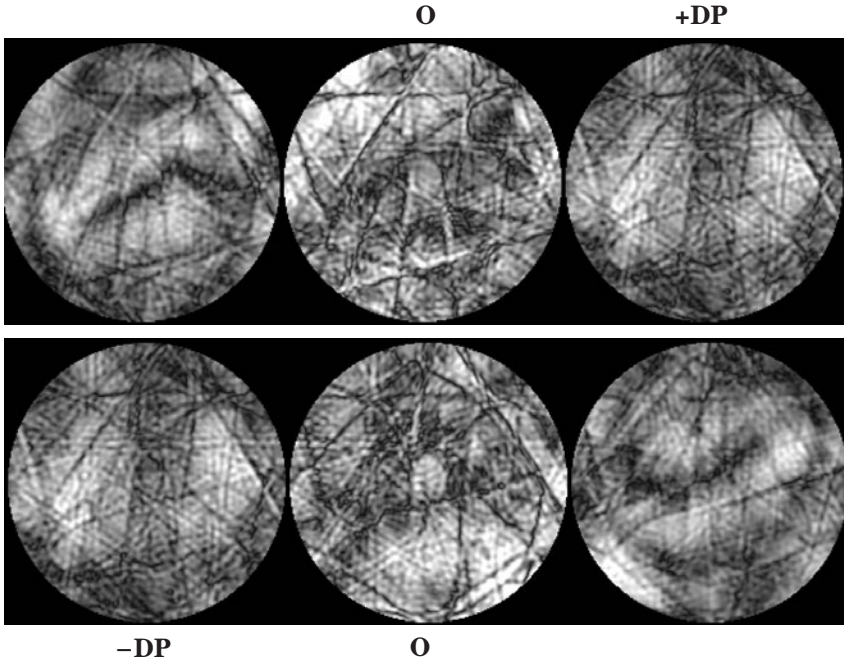

$a = b = 1.016$nm, $c = 0.377$nm, $\alpha = \beta = \gamma = 90°$.

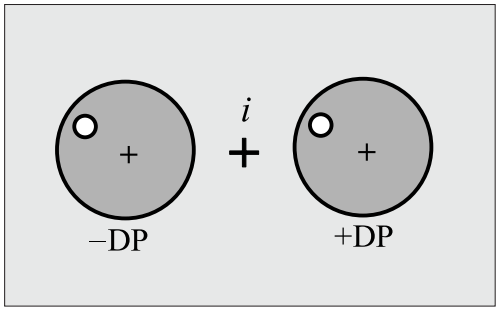

Symmetry 2_R

Symmetry 4_R

The fourfold rotoinversion or $\bar{4}$-axis is illustrated in Fig. (a). It is noted that the $\bar{4}$-axis contains a twofold rotation axis. The symmetry element causes symmetry 4_R in a set of CBED patterns as shown in Fig. (b). The cross at the center shows the direction parallel to the $\bar{4}$-axis. The four large circles represent the exactly excited diffraction disks appearing in the four different CBED patterns. The center of each disk corresponds to the exact Bragg position of the reflection. A set of the four small circles in the disks denotes the symmetry due to the $\bar{4}$-axis. This symmetry is called 4_R, which is a combination of a rotation $2\neq/4$ of a disk about the zone axis and a rotation $\neq$ of the disk with respect to the exact Bragg position.

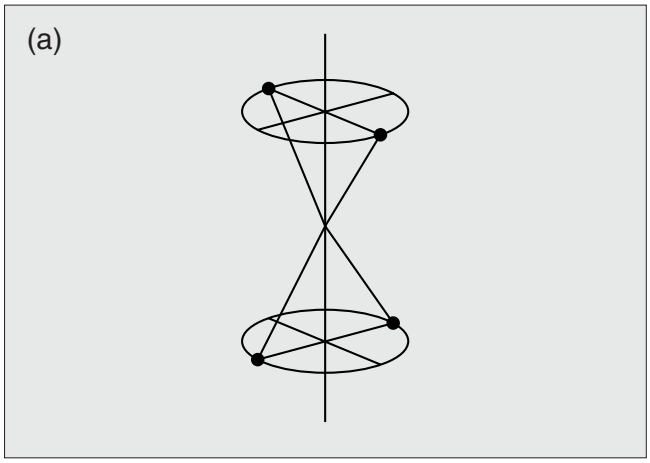

Rotoinversion symmetry $\bar{4}$

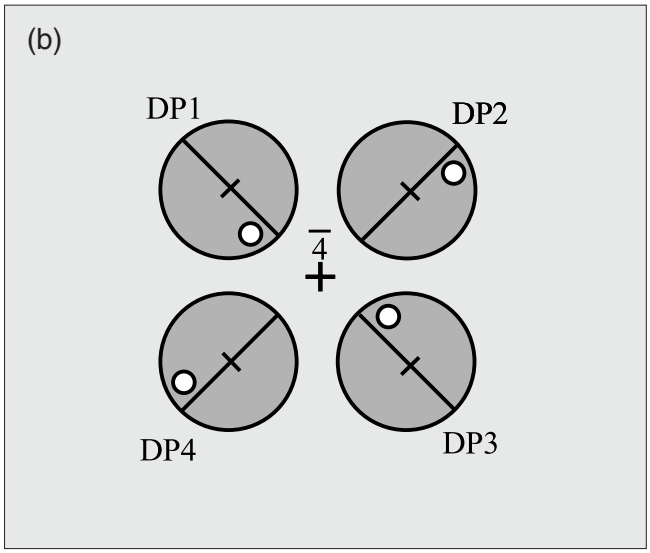

Symmetry 4_R ($\bar{4}$: parallel to electron beam)

Reference

[a] M. Tanaka, M. Terauchi and F. Sato: *Ultramicroscopy*, **55** (1994) 241.

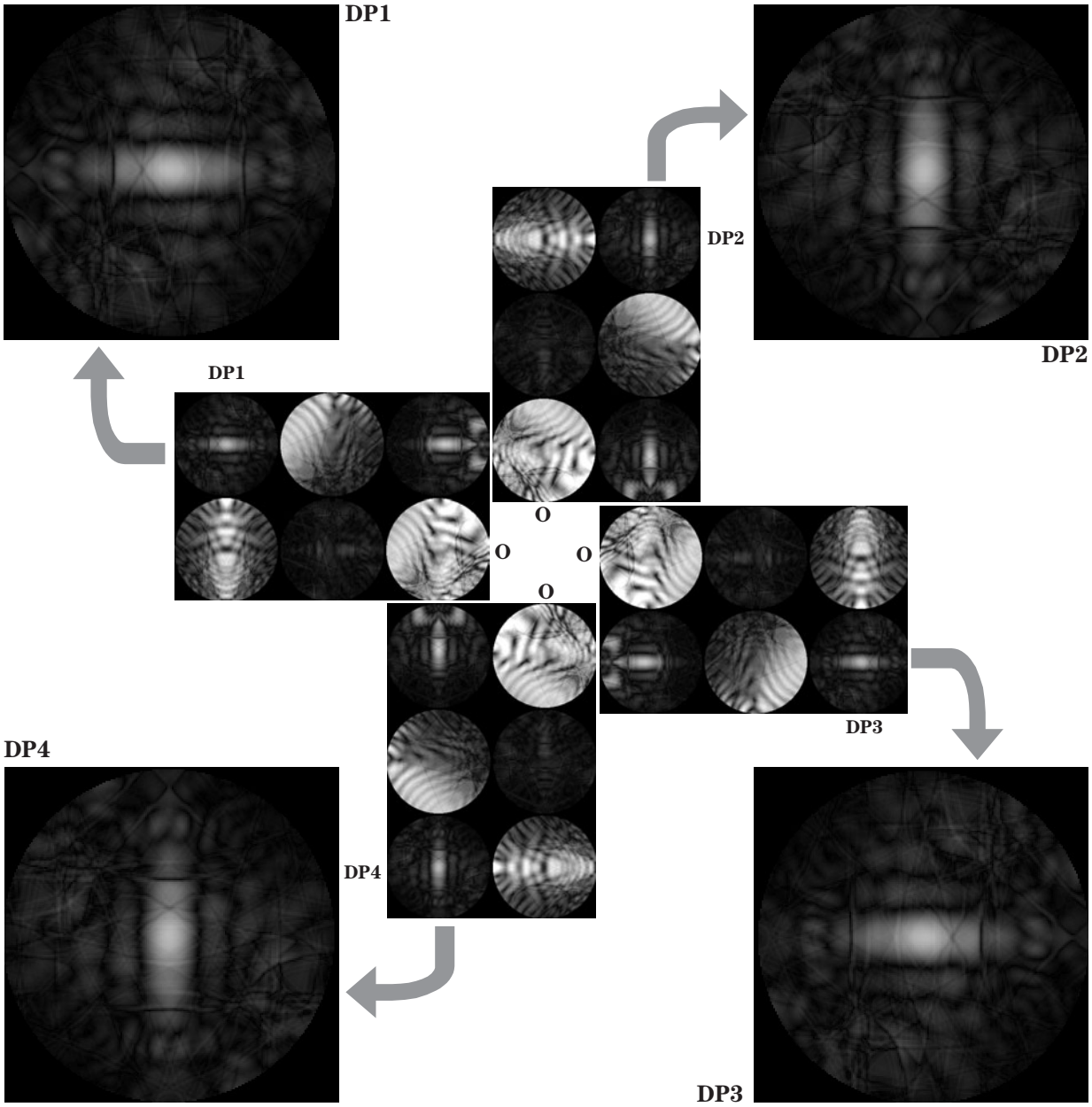

$a = b = c = 0.565$nm, $\alpha = \beta = \gamma = 90°$.

Symmetry 4_R due to a $\bar{4}$-axis of GaAs

At the central part of the figure, four CBED patterns are placed, in which the diffraction disks of DP1, DP2, DP3 and DP4 are exactly excited, respectively. Those patterns are enlarged to clarify the pattern symmetry. Symmetry 4_R is confirmed by these photos and the figures on the left-side page.

Dynamical Extinction Lines

Figures (a) and (b) illustrate the formation of dynamical extinction lines. *Umweganregung* paths a, b and c to a forbidden reflection G via zeroth- and higher-order Laue-zone reflections are shown in Figs. (a) and (b), respectively. The $h00$ (h = odd) reflections are assumed to be kinematically forbidden owing to an a-glide plane parallel to the c-axis and/or 2_1-screw axis in the a-direction.

The dynamical extinction lines parallel to the diffraction vectors are called A lines, and those perpendicular to the vectors B lines. A lines can appear even in inexactly excited diffraction disks but B lines appear only in the exactly excited disks. The suffix 2 of A and B stands for the lines formed by two-dimensional (ZOLZ) interaction. The suffix 3 stands for the lines formed by three-dimensional (HOLZ) interaction. Both the glide planes and screw axes give rise to A_2 and B_2 lines. Thus, those two space-group symmetry elements can not be distinguished by the A_2 and B_2 lines. The glide planes produce A_3 lines but the screw axes produce B_3 lines. Therefore, the two symmetry elements can be identified by observing the A_3 and B_3 lines. The glide planes parallel to the specimen surface cause the extinction of the intensity at the intersection of the A_3 and B_3 lines due to a three-dimensional (HOLZ) interaction. These results are summarized in the table below. Examples of those extinction lines are given on the following pages. Further details of the dynamical extinction are consulted by references [a], [b], [33], [41].

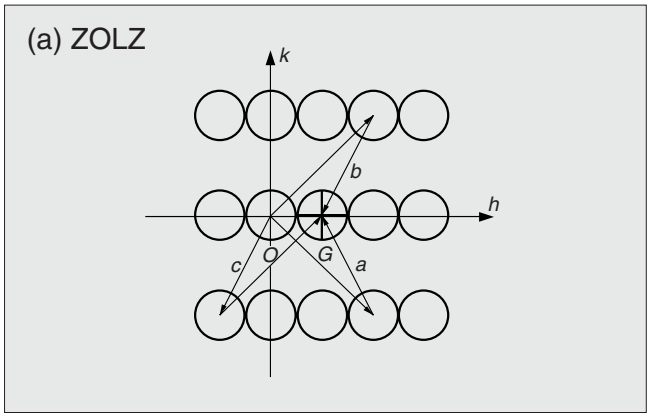

Formation of A_2 and B_2 lines due to a 2_1-screw axis and an a-glide plane.

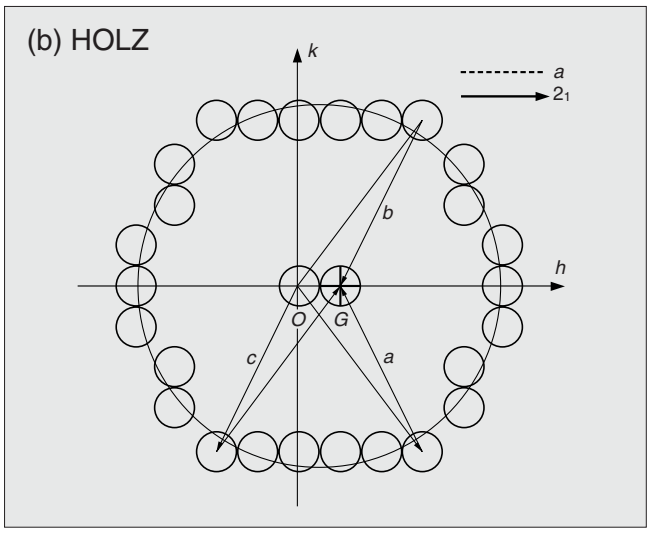

Formation of an A_3 line due to an a-glide plane and a B_3 line due to a 2_1-screw axis.

Symmetry elements of plane-parallel specimen	Orientation to specimen surface	Dynamical extinction lines	
		ZOLZ interaction	HOLZ interaction
Glide planes	Perpendicular: g	A_2 and B_2	A_3
	Parallel: g'		Intersection of A_3 and B_3
Two-fold screw axis	Perpendicular: 2_1		
	Parallel: $2_1'$	A_2 and B_2	B_3

References

[a] M. Tanaka, H. Sekii and T. Nagasawa: *Acta Cryst.*, **A39** (1983) 825.

[b] M. Tanaka, M. Terauchi and H. Sekii: *Ultramicroscopy*, **21** (1987) 245.

Dynamical extinction lines A_2, B_2, A_3 *and* B_3

FeS_2 [$\bar{1}10$] $Pa\bar{3}$ **80kV**

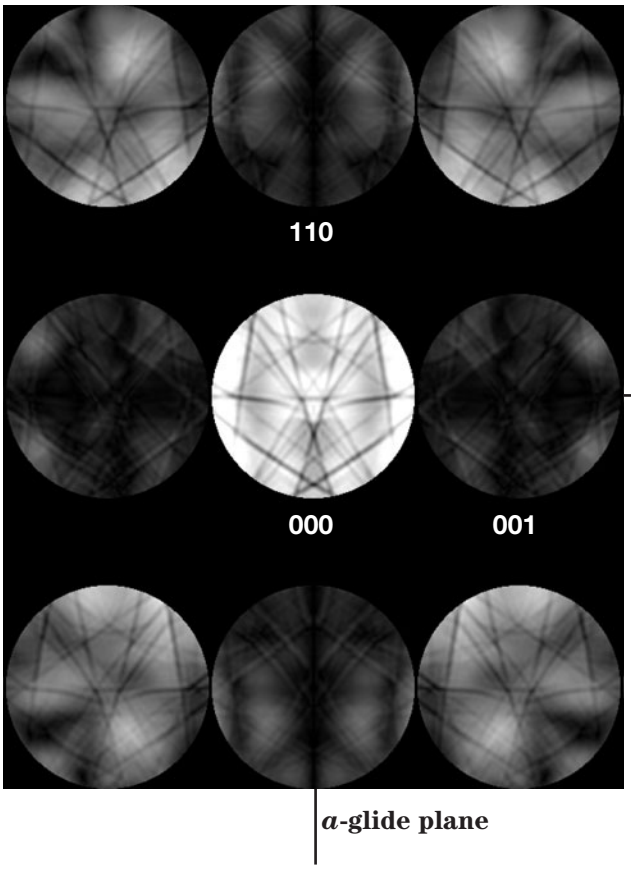

The simulated pattern (a) shows a CBED pattern of FeS_2 at the [$\bar{1}10$] zone-axis incidence. A_2 lines are seen in both the ± 001 and ± 110 disks. The A_3 (and B_3) lines cannot be seen directly due to the existence of the A_2 lines. By observing the symmetry of fine lines due to HOLZ reflections with respect to the A_2 lines, it is found that the A_3 lines are produced in the ± 110 reflections but are not produced in the ± 001 reflections. In other words, the ± 110 reflections show that the extinction is due to an *a*-glide plane, but the ± 001 reflections show that it occurs due to a 2_1-screw axis. Therefore, the *a*-glide plane exists parallel to the (001) plane and the 2_1-screw axis exists parallel to the [001] direction. It is noted that the A_2 lines in ± 001 reflections are somewhat obscured by the fine lines which do not form an A_3 line.

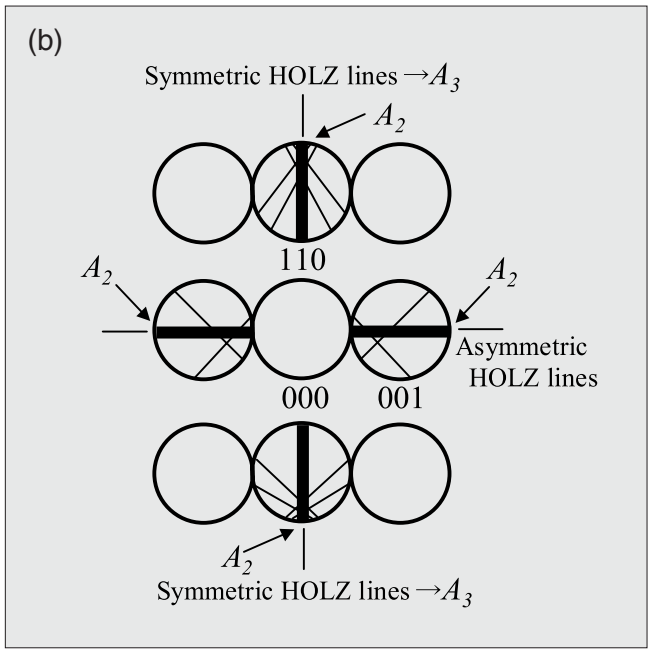

Schematic figure of A_2 and A_3 GM line symmetries in (a).

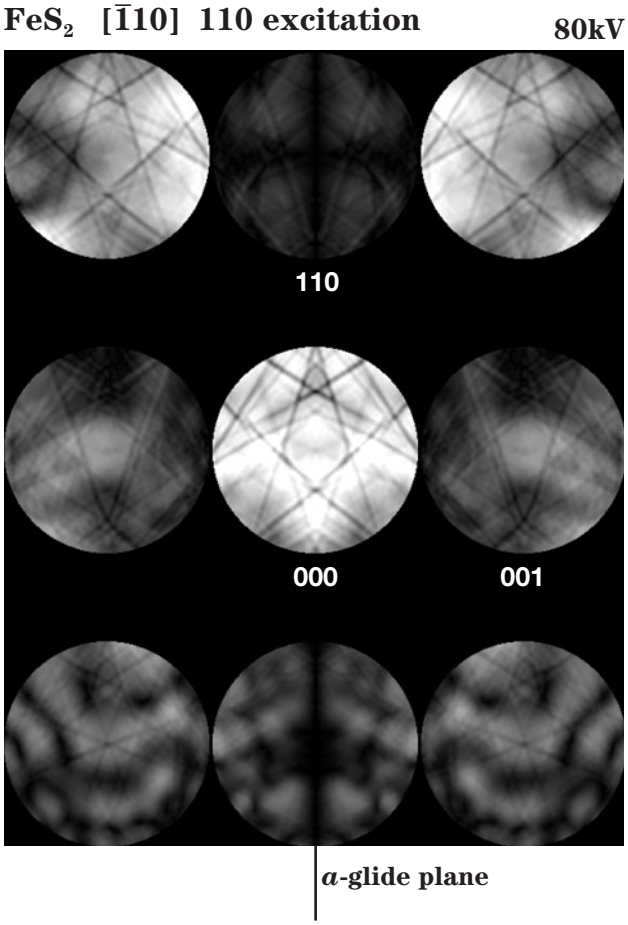

(c)

The simulated pattern (c) shows a CBED pattern of FeS_2 for the exact excitation of the 110 reflection at the [$\bar{1}$10] electron incidence. The fine HOLZ lines are symmetric with respect to the A_2 line in the 110 reflection disk but asymmetric with respect to the B_2 line. This proves that the A_3 line is produced in the 110 reflection but no B_3 line exists. These features again prove the existence of the *a*-glide plane parallel to the (001) plane.

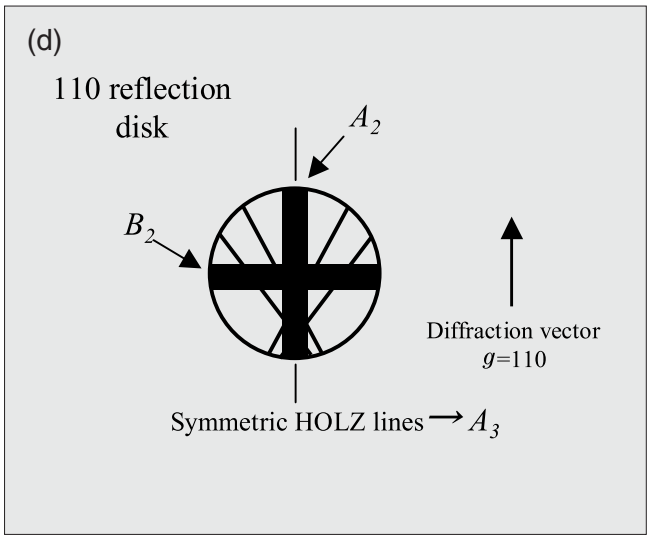

Schematic figure of A_2, A_3 and B_2 lines in the 110 reflection disk of (c).

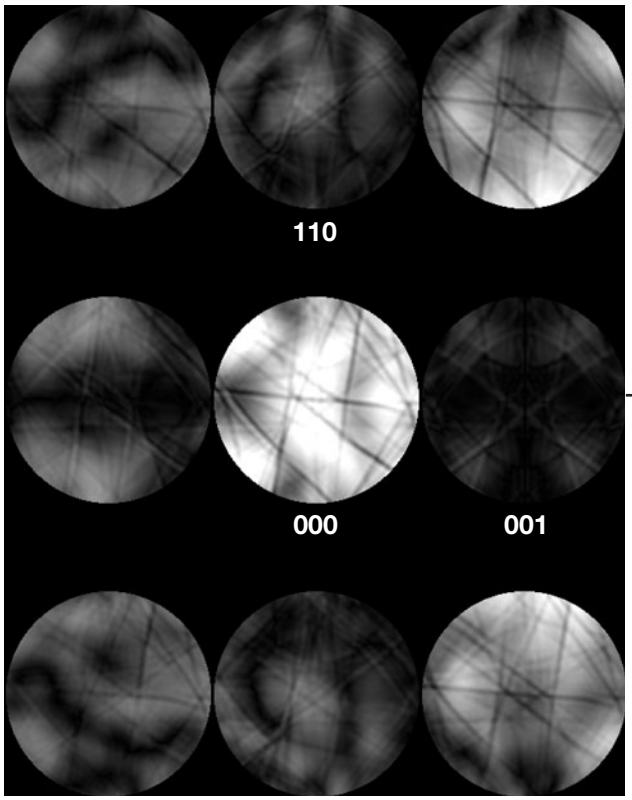

(e)

The simulated pattern (e) shows a CBED pattern of FeS_2 for the exact excitation of the 001 reflection at the $[\bar{1}10]$ electron incidence. The fine HOLZ lines are symmetric with respect to the B_2 line in the 001 reflection disk but asymmetric with respect to the A_2 line. This proves that the B_3 line is produced in the 001 reflection but no A_3 line exists. These features again prove the existence of the 2_1-screw axis parallel to the [001] direction.

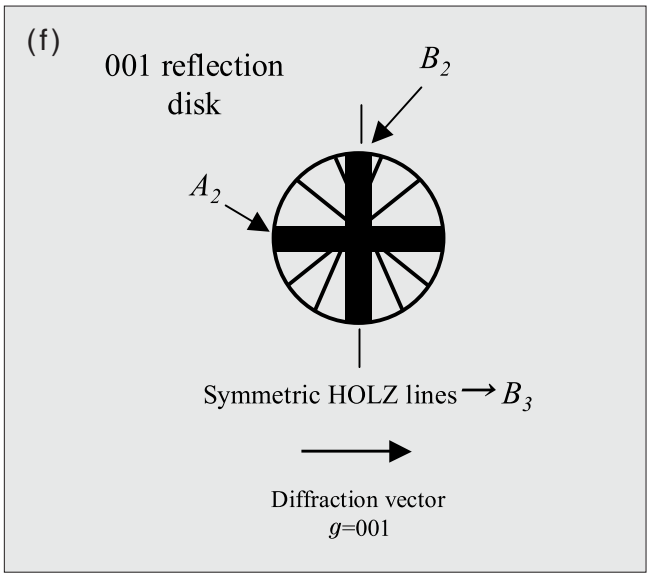

Schematic figure of A_2, B_2 and B_3 lines in the 001 reflection disk of (e).

Dynamical extinction at the intersection of A_3 and B_3

The figure shows *Umweganregung* paths to the 200 reflection via HOLZ reflections at the [001] electron incidence for silicon. The 200 reflection is assumed to be exactly excited. The projection of the Laue point L in the [001] direction is located at the center of the 000 and 200 disks. The electron beams passing through the paths A and B (solid lines), which are symmetric with respect to the point L, lose their intensity at the exact excitation position of the 200 reflection. The reason is that their phase difference is ≠ due to the *d*-glide plane perpendicular to the [001] direction. Since the beams passing through the paths A' and B' (dotted lines) also cause the extinction, an extinction line is formed by the interference of the beams passing through those two paths via HOLZ reflections H and H'. It should be noted that to observe the extinction the accelerating voltage has to be chosen so that the reflections via paths A (A') and B (B') meet at the same point in the 200 reflection disk.

A spot-shaped extinction is produced by the superposition of such extinction lines running in different directions, which meet near the exact 200 Bragg position. The simulated pattern below shows the dynamical extinction of (001) Si with the [001] incidence at an accelerating voltage of 59.3kV. It is seen that the several extinction lines form a spot-shaped extinction at the exact Bragg position. This proves the existence of the *d*-glide plane parallel to the (001) plane.

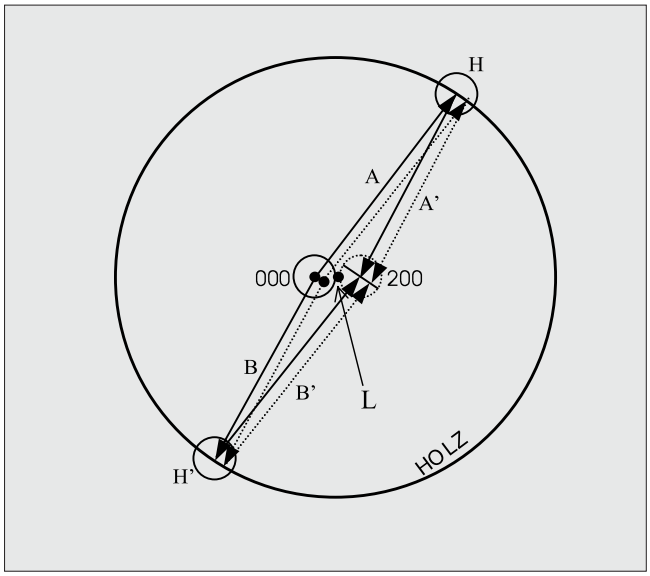

Reference

[a] M. Tanaka, M. Terauchi and H. Sekii: *Ultramicroscopy*, **21** (1987) 245.

Si [001] $Fd\bar{3}m$ 200 excitation

59.3kV

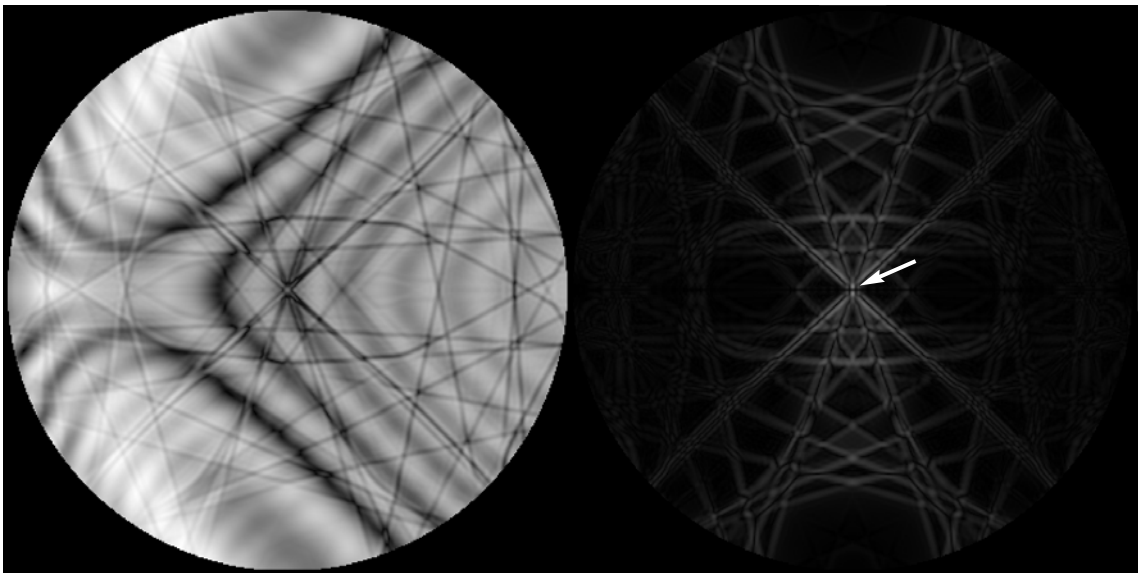

000 **200**

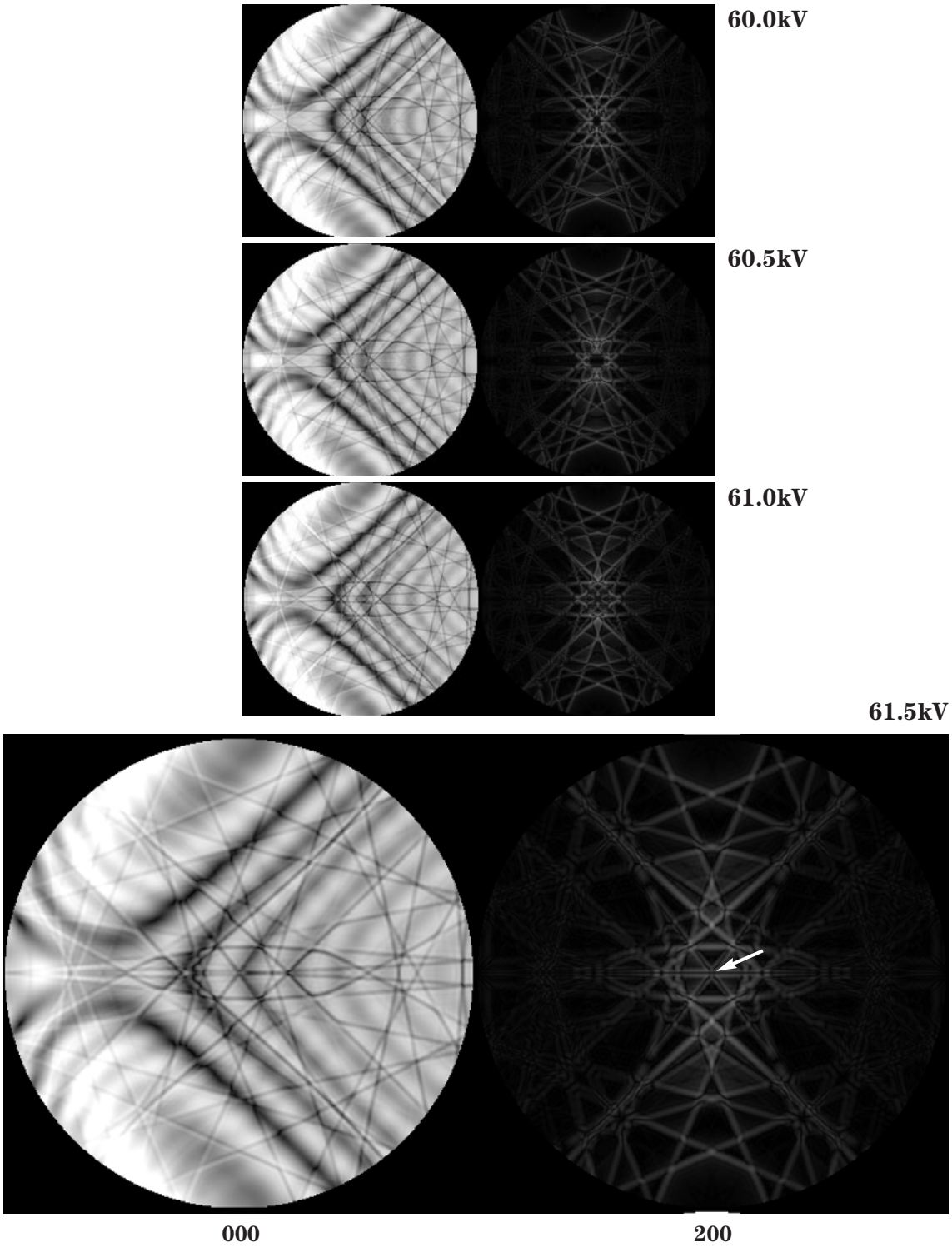

Changes of the features of the dynamical extinction due to the *d*-glide plane parallel to the Si (001) plane with the accelerating voltage.

Attraction

K. Saitoh

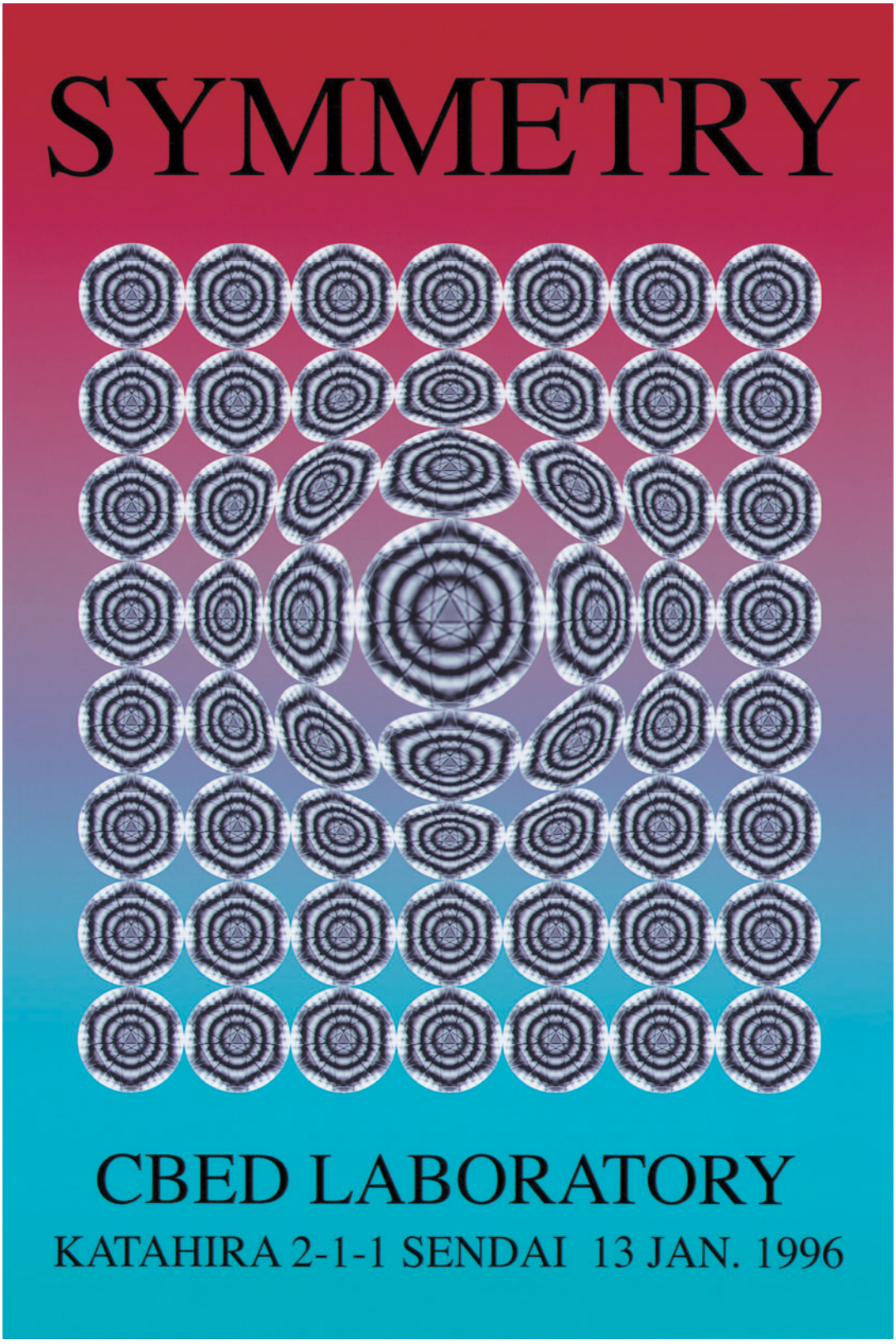

K. Tanaka and K. Saitoh

N. Kanda

S. Amamiya and K. Tsuda


MAGRITTE CBED
LA GRANDE FAMILLE
Tanaka Lab. RISM. Tohoku Univ.

K. Saitoh

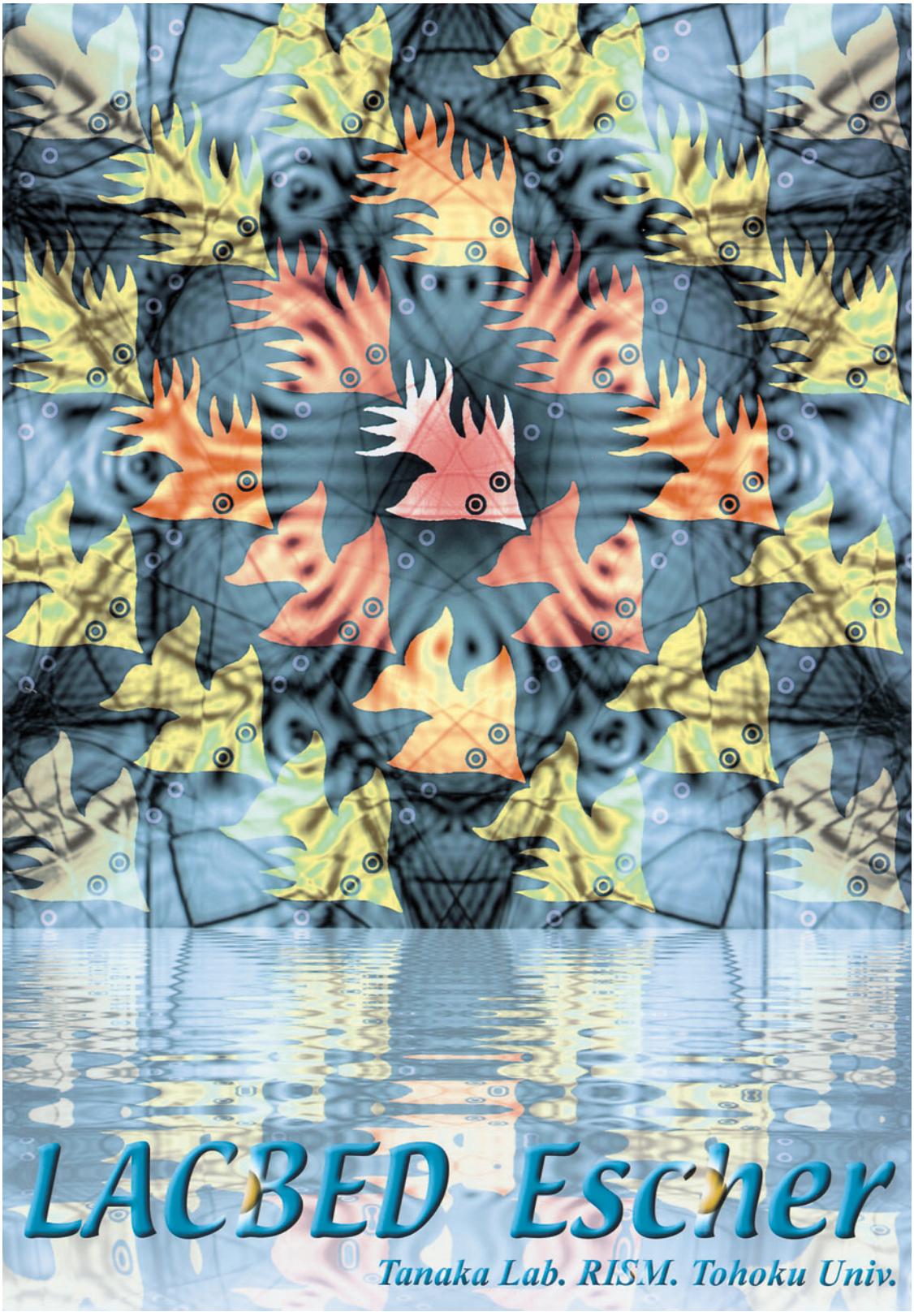

K. Omoto

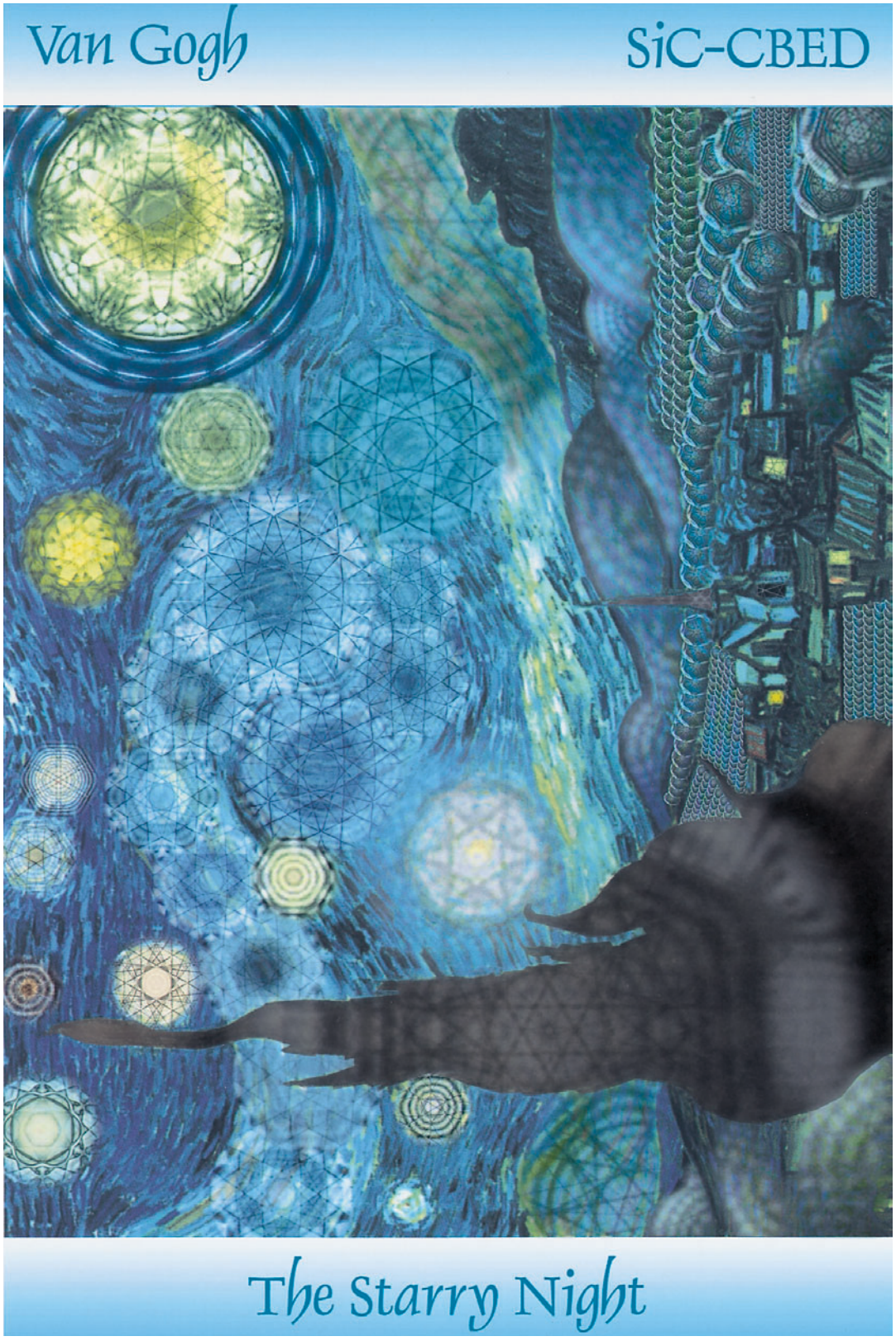

U. Kaiser, T. Yokosawa and K. Saitoh

S. Amamiya

"Looking back beauty" (Moronobu Hishikawa) K.Saitoh

“Beauty under blossoms” (Toyonobu Ishikawa) K.Saitoh

T. Yokosawa K. Shibata K. Saitoh K. Tsuda M. Tanaka M. Terauchi F. Sato K. Omoto

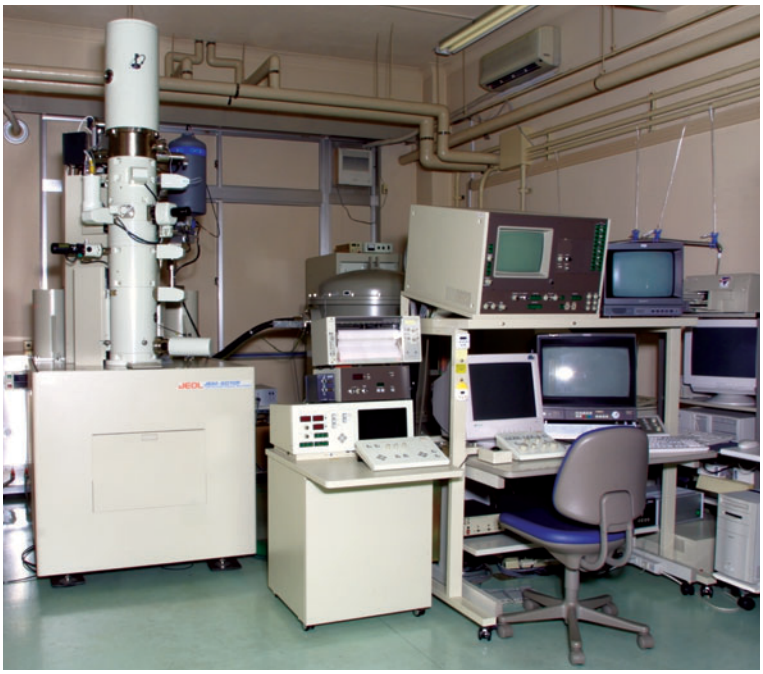

JEM-2010FEF